U.PORTO

FEUP FACULDADE DE ENGENHARIA
UNIVERSIDADE DO PORTO

Machine Learning Methodologies in the Development of Accurate Modeling Applied to Stamping of Advanced High Strength Steels

---

Author:

Daniel Jácome da Cruz

Supervisor:

Manuel Romano Barbosa

Co-supervisors:

Abel Dias dos Santos

José César de Sá

Doctoral Program in Mechanical Engineering (PRODEM)

Faculty of Engineering of the University of Porto

January 14, 2026

© **Daniel Jácome da Cruz**
Departamento de Engenharia Mecânica
Faculdade de Engenharia da Universidade do Porto

Rua Dr. Roberto Frias, s/n
4200-465 Porto
Portugal

Abstract

The increasing use of Advanced High-Strength Steels (AHSS) in the automotive industry presents significant challenges for sheet metal forming processes, especially in predicting strain distributions, formability and springback of stamping components through finite element simulations. Although advanced phenomenological constitutive models can address some of these challenges, they often require the calibration of numerous empirical parameters, making the process costly and time-consuming. In this context, Machine Learning (ML) offers a powerful alternative for parameter identification and for the development of fully data-driven constitutive surrogate models. This thesis explores the potential of ML techniques to constitutive modeling of AHSS, aiming to enhance both the accuracy and efficiency of stamping simulations.

Initially, a comprehensive experimental program was conducted to characterize the mechanical behavior of three dual-phase steels (DP500, DP600 and DP780) using both standardized and novel tests. A miniaturized specimen device was developed for monotonic and reverse tests (tensile/compressive and shear) and a reverse bending setup was developed for characterizing the cyclic behavior of materials. Together with full-field digital image correlation, these tests provided a robust dataset for the evaluation of anisotropy, the Bauschinger effect and elastic modulus degradation of the selected AHSS.

In a second stage, ML models were applied to constitutive parameter identification. Long Short-Term Memory (LSTM) networks trained on bending and reverse bending data successfully identified isotropic and anisotropic hardening parameters demonstrating, once trained, greater efficiency than traditional optimization methods. The isotropic hardening parameters were predicted with mean relative errors between 0.7-1.5% and more than 90% of the predictions presented relative errors below 4%, with only 6–9% of the cases classified as outliers. In contrast, the kinematic parameters exhibited higher variability, with mean relative errors of about 7% and the majority of cases having relative errors below 10%. Approximately 11%

of the predictions were identified as outliers and in some cases the network produced non-physically supported results. Incorporating physical constraints into the loss function reduced predictions that were clearly incompatible with the considered constitutive model, in particular negative values of the kinematic parameters. Moreover, transfer learning approaches, in which pre-trained models are reused and fine-tuned with new data, further improved the adaptability of the model to variations in test conditions while reducing training time by up to 80%.

Beyond parameter identification, this work also explores the development of fully data-driven constitutive models capable of directly learning the stress–strain response without relying on predefined constitutive equations. Recurrent neural networks, specifically Linearized Minimal State Cells (LMSCs), were trained to directly approximate the stress–strain response of DP780 under monotonic, reverse and multiaxial loading paths. Using synthetic datasets, the optimized LMSC achieved mean squared errors of 10^{-3}, when evaluated on normalized stress data, accurately capturing anisotropy evolution and Bauschinger effects. In particular, the network was able to surrogate the anisotropic behavior described by the Yld2000-2d yield function and the hardening behavior represented by the Homogeneous Anisotropic Hardening (HAH) model. Offline evaluation against FE-generated strain paths, including benchmark forming cases, demonstrated strong self-consistency across static and dynamic schemes, confirming the potential for integration into UMAT/VUMAT subroutines of Abaqus FE code. While challenges remain, concerning data availability and generalization, this work pave the way for future integration of ML-based constitutive models into finite element simulations and their application to industrial sheet metal forming processes.

Keywords: Sheet metal forming; Advanced High-Strength Steels (AHSS); Constitutive modeling; Machine Learning (ML); Data-driven models; Recurrent Neural Networks (RNNs); Long Short-Term Memory (LSTM); Linearized Minimal State Cells (LMSCs).

Resumo

O uso crescente de aços avançados de alta resistência (AHSS) na indústria automóvel apresenta desafios significativos para os processos de conformação de chapas metálicas, especialmente na previsão de distribuições de deformação, conformabilidade e retorno elástico de componentes estampados, com base na simulação pelo método dos elementos finitos. Embora modelos constitutivos fenomenológicos avançados possam resolver alguns desses desafios, eles geralmente exigem a calibração de vários parâmetros empíricos, tornando o processo caro e demorado. Neste contexto, *Machine Learning* (ML) oferece uma alternativa poderosa para a identificação de parâmetros e para o desenvolvimento de modelos constitutivos de substituição totalmente baseados em dados. Esta tese explora o potencial das técnicas de ML para a modelação constitutiva de AHSS, com o objetivo de melhorar a precisão e a eficiência das simulações de estampagem.

Inicialmente, foi realizado um programa experimental abrangente para caracterizar o comportamento mecânico de três aços bifásicos (DP500, DP600 e DP780) utilizando testes padronizados e inovadores. Foi desenvolvido um dispositivo de amostra miniaturizado para testes monotónicos e com inversão (tração/compressão e corte) e uma configuração de flexão reversa para caracterização do comportamento cíclico dos materiais. Juntamente com técnicas de correlação digital de imagem, estes testes forneceram um conjunto de dados robusto para a avaliação da anisotropia, do efeito Bauschinger e da degradação do módulo de elasticidade dos AHSS selecionados.

Numa segunda etapa, os modelos de ML foram aplicados à identificação de parâmetros constitutivos. Redes *Long Short-Term Memory* (LSTM), treinadas com dados de ensaios de flexão, identificaram com sucesso os parâmetros de encruamento isotrópico e anisotrópico, demonstrando maior eficiência do que os métodos tradicionais de otimização. Os parâmetros de encruamento isotrópico foram preditos com erros relativos médios entre 0,7–1,5%, sendo que mais de 90% das previsões apresentaram erros relativos inferiores a 4%, com apenas 6–9% dos casos classificados como

outliers. Em contraste, os parâmetros cinemáticos exibiram maior variabilidade, com erros relativos médios de cerca de 7% e a maioria dos casos com erros abaixo de 10%. Aproximadamente 11% das previsões foram identificadas como *outliers* e, em alguns casos, a rede produziu resultados sem suporte físico. A incorporação de restrições físicas na função de perda reduziu previsões claramente incompatíveis com o modelo constitutivo considerado, em particular valores negativos dos parâmetros cinemáticos. Além disso, as abordagens de *transfer learning*, nas quais modelos pré-treinados são reutilizados e ajustados com novos dados, melhoraram ainda mais a adaptabilidade do modelo a variações nas condições de ensaio, reduzindo simultaneamente o tempo de treino em até 80%.

Para além da identificação de parâmetros, este trabalho explora o desenvolvimento de modelos constitutivos totalmente *data-driven*, capazes de aprender diretamente a resposta em extensão sem recorrer a equações constitutivas pré-definidas. Redes neuronais recorrentes, especificamente as *Linearized Minimal State Cells* (LMSCs), foram treinadas para aproximar diretamente a resposta tensão–extensão do aço DP780 sob trajetórias de carregamento monotónicas, reversas e multiaxiais. Utilizando *datasets* sintéticos, a LMSC otimizada alcançou erros quadráticos médios da ordem de 10^{-3}, quando avaliada sobre dados de tensão normalizados, captando com precisão a evolução da anisotropia e os efeitos de Bauschinger. Em particular, a rede foi capaz de reproduzir o comportamento anisotrópico descrito pela função de escoamento Yld2000-2d e o comportamento de encruamento representado pelo modelo de *Homogeneous Anisotropic Hardening* (HAH). A avaliação *offline* em trajetórias de deformação geradas por elementos finitos, incluindo casos de estampagem de referência, demonstrou forte auto-consistência em regimes estáticos e dinâmicos, confirmando o potencial de integração em sub-rotinas UMAT/VUMAT do código de elementos finitos Abaqus. Apesar de persistirem desafios, relacionados com a disponibilidade e generalização dos dados, este trabalho abre caminho para a futura integração de modelos constitutivos baseados em *Machine Learning* em simulações por elementos finitos e a sua aplicação em processos industriais de estampagem de chapas metálicas.

Palavras-chave: Estampagem de chapas metálicas; Aços Avançados de Alta Resistência (AHSS); Modelação constitutiva; *Machine Learning* (ML); Modelos baseados em dados; Redes Neuronais Recorrentes (RNNs); *Long Short-Term Memory* (LSTM); *Linearized Minimal State Cells* (LMSCs).

Acknowledgments

I would like to express my sincere gratitude to Professor Doctor Manuel Romano Barbosa, my supervisor, for his guidance, support and encouragement throughout the course of this thesis. His expertise, patience and availability were fundamental to the successful completion of this work. My deepest appreciation also goes to my co-supervisors, Professor Doctor Abel Dias dos Santos and Professor Doctor José Manuel de Almeida César de Sá. Their valuable advice, critical insight and continuous support were indispensable for the coherence and consistency of this research.

I would like to thank INEGI (Institute of Science and Innovation in Mechanical and Industrial Engineering) for providing the means and resources necessary for the development of this work. The access to INEGI's scientific and technological infrastructure was crucial to the extensive experimental work that forms the basis of this thesis. My gratitude also extends to my colleagues from UTAF (Advanced Manufacturing Processes Unit), whose collaboration, friendship and support greatly contributed to the development of this research. I am also indebted to Doctor Rui Amaral, for his companionship and valuable contributions during this journey.

A heartfelt thanks to my family, for their unconditional support, patience and encouragement and to Catarina, for her understanding and constant presence, which gave me the strength to persevere.

Finally, I gratefully acknowledge the financial support of the Portuguese Foundation for Science and Technology (FCT) through the Doctoral grant 2022.12657.BD, awarded under the POCH program and co-funded by the European Social Fund (FSE) and Portuguese national funds from MCTES.



Declaration on the Use of AI Tools

During the preparation of this thesis, the author used *ChatGPT-4.0* exclusively for language polishing. All content suggested by the tool was carefully reviewed, edited and validated by the author, who assumes full responsibility for the final version of this work.

Contents

Abstract i

Resumo iii

Acknowledgments v

List of Figures xxviii

List of Tables xxxi

List of Acronyms xxxiii

List of Symbols xxxv

List of Publications xxxvii

1 Introduction 1

1.1 Objectives 4

1.2 Outline of the thesis 5

2 Machine Learning Approaches in Constitutive Modeling 7

2.1 Machine Learning based on Artificial Neural Networks 9

2.1.1 Feedforward Neural Networks 11

2.1.2 Convolutional Neural Networks 13

2.1.3 Recurrent Neural Networks 15

2.1.4 Physics-Guided Neural Network Strategies 18

2.1.5 Implementation Considerations in Machine Learning 21

2.2 Phenomenological Models 25

2.2.1 Plasticity Yield Surface Models 27

2.2.1.1 Yield Criteria for Isotropic Materials 27

2.2.1.2 Yield Criteria for Anisotropic Materials 28

2.2.2 Hardening . . . 32
2.2.2.1 Isotropic Hardening . . . 33
2.2.2.2 Anisotropic Hardening . . . 34
2.3 Applications of Artificial Neural Networks in Constitutive Modeling . 43
2.3.1 Parameter Identification Inverse Modeling . . . 44
2.3.2 Data-Driven Material Modeling . . . 49
2.3.2.1 Data-Driven ANN Models from Experimental Data . 51
2.3.2.2 Data-Driven Surrogate ANN Models from Synthetic Numerical Data . . . 52

3 Experimental Work for Material Characterization 63
3.1 Overview of Homogeneous Mechanical Tests . . . 67
3.1.1 Monotonic Loading Tests . . . 67
3.1.2 Reverse Loading Tests . . . 67
3.2 Materials . . . 70
3.3 Experimental Results for Monotonic Loading Tests . . . 71
3.3.1 Uniaxial Tension and Compression Tests . . . 72
3.3.1.1 Uniaxial Tensile Results - Macro Samples . . . 73
3.3.1.2 Development of an Uniaxial Test Equipment for Miniaturized Specimens . . . 76
3.3.1.3 Uniaxial Tension Results - Miniaturized Samples . . 84
3.3.1.4 Uniaxial Compression Results - Miniaturized Samples 85
3.3.2 Shear Test . . . 87
3.3.3 Hydraulic Bulge Test . . . 91
3.3.4 Stacked Disc Compression Test . . . 93
3.3.5 Three-Point Bending Test . . . 95
3.4 Experimental Results for Reverse Loading Tests . . . 96
3.4.1 Tension-Compression Tests . . . 97
3.4.2 Reverse Shear Tests . . . 100
3.4.3 Reverse Bending Tests . . . 102
3.4.3.1 Development of an Reverse Bending Equipment . . 102
3.4.3.2 Experimental Test Conditions . . . 105
3.4.3.3 Reverse Bending Results . . . 107
3.5 Experimental Analysis of Elastic Modulus Degradation . . . 109
3.6 Concluding Remarks . . . 112

4 Identification of Material Constitutive Parameters using Machine Learning 115
4.1 Identification of Material Parameters using Conventional Methods and Tension-Compression Tests . . . 117
4.1.1 Material Parameters for Anisotropic Yield Functions . . . 117
4.1.2 Material Parameters for Hardening Models . . . 121
4.1.2.1 Isotropic Hardening . . . 121
4.1.2.2 Anisotropic Hardening . . . 122
4.2 Identification of Isotropic Hardening Parameters using Machine Learning and a Three-Point Bending Test . . . 124
4.2.1 Methodology . . . 125
4.2.1.1 FE Model - Three-Point Bending Test . . . 127
4.2.1.2 Sensitivity Analysis for Key Variables . . . 129
4.2.1.3 Dataset Generation . . . 137
4.2.2 Neural Network Implementation: ML Model — Plasticity . . . 140
4.2.2.1 Feedforward Neural Networks . . . 141
4.2.2.2 Recurrent Neural Networks . . . 145
4.2.3 Neural Network Implementation: ML Model — Elasticity . . . 151
4.2.4 Results and Validation of Developed ML models . . . 153
4.2.4.1 ML Model — Elasticity . . . 153
4.2.4.2 ML Model — Plasticity . . . 154
4.2.4.3 Results for Materials with Thickness Variations . . . 159
4.2.4.4 Experimental Validation . . . 161
4.3 Identification of Isotropic and Anisotropic Hardening Parameters using Machine Learning and a Reverse Bending Test . . . 164
4.3.1 Methodology . . . 165
4.3.1.1 FE Model - Reverse Bending Test . . . 165
4.3.1.2 Dataset Generation . . . 168
4.3.2 Neural Network Implementation: Isotropic Parameters . . . 173
4.3.2.1 Results . . . 177
4.3.2.2 Transfer Learning Approach for different Test Conditions . . . 179
4.3.3 Neural Network Implementation: Anisotropic Parameters . . . 183
4.3.3.1 Results . . . 189
4.3.3.2 Penalty in Loss Function based on Kinematic Parameters Analysis . . . 194
4.4 Final Remarks . . . 204

5 Data Driven Constitutive Modeling **209**
5.1 Linearized Minimal State Cells (LMSCs) . . . 210
5.2 Data Generation . . . 213
5.2.1 Random Walks . . . 214
5.2.2 Smooth Walks . . . 217
5.2.3 Dataset Division . . . 220
5.3 Training Methodology . . . 221
5.3.1 Training Strategy . . . 221
5.3.2 Models Performance . . . 222
5.4 Results . . . 228
5.4.1 Evaluation on Standard Experimental Loading Paths . . . 232
5.4.1.1 Monotonic Loading Cases . . . 232
5.4.1.2 Reverse Loading Cases . . . 234
5.4.2 Evaluation on FEA-Based Strain Histories . . . 239
5.4.2.1 Tensile Test . . . 241
5.4.2.2 Reverse Bending Test . . . 246
5.4.2.3 Cylindrical Cup Forming . . . 249
5.4.2.4 3DS Benchmark – Rail Forming . . . 255
5.5 Discussion and Final Remarks . . . 259

6 Conclusions **263**
6.1 Future Work . . . 265

References **267**

A Classical Monotonic Tests for Material Mechanical Characterization **313**
A.1 Uniaxial Tensile Test . . . 313
A.2 Hydraulic Bulge Test . . . 314
A.3 Stacked Disc Compression Test . . . 317
A.4 In-Plane Compression Test . . . 318
A.5 Shear Test . . . 321
A.6 Three-Point Bending Test . . . 323

B Article: *"Application of Digital Image Processing Techniques to Detect Through-Thickness Crack in Hole Expansion Test"* **327**

C R^2 Analysis for the Prediction of Hardening Parameters **343**

D Evaluation Cases for Standard Experimental Loading Paths **345**

E Training and Validation Loss Curves for Random-Walk and Smooth-Walk Models **349**

F Evaluation on FEA-Based Deformation Histories: Cylindrical Cup Forming **351**

F.1 Results - Static/Implicit 351

F.2 Strain Paths - Dynamic/Explicit 352

F.3 Results - Dynamic/Explicit 353

G Article: *"Application of Recurrent Neural Networks in Uncertainty Analysis of Sheet Metal Forming"* **355**

List of Figures

1.1 Schematic illustration representing the different loadings states presented in a typical deep drawing process. 2

2.1 Representation of (a) the hierarchical relationship between Artificial Intelligence (AI), Machine Learning (ML) and Deep Learning (DL) [45]; and (b) the main types of ML models; adapted from [46]. . 10

2.2 Example of a feedforward neural network, with m input nodes, several hidden layers with specific numbers of processing elements (PE) each implementing a nonlinear function (i.e., sigmoid), n output nodes implementing a linear function and interconnections weights (i.e., W_{kn} and W_{mr}). 12

2.3 Network structure of a convolutional neural network (CNN). 14

2.4 Network structure of a (a) feed-forward neural network (FNN) and (b) recurrent neural network (RNN). 15

2.5 Network structure of an LSTM: $\boldsymbol{x}_t$ represents the input, $\boldsymbol{h}_t$ the hidden state and $\boldsymbol{c}_t$ the cell state. 17

2.6 Illustration of two physics-guided neural network formulations: (a) hybrid physics–data (HPD) model; (b) residual model. White boxes represent physics-based models, black boxes represent ML models. . . 19

2.7 The framework of the physics-informed neural networks (PINNs) for a viscous Burgers' equation. 21

2.8 Supervised learning workflow. 22

2.9 Visual comparison of sampling strategies (Grid, Random, Latin Hypercube and Sobol), showing decreasing discrepancy. 23

2.10 Representation of stress and plastic strain increment direction applied to the von Mises yield surface. 25

2.11 Graphical representation of the Tresca and von Mises yield criteria in (a) the principal stress space and (b) $\sigma_3 = 0$ plane. 29

2.12 Schematic representation of (a) tensile specimen produced at the angle θ (measured from the RD) and (b) relationship between the yield stress and the direction of loading in the plane of the sheet metal. . . 29
2.13 Evolution of the yield surface in the σ_1 -σ_2 plane and the correspondent Stress-Strain (σ_1-ε_1) behavior considering both isotropic and kinematic hardening models. 34
2.14 Schematic illustration of stress-strain response during forward and reverse deformation. 36
2.15 Evolution of the yield surface according to the type of hardening: (a) kinematic hardening and (b) distortional hardening; adapted from [102]. 37
2.16 Schematic illustration of Yoshida–Uemori model. 39
2.17 Schematic representation of (a) the direct problem, where numerical data is generated using finite element simulations based on known material parameters and (b) the inverse problem, where a machine learning model is trained to infer material parameters from experimental data (e.g., DIC-based displacement and strain fields). 46
2.18 Sources of training data for ANN-based constitutive modeling. 50
2.19 Schematic representation of modeling strategies in constitutive mechanics based on their interpretability and data requirements; adapted from [15]. 59

3.1 Mechanical tests for material characterization: (a) examples of monotonic homogeneous tests along with the corresponding stress states in the principal axes (σ_1–σ_2); (b) examples of specimen geometries used in heterogeneous mechanical tests [193; 194; 197]. 64
3.2 Different reverse loading tests: (a) tension-compression test; (b) reverse shear test; (c) reverse bending test. 68
3.3 Bending-reverse bending test setup proposed by Omersphahic et al [216]. 69
3.4 Initial microstructure obtained from SEM of the dual-phase steels. A - hard martensite phase; B - soft ferrite phase. 70
3.5 Experimental engineering stress-strain curves (left) and true stress-strain curves (right) considering different loading directions for DP500 (a-b), DP600 (c-d) and DP780 (e-f). 74

3.6 Evolution of transverse (ε_{22}) and thickness (ε_{33}) plastic strains considering different angles relative to the rolling direction for (a) DP500, (c) DP600 and (e) DP780 and corresponding anisotropic coefficients (r-values) and normalized stress values (σ_y) for (b) DP500, (d) DP600 and (f) DP780. 75
3.7 Miniaturized Specimen Tester Device: (a) MSTD setup and (b) geometry of the miniaturized specimen. 76
3.8 Points of reference used in evaluating the reconstruction of the ε_{xx} strain signal with regard to the DIC settings and as a function of the VSG for both: (a) tension and (b) compression tests. 80
3.9 Evaluation of ε_{xx} for point A, B and C (Figure 3.8) as a function of DIC parameters expressed with regard to Virtual Strain Gauge (VSG) for both tension and compression tests, at two stages of deformation corresponding to low and high strains. 81
3.10 Evaluation of ε_{xx} at point B (Figure 3.8) as a function of DIC parameters expressed with regard to Virtual Strain Gauge (VSG). 83
3.11 Evaluation of ε_{xx} as a function of the coordinate x for several Virtual Strain Gauge (VSG) values for both tension and compression tests. . 83
3.12 Experimental curves obtained with macro specimens (dotted) and mini specimens (continuous lines) (a) engineering stress-strain and (b) true stress-strain curves for DP500, DP600 and DP780 materials. 84
3.13 Miniaturized monotonic uniaxial compression test for (a) DP500, (b) DP600 and (c) DP780. 86
3.14 Representation of the point where buckling occurs in the uniaxial compression test. 86
3.15 Illustration of the (a) Miniaturized Specimen Tester Device and (b) modified shear specimen. 87
3.16 Schematic representation of (a) longitudinal (A-B) and transverse (C-D) sections used to analyze the homogeneity of strain distribution; shear strain distributions for different values of deformation at point P: (b) $\varepsilon_{xy} = 0.1$, (c) $\varepsilon_{xy} = 0.2$ and (d) $\varepsilon_{xy} = 0.3$. 88
3.17 Strain distributions (ε_{xy}, ε_{xx} and ε_{yy}) for DP500 material, considering the longitudinal section (a, c, e) and transverse section (b, d, f) at three different deformation levels. 90

3.18 Experimental (a) monotonic shear curves (τ_{xy}-ε_{xy}) for the selected materials (DP500, DP600 and DP780) and (b) corresponding strain path evolution ($\varepsilon_{22}/\varepsilon_{11}$) during the test at the center point of the shear zone. 91
3.19 Experimental (a) biaxial stress-strain curves and (b) hydraulic pressure-height profiles obtained for the selected dual-phase steels (DP500, DP600 and DP780). 92
3.20 Equivalent stress-strain curves for the selected materials obtained using biaxial bulge data combined with tensile test results. 93
3.21 Longitudinal (ε_{11}) and transverse (ε_{22}) strain from axial compression of stacked discs for (a) DP500, (b) DP600, (c) DP780; (d) biaxial r_b anisotropy. 94
3.22 Influence of friction conditions (dry and abundant lubrication) on the experimental three-point bending test results. 96
3.23 Reverse-loading experimental stress-strain curves of tension-compression test for (a-b) DP500, (c-d) DP600, (e-f) DP780. 98
3.24 (a) Yield stress, σ_Y and (b) Bauschinger Ratio, β , values for different pre-strains, ε_p^*. 99
3.25 Reverse-loading shear stress-strain curves for: (a) DP500, (b) DP600 and (c) DP780. 100
3.26 Shear device: (a) setup on a universal tensile test machine; (b) geometry of the single gauge area specimen [262]. 101
3.27 Comparison of reverse shear curves for the DP600 material using the modified ASTM B831-05 shear specimen (blue - Figure 3.15b.) and the single gauge area specimen (grey - Figure 3.26). 102
3.28 Boundary conditions of (a) the full contact model based on Zhou and Lee [263] and (b–d) equivalent non-contact models that preserve bending moments at Point A. 103
3.29 Representation of (a) the reverse bending setup and (b) the corresponding schematic illustrating the clamped end, roller spacing (b), loading distance (L) and applied force (F). 104
3.30 Overview of the reverse bending test, showing the sequential application of displacements d_1, d_2 and d_3 and the resulting springback angles α_1, α_2 and α_3 of the sheet material. 105

3.31 Images captured during the reverse bending test for the DP500 material, at the end of (a-b) step 1, (c-d) step 2 and (e-f) step 3. The left image shows the specimen before elastic recovery, while the right image depicts the specimen after elastic recover. 106
3.32 Reverse bending test results for (a-b) DP500, (c-d) DP600 and (e-f) DP780; the first column shows the punch force-displacement curves for the three test steps and the second column presents the evolution of the bending angle before (BSP) and after springback (ASP) and the corresponding springback angle (α) for each step. 108
3.33 Representation of (a) elastic moduli under uniaxial tensile loading and (b) the influence of ξ on Young's modulus degradation with plastic strain, based on the Yoshida-Uemori model [113]. 109
3.34 Elastic modulus degradation analysis for DP500, DP600 and DP780: (left) true stress–strain curves from miniaturized tensile specimens and (right) evolution of the elastic modulus as a function of plastic strain for each material. 111

4.1 Predicted yield surfaces of Hill'48 and Yld2000-2d models for (a) DP500, (b) DP600 and (c) DP780 steel. 119
4.2 Predicted normalized yield stresses and r-values of Hill'48 and Yld2000-2d models for (a-b) DP500, (c-d) DP600 and (e-f) DP780. 120
4.3 Comparison between the experimental stress-strain curves and Swift hardening curves for the different dual-phase steels. 121
4.4 Comparison of experimental stress-strain curves with calculated results using the IKH and HAH anisotropic hardening models for (a-b) DP500, (c-d) DP600 and (e-f) DP780. 124
4.5 Schematic illustration of the three-point bending test and definition of the main problem objectives. 125
4.6 Overview of the proposed methodology combining machine learning and bending tests for material parameter identification. 126
4.7 Three-point bending test geometry and variables defined. 128
4.8 Three-point bending force–displacement curves (F_p-y_p) for the selected dual-phase steels (DP500, DP600, DP780) obtained by FEA, with comparison to experimental results. 128

4.9 Representation of (a) the effect of Young's modulus variations on DP500 and DP780 three-point bending curves and (b) the corresponding analytical estimation of Young's modulus using Equation 4.3. . . 130
4.10 Influence of the Swift hardening law parameters on (left) the force –displacement response in the three-point bending test and (right) the corresponding Swift hardening curves: (a, b) parameter K, (c, d) parameter ε_0 and (e, f) parameter n; the reference combination is $K = 1000$ MPa, $\varepsilon_0 = 0.001$ and $n = 0.2$. 132
4.11 Distribution of (a) stress and (b) equivalent plastic strain (PEEQ) through the thickness of the material for the reference Swift hardening parameters ($K = 1000$ MPa, $\varepsilon_0 = 0.001$, $n = 0.2$) during a three-point bending test with a punch displacement of $y_p = 7$ mm. 133
4.12 Influence of material thickness in three-point bending curves in the case of DP600: (a) original punch force–displacement curves ($F_p - y_p$); (b) corrected punch force–displacement curves ($F_p^* - y_p$). 134
4.13 Stress distribution on a normal section in bending, considering a strain-hardening material. 134
4.14 Influence of the friction coefficient, μ, on the force–displacement curves of the three-point bending for (a) DP500, (b) DP600 and (c) DP780; 136
4.15 Flowchart illustrating the proposed methodology for predicting elastic and plastic parameters of sheet metal materials using experimental three-point bending test curves and neural networks. 138
4.16 Combinations of Swift hardening parameters (K, n, ε_0) selected to generate the dataset for training the *ML Model — Plasticity* consist of 13 values for the K variable ranging between 400 and 1600 MPa with increments of 100 MPa, 7 values for the n variable ranging between 0.05 and 0.35 with increments of 0.05 and 7 values for ε_0 {0.0001, 0.0005, 0.001, 0.0025, 0.005, 0.0075, 0.01}. 139
4.17 Distribution of cases in (a) training dataset (shades of grey), (b) validation dataset (shades of black) and (c) testing dataset (shades of red color), resulting from the random division of the complete dataset (637 cases). 140

4.18 Implementation of material characterization problem: (a) punch force-displacement curve and the selected five pairs of values (P1-P5); (b) structure of the neural network with ten processing elements in the input layer corresponding to the five pairs of punch force-displacement values and three nodes in the output layer (Swift parameters — K, ε_0 and n). 142
4.19 Coefficient of determination (R^2) for each dataset—training (gray), validation (black) and testing (red) across the variables K, ε_0 and n obtained considering FNNs. 145
4.20 Boxplots of relative error percentages for the variables K, ε_0 and n across the training, validation and test datasets, obtained considering FNNs; (Relative Error (%) = $(y_{\text{pred}} - y_{\text{true}})/y_{\text{true}} \times 100$). 146
4.21 Coefficient of determination (R^2) for each dataset - training (grey), validation (black) and testing (red) across the variables K, ε_0 and n obtained using recurrent neural networks. 148
4.22 Boxplots of relative error percentages for the variables K, ε_0 and n across the training, validation and test datasets, obtained considering RNNs; (Relative Error (%) = $(y_{\text{pred}} - y_{\text{true}})/y_{\text{true}} \times 100$). 149
4.23 Histograms of the relative errors for the three variables (K, n and ε_0) obtained using FNNs (left side) and LSTMs (right side);(Relative Error (%) = $(y_{\text{pred}} - y_{\text{true}})/y_{\text{true}} \times 100$). 150
4.24 Punch force–displacement curves for cases in the training (grey), validation (black) and testing (red) datasets, illustrating selected points for ML development within the $y_p = 0$ mm to $y_p = 2$ mm range. . . . 151
4.25 Training and performance evaluation figures illustrating (a) the convergence of error curves and (b) coefficient of determination (R^2) in the training, validation and testing datasets. 152
4.26 Three-point bending punch force–displacement curves obtained by FEA for virtual materials *VM1*, *VM2* and *VM3* with Young's modulus (E) values of 75, 215 and 225 GPa, respectively. 154
4.27 Schematic representation of the comparison between the target (circles) and the prediction (blue stars) for (a) the training dataset (grey color), (b) the validation dataset (black color) and (c) the testing dataset (red color). 155

4.28 Comparison of predicted (dashed/dotted line) and expected (solid line) true stress–strain curves ($\sigma - \varepsilon_p$) for cases W_K, W_{ε_0} and W_n for the training (a), validation (b) and testing (c) datasets and respective true stress errors, $\Delta\sigma$, for the training (d), validation (e) and testing (f) datasets; $Best|_{Train}$, $Best|_{Valid}$ and $Best|_{Test}$ $Best|_{Train}$ are examples of cases with an accurate prediction result. 156
4.29 Representation of (a) histogram of maximum absolute stress errors $|\Delta\sigma|_{max}$ and (b) respective quartile analysis. 157
4.30 Influence of material thickness for *VM4* and *VM5* on (a) punch force–displacement curve, (b) corrected punch displacement curve, (c) true stress–strain curves predicted by the trained LSTM and (d) stress error. 160
4.31 Influence of Swift hardening parameters obtained based on the experimental tensile test and three-point bending Test on (a) true stress–strain curves and (b) respective stress error, $\Delta\sigma$, analysis for DP500 dual-phase steel. 163
4.32 Influence of Swift hardening parameters obtained based on experimental tensile test and three-point bending test on (a) true stress–strain curves and (b) respective stress error, $\Delta\sigma$, analysis for DP600 dual-phase steel. 163
4.33 Influence of Swift hardening parameters obtained based on experimental tensile test and three-point bending test on (a) true stress–strain curves and (b) respective stress error, $\Delta\sigma$, analysis for DP780 dual-phase steel. 164
4.34 Schematic representation of the methodology for identifying hardening parameters using reverse bending tests. 165
4.35 Schematic representation of the finite element model used for the reverse bending test. 166
4.36 Comparison between experimental and numerical force-displacement curves for DP500, DP600 and DP780 steels; the left subfigures illustrate the results using a pure isotropic hardening (IH) model, while the right subfigures show the results with a combined isotropic-kinematic hardening (IKH) model. 167
4.37 Comparison of experimental and numerical springback angles α_1, α_2 and α_3 for (a) DP500, (b) DP600 and (c) DP780 steels and (d) schematic definition of the springback angles (α_1, α_2 and α_3). 168

4.38 Parameter distributions for the *RB - IsoDataset*; the diagonal subplots show histograms of individual parameters, while the off-diagonal subplots display scatter plots of parameter pairs. 169
4.39 Parameter distributions for the *RB - AnisoDataset*; the diagonal subplots show histograms of individual parameters, while the off-diagonal subplots show scatter plots of parameter pairs. 170
4.40 Example Punch Force Displacement (F_p-y_p) curves for (a) the *RB - IsoDataset* and (b) the *RB - AnisoDataset*. 171
4.41 Evolution of force and displacement during the test for cases A and B under the IKH model. 172
4.42 Evolution of (a) normal stress σ_{11} versus normal strain ε_{11} for cases A and B and (b) von Mises equivalent stress-strain behavior for the same cases at point (A). 173
4.43 Error curves for the training and validation datasets using the *RB - IsoDataset*: (a) pre-trained model and (b) model trained from scratch. 174
4.44 Combinations of the parameters K, ε_0 and n for three different values of n_{cases}: (a) 50, (b) 500 and (c) 5000. 175
4.45 Influence of n_{cases} on (a) MSE and (b) runtime, demonstrating how the amount of data used for fine-tuning influences model accuracy and computational efficiency. 176
4.46 Histograms of the relative errors for the three variables (K, n and ε_0) obtained considering 2000 and 5000 cases. 178
4.47 Analysis of stress prediction errors for the the pre-trained network considering (a) 2000 cases and (b) 5000 cases. 180
4.48 Evolution of the Mean Squared Error (MSE) over the epochs for different numbers of cases: (a) training dataset, (b) validation dataset, ... 181
4.49 Histograms of relative errors for (a) K, (b) ε_0 and (c) n using the model trained with $n_{\text{cases}} = 2000$ for $t = 1.2\,\text{mm}$. 182
4.50 Histogram of the maximum absolute stress error and corresponding quartile analysis of the maximum relative stress error for the ML model for materials with t=1.2 mm, trained with 2000 cases. 183
4.51 Dataset visualization with 5000 parameter combinations, divided into training (grey, 70%), validation (black, 15%) and testing (red, 15%) subsets. 185

4.52 Evolution of the Mean Squared Error (MSE) over the epochs for different numbers of Bi-LSTM units: (a) Training dataset, (b) Validation dataset, (c) Best validation loss and test loss for the different numbers of LSTM units. 186
4.53 Prediction results for the network with 40 Bi-LSTM units. The rows represent the training (top), validation (middle) and test (bottom) datasets, showing the alignment between predicted and true values for K, σ_0, n, C and γ, along with their R^2 values. 187
4.54 Histograms of (a) absolute and (b) relative errors across training (grey), validation (black) and test (red) datasets for variables K, σ_0, n, C and γ. 188
4.55 Correlation between true values and absolute relative errors on a logarithmic scale with error lines at 10% (black) and 100% (blue). 189
4.56 Boxplot representation of the Mean Squared Error (MSE) distribution for normalized output values across the Training, Validation, Test and Total datasets. 190
4.57 Schematic representation of uniaxial loading conditions applied to a single element, illustrating the three distinct stages: initial tension, compression and subsequent tension. 192
4.58 Tension-compression-tension (TCT) stress-strain (σ_{xx}-ε_{xx}) curves for three distinct cases: (a) Case Q2, (b) Case Q3 and (c) Case Max. . . 192
4.59 Tension-compression-tension (TCT) stress-strain (σ_{xx}-ε_{xx}) curves for three distinct cases: (a) Outlier A, (b) Outlier B and (c) Outlier C. . 194
4.60 Influence of the penalty parameter λ on (a) test mean squared error and (b) number of predicted negative values for C and γ. 197
4.61 Tension-compression-tension (TCT) stress-strain (σ_{xx}-ε_{xx}) curves for (a) Outlier D, (b) Outlier E and (c) Outlier F. 199
4.62 Comparison of (a) equivalent stress and (b) backstress evolution for Outliers G and H as a function of plastic strain (ε_p). 201
4.63 Tension-compression-tension (TCT) stress-strain (σ_{xx}-ε_{xx}) curves for (a) Outlier G, (b) Outlier H. 201
4.64 Error analysis for isotropic (σ) and kinematic (α) hardening components. (a) Maximum absolute error distribution for σ; (b) maximum absolute error for α; (c) boxplot of the maximum relative error (%). . 202

4.65 Comparison of the springback angles (α_1, α_2 and α_3) obtained from FEA using the hardening parameters identified from the TC and RB tests alongside the corresponding experimental values for (a) DP500 and (b) DP780. 204

5.1 Network structure of a Linearized Minimal State Cell (LMSC): $\Delta\boldsymbol{\varepsilon}_t$ represents the input, $\boldsymbol{\chi}_t$ the memory state and $\boldsymbol{\sigma}_t$ the output. 212
5.2 Random walk strain path generated by adding scaled noise to a piecewise-linear main path. 215
5.3 Stress and strain components over time for a single random walk simulation; (a,c,e): strain components ε_{xx}, ε_{yy}, ε_{xy}; (b,d,f): corresponding stress components σ_{xx}, σ_{yy}, σ_{xy}. 216
5.4 Processed input-output data used for model training. (a) strain history; (b) raw stress outputs; (c) strain increments $\Delta\varepsilon$; (d) normalized stress outputs used for LMSC training. 217
5.5 Strain and stress components along a smooth path; left plots: ε_{xx}, ε_{yy}, ε_{xy}; right plots: σ_{xx}, σ_{yy}, σ_{xy}. 218
5.6 Smooth path data used for model training: (a) strain history, (b) stress response, (c) strain increments, (d) normalized outputs. 219
5.7 Comparison of strain path characteristics between random and smooth paths: (a) strain norm, (b) strain increment norm. 220
5.8 Test, validation and training MSE as a function of the total number of trainable parameters for different memory sizes n_s; left plots: random walks (RW); right plots: smooth walks (SW). 224
5.9 Test set MSE as a function of network depth d and width w, for memory sizes $n_s = 20$ (top) and $n_s = 40$ (bottom); left plots: random walks; right plots: smooth walks. 225
5.10 Distribution of absolute errors on the test dataset for selected LMSC architectures with $n_s = 20$ (top) and $n_s = 40$ (bottom); left plots: random walks; right plots: smooth walks. 227
5.11 Evolution of: (a) training and (b) validation loss across three independent training runs with different random seeds for the u40_d4_w100 model. 228
5.12 Distribution of absolute (top) and relative (bottom) errors for each stress component in the test set; left plots: random walks; right plot: smooth walks; 229

5.13 Boxplots of mean relative error per test sample for each stress component for (a) random walks and (b) smooth walks. 230
5.14 Comparison between predicted and true stress histories: (a, c) representative median-error cases for random walk (RW) and smooth walk (SW); (b, d) worst-case examples based on mean relative error for RW and SW. 232
5.15 Predicted vs. reference stress responses for standard monotonic loading cases: (a) uniaxial tension in the rolling direction (RD), (b) uniaxial tension in the transverse direction (TD), (c) biaxial tension and (d) simple shear. 233
5.16 Stress predictions for reverse loading scenarios; left plots: TC paths with strain reversal applied at different strain levels ($\varepsilon^*_{xx} = 0.025$, 0.05 and 0.075); right plots: RS paths with reversal applied at different strain levels ($\varepsilon^*_{xy} = 0.1$, 0.2 and 0.3). 235
5.17 Additional training examples for strain-path reversals: (a–b) noise-free random walk and its stress response; (c–d) uniaxial ε_{xx} trajectory and response. 236
5.18 Stress predictions for reverse loading scenarios using the retrained LMSC model; left plots: TC paths with strain reversal applied at different strain levels ($\varepsilon^*_{xx} = 0.025, 0.05$ and 0.075); right plots: RS paths with reversal applied at different shear strain levels ($\varepsilon^*_{xy} = 0.1, 0.2$ and 0.3). 237
5.19 Comparison between predicted and reference stress–strain curves for reverse loading paths using the retrained model: (a) TC paths at reversal strains $\varepsilon^*_{xx} = 0.025$, 0.05 and 0.075; (b) RS paths at reversal strains $\varepsilon^*_{xy} = 0.1$, 0.2 and 0.3. 239
5.20 Comparison between UMAT and VUMAT implementations of the constitutive model under a tension-compression-tension (TCT) path. 240
5.21 Finite element mesh and contour plot of the equivalent stress distribution (`SDV2`) for the tensile test simulation. 241
5.22 Strain paths and corresponding increments extracted from the static/implicit tensile simulation: (a)–(b) IntPtA, (c)–(d) IntPtB. 242
5.23 Comparison between LMSC predictions ('Pred') and UMAT reference ('Real') at selected integration points in the static/implicit tensile test: (a) IntPtA; (b) IntPtB. 242

5.24 Strain evolution for IntPtA in the dynamic/explicit tensile simulation: (a) strain components and (b) corresponding incremental strain steps. 243
5.25 Comparison between VUMAT reference ('Real') and LMSC prediction ('Pred') at IntPtA in the dynamic explicit tensile test: (a) stress components versus increments; (b) σ_{xx} versus ε_{xx}. 244
5.26 Strain paths and corresponding increments for the (a-b) static and (c-d) dynamic tension-compression simulation. 245
5.27 Comparison between reference ('Real') and LMSC prediction ('Pred') for the tension–compression simulation: (a) static and (b) dynamic case. 245
5.28 Finite element model of the reverse bending test using 3D shell elements and the distribution of principal stress (S11) at the end of the (a) first step (bending) and (b) second loading step (unbending). . . . 246
5.29 Strain components ε_{xx}, ε_{yy}, ε_{xy} and their increments $\Delta\varepsilon$ during the reverse bending test: (a–b) correspond to top integration point (IntPtA) and (c–d) to bottom integration point (IntPtB). 247
5.30 Comparison between the LMSC-predicted ('Pred') and reference ('Real') stress components during the reverse bending test for: (a) top integration point (IntPtA) and (b) bottom integration point (IntPtB). . . 248
5.31 Comparison of LMSC-predicted ('Pred') and reference ('Real') stress–strain curves (σ_{xx} vs. ε_{xx}) for the reverse bending test for: top integration point (IntPtA) and (b) bottom integration point (IntPtB). 249
5.32 Cylindrical cup forming setup: (a) tooling geometry and main dimensions and (b) finite element mesh of the blank. 250
5.33 Equivalent stress distribution (`SDV2`) in the final formed cup, showing the selected integration points for analysis. 250
5.34 Strain components (ε_{xx}, ε_{yy} and ε_{xy}) and corresponding strain increments ($\Delta\varepsilon$) for the selected integration points during the cup forming static/implicit simulation: (a–b) IntPtA, (c–d) IntPtB and (e–f) IntPtC. 251
5.35 Comparison between LMSC-predicted ('Pred') and reference ('Real') stress components (σ_{xx}, σ_{yy} and σ_{xy}) at the selected integration points during the cup forming static/implicit simulation: (a) IntPtA, (b) IntPtB and (c) IntPtC. 252

5.36 Comparison of LMSC-predicted ('Pred') and reference ('Real') stress–strain evolution at IntPtB during cylindrical cup forming static/implicit simulation. 253
5.37 Comparison between LMSC-predicted ('Pred') and reference ('Real') stress components (σ_{xx}, σ_{yy} and σ_{xy}) at the selected integration points during the cup forming dynamic/explicit simulation: (a) IntPtA, (b) IntPtB and (c) IntPtC. 254
5.38 Comparison of LMSC-predicted ('Pred') and reference ('Real') stress–strain evolution at IntPtB during cylindrical cup forming dynamic/explicit simulation. 255
5.39 3DS 2D-Rail forming (a) geometry and (b) blank finite-element discretization used in the 3DS benchmark 256
5.40 Equivalent stress distribution (`SDV2`) in the final formed cup, showing the selected integration points for analysis. 256
5.41 Strain components (ε_{xx}, ε_{yy} and ε_{xy}) and corresponding strain increments ($\Delta\varepsilon$) for the selected integration points during the 3DS Rail Forming static/implicit simulation at IntPtA. 257
5.42 Comparison between (a) LMSC-predicted ('Pred') and reference ('Real') stress components (σ_{xx}, σ_{yy} and σ_{xy}) at IntPtA and (b) LMSC-predicted ('Pred') and reference ('Real') stress–strain evolution ($\sigma_{yy} - \varepsilon_{yy}$) at IntPtA points during the 3DS rail forming static/implicit simulation. 257
5.43 Strain components (ε_{xx}, ε_{yy} and ε_{xy}) and corresponding strain increments ($\Delta\varepsilon$) for the selected integration points during the 3DS rail forming dynamic/explicit simulation at IntPtA. 258
5.44 Comparison between (a) LMSC-predicted ('Pred') and reference ('Real') stress components (σ_{xx}, σ_{yy} and σ_{xy}) at IntPtA and (b) LMSC-predicted ('Pred') and reference ('Real') stress–strain evolution ($\sigma_{yy} - \varepsilon_{yy}$) at IntPtA points during the 3DS rail forming dynamic/explicit simulation. 259

A.1 Schematic representation of the hydraulic bulge test and its key variables. 315
A.2 Scheme of the mechanical measuring system constituted by an extensometer and a spherometer. 316

A.3 Stacked disk compression test: (a) specimen; (b) disk diameters before and after deformation. 318
A.4 Different methodologies presented in literature to perform in-plane compression tests. 320
A.5 Shear test specimen with a single gauge area. 321
A.6 Shear test specimens according to (a) Miyauchi and (b) ASTM B831-05. 322
A.7 Representation of torsional shear tests proposed by (a) Marciniak and (b) Brosius. 323
A.8 Schematic illustration of a (**a**) three-point bending test setup and the main variables: support span (V), support radius (Rm), specimen length (L), specimen width (W), specimen thickness (t) and punch radius (Rp); (**b**) example of a punch force–displacement (F_p - y_p) curve of a sheet metal material. 324

C.1 Prediction results for the network with 40 Bi-LSTM units. 344

D.1 Stress and strain evolution for uniaxial tension tests along the rolling (a–b) and transverse (c–d) directions; left: imposed strains ε_{xx}, ε_{yy}, ε_{xy}; right: resulting stresses σ_{xx}, σ_{yy}, σ_{xy}. 345
D.2 Monotonic biaxial tension (a,b) and monotonic shear (c,d). 346
D.3 Tension-compression paths showing reversal in loading direction (a–f). 347
D.4 Reverse shear tests with loading and unloading in ε_{xy}. 348

E.1 MSE convergence during progressive training for the LMSC model ($n_s = 40$, $d = 4$, $w = 100$) trained exclusively on (a) random-walk (RW) data and (b) smooth-walk (SW) data. 349

F.1 Comparison of predicted and reference stress–strain evolution at IntPtA during cylindrical cup forming static/implicit simulation. 351
F.2 Comparison of predicted and reference stress–strain evolution at IntPtC during cylindrical cup forming static/implicit simulation. 351
F.3 Strain components (ε_{xx}, ε_{yy} and ε_{xy}) and corresponding strain increments ($\Delta\varepsilon$) for the selected integration points during the cup forming dynamic/explicit simulation: (a–b) IntPtA, (c–d) IntPtB and (e–f) IntPtC. 352
F.4 Comparison of predicted and reference stress–strain evolution at IntPtA during cylindrical cup forming dynamic/explicit simulation. 353

F.5 Comparison of predicted and reference stress–strain evolution at IntPtC during cylindrical cup forming dynamic/explicit simulation. 353

List of Tables

3.1 Chemical composition of the dual-phase steels (DP500, DP600, DP780). 71
3.2 Thickness measurements (average, μ and standard deviation, σ) of DP500, DP600 and DP780 sheet metal samples. 71
3.3 Experimental conditions for macro and miniaturized samples. 72
3.4 Measured experimental anisotropy coefficients of dual-phase steels using DIC techniques. 73
3.5 Camera-lens optical system for the miniaturized tests. 79
3.6 Parameters used in the Performance Analysis Tool of MatchID 2D DIC. 80
3.7 DIC and strain settings selected in the full-field measurements. 82
3.8 Experimental conditions used in hydraulic bulge test. 91
3.9 Obtained properties from hydraulic bulge test for the different dual-phase steels. 92
3.10 Hydraulic bulge test results for dual-phase steels; k (Eq. A.12) is the proportionality factor between bulge and tensile tests. 93
3.11 Three-point bending test geometry, test conditions and sample geometry. 95
3.12 Parameters of the Yoshida-Uemori model (Equation 2.50) for dual-phase steels (DP500, DP600 and DP780). 112

4.1 Material parameter identification for Hill'48 yield criterion for DP500, DP600 and DP780. 118
4.2 Material parameter identification for Yld2000-2d yield criterion of DP500, DP600 and DP780 steels. 118
4.3 Identified parameters for the Swift hardening law based on experimental stress–strain data for dual-phase steels. 121
4.4 Identified parameters for the isotropic-kinematic hardening (IKH) model applied to dual-phase steels. 122

4.5 Identified parameters for the homogeneous anisotropic hardening (HAH) model applied to dual-phase steels. 123
4.6 Elastic properties and Swift law hardening parameters considered to develop the ML models. 139
4.7 Summary of hyperparameter ranges and fixed training parameters used for the FNN model. 144
4.8 Summary of hyperparameter ranges and fixed training parameters used for the bidirectional LSTM model. 147
4.9 Plastic parameters (K, ε_0, n) and corresponding Young's modulus (E) predictions for virtual materials (*VM1*, *VM2*, *VM3*), compared with true values. 154
4.10 Swift parameters and Young's modulus of virtual materials *VM4* and *VM5*. 159
4.11 Comparison of Young's modulus predicted by the *ML model — Elasticity* with the analytical approach (Equation 4.3) and comparison of Swift parameters predicted by the *ML model — Plasticity* with the parameters obtained from experimental tensile test curves. 161
4.12 Isotropic and kinematic hardening parameters for representative cases (A and B) from the *RB-IsoDataset* and *RB-AnisoDataset*. 172
4.13 Expected and predicted parameters for Cases Q2, Q3 and Max, along with the relative prediction error for each variable. 191
4.14 Expected and predicted parameters for Outliers A, B, C and D, along with the relative prediction error for each variable. 193
4.15 Comparison of expected and predicted material parameters for outliers D, E and F. Predicted values are shown for two regularization levels: $\lambda = 0$ and $\lambda = 0.9$. 198
4.16 Expected and predicted parameters for Outliers G and H, along with the relative prediction error for each variable. 200
4.17 Anisotropic hardening parameters of the combined isotropic-kinematic hardening (IKH) model, identified based on tension-compression tests (TC) and reverse bending tests (RB). 203

5.1 Test MSE, outlier percentage and maximum error for models with $n_s = 40$, comparing random walk (RW) and smooth walk (SW) data across different network depths and widths. 227

5.2 Mean relative error (%) in σ_{xx} for tension–compression (TC) cases and in σ_{xy} for reverse-shear (RS) cases, comparing baseline and expanded datasets. 238

List of Acronyms

AFR	Associated Flow Rule
AHSS	Advanced High-Strength Steels
AI	Artificial Intelligence
ANN	Artificial Neural Network
BCC	Body-Centered Cubic
BPTT	Backpropagation Through Time
CEGM	Constitutive Equation Gap Method
CNN	Convolutional Neural Network
DIC	Digital Image Correlation
DL	Deep Learning
DP	Dual-Phase
EDM	Eletrical Discharge Machining
EGM	Equilibrium Gap Method
FCC	Face-Centered Cubic
FEA	Finite Element Analysis
FEM	Finite Element Method
FEMU	Finite Element Model Updating
FNN	Feed-forward Neural Network
GRU	Gated Recurrent Unit
HAH	Homogeneous Anisotropic Hardening
HPD	Hybrid Physics-Data
IH	Isotropic Hardening
IKH	Isotropic-kinematic Hardening
LHS	Latin Hypercube Sampling
LMSC	Linearized Minimal State Cells
LSTM	Long Short-Term Memory

MAE	Mean Absolute Error
ML	Machine Learning
MLP	Multi-Layer Perceptrons
MRE	Mean Relative Error
MSE	Mean Squared Error
MSC	Minimal State Cells
MSTD	Miniaturized Specimen Tester Device
MTT	Miniaturized Tensile Test
NANN	Nested Adaptive Neural Network
ND	Normal Direction
OM	Optical Microscopy
PCA	Principal Component Analysis
PDE	Partial Differential Equations
PEEQ	Plastic Equivalent Strain
PINN	Physics-Informed Neural Network
RD	Rolling Direction
ReLU	Rectified Linear Unit
RNN	Recurrent Neural Network
RVE	Representative Volume Element
RW	Random Walk
SD	Stress Differential
SEM	Scanning Electron Microscopy
SPD-NN	Symmetric Positive Definite Neural Network
SS	Subset Size
StW	Strain Window
STM	Scanning Tunneling Microscope
SW	Smooth Walk
TANN	Thermodynamics-Based Artificial Neural Network
TD	Transverse Direction
VFM	Virtual Fields Method
VSG	Virtual Strain Gauge

List of Symbols

$\mathbf{W}$	Weights of neural networks
b	Bias terms of neural networks
ϕ	Activation function
$\mathbf{h}_t$	Hidden state of recurrent neural networks (RNNs)
$\mathbf{c}_t$	Cell candidate of RNNs
$\mathbf{O}_t, \mathbf{I}_t, \mathbf{F}_t$	Output, input and forget gates of RNNs
$\boldsymbol{\chi}$	Internal state variables of LMSC networks
$\boldsymbol{\alpha}, \boldsymbol{\beta}$	Update vectors of LMSC networks
Φ	Yield function
Ψ	Potential function
$\bar{\sigma}$	Equivalent yield stress
$\boldsymbol{\sigma}$	Cauchy stress tensor
σ_i	Principal stresses ($i = 1...3$)
σ_y	Flow stress
I_i	Invariants of Cauchy stress tensor ($i = 1...3$)
J_i	Invariants of deviatoric stress tensor ($i = 1...3$)
$\boldsymbol{\varepsilon}$	Strain tensor
$\boldsymbol{\varepsilon}_p$	Plastic strain tensor
ε_i	Principal strains ($i = 1...3$)
λ	Plastic multiplier
r	Plastic anisotropic coefficient
r_θ	Directional plastic anisotropic coefficient
Δr	Planar anisotropic coefficient
r_b	Biaxial anisotropic coefficient

$\mathbb{N}$	Anisotropic tensor (Hill's criterion)
$\boldsymbol{\alpha}$	Back stress tensor
$\boldsymbol{s}$	Equivalent deviatoric stress tensor
$\bar{\varepsilon}_p$	Accumulated plastic strain
$\boldsymbol{\eta}$	Relative stress tensor
$\mathbf{L}$	Anisotropic tensor acting on Cauchy stress tensor (Yld2000-2d)
$\mathbf{N}$	Normalized deviatoric stress tensor
χ	Schmitt factor
ψ	Helmholtz free energy potential
ζ_i	Kinematic internal variables
$\mathbf{h}^s$	Microstructure deviator
E	Elastic (Young's) modulus
E_0	Initial Young's modulus
E_a	Saturated Young's modulus
ν	Poisson's ratio
σ_0	Initial yield stress
K, n, ε_0, σ_{y0}, Q, β, α	Isotropic hardening parameters
C, γ	Kinematic hardening parameters (Armstrong–Frederick law)
F, G, H, L, M, N	Hill'48 anisotropy parameters
α_i	Yld2000-2d anisotropy parameters ($i = 1...8$)
a	Material parameter (crystallographic structure)
a, b, c	Yoshida–Uemori model parameters
$q, k, k_1, k_2, k_3, k_4, k_5$	HAH model parameters
B	Size of the bounding surface
R_{sat}	Saturated isotropic hardening stress at infinite plastic strain
L_0	Gauge length
ρ	Radius of curvature
F_p	Punch force
y_p	Punch displacement
t	Material thickness
μ	Friction coefficient
V	Support span

List of Publications

Publications in the scope of the thesis

1. Cruz, D. J., Barbosa, M. R., Santos, A. D., Amaral, R. L., de Sa, J. C., & Fernandes, J. V. (2024). *Recurrent Neural Networks and Three-Point Bending Test on the Identification of Material Hardening Parameters.* Metals, 14(1), 84. https://doi.org/10.3390/met14010084

2. Cruz, D. J., Xavier, J., Amaral, R. L., & Santos, A. D. (2022). *A Miniaturized Device Coupled with Digital Image Correlation for Mechanical Testing.* Micromachines, 13(11), 2027. https://doi.org/10.3390/mi13112027

3. Cruz, D. J., Pereira, A. F. G., Simões, V. M., Amaral, R. L., Santos, A. D., & Oliveira, M. C. (2022). *Work Hardening of Metallic Sheets under Tension-Compression and Simple Shear Reverse Loading.* Key Engineering Materials, 926. Trans Tech Publications.

4. Cruz, D. J., Barbosa, M. R., Santos, A. D., Miranda, S. S., & Amaral, R. L. (2021). *Application of Machine Learning to Bending Processes and Material Identification.* Metals, 11(9), 1418. https://doi.org/10.3390/met11091418

Publications regarding sheet metal forming research

1. Amaral, R. L., Cruz, D. J., Almeida, M., Barros, M., Santos, A. D., Reis, A. (2025). *Analysis of Springback in Rotary Draw Bending Process: Numerical Modelling with Experimental Validation.* MATEC Web of Conferences, 408, 01077. https://doi.org/10.1051/matecconf/202540801077

2. Cruz, D. J., Parreira, T., Marques, A., Prates, P., Oliveira, M., Neto, D., Santos, A., Amaral, R., Barbosa, M., Pereira, A. (2025). *Application of Recurrent Neural Networks in Uncertainty Analysis of Sheet Metal Forming.* MATEC

Web of Conferences, 408, 01071. https://doi.org/10.1051/matecconf/202540801071

3. Parreira, T., Cruz, D. J., Marques, A., Prates, P., Oliveira, M., Neto, D., Santos, A., Fernandes, V., Pereira, A. (2025). *Uncertainty analysis in sheet metal forming processes: Troubleshooting with machine learning.* In Materials Research Proceedings (Vol. 54, pp. 1577–1586). Material Forming. Materials Research Forum LLC. https://doi.org/10.21741/9781644903599-170

4. Cruz, D. J., Amaral, R. L., Santos, A. D., Tavares, J. M. R. S. (2023). *Application of Digital Image Processing Techniques to Detect Through-Thickness Crack in Hole Expansion Test.* Metals, 13(7), 1197. https://doi.org/10.3390/met13071197

5. Habraken, A. M., Aksen, T. A., Alves, J. L., Amaral, R. L., Betaieb, E., Chandola, N., Corallo, L., Cruz, D. J., Duchêne, L., Engel, B., Esener, E., Firat, M., Frohn-Sörensen, P., ... Vincze, G. (2022). *Analysis of ESAFORM 2021 cup drawing benchmark of an Al alloy, critical factors for accuracy and efficiency of FE simulations.* International Journal of Material Forming, 15(5). https://doi.org/10.1007/s12289-022-01672-w

6. Jimenez, M., dos Santos, A., Amaral, R., Cruz, D. J., de Sá, J. C. (2022). *Fracture Prediction of Third Generation Advanced High Strength Steels Using Hosford-Coulomb Damage Model.* Key Engineering Materials, 926, 1986–1992. https://doi.org/10.4028/p-sz798f

7. Oliveira, M. C., Cazacu, O., Revil-Baudard, B., Neto, D. M., Frohn-Sörensen, P., Ma, J., Liu, W., Cruz, D. J., Santos, A. D., Van Bael, A., Ghiabakloo, H., Habraken, A. M. (2023). *ESAFORM 2021 cup drawing benchmark of an Al alloy: Critical follow up analysis of its potentials.* In Materials Research Proceedings (Vol. 28, pp. 1491–1502). Material Forming. Materials Research Forum LLC. https://doi.org/10.21741/9781644902479-161

8. Cruz, D. J., Santos, A. D., Pereira, C., Miranda, S. S., Amaral, R. L. (2022). *Investigations on contact pressure in sheet metal forming of advanced high-strength steels.* Engineering Manufacturing Letters, 1(1), 2–7. https://doi.org/10.24840/2795-5168001-0010002

Chapter 1

Introduction

Advances in digital and industrial technologies have significantly reshaped modern economies and societies, playing a central role in sustainable development by redefining industrial processes and enabling new products and services [1; 2]. These developments are often described as part of the so-called Fourth Industrial Revolution, a term used to capture the integration of digital, physical and biological systems in industry [3]. Within this framework, concepts such as artificial intelligence (AI), machine learning (ML), advanced statistics, the internet of things and big data management strategies drive the emergence of smart factories, where virtual and physical systems cooperate flexibly and efficiently on a global scale [4].

One of the key elements of the fourth industrial revolution is artificial intelligence, with special emphasis on the subfield of machine learning. The goal of ML is to design algorithms capable of learning and improving without being explicitly programmed [5]. Such algorithms are particularly valuable for problems traditionally described by complex first-principles models, since ML can directly capture nonlinear relationships from data. The growing availability of large datasets, combined with exponential increases in computing power, has accelerated ML adoption across many industrial domains, including sheet metal forming [6].

Sheet metal forming is one of the most important and efficient processes for manufacturing metallic components, with applications in the automotive, naval, electrical, aeronautical and aerospace industries [7]. These processes, generally referred to as stamping when applied at industrial scale, range from relatively simple operations such as bending and stretch-forming to more complex operations such as roll-forming and deep drawing. In all cases, forces are applied to metallic sheets to modify their geometry, enabling the production of complex and functional components. Deep drawing, illustrated in Figure 1.1, is a representative example of such

processes. A flat sheet (blank) is plastically deformed into a desired shape using a punch, die and blank holder. The blank holder applies pressure on the flange region, controlling material flow into the die cavity. Even in such a basic process, different design variables, including material properties, tool geometry and process parameters (e.g., blank holder force), must be optimized to ensure part quality [8]. As shown in Figure 1.1, the deformation of the material during the process is not uniform and the different regions of the blank are subjected to different loading paths. While the flange area experiences compression under the action of the blank holder, the material in the die radius undergoes bending, followed by unbending and consequent stretching. These combined loading states illustrate the mechanical complexity of the process, which makes its accurate modeling particularly challenging.

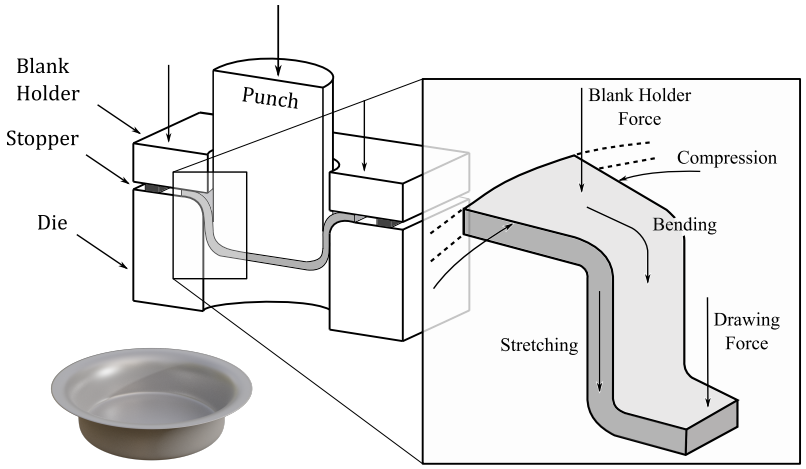


Figure 1.1: Schematic illustration representing the different loadings states presented in a typical deep drawing process.

Traditionally, developing forming processes relied heavily on trial and error, requiring extensive industrial expertise. However, the increasing complexity of products, shorter development cycles and introduction of new lightweight materials have made these approaches costly and time-consuming. Industries now seek for "first-time-right" solutions that minimize waste, reduce costs and accelerate the path from design to production. This requires not only advances in forming technologies and materials, but also in computational modeling and predictive tools.

The automotive industry is one of the main drivers for advances in sheet metal forming, fostering the development of new materials, innovative forming technologies and numerical tools that enable the virtual try-out of components. This industry is currently acting to follow the compelling and widespread efforts in addressing environmental concerns of energy savings while also ensuring the demanding safety

requirements. To achieve these goals, vehicle manufacturers try to reduce the mass of their products, mainly through the weight of vehicle's structure, by using lighter and stronger materials, such as advanced high-strength steels (AHSS) and aluminum alloys [9]. However, the behavior of these new materials differs from that observed in conventional materials. For example, springback, i.e., elastic recovery after unloading, is more pronounced in these materials, due to their unique material properties, thus leading to additional processing difficulties and costs for industrial applications.

To take advantage of the promising properties of AHSS, finite element analysis (FEA) of sheet metal forming processes has become indispensable for predicting and optimizing the product's manufacturing process. In this context, the constitutive models chosen to represent the behavior of the material have a significant impact on the accuracy of sheet metal forming simulations by FEA. This behavior normally includes four independent but interconnected phenomena [10]: (a) the elastic behavior and its influence on springback; (b) the yield criterion; (c) the forming limits and (d) the hardening model. Recent advances in this topic have led to the increased complexity of modern constitutive models with additional empirical parameters, making the calibration procedure more difficult and time-consuming, particularly when multiple experimental tests are required [11]. These difficulties have motivated the use of machine learning, including deep learning (DL) networks, as a complementary tool in this field.

One of the most promising applications of machine learning in sheet metal forming is inverse identification of material constitutive parameters. Rather than relying solely on extensive experimental campaigns and iterative optimization algorithms, ML-based approaches provide an efficient alternative for parameter calibration. Direct identification strategies use trained neural networks to map experimental data, such as stress-strain curves or force-displacement responses, directly to material parameters. Hybrid approaches combine machine learning surrogates with optimization algorithms to accelerate the fitting procedure [12; 13]. These methods significantly reduce the computational costs of traditional inverse analysis and can mitigate the challenges posed by nonlinear parameter interactions. Despite these advantages, several limitations remain. Most applications are limited to relatively simple constitutive models, whereas more advanced formulations, such as anisotropic hardening laws, remain unexplored. Because these models are inherently path dependent and sensitive to deformation history, their calibration would require surrogate architectures capable of capturing sequential dependencies. In addition, the parameters identified through ML often lack physical interpretability and may lead

to mechanically inconsistent behavior when the model is applied outside the training domain In particular, extrapolation may lead to non-physical responses, such as loss of convexity of the yield surface, violation of invariance principles, or inadmissible plastic flow, which undermines the robustness of ML-identified models in predictive applications.

Beyond parameter identification, machine learning is increasingly applied to develop fully data-driven constitutive models. Instead of relying on predefined functional forms, neural networks can approximate stress–strain relations directly from experimental or simulated data [14; 15]. These so-called constitutive neural networks range from simple feedforward architectures used as universal function approximators, to advanced recurrent and convolutional networks that account for load history and spatial dependencies. More recently, physics-informed neural networks have been introduced to incorporate physical laws, improving robustness and generalization [16]. These developments promise significant advantages, including accurate representation of highly nonlinear material behavior and near real-time execution within FEA. Nevertheless, limitations remain regarding data availability, extrapolation beyond training regimes and integration into component-scale simulations. Addressing these challenges constitutes an open research opportunity in applying ML to sheet metal forming processes.

1.1 Objectives

This thesis aims to advance research on sheet metal forming processes by exploring the use of machine learning techniques for the development and refinement of constitutive models for advanced high-strength steels. The work combines experimental characterization with parameter identification and data-driven modeling, leveraging machine learning as an alternative to classical phenomenological formulations and placing particular emphasis on anisotropy and path-dependent hardening behavior.

The work is structured around three specific goals. First, an extensive experimental campaign is carried out on AHSS grades (DP500, DP600, DP780), including conventional monotonic tests as well as innovative reverse-loading setups, in order to capture anisotropy, strain-path changes and Young's modulus degradation. Second, inverse strategies for parameter identification are investigated to calibrate classical constitutive models, relying both on conventional optimization approaches and on machine learning techniques, with particular focus on isotropic and anisotropic

hardening laws. Finally, data-driven constitutive modeling is explored through the development of ML-based surrogate models capable of directly reproducing nonlinear path-dependent stress–strain behavior from simulated data, while also assessing their robustness and generalization across complex loading paths relevant to forming processes.

By achieving these objectives, this thesis aims to bridge experimental mechanics, inverse parameter identification and data-driven modeling, thereby advancing the understanding and predictive capabilities of constitutive descriptions for AHSS. The developments are intended to improve the description of path-dependent material behavior and lay the groundwork for future integration of ML-based constitutive models into finite element simulations and industrial applications.

1.2 Outline of the thesis

This thesis is structured into six chapters. Beyond this introductory chapter, which presents the motivation, objectives and scope of the work, the document is organized as follows:

- **Chapter 2** provides a comprehensive overview of machine learning approaches in constitutive modeling. It introduces the fundamental concepts of machine learning, with emphasis on artificial neural networks and deep learning techniques. The chapter also reviews classical phenomenological models, including yield criteria and hardening laws and highlights recent advances in applying ML to parameter identification and data-driven constitutive modeling. Key research challenges and open directions are also identified.

- **Chapter 3** describes the experimental campaign performed to characterize the mechanical behavior of three AHSS grades (DP500, DP600 and DP780). Both classical monotonic tests (tension, compression, shear, biaxial and bending) and innovative setups for reverse loading were employed, with particular emphasis on digital image correlation and miniaturized specimen testing. Novel experimental devices, such as the *Miniaturized Specimen Tester Device* and a reverse bending setup, were developed to capture the behavior of the materials for different strain path changes. The experimental results provide the foundation for model calibration and validation in the subsequent chapters.

- **Chapter 4** focuses on the identification of constitutive parameters for dual-

phase steels (DP500, DP600 and DP780). It starts with conventional inverse identification techniques using tension and compression tests to calibrate anisotropic yield criteria and both isotropic and anisotropic hardening laws. The chapter then explores the application of machine learning approaches to parameter identification: first, using neural networks to process three-point bending test data for isotropic hardening calibration and then extending the methodology to reverse bending tests for the simultaneous identification of isotropic and anisotropic hardening parameters.

- **Chapter 5** explores the development of fully data-driven constitutive models using recurrent neural networks. Unlike the previous chapter, which focused on parameter identification, this chapter investigates the ability of recurrent neural networks to directly learn the stress–strain response of DP780 steel from data, capturing anisotropic yielding and hardening evolution under non-proportional loading. Key aspects of training, dataset design and hyperparameter optimization are analyzed and the generalization of the models is assessed under monotonic and reverse strain paths. Finally, the performance of the proposed ML-based models is validated against conventional constitutive formulations in both quasi-static and dynamic finite element simulations.

- **Chapter 6** presents the main conclusions of this thesis and suggestions for future works.

Chapter 2

Machine Learning Approaches in Constitutive Modeling

Material constitutive models play a critical role in both materials scientific research and manufacturing processes, providing insights into the physical phenomena and behavior of materials. These models enable accurate predictions of material behavior under different loading conditions, with the primary goal of accurately reproducing real-world material behavior under a wide range of assumptions and requirements [17]. In case of sheet metal materials, two main modeling strategies are typically adopted, leading to two distinct categories of constitutive models: (i) crystallographic texture-based models and (ii) phenomenological models.

Crystallographic texture-based models are based on the theory of crystal plasticity originally proposed by Taylor and Elam [18] and Schmid et al. [19]. These models simulate deformation by slip on crystallographic planes, capturing both elastic and plastic behavior as well as the evolution of internal material properties [20]. A major advantage of this approach is that it relies on crystallographic texture as input, reducing the extensive mechanical testing typically required for complex anisotropic phenomenological models. In addition, by integrating microscale heterogeneities directly into the constitutive relations [21], these models can naturally represent anisotropic material behavior. However, this increased physical fidelity comes at the cost of higher computational requirements, which may limit their applicability in large-scale or real-time forming simulations [22].

Phenomenological models, on the other hand, consist of empirical mathematical relationships derived from macroscopic experimental observations. Although some phenomenological models are inspired by the crystallographic structure of materials, the corresponding constitutive parameters are calibrated using experimental data to minimize the error between numerical predictions and experimental results. The increasing complexity of advanced materials exhibiting nonlinear behavior has led

to the development of more complex constitutive laws capable of capturing phenomena, such as hardening and anisotropy. Consequently, these models often involve a large number of empirical parameters, which not only complicates their mathematical formulation, but also makes the calibration process more demanding, requiring extensive experimental campaigns [23].

To address the challenges of parameter identification in phenomenological models, several inverse strategies have been proposed. These methods leverage homogeneous and heterogeneous mechanical tests to characterize material behavior across diverse stress and strain states. Common inverse identification techniques include Finite Element Model Updating (FEMU) [24], the Constitutive Equation Gap Method (CEGM) [25], the Virtual Fields Method (VFM) [26] and the Equilibrium Gap Method (EGM) [27]. These techniques often employ either gradient-based or derivative-free optimization algorithms. While effective, both gradient-based and derivative-free methods can converge to local minima rather than the global solution. To overcome this limitation, global optimization methods such as genetic algorithms have been explored, despite their higher computational costs [28]. Advances in imaging technologies have further enriched experimental mechanics. Techniques such as digital image correlation (DIC) [29] have become popular because of their non-contact nature and their ability to provide full-field data with high spatial resolution and accuracy. Despite these advances, conventional phenomenological models often struggle to fully exploit the rich full-field data provided by modern techniques such as DIC. This limitation arises because their explicit mathematical formulations are typically calibrated using global stress–strain curves, making it difficult to directly incorporate heterogeneous strain distributions revealed experimentally [30; 31].

In recent years, the increase in data availability and computational power has brought data-driven approaches such as ML to the forefront of research in many scientific fields. In the field of computational materials science, ML techniques are increasingly used for tasks such as designing new materials [32–34], optimizing processing routes [35; 36], developing digital twins, soft sensors [37] and supporting multiscale simulations and homogenization strategies [38; 39]. In the context of constitutive modeling, ML introduces a fundamentally different paradigm by eliminating the need for predefined mathematical formulations or empirical parameter calibration [40]. In particular, neural network-based approaches are particularly powerful due to their highly flexible approximation capabilities [41], which allow them to represent arbitrarily complex and non-linear material behaviors directly from data. As a result, these data-driven models can fully exploit the rich datasets generated by

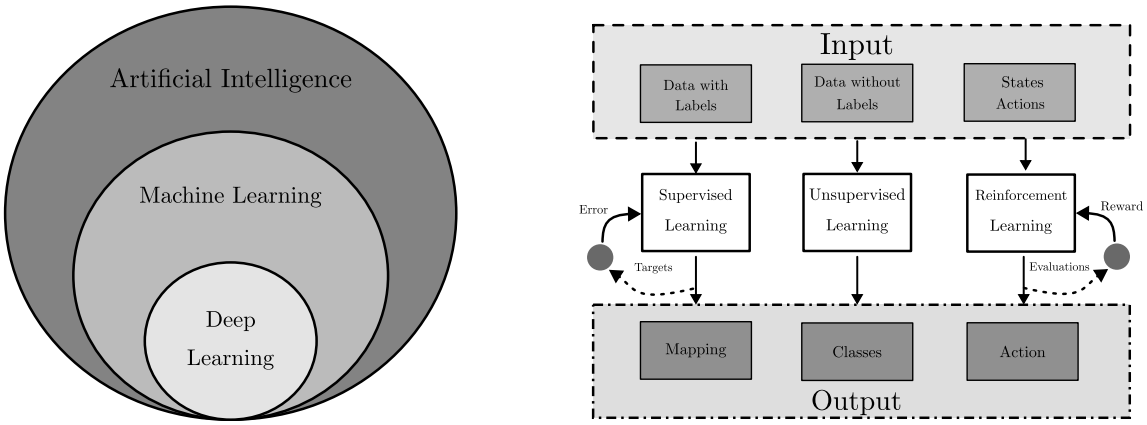
modern experimental techniques while reducing the modeling bias often present in phenomenological constitutive approaches [30].

This chapter provides an overview of machine learning techniques and their integration into constitutive modeling. The first section introduces basic ML concepts, including an overview of the main categories of ML algorithms, with a focus on artificial neural networks, deep learning approaches and practical aspects related to the implementation of ML models. The second section covers the fundamentals of phenomenological constitutive models for sheet metal materials, with particular emphasis on the mathematical formulation of plasticity theories, yield surface models and hardening laws. The chapter then presents a literature review on the application of ML in constitutive modeling, highlighting two main approaches: (i) the use of ML for parameter identification in traditional constitutive models and (ii) the development of ML-based metamodels that serve as data-driven surrogates for conventional phenomenological formulations. Finally, key research challenges and possible future directions are discussed.

2.1 Machine Learning based on Artificial Neural Networks

Machine learning is a growing field of study that enables computers to learn from data and make decisions without being explicitly programmed [42]. Once developed, ML algorithms can operate effectively and accurately without human intervention, making them highly adaptable to a wide range of applications. This adaptability stems from their ability to model and represent knowledge through mathematical algorithms that can be used for tasks such as regression and classification [43]. As shown in Figure 2.1a, ML is a subfield of artificial intelligence that focuses on the development of algorithms capable of learning patterns and relationships from data. Within ML, deep learning is emerging as a more specialized branch that expands the conventional multi-layer neural networks to include larger number of internal layers and elements and therefore increases their capability to learn more complex patterns from large datasets. ML algorithms are designed to automatically adjust their internal parameters through a process known as training. During training, the algorithm refines its performance by repeatedly processing input-output data pairs and optimizing its parameters to improve accuracy. This process allows the model not only to produce correct outputs for known data, but also to develop the

capacity for generalization, enabling reliable predictions on new, unseen examples or instances of the problem [44]. Developing a machine learning model begins with assembling a dataset that represents instances of the problem at hand. This dataset is typically associated into input features and output labels (or target values). The learning algorithm processes this data to construct a meaningful representation of the underlying patterns. Depending on the chosen approach, the resulting model may take various forms, including rule-based models such as decision trees, clustering algorithms (e.g., k-means), regression functions or artificial neural networks (ANNs) [43].



(a) (b)

Figure 2.1: Representation of (a) the hierarchical relationship between Artificial Intelligence (AI), Machine Learning (ML) and Deep Learning (DL) [45]; and (b) the main types of ML models; adapted from [46].

From a methodological perspective, machine learning approaches can be categorized according to different criteria. One common distinction is based on the type of output, leading to classification or regression problems. In classification tasks, the objective is to assign each input sample to one of a finite number of discrete categories or classes, whereas in regression problems the goal is to predict continuous-valued outputs. Another important categorization concerns the structure of the data being processed, which may include tabular datasets, time series or spatially structured data such as images. Finally, machine learning methods can be distinguished according to the learning paradigm. As represented in Figure 2.1b, ML models are generally divided into three main types based on data labeling and learning strategy [46]. Supervised learning uses labeled data to learn a mapping from inputs to corresponding outputs. During training, input-output

pairs are presented to the algorithm, allowing it to minimize the error between predicted and true labels through iterative optimization. This process is driven by the availability of ground truth targets, enabling accurate regression and classification tasks [47]. Unsupervised learning, on the other hand, works with data that has no explicit labels. Instead of learning a direct mapping, the goal is to discover hidden structures, patterns or groupings inherent in the input data. A key application of this type of learning is clustering, where similar data points are grouped together based on intrinsic characteristics, often revealing underlying relationships. Unlike supervised learning, the absence of labelled results means that there is no ground truth against which to evaluate performance and learning is guided by the internal statistical properties of the dataset [5]. In reinforcement learning (RL), learning occurs through interaction with an environment. An RL agent learns to perform actions in particular states in order to maximise a cumulative reward signal over time [44; 48]. Feedback is provided in the form of rewards or penalties, allowing the agent to iteratively refine its policy. This structure is particularly useful in domains that require sequential decision making under uncertainty, such as robotics and autonomous systems.

The applications addressed in this thesis employ supervised learning techniques, with a specific focus on regression problems. Among the available algorithms, artificial neural networks were selected due to their ability to model complex, nonlinear relationships. The following sections provide a brief theoretical background on supervised learning, with particular emphasis on both shallow and deep artificial neural networks.

2.1.1 Feedforward Neural Networks

Feedforward Neural Networks (FNNs) are a widely used class of neural networks, inspired by the structure and function of the human brain, suitable for both classification and regression tasks. Also known as Multi-Layer Perceptrons (MLPs), FNNs consist of multiple layers of interconnected nodes (neurons) arranged in a unidirectional, feedforward structure. The basic idea behind FNNs, whether shallow or deep, is to use multiple simple processing elements (PE) or nodes, connected to nodes in the immediately preceding layer to process information for the nodes in the next layer. Each node receives inputs, applies a transformation and passes the output forward through the network [49]. In supervised learning, the learning process involves adjusting the parameters of the network, specifically the weights

of the connections, to minimize an error function that measures the deviation between the predicted response and the target response. A typical FNN architecture is shown in Figure 2.2, where the nodes are organized in successive layers, from the input layer to the output layer, without backward connections, forming a feedforward topology [50]. The use of nonlinear activation functions in the processing elements, combined with multiple layers of computation, allows FNNs to approximate highly nonlinear and complex functions.

The structure of the input and output layers determines how the problem is formulated and encoded within the FNN. Before an FNN can be used in a deployment phase, its internal parameters must be optimized during a dedicated training phase. This process involves selecting an appropriate loss function and an optimization algorithm to iteratively adjust the network's weights to minimize the error between predicted and target outputs. A common choice for the loss function in regression tasks is mean squared error (MSE), while optimization is typically performed using gradient-based methods such as backpropagation. Once the architecture is defined and training is complete, the FNN effectively represents a defined set of mathematical functions capable of producing accurate results (outputs) for each instance of the problem (inputs) [46].

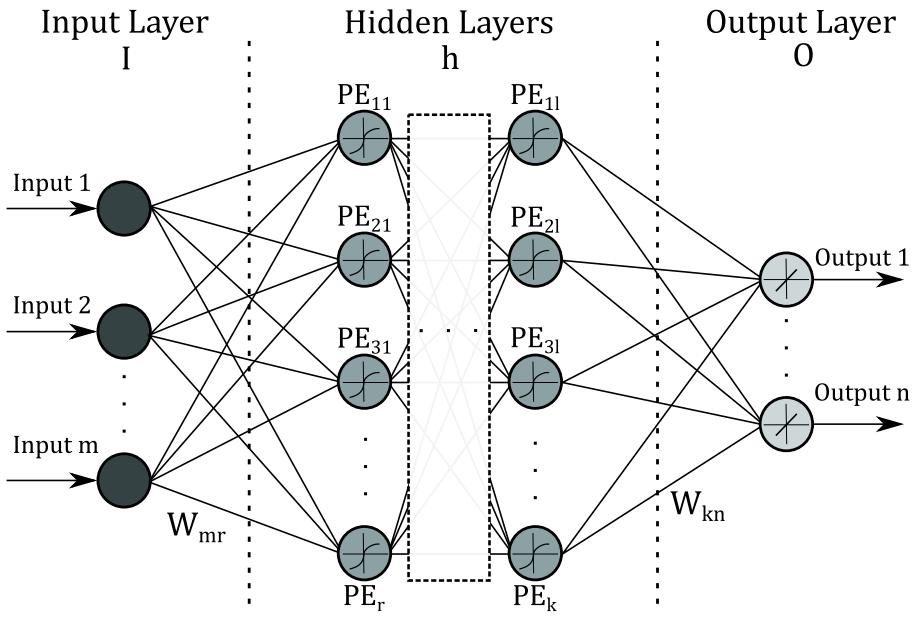


Figure 2.2: Example of a feedforward neural network, with m input nodes, several hidden layers with specific numbers of processing elements (PE) each implementing a nonlinear function (i.e., sigmoid), n output nodes implementing a linear function and interconnections weights (i.e., W_{kn} and W_{mr}).

The ouput of a single node from a hidden layer is given by:

$$y_i = \phi\left(\sum_j W_{ij} y'_j + b_i\right), \tag{2.1}$$

where y_i is the output of the ith neuron in the hidden layer. The term ϕ denotes the activation function applied to the weighted sum of the inputs (j) from the previous layer plus the bias term (b_i). The activation function ϕ can be any nonlinear function, such as the sigmoid function, the hyperbolic tangent (tanh) or the rectified linear unit (ReLU) [51], depending on the design of the network. The symbol W_{ij} represents the weight associated with the connection from the j-th neuron in the previous layer to the i-th neuron in the current layer. The term y'_j indicates the output of the j-th neuron of the previous layer or the input value if j corresponds to a neuron of the input layer. Finally, b_i is the bias term for the i-th neuron, which helps to shift the activation function and allows the model to better fit the data.

The significant increase in computing power, combined with the large volumes of data available, has driven the development of DL approaches [50; 52]. In recent years, DL algorithms have gained widespread popularity due to their ability to solve complex pattern recognition problems, such as natural language processing, handwriting recognition and image classification [46]. Although deep learning models share conceptual similarities with traditional shallow FNNs, their primary distinction lies in the depth and architectural complexity of the network. DL models consist of multiple layers of hierarchically organized processing units that progressively learn to extract relevant features from input data and represent them at increasingly abstract levels. This hierarchical structure more easily enables DL algorithms to perform feature extraction automatically, removing the need for manual feature engineering and significantly improving performance in tasks involving high-dimensional or unstructured data. However, this capability comes at the cost of increased computational demand, larger training datasets and longer training times. Some examples of deep learning architectures are presented next.

2.1.2 Convolutional Neural Networks

Convolutional Neural Networks (CNNs) are a special type of feed-forward neural networks designed to identify image information and are widely used in pattern recognition and image processing. Their simple structure allows for high adaptability, reducing the complexity of the network model and the number of parameters to

be adjusted [53]. As shown in Figure 2.3, a CNN consists of four types of layers: the input layer, convolutional layers, pooling layers and fully connected layers. The input layer is responsible for introducing the initial data into the network, typically the pixel values of the image. The convolutional layer contains a set of filters whose parameters are learned during training. These filters determine the output of the neurons by connecting to local regions of the input and computing the scalar product between their weights and the input region. Each filter detects specific patterns or features of interest, producing a unique two-dimensional activation map that captures the filter's response at each spatial location [46].

The output of a convolutional layer is computed by sliding a filter (or kernel) over the input feature map and computing the dot product between the filter weights and the local input region. Formally, for an input $\boldsymbol{x}$ and a filter $\boldsymbol{w}$, the operation is defined as:

$$(\boldsymbol{x} * \boldsymbol{w})_{i,j} = \sum_m \sum_n \boldsymbol{x}_{i+m,j+n} \cdot \boldsymbol{w}_{m,n} \tag{2.2}$$

where m and n are indices that iterate over the height and width of the filter, respectively. The pooling layer applies dimensionality reduction by downsampling the spatial dimensions of the input, reducing the number of parameters and computational load and helping to control overfitting. A CNN can have any combination of convolutional and pooling layers, but it always starts with a convolutional layer.

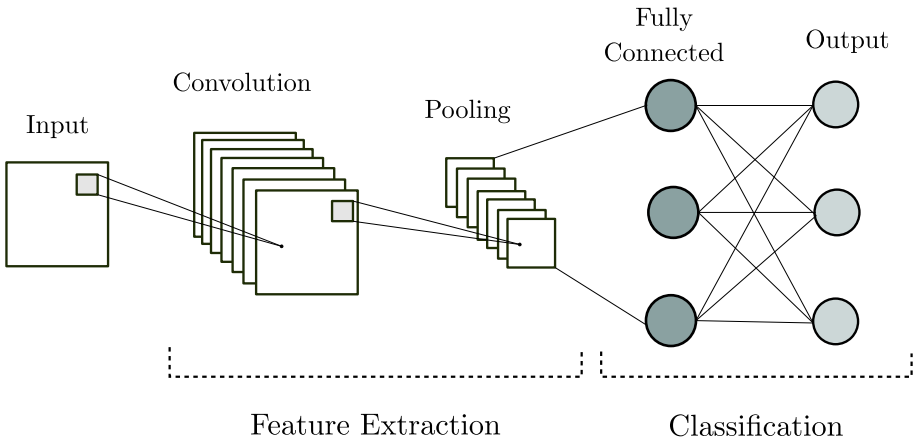


Figure 2.3: Network structure of a convolutional neural network (CNN).

Finally, the fully connected layers take the output from the convolutional and pooling layers and generate class scores for classification or regression problems. These last layers work in a similar way to standard FNNs, connecting each neuron to all the activations from the previous layer. This layered structure allows CNNs

to transform the original input through successive convolutional and downsampling operations, ultimately producing class scores for tasks such as classification and regression [54].

2.1.3 Recurrent Neural Networks

Recurrent Neural Networks (RNNs) are a powerful class of supervised machine learning models specifically designed to handle sequential data and time series analysis. Unlike feedforward networks (Figure 2.4a), which propagate information unidirectionally through the network without loops, RNNs (Figure 2.4b) incorporate cyclic connections, allowing them to process information and memorize dependencies in sequential data by incorporating insights from previous inputs, $\boldsymbol{x}_{0:t-1}$ and not just the current input, $\boldsymbol{x}_t$ [55; 56]. This memory capability increases the versatility of RNNs, making them essential for various applications, including natural language processing tasks [57] and speech recognition applications [58; 59].

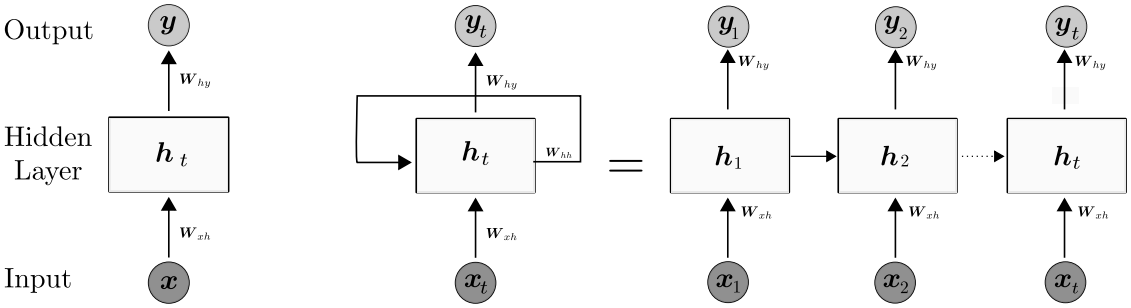


Figure 2.4: Network structure of a (a) feed-forward neural network (FNN) and (b) recurrent neural network (RNN).

RNNs are composed of a hidden layer that can be "unfolded" into several high-dimensional hidden states with non-linear dynamics, forming the network's memory of previous states. This unfolding technique allows RNNs to be trained using back-propagation through time (BPTT), where a consistent set of weights is applied to a layer over different timesteps. At time step t, the hidden state is denoted as $\boldsymbol{h}_t \in \mathbb{R}^{n \times h}$ and the input as $\boldsymbol{x}_t \in \mathbb{R}^{n \times d}$, where n represents the number of samples, d the number of inputs for each sample and h the number of hidden units. The trained parameters during the BPTT include the weight matrix $\boldsymbol{W}_{xh} \in \mathbb{R}^{d \times h}$, the hidden-state-to-hidden-state matrix $\boldsymbol{W}_{hh} \in \mathbb{R}^{h \times h}$ and the bias parameter $\boldsymbol{b}_h \in \mathbb{R}^{1 \times h}$. These elements form the basic structure of the recurrent neural network. The informa-

tion from the hidden state and input at each time step undergoes transformation through an activation function ϕ, often a *sigmoid* function such as the logistic or the *tanh* function, which is crucial for calculate the gradients in the subsequent BPTT algorithm [55].

Using the presented notation, the hidden state, $\boldsymbol{h}_t$, can be defined by Equation 2.3, while the output variable, $\boldsymbol{y}_t$, can be determined by Equation 2.4 [60]:

$$\boldsymbol{h}_t = \phi(\boldsymbol{W}_{hh}\boldsymbol{h}_{t-1} + \boldsymbol{W}_{xh}\boldsymbol{x}_t + \boldsymbol{b}_h), \tag{2.3}$$

$$\boldsymbol{y}_t = \phi(\boldsymbol{W}_{hy}\boldsymbol{h}_t + \boldsymbol{b}_y). \tag{2.4}$$

Training recurrent neural networks poses several challenges, in particular their ability to retain information over time. Although RNNs are theoretically able to model long-term dependencies through their recurrent connections, in practice their memory capacity is often limited by the way gradients are propagated during training. A major difficulty in training is the vanishing and exploding gradient problem. These problems are characterized by the behavior of the gradients during backpropagation through time. If the gradients become too small, they gradually disappear, resulting in minimal updates of the network weights. As a result, the learning process stalls and the network fails to capture long-term dependencies in the data. Conversely, if the gradients become too large, they can cause the weights to increase uncontrollably, leading to numerical instability and poor convergence [61]. These challenges significantly impact the training of standard RNNs, especially for tasks involving long sequences. As a result, alternative architectures such as Long Short-Term Memory (LSTM) networks and Gated Recurrent Units (GRUs) have been proposed to overcome these limitations by improving gradient propagation and enabling more effective learning of long-term dependencies. While LSTM use a more complex gating structure with separate input, forget and output gates, GRU offer a simplified variant that combines these functions into fewer gates. Both architectures share the key idea of gated units, which regulate the information propagation through the network and help preserve important signals over time.

Long-Short Term Memory

Several modified versions of recurrent neural networks have been proposed to improve the ability to retain information over time. Long short-term memory [57] is one of the most popular and effective solutions to mitigate the vanishing and exploding gradient problems. This architecture introduces the concept of ”memory

cells" (Figure 2.5), which extend the standard hidden units to retain information over longer sequences using structures known as gated cells. These gates regulate the flow of information into and out of the memory cell, preserving features from previous inputs and controlling how much new information is integrated.

An LSTM cell contains three primary gates: the output gate $\boldsymbol{O}_t$, input gate $\boldsymbol{I}_t$ and forget gate $\boldsymbol{F}_t$. The input gate controls how much new information flows into the memory cell, the forget gate determines how much of the previous cell state is retained and the output gate controls the exposure of the internal state to the next layer.

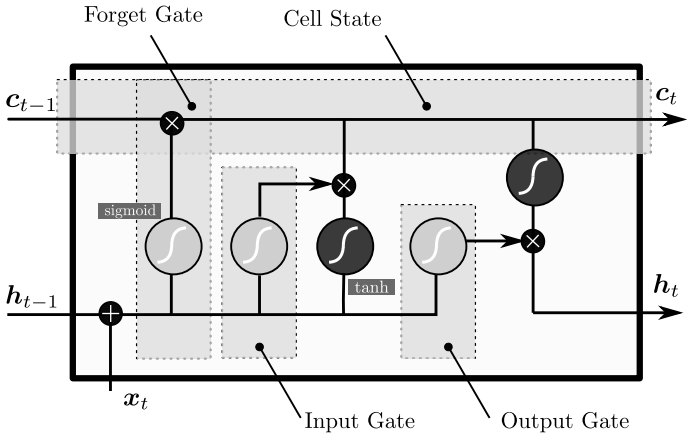


Figure 2.5: Network structure of an LSTM: $\boldsymbol{x}_t$ represents the input, $\boldsymbol{h}_t$ the hidden state and $\boldsymbol{c}_t$ the cell state.

These gates are computed as follows:

$$\boldsymbol{O}_t = \sigma(\boldsymbol{x}_t \boldsymbol{W}_{xo} + \boldsymbol{h}_{t-1} \mathbf{W}_{ho} + \boldsymbol{b}_o), \tag{2.5}$$

$$\boldsymbol{I}_t = \sigma(\boldsymbol{x}_t \boldsymbol{W}_{xi} + \boldsymbol{h}_{t-1} \mathbf{W}_{hi} + \boldsymbol{b}_i), \tag{2.6}$$

$$\boldsymbol{F}_t = \sigma(\boldsymbol{x}_t \boldsymbol{W}_{xf} + \boldsymbol{h}_{t-1} \mathbf{W}_{hf} + \boldsymbol{b}_f), \tag{2.7}$$

where $\boldsymbol{W}_{xo}$, $\boldsymbol{W}_{xi}$, $\boldsymbol{W}_{xf} \in \mathbb{R}^{d \times h}$ and $\boldsymbol{W}_{ho}$, $\boldsymbol{W}_{hi}$, $\boldsymbol{W}_{hf} \in \mathbb{R}^{h \times h}$ are the weight matrices, $\boldsymbol{b}_o$, $\boldsymbol{b}_i$, $\boldsymbol{b}_f \in \mathbb{R}^{1 \times h}$ are bias terms and σ is the logistic sigmoid activation function, mapping the outputs to the range (0, 1). An intermediate component, known as the cell candidate $\boldsymbol{c}'_t$, stores potential new information derived from the current input and previous hidden state:

$$\boldsymbol{c}'_t = \tanh(\boldsymbol{x}_t \boldsymbol{W}_{xc} + \boldsymbol{h}_{t-1} \boldsymbol{W}_{hc} + \boldsymbol{b}_c), \tag{2.8}$$

where $\boldsymbol{W}_{xc}$ and $\boldsymbol{W}_{hc}$ are weight matrices and $\boldsymbol{b}_c$ is the bias term. The final cell state $\boldsymbol{c}_t$ is then updated by combining the retained past state and the candidate memory content, modulated by the forget and input gates:

$$\boldsymbol{c}_t = \boldsymbol{F}_t \odot \boldsymbol{c}_{t-1} + \boldsymbol{I}_t \odot \boldsymbol{c}'_t, \tag{2.9}$$

where $\odot$ denotes the Hadamard (element-wise) product. The hidden state $\boldsymbol{h}_t$, which serves as output to the next layer or time step, is determined by:

$$\boldsymbol{h}_t = \boldsymbol{O}_t \odot \tanh(\boldsymbol{c}_t). \tag{2.10}$$

This gated mechanism allows LSTM to maintain and update long-term dependencies more effectively than standard RNNs.

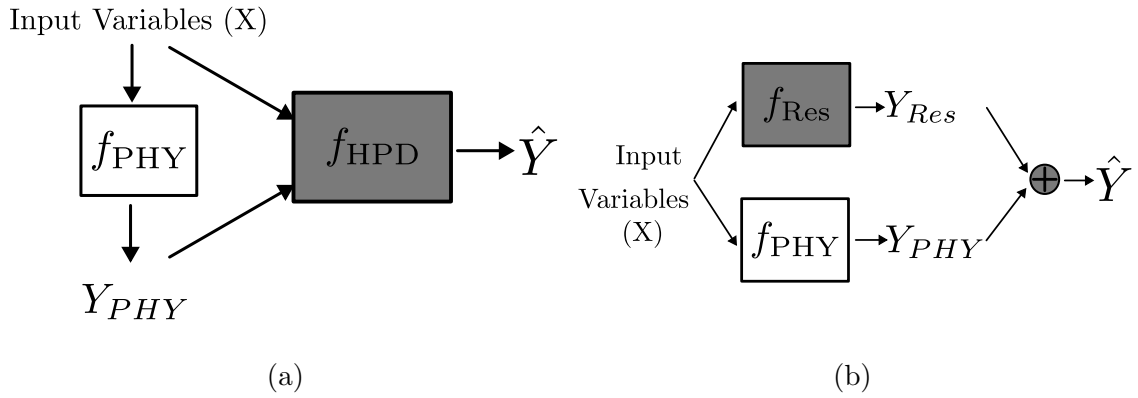
2.1.4 Physics-Guided Neural Network Strategies

Several strategies have been developed to integrate physical knowledge into neural networks. The goal of these methods is not only to improve predictive accuracy, but also to ensure that the predictions produced by the neural networks remain consistent with established physical principles, even in the presence of imperfect data such as missing values, noise or outliers. Different approaches to physics-informed neural networks have emerged in the literature, reflecting multiple ways in which physical knowledge can be combined with data-driven models.

According to Daw et al. [62], two complementary strategies can be highlighted. The first is the hybrid physics–data model (HPD), shown in Figure 2.6a. In this approach, the input variables of the system, X, are combined with the output of a simplified physics-based model, $Y_{\mathrm{PHY}} = f_{\mathrm{PHY}}(X)$. Both components are then used as inputs to a machine learning model, f_{HPD}, which produces the final prediction $\hat{Y} = f_{\mathrm{HPD}}(X, Y_{\mathrm{PHY}})$. This hybrid design allows the neural network to exploit the structured information provided by the physics-based model while simultaneously learning data-driven corrections from the input variables. It is particularly effective when the physics-based model captures the dominant behavior of the system but suffers from systematic biases or limited accuracy. An alternative hybrid formulation is the residual model, shown in Figure 2.6b. Here, the physics-based model f_{PHY} produces an initial prediction Y_{PHY} from the input variables, X, while a separate residual network f_{Res} is trained to estimate the discrepancy Y_{Res} between the physical model and the true response. The final prediction is then obtained by adding both contributions;

$$\hat{Y} = Y_{\text{PHY}} + Y_{\text{Res}}. \tag{2.11}$$

Since the residuals are typically of smaller magnitude and smoother than the full response, the learning task becomes less complex and more stable. This formulation is particularly valuable when the physical model captures the dominant trends but systematic deviations remain, which can then be corrected by the data-driven residual.



(a) (b)

Figure 2.6: Illustration of two physics-guided neural network formulations: (a) hybrid physics–data (HPD) model; (b) residual model. White boxes represent physics-based models, black boxes represent ML models.

Another strategy is the use of physics-based loss functions. In this formulation, known physical relationships are encoded as equality or inequality constraints, such as $G(Y, Z) = 0$ or $H(Y, Z) \leq 0$, where Y denotes the target variables and Z represents auxiliary physical quantities. These constraints are incorporated into the training process through a physics loss term:

$$\mathcal{L}_{\text{PHY}}(\hat{Y}) = \|G(\hat{Y}, Z)\|^2 + \text{ReLU}\big(H(\hat{Y}, Z)\big). \tag{2.12}$$

The overall cost function then combines two contributions:

$$\arg\min_{f} \underbrace{\mathcal{L}_{\text{DATA}}(\hat{Y}, Y)}_{\text{empirical error}} + \lambda_{\text{PHY}} \underbrace{\mathcal{L}_{\text{PHY}}(\hat{Y})}_{\text{physics constraints}}. \tag{2.13}$$

where $\mathcal{L}_{\text{DATA}}$ quantifies the error with respect to labeled data, $\mathcal{L}_{\text{PHY}}$ penalizes violations of physical laws and the weighting factor λ_{PHY} balances the relative importance of data fit and physical consistency during training. A key advantage of this formulation is that the physics-based loss can also be evaluated on unlabeled samples, since it only requires consistency with physical principles rather than

ground-truth labels. This property makes the approach particularly attractive in scientific and engineering applications, where experimental data are often limited or expensive to obtain, but robust physical knowledge is available to guide the learning process.

Meng et al. [63] provide a broader classification of physics-guided ML methods according to the level at which physical knowledge is introduced: data-level, model-level and optimization-level. At the data level, physics can be embedded by manipulating the training data before model learning. Examples include generating synthetic datasets through numerical simulations [64], applying transfer learning from domains where physics-rich data are available [65], or using multitask learning to couple related physical quantities [66]. These strategies guide the network towards physically plausible patterns, although their success strongly depends on the fidelity of the underlying physical models used to create synthetic data.

At the model level, physics is incorporated directly into the neural network architecture. This can be achieved by designing networks that encode invariances, conservation laws, or partial differential equation (PDE) structures. Examples include Physics-Informed Neural Networks (PINNs), which enforce PDE residuals through automatic differentiation. As shown in Figure 2.7, PINNs incorporate the governing physical laws directly into the loss function using automatic differentiation, which allows for the simultaneous minimization of data mismatch and PDE residuals during training. The inputs are the spatial coordinate x and time t and the output is $u(x,t)$, the state variable of interest. The training loss has two parts. The first, L_{data}, is the standard supervised error that penalizes the difference between predictions $\hat{u}(x,t)$ and available data. The second, L_{PDE}, enforces the governing equation by computing its residual for each predicted output using automatic differentiation with respect to x and t. The final objective combines both terms so that the network learns representations that are simultaneously consistent with data and with the PDE. This regularization enhances model stability and allows the use of simpler neural network architectures without sacrificing accuracy [67; 68].

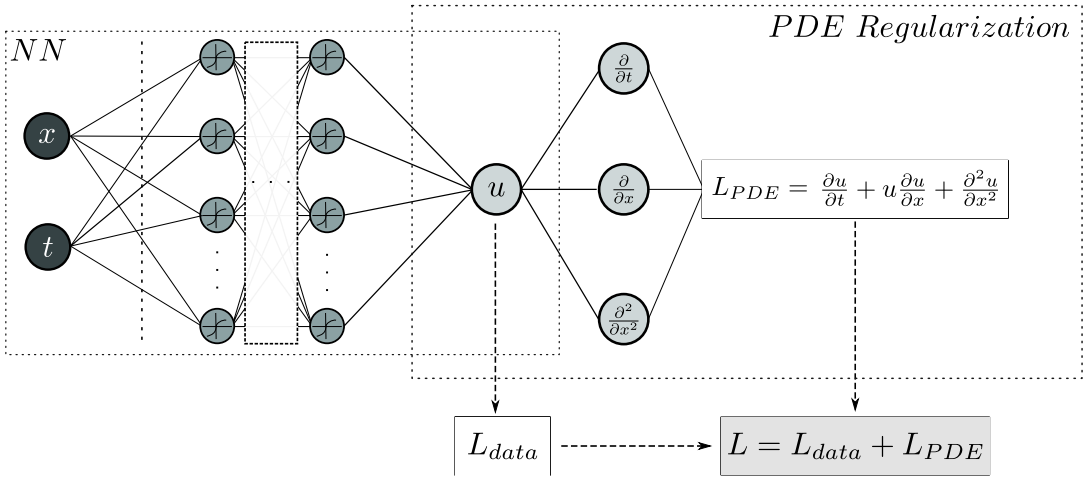


Figure 2.7: The framework of the physics-informed neural networks (PINNs) for a viscous Burgers' equation; adapted from [67].

At the optimization level, physical knowledge is introduced during training by modifying the loss function directly derived from task-specific knowledge or regularizations from physics principles. Beyond the standard empirical error, additional penalty terms are included to discourage violations of known constraints. This approach is flexible and can be applied even when data are scarce or noisy, but the choice of penalty weights is critical, as excessively large values may compromise data fit while very small values may lead to physically inconsistent predictions.

2.1.5 Implementation Considerations in Machine Learning

The successful application of machine learning models depends not only on selecting the most appropriate algorithm for a given problem, but also on several practical aspects that affect model accuracy, generalization and robustness. This section highlights key considerations in the development and implementation of ML models, such as: (i) **data generation**, which involves collecting representative and diverse samples that adequately cover the relevant aspects of the problem domain; (ii) **data preprocessing**, which involves transforming raw inputs into formats suitable for the model architecture, including normalization, encoding, handling missing values and often feature engineering; (iii) **model configuration**, which involves selecting an appropriate model architecture and tuning hyperparameters. These are set before training and not updated during learning (e.g., learning rate, batch size, regularization strength) These parameters govern how the model learns and influence the trade-off between complexity and generalization; and (iv) **training and evalu-**

ation, during which the model's internal parameters are iteratively updated using the training data, based on the chosen configuration, while performance is continuously monitored on validation data to adjust the learning process, prevent overfitting and ensure generalization. After training is complete, the final model is evaluated on a separate test set, which provides an unbiased estimate of its performance on previously unseen data.

The development of supervised learning models typically follows a structured sequence of steps aimed at producing models that are both accurate and capable of generalizing to unseen data. Figure 2.8 illustrates a standard supervised learning workflow.

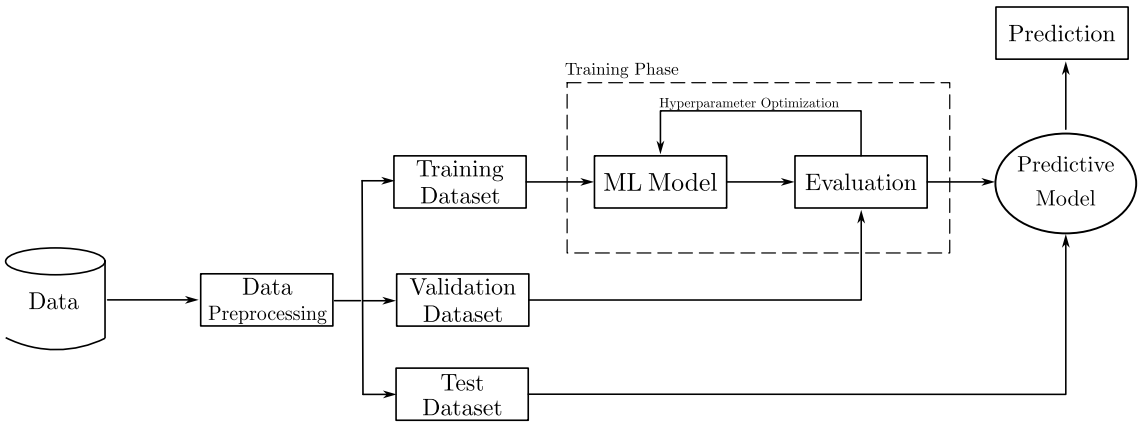


Figure 2.8: Supervised learning workflow.

The process begins with the creation of a dataset appropriate to the problem at hand. In the context of constitutive modeling, data can come from experimental tests or numerical simulations such as finite element analysis. In particular, FEA is widely used to generate synthetic datasets under a wide range of loading paths, boundary conditions and material parameters, allowing systematic exploration of constitutive behavior beyond the limitations of physical experiments. To ensure adequate coverage of the input space, different sampling strategies can be employed depending on the dimensionality and complexity of the problem. Figure 2.9 illustrates the differences between common sampling methods, including grid, random, Sobol [69] and Latin Hypercube sampling [70]. A key concept for comparing these methods is the discrepancy, a quantitative measure of how uniformly the sample points cover the input domain. Lower discrepancy indicates that points are more evenly distributed, which typically results in more accurate and generalizable models, especially in high-dimensional settings [71]. Grid sampling provides structured and uniform coverage and works well in low-dimensional spaces, but becomes in-

efficient as dimensionality increases due to the exponential growth in the number of required points. Random sampling offers simplicity and flexibility, particularly in high-dimensional spaces, but it can produces irregular point distributions with clusters and voids, leading to poor coverage of the input domain. More advanced sampling strategies have been developed to reduce discrepancy and improve the uniformity of point distributions across the input domain. Latin Hypercube Sampling (LHS) is a stratified method that ensures each input dimension is sampled uniformly by dividing the range of each variable into equal intervals and selecting one sample per interval. While the placement of samples within intervals is randomized, this approach guarantees good marginal coverage and offers significantly better space-filling properties than purely random sampling [70]. Sobol sequences, in contrast, are a type of deterministic quasi-random sampling that generate low-discrepancy point sets. Unlike LHS, Sobol sampling focuses on achieving uniformity not just in each individual dimension but across the entire multidimensional space [69; 72].

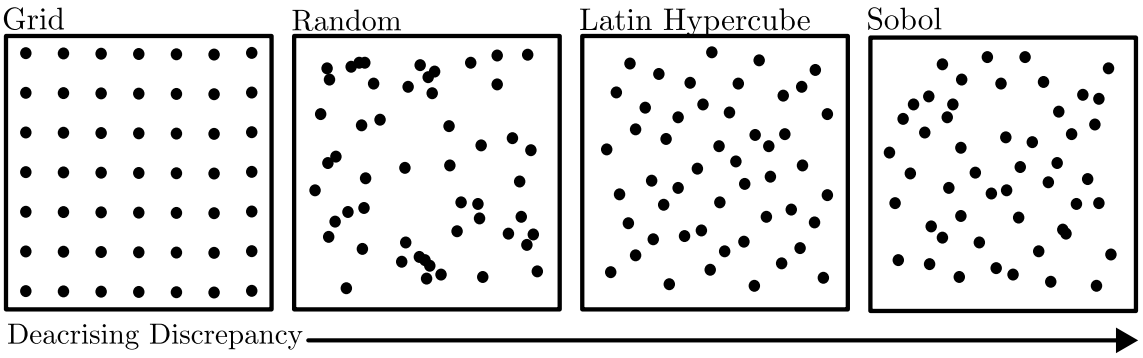


Figure 2.9: Visual comparison of sampling strategies (Grid, Random, Latin Hypercube and Sobol), showing decreasing discrepancy.

Once the dataset has been sampled, preprocessing steps are applied to improve data quality and consistency. These include correcting or removing invalid entries, applying transformations such as scaling or coding and eliminating redundant or irrelevant features. For models that are sensitive to different scales of input features, such as neural networks, normalization or standardization is essential for successful training. Common techniques include min-max scaling, which maps data to fixed intervals such as [0, 1] or [-1, 1] and z-score standardization, which transforms features to a normal distribution with zero mean and unit variance. Without proper normalization, the optimization process may be biased toward features with larger numerical ranges or exhibit unstable convergence behavior [5]. These preprocessing steps help ensure that the dataset is consistent and well suited for machine learning

algorithms [46].

The original dataset is typically divided into three subsets: the training set, the validation set and the test set. The training set is used to learn patterns and relationships within the data. The validation set supports hyperparameter tuning and generalization monitoring during training and plays a critical role in detecting problems such as overfitting. The test set is reserved exclusively for final model evaluation, providing an unbiased estimate of generalization performance [73]. Common partitioning schemes include 70% for training, 15% for validation and 15% for testing or alternatively 80-10-10, depending on dataset size.

Model training involves optimizing parameters based on the training data, governed by hyperparameters that define the learning process itself. These include the learning rate, batch size, number of layers or neurons and regularization coefficients. Since these values are not learned directly from the data, their selection has a significant impact on model performance. Sampling strategies such as grid search, random search and Bayesian optimization are commonly used to explore the hyperparameter space, guided by performance on the validation set [74]. A major challenge during training is overfitting, where the model learns to fit too closely the training data, including noise and outliers, impairing its ability to generalize. This is particularly problematic for highly flexible models such as deep neural networks. To mitigate overfitting, techniques such as early stopping, dropout, L1/L2 regularization and data augmentation are often employed. In cases with limited data, cross-validation can also provide more robust performance estimates [75; 76].

In cases where data is limited or training a model from scratch is computationally expensive, transfer learning can be an effective alternative. Transfer learning involves using knowledge gained from pre-training a model on a related task, typically with a large dataset and adapting it to a new but related problem. This technique is particularly useful in domains such as image recognition and natural language processing [77], where pre-trained deep learning models can be fine-tuned with smaller, task-specific datasets. In the context of constitutive modeling, transfer learning can be applied by reusing models trained on similar materials or loading conditions, thereby accelerating training and potentially improving generalization. Reusing pre-trained feature representations reduces the dependence on large amounts of labeled data and often improves convergence rates and overall performance.

Evaluating the predictive performance of the model requires appropriate metrics tailored to the task. Since this work focuses on regression problems, standard metrics such as mean squared error, mean absolute error (MAE) and coefficient of

determination (R^2 value) are commonly used [78]. Complementary to these indicators, the analysis of extreme error values or outliers can reveal systematic weaknesses of the model and pinpoint specific regions of the input space where predictions are less reliable.

These considerations form the basis for the development and use of robust ML models in this thesis. In the following sections, these principles are systematically applied and tailored to the specific challenges of data-driven constitutive modeling.

2.2 Phenomenological Models

In the context of phenomenological elastoplastic constitutive models, material behavior can be described in two distinct domains: elastic and elastoplastic. Within the elastic domain, the mechanical response follows an elastic law, where stress is derived from an energy potential expressed as a function of an appropriate measure of elastic deformation [20]. In contrast, the elastoplastic domain introduces a yield criterion that limits the elastic behavior, as shown in Figure 2.10. When the stress state reaches this limit, the material begins to deform plastically. Three-dimensional phenomenological elastoplastic models are based on three fundamental principles: (a) **yield criterion**, which specifies the stress conditions that initiate plastic yielding; (b) **hardening law**, which describes the evolution of the yield surface as the material undergoes plastic deformation; and (c) **plastic flow rule**, which defines the relationship between the strain rate and the stress components [23].

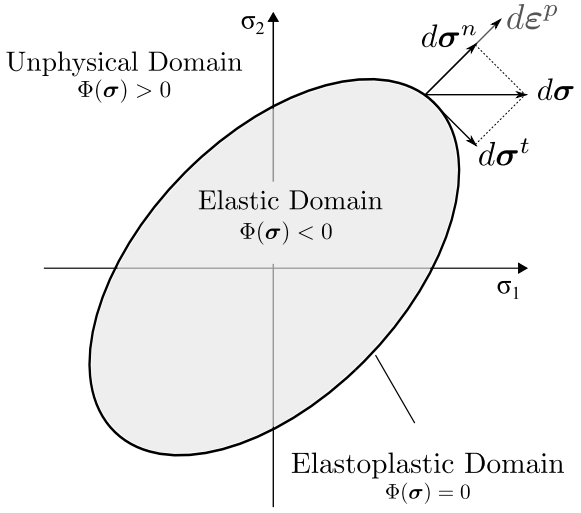


Figure 2.10: Representation of stress and plastic strain increment direction applied to the von Mises yield surface.

The yield condition is defined by a function of the stress tensor and is given by:

$$\Phi(\boldsymbol{\sigma}) = \bar{\sigma} - \sigma_y = 0, \tag{2.14}$$

where $\bar{\sigma}$ is the equivalent stress of a known yield function and σ_y is a material property, usually associated with the scalar flow stress value from the hardening law. For an arbitrary loading point, if $\Phi(\boldsymbol{\sigma}) < 0$, the stress state is within the yield surface and the material response remains purely elastic. When the yield point is reached ($\Phi(\boldsymbol{\sigma}) = 0$), further loading leads to plastic deformation and the onset of hardening. The evolution of the yield surface during plastic flow - whether by expansion, translation, rotation - is given by the hardening law. While the yield function defines the onset of plasticity, determining the material response in the plastic domain also requires relating stresses to strain increments. This is done by decomposing the stress increment vector $d\boldsymbol{\sigma}$ into two components: a tangential part $d\boldsymbol{\sigma}^t$, which does not produce plastic deformation and a normal part $d\boldsymbol{\sigma}^n$, which governs the plastic strain increment $d\boldsymbol{\varepsilon}_p$. The latter is oriented perpendicular to the yield surface and is given by:

$$d\boldsymbol{\varepsilon}_p = \dot{\lambda}\frac{\partial \Psi}{\partial \boldsymbol{\sigma}}, \tag{2.15}$$

where Ψ is the plastic potential function, $\dot{\lambda}$ is the plastic multiplier (a non-negative scalar dependent on loading conditions) and $\frac{\partial \Psi}{\partial \boldsymbol{\sigma}}$ is the gradient of the potential, normal to the yield surface at the loading point. In metal plasticity, it is common to assume that the plastic potential and the yield function coincide ($\Psi = \Phi$). This assumption leads to the associated flow rule (AFR), which can be expressed as:

$$\dot{\boldsymbol{\varepsilon}}_p = \dot{\lambda}\frac{\partial \Phi}{\partial \boldsymbol{\sigma}} = \begin{cases} \dot{\lambda} = 0, \text{ if } \Phi(\boldsymbol{\sigma}) < 0 \\ \dot{\lambda} > 0, \text{ if } \Phi(\boldsymbol{\sigma}) = 0 \end{cases} \tag{2.16}$$

This principle of normality, which is central to the AFR, requires that the direction of the plastic strain increase be perpendicular to the yield surface. This is visually represented in the principal stress space (σ_1-σ_2) in Figure 2.10. Different yield criteria - both isotropic and anisotropic - can be used to model different plastic behaviors. These, along with detailed discussions of nonlinear hardening behavior and modern hardening laws, will be explored in the following sections.

2.2.1 Plasticity Yield Surface Models

As previously stated, plastic yielding occurs when a yield criterion is satisfied. Generically, yield criteria are expressed by Equation 2.14 and state the elastoplastic boundary ($\Phi(\boldsymbol{\sigma}) = 0$). Therefore, the elastic domain is characterized mathematically by stress states in which the condition $\Phi(\boldsymbol{\sigma}) < 0$ is verified. The stress states located outside the admissible domain, i.e., $\Phi(\boldsymbol{\sigma}) > 0$, have no physical meaning. For numerical implementation, the yield surface must be closed, piecewise smooth and convex to ensure both stability and convergence. In the following sections, several isotropic and anisotropic yield criteria that will be considered in this work are presented.

2.2.1.1 Yield Criteria for Isotropic Materials

An isotropic material represents a material whose mechanical properties are independent of the loading direction (e.g., rolling or transverse directions). Accordingly, isotropic yield criteria can be formulated in terms of the principal stresses σ_i, where $i = 1, 2, 3$ or in terms of stress invariants:

$$I_1 = tr(\boldsymbol{\sigma}), \tag{2.17}$$

$$I_2 = \frac{1}{2} tr(\boldsymbol{\sigma}^2), \tag{2.18}$$

$$I_2 = \frac{1}{3} tr(\boldsymbol{\sigma}^3). \tag{2.19}$$

Tresca Yield Criterion

The oldest yield criterion was proposed by Tresca [79] and considers that the plastic deformation starts by crystallographic gliding when the maximum shear stress reaches a critical value. In the general case, it can be expressed as:

$$\Phi(\boldsymbol{\sigma}) = max\left\{|\sigma_1 - \sigma_2|, |\sigma_2 - \sigma_3|, |\sigma_3 - \sigma_1|\right\} - \sigma_y, \tag{2.20}$$

where σ_1, σ_2 and σ_3 are principal stresses, with $\sigma_1 \geq \sigma_2 \geq \sigma_3$. For a uniaxial condition ($\sigma_1 = \sigma_y$ and $\sigma_2 = \sigma_3 = 0$), the relationship between the value of the critical shear and the elastic limit (yield stress) of the uniaxial tensile test is given by:

$$\tau_{max} = \frac{\sigma_y}{2}. \tag{2.21}$$

As represented in Figure 2.11a, in the three-dimensional principal stress space, also known as Haig-Westergaard space, the yield surface of this criterion is represented by a hexagonal cylinder parallel to the hydrostatic axis. The intersection of the Tresca surface by a plane $\sigma_3 = 0$ gives a distorted hexagon, as shown in Figure 2.11b.

Huber–Mises–Hencky Yield Criterion

This criterion was proposed independently by Huber [80] and von Mises [81] and further developed by Hencky [82]. Also referred to as the J_2 yield criterion, it postulates that yielding begins when the distortional energy reaches a critical level, independent of the hydrostatic component of stress. The von-Mises's yield criterion can then be written as:

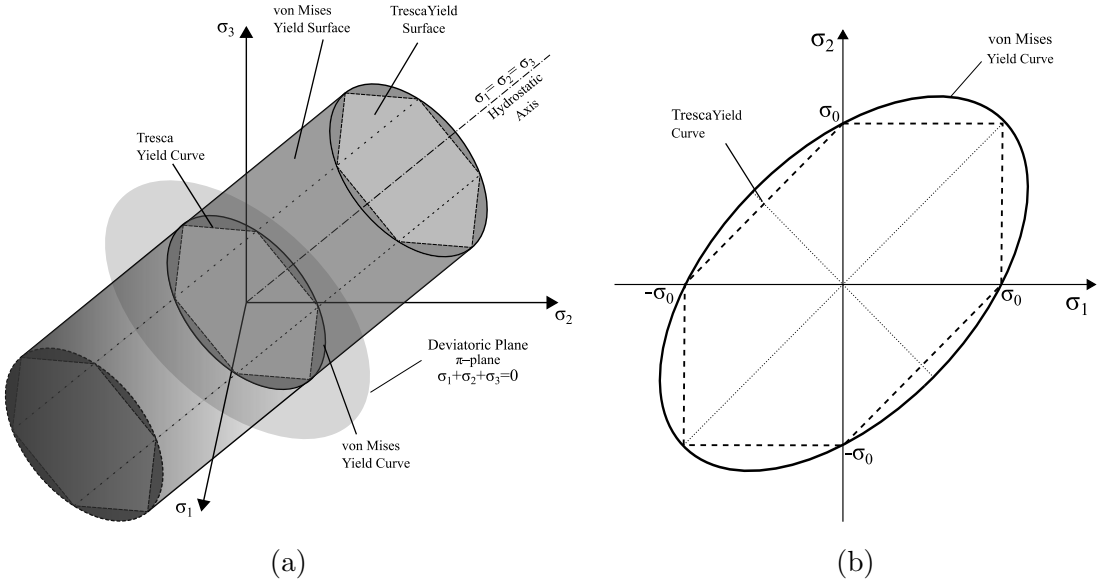
$$\begin{aligned}\Phi(\boldsymbol{\sigma}) &= \sigma_{\text{eq}} - \sigma_y \\ &= \sqrt{\frac{1}{2}\Big[(\sigma_{11}-\sigma_{22})^2 + (\sigma_{22}-\sigma_{33})^2 + (\sigma_{33}-\sigma_{11})^2\Big] + 3\Big(\sigma_{12}^2 + \sigma_{13}^2 + \sigma_{23}^2\Big)} - \sigma_y \\ &= \sqrt{3J_2} - \sigma_y.\end{aligned} \tag{2.22}$$

In the Haigh–Westergaard space, the von Mises yield surface is a circular cylinder of radius σ_y, enclosing the hexagonal prism of the Tresca criterion (see Figures 2.11a and 2.11b).

2.2.1.2 Yield Criteria for Anisotropic Materials

Sheet metals typically exhibit significant anisotropy in both mechanical and metallurgical properties, primarily due to their crystallographic texture and the heterogeneous plastic deformation introduced during the rolling process. This directional dependence of properties, known as orthotropy, results from material symmetry in three mutually perpendicular planes. The intersections of these planes define the orthotropic directions: rolling direction (RD), transverse direction (TD) and normal direction (ND). The plastic anisotropy of sheet metal is commonly characterized by the Lankford coefficient or r value, which quantifies the material's resistance to thinning during plastic deformation [83]. This parameter is typically obtained from a standard uniaxial tensile test [84] and is defined as

$$r = \frac{\varepsilon_{22}}{\varepsilon_{33}}, \tag{2.23}$$

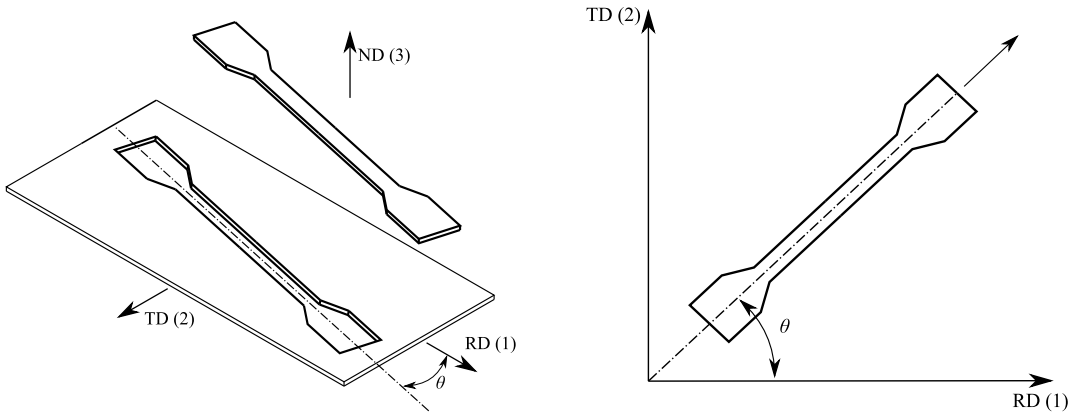


(a) (b)

Figure 2.11: Graphical representation of the Tresca and von Mises yield criteria in (a) the principal stress space and (b) $\sigma_3 = 0$ plane.

where ε_{22} and ε_{33} are the strains in the width and thickness directions, respectively.

It is well known that anisotropy coefficient, r, is variable in the sheet plane. As represented in Figure 2.12, tensile specimens obtained in different directions will provide different Lankford parameters, r_θ. The angle θ represents the angle between the axis of the specimen and the rolling direction. If $r_\theta > 1$ the strains in the width direction are dominant. On the other hand if $r_\theta < 1$ the thickness strains are dominant, which lead to excessive thinning and failure.



(a) (b)

Figure 2.12: Schematic representation of (a) tensile specimen produced at the angle θ (measured from the RD) and (b) relationship between the yield stress and the direction of loading in the plane of the sheet metal.

To evaluate the variation of r-values across the sheet plane, the planar anisotropy coefficient Δr is defined as:

$$\Delta r = \frac{r_0 - 2r_{45} + r_{90}}{2}, \tag{2.24}$$

where r_0, r_{45} and r_{90} are the r values measured at 0°, 45° and 90° with respect to the rolling direction, respectively. More recently, a biaxial anisotropy coefficient, r_b, has been introduced [85] to characterize the anisotropy under equi-biaxial or plane strain conditions. This coefficient is defined by the in-plane principal strain ratio:

$$r_b = \frac{\varepsilon_{22}}{\varepsilon_{11}}. \tag{2.25}$$

A robust yield criterion for anisotropic materials should be capable of describing both the evolution of the r value and the variation of the yield stress as a function of the loading direction in the plane of the sheet. To evaluate this capability, it is useful to establish analytical relationships between the stress components and the loading angle θ. For uniaxial loading at any angle θ with respect to the RD, the stress tensor components can be expressed as:

$$\begin{cases} \sigma_{11} = \sigma_\theta \cdot \cos^2\theta, \\ \sigma_{22} = \sigma_\theta \cdot \sin^2\theta, \\ \sigma_{21} = \sigma_{12} = \sigma_\theta \cdot \sin\theta\cos\theta, \end{cases} \tag{2.26}$$

where σ_θ is the yield stress in the direction defined by the angle θ from the RD. The increasing use of highly anisotropic advanced materials in sheet metal forming has led to the development of several anisotropic yield criteria. The following sections present the most relevant models adopted in this work.

Hill'48 Yield Criterion

In 1948, Hill proposed a generalization of the Huber-Mises-Hencky (or von Mises) quadratic isotropic yield criterion to account for anisotropic behavior in materials [86]. When the coordinate system is aligned with the material's orthotropic axes, the Hill'48 yield criterion is given by:

$$\Phi(\boldsymbol{\sigma}) = \sqrt{F(\sigma_{22} - \sigma_{33})^2 + G(\sigma_{33} - \sigma_{11})^2 + H(\sigma_{11} - \sigma_{22})^2 + 2\left(L\sigma_{23}^2 + M\sigma_{31}^2 + N\sigma_{12}^2\right)} - \sigma_y \tag{2.27}$$

where F, G, H, L, M and N are material constants that characterize the anisotropic behavior. The terms σ_{11}, σ_{22} and σ_{33} represent the normal stresses in the rolling, transverse and normal directions, respectively, while σ_{12}, σ_{23} and σ_{31} are the corresponding shear stress components. In this context, the von Mises yield criterion is retrieved when the anisotropy parameters satisfy $F = G = H = 0.5$ and $L = M = N = 1.5$. Alternatively, the Hill'48 criterion can be compactly written using tensor notation as:

$$\Phi(\boldsymbol{\sigma}) = \sqrt{\boldsymbol{\sigma} : \mathbb{N} : \boldsymbol{\sigma}} - \sigma_y, \tag{2.28}$$

where $\mathbb{N}$ is a fourth-order tensor that represent the anisotropy of the material given by:

$$\mathbb{N} = \begin{bmatrix} H+G & -H & -G & 0 & 0 & 0 \\ -H & H+F & -F & 0 & 0 & 0 \\ -G & -F & G+F & 0 & 0 & 0 \\ 0 & 0 & 0 & 2N & 0 & 0 \\ 0 & 0 & 0 & 0 & 2L & 0 \\ 0 & 0 & 0 & 0 & 0 & 2M \end{bmatrix}. \tag{2.29}$$

The anisotropy coefficients can be calibrated either from experimental yield stress data or from Lankford r-values, depending on the available material characterization. Despite its widespread use due to its simplicity and low computational cost, the Hill'48 yield criterion exhibits several well-known limitations. In particular, it provides a poor representation of material behavior under biaxial stress states and is unable to simultaneously capture both the directional dependence of the yield stress and the anisotropy of plastic strain (i.e., r-values) within the plane of the sheet.

Yld2000-2d yield criterion

The Yld2000-2d model, proposed by Barlat et al. [85], is a non-quadratic plane stress yield function developed to accurately describe the anisotropic plastic behavior of sheet metals, particularly those with body-centered cubic (BCC) or face-centered cubic (FCC) crystal structures. This formulation overcomes limitations observed in classical quadratic models, such as Hill'48, by allowing independent control over the yield stress and plastic strain anisotropy. The yield function is defined as:

$$\Phi = \left[\frac{1}{2}(|\tilde{s}'_1 - \tilde{s}'_2|^a + |2\tilde{s}''_2 + \tilde{s}''_1|^a + |2\tilde{s}''_1 + \tilde{s}''_2|^a)\right]^{\frac{1}{a}} - \sigma_y, \tag{2.30}$$

where the exponent a is a material dependent parameter associated with the crystallographic structure of the material. The quantities $\tilde{s}'_i$ and $\tilde{s}''_i$ (for $i = 1, 2$) correspond to the principal values of the transformed stress tensors $\tilde{\mathbf{s}}' = \mathbf{L}'\boldsymbol{\sigma}$ and $\tilde{\mathbf{s}}'' = \mathbf{L}''\boldsymbol{\sigma}$, respectively. These transformations introduce anisotropy into the yield function through two linear operators, $\mathbf{L}'$ and $\mathbf{L}''$, each defined by specific combinations of anisotropy parameters. The matrices $\mathbf{L}'$ and $\mathbf{L}''$ are shown in Equations 2.31 and 2.32:

$$\mathbf{L}' = \begin{bmatrix} L'_{11} & L'_{12} & 0 \\ L'_{21} & L'_{22} & 0 \\ 0 & 0 & L'_{66} \end{bmatrix} = \frac{1}{3} \begin{bmatrix} 2\alpha_1 & \alpha_1 & 0 \\ -\alpha_2 & 2\alpha_2 & 0 \\ 0 & 0 & 3\alpha_7 \end{bmatrix}, \tag{2.31}$$

$$\mathbf{L}'' = \begin{bmatrix} L''_{11} & L''_{12} & 0 \\ L''_{21} & L''_{22} & 0 \\ 0 & 0 & L''_{66} \end{bmatrix} = \frac{1}{9} \begin{bmatrix} 8\alpha_5 - 2\alpha_3 - 2\alpha_6 + 2\alpha_4 & 4\alpha_6 - 4\alpha_4 - 4\alpha_5 + \alpha_3 & 0 \\ 4\alpha_3 - 4\alpha_5 - 4\alpha_4 + -4\alpha_6 & 8\alpha_4 - 2\alpha_6 - 2\alpha_3 + 2\alpha_5 & 0 \\ 0 & 0 & 9\alpha_8 \end{bmatrix}. \tag{2.32}$$

The model contains a total of eight independent anisotropy coefficients α_k calibrated with experimental data. These typically include uniaxial yield stresses and Lankford r values measured at 0°, 45° and 90° with respect to the rolling direction, as well as results from equi-biaxial tensile tests. Each coefficient α_k affects the shape and orientation of the yield surface in stress space. For example, α_1, α_2 and α_3 primarily control the in-plane uniaxial response, while α_4 through α_8 allow fine-tuning of the diagonal and biaxial stress behavior.

2.2.2 Hardening

Metals are commonly classified as strain-hardening materials due to their behavior during plastic deformation, which results in an increase in stress with continued straining. This phenomenon, known as hardening, reflects the evolution of the yield surface as plastic deformation progresses and is directly influenced by the accumulated plastic strain. The hardening response is inherently path-dependent, meaning that it is influenced by the specific deformation history experienced by the material [20]. Under monotonic loading, materials typically exhibit isotropic hardening. This is characterized by a uniform expansion of the yield surface in all directions without changing its shape. As a result, the hardening behavior in different loading directions can be approximated by a single, uniform stress-strain curve. However,

in most sheet metal forming processes, materials are subjected to complex multi-axial loading conditions, making changes in the loading path highly probable [23]. For example, during deep drawing, the stress state at the flange edge gradually changes from compression to radial tension. In addition, load path changes are almost inevitable in multi-stage forming processes. Under such conditions, isotropic hardening models may no longer be adequate. Instead, constitutive models that incorporate the deformation history of the material - known as anisotropic hardening models - become essential. These models improve the predictive accuracy of sheet metal forming simulations, particularly with respect to springback [87; 88] and are critical for predicting residual stresses [89; 90] and failure mechanisms [91–93]. In the following sections, both types of hardening models will be presented and the most widely used hardening laws found in the literature will be introduced.

2.2.2.1 Isotropic Hardening

The isotropic hardening model assumes that the yield surface expands uniformly in all directions without changing its shape. The evolution of the yield stress, σ_y, is expressed as a function of the equivalent plastic strain, i.e., $\sigma_y = \sigma_y(\bar{\varepsilon}_p)$ and is typically derived from a uniaxial stress-plastic strain curve. Figure 2.13 shows a schematic illustration of a uniaxial stress-strain curve with isotropic hardening, along with the corresponding evolution of the yield surface. As shown, the yield stress remains symmetric in both forward (σ_D) and reverse (σ_C) loading due to the uniform expansion of the yield surface. Several empirical laws have been proposed in the literature to describe isotropic hardening. The most well-known isotropic hardening laws are:

Ludwik (1909) [94]	$\sigma_y = \sigma_{y_0} + K \cdot \bar{\varepsilon}_p^n,$	(2.33)
Hollomon (1945) [95]	$\sigma_y = K \cdot \bar{\varepsilon}_p^n,$	(2.34)
Swift (1952) [96]	$\sigma_y = K(\varepsilon_0 + \bar{\varepsilon}_p)^n,$	(2.35)
Voce (1948) [97]	$\sigma_y = \sigma_{y_0} + Q(1 - e^{-\beta\bar{\varepsilon}_p}),$	(2.36)
Hollomon - Voce (2010) [98]	$\sigma_y = \alpha K \cdot \bar{\varepsilon}_p^n + (1-\alpha)[\sigma_{y_0} + Q(1 - e^{-\beta\bar{\varepsilon}_p})],$	(2.37)
Swift - Voce (2006) [99]	$\sigma_y = \alpha\,[K(\varepsilon_0 + \bar{\varepsilon}_p)^n] + (1-\alpha)[\sigma_{y_0} + Q(1 - e^{-\beta\bar{\varepsilon}_p})],$	(2.38)

where K, n, ε_0, σ_{y0}, Q, β and α are materials parameters. The Hollomon and Swift models are well-suited for materials exhibiting continuous hardening without saturation, such as many steel alloys. In contrast, the Voce law is commonly used for materials that display hardening saturation, such as aluminum alloys. Hybrid laws

such as Hollomon–Voce [98] and Swift–Voce [99] have been developed to improve model flexibility by combining power-law and saturation behaviors. Despite their widespread use, isotropic hardening models are not capable of accurately capturing cyclic plasticity phenomena. This limitation has motivated the development of more advanced constitutive models, such as anisotropic hardening laws, which will be discussed in the following sections.

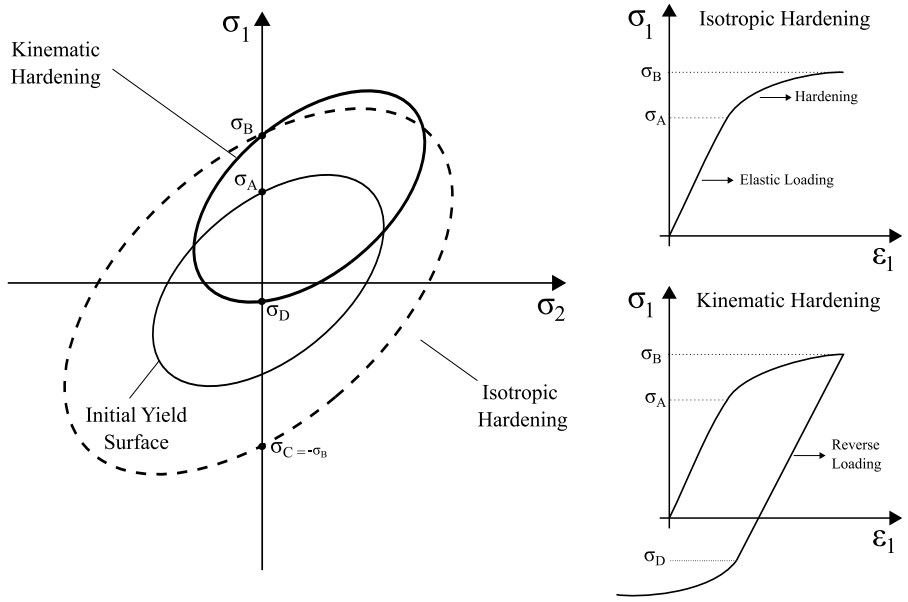


Figure 2.13: Evolution of the yield surface in the σ_1 -σ_2 plane and the correspondent Stress-Strain (σ_1-ε_1) behavior considering both isotropic and kinematic hardening models.

2.2.2.2 Anisotropic Hardening

For a comprehensive understanding of anisotropic hardening behavior, it is important to describe the phenomena arising from changes in loading paths. Different modes of load path changes can activate distinct slip systems, resulting in different strain path change effects. The characterization of these loading modes depends on the direction of loading before and after the path change and can be quantified using the Schmitt factor [100], defined as:

$$\cos\chi = \boldsymbol{N_{pre}} : \boldsymbol{N}, \tag{2.39}$$

where $\boldsymbol{N_{pre}}$ and $\boldsymbol{N}$ denote the normalized deviatoric stress tensors before and after the load path change, respectively and χ is the Schmitt angle. According to Barlat et al. [101], the directional tensor $\boldsymbol{N}$ can be calculated as:

$$\boldsymbol{N} = \frac{\boldsymbol{s}}{||\boldsymbol{s}||}, \tag{2.40}$$

where $\boldsymbol{s}$ is the stress deviator tensor. Based on the value of $\cos\chi$, different load path scenarios can be classified. When $\cos\chi = 1$, there is no load path change, indicating monotonic proportional loading, which corresponds to isotropic hardening as described in Section 2.2.2.1. A value of $\cos\chi = -1$ indicates reverse loading, such as compression following tension, which is the most severe form of strain path change. If $\cos\chi = 0$, the loading is orthogonal, i.e. the stress deviators before and after the change are perpendicular, as in the case of torsion following axial tension. Intermediate values between -1 and 1 represent more complex load transitions [102]. In practice, forming processes often involve deformation histories with multiple or continuously varying strain paths [103]. When the load path changes abruptly, the material response deviates significantly from that under monotonic loading. This phenomenon, known as the strain path change effect, is associated with a reorganization of the microstructure to adapt to the new loading conditions, resulting in significant macroscopic changes in mechanical behavior. A useful concept for describing such behavior is the modulus of rigidity, defined as $h = \frac{d\sigma}{d\epsilon}$. A positive value of h corresponds to hardening, values near zero indicate stagnation and negative values reflect softening. The hardening behavior under reverse loading involves several phenomena, as shown in Figure 2.14. The Bauschinger effect describes the reduction in yield stress when the load is reversed relative to the forward direction. This is followed by transient behavior characterized by an elasto-plastic transition and a change in work hardening rate. This is accompanied by work-hardening stagnation, where the material exhibits a stress-strain plateau. Finally, permanent softening is observed as a lower stress level compared to that under monotonic loading. Together, these effects are commonly referred to as Bauschinger behavior.

In orthogonal loading, the anisotropic response may be classified as orthogonal hardening or orthogonal softening, depending on whether the material strengthens or weakens relative to monotonic loading. Similar to reverse loading orthogonal loading can result in permanent softening. For load path changes that are not strictly orthogonal or reversed, the hardening behavior typically represents a transition state between proportional orthogonal and reverse loading conditions [104].

Constitutive anisotropic hardening models are generally divided into two main types: kinematic and distortional hardening. Figure 2.15 shows the evolution of the yield surface for both approaches, relative to the case of isotropic hardening.

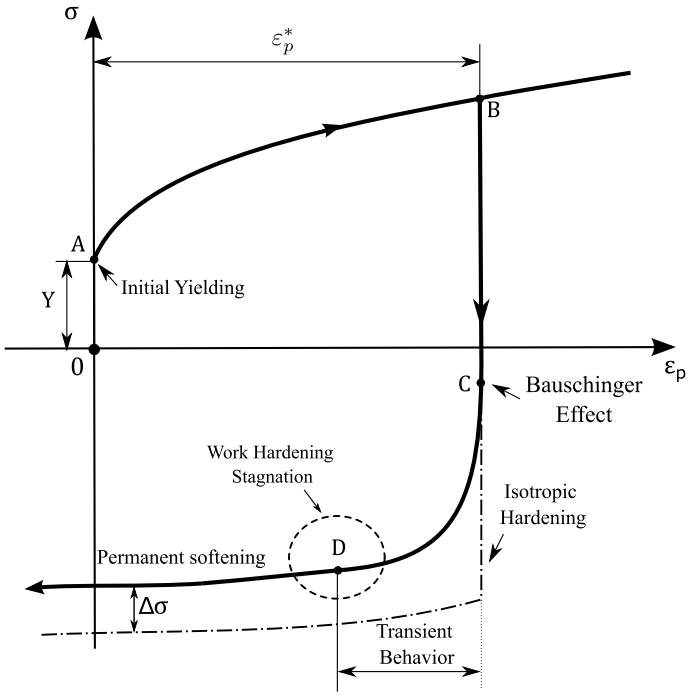


Figure 2.14: Schematic illustration of stress-strain response during forward and reverse deformation.

Kinematic hardening models describe a translation of the yield surface in stress space during plastic deformation. They are particularly good at capturing the material response under forward and reverse loading, represented by the red dots in Figure 2.15a, but are limited in describing the response under other loading scenarios. In contrast, distortional hardening models account for both translation and distortion of the yield surface and can therefore capture more complex responses associated with reverse orthogonal and intermediate load paths, as shown by the blue dots in Figure 2.15b [102].

Kinematic Hardening

Kinematic hardening is a traditional and widely used approach for simulating anisotropic hardening behavior, especially in industrial applications, due to its simplicity [23]. The basic assumption of pure kinematic hardening is that the yield surface translates in stress space during plastic deformation without undergoing homogeneous expansion, as shown in Figure 2.15a. In practical applications, however, it is common to use a combined description that includes both translation and expansion. In the case of pure kinematic hardening, two main modeling strategies can be identified: translation of a single yield surface or the use of multiple yield

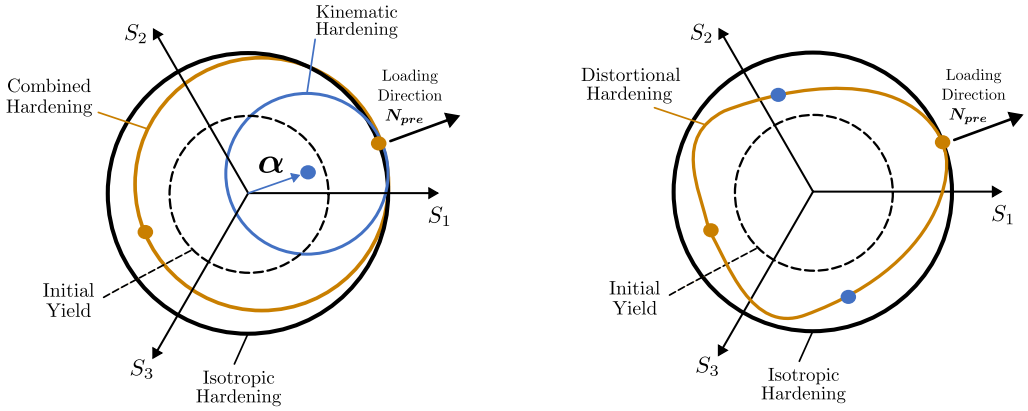


Figure 2.15: Evolution of the yield surface according to the type of hardening: (a) kinematic hardening and (b) distortional hardening; adapted from [102].

surfaces.

The concept of kinematic hardening was originally introduced by Prager [105] to describe Bauschinger behavior. According to this model, the yield surface translates in stress space as a rigid body without changing its size, orientation or shape. The evolution of this translation is described by the back stress tensor, $\boldsymbol{\alpha}$, which defines the center of the yield surface in stress space. As a result, the effective stress, $\bar{\eta}$, is expressed using the relative stress tensor, $\boldsymbol{\eta} = \boldsymbol{\sigma} - \boldsymbol{\alpha}$, instead of the total stress tensor, $\boldsymbol{\sigma}$. Prager's original formulation is linear and the evolution of the back stress rate, $\dot{\boldsymbol{\alpha}}$, is proportional to the rate of the plastic strain tensor, $\dot{\boldsymbol{\varepsilon}}_p$:

$$\dot{\boldsymbol{\alpha}} = C\dot{\boldsymbol{\varepsilon}}_p. \tag{2.41}$$

Ziegler [106] later proposed a linear law that directly relates the rate of the back stress tensor to the relative stress tensor:

$$\dot{\boldsymbol{\alpha}} = C\boldsymbol{\eta}\dot{\bar{\varepsilon}}_p. \tag{2.42}$$

Although classical kinematic hardening models can describe the Bauschinger effect, they often overpredict permanent softening and fail to capture other reverse loading phenomena. To address these limitations, Armstrong and Frederick [107] introduced a nonlinear evolution law for the back stress tensor by adding a dynamic recovery term that is collinear with the back stress tensor. This term introduces a memory effect that leads to an exponential evolution of the back stress tensor:

$$\dot{\boldsymbol{\alpha}} = C\dot{\boldsymbol{\varepsilon}}_p - \gamma\boldsymbol{\alpha}\dot{\bar{\varepsilon}}_p, \tag{2.43}$$

where C and γ are material parameters. This evolution law has been widely adopted to describe Bauschinger and ratcheting effects, as well as transient behavior [20].

To better capture the material behavior over different strain ranges, Chaboche [108] proposed a decomposition into several nonlinear kinematic terms based on the Armstrong-Frederick model. This formulation uses a superposition of multiple back-stress components, each with its own evolution law:

$$\dot{\boldsymbol{\alpha}} = \sum_{i=1}^{n} \dot{\boldsymbol{\alpha}}_i, \text{ with } \dot{\boldsymbol{\alpha}}_i = C_i\dot{\boldsymbol{\varepsilon}}_p - \gamma_i\boldsymbol{\alpha}_i\dot{\bar{\varepsilon}}_p. \tag{2.44}$$

The inclusion of multiple back stress components increases the flexibility of the model and allows for a more accurate representation of transient behavior and permanent softening.

To describe the combined effects of Bauschinger behavior, transient hardening and permanent softening, Mroz [109] introduced the concept of multi-surface kinematic hardening, which was later refined by Krieg [110] and Dafalias and Popov [111]. This approach considers multiple nested yield surfaces embedded in stress space, each representing a different stage of the material's inelastic response. Plastic deformation begins when the stress reaches the innermost yield surface, which defines the elastic limit. As loading progresses, the active surface translates linearly and when the stress reaches the next surface, both begin to translate simultaneously, albeit at a reduced rate. This sequential activation and movement of multiple surfaces allows the model to replicate the non-linear hardening behavior. Each surface is associated with a constant elastoplastic modulus, allowing a piecewise linear approximation of the full stress-strain curve.

To reduce model complexity while retaining the ability to capture key hardening phenomena, Dafalias and Popov [111] later proposed a simplified version of this concept involving only two yield surfaces and a set of internal state variables. This two-surface concept provides a balance between accuracy and computational efficiency, making it particularly attractive for practical applications. As a result, several two-surface models have been developed and validated over the years [112–115]. Among them, one of the most prominent is the Yoshida-Uemori (Y-U) model [116]. Known for its simplicity, the Y-U model can accurately reproduce Bauschinger effects, transient hardening and permanent softening with a relatively small number of material parameters.

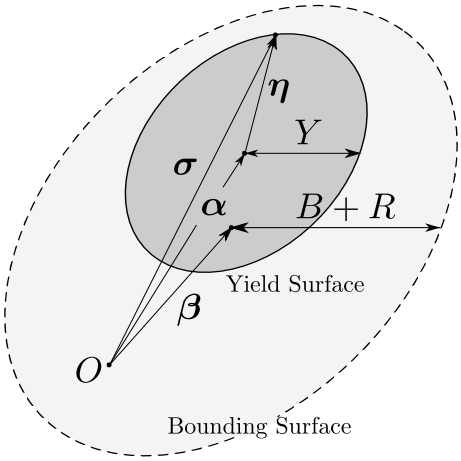


Figure 2.16: Schematic illustration of Yoshida–Uemori model; adapted from [116].

As shown in Figure 2.16, the Yoshida-Uemori model uses two surfaces in stress space, each governed by its own kinematic hardening rule. The inner surface defines the elastic domain, while the outer (bounding) surface governs global work hardening and permanent softening. Both surfaces can expand and translate. During plastic deformation, the yield surface translates while maintaining its size. The relative motion of the yield surface with respect to the bounding surface is expressed by:

$$\dot{\boldsymbol{\theta}} = c \left[\frac{a}{Y} \boldsymbol{\eta} - \sqrt{\frac{a}{\bar{\theta}} \boldsymbol{\theta}} \right] \dot{\varepsilon}_p, \tag{2.45}$$

where $\boldsymbol{\theta}$ is the position of the yield surface relative to the center of the bounding surface, c is a material parameter, Y is the size of the yield surface, $\boldsymbol{\eta} = \boldsymbol{\sigma} - \boldsymbol{\alpha}$ is the relative stress and $\dot{\varepsilon}_p$ is the effective plastic strain rate. The a parameter is defined as:

$$a = B + R - Y, \tag{2.46}$$

where B is the initial size and R is the isotropic hardening component of the bounding surface. The evolution of R is governed by:

$$\dot{R} = k(R_{sat} - R)\dot{\varepsilon}_p, \tag{2.47}$$

where R_{sat} is the saturation value and k controls the rate of isotropic hardening.

The kinematic hardening of the bounding surface is described by:

$$\dot{\boldsymbol{\beta}} = k \left(\frac{b}{Y} \boldsymbol{\eta} - \boldsymbol{\beta} \right) \dot{\varepsilon}_p, \tag{2.48}$$

where b is a material parameter. The overall evolution of the back stress tensor is the sum of these two components:

$$\dot{\boldsymbol{\alpha}} = \dot{\boldsymbol{\beta}} + \dot{\boldsymbol{\theta}}. \tag{2.49}$$

An important extension of the Yoshida-Uemori model is the inclusion of elastic modulus degradation, which significantly improves the accuracy of springback predictions in finite element simulations. While conventional plasticity theory assumes that unloading occurs at a constant modulus, experimental studies have shown that the elastic modulus of materials decreases progressively with accumulated plastic deformation. Young's modulus degradation has a direct impact on the predicted springback and its inclusion in the Y-U model allows the formulation to more realistically replicate the unloading path. In this regard, the Y-U model introduces a specific evolution equation for the Young's modulus based on the accumulated plastic strain:

$$E = E_0 - (E_0 - E_a)\left(1 - \exp(-\xi \bar{\varepsilon}_p)\right), \tag{2.50}$$

where E_0 is the initial elastic modulus, E_a is the asymptotic value at large strains and ξ controls the degradation rate. This formulation ensures that the material exhibits a gradual loss of rigidity as the plastic deformation progresses, which in turn affects the residual stress state after unloading. Yoshida et al. [113] reported reductions in elastic modulus of up to 30% for mild steels, while Yang et al. [117] observed similar trends in high strength steels (20%) and aluminum alloys (10%). Subsequent studies have highlighted the need to include this effect in finite element simulations. Kuwabara et al. [118] demonstrated that omitting modulus degradation leads to significant errors in springback prediction. In addition, Yoshida and Uemori [119] validated the benefits of including this mechanism through comparisons with experimental results from U-draw bending and cyclic tension-compression tests.

Kinematic hardening models, whether based on one or two surfaces, describe the evolution of the yield surface by translating and expanding a fixed shape while maintaining a constant normal direction at each point. As such, they are well suited for modeling processes dominated by reverse loadings. However, their ability to capture anisotropic hardening under cross loading remains limited [102].

Distortional Hardening

Distortional hardening models differ from kinematic hardening approaches by allowing the shape of the yield surface to evolve with plastic deformation, rather than simply translating in stress space. This ability to distort the yield surface allows for a more accurate and consistent description of anisotropic hardening under different loading paths, such as reverse, cross and non-proportional loading. In this context, Barlat et al. [101] proposed the Homogeneous Anisotropic Hardening (HAH) model as an alternative to kinematic hardening. Unlike models that use a back stress tensor to translate the yield surface, the HAH model keeps the surface fixed in stress space. Instead, it introduces shape distortion to reflect changes in material behavior resulting from the loading history. As a result, the model can naturally capture phenomena such as the Bauschinger effect and permanent softening under different loading scenarios without relying on back stress evolution. The central idea of the HAH model is the introduction of a fluctuating component into a conventional yield function, which allows for shape changes in the surface. The yield function is defined as a combination of a stable component, $\bar{\sigma}$ and a fluctuating component, $\bar{\sigma}_h$, as follows:

$$\Phi = (\bar{\sigma}^q + \bar{\sigma}_h^q)^{\frac{1}{q}} - \sigma_y, \tag{2.51}$$

where q is a material parameter. The fluctuating term is further defined as:

$$\bar{\sigma}_h^q = f_1^q \left| \hat{\mathbf{h}}^s : \mathbf{s} - |\hat{\mathbf{h}}^s : \mathbf{s}| \right|^q + f_2^q \left| \hat{\mathbf{h}}^s : \mathbf{s} - |\hat{\mathbf{h}}^s : \mathbf{s}| \right|^q, \tag{2.52}$$

where $\hat{\mathbf{h}}^s$ is the microstructure deviator, a normalized traceless tensor that encodes the loading history and the current microstructural state:

$$\hat{\mathbf{h}}^s = \frac{\mathbf{h}^s}{\sqrt{\frac{8}{3}\mathbf{h}^s : \mathbf{h}^s}}. \tag{2.53}$$

This tensor acts similarly to a normalized plastic strain rate and evolves as the loading direction changes. If the material is unloaded and reloaded in a different direction, $\hat{\mathbf{h}}^s$ rotates progressively toward the new stress deviator. In near-reverse loading ($\cos\chi \approx -1$), it rotates toward the opposite direction. Importantly, $\hat{\mathbf{h}}^s$ and $-\hat{\mathbf{h}}^s$ represent the same microstructural state, reflecting the fact that the same slip systems are active in both tension and compression for a given direction. Thus, $\hat{\mathbf{h}}^s$

serves as a continuum representation of the dominant slip system set in a polycrystalline volume element [101]. The fluctuating components are scaled by functions f_1 and f_2, which depend on the internal state variables g_1 and g_2:

$$f_k = \left(\frac{1}{g_k^q} - 1\right), \quad k = 1, 2. \tag{2.54}$$

When $f_1 = f_2 = 0$, the fluctuating component vanishes and the formulation reduces to a conventional isotropic or anisotropic yield function, without distortional hardening. At the first increment of plastic deformation, $\mathbf{h}^s$ is initialized to the current stress deviator $\mathbf{s}$ and remains unchanged as long as the loading direction does not change. When loading direction changes such that $\mathbf{h}^s \neq \mathbf{s}$, the evolution of $\hat{\mathbf{h}}^s$ and the internal variables depends on the scalar product $\hat{\mathbf{h}}^s : \mathbf{s}$, following different evolution equations:

If $\hat{\mathbf{h}}^s : \mathbf{s} \geq 0$:

$$\frac{dg_1}{d\bar{\varepsilon}} = k_2 \left(k_3 \frac{\bar{\sigma}_0}{\bar{\sigma}} - g_1\right) \tag{2.55}$$

$$\frac{dg_2}{d\bar{\varepsilon}} = k_1 \frac{g_3 - g_2}{g_2} \tag{2.56}$$

$$\frac{dg_4}{d\bar{\varepsilon}} = k_5(k_4 - g_4) \tag{2.57}$$

$$\frac{d\hat{\mathbf{h}}^s}{d\bar{\varepsilon}} = k \left(\hat{\mathbf{s}} - \frac{8}{3}\hat{\mathbf{h}}^s(\hat{\mathbf{h}}^s : \mathbf{s})\right) \tag{2.58}$$

If $\hat{\mathbf{h}}^s : \mathbf{s} < 0$:

$$\frac{dg_1}{d\bar{\varepsilon}} = k_1 \frac{g_4 - g_1}{g_1} \tag{2.59}$$

$$\frac{dg_2}{d\bar{\varepsilon}} = k_2 \left(k_3 \frac{\bar{\sigma}_0}{\bar{\sigma}} - g_2\right) \tag{2.60}$$

$$\frac{dg_4}{d\bar{\varepsilon}} = k_5(k_4 - g_3) \tag{2.61}$$

$$\frac{d\hat{\mathbf{h}}^s}{d\bar{\varepsilon}} = k \left(-\hat{\mathbf{s}} + \frac{8}{3}\hat{\mathbf{h}}^s(\hat{\mathbf{h}}^s : \mathbf{s})\right) \tag{2.62}$$

The constants k and k_1 through k_5 are material parameters, while the internal variables g_3 and g_4 govern behavior related to permanent softening. The system simplifies to a non-softening model when $k_4 = k_5 = 0$ and $g_3 = g_4 = 1$. According to this framework, as loading progresses in a given direction, the yield surface

distorts—typically flattening in the opposite direction. The evolution of the surface is dictated by the state variables f_1, f_2 and the microstructure deviator $\hat{\mathbf{h}}^s$, which together allow the model to capture complex anisotropic effects.

In recent years, extended versions of the HAH model have been proposed to improve the prediction accuracy of forming simulations. Notable examples include the HAH_{20} and HEXAH models, which incorporate up to 15 anisotropic coefficients to better reflect complex material behavior under multiaxial loading [120]. At the same time, the increase in model complexity has led to the development of advanced numerical strategies aimed at reducing computational costs. These include multi-stage return-mapping algorithms [121], fully implicit solvers capable of solving complete residual systems and robust stress-update procedures based on generalized cutting plane methods [122]. Together, these developments contribute to making strain hardening models more applicable in industrial contexts where both accuracy and computational efficiency are essential for the simulation of anisotropic plastic deformation.

2.3 Applications of Artificial Neural Networks in Constitutive Modeling

Material constitutive models are mathematical representations designed to describe the mechanical response of materials under different loading conditions. They are typically formulated either as phenomenological models, based on macroscopic observations, or as crystallographic models. In both cases, these models involve material-dependent parameters, such as hardening coefficients, anisotropy parameters or evolution laws for internal variables, that must be determined through calibration against experimental or numerical data. Additionally, classical constitutive models are grounded in physical principles such as the second law of thermodynamics which makes them less prone to unreliable predictions or outlier responses. However, this same predefined mathematical structure inherently limits their predictive capability, as they can only reproduce behaviors explicitly encoded in the chosen formulation [123]. As a result, their ability to capture highly nonlinear or history-dependent phenomena remains restricted. In this context, machine learning and in particular artificial neural networks, offer a promising alternative by providing flexible function approximators that can learn complex stress–strain relationships directly from data. The potential advantages include bypassing restrictive assump-

tions about material law, leveraging high-dimensional experimental or simulation datasets and accelerating parameter identification tasks [15].

Supervised machine learning techniques have emerged in recent decades as promising tools for modeling nonlinear behavior, including the complex responses of materials captured by constitutive models. In particular, artificial neural networks are well suited to represent such dependencies due to their ability to provide continuous and highly flexible function approximation. Depending on the modeling objective, machine learning techniques are typically integrated into constitutive modeling in one of two forms [13]: (a) to support the inverse identification of material parameters in predefined constitutive models, improving calibration procedures [12; 124–126]; and (b) to construct fully data-driven constitutive formulations, commonly referred to as implicit constitutive models, where stress-strain relationships are learned directly from data without assuming an explicit symbolic structure [14; 127; 128].

In the first method, ANNs are used to assist in the identification of material parameters by emulating a specific process, typically a mechanical test, from which constitutive parameters are identified. The ANN model acts as a curve-fitting tool within a predefined constitutive model, improving calibration efficiency but remaining limited by the underlying symbolic structure. In the second method, the ANN model directly replaces the constitutive formulation, learning the stress-strain relationship from data without assuming a predefined model form. These data-driven models, trained on experimental or synthetic data, are often referred to as surrogate models and can be integrated into finite element simulations. Although these approaches show great potential, ANN-based constitutive modeling remains an emerging field and further research is needed to fully establish its capabilities and limitations [128]. This section reviews the state of the art in the application of machine learning to constitutive modeling. Within this broad field, artificial neural networks have received particular attention due to their capacity to approximate complex nonlinear relationships.

2.3.1 Parameter Identification Inverse Modeling

The identification of material parameters in constitutive models is commonly formulated as an optimization problem, where the objective is to minimize the difference between experimental measurements and numerical predictions of material behavior based on existing mathematical models [125]. This discrepancy is typically quantified by a cost function, which is minimized using optimization algorithms that

iteratively adjust the constitutive parameters to best fit the available data.

A well-established inverse strategy in this context is the finite element model updating technique [129], in which a finite element simulation of a mechanical test is repeatedly run. At each iteration, the deviation between experimental and simulated responses is evaluated, guiding the optimization process toward the optimal set of material parameters. FEMU offers high flexibility, allowing the integration of local, global or full-field data sources [125]. In addition to FEMU, several alternative inverse methods have been developed, including the equilibrium gap method [130] and the virtual fields method [131]. These approaches often rely on full-field measurements obtained via digital image correlation and enable a broader identification of material behavior under heterogeneous deformation states [132].

To address some limitations of traditional optimization-based strategies, such as sensitivity to local minima and high computational cost, several authors have proposed using ANNs to solve the inverse problem more efficiently [12; 13; 124; 133]. In this approach a neural network is trained to establish a surrogate mapping between measurable input data (e.g., displacements, strains) and the underlying material parameters. As shown in Figure 2.17, the method consists of two steps. In the direct problem (Figure 2.17a), a synthetic dataset is generated using finite element simulations under varying boundary conditions, geometries and material parameters. For each simulation, relevant outputs such as strain and displacement fields are recorded. This data is then used to train a neural network that learns to approximate the inverse function, as shown in the inverse problem (Figure 2.17b). Once trained, the network can quickly predict material parameters from experimental measurements, enabling near real-time identification.

Huber et al. [134] demonstrated the feasibility of this approach by developing an FNN to identify parameters of a finite deformation viscoplasticity model, achieving good agreement with experimental data even under complex loading histories. Similarly, Ktari et al. [135] applied FNNs to identify anisotropic parameters of thin-walled tubes based on the ring hoop tensile test. Bouchard et al. [136] highlighted the integration of inverse identification procedures with full-field measurement techniques, reinforcing the effectiveness of ANN-based strategies in experimental settings.

Beyond the standard ANN-based inverse approaches, some authors have developed hybrid methods that couple neural networks with genetic algorithms. Aguir et al. [12] focused on calibrating the Karafillis–Boyce yield surface [137] combined with a Voce hardening law for AISI 304 stainless steel. Their methodology relied on ANNs trained with finite element data from bulge and plane strain tensile tests

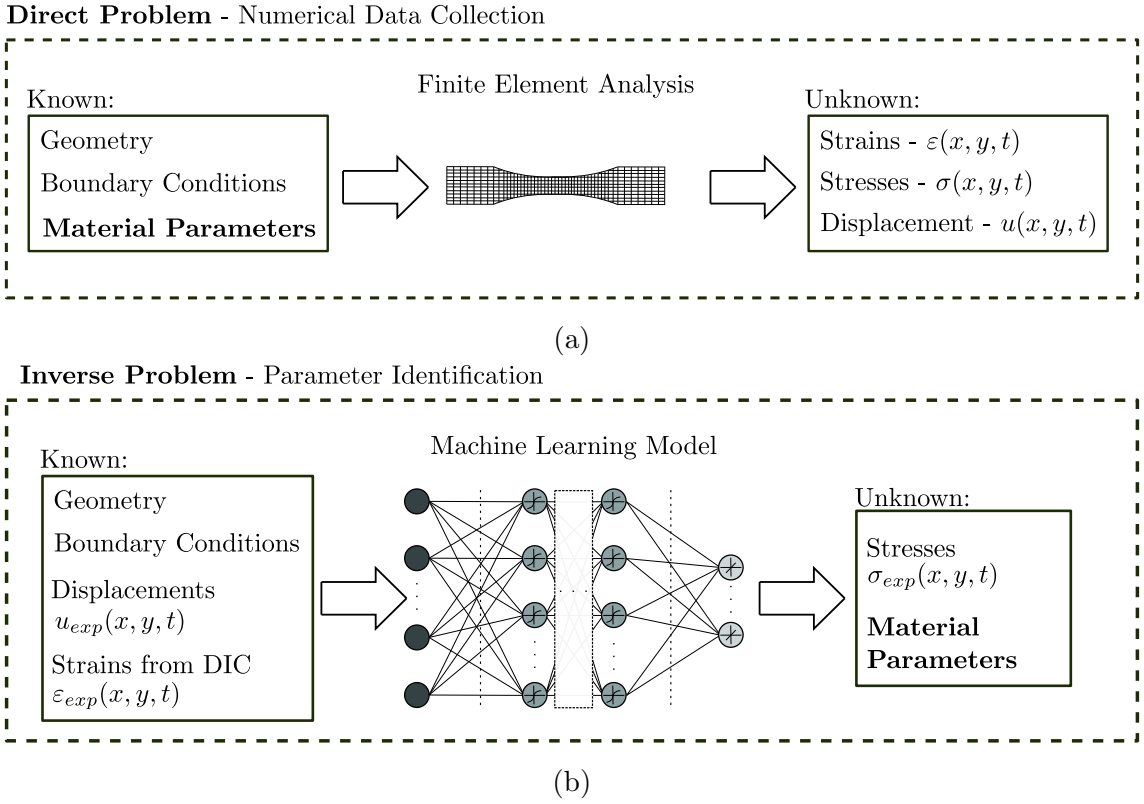


Figure 2.17: Schematic representation of (a) the direct problem, where numerical data is generated using finite element simulations based on known material parameters and (b) the inverse problem, where a machine learning model is trained to infer material parameters from experimental data (e.g., DIC-based displacement and strain fields).

to approximate the mechanical response for given sets of constitutive parameters. A genetic algorithm then explored the parameter space, iteratively updating the candidates until the ANN-predicted displacements converged with the experimental measurements. The procedure was later validated against an elliptical bulge test. Yao et al. [138] extended this concept to a viscoplastic-damage model, using ANNs to generate an informed initial population for the optimization loop. Trained on tensile curves at different strain rates and temperatures for an AA6061 aluminium alloy, the approach achieved accurate parameter identification under diverse loading conditions.

An important advancement was introduced by Morand and Helm [139], who addressed the issue of non-uniqueness in parameter identification. In certain hardening models, different sets of parameters can reproduce similar macroscopic responses, making the inverse problem inherently ambiguous. Conventional single ANN meta-

models tend to average across these possible solutions, which severely reduces prediction accuracy. To overcome this limitation, the authors proposed a "mixture of experts" approach, in which several ANNs are trained in parallel and dynamically combined through a gating network. This ensemble strategy achieved superior performance in both numerical benchmarks and experimental validation, where it was applied to tensile test data of AA6014 aluminium, DC04 and DP600 steels. The study demonstrated that ensemble-based architectures are more robust and reliable than single ANN models when dealing with non-unique parameter identification problems.

Recent developments have also highlighted the use of deep learning architectures, such as combinations of convolutional neural networks and long short-term memory networks, to handle noisy or high-dimensional full-field data, enabling robust identification in experimental conditions. Guo et al. [140] developed a hybrid CNN–LSTM metamodel, in which the convolutional layers were used to filter experimental noise and extract strain field features, while the recurrent LSTM layers captured the sequential nature of the loading process. The model was trained on a large synthetic dataset generated by finite element simulations of uniaxial tensile tests, covering variations in geometry, material parameters and load histories. Five elastoplastic parameters were identified with high accuracy, even when the input data were corrupted by noise. Validation against experimental tests on AA6061 aluminium confirmed that the approach achieved accuracy comparable to FEMU-based identification, while offering the advantage of almost instantaneous predictions once trained.

In addition to ANN-based models, alternative machine learning models have also been explored. Huang et al. [141] applied Gaussian Process Regression (GPR), a non-parametric Bayesian approach for the inverse identification of Swift hardening and Lemaitre damage model parameters, based on tensile test simulations of AA2017-T4 aluminium. The surrogate predictions were then integrated into finite element analyses and successfully validated against experimental results, highlighting the potential of probabilistic surrogate models in constitutive parameter calibration. Bastos et al. [142] applied the XGBoost algorithm for the identification of elastoplastic constitutive parameters, using synthetic full-field data generated by finite element simulations of heterogeneous dogbone tests. Their study showed that gradient-boosted trees could achieve highly accurate predictions with relatively small training datasets and that dimensionality reduction techniques such as Principal Component Analysis (PCA) significantly improved computational efficiency

without compromising accuracy.

Discussion

In the context of parameter identification, ML methods, specially ANNs, have shown strong potential for inverse mapping of stress-strain data into constitutive model parameters, often outperforming traditional optimization techniques in terms of computational efficiency. Once trained, ML-based surrogates provide predictions that are nearly instantaneous, which makes them highly attractive for applications involving repeated evaluations

Despite these advantages, several important challenges remain. A major limitation of current ML-based frameworks is their predominant focus on relatively simple constitutive models with a small number of continuous parameters, with the exception of the work of Yao et al. [138], which naturally fit regression-based frameworks. However, advanced formulations such as the CPB'06 yield criterion [143] or modern anisotropic hardening laws introduce additional complexity by combining continuous and discrete parameters. These mixed parameter spaces pose a significant challenge for conventional regression algorithms and the development of ML strategies capable of handling such hybrid identification problems remains an open area of research [144].

In addition, the majority of existing applications have been restricted to isotropic hardening models. Extending these approaches to anisotropic or kinematic hardening formulations is considerably more challenging, as such models are inherently history-dependent and sensitive to the loading sequence. Applications of neural networks to the identification of kinematic hardening parameters have been reported before using FNNs, for example by Huber et al. [134], but not applied to sheet metal materials. Accurately modeling such path-dependent behavior can be enhanced by surrogate architectures designed to capture sequential dependencies, with recurrent neural networks representing a particularly promising option. The application of such structures in identification of constitutive parameters, however, is still very limited. A notable exception is the work of Guo et al. [140], where a recurrent architecture was applied to an isotropic hardening model. Beyond this example, the use of recurrent networks for the calibration of isotropic and anisotropic hardening models, particularly in the context of sheet metal materials, remain limited leaving a clear opportunity for further research.

Another challenge is the physical validity of the identified parameters. Most ex-

isting approaches rely exclusively on numerically generated datasets, which provide no inherent guarantee that the parameters learned will remain consistent under unseen loading conditions. In some cases, can result in non-physical outcomes, such as negative material parameters that violate basic principles. In the literature, the systematic integration of physical-guided neural network strategies into the training process is still limited [145]. Song et al. [146], for example, employed physics-informed neural networks for the calibration of hyperelastic models from full-field data. By embedding equilibrium and constitutive relations directly into the loss function, their framework reduced the dependence on large numerical datasets and ensured that the identified parameters remained physically consistent even in the presence of noise. These results highlight the potential of physics-based strategies to mitigate the risk of obtaining non-physical solutions when extrapolating beyond the training domain. Addressing these issues through the integration of sequence-aware architectures and physics-guided training strategies defines the central motivation of Chapter 4 of this work.

2.3.2 Data-Driven Material Modeling

A higher level of integration of machine learning into constitutive modeling involves the use of artificial neural networks to represent material behavior without relying on predefined constitutive equations. In this fully data-driven framework, ANNs are trained directly on experimental or synthetic data to approximate the stress–strain behavior, bypassing the need for explicit symbolic formulations. The main advantage of this approach lies in the flexibility of ANNs as universal function approximators, capable of capturing highly nonlinear relationships and being continuously refined as new data become available [31]. However, this flexibility comes at the cost of interpretability, since as the learned parameters have no direct physical meaning and of robustness, as purely data-driven models may fail to extrapolate reliably beyond the range of training data [15].

As shown in Figure 2.18, two main types of data can be used to train ANN-based constitutive models: experimental and synthetic. Both fall under the category of direct supervised learning, but differ in motivation and data requirements. In the first case, shown in Figure 2.18a, the training data is obtained from mechanical tests and full-field measurements, making this approach particularly suitable when there is limited prior knowledge about the material. However, building robust models from experimental data alone requires a sufficiently large dataset, which is typi-

cally limited by the cost and complexity of testing. In addition, standard tests often assume uniform stress and strain states, limiting data diversity and typically covering only one-dimensional behavior [147]. In the second approach, shown in Figure 2.18b, synthetic data are generated by sampling from classical constitutive models using numerical simulations. The main objective is to train surrogate neural networks that reproduce the behavior of the reference constitutive model in a computationally efficient manner, thereby accelerating FEA simulations. Although the training data are numerical, their physical relevance still depends on the experimental calibration of the underlying models. Although powerful, surrogate approaches inevitably inherit the assumptions of the reference model used to generate the training data. This constrains their ability to reveal new material mechanisms. Nevertheless, these approaches show promise in bridging multiple length scales because knowledge embedded at one scale can be transferred to construct effective models at higher scales [15].

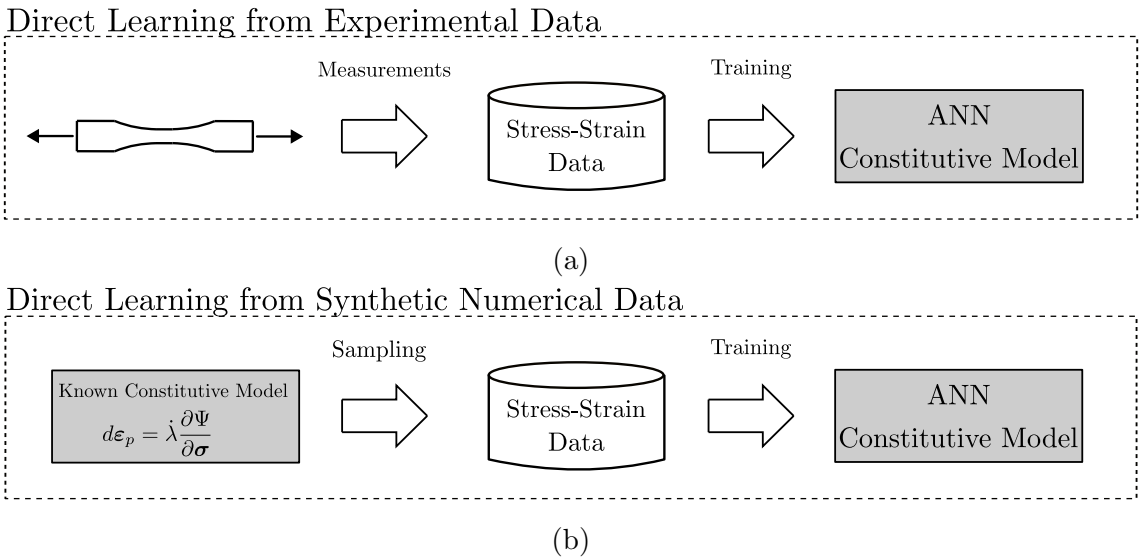


Figure 2.18: Sources of training data for ANN-based constitutive modeling.

A complementary strategy is indirect learning [148], which leverages numerical simulations in combination with experimental data. In this case, the network is not trained directly on stress–strain data, but instead updated iteratively by minimizing discrepancies between finite element method (FEM) predictions and experimental observations. This incremental framework allows for the use of rich structural test information, though it relies heavily on the consistency of simulations and experiments. While promising, this line of research will not be the focus of this thesis.

2.3.2.1 Data-Driven ANN Models from Experimental Data

The first application of ANNs for constitutive modeling based on experimental data was presented by Ghaboussi et al. [14; 149]. In [149], the behavior of concrete under plane stress was characterized using feedforward neural networks trained on biaxial monotonic and uniaxial cyclic loading tests. Two modeling strategies were proposed. In the stress-controlled formulation, the network predicts the strain increment based on the previous stress and strain history together with the current stress increment. In the strain-controlled formulation, the network predicts the stress increments based on the previous stress and strain history together with the current strain increment. The latter is particularly relevant for finite element implementations. The trained networks showed good generalization to unseen monotonic loading paths, although performance was limited for low-stress cyclic paths. The follow-up work [14] introduced the nested adaptive neural network (NANN), a structured FNN that learns variable-length stress–strain paths using a hierarchical training approach, which was applied to geomaterials. The model was able to reproduce stress–strain responses in drained conditions, while showing larger deviations for undrained cyclic loading tests. While this model enabled the learning of complex time-dependent behavior, its size and computational cost grew with sequence length, restricting it to short loading histories. Nonetheless, the architecture anticipated later developments in recurrent neural networks [15].

In the field of metal plasticity, Furukawa and Yagawa [150] developed one of the earliest implicit constitutive models based on the state space method, where a feedforward neural network was trained on input-output data generated from the Chaboche viscoplastic model. The ANN-based model was able to reproduce the stress-strain curves within the training domain, but showed limited extrapolation capability beyond the training domain. Gorji et al. [151] trained FNNs on synthetic data from the Zerilli-Armstrong model and J2 plasticity using over 900 simulated loading paths across strain rates, temperatures and biaxial stress states. The networks reproduced the reference stress–strain curves with errors below 1% and achieved good agreement in validation tests, including notched tensile simulations with deviations under 7%. Similarly, du Bos et al. [152] trained FNNs to map entire strain paths to stress responses in a single pass, rather than incrementally. Using a relatively small dataset of 100 synthetic curves and validating against 2000 additional cases, the networks achieved mean errors below 3 MPa, although accuracy decreased for low-amplitude strain paths. Despite these limitations, their approach

showed promising results in reverse loading scenarios, highlighting the need for richer datasets to improve generalization.

In the context of hot forming, neural networks have been used to learn complex hardening and softening behavior from high-temperature experimental tests. These processes involve multiple nonlinear phenomena such as work hardening, dynamic recovery and recrystallization, all of which are strongly dependent on temperature and strain rate. For example, Kessler et al. [99] developed an FNN model for 6061 aluminum using high-temperature deformation data and successfully implemented it in commercial FE software for virtual forming simulations. Similar ANN approaches have been proposed for steels [153–155], aluminum alloys [99; 156], titanium and magnesium alloys [157; 158].

Direct learning from experimental data is typically based on standard mechanical tests conducted under homogeneous and nearly proportional loading conditions. However, real parts often experience heterogeneous deformation paths that fall outside the domain of the training data [15]. In such situations, purely data-driven models have been shown to reproduce well the behavior within the calibrated range but to lose accuracy when extrapolated to unseen loading paths [152]. To overcome this limitation, hybrid strategies have been proposed, in which experimental data is complemented by numerically generated data and physical constraints are embedded directly into the neural network architecture. These approaches aim to enhance generalization and reduce impossible or outliers solutions while maintaining the adjustability of data-driven models. An example of such a hybrid approach was presented by Pandya et al. [159], who developed a machine learning model based on FNNs to predict the plastic and fracture behavior of the aluminum alloy AA7075. The model was trained on a combination of experimental and synthetic data covering tensile, notched, central-hole and shear tests performed at different temperatures. Compared to a modified Johnson–Cook formulation, the ANN-based approach achieved superior performance, particularly in the post-necking regime and at elevated temperatures, where the Johnson–Cook model failed to reproduce the observed softening behavior.

2.3.2.2 Data-Driven Surrogate ANN Models from Synthetic Numerical Data

To develop constitutive surrogates, neural networks are trained using data generated from numerical simulations of a reference constitutive model. Once trained, the neural network surrogate model is used to replace the reference model in numerical

FEA simulations with the goal of speeding up the simulation process [160]. This acceleration is particularly valuable in the early stages of design, where many iterations are required and computational efficiency is critical. For example, surrogate models can reduce simulation times for large FEM problems from several hours to a few minutes, enabling faster exploration of design alternatives. As the design progresses, however, high-fidelity physics-based constitutive models remain necessary to provide more accurate and comprehensive results. In this sense, surrogate models are best understood not as replacements but as complementary tools that accelerate and support conventional modeling strategies. Surrogate constitutive models have been implemented with different neural network architectures. Feedforward networks are commonly used for direct stress–strain approximations, while CNNs are better suited for handling full-field data and RNNs for capturing history-dependent behavior.

Feedforward Neural Networks for Constitutive Modeling

Feedforward neural networks have been extensively applied as surrogate models to replace classical constitutive formulations in finite element simulations. When trained on synthetic datasets generated from reference material models, FNNs are capable of approximating complex stress–strain responses without the need for explicit yield surfaces and hardening rule equations. This data-driven strategy offers a flexible and computationally efficient alternative, especially in early-stage design or multiscale simulations. Early applications focused on rate-dependent and cyclic behavior in materials such as concrete and steel. Jung and Ghaboussi [161] proposed a rate-dependent FNN model for viscoelastic behavior, trained on synthetic data from creep and relaxation tests. Their network incorporated strain, stress and strain rate information from multiple previous time steps to predict the current stress rate and was validated against experimental data from reinforced concrete beams. Yun et al. [162] extended this approach by including internal variables to model cyclic hysteresis. Both studies demonstrated that FNNs could outperform earlier constitutive models based on ANNs in both accuracy and implementation flexibility within FEM frameworks.

More recent developments have addressed more complex material behaviors, such as multiaxial plasticity and microstructure-sensitive deformation. Bessa et al. [32] used FNNs to learn the hyperelastic response of 2D composites based on representative volume elements (RVEs), comparing their approach to Gaussian process models

and emphasizing the role of uncertainty quantification and design of experiments. Zhang and Mohr [93] proposed a neural surrogate for von Mises plasticity with isotropic hardening, which predicts the apparent stiffness matrix without assuming any explicit flow rule or yield surface. While their model accurately captured large-strain multiaxial behavior, the transition between elastic and plastic regimes had to be smoothed manually, which could lead to approximation errors in yield point prediction. Jang et al. [163] further explored the potential of FNNs by replacing the classical stress-integration scheme of J2 plasticity under isotropic hardening with a neural model. The network was trained to predict the stress response directly from strain inputs, allowing its integration into finite element simulations without relying on conventional numerical solvers. In validation tests, including single-element uniaxial tension and circular cup drawing, the FNN-based model showed excellent agreement with reference results.

Although FNN-based surrogate models offer promising alternatives to classical constitutive formulations, their practical implementation still faces several challenges. One of the major limitations is the large amount of data required to properly train the networks. For example, Zhang and Mohr [93] observed that achieving accurate predictions for J2 plasticity at strain levels up to 20% required the generation of tens to hundreds of thousands of training samples. Similarly, Huang et al. [164] developed a 3D neural surrogate using over 8100 simulated loading paths, but limited their dataset to monotonic loading due to the impracticality of collecting sufficient unloading data.

When it comes to computational efficiency, several studies have demonstrated that neural network-based surrogates can significantly accelerate simulations. Jang et al. [163], for example, reported a speed-up of about 11% compared to the reference constitutive model, while Stoffel et al. [165] achieved a reduction of nearly 50% in total simulation time by introducing a simplified FNN-based integration scheme. Even larger gains have been reported in computationally intensive contexts, such as polycrystal plasticity, where constitutive neural networks can reduce the cost of multiscale simulations by orders of magnitude [166]. An exception is the work of Huang et al. [164], who found that their ANN-based surrogate was slightly slower than the analytical constitutive law in both 2D and 3D benchmark problems. This was attributed not to the ANN framework itself, but to the proposed integration scheme.

Convolution Neural Networks for Constitutive Modeling

Convolutional neural networks are increasingly used for constitutive modeling in solid mechanics, especially in multi-scale and microstructure-informed frameworks. Unlike traditional neural networks that treat each input independently, CNNs can exploit spatial correlations, making them well suited for learning mechanical behavior from image-based or graph-based representations of materia In this context, CNNs are typically employed to map microstructural descriptors, such as voxelized grain orientations, binary phase distributions, or crystallographic connectivity, into homogenized stress responses, local stress fields, or energy functionals [15].

An early contribution in this field was made by Frankel et al. [167], combining recurrent neural networks with 3D convolutional layers to predict the homogenized stress response of oligocrystalline materials. The model used both the strain history and a 3D voxelized image encoding the initial grain orientations as input, demonstrating the feasibility of incorporating spatial and temporal features in constitutive learning. To overcome the resolution and noise limitations of voxel-based data, Vlassis et al. [168] proposed a graph-based convolutional neural network for modeling elastic energy functionals in polycrystals. In their formulation, the microstructure is represented as a graph in which nodes correspond to individual grains and edges reflect crystallographic connectivity. This graph-based structure allows the model to preserve essential symmetries, such as frame indifference and rotational invariance, while improving learning efficiency. Yang et al. [169] explored the use of CNNs to learn homogenized stress-strain curves from two-dimensional binary images of composite microstructures under uniaxial loading. Trained on a dataset of 100000 synthetic microstructures, their model achieved good predictive accuracy, with mean absolute errors below 10% of the data range for key mechanical properties such as modulus, strength and toughness, demonstrating the ability of CNNs to integrate microstructure-sensitive features into constitutive predictions. Mianroodi et al. [170] presented a U-net-based [171] CNN architecture designed to be used as a surrogate for spectral solvers. The model was trained to map 2D patches of local material properties to corresponding von Mises stress fields and achieved remarkable efficiency gains - over 100 times faster for elastic and over 8000 times faster for elasto-plastic problems - while maintaining good accuracy over heterogeneous microstructures.

Despite these promising results, most CNN-based approaches rely exclusively on synthetic datasets generated from numerical simulations and their validation

against experimental microstructural data remains limited. Moreover, 3D convolutional models are computationally demanding, particularly at high resolution, while CNNs alone cannot capture loading-path dependencies, often requiring integration with recurrent layers. Nevertheless, by bridging microstructural information with macroscopic responses, CNN-based constitutive models offer a powerful and efficient framework to capture complex heterogeneous material behavior.

Recurrent Neural Networks for Constitutive Modeling

Several authors [172–176] have recently shown that recurrent neural networks can be particularly useful for modeling path-dependent plasticity, since plastic deformation of materials is a history-dependent process. Unlike FNNs, RNNs are designed to handle sequences and can incorporate data from past inputs into future predictions in a way that allows more easily to increase the deepness of the ANN due to history-dependent hidden states represented in the network structure. In an RNN, the input layer processes data from the current time step, while the recurrent connections allow the transfer of information across time steps. Consequently, the current output, $\boldsymbol{y}_t$, is influenced not only by the current input, $\boldsymbol{x}_t$, but also by all previous inputs, $\boldsymbol{x}_{t-i}$, where $i \in [0, t]$. The history-dependent hidden states can be used, for example, to emulate plastic strains and backstresses in plasticity.

Well-established recurrent neural network architectures, such as long short-term memory and gated recurrent units, have been applied to various aspects of constitutive modeling. Chen [177] used LSTM networks to model viscoelastic material behavior under infinitesimal strain. Similarly, Shah and Rimoli [178] developed an LSTM-based surrogate model for the representative unit cell to predict the dynamic response of large, arbitrarily heterogeneous structures. In the context of granular materials, Zhang et al. [179] proposed an LSTM-based approach to characterize the cyclic behavior of sand under both drained and undrained conditions. Their model consisted of two separate LSTM networks, one for strain-controlled behavior and another for stress-controlled behavior. Trained on synthetic data, the model accurately reproduced the behavior of real sands under cyclic loading, as validated by experimental results. Qu et al. [180] extended this work by incorporating physically interpretable variables into GRU models to simulate granular media. Focusing on plasticity at large deformations, Gorji et al. [175] introduced and evaluated GRUs as an alternative to traditional physics-based mathematical models. Their model, trained on single-element simulations using the Yld2000-2d yield criterion and homo-

geneous anisotropic hardening model, was tested under various conditions, including arbitrary multiaxial loading paths and unit cell analyses of two-dimensional foams. Abueidda et al. [173] compared different sequence models for predicting strain and temperature dependent behavior and further proposed the use of temporal convolutional networks, which offer reduced training times due to their non-recursive structure. In the context of multiscale modeling, GRUs have been used to reproduce the homogenized mechanical behavior of battery cells [181]. In addition, Hu et al. [182] used RNNs trained on microstructural evolution in PCA-compressed latent spaces to accelerate phase field simulations.

While LSTM and GRU networks have shown promise results in constitutive modeling, they were originally developed for very different tasks, such as speech recognition [57; 183]. When adapted to constitutive applications, RNNs naturally encode internal variables that resemble state variables. However, these internal representations often lack physical interpretability and are difficult to constrain. For example, the GRU model used by Gorji et al. [175] used over 200 internal variables, although the underlying phenomenological model used only 10. This redundancy arises because increasing the number of trainable parameters inevitably expands the state space. To address this limitation, Bonatti and Mohr [184] proposed the Minimal State Cell (MSC) architecture, specifically designed for constitutive modeling. Unlike GRUs or LSTM, MSCs compress the number of state variables to physically meaningful values that closely match those of the corresponding reference models. Despite this significant reduction, MSCs retain high predictive accuracy while using an order of magnitude fewer trainable parameters than conventional GRUs/LSTMs. This makes them more interpretable and significantly more efficient.

Another major challenge of standard RNN-based models is the lack of self-consistency with respect to the temporal discretization of the input strain history. The predicted stress response should converge as the strain history is refined and ideally be invariant under different discretizations of the same continuous path. To address this issue, Bonatti and Mohr [185] proposed the Linearized Minimal State Cell (LMSC) architecture, which guarantees consistent predictions across different temporal resolutions and is thus suitable for explicit FE analyses with adaptive time stepping. In their study, an isotropic von Mises elastoplastic model with Swift hardening model was considered. The training data comprised 10000 random multiaxial strain paths, with an additional 1000 paths for validation. Each path was first built as a piecewise-linear curve with 125 segments and then re-sampled to create datasets with different numbers of increments $m \in \{125, 250, 500, 1000, 2000\}$.

Results showed that, unlike conventional RNNs (e.g., GRUs) whose errors increased as the increment size decrease, the LMSC maintained self-consistency and achieved mean-squared errors on the order of 10^{-3} for smooth trajectories not seen in training. However, the evaluation focused on average error measures and global responses. Therefore, no explicit analysis of outliers or extreme local errors was reported, which remains important because localized inaccuracies can compromise FE stability even when mean errors are small.

A further limitation, common to most ML-based constitutive surrogate models, is that the trained networks are inherently material dependent, meaning the trained models are only applicable for the same material that the training data was originally obtained from. To address this issue, Heidenreich et al. [186] proposed a transfer learning framework for RNN-based plasticity models. By reusing weights from previously trained networks, their approach substantially reduced the amount of data needed for new materials. Although still recent and preliminary, these results highlight the potential of transfer learning to enable the construction of robust and efficient RNN-based constitutive models from small and possibly experimental datasets.

Physics-Guided Neural Networks for Constitutive Modeling

ANNs have shown considerable success in capturing complex constitutive behavior, especially in modeling nonlinear and history dependent material responses. However, ANNs suffer from several critical limitations. They often require large and diverse datasets to achieve robust generalization and typically operate as black-box models, providing little to no insight into the underlying physical mechanisms. More importantly, they do not inherently enforce essential physical principles such as energy conservation or thermodynamic consistency [16; 187]. As a result, their predictions may become unreliable when applied to loading scenarios beyond those encountered during training, limiting their applicability in extrapolative contexts.

At the same time, their main strength lies in their high flexibility as universal function approximators, since they can, in principle, represent arbitrarily complex constitutive relationships if sufficient data is available. This trade-off between flexibility and physical reliability is summarized in Figure 2.19, which contrasts different modeling paradigms. Traditional physics-based constitutive models occupy the upper left corner, being interpretable and robust but less flexible. Purely data-driven models, such as deep ANNs without constraints, lie at the lower right, offering

maximum flexibility at the expense of interpretability. Between these extremes are physics-guided models, which seek to combine the strengths of both paradigms by embedding physical knowledge into data-driven frameworks.

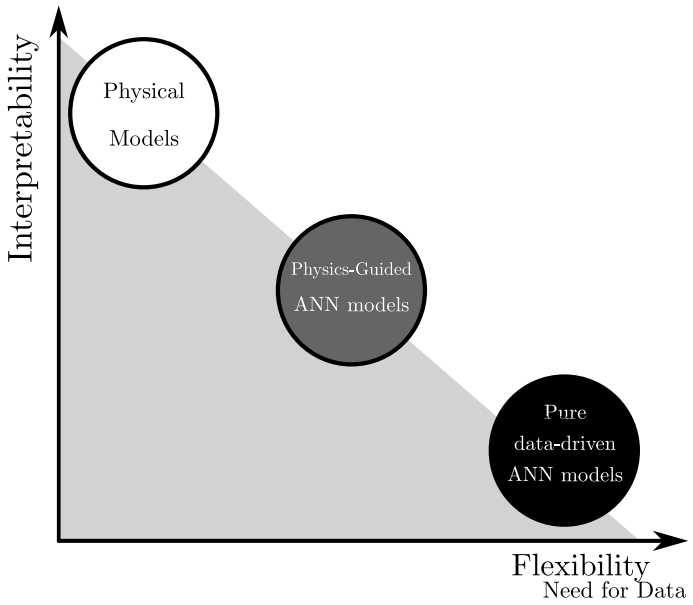


Figure 2.19: Schematic representation of modeling strategies in constitutive mechanics based on their interpretability and data requirements; adapted from [15].

Raissi et al. [187] introduced the concept of physics-informed neural networks, which embed governing physical laws directly into the training process. Instead of relying solely on empirical data, PINNs incorporate differential equations, boundary conditions and other physical constraints into the loss function. A common strategy is to formulate the loss function to include terms that penalize violations of conservation laws, energy balance or dissipation inequalities. By penalizing outputs that violate these constraints, the learning algorithm is guided toward solutions that are not only accurate with respect to the data, but also consistent with fundamental physical laws. The advantages of integrating physics into learning are that models typically require less training data than purely black-box approaches and that their predictions are more reliable in extrapolative settings, as they more directly include mechanisms to help enforcing consisting values.

Thermodynamics-based neural networks (TANNs), proposed by Masi et al. [16], represent a subclass of PINNs that explicitly enforce the first and second laws of thermodynamics during training. In these models, the balance of energy and the dissipation inequality are defined as:

$$\boldsymbol{\sigma} = \frac{\partial \Psi}{\partial \boldsymbol{\varepsilon}}, \tag{2.63}$$

$$\Phi = -\sum_{i=1}^{N} \frac{\partial \psi}{\partial \zeta_i} \dot{\zeta}_i, \tag{2.64}$$

where Ψ denotes the Helmholtz free energy potential, $\boldsymbol{\sigma}$ is the Cauchy stress tensor, $\boldsymbol{\varepsilon}$ is the strain tensor, Φ is the mechanical dissipation rate and ζ_i are kinematic internal variables. The network architecture proposed consists of two coupled feed-forward neural networks: the first predicts the increments of the internal variables, while the second estimates the energy potential at the next time step. Stress and dissipation are then computed from the network outputs using automatic differentiation. During training, the dissipation rate is constrained to be non-negative, ensuring consistency with the second law of thermodynamics. In benchmark tests, the authors demonstrated that this thermodynamics-based formulation outperforms conventional black-box FNNs, providing superior generalization and accuracy even under loading conditions not included in the training data.

Borkowski et al. [160] proposed a hybrid RNN-based surrogate model for multiaxial plasticity that incorporates physics-informed constraints via regularization. The architecture combines GRUs with FNNs to predict stress and plastic power from strain histories. A key innovation of their approach is the inclusion of a physics-based regularization term in the loss function, specifically designed to enforce non-negative plastic power throughout the deformation process. This constraint ensures compliance with the second law of thermodynamics, improving the physical consistency of the model.

Other research directions have explored incorporating physical structure in alternative ways. Vlassis et al. [188] developed an ANN model that includes a yield surface and plastic flow rule by representing the surface as a time-evolving level-set function in stress space. While this approach offers interpretability, it depends on prior knowledge of the initial yield surface, an assumption that may not be practical when using experimental data. Xu et al. [189] proposed a symmetric positive-definite neural network (SPD-NN) that guarantees the generation of admissible stiffness tensors by satisfying Hill's criterion, time consistency and convexity of the strain energy function. Their framework showed excellent performance across elasto-plastic, hyperelastic and multi-scale material systems.

Discussion

To fully realize the potential of data-driven constitutive modeling in both academic and industrial settings, several challenges remain open. A primary limitation is the generalizability of neural network models, which remains highly dependent on the availability, quality and variety of training data. Although recent efforts have focused on the development of heterogeneous experimental tests [190] capable of capturing material behavior under continuous strain path changes, these datasets are still insufficient to support robust model training across the full range of loading conditions encountered in practice. As a result, most applications reported in the literature rely on surrogate models trained on synthetic data generated from classical constitutive formulations, rather than on purely experimental datasets.

An alternative strategy for training models directly from experiments is indirect learning, in which constitutive relations are identified using only experimentally measurable quantities such as displacements and forces. Its application to constitutive modeling remains very limited and only recently has it been extended to recurrent neural networks by Lourenço et al. [191], who coupled GRU-based RNNs with the virtual fields method. Their framework enables training directly from full-field DIC data without requiring stress labels. While promising, particularly for experimental integration, the study also reported numerical instabilities in finite element implementations, highlighting the need for further developments to ensure robustness in practical applications.

Complementary to such data-driven approaches, another major challenge is the integration of physical knowledge into the training process. While incorporating thermodynamic consistency or known constitutive behavior can improve model reliability and reduce unphysical consistent predictions, it often comes at the cost of reduced model flexibility. Finding the optimal trade-off between purely data-driven learning and regularization is in the loss function remains an open and highly problem-specific question.

The introduction of self-consistent neural architectures, such as the LMSC, marks a significant step forward in modeling history dependent material behavior. These models have shown promising results in ensuring path-independent predictions across different time discretizations, a property that is particularly important for integration into explicit finite element simulations. However, several key issues regarding their applicability in the context of sheet metal materials remain unexplored. To date, most LMSC-based studies have been limited to von Mises yield criteria com-

bined with isotropic hardening laws. Extending these approaches to capture more complex anisotropic behavior, especially in AHSS, where anisotropy and Bauschinger effects play a critical role, remains unexplored. Equally important is the validation of LMSC-based models in realistic sheet metal forming applications. Beyond single-element tests, their performance must be assessed in finite element simulations of stamped components, where static and dynamic formulations and different increment sizes can strongly affect accuracy and stability. Addressing these gaps, along with practical aspects such as, type and representativeness of training data, the comparative impact of training strategies and the role of hyperparameter selection on convergence stability and generalization performance, defines the central motivation of Chapter 5 of this work.

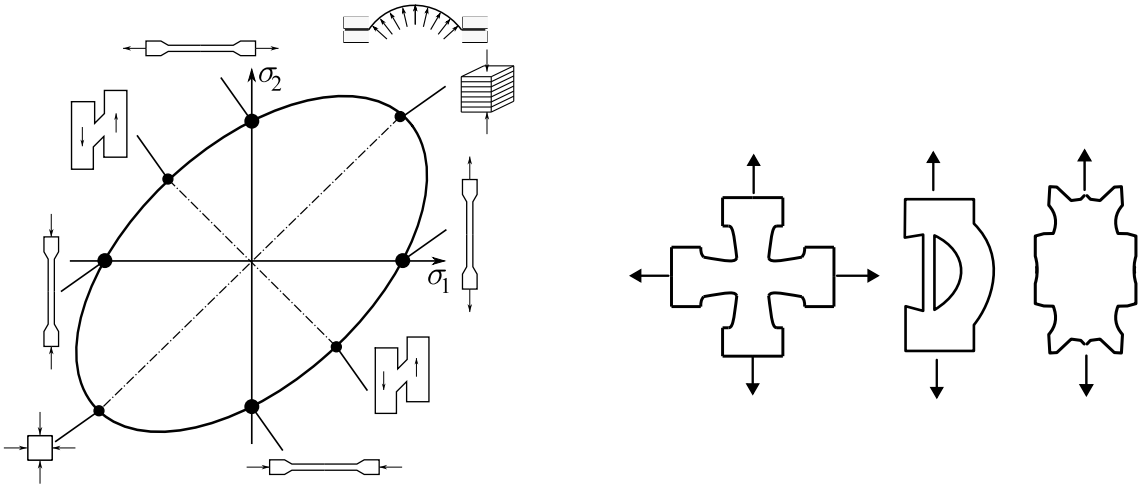
Chapter 3

Experimental Work for Material Characterization

To support the development and calibration of advanced constitutive models, experimental methods must be capable of capturing material behavior under both simple and complex loading conditions. With the increasing use of ML techniques in material modeling, the need for large and high quality experimental datasets has become even more critical, since building robust predictive models requires extensive databases containing detailed information on the mechanical response of materials under different loading paths. Therefore, a substantial amount of accurate and representative experimental data is essential for the development of state-of-the-art data-driven constitutive models [15]. In recent years, significant advances in experimental mechanics have led to more accurate, efficient and data-rich experimental strategies. Among these, digital image correlation [29] has emerged as a key technique. DIC provides full-field, non-contact and high-resolution strain measurements, making it particularly suitable for capturing complex deformation patterns. Unlike traditional point-based methods such as strain gauges or extensometers, which provide only localized data, DIC provides continuous strain fields over the entire sample surface [192].

Experimental characterization of metallic materials typically involves inducing plastic deformation under different stress states, as shown in Figure 3.1a. These include uniaxial tension, uniaxial compression, plane-strain tension, equal-biaxial tension and simple shear, allowing a detailed evaluation of the yield surface and its evolution with plastic strain. In addition, material anisotropy can be evaluated by testing specimens at different angles relative to the rolling direction. In these classical tests, the strain field is generally assumed to be homogeneous, which simplifies the analysis and allows straightforward extraction of stress-strain relationships under well-defined loading conditions. However, extracting a comprehensive set of constitu-

tive parameters from a single homogeneous test is challenging. As a result, multiple tests under different loading conditions are typically required to fully calibrate a single constitutive model [23]. While classical tests remain fundamental, their limitations in parameter identification have motivated the development of heterogeneous mechanical tests that are better suited for calibrating advanced constitutive models, particularly in the context of modern data-driven strategies [193]. These tests are specifically designed to induce non-uniform strain fields within a specimen through the use of optimized geometries or boundary conditions, allowing a wider range of stress and strain states to be captured in a single experiment [194]. When combined with DIC, heterogeneous testing enables the simultaneous identification of multiple constitutive parameters, significantly reducing the number of tests required. As represented in Figure 3.1b various geometries have been proposed to maximize strain diversity and improve parameter identification [195]. These developments are part of a growing movement in experimental mechanics known as the Material Testing 2.0 paradigm [196]. This approach emphasizes the design of high-information tests that integrate heterogeneous loading conditions, full-field strain measurements and inverse identification methods.



(a) (b)

Figure 3.1: Mechanical tests for material characterization: (a) examples of monotonic homogeneous tests along with the corresponding stress states in the principal axes (σ_1–σ_2); (b) examples of specimen geometries used in heterogeneous mechanical tests [193; 194; 197].

To improve the efficiency of experimental characterization, robotic mechanical testing is being integrated into materials testing. Robotic experimental setups

equipped with advanced full-field measurement techniques can perform a wide range of mechanical tests with minimal human intervention, significantly increasing performance while ensuring high quality data acquisition [198].

In parallel with these advances, the use of miniaturized specimens in mechanical testing has gained increasing attention. The mechanical behavior of engineering materials is typically determined by experimental tests using the so-called "macro specimens", with dimensions in the scale of millimeters. However, in some applications, the material to be characterized is not available in the form of large blocks [199], which has recently motivated an increasing interest in evaluating the mechanical properties of materials with "miniaturized" specimens, also known by other names such as "small-size", "sub-size", or "mini" specimens [200; 201]. Miniaturized specimens were first developed in the 1970s to characterize materials for in-service nuclear reactor pressure vessels [202]; this is an application in which surveillance capsules are used to periodically monitor the degradation of vessel materials. These capsules typically have limited storage space and for this reason, a limited specimen size is required [203]. As a result, Small Specimen Testing Technology (SSTT) has been developed and applied in different application fields such as residual life assessment of in-service components [204], local properties measurement in the welding industry [205; 206], additive manufacturing process [207; 208] and mechanical properties evaluation of miniature devices, such as microelectromechanical systems (MEMS) [209; 210].

Several non-standard test techniques are currently available to evaluate the mechanical behavior of materials using miniaturized specimens [201]. One of the most used SSTT is the miniaturized tensile test (MTT) [211], which uses specimens with dog-bone geometry with nominal dimensions ranging from several millimeters to hundreds of microns. No standards have yet been established for MTT, which has resulted in different specimen designs. The design of miniaturized specimens currently uses one of two approaches: (1) simply scaling down from standard specimens; or (2) scaling down from standard specimens, with a subsequent adjustment of some dimensions. A comprehensive and complete review about this topic can be found in the recent work of [200].

Miniaturized tensile testing encompasses several challenges related to specimen manufacturing, handling and procedural issues. In addition, the miniaturization may cause the so-called "specimen size effect", which leads to different behaviors at the miniaturized and macro scales. Specimen size effects can be categorized into two different levels. At the first level, the test results obtained from miniaturized

specimens reflect the bulk mechanical properties described by continuum mechanics. However, for some materials, the results may deviate from standard specimens and additional data processing techniques, e.g., the inverse finite element method, are required [212–214]. On the other hand, at the second level, the specimen can no longer reflect the bulk properties as the thickness or diameter is further decreased. Typically, the critical thickness value is defined by the ratio t/d between thickness, t and grain size, d, of the material. Generally, miniaturized specimens with a t/d ratio between 6 and 10 can achieve standard bulk behavior.

In sheet metal forming processes, it is crucial to characterize the material behavior not only under monotonic loading but also under strain path changes, particularly in scenarios such as reverse loading and cross-loading. Reverse loading refers to the reversal of the loading direction along the same axis, as in tension-compression tests [215] or reverse-bending cycles [216]. This type of loading is essential for capturing phenomena such as the Bauschinger effect, permanent softening and stress differential (SD). In this context, various experimental techniques have been developed to characterize material behavior under reverse loading conditions. However, a significant challenge lies in performing compression tests on sheet metal, mainly due to the buckling of the specimens, which makes it difficult to obtain reliable and accurate data. Cross-loading, on the other hand, nvolves changing the loading direction. For example, it could mean switching from uniaxial tension to shear or applying the load at an angle relative to the original direction. This type of test usually requires extracting smaller specimens from a larger original sample to study the material's behavior under different loading orientations. Therefore, the use of miniaturized specimens can play a key role in reverse and cross-loading experiments.

This chapter presents the experimental work performed for the mechanical characterization of three different advanced high-strength steels: DP500, DP600 and DP780. The experimental campaign included standard and well-established homogeneous mechanical tests, as well as the design and implementation of novel test setups specifically designed for reverse loading scenarios. This chapter is organized as follows. Section 1 provides a state-of-the-art review of the experimental techniques commonly used to characterize sheet metals, including standard test procedures, specimen geometries and measurement methods. Section 2 introduces the selected AHSS grades. Sections 3 and 4 present the experimental results obtained for these materials, covering both classical monotonic tests and reverse loading tests, which are critical for capturing material behavior under complex strain path conditions. Section 5 present the determination of the Young's modulus degradation

of the selected dual-phase steels. Finally, Section 6 summarizes the main results of the experimental work and discusses their relevance to the modeling approaches presented in the subsequent chapters.

One of the innovations presented in this chapter is the design and development of dedicated experimental testing devices. One of these is the *Miniaturized Sample Tester Device* (MSTD), a custom-designed experimental setup for testing miniaturized specimens. Equipped with a DIC system for full-field strain measurements, this device supports both monotonic and reverse loading conditions, including tension, compression and shear. It can also be used to evaluate Young's modulus degradation with plastic deformation. Additionally, a new experimental setup was developed to perform reverse bending tests providing valuable experimental data for the calibration of anisotropic hardening models. The experimental results presented in this chapter provide the basis for validating the numerical models introduced in the subsequent chapter.

3.1 Overview of Homogeneous Mechanical Tests

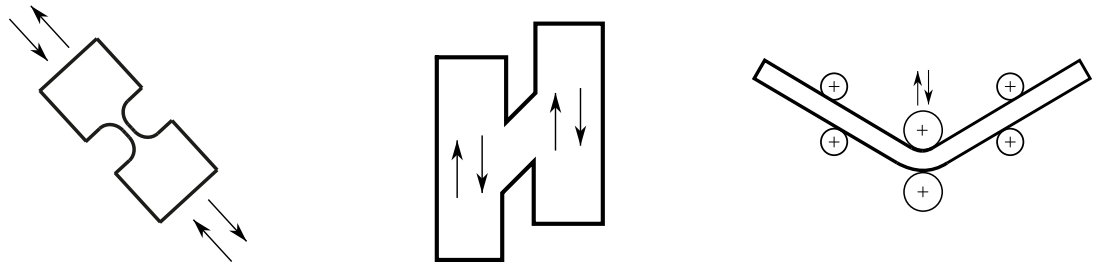
3.1.1 Monotonic Loading Tests

A large number of standardized tests have been established in the literature to obtain the experimental data required for calibrating advanced constitutive models. Some of these tests and their associated stress states in the principal stress axes (σ_1–σ_2) are illustrated schematically in Figure 3.1. In the first quadrant, the uniaxial tensile test is the most widely used, although it provides only one-dimensional stress data. Therefore, additional tests are needed to experimentally determine the remaining points of a yield locus. For biaxial tensile stress states, methods such as bulge, stack compression, or biaxial tensile tests can be applied. Shear and in-plane torsion tests are used to characterize the shear stress states, in the second and fourth quadrants. Finally, for the third quadrant, uniaxial and biaxial compression tests can be performed [217]. A comprehensive description of monotonic mechanical tests can be found in the Appendix A.

3.1.2 Reverse Loading Tests

As presented in Section 2.2.2.2, the description of Bauschinger behavior using a combination of isotropic and anisotropic hardening models has been shown to im-

prove the reliability of numerical predictions, particularly in cases involving springback. However, the accuracy of these material models strongly depends on the experimental testing methodology and the calibration procedure used to determine the constitutive parameters. Experimentally, parameter calibration is typically performed based on reverse strain path tests. Several experimental methods have been used to characterize load path changes in sheet metal materials [218]. However, there is no consensus on the best method, as each has its own advantages and disadvantages. These experiments can be divided into three main categories, as shown in Figure 3.2: (i) in-plane uniaxial tension-compression test; (ii) reverse shear test; and (iii) reverse bending test.



(a) (b) (c)

Figure 3.2: Different reverse loading tests: (a) tension-compression test; (b) reverse shear test; (c) reverse bending test.

The in-plane uniaxial tension-compression test is widely used to calibrate Bauschinger behavior due to its simplicity and popularity [219–221]. In this test, a sheet metal specimen undergoes uniaxial tensile loading followed by compression in the same direction using the experimental methods presented in Section A.4 to prevent buckling in the compression step. The main advantage of this test is the generally uniform strain distribution in the gauge region, which simplifies the determination of the material behavior. However, there are several challenges: on the one hand, the assumption of uniform material properties across the sheet thickness holds for thin sheets but becomes less accurate for thicker materials; on the other hand, necking during tensile loading limits the usable range of strain hardening curves, making it difficult to obtain stress-strain responses at high strain levels. Additionally, buckling during compression makes data interpretation more complicated and reduces the reliability of the results [222; 223].

The in-plane cyclic shear test, using the specimens described in Section A.5, is widely used to characterize the hardening behavior of sheet metals, especially to achieve large plastic deformations beyond the limits of conventional tensile testing

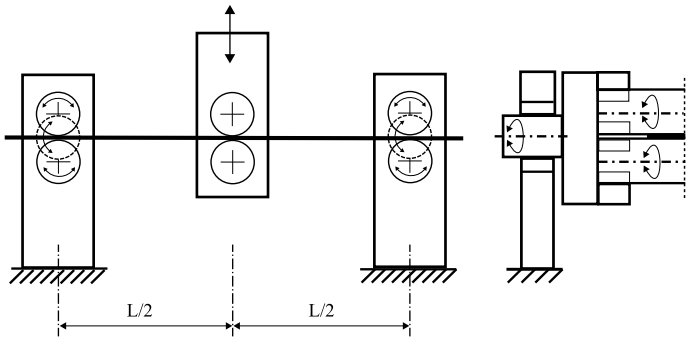


Figure 3.3: Bending-reverse bending test setup proposed by Omersphahic et al [216].

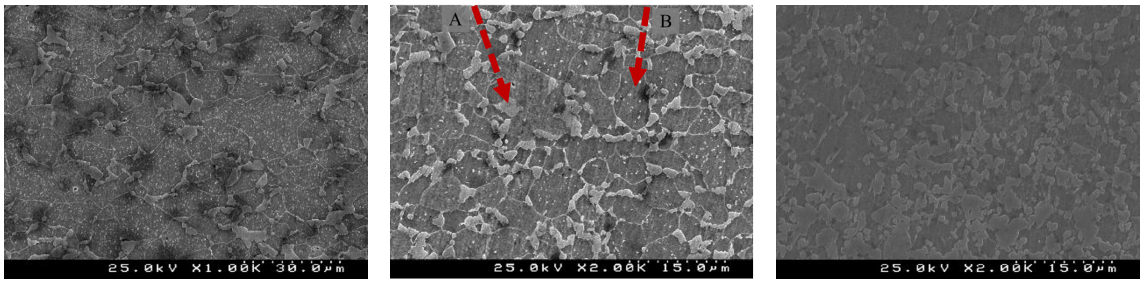
methods [224–226]. Lee et al. [227] used forward and reverse shear tests to obtain yield stress curves for different steel sheets. Similarly, Rauch et al. [228] validated a new work-hardening model using stress-strain responses derived from planar simple shear and reverse shear tests. Weiss et al. [229] achieved Bauschinger calibration at high strain levels using shear and reverse shear tests, highlighting the effectiveness of these methods compared to traditional tension-compression tests, which often encounter problems such as necking and buckling. Cyclic shear testing also presents several challenges: accurate measurement of local strain is difficult due to the narrow shear zones [230] and the stress-strain field can exhibit heterogeneity due to end effects and plastic deformation near specimen grips [231]. In addition, studies have identified the presence of normal stress components that can rival the magnitude of the shear stress, thereby affecting the pure shear state of the material. Neglecting these components can significantly affect the results, especially in determining equivalent stress-strain curves and identifying critical material parameters [224; 225].

In addition to the reverse shear test, the reverse bending test has gained attention for its relevance to sheet metal forming processes where bending deformation is predominant. This test is particularly valued for its ability to account for the non-uniform material properties across the sheet thickness resulting from rolling operations. Several researchers have investigated the applicability of the reverse bending test for identifying constitutive parameters in sheet metal forming and have proposed experimental setups tailored for this purpose. This test was first introduced by Yoshida et al. [232] using a uniform bending apparatus for cyclic loading. Later, Geng et al. [112] developed a three-point cyclic bending configuration, shown in Figure 3.3, which was later improved by Omerspahic et al. [216]. In this design, a moment-free support allows the plate to slide freely in the axial direction. During testing, the inner region of the plate undergoes compression-tension deformation,

while the outer region undergoes tension-compression [233]. Zang et al. [234] introduced an innovative alternative to evaluate the Bauschinger effect without cyclic loading, using pre-strained specimens subjected to three-point bending. In this configuration, the inner material undergoes tension-compression after bending, which influences the bending moment before springback. Compared to tension-compression and cyclic shear tests, reverse bending is less standardized, mainly due to the lack of direct stress-strain measurements under one-dimensional loading. As a result, inverse methods are typically required to extract hardening parameters from the load-displacement or moment-curvature curves [234]. However, the main advantage of this test lies in its deformation mode, which closely resembles real forming operations where the sheet is drawn over multiple die radii [235].

3.2 Materials

In this work, three dual-phase (DP) steel grades (DP500, DP600 and DP780) are considered, all supplied with an initial nominal thickness of 0.8 mm. These steels belong to the first generation of advanced high-strength steels and are known for their superior mechanical properties compared to conventional steels. Their unique combination of high strength, good formability and pronounced hardening behavior allows the production of thinner automotive components without compromising performance. In addition to these properties, DP steels also exhibit exceptional energy absorption capacity. Their microstructure, shown in Figure 3.4, consists of a soft ferrite matrix that provides ductility, combined with hard martensitic islands that contribute to strength [236]. The mechanical performance of DP steels can be tailored by adjusting the ferrite-to-martensite ratio and by grain refinement. The chemical composition of selected DP grades is given in Table 3.1.



(a) DP500 (b) DP600 (c) DP780

Figure 3.4: Initial microstructure obtained from SEM of the dual-phase steels. A - hard martensite phase; B - soft ferrite phase.

Table 3.1: Chemical composition of the dual-phase steels (DP500, DP600, DP780).

Element [%]	**C**	**Si**	**Mn**	**P**	**S**	**Cr**	**Ni**	**V**	**Cu**	**Al**	**Nb**	**B**	**N**
DP500	0.079	0.31	0.65	0.003	0.003	0.03	0.03	0.01	0.01	0.038	0.0	0.0003	0.003
DP600	0.089	0.20	0.85	0.014	0.004	0.03	0.03	0.01	0.01	0.046	0.019	0.0003	0.004
DP780	0.138	0.20	1.52	0.011	0.002	0.03	0.03	0.02	0.01	0.038	0.014	0.0002	0.003

Table 3.2 shows the measured average thickness values for each material. To account for possible thickness variations, measurements were taken at multiple locations across the material. A digital micrometer (Mitutoyo Digimatic) with an accuracy of 2 μm and a resolution of 0.001 mm was used and a total of 25 measurement points per material were considered to calculate the average sheet thickness. The average thicknesses of DP500 and DP780 were close to the nominal value of 0.8 mm. In contrast, the average measured thickness of DP600 steel was 0.817 mm, slightly above the nominal value. In addition to these average measurements, the thickness of each specimen was individually measured during the mechanical tests presented in the following sections.

Table 3.2: Thickness measurements (average, μ and standard deviation, σ) of DP500, DP600 and DP780 sheet metal samples.

	$\boldsymbol{\mu}$ [mm]	$\boldsymbol{\sigma}$ [mm]
DP500	0.802	0.004
DP600	0.817	0.007
DP780	0.801	0.007

3.3 Experimental Results for Monotonic Loading Tests

This section presents the experimental results obtained from different monotonic mechanical tests performed on DP500, DP600 and DP780 steel grades. The tests include uniaxial tension, compression and shear tests conducted using a specially designed testing device for testing miniaturized sheet metal specimens. In addition, bulge tests, disk compression and three-point bending tests are considered to characterize the mechanical behavior of the materials under biaxial and bending loading conditions. A detailed description of the experimental setups and procedures for all

these tests is provided in the Appendix A.

3.3.1 Uniaxial Tension and Compression Tests

To evaluate the monotonic mechanical behavior of the selected materials, macro-scale tensile tests were performed according to the ISO 6892-1 standard [237]. In addition, miniaturized specimens, shown in Figure 3.7b, were tested using the same materials. This miniaturized geometry allows for both uniaxial tensile and compression testing, offering a major advantage in compression by effectively minimizing buckling effects (see Section A.4). Five different loading conditions were defined for the macro specimens: 0, 22.5, 45, 67.5 and 90°, relative to the rolling direction. Miniaturized specimens were tested only along the rolling direction. The geometry of the macro specimens was obtained by machining a rectangular strip, while the miniaturized specimens were produced by wire electrical discharge machining (EDM).

Standard macro tensile tests were performed on a 300 kN Instron 5900R testing machine. Strain measurements were obtained using the digital image correlation technique by capturing images at a frequency of 20 Hz using a 5MP camera (Basler acA2440-75um) coupled with a high resolution lens (Fujinon HF50HB-1B, f2.3/50 mm). The commercial software VIC-2D.v6 was used to calculate the strain field, specifically the logarithmic strain, with a step size of 7 and a set size of 25 within a defined region of interest. Miniaturized specimens were tested using a miniaturized specimen tester device described in detail in Section 3.3.1.2.

Table 3.3: Experimental conditions for macro and miniaturized samples.

	Macro Sample	**Miniaturized Sample**
Number of samples	3	3
Gauge length (L_0)	50 mm	2 mm
Crosshead speed	5 mm/min	0.5 mm/min
Frequency for data acquisition	20 Hz	20 Hz
Temperature	23 °C	23 °C
Humidity	53 %	53%

The experimental conditions for both geometries are summarized in Table 3.3. All tests were performed at a constant rate, resulting in an initial strain rate of approximately $10^{-3}\ s^{-1}$, until the material failed. To ensure repeatability of results,

three specimens were systematically tested for each geometry. However, for a clear and simple analysis of the stress-strain curves, only one representative result is shown.

3.3.1.1 Uniaxial Tensile Results - Macro Samples

Figure 3.5 shows the engineering stress-strain curves obtained from uniaxial tensile tests and the corresponding true stress-strain curves for the three AHSS grades. All materials exhibit an initial region of pronounced strain hardening followed by a reduction in hardening rate as the maximum stress is approached, a behavior typical of dual-phase steels. Among the grades tested, DP780 has the highest yield strength but the lowest ductility. DP600, although stronger than DP500, has strain limits similar to those of DP500 and does not follow the usual rule of increasing strength and decreasing ductility that DP780 follows. Despite the differences in tensile strength, the true stress-strain curves show a relatively high slope at lower strains, indicating that these AHSS exhibit higher initial work hardening.

Table 3.4: Measured experimental anisotropy coefficients of dual-phase steels using DIC techniques.

Material	r_0	$r_{22.5}$	r_{45}	$r_{67.5}$	r_{90}	$\bar{r}$	Δr
DP500	0.971	0.888	0.851	1.002	1.110	0.946	0.190
DP600	0.695	0.783	0.935	0.899	0.811	0.844	-0.182
DP780	0.648	0.802	0.922	0.891	0.824	0.829	-0.186

The evaluation of true plastic strains and corresponding r-values was performed using the digital image correlation technique, following a standardized procedure. DIC allows high-resolution measurement of strain evolution in both the loading direction (ε_{11}) and the transverse direction (ε_{22}) within a predefined region of interest, thereby capturing the anisotropic behavior of the material. Figure 3.6 shows the experimental correlation between thickness strain ε_{33} and transverse strain ε_{22} for each material and loading direction during the tensile test. The data points are fitted using linear regression, with the slope of the fitted line providing the anisotropic r-value. These values, along with the calculated average normal anisotropy ($\bar{r}$) and planar anisotropy (Δr), are summarized in Table 3.4.

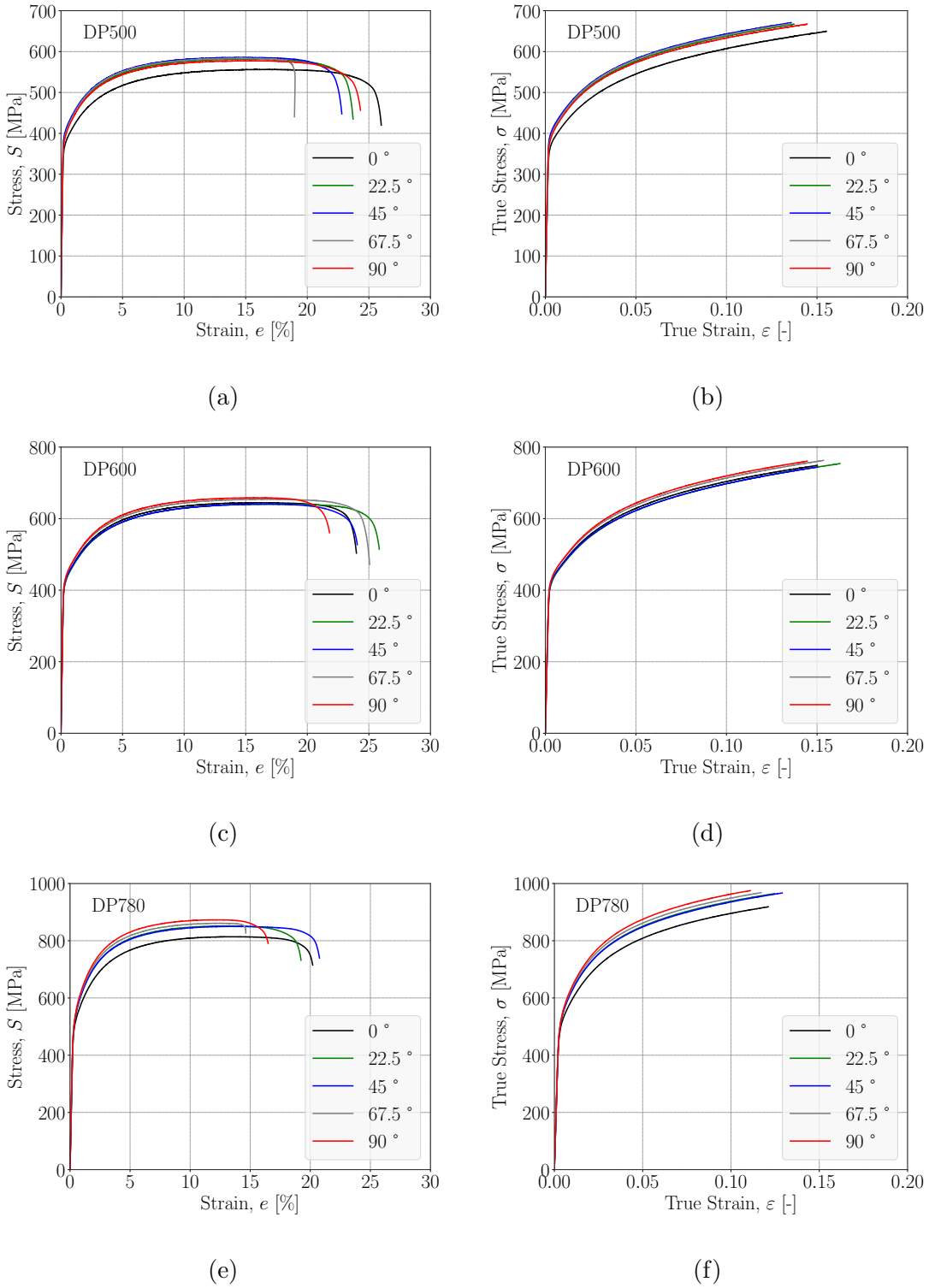


Figure 3.5: Experimental engineering stress-strain curves (left) and true stress-strain curves (right) considering different loading directions for DP500 (a-b), DP600 (c-d) and DP780 (e-f).

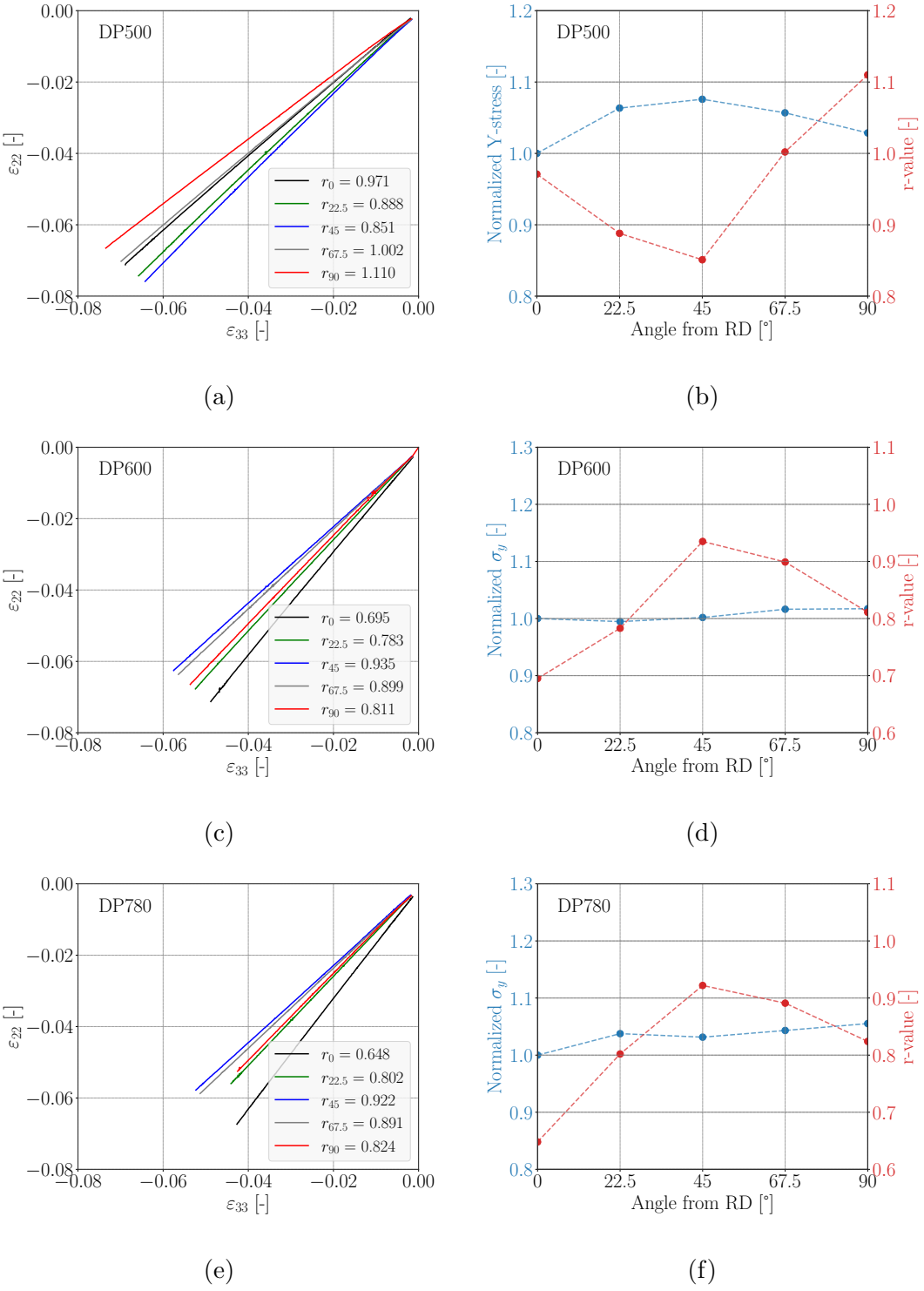
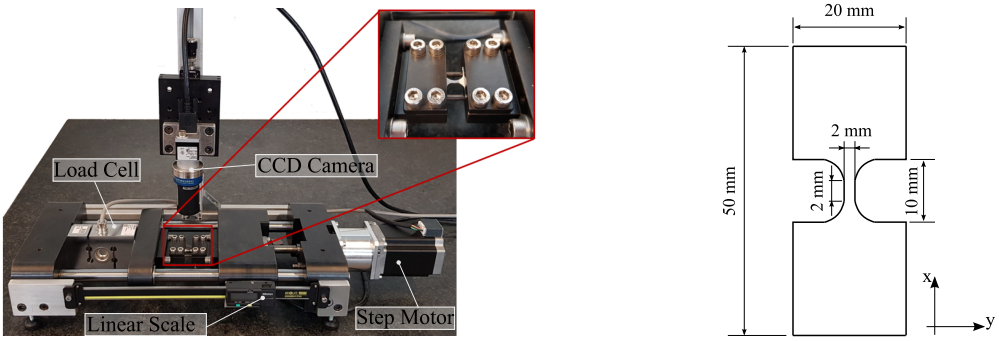


Figure 3.6: Evolution of transverse (ε_{22}) and thickness (ε_{33}) plastic strains considering different angles relative to the rolling direction for (a) DP500, (c) DP600 and (e) DP780 and corresponding anisotropic coefficients (r-values) and normalized stress values (σ_y) for (b) DP500, (d) DP600 and (f) DP780.

3.3.1.2 Development of an Uniaxial Test Equipment for Miniaturized Specimens

The experimental test procedure for miniaturized specimens followed a procedure similar to that typically used for conventional standard specimens, which is based on moving grips and results of force as a function of strain data. However, a very accurate procedure is required because the results can be significantly affected by the test protocol, including specimen preparation, test setup, experimental operation, measurements and data processing [200]. Several authors have emphasized different aspects to be considered when testing miniaturized samples [201]: (a) the importance of the specimen fabrication technique, which can affect the measured properties, especially the yield strength; (b) good control and accuracy of the specimen dimensions, which is directly related to the reliability and reproducibility of the test data; (c) high-quality measuring instruments and (d) the importance of a precise and well-aligned test frame to minimize the extraneous bending stresses.



(a) (b)

Figure 3.7: Miniaturized Specimen Tester Device: (a) MSTD setup and (b) geometry of the miniaturized specimen.

Based on these considerations, a new device has been developed that is specifically designed to test miniaturized specimens at a reduced scale and is defined as the *Miniaturized Specimen Tester Device* [238]. As shown in Figure 3.7, the MSTD consists of three groups of components with their well-defined functions. First, there is the "motor group", which includes a ball screw driven by a stepper motor that ensures continuous and precise movement of the specimen, thus guaranteeing a minimum displacement of 2 µm for each step of the motor. Secondly, there is the "frame group", which ensures the positioning and guidance of the various components and is composed of four linear bearings sliding on two ground shafts. Finally,

there is the "instrumentation group", consisting of a 5 kN "S" type load cell and two extension measurement components - a linear ruler for measuring and controlling the positioning of the moving table and a digital image correlation system. The MSTD layout allows all components to be on a common plane, which is advantageous for precise specimen alignment during testing. This minimizes the occurrence of unwanted bending moments, especially in compression, which is also essential to prevent specimen buckling. Designed to test miniaturized specimens, the equipment can withstand a maximum axial force of 2.5 kN.

In miniaturized tensile testing, specimen preparation is crucial because miniaturized specimens are more susceptible to large dimensional variations. Accordingly, in this work, the specimen profile was obtained by EDM using a 0.25 mm wire diameter. This process is widely used to fabricate miniaturized specimens, resulting in good dimensional accuracy and surface finish [200].

Choice of the optical technique for strain measurement

The DIC technique was coupled with the mechanical tests to quantify the deformation of the material over the central region of interest for both macro and miniaturized specimens with an appropriate spatial resolution and accuracy at the scale of observation. Traditionally, when performing experimental tests (*e.g.*, macro tensile test [237]), the strain components are measured using a strain gauge attached to the specimen. However, for miniaturized specimens, these instruments may not be suitable due to the reduced specimen size. Therefore, a non-contact optical technique can be used to conveniently access full-field strains over the target region. For this purpose, several white light and interferometric optical methods have been proposed in the literature [239]. Among them, DIC has been increasingly used in recent years in the field of experimental solid mechanics [240; 241]. This technique was introduced in the 1980s [29; 242] and allows the measurement of full-field kinematic quantities by tracking unique features on images taken at different stages of deformation, typically using a subset-based approach [192; 243–245]. The DIC technique uses a camera-lens optical setup and allows variable sensitivity and resolution in strain measurements. Since the DIC method uses digital images, several high spatial resolution digital devices can be used for image acquisition. For example, DIC can be coupled with Optical Microscopy (OM) [246; 247], Scanning Electron Microscopy (SEM) [248; 249], Scanning Tunneling Microscope (STM) [250] to realize deformation measurement from the microscale to the nanoscale. In the 2D DIC

setup, the planar surface of a sample is imaged strictly parallel to the camera sensor and the surface must have a random pattern of contrasting speckle pattern. The creation of a quality pattern for DIC at reduced scales can be challenging [251] and the accuracy of the measurements is highly dependent on the spatial resolution of the imaging system [192].

Optical system and speckle pattern

A 2D DIC setup using a 5 MPixel CMOS digital camera was selected in this work. The mounted lens was chosen with respect to the sample size. The details of the camera-lens system used for the miniaturized experiments are summarized in Table 3.5. In this case, a telecentric lens was selected in contrast to a standard 50 mm focal length lens (Fujinon HF50HB-1B, f2.3/50 mm) used for the macroscopic tensile tests. It had the advantage of keeping the image magnification unchanged during the mechanical test, thus avoiding artifacts due to, for example, Poisson effects or slight out-of-plane movements during the test. In this case, the undeformed image was focused by setting the working distance to 63.3 mm with a magnification factor of 1×. Images were acquired during the tests at a frame rate of 5 Hz. The central part of the samples was first painted by spraying a thin layer of white paint to uniform the diffuse reflectivity of the surface. The final speckle pattern was then created by applying dark paint using an airbrush (Evolution Silverline Solo) with a 0.2 mm nozzle set. Considering the region of interest and the camera-lens system, an average speckle size of about 6 pixels (21 µm) was obtained in the speckle quality evaluation. According to international guidelines [252], this means that a subset size larger than 21 pixels (0.075 mm) or 31 pixels (0.111 mm) must be used in DIC measurements for accuracy.

Selecting DIC setting parameters

When performing DIC measurements, a convergence analysis must be performed for the parameters inherent in the numerical imaging method [253; 254]. The set of DIC parameters plays an important role in the spatial resolution and accuracy associated to both displacement and strain measurements [255]. Therefore, a parametric analysis was performed in this study using the performance analysis tool of the MatchID subset-based 2D DIC software [256]. The parametric tool allows multiple DIC analyses to be performed on the same set of images by considering multiple combinations of parameters, as listed in Table 3.6. Each relevant parameter was

Table 3.5: Camera-lens optical system for the miniaturized tests.

Camera	Basler acA2440-75um, 5 MPixel, CMOS sensor
Pixel resolution	2448 px × 2048 px
Lens	Opto Engineering TC 23 09
Field of view	8.8 mm × 6.6 mm
Magnification factor	1 ×
Working distance	63.3 mm
Image conversion factor	3.5 μm/px
Image acquisition frequency	5 Hz
Speckle pattern technique	Airbrush (nozzle set of 0.2 mm)
Average speckle size	6 px | 21.5 μm

considered over an appropriate design space by defining minimum and maximum values and a step of an integer increment (i.e. a subset size with a minimum of 21×21 pixels^2, a maximum of 91×91 pixels^2 and an increment of 10 pixels, Table 3.6). The results in terms of signal evaluation at the center of the sample can then be discussed in the light of the preselected DIC setting parameters. The linear strain component in the x direction (ε_{xx}) was used as a reference since uniaxial tests were performed along this axis. Each set of DIC parameters can be associated with a corresponding spatial resolution. To quantify this metric, the following Virtual Strain Gauge (VSG) measure was used [252; 256]:

$$\text{VSG} = [(\text{StW} - 1) \times \text{ST}] + \text{SS} \quad [\text{pixels}] \tag{3.1}$$

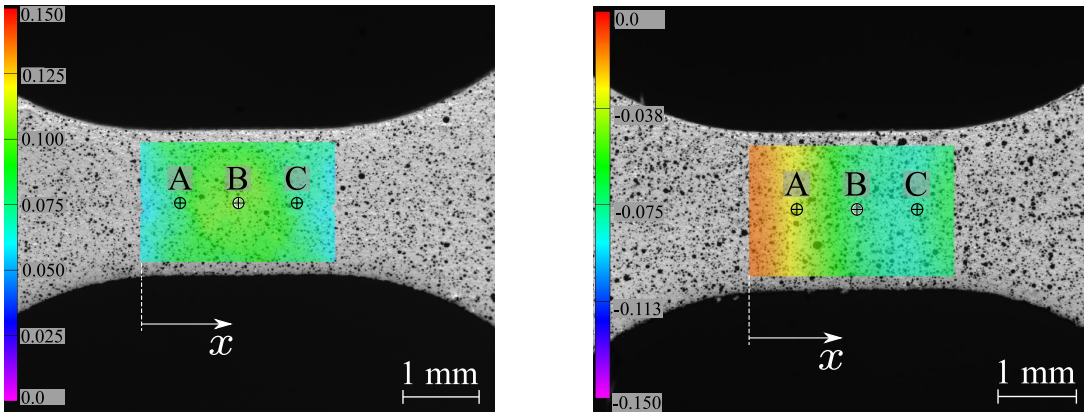
where StW stands for a strain window, *i.e.* the number of displacement data points used to fit a local polynomial in the neighborhood of the subset centroid under evaluation, ST is the subset step and SS is the subset size. The VSG can be expressed in physical units of millimeters if the image conversion factor of the optical system is taken into account (Table 3.5).

Table 3.6: Parameters used in the Performance Analysis Tool of MatchID 2D DIC.

Subset-based settings	
Subset size	SS $\in \{21, 31, 41, 51, 61, 71, 81, 91\}$ px
Subset step	ST = 10 px (fixed)
Shape function	{Affine, Quadratic}
Strain reconstruction-based settings	
Strain window	StW $\in \{3, 5, 7, 11, 13, 15, 17, 19\}$ data points
Polynomial order*	Bilinear (Q4), Biquadratic (Q8)
Strain convention	Green–Lagrange

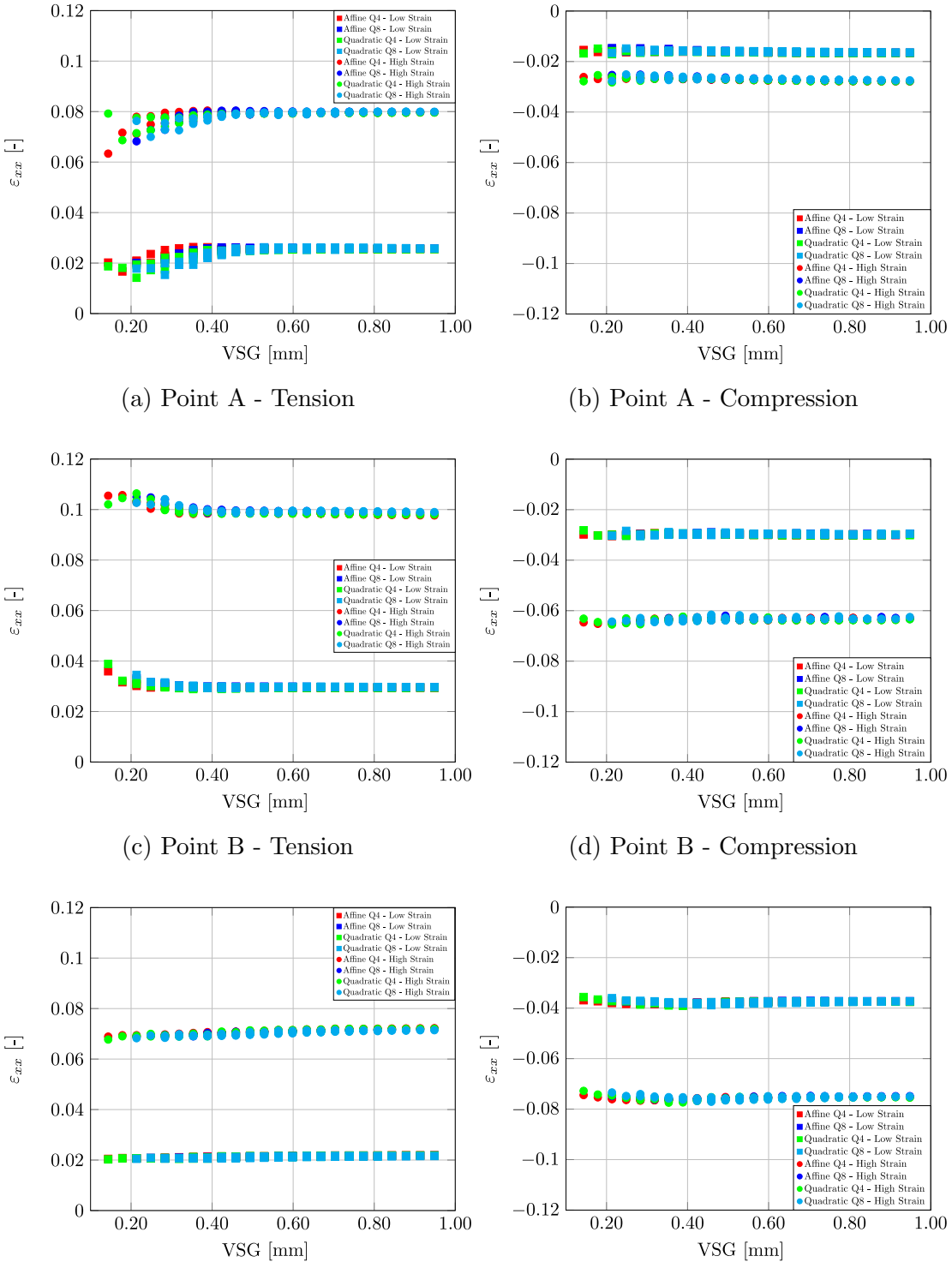
* Local least-squares fitting approach for the strain evaluation.

In order to evaluate the ε_{xx} strain signal with respect to the DIC settings as a function of the VSG, three reference points in the center of the specimen were systematically analyzed for both tensile and compression tests for the DP500 steel, as schematically shown in Figure 3.8.



(a) Tension (b) Compression

Figure 3.8: Points of reference used in evaluating the reconstruction of the ε_{xx} strain signal with regard to the DIC settings and as a function of the VSG for both: (a) tension and (b) compression tests.



(a) Point A - Tension

(b) Point A - Compression

(c) Point B - Tension

(d) Point B - Compression

(e) Point C - Tension

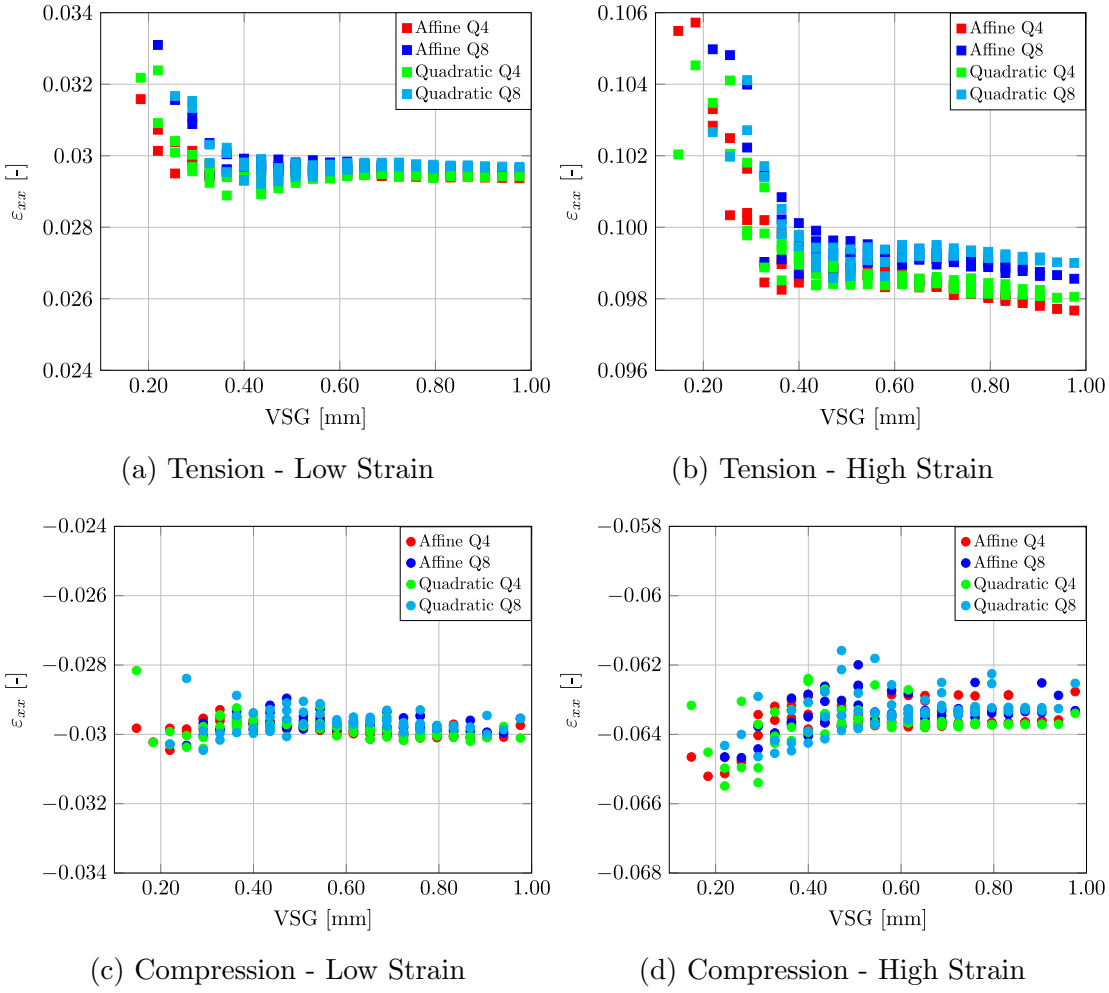
(f) Point C - Compression

Figure 3.9: Evaluation of ε_{xx} for point A, B and C (Figure 3.8) as a function of DIC parameters expressed with regard to Virtual Strain Gauge (VSG) for both tension and compression tests, at two stages of deformation corresponding to low and high strains.

Figure 3.9 shows the evolution of ε_{xx} as a function of VSG for points A, B and C (Figure 3.8)) for both tensile and compression tests at two different deformation stages corresponding to low and high average strains, respectively. It can be observed that the DIC setting parameters systematically converge to an average linear strain reconstruction. In a more local analysis, Figure 3.10 shows the results of the reconstructed ε_{xx} value at point B in the center of the specimen (see Figure 3.8) as a function of VSG, for the different DIC setting parameters for both tensile and compression tests and for two stages at low and high strain values, respectively. A good balance between spatial resolution and strain field reconstruction can be found. As can be seen in all scenarios, the signal is quite stable with respect to a number of parameters. This is to be expected for a homogeneous material and a uniaxial loading configuration. Figure 3.11 shows a complementary analysis plotting the ε_{xx} value along the coordinate x at the center of both the tensile and compression tests, for several VSG values. It can be seen that the DIC setting corresponding to higher VSG values shows a smooth signal evaluation, as expected, in contrast to lower VSG DIC settings. In conclusion, from the analysis in this work, the DIC settings reported in Table 3.7 were finally selected in a suitable balance between spatial resolution and accuracy of results for the current application. For the reconstruction of the strain signal during the mechanical tests, an average value was systematically calculated at the centre of the specimen corresponding to a region of 2 mm $\times$ 2 mm.

Table 3.7: DIC and strain settings selected in the full-field measurements.

DIC Settings	
Correlation criterion	ZNSSD
Interpolant	Bicubic spline
Subset shape function	Affine
Subset size	71 px
Step size	10 px
Image pre-filtering	Gaussian, 5 px kernel
Strain Settings	
Strain window size	9 data points
Strain interpolation	Bilinear Q4
Strain convention	Green–Lagrange



(a) Tension - Low Strain

(b) Tension - High Strain

(c) Compression - Low Strain

(d) Compression - High Strain

Figure 3.10: Evaluation of ε_{xx} at point B (Figure 3.8) as a function of DIC parameters expressed with regard to Virtual Strain Gauge (VSG).

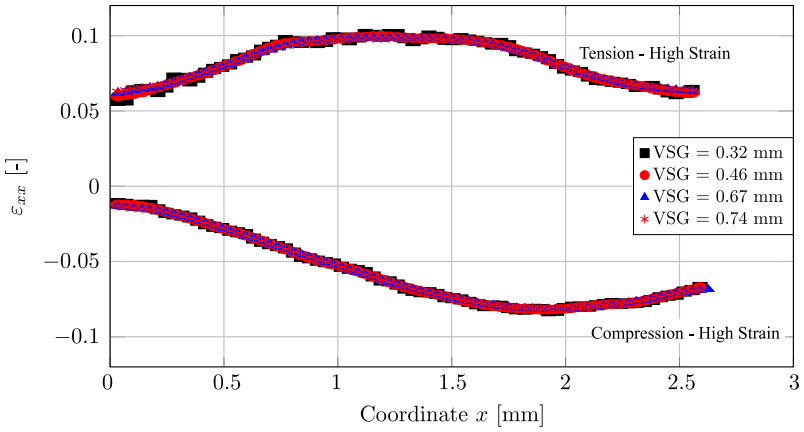
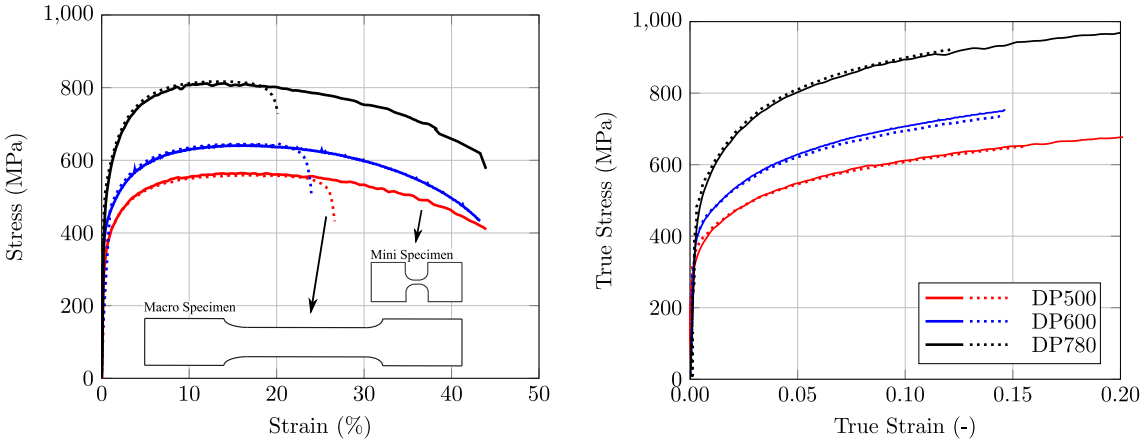


Figure 3.11: Evaluation of ε_{xx} as a function of the coordinate x for several Virtual Strain Gauge (VSG) values for both tension and compression tests.

3.3.1.3 Uniaxial Tension Results - Miniaturized Samples

The uniaxial stress-strain curves for the selected dual-phase steels (DP500, DP600 and DP780) are shown in Figure 3.12. For each material, the results obtained using mini (solid line) and macro (dotted line) specimens are shown. The engineering stress-strain curves, Figure 3.12a show that the results obtained for both geometries are very similar.



(a) (b)

Figure 3.12: Experimental curves obtained with macro specimens (dotted) and mini specimens (continuous lines) (a) engineering stress-strain and (b) true stress-strain curves for DP500, DP600 and DP780 materials.

Overall, the results of the miniaturized specimen are in very good agreement with the macro tensile test. However, it can be seen that after the point of maximum tensile strength, the miniaturized geometry shows a higher total strain compared to the macro geometry. This difference can be explained by the local necking that occurs after the point of maximum stress is reached, resulting in a localized strain zone whose size is independent of the gauge length. Therefore, for smaller gauge lengths, the localized strain has a greater effect on the total strain value. In addition, the variation in necking behavior should also be considered. As reported by [257], total elongation and post-necking elongation tend to increase with decreasing ratio, w/t, between specimen width and thickness. In fact, when w/t decreases, the shear deformation can occur in both the top (bottom) and side planes, resulting in complex stress distribution and the localized necking changes to diffuse necking, resulting in higher post-necking elongation.

Despite this difference, the elastic part and the hardening behavior are very

similar for both specimen geometries, as it can be seen from the true stress-strain curves shown in Figure 3.12b for the dual-phase steels. It can also be seen that it is possible to characterize the true stress-strain relationship for the same range of strain values obtained with macro specimens using mini specimens. However, for some materials (i.e. DP500 and DP780), the use of miniature specimens allows the hardening behavior to be characterized for higher strain values ($\varepsilon = 0.2$) compared to macro tensile specimens ($\varepsilon \approx 0.13$).

3.3.1.4 Uniaxial Compression Results - Miniaturized Samples

The hardening behavior of the dual-phase steels under compressive loading was also evaluated using the miniaturized specimens (Figure 3.7b). The true stress–strain curves for DP500, DP600 and DP780 are shown in Figure 3.13a-c, respectively. Additionally, each figure represents the tensile hardening curve obtained using miniaturized samples (curve defined by points). For an easy comparison with these two tensile curves, the compression results were reflected for the first quadrant and represented as a dashed line.

The results show that the work hardening behavior is similar under tension and compression for each of the three materials and no evident stress differential effect is observed. However, the maximum strain values in the compression test were lower than those reached in tension, as explained next. As seen in Figure 3.14, for a strain value close to 7%, the force reaches a maximum value. At this point, the test becomes non-planar and the buckling phenomenon becomes evident. This instability is translated in the decay of the stress, which means that the test is not longer valid.

In conclusion, the experimental results presented in this section provide a solid foundation for understanding the mechanical behavior of dual-phase steels under monotonic loading conditions. Tensile and compression tests conducted with miniaturized specimens demonstrate the reliability of the developed methodology for accurately characterizing materials. These results are an important reference for investigating reverse loading behavior and support the development of advanced constitutive models for dual-phase steels.

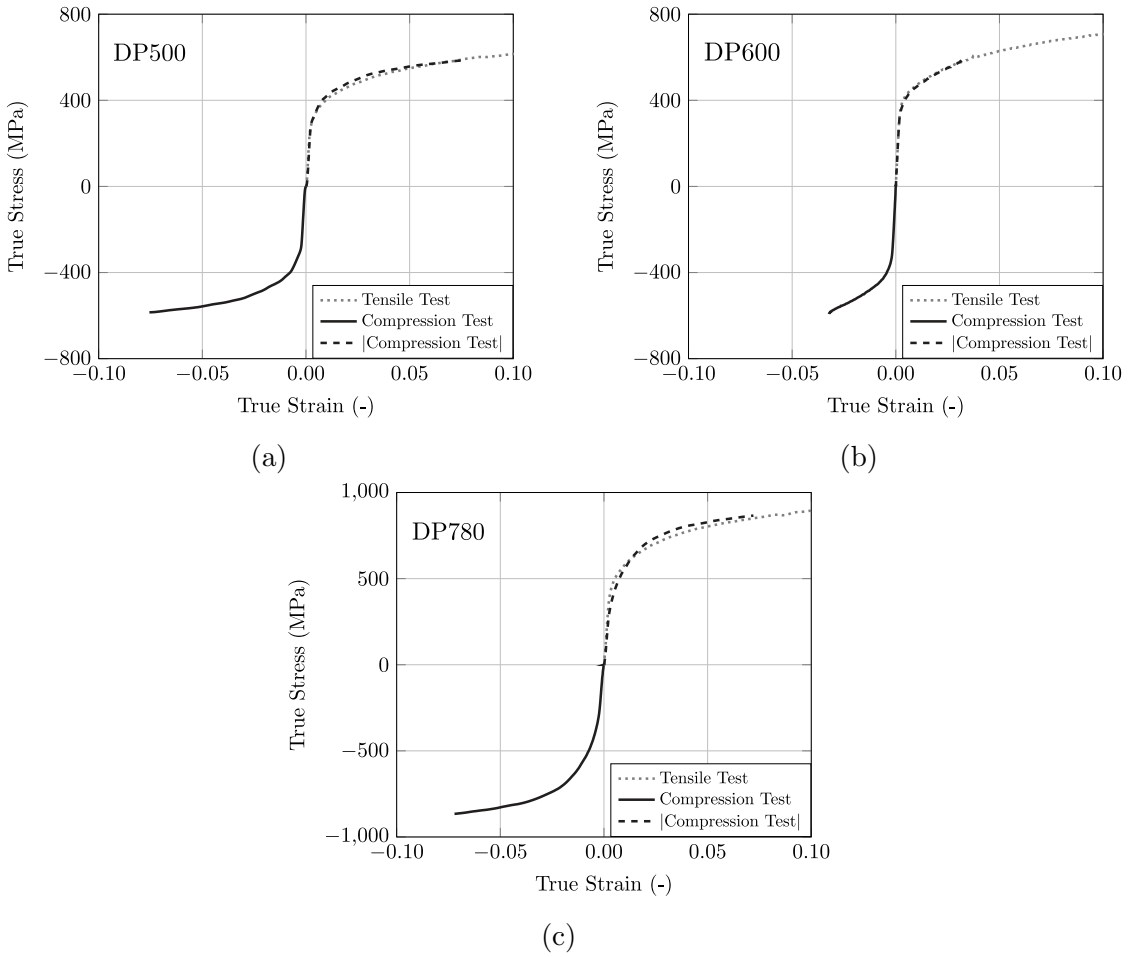


Figure 3.13: Miniaturized monotonic uniaxial compression test for (a) DP500, (b) DP600 and (c) DP780.

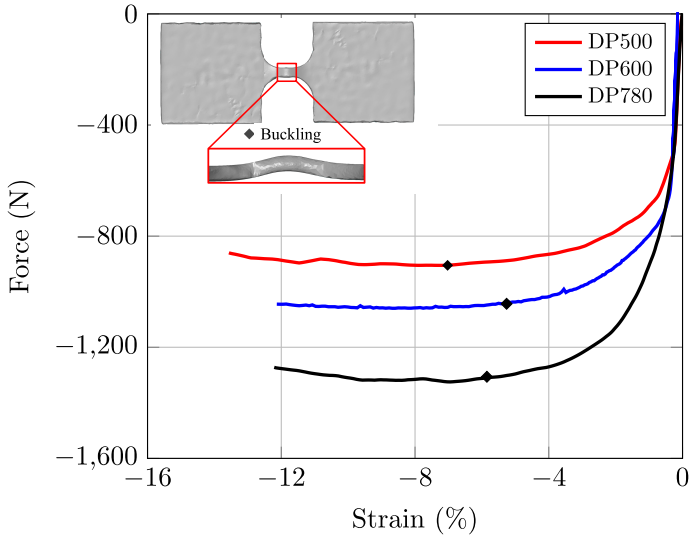
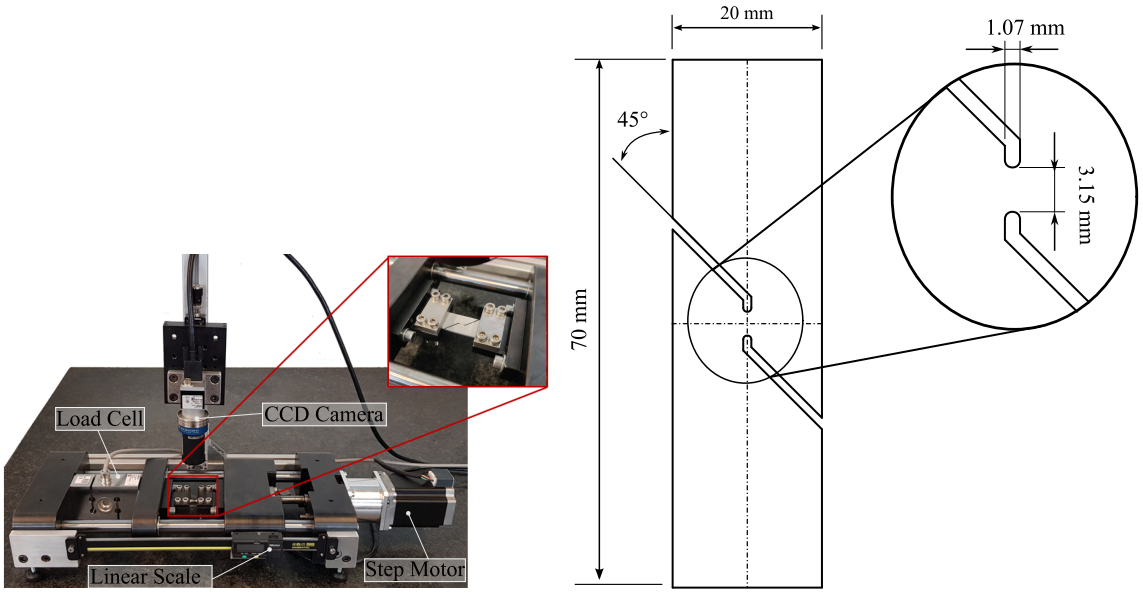


Figure 3.14: Representation of the point where buckling occurs in the uniaxial compression test.

3.3.2 Shear Test

The geometry used for the shear tests is a modified version of the standard ASTM B831–05 test geometry originally developed by Merklein and Biasutti [258] to perform monotonic and reverse shear tests. The geometry was adapted to be tested in the miniaturized specimen tester device described in Section 3.3.1.2 and shown in Figure 3.15a. As shown in Figure 3.15b, the shear zone of the specimen has an initial length of $l_0 = 3.15$ mm and a width of $b_0 = 1.07$ mm, giving a length to width ratio of 2.9:1 and a width to thickness ratio of 1.33:1 for the selected materials. The geometry was obtained by EDM and cut along the rolling direction of each material. The crosshead was set at a constant machine speed of 0.1 mm/min, corresponding to a shear strain rate of 0.001 s^{-1}. Three specimens were tested for each material to verify repeatability and a representative curve was selected for analysis.



(a) (b)

Figure 3.15: Illustration of the (a) Miniaturized Specimen Tester Device and (b) modified shear specimen.

The strain distributions within the shear zones were measured using the DIC technique, considering the same parameters as described in Section 3.3.1.2. The homogeneity of the strain distributions along two different directions in the shear zones is discussed next. As shown in Figure 3.16a, two different sections are considered: the longitudinal section, defined by points A and B and the transverse section, defined by points C and D. The homogeneity of the shear zone is evaluated for three

different levels of shear strains, ε_{xy}, of 0.1, 0.2 and 0.3 measured at point P, as shown in Figure 3.16b, 3.16c and 3.16d, respectively. Figure 3.17 shows the strain distributions (ε_{xy}, ε_{xx} and ε_{yy}) in both the longitudinal section (left-hand plots) and the transverse section (right-hand plots) for the DP500 material. Each strain variable is plotted along a normalized length, x/l for the longitudinal section and y/l for the transverse section. The reference point for x is point A and the reference point for y is point C.

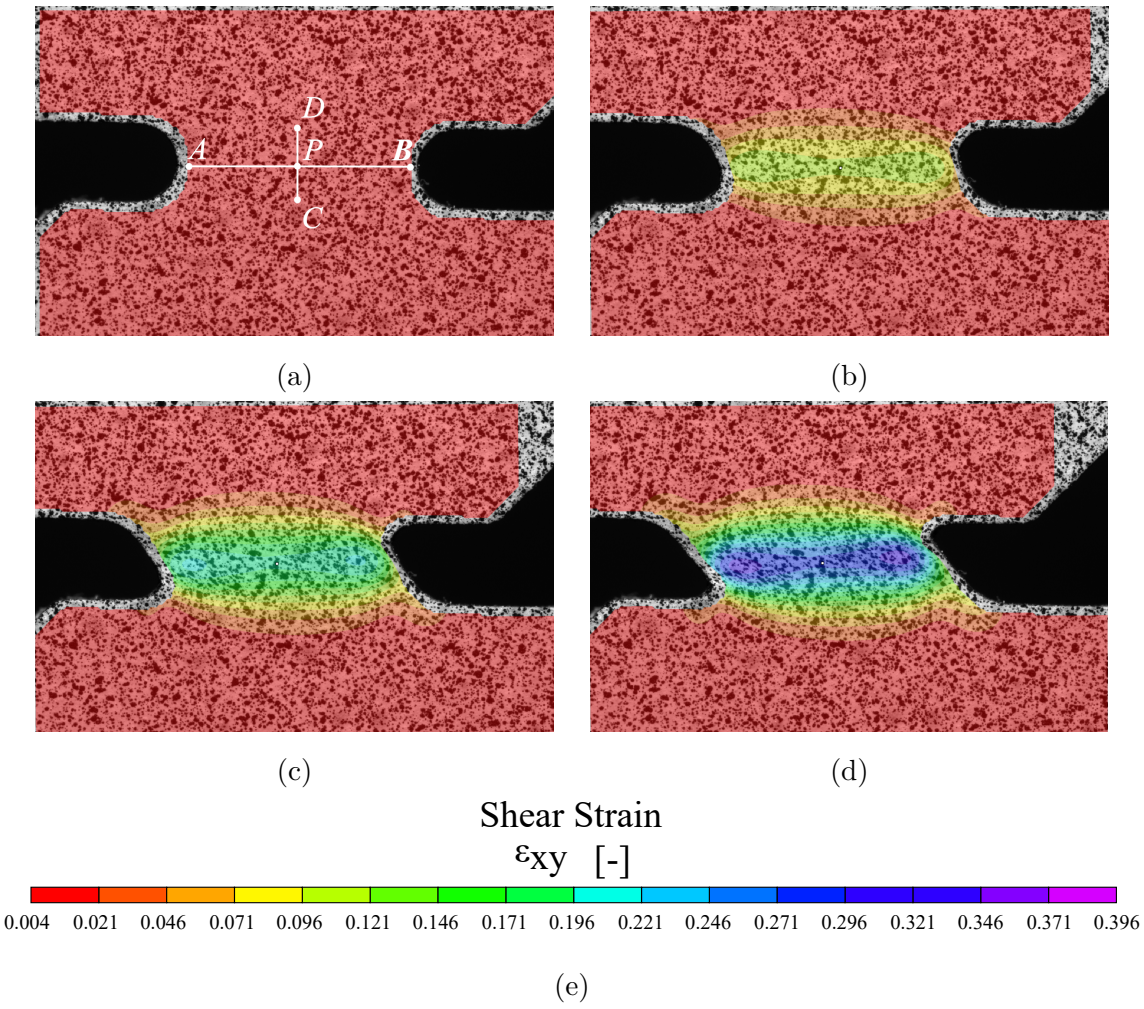
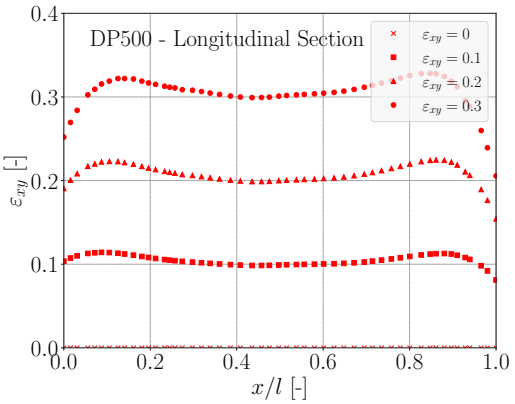


Figure 3.16: Schematic representation of (a) longitudinal (A-B) and transverse (C-D) sections used to analyze the homogeneity of strain distribution; shear strain distributions for different values of deformation at point P: (b) $\varepsilon_{xy} = 0.1$, (c) $\varepsilon_{xy} = 0.2$ and (d) $\varepsilon_{xy} = 0.3$.

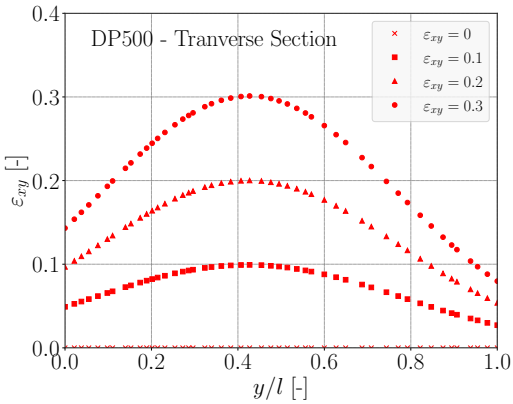
The results show that the strain distributions are approximately homogeneous in the longitudinal section, as shown in Figures 3.17a, 3.17c and 3.17e for ε_{xy}, ε_{xx} and ε_{yy}, respectively. For a relative distance of $x/l \approx 0.5 \pm 0.1$, corresponding to the

center of the longitudinal section the strain values are nearly homogeneous, but they begin to diverge outside this interval. It is also evident that the strain inhomogeneity in the longitudinal section increases with higher deformation levels, being smaller for a shear strain ε_{xy} of 0.1 and more pronounced for a shear strain of 0.3.

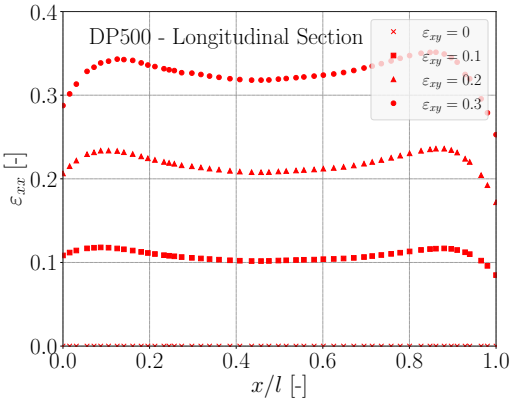
In the transverse section shown in Figures 3.17b, 3.17d and 3.17f for ε_{xy}, ε_{xx} and ε_{yy}, respectively, the uniformity of the strains is not so pronounced. The strain values increase rapidly from the edges and reach a maximum, in absolute values, in the centre of the analysis zone, corresponding to point D. This heterogeneity is also more pronounced at higher values of plastic deformation. In this section, the shear strain ε_{xy} is significantly greater than the normal strain components, ε_{xx} and ε_{yy}. This contrast is not observed in the longitudinal section. For each sections, the strain distributions along the xx and yy directions are very similar but have opposite signs. Finally, it can be seen that the shear strain, ε_{xy}, at the center of the shear zone is identical in the transverse and longitudinal directions, indicating that the specimens produce a shear deformation close to the ideal case.



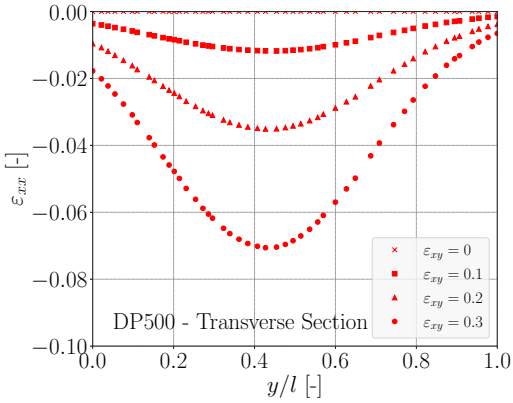
(a)



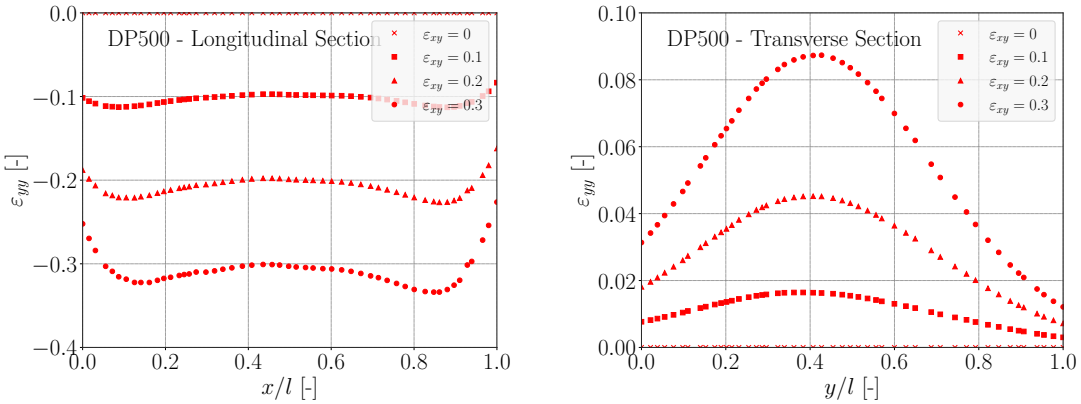
(b)



(c)



(d)



(e) (f)

Figure 3.17: Strain distributions (ε_{xy}, ε_{xx} and ε_{yy}) for DP500 material, considering the longitudinal section (a, c, e) and transverse section (b, d, f) at three different deformation levels.

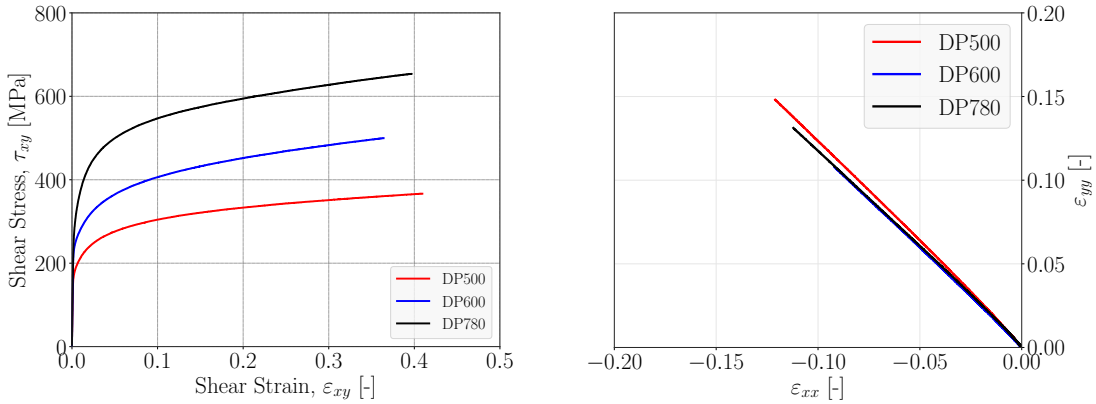
The experimental monotonic shear curves for the three considered materials are shown in Figure 3.18a. The shear strain evolution was obtained at point D as shown in Figure 3.16a, since the strain distribution is uniform in the central region of the specimen. The shear stress was calculated using Equation A.15. As expected, the stress-strain curves show similar trends, with DP780 having the highest shear strength and DP500 having the lowest. This type of specimen allowed characterization of the hardening behavior up to a shear strain ε_{xy} of about 0.4.

The equivalent plastic strain, ε_{eq}, corresponding to the shear strain levels reached in the tests, can be estimated using the von Mises plasticity criterion. According to this criterion, for a simple shear stress state, the equivalent strain is given by:

$$\varepsilon_{eq} = \frac{\gamma}{\sqrt{3}}, \tag{3.2}$$

where γ is the engineering shear strain, which, for simple shear loading, is related to the tensorial shear strain by $\gamma = 2\varepsilon_{xy}$. Therefore, for the maximum shear strain of approximately $\varepsilon_{xy} = 0.4$ achieved in these tests, the equivalent von Mises strain is approximately $\varepsilon_{eq} = 0.46$.

Finally, Figure 3.18b shows the evolution of the strain path at point D during the tests for all three materials. The results suggest that the selected shear specimen follows a nearly pure shear path, as the ratio between the principal strain components remains close to -1, i.e., $\varepsilon_{22}/\varepsilon_{11} \approx -1$.



(a) (b)

Figure 3.18: Experimental (a) monotonic shear curves (τ_{xy}-ε_{xy}) for the selected materials (DP500, DP600 and DP780) and (b) corresponding strain path evolution ($\varepsilon_{22}/\varepsilon_{11}$) during the test at the center point of the shear zone.

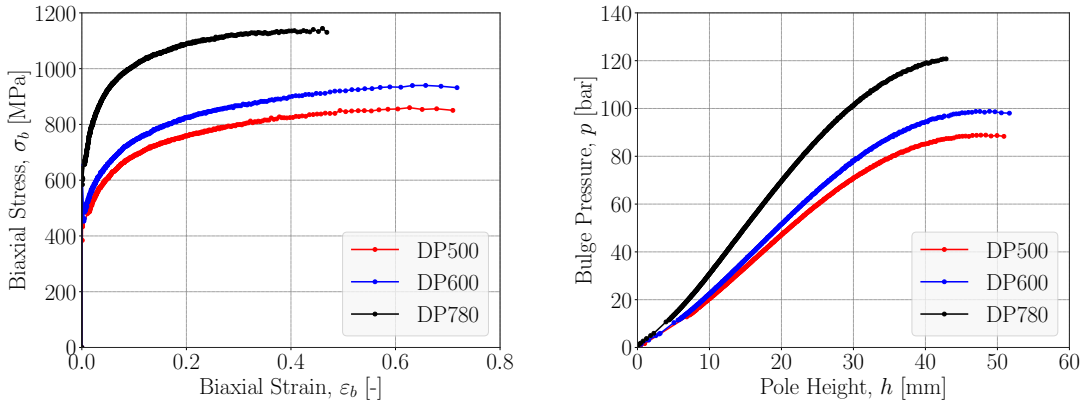
3.3.3 Hydraulic Bulge Test

The biaxial experimental characterization using the hydraulic bulge test presented in Section A.2 was performed using the equipment developed by Santos et al. [259] with a constant pressure increment. The test conditions are detailed in Table 3.8.

Table 3.8: Experimental conditions used in hydraulic bulge test.

Parameter	Value
Number of samples	2
Specimen Diameter	250 mm
Hydraulic pressure increment	1 bar/s
Room temperature	23C
Relative humidity	56%

The resulting biaxial stress-strain curves, obtained using Equations A.6 and A.10, are shown in Figure 3.19a. In addition, Figure 3.19b shows the evolution of the hydraulic bulge pressure, p, with the total height of the specimen pole, h. Table 3.9 shows the values of the bulge burst pressure at failure, the corresponding total dome height and also the corresponding initial biaxial stress and maximum achieved biaxial strain for each material.



(a) (b)

Figure 3.19: Experimental (a) biaxial stress-strain curves and (b) hydraulic pressure-height profiles obtained for the selected dual-phase steels (DP500, DP600 and DP780).

As observed in the tensile test, DP780 steel has the highest strength of the materials tested, while DP500 has the lowest strength. However, DP500 shows greater plastic deformability compared to DP780, which is in line with expectations. The DP600 steel strikes a good balance between strength and formability, as its properties fall between those of DP500 and DP780. In particular, DP600 shows similar ductility characteristics to DP500. As observed, all materials achieve higher levels of strain when compared to those obtained in uniaxial tests, Section 3.3.1.1. For all materials, it was possible to characterize the stress-strain relationship for a biaxial strain up to 0.5-0.7, while in the uniaxial tensile tests the strain limits correspond to 0.1-0.15. These results underscore the importance of the biaxial bulging test for an extended characterization of the hardening behavior of metallic materials.

Table 3.9: Obtained properties from hydraulic bulge test for the different dual-phase steels.

Material	Burst pressure [bar]	Total height [mm]	Biaxial stress [MPa]
DP500	88.4	52.7	414.8
DP600	98.0	51.7	442.6
DP780	120.8	42.9	585.1

Following the procedure presented in Section A.2 to convert the biaxial bulge curve into an equivalent curve, the corresponding identified k-values , Equation A.12, are presented in Table 3.10. In this context, k is the proportionality factor relating bulge test biaxial behavior to the equivalent uniaxial tensile behavior. The obtained stress-strain curves based on the combination of tensile and bulge test hardening data are shown in Figure 3.20.

Table 3.10: Hydraulic bulge test results for dual-phase steels; k (Eq. A.12) is the proportionality factor between bulge and tensile tests.

Material	DP500	DP600	DP780
k	0.898	0.955	0.874

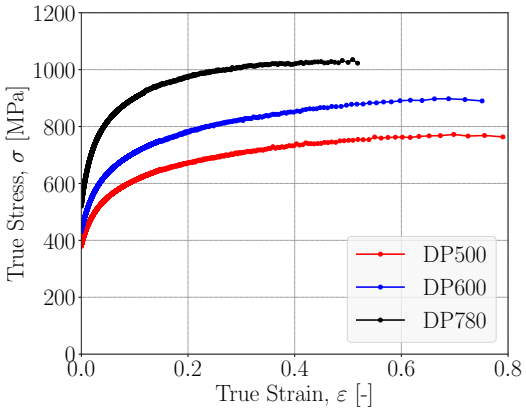


Figure 3.20: Equivalent stress-strain curves for the selected materials obtained using biaxial bulge data combined with tensile test results.

3.3.4 Stacked Disc Compression Test

To perform the stacked compression tests presented in Section A.3, 10 mm diameter disks, obtained by punching, were stacked and then loaded in compression by two polished parallel plates. A hydraulic INSTRON 5900R testing machine with a 100 kN load cell was used to apply the biaxial compression load. A lubricant was applied between the faces of the specimens and a Teflon film (0.15 mm) was also considered between the contact surfaces with the tools. The crosshead speed considered was 1 mm/min. Concentricity and axial alignment were maintained to prevent any deviation from the axial compressive load and to ensure homogeneous deformation of the specimens under frictionless conditions.

A preliminary compression test was performed to determine the appropriate load range for the experiments. Five stacked disks were used for this test. The results indicated that the force should be between 70 kN and 90 kN to ensure sufficient displacement to reach the plastic regime and to prevent specimen failure when the maximum load capacity is reached. Therefore, three load levels were defined: 70, 85 and 90 kN. Two tests were performed at each load level to verify the repeatability of the results. As shown in Figure 3.21, the mean transverse strains (ε_{22}^{p}) were plotted against the longitudinal strains (ε_{11}^{p}) and a linear fit was applied to all load cases to model the experimental data. The value of r_b, defined by Equation A.13, was determined as the slope of the linear fit. The experimental values of this parameter were 0.96 for DP500, 0.92 for DP600 and 0.91 for DP780, as summarized in Figure 3.21d.

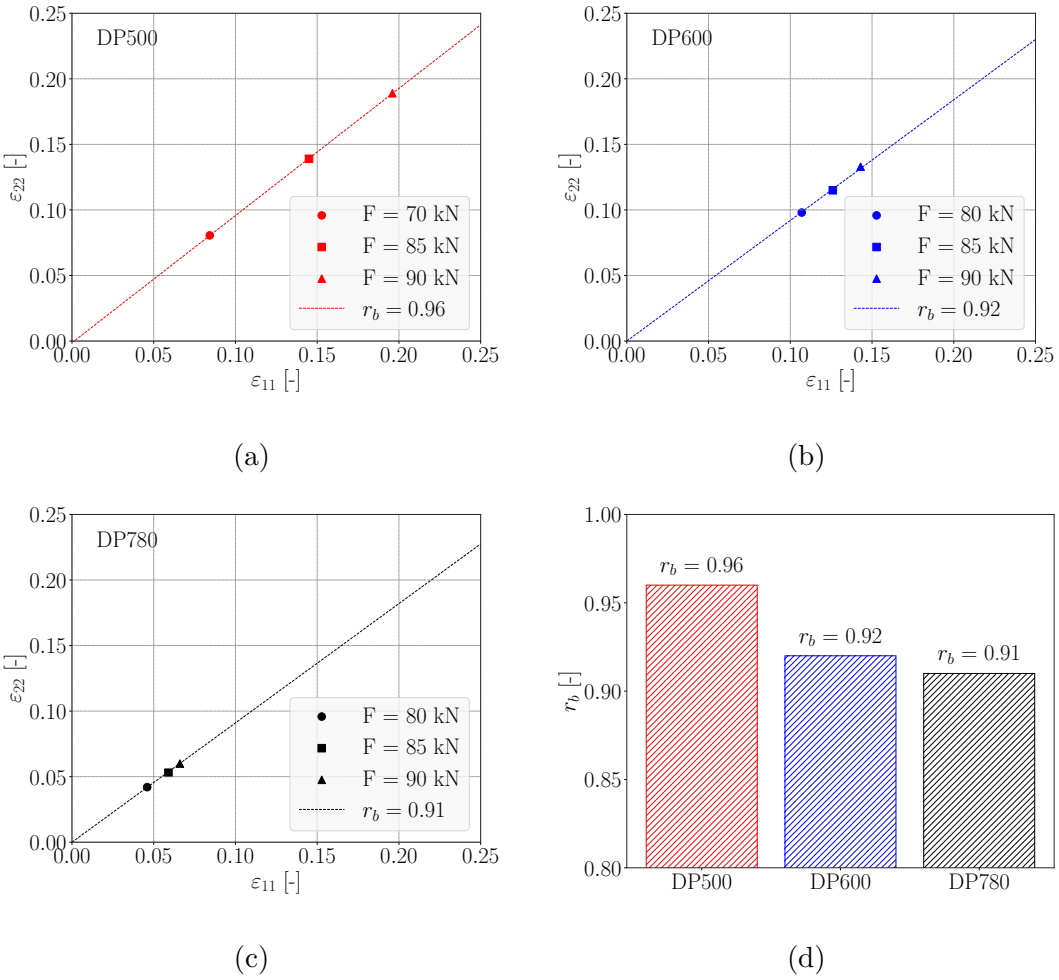


Figure 3.21: Longitudinal (ε_{11}) and transverse (ε_{22}) strain from axial compression of stacked discs for (a) DP500, (b) DP600, (c) DP780; (d) biaxial r_b anisotropy.

Although these values are close to unity (indicative of isotropy), all dual-phase steels exhibit biaxial anisotropy, which is more pronounced in DP600 and DP780 than in DP500. In general, the materials have a tendency for higher deformation along the rolling direction and thus to adopt an elliptical shape. Conversely, the dual-phase steels show some resistance to plastic deformation in the transverse direction under biaxial compressive stress.

3.3.5 Three-Point Bending Test

The experimental three-point bending tests, presented in Section A.6 were conducted on an Instron 3900-R universal testing machine equipped with a 1 kN load cell. Detailed information on the test setup and specimen geometry can be found in Table 3.11. Regarding the test conditions, the maximum displacement, y_{pmax}, was set to 20 mm and a crosshead speed of 200 mm/min was used. During the experimental three-point test, a noticeable discrepancy was observed between the predicted and experimentally measured elastic moduli of the tested materials. This variation is attributed to the stiffness (compliance) of the testing machine, which is influenced by the tested materials and the load cell. To correct for this effect, the compliance of the testing system, K_s, was determined following the methodology outlined in [260]. In this process, a load is applied to the specimen supported on a rigid surface. Compliance is then evaluated within the linear region where the curved region induced by indentation effects disappears [261]. For the specific setup used in this study, the measured system compliance was $K_s = 5335$ N/mm.

Table 3.11: Three-point bending test geometry, test conditions and sample geometry.

Three-Point Bending Test Geometry			**Test Conditions**	
Punch Radius	Support Radius	Support Span	Max. Displacement	Test Speed
Rm	Rp	V	y_{pmax}	v
4 mm	6.25 mm	50 mm	20 mm	200 mm/min
Sample Geometry				
Lenght		Thickness		Width
L		t		W
150 mm		0.8 mm		45 mm

Two lubrication conditions were tested: dry and abundant application of lubricant to both the supports and the sheet metal, using Quaker 6130 lubricant. The results for both lubrication conditions are shown in Figure 4.14 for DP500, DP600 and DP780. As seen, the presence of lubricant does not significantly change the force values for the current experimental setup. In addition, the decrease in force for a punch displacement, y_p, of 20 mm is approximately the same for both conditions and it is consistent across the three materials. Using equation A.16, it is possible to estimate the coefficient of friction in the three-point bending setup. Considering the DP780 material in dry conditions, the bending angle for a punch displacement of $y_p = 20$ mm is $\alpha = 83.83°$. In addition, F_m is 348.19 N and ΔF is 58.55 N. These values suggest an estimated coefficient of friction of $\mu = 0.1$.

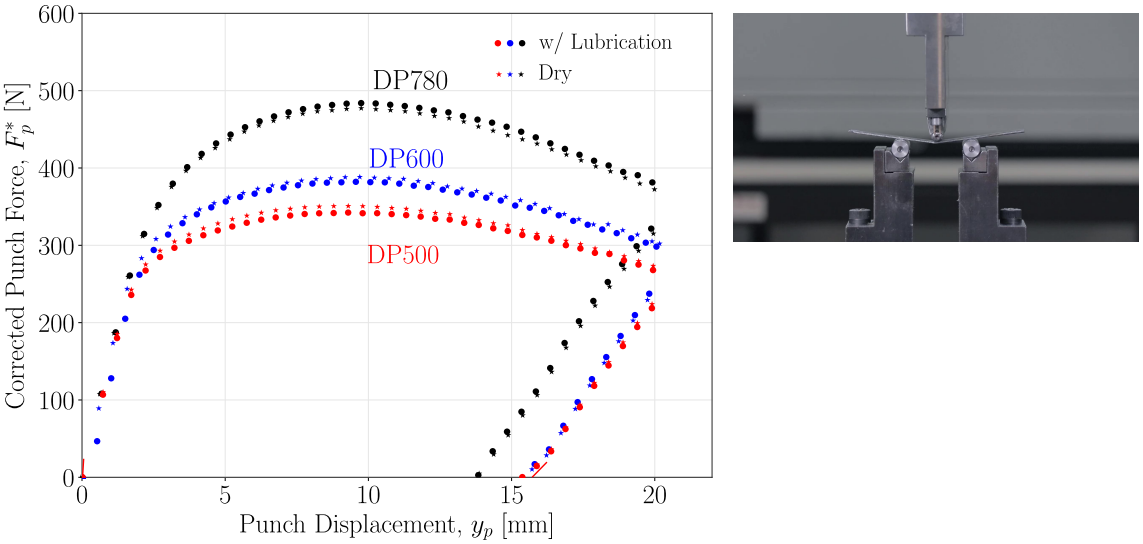


Figure 3.22: Influence of friction conditions (dry and abundant lubrication) on the experimental three-point bending test results.

3.4 Experimental Results for Reverse Loading Tests

This section presents the experimental results of reverse loading tests performed on the selected dual-phase steels (DP500, DP600 and DP780). Three different tests were performed: the tension-compression test using the miniature specimen testing device presented in Section 3.3.1.3, the reverse shear test using a modified version of the ASTM B831-05 standard (presented in Section 3.3.2) and the reverse bending test. For the reverse bending test, a new experimental setup was developed based on the equipment introduced by Omerspahic et al. [216], capable of performing bending-unbending loading on sheet metal materials.

3.4.1 Tension-Compression Tests

The tension-compression test is performed in two distinct sequential steps: first, the material is subjected to a tensile loading step, up to a specified pre-strain value, ε_p^*, followed by a compression step. The test is stopped when buckling of the specimen is detected, typically indicated by an abnormal change in the force signal. Three different tensile pre-strain nominal values were selected: $\varepsilon_p^* = 0.025, 0.050, 0.075$. Since the strain measurements are obtained via DIC in post-processing, it is not possible to precisely monitor the principal strains during the test. As a result, it is not always possible to change the loading direction exactly at the nominal pre-strain value. In this test, the experimental conditions used in the monotonic tests were considered (see Tables 3.3 and 3.7).

The experimental results for the selected dual-phase steels are shown in Figure 3.23. In this figure, the left-hand plots show the tension-compression true stress–strain curves for each material, considering the three pre-strain levels. In addition, the uniaxial monotonic tensile curve is also included for comparison. As seen, the tensile step of the tension–compression test closely matches the uniaxial tensile curve, confirming the reliability and repeatability of the experimental setup and procedure. The compression step curves for the three different pre-strain values show a similar changing trend across the entire strain range, indicating that the device can provide reliable results for the selected materials in this study. However, the amount of plastic strain achieved in compression prior to the onset of buckling is different depending on the applied tensile pre-strain. In general, the higher the pre-strain introduced during the tensile step, the lower the compressive strain achieved before buckling occurs. For the three materials, a pre-strain of $\varepsilon_p^* = 0.025$ allowed characterization of the compressive behavior up to about -0.05. In contrast, for a pre-strain of 0.050, the maximum compressive strain was in the range from -0.01 to 0.01. For a pre-strain of 0.075, the maximum compressive strain decreased to about 0.025. These differences can be attributed to the increase in specimen length caused by plastic deformation during the tensile step, which increases the probability of buckling during compression.

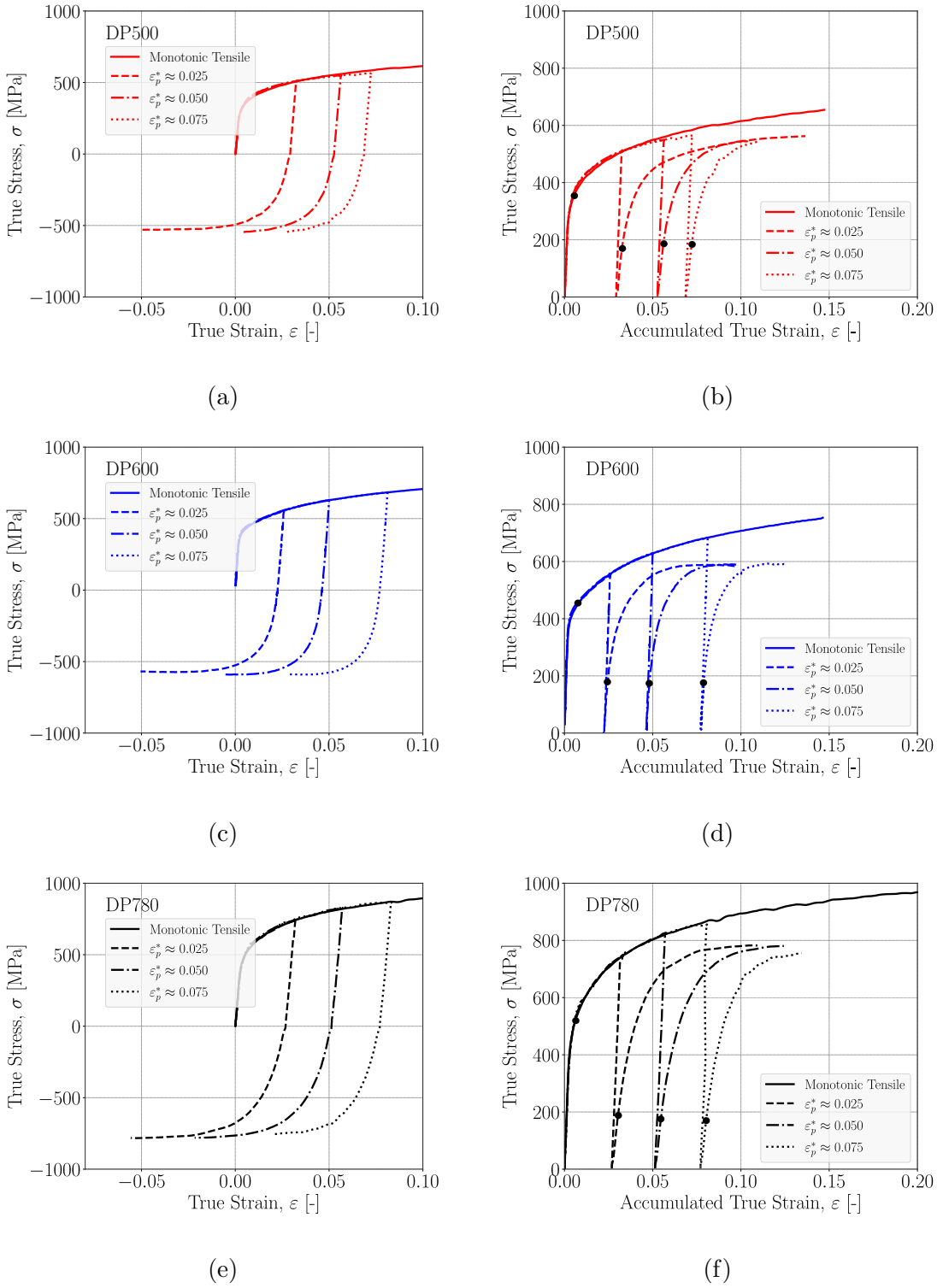


Figure 3.23: Reverse-loading experimental stress-strain curves of tension-compression test for (a-b) DP500, (c-d) DP600, (e-f) DP780.

To analyze the Bauschinger behavior of the selected dual-phase steels, the right-hand plots show the evolution of true stress with accumulated true strain. To enable

direct comparison with the uniaxial tensile curve, the hardening curves from the compression step were reflected into the first quadrant, as shown in Figures 3.23b, 3.23d and 3.23f. The yield points of both the uniaxial tensile curve and the reflected reverse loading curves, indicated by circular markers, were determined at 0.2% plastic strain and are summarized in Figure 3.24a. As observed, the materials present a strong Bauschinger effect since the reverse yield stress is significantly reduced during the reverse loading. A strong permanent softening effect is also visible, since the curves do not coincide with the monotonic tensile curve and tend to be approximately parallel.

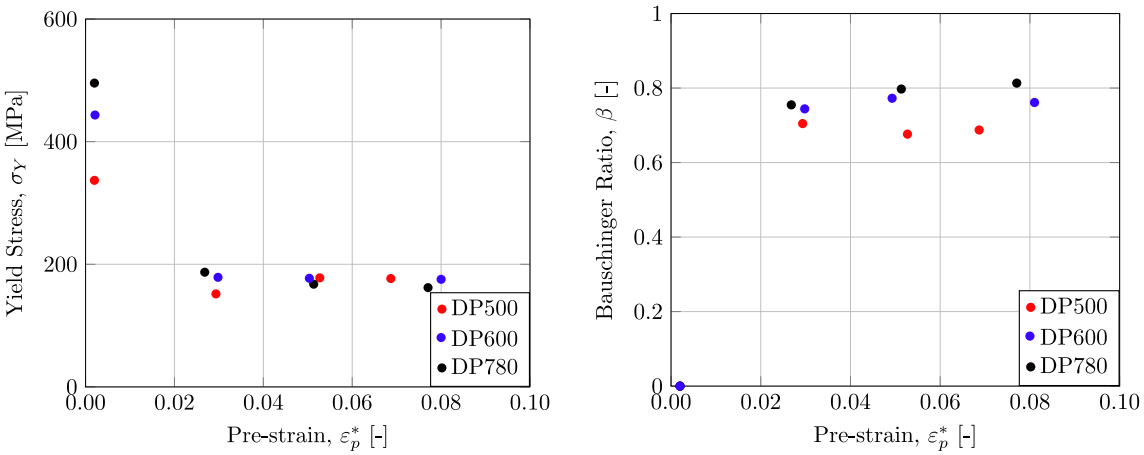


Figure 3.24: (a) Yield stress, σ_Y and (b) Bauschinger Ratio, β , values for different pre-strains, ε_p^*.

To quantify the Bauschinger effect several indicators have been proposed over the years. One of the most used, the so-called Bauschinger ratio, β, is based on stress values and is expressed mathematically by Equation 3.3:

$$\beta = \frac{\sigma_{max}^T + \sigma_{Yield}^C}{\sigma_{max}^T} \tag{3.3}$$

where σ_{max}^T represents the maximum stress in the forward load (tensile step) and σ_{Yield}^C represents the yield stress in the backwards or reverse load (compression step) - point B and C, respectively, in Figure 2.14. The Bauschinger ratio quantifies the magnitude of the Bauschinger effect. The higher the parameter, the greater the Bauschinger effect of the material. In the case of isotropic hardening, the Bauschinger ratio is equal to zero. The Bauschinger ratio for the materials under this study is represented in Figure 3.24b, which is dependent on the applied

pre-strain. From these results, it is possible to observe that both materials have a strong Bauschinger effect, since whenever the loading direction is reversed, the yield stress is reduced by about 70-80% when compared to the value of the stress in the opposite direction.

3.4.2 Reverse Shear Tests

The reverse shear tests were conducted using the modified ASTM B831-05 geometry, as shown in Figure 3.15b. The tests were performed in the MSTD, imposing the load inversion at three different nominal shear pre-strain values, ε^*_{xy}, approximately 0.1, 0.2 and 0.3. The resulting reverse shear stress-strain curves for the selected dual-phase steels are shown in Figure 3.25. Each figure also includes the monotonic shear curve for comparison.

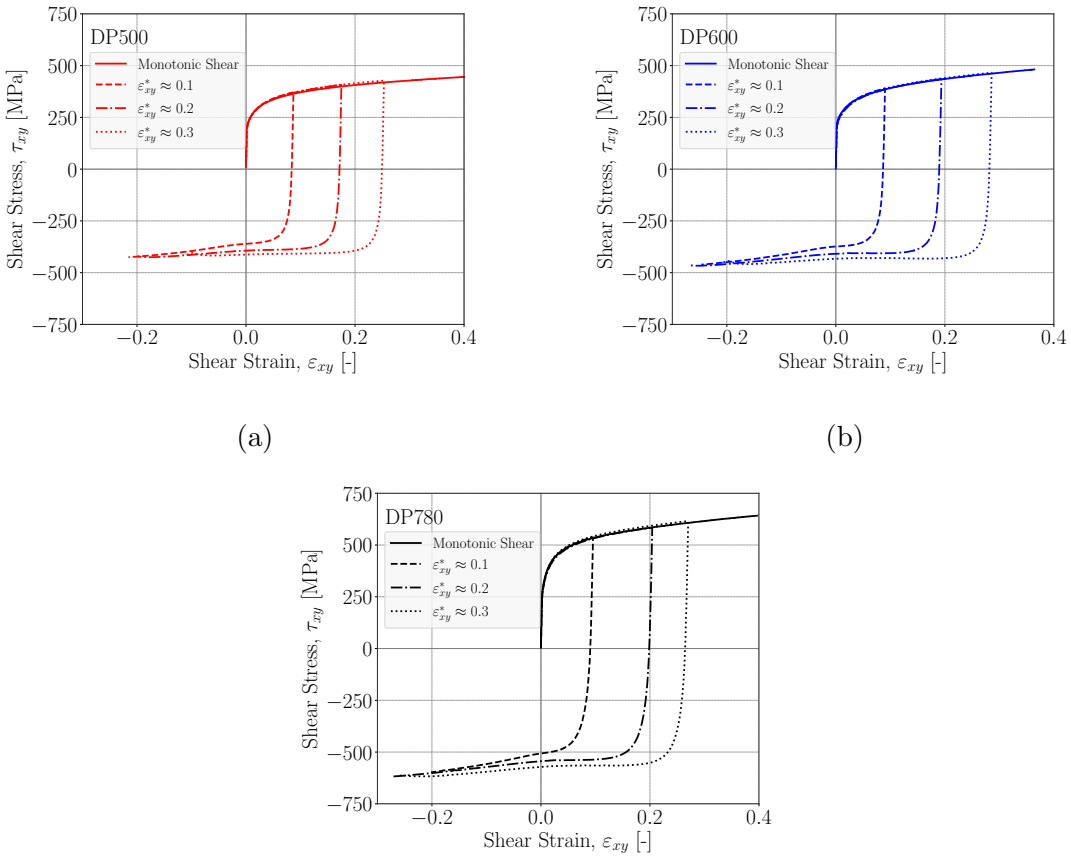
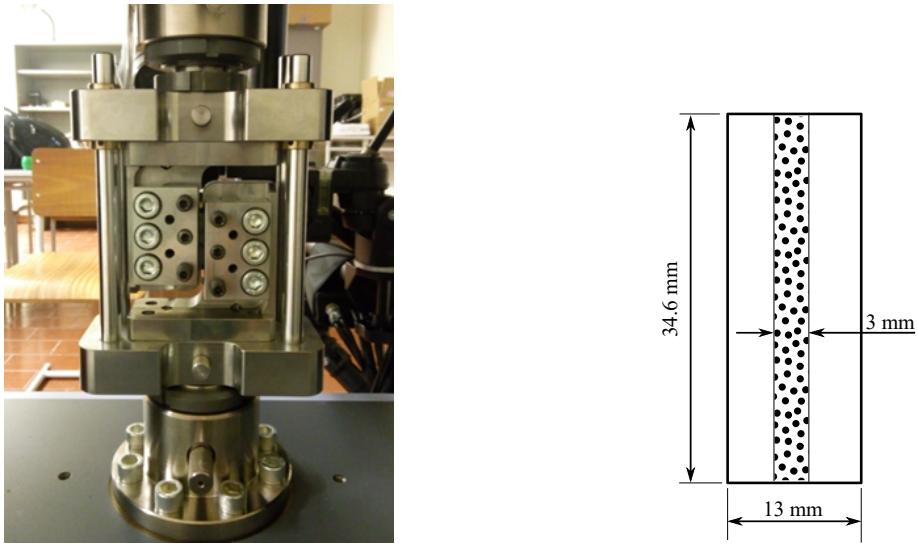


Figure 3.25: Reverse-loading shear stress-strain curves for: (a) DP500, (b) DP600 and (c) DP780.

The figures show a good agreement between the monotonic shear curve and the initial stage of the reverse shear curves, indicating similar material behavior prior to load reversal. As already observed in the tension-compression test results the Bauschinger and permanent softening effect are also visible in this type of test. To validate these results, an alternative shear specimen with a single gauge area was considered [231; 262], as shown in Figure A.5 (Appendix A). The tests were performed on a Shimadzu 100kN universal tensile testing machine using a shear fixture based on the design of Yoon et al. [224] (see Figure 3.26). The geometry of the shear specimens has a length, l_0, of 34.6 mm and a width, w_0, of 13 mm, as shown in Figure 3.26b.



(a) (b)

Figure 3.26: Shear device: (a) setup on a universal tensile test machine; (b) geometry of the single gauge area specimen [262].

In this setup, the specimen is clamped between two grips that are subjected to parallel displacement, inducing shear deformation in a 3 mm wide gauge region. During the tests, the shear strain was measured using the DIC technique. For comparison, only the DP600 material was tested. Two shear pre-strain levels, ε^*_{xy} 0.1 and 0.2, were considered. The results are shown in Figure 3.27. The data obtained using the modified ASTM B831-05 specimen are shown in blue, while the results from the single gauge area specimens are shown in gray. A strong agreement between the results of the two geometries is observed, especially for the test with $\varepsilon^*_{xy} = 0.2$, where the inversion point coincides in both cases. Under this condition, the overall material behavior is very similar. However, the modified geometry allows

for a more extensive characterization of the post-inversion behavior, allowing for significantly higher strain values. While the single-gauge area specimen achieved nearly zero post-inversion shear strains, the modified specimen allowed testing up to $\varepsilon_{xy} = -0.2$.

These results validate the use of specimens based on the modified ASTM B831-05 geometry for characterizing sheet metal materials under both monotonic and reverse shear loading. In addition, these specimens, when tested with the developed MSTD fixture, allow testing at higher plastic strain levels compared to geometries commonly found in the literature. This improvement is due to the design of the equipment, which ensures proper specimen alignment throughout the test in both the monotonic and reverse phases. This minimizes the occurrence of unwanted bending moments while maintaining test stability and specimen alignment.

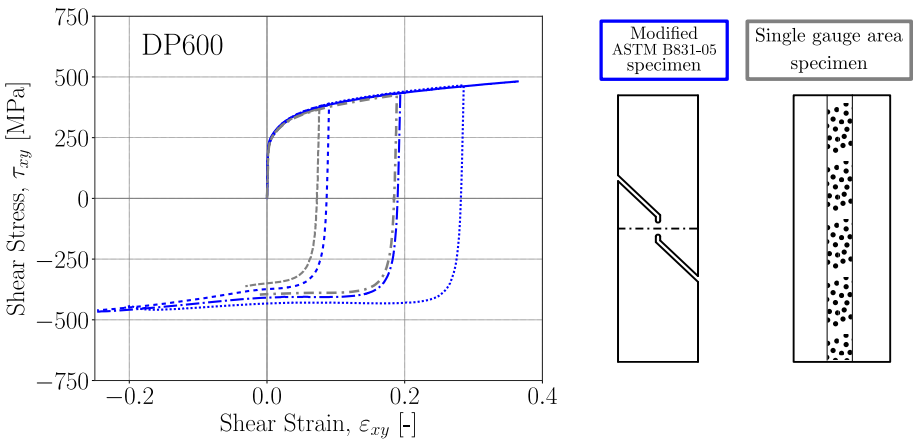


Figure 3.27: Comparison of reverse shear curves for the DP600 material using the modified ASTM B831-05 shear specimen (blue - Figure 3.15b.) and the single gauge area specimen (grey - Figure 3.26).

3.4.3 Reverse Bending Tests

3.4.3.1 Development of an Reverse Bending Equipment

To evaluate the behavior of sheet metal materials under reverse bending conditions, a new experimental setup has been developed, inspired by the work of Omerspahic et al. [216]. The apparatus designed by the authors is shown schematically in Figure 3.3. In this experimental setup, the specimen is supported on three sets of rollers: two outer sets that are free to rotate but constrained against translational movement and a central set of rollers that applies the cyclic vertical load. Each support consists of a precisely aligned and spaced pair of upper and lower rollers to

apply bending and unbending loads with control and repeatability throughout the loading cycles.

The corresponding boundary conditions of this solution are summarized in Figure 3.28(a), following the approach originally proposed by Zhao and Lee [263] for the numerical simulation of this test. The symmetry of the setup is intentionally used to reduce the complexity and computational effort. As demonstrated by the authors, these boundary conditions can be further simplified using equivalent non-contact models, as shown in Figure 3.28b-d. These models provide results equivalent to those of the full contact model, assuming that the bending moments at the fixed ends (point A) are maintained. Three equivalent non-contact configurations with different boundary conditions can be assumed, significantly reducing the computational cost typically associated with contact-based models. The effective length, L_1, in the non-contact model can be set to $1.03\,L_0$ as recommended by Zhao and Lee [263].

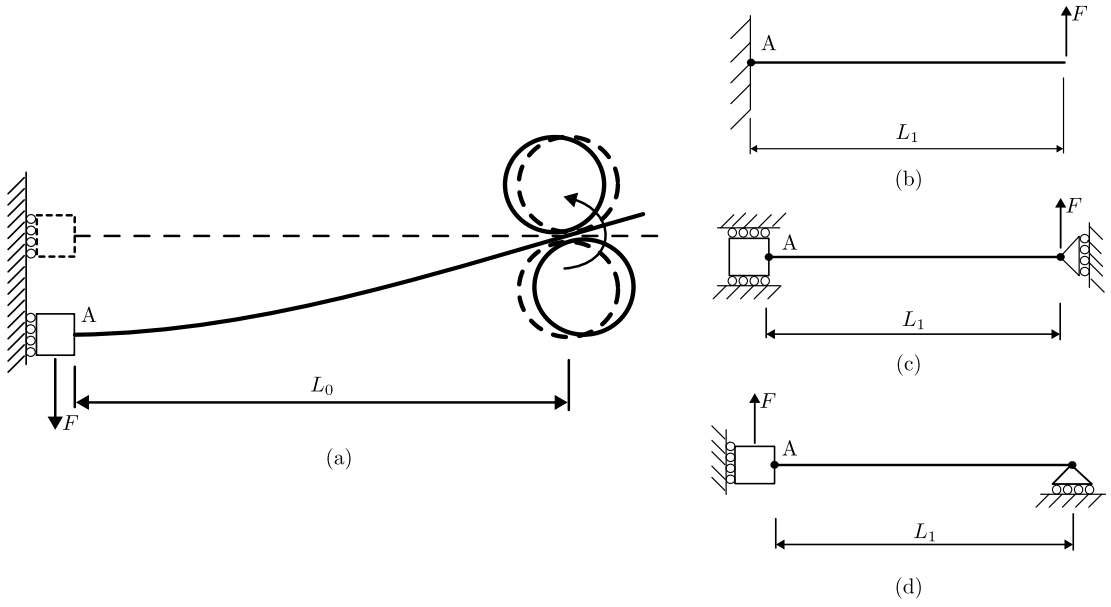
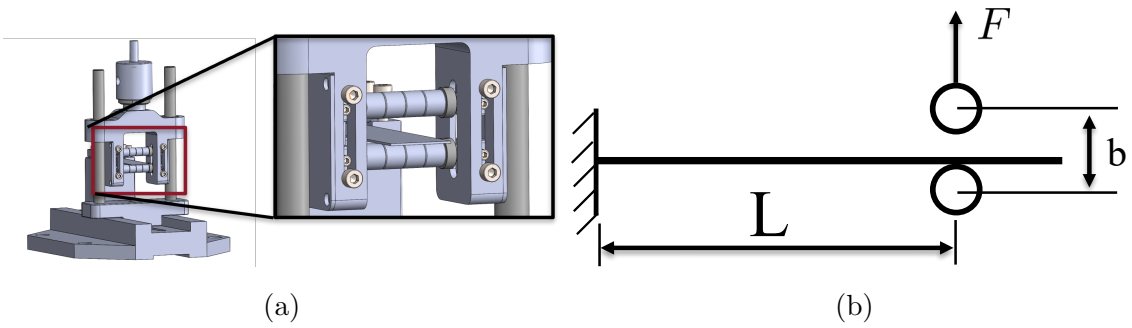


Figure 3.28: Boundary conditions of (a) the full contact model based on Zhou and Lee [263] and (b–d) equivalent non-contact models that preserve bending moments at Point A.

Based on these non-contact models, a novel reverse bending apparatus has been developed. Its layout is shown in Figure 3.29. In this setup, a rectangular specimen is clamped at one end, where bending occurs, while two rollers apply cyclic vertical displacements at a point located at a distance L from the clamped edge. The main geometric parameters governing the test are the distance L between the loading point

and the clamped end and the distance b between the upper and lower rollers. The specimen is first bent in one direction until a predefined displacement d is reached. The loading direction is then reversed to induce a reverse bending condition. This process is repeated for a predefined number of cycles n, allowing characterization of the material response under repeated bending and unbending conditions.



(a) (b)

Figure 3.29: Representation of (a) the reverse bending setup and (b) the corresponding schematic illustrating the clamped end, roller spacing (b), loading distance (L) and applied force (F).

The distance, b, between the upper and lower rollers allows characterization of the elastic recovery of the material during reverse loading, specifically by measuring the springback angles, α_i, in each cycle, as shown in Figure 3.30. This figure schematically shows a reverse bending test consisting of three steps ($n = 3$). In each step, the rollers move together by a predefined displacement d_i. In the first step, a displacement d_1 is applied, inducing tensile stress on the lower surface and compressive stress on the upper surface of the sheet. When the maximum upward displacement is reached, the direction of motion is reversed, allowing the specimen to recover elastically and bend in the opposite direction. When the rollers lose contact during this reverse motion, the springback angle α_1 is recorded. In the second step, a displacement d_2 is applied, now inducing compressive stress on the lower surface and tensile stress on the upper. After measuring the springback angle α_2, the rollers move upward again by a fixed displacement d_3. The test concludes after the springback angle for this step, α_3, is measured, indicating that the lower roller has lost contact with the sheet material.

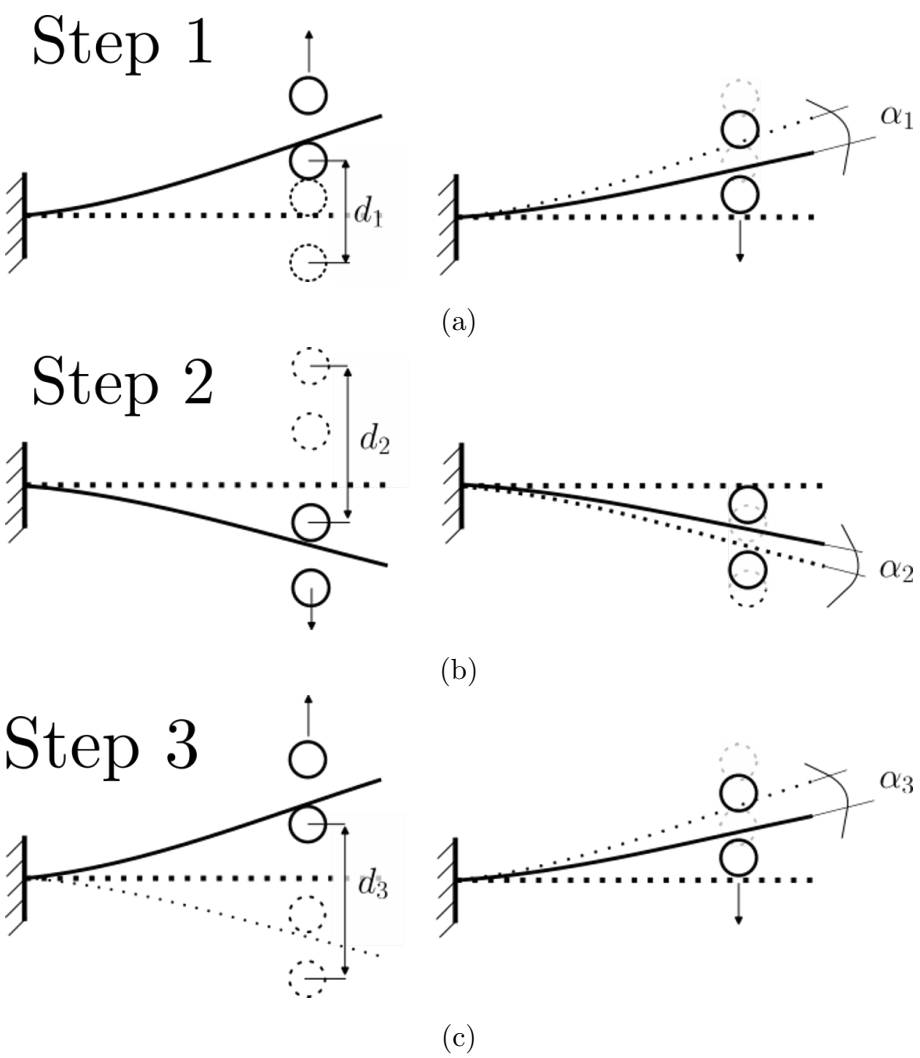


Figure 3.30: Overview of the reverse bending test, showing the sequential application of displacements d_1, d_2 and d_3 and the resulting springback angles α_1, α_2 and α_3 of the sheet material.

3.4.3.2 Experimental Test Conditions

To evaluate the behavior of the dual-phase steels (DP500, DP600 and DP780), the developed experimental setup was mounted on a universal testing machine (Instron 5900R 300 kN) using a 1 kN load cell. During the test, force and displacement data were recorded from the moving crosshead at a sampling rate of 10 Hz. In addition, images were taken during the test to measure the springback angle at each stage. A representation of these images is shown in Figure 3.31 for the DP500 material. In this figure, each row shows the images at the end of each stage: the left image shows the specimen before elastic recovery and the right image shows it after elastic recovery. Three steps were considered, i.e. $n = 3$. A displacement value d_1 of

20 mm was used for the first step, while displacements of 40 mm were used for the second and third steps. The rectangular sample was cut to a size of 145 x 30 mm by EDM. To ensure the repeatability of the results, five specimens were considered for each material. The value of L was set to 30 mm, while the distance between the top and bottom rollers, b, was set to 10 mm.

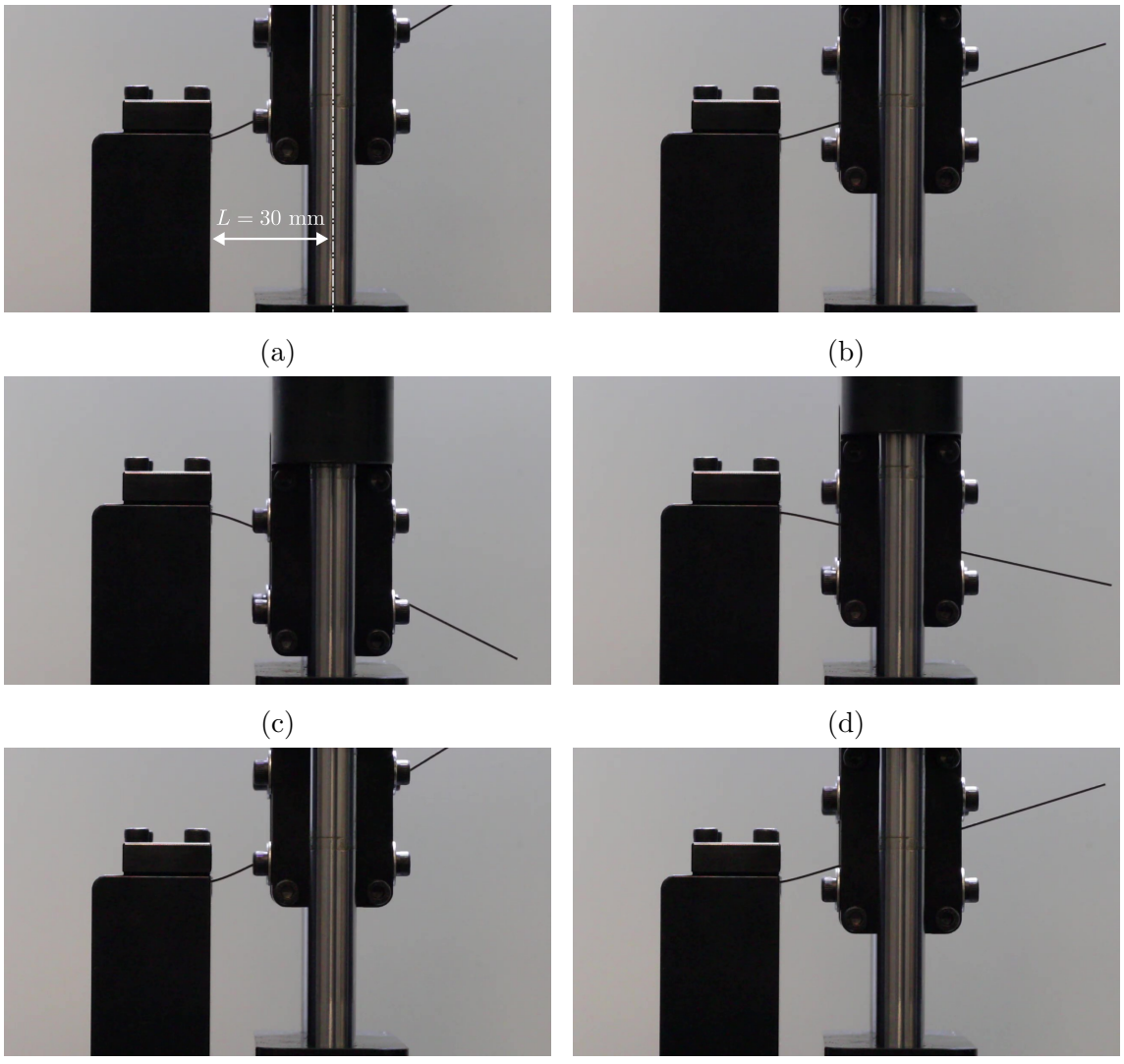


Figure 3.31: Images captured during the reverse bending test for the DP500 material, at the end of (a-b) step 1, (c-d) step 2 and (e-f) step 3. The left image shows the specimen before elastic recovery, while the right image depicts the specimen after elastic recover.

3.4.3.3 Reverse Bending Results

The reverse bending results for DP500, DP600 and DP780 are presented in Figure 3.32. Since five samples were considered for each material, the average results are shown. In the first column of the figure, the punch force-displacement curves for the three steps of the test are displayed, while the second column presents the evolution of the bending angle and the corresponding springback angle for each step. Six different angles of interest can be selected, corresponding to the bending angles at the end of each step, both before (BSP) and after springback (ASP). For example, for the DP500 material, at the end of step 1, (see Figure 3.32b) the bending angle before springback (1-BSP) was approximately 42.5°, while the bending angle after springback (1-ASB) was about 31.9°. The difference between the angle before and after springback is equivalent to the springback angle that in this case is approximately $\alpha_1 = 10.6°$.

When comparing the experimental results for the three dual-phase steels, a similar trend can be observed in both the punch force-displacement curves and the evolution of springback angles across the steps. The punch force-displacement curves shows a relatively smooth, symmetrical shape for the forward and reverse bending cycles. As expected, DP500 requires the lowest force, DP780 the highest and DP600 falls in between. For all materials, two horizontal zones are evident, labeled as Zone A and Zone B in Figure 3.32a, corresponding to the transitions between steps 1-2 and 2-3, respectively. In these zones, the punch moves continuously without contacting the specimen.

When comparing the springback angles, a similar behavior can be observed across the three materials. DP780 exhibits the largest springback angles in all stages compared to the other two steels. On the other hand, DP500 shows the smallest springback angles, while DP600 presents intermediate values between the two. It is also evident for all three materials that the springback angle in the second stage is significantly smaller than the angles in stages 1 and 3. This can be explained by the different levels of plastic deformation reached in each stage. Although the reverse bending test is displacement-controlled, with limits between -20 mm and 20 mm, not all of the punch displacement contributes to plastic deformation in the material, due to the spacing between the upper and lower rollers. This affects how much the material bends and recovers elastically in each stage.

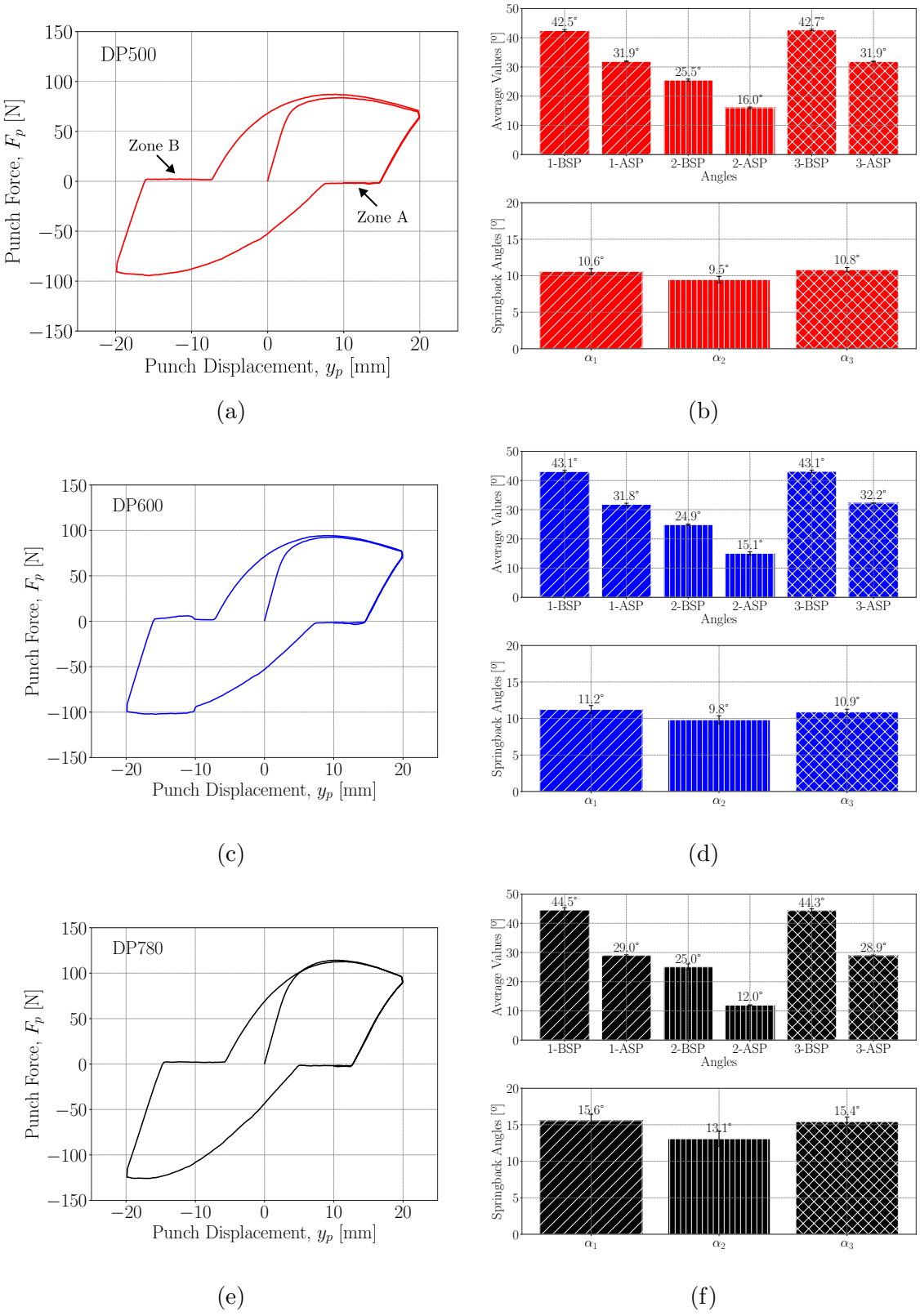
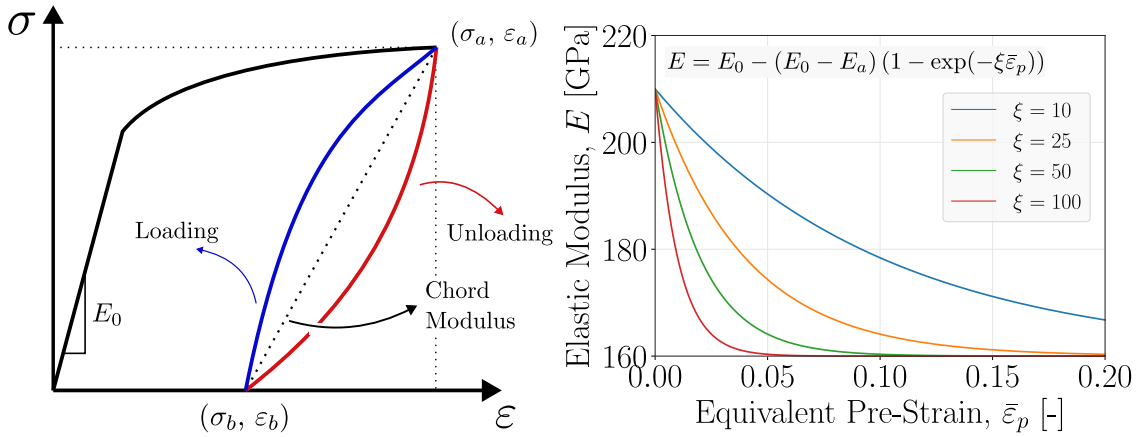


Figure 3.32: Reverse bending test results for (a-b) DP500, (c-d) DP600 and (e-f) DP780; the first column shows the punch force-displacement curves for the three test steps and the second column presents the evolution of the bending angle before (BSP) and after springback (ASP) and the corresponding springback angle (α) for each step.

In conclusion, the experimental results from the reverse bending tests show that the new testing setup effectively characterizes the cyclic bending behavior of dual-phase steels. Using flat sheet specimens instead of complex machining significantly simplified specimen preparation while enabling an accurate assessment of cyclic hardening behavior under reverse loading conditions. These tests provide a valuable dataset essential for identifying anisotropic constitutive model parameters using machine learning–based approaches, which will be explored in the next chapter.

3.5 Experimental Analysis of Elastic Modulus Degradation

To evaluate the Young's modulus degradation with plastic strain, the methodology proposed by Yoshida and Uemori [113] and summarized in Figure 3.33 was followed. As shown in Equation 2.50, this model has three parameters that require calibration: E_0 is the initial elastic modulus of the material, E_a is the value of the elastic modulus at infinite plastic strain and ξ is a material parameter that controls the rate of modulus degradation. Figure 3.33a shows a graphical example of the influence of the parameter ξ on the evolution of the Young's modulus. In this case, the initial Young's modulus is defined as 210 GPa, while the Young's modulus at infinite plastic strain is set to 160 GPa. The graph shows that higher values of ξ result in a faster decrease of Young's modulus.

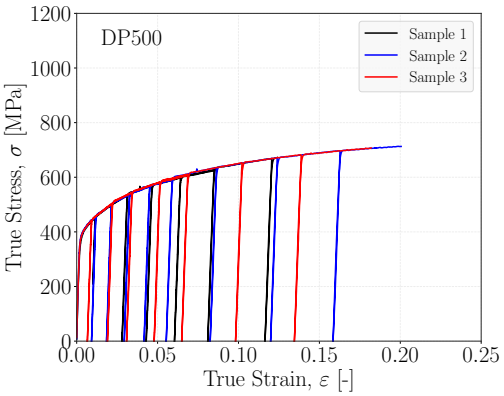


(a) (b)

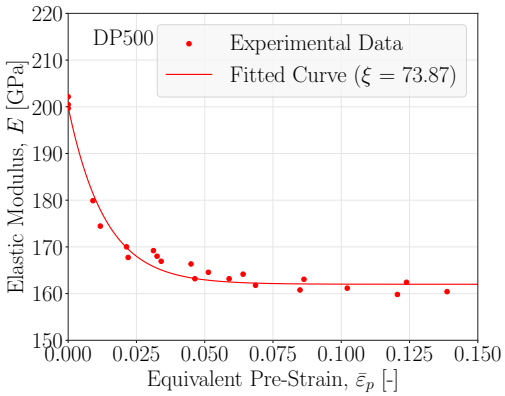
Figure 3.33: Representation of (a) elastic moduli under uniaxial tensile loading and (b) the influence of ξ on Young's modulus degradation with plastic strain, based on the Yoshida-Uemori model [113].

Young's modulus degradation is typically determined by uniaxial loading-unloading cycle tensile tests using macro-tensile specimens with lateral supports to prevent buckling during the unloading phase [218; 264]. Alternative methods, such as bi-axial load-unload tests [265] and three-point bending tests [266], have also been reported in the literature. This study takes a different approach by evaluating the Young's modulus degradation of dual-phase steels (DP500, DP600 and DP780) using miniaturized tensile specimens (Figure 3.7b), a methodology not commonly found in the literature. For this purpose, loading and unloading tests were considered for the selected materials, taking into account different strain levels for unloading. Three specimens were considered for each material and the corresponding true strain-stress curves are shown in Figure 3.34. The analysis of the different curves shows significant discrepancies, especially during the unloading phase. The strain levels at which unloading occurs vary from sample to sample, due to the fact that the test is controlled by stress rather than strain. Since the strain values are measured by digital image correlation and analyzed in post-processing, it is not possible to obtain perfect real-time control of the deformation imposed on the material during the test.

Figure 3.34 b, d and f show the evolution of the elastic modulus values obtained for different levels of plastic deformation for DP500, DP600 and DP780, respectively. The elastic modulus at different plastic strain levels was calculated using the chord modulus concept, presented in Figure 3.33 which minimizes the influence of non-linear effects during loading and unloading. The slope of the chord between points $(\sigma_a, \varepsilon_a)$ and $(\sigma_b, \varepsilon_b)$ was used to represent the modulus for the entire unloading-loading cycle.



(a)



(b)

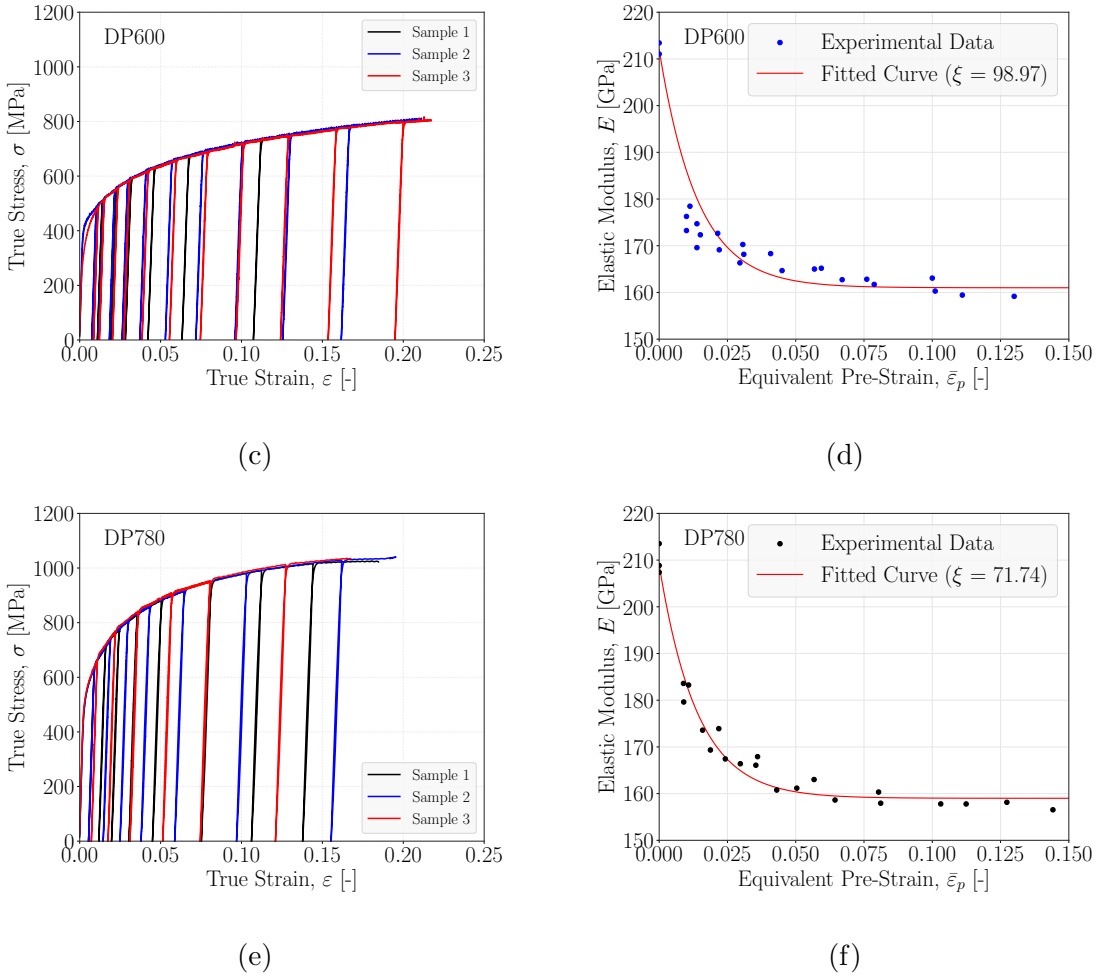


Figure 3.34: Elastic modulus degradation analysis for DP500, DP600 and DP780: (left) true stress–strain curves from miniaturized tensile specimens and (right) evolution of the elastic modulus as a function of plastic strain for each material.

The calibrated values of the Yoshida-Uemori model parameters based on the experimental tests are summarized in Table 3.12. The experimental results show a significant decrease in Young's modulus of all dual-phase steels tested with increasing plastic strain. The fitted curves obtained using the Yoshida-Uemori model show good agreement with the experimental data, confirming the applicability of the model to current materials in this study. For DP500, the initial Young's modulus E_0 was 200.7 GPa and the asymptotic value E_a at infinite plastic strain was 162 GPa, resulting in a total decrease of approximately 19.3%. For DP600 and DP780, the decrease was more pronounced, with reductions of about 24.2% and 23.9%, respectively. The ξ parameter plays a critical role in determining how quickly the modulus decreases with increasing plastic strain. The analysis shows that DP600 with

$\xi = 98.97$ has the fastest degradation rate, followed by DP500 ($\xi = 73.87$) and DP780 ($\xi = 71.74$). The modulus degradation tends to stabilize after a certain amount of plastic strain. For all three materials, the Young's modulus shows a tendency to plateau for equivalent plastic strains greater than about 0.06–0.07. This indicates that most of the degradation occurs at lower strain levels and beyond this point the elastic modulus approaches its asymptotic value (E_a). Overall, the results show the adequacy of the Yoshida-Uemori model (Equation 2.50) for capturing Young's modulus degradation in dual-phase steels. The use of miniaturized tensile specimens proved effective for this purpose and the model parameters obtained provide a reliable basis for incorporating this phenomenon into numerical simulations.

Table 3.12: Parameters of the Yoshida-Uemori model (Equation 2.50) for dual-phase steels (DP500, DP600 and DP780).

Material	E_0 [GPa]	E_a [GPa]	ξ
DP500	200.7	162	73.87
DP600	212.2	161	98.97
DP780	209.1	159	71.74

3.6 Concluding Remarks

This chapter describes an experimental program that was conducted to characterize the mechanical behavior of three dual-phase steels (DP500, DP600 and DP780) under various loading conditions, including monotonic and reverse loading scenarios. The experimental campaign was designed to generate a comprehensive dataset to support the calibration and validation of advanced constitutive models, a topic discussed in detail in the following two chapters.

A key contribution of this study lies in the use of miniaturized specimens for sheet metal material characterization and the development of the *Miniaturized Specimen Tester Device*. This novel setup enables the efficient performance of monotonic and reverse loading tests while significantly reducing material consumption and costs. Integrating DIC techniques enabled full-field strain measurements with high spatial resolution, providing a more precise assessment of deformation behavior under complex loading conditions. The MSTD successfully performed monotonic tests under tension, compression and shear loading conditions. Results from these miniaturized tests were consistent with reference data from conventional and macroscale

specimens, confirming the validity and robustness of the methodology. Notably, using miniaturized specimens effectively suppressed issues such as buckling during compression tests. This eliminated the need for lateral supports or the complex experimental setups typically required in macroscale testing. In monotonic compression tests, the material could be characterized up to approximately 7% plastic strain without buckling instabilities occurring.

Reverse shear tests were conducted using miniaturized specimens adapted from the ASTM B831-05 standard geometry, demonstrating good agreement with reference single-gauge specimens from the literature. The miniaturized configuration allowed stable characterization at higher strain levels after inversion, without the occurrence of instabilities, confirming the suitability of the MSTD for studying reverse shear behavior. The MSTD's design ensured proper specimen alignment and minimized unwanted bending moments, proving to be a good solution for investigating the anisotropic and kinematic hardening behavior of dual-phase steels.

Finally, dedicated tests were conducted using the MSTD to investigate the degradation of Young's modulus in the selected materials as a function of plastic strain. The results confirmed a progressive decrease in Young's modulus, with the degradation rate varying across the different dual-phase steels. The experimental data were used to calibrate the Yoshida-Uemori model, which showed excellent agreement with the observations, validating its applicability for modeling elastic modulus degradation in dual-phase steels.

In addition to the MSTD device for tension, compression and shear tests, a custom setup was developed to enable reverse bending experimental characterization. This novel reverse bending setup provides a simple and efficient solution for characterizing material behavior under cyclic bending conditions, which are commonly encountered in industrial sheet forming processes. A key advantage of this setup is its ability to evaluate elastic recovery of the material at the end of each intermediate loading step, providing direct insights into the material's behavior under cyclic loading.

The experimental campaign described in this chapter provides a robust and comprehensive dataset for characterizing the mechanical behavior of dual-phase steels under monotonic and reverse loading paths capturing essential phenomena, such as Young's modulus degradation, the Bauschinger effect and anisotropic hardening behavior. This makes the dataset highly valuable for validating constitutive models and for the reliable identification of model parameters, including when using machine learning approaches. At the same time, it is important to acknowledge the inherent

limitations of the dataset generated through this experimental program. The loading conditions explored (tension–compression, reverse shear and reverse bending) represent only a small subset of the wide range of deformation paths encountered in industrial forming processes. As such, while the dataset is well suited for parameter identification and model validation, it remains insufficient as a standalone basis for developing fully data-driven constitutive models, which require a broader coverage of strain-path diversity. To address this challenge, future efforts should focus on expanding the range of deformation histories explored experimentally. Recent developments, such as mechanical tests incorporating continuous strain-path changes within a single specimen, thus eliminating the need for unloading or repositioning [190], represent promising steps toward generating richer datasets for ML applications. In parallel, indirect approaches such as crystal plasticity simulations offer a valuable complement to experimental data by providing synthetic datasets across a wide variety of strain paths. These methods can help bridge the gap between limited experimental observations and the broader modeling space required for robust constitutive model development. Furthermore, applying advanced image processing techniques, as demonstrated in the work presented in Appendix B, can significantly enhance the information extracted from experimental tests. Techniques such as feature detection, image segmentation and data augmentation enrich the datasets available for ML algorithms, especially convolutional neural networks. Integrating image-based data into ML pipelines holds great promise for developing more accurate and generalizable constitutive models, ultimately bridging the gap between experimental mechanics and data-driven material modeling.

Chapter 4

Identification of Material Constitutive Parameters using Machine Learning

An essential requirement for the effective description of material behavior using phenomenological constitutive models is the accurate identification of constitutive parameters. This process involves a consistent comparison between mathematical predictions and experimental observations by defining an cost function that quantifies the deviations between the numerical model and the experimental data, then minimizing this function to achieve the best fit. When using the finite element method to numerically reproduce the material behavior, a common technique is the finite element model updating [24], in which, a FEM model of a mechanical test is created and relevant data, such as force, strain and displacement are collected at selected nodes. A cost function is then calculated based on the difference between numerical predictions and experimental measurements and its minimisation with respect to the unknown constitutive parameters provides the optimal parameter set. FEMU is particularly versatile as it can be applied to local, average or full-field measurements. Alternative methods such as the constitutive equation gap method [25], the equilibrium gap method [27] and the virtual fields method [26] have also been proposed to address similar challenges.

Another promising approach is to use machine learning techniques to identify material parameters more efficiently [13]. This strategy uses data-driven models - often called metamodels - to directly solve the inverse identification problem. These models are typically trained on synthetic data obtained from finite element analysis. However, instead of repeatedly running computationally expensive finite element simulations during the identification process, these simulations are run in advance to generate a comprehensive dataset that is used to train the metamodel. The cho-

sen inputs to the metamodel correspond to the data available for new materials at the time of identification (usually results from mechanical tests, such as forces, displacements and strains), while the outputs are the constitutive model parameters. During training, optimisation algorithms are used to obtain the optimal set of internal metamodel parameters. Once trained, the ML model can efficiently predict constitutive parameters by processing experimental data from the material under investigation, making identification almost instantaneous.

This chapter explores the application of ML approaches, in particular neural networks, to the identification of constitutive hardening parameters using bending test results. Bending tests are usually not the most commonly used method to experimentally determine the hardening behavior of a material because they lead to inhomogeneous stress and strain distributions across the thickness of the material [267]. This inhomogeneity makes direct stress-strain relationships difficult to determine. As a result, monotonic and reverse tensile tests are usually preferred. Converting the raw experimental data of a bending test, usually represented as punch displacement (y_p) and punch force (F_p), into a stress–strain response (σ–ε) often requires the use of inverse fitting models [268–270] or analytical approaches [271]. These methods are based on accurate modeling of the test conditions and usually involve predefined hardening models combined with iterative optimization cycles. Although effective, this traditional approach can be time consuming, especially when multiple experimental tests are performed. The methodology proposed in this chapter aims to overcome this limitation by efficiently determining the stress-strain behavior of a material using only the results of an experimental bending test and ML approaches. By leveraging the simplicity of this test, the proposed approach provides an effective alternative to traditional inverse and analytical fitting methods for characterizing the hardening behavior of a material.

This chapter is organized into four main sections. In the first section, conventional inverse identification techniques using tension and compression tests are used to determine the constitutive parameters of selected dual-phase steels (DP500, DP600 and DP780). These parameters not only provide a baseline for comparison with ML approaches, but also lay the foundation for the developments discussed in Chapter 5. This section focuses on the identification of material parameters for anisotropic yield functions, specifically the Hill '48 yield criterion and the Yld2000-2d model and also presents the identification of both isotropic and anisotropic hardening parameters. On the other hand, sections two and three explore the application of ML to the identification of hardening parameters. The second section presents a

novel method using neural networks to analyze experimental data from three-point bending tests to identify isotropic hardening parameters. The third section extends the developments previously proposed, by applying them to reverse bending tests - a more comprehensive method that allows the simultaneous identification of both isotropic and anisotropic hardening parameters. These methods have been developed specifically for high-strength steels, which are the focus of this thesis, but the ultimate goal is to establish a generalized methodology applicable to a wider range of materials and adaptable to different experimental tests. Finally, section four concludes the chapter by summarizing the key findings and outlining directions for future research.

4.1 Identification of Material Parameters using Conventional Methods and Tension-Compression Tests

4.1.1 Material Parameters for Anisotropic Yield Functions

In order to accurately model the anisotropic behavior of dual-phase steels, two different yield criteria were chosen: Hill'48 and Yld2000-2d. For the Hill'48 criterion, the corresponding parameters can be identified using two different approaches: based on stresses (Hill'48 σ-based) or based on r-values (Hill'48 r-based). For the Hill'48 yield criterion, the explicit expressions were used to identify the parameters. However, in the case of the Yld2000-2d yield criterion, a genetic algorithm was used to minimize the cost function. Since the error associated with the yield stresses is greater than the error when using r-values, the normalized yield stresses were adopted, with the yield stress in the rolling direction as the reference value. The experimental reference data used for parameter identification includes the uniaxial tensile yield strengths (σ_0, $\sigma_{22.5}$, σ_{45}, $\sigma_{67.5}$, σ_{90}), biaxial stress (σ_b), plastic anisotropy coefficients (r-values: r_0, $r_{22.5}$, r_{45}, $r_{67.5}$, r_{90}) and biaxial plastic anisotropy coefficient (r_b).

The parameters obtained for Hill'48 and Yld2000-2d models for selected dual-phase steels are presented in Table 4.1 and 4.2, respectively. For Hill'48 criterion, the parameters related to the through-thickness material properties were assumed to follow isotropic conditions with L and M set to 1.5. The exponent a in the Yld2000-2d model was assigned a value of 6, reflecting the BCC structure of the materials. The yield surface contours for the three steels are shown in Figure 4.1. In

addition, the predicted evolution of the normalized yield stresses and r-values with angle relative to the rolling direction is shown in Figure 4.2.

Table 4.1: Material parameter identification for Hill'48 yield criterion for DP500, DP600 and DP780.

		Hill'48 Parameters			
		F	G	H	N
DP500	r-based	0.4438	0.5074	0.4926	1.2850
	σ-based	0.3914	0.4465	0.5535	1.3090
DP600	r-based	0.5056	0.5900	0.4100	1.5721
	σ-based	0.4543	0.4878	0.5122	1.5215
DP780	r-based	0.4772	0.6068	0.3932	1.5414
	σ-based	0.3458	0.4477	0.5523	1.4831

Table 4.2: Material parameter identification for Yld2000-2d yield criterion of DP500, DP600 and DP780 steels.

	Yld2000-2d Parameters								
	a	α_1	α_2	α_3	α_4	α_5	α_6	α_7	α_8
DP500	6	0.9770	0.9620	0.8593	0.9427	0.9608	0.7867	0.9064	0.9800
DP600	6	0.9298	0.9700	0.9271	0.9822	1.0018	0.8899	0.9811	1.0514
DP780	6	0.8558	0.9495	0.8224	0.9310	0.9703	0.6808	0.9374	1.0981

Figure 4.2 show that the Yld2000-2d model accurately captures both yield stresses and r-values. However, for DP500 steel the model tends to underestimate the r-value at 62.5° and 90° and for DP780 steel it underestimates the r-value at 22.5°. It also tends to underestimate the equivalent stress at 22.5° for both DP500 and DP780 steels. In contrast, the Hill'48 r-based yield criterion accurately represents the r-value but shows slight discrepancies in the yield stresses at 45° and 90°, particularly for DP600 and DP780. In this case, the Hill'48 r-based criterion tends to underestimate the equivalent stress at 45° and overestimate it at 90°. Conversely, the Hill'48 σ-based model effectively captures the yield stress anisotropy for all three materials. However, this criterion still underestimates the equivalent stress at 22.5° for both

DP500 and DP780 steels. It also significantly overestimates the r-values over the full range of angles relative to the rolling direction. These results suggest that the Hill'48 model struggles to describe the anisotropy in both yield stress and r-value simultaneously. In contrast, the Yld2000-2d model, although slightly less accurate in its predictions in some cases, generally provides a more reliable representation of the anisotropy in both yield stresses and r-values, but at the cost of requiring a greater number of parameters to be calibrated. Regarding the yield surfaces, it can be seen that the Yld2000-2d yield criterion satisfactorily reproduces every point of the experimental data, except for the prediction of the uniaxial compression stress, σ_c^0, for DP500, where it overestimates the value. The anisotropic yield parameters identified in this section will be used mainly in Chapter 5.

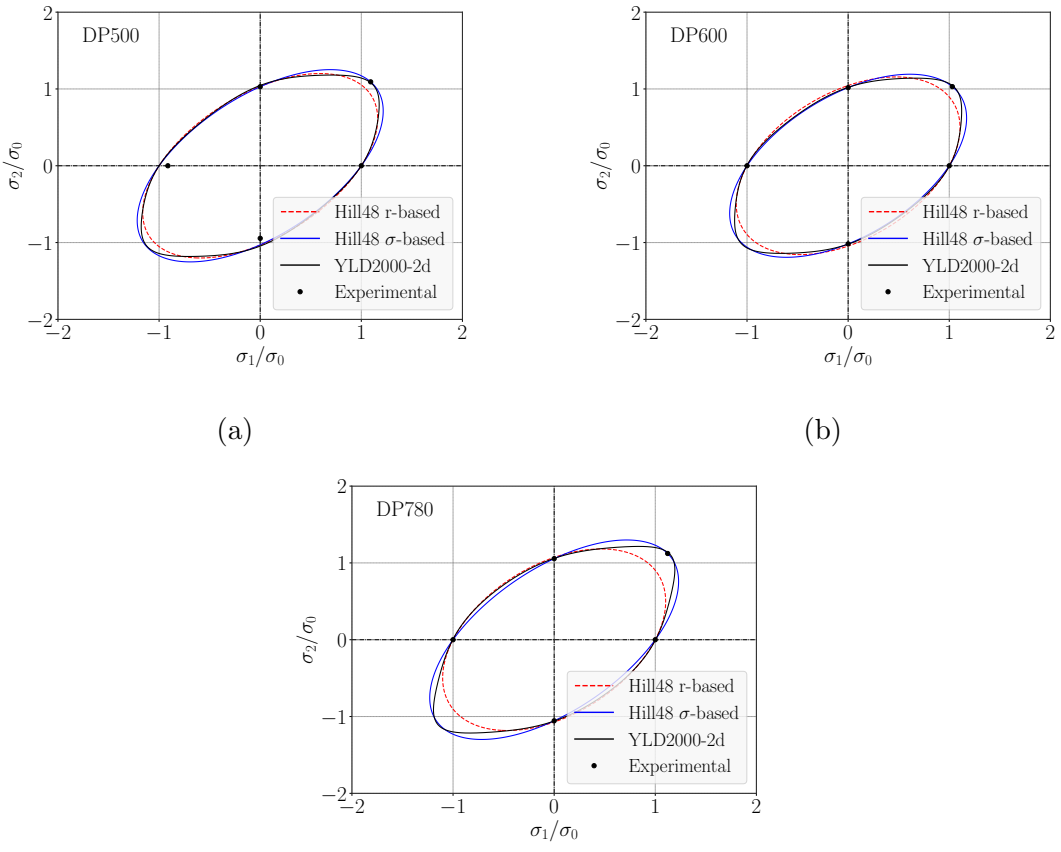


Figure 4.1: Predicted yield surfaces of Hill'48 and Yld2000-2d models for (a) DP500, (b) DP600 and (c) DP780 steel.

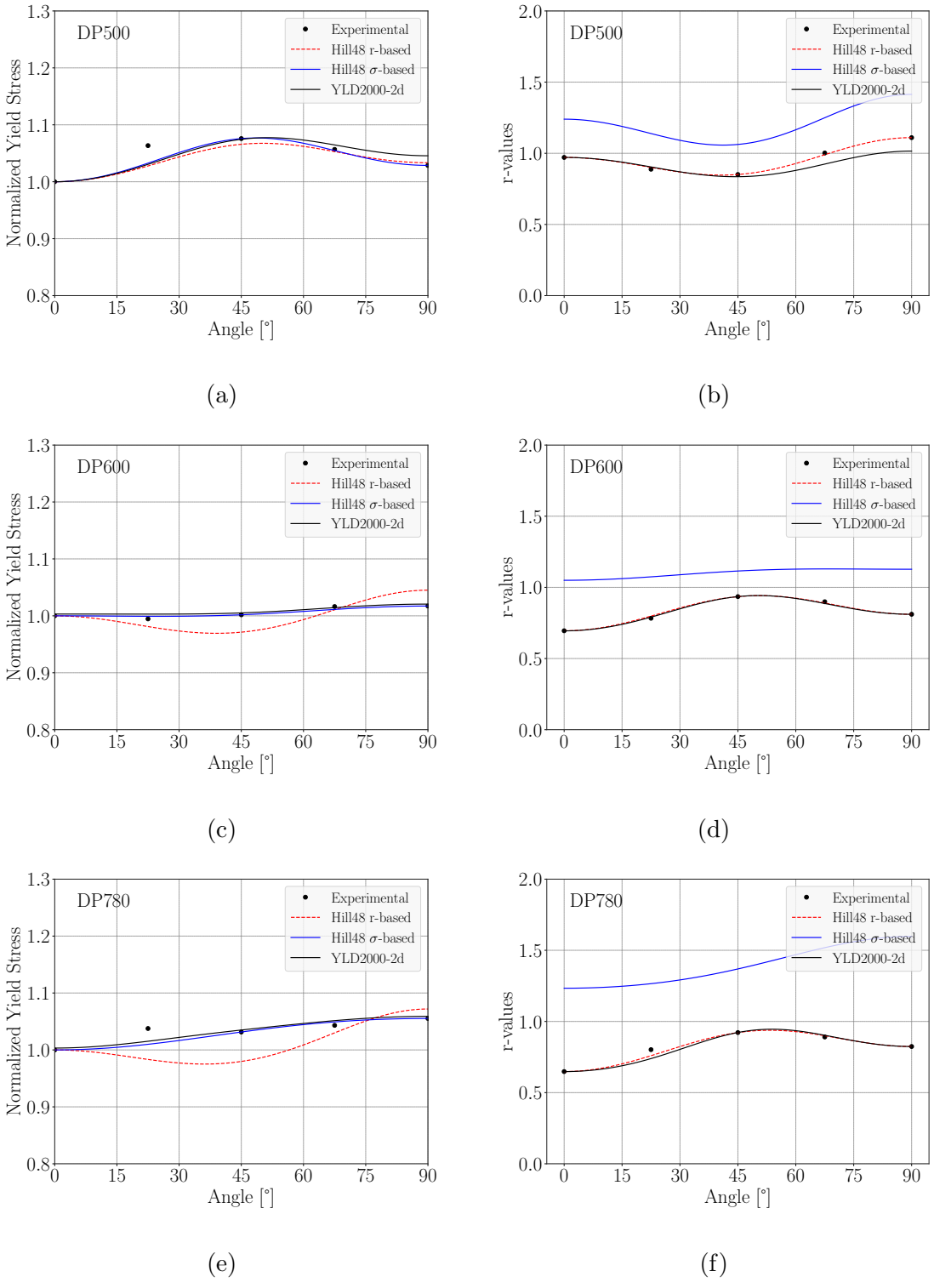


Figure 4.2: Predicted normalized yield stresses and r-values of Hill'48 and Yld2000-2d models for (a-b) DP500, (c-d) DP600 and (e-f) DP780.

4.1.2 Material Parameters for Hardening Models

4.1.2.1 Isotropic Hardening

Isotropic hardening for the selected dual-phase steels was modeled using a Swift hardening law represented by the Equation 2.35. The Swift parameters (K, ε_0 and n) were optimized using the Nelder-Mead method [272], also known as the simplex direct search method. This method identifies the minimum mean square error between the hardening law prediction and the experimental stress-strain curve obtained from the uniaxial macro tensile tests. The identified isotropic hardening parameters are summarized in Table 4.3 and the corresponding hardening evolution curves are plotted in Figure 4.3. These parameters will be crucial for validating the developments proposed in Sections 4.2 and 4.3, as well as for verifying the accuracy of the isotropic parameters identified by bending tests and ML techniques.

Table 4.3: Identified parameters for the Swift hardening law based on experimental stress–strain data for dual-phase steels.

Isotropic Hardening (IH)			
	K [MPa]	ε_0	n
DP500	865.32	0.0026	0.1530
DP600	1011.01	0.0019	0.1563
DP780	1253.72	0.0001	0.1431

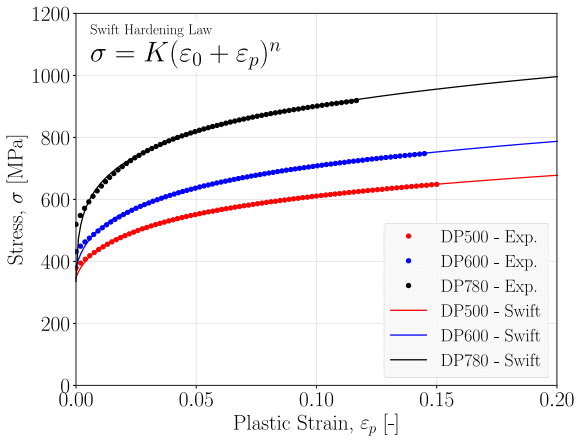


Figure 4.3: Comparison between the experimental stress-strain curves and Swift hardening curves for the different dual-phase steels.

4.1.2.2 Anisotropic Hardening

The anisotropic hardening behavior of the dual-phase steels was described using two different models: (a) a combined isotropic-kinematic hardening model (IKH) and (b) the homogeneous hardening model (HAH) [101]. For the combined model, the isotropic component is represented by the Swift hardening model characterized by three parameters (K, ε_0 and n), while the kinematic component is modeled by the Frederick-Armstrong model [107] with two parameters (C and γ) that require calibration. For the HAH model, six parameters, denoted as k and k_1-k_5, must be identified to control the evolution of state variables during reverse loading. As mentioned in Section 2.2.2.2, the HAH model also includes an isotropic component, which in this case was characterized using the Swift parameters listed in Table 4.3. The material parameters were identified based on tension–compression tests using miniaturized specimens (Section 3.4.1 performed along the rolling direction.

For the identification of the IKH hardening parameters, a genetic optimization algorithm was developed to minimize the MSE between the tension-compression experimental results and the numerical solution. For the calibration of the HAH model, the optimization code provided by Yoon [273] was used. The parameters for the IKH and HAH models are summarized in Table 4.4 and 4.5, respectively. Figure 4.4 shows a comparison between the experimental stress-strain curves and the numerical results based on both anisotropic hardening models for DP500, DP600 and DP780. For each material, the left plot shows the results for the IKH model compared to the purely isotropic hardening model. On the right side, the same experimental data is shown but with the HAH model applied.

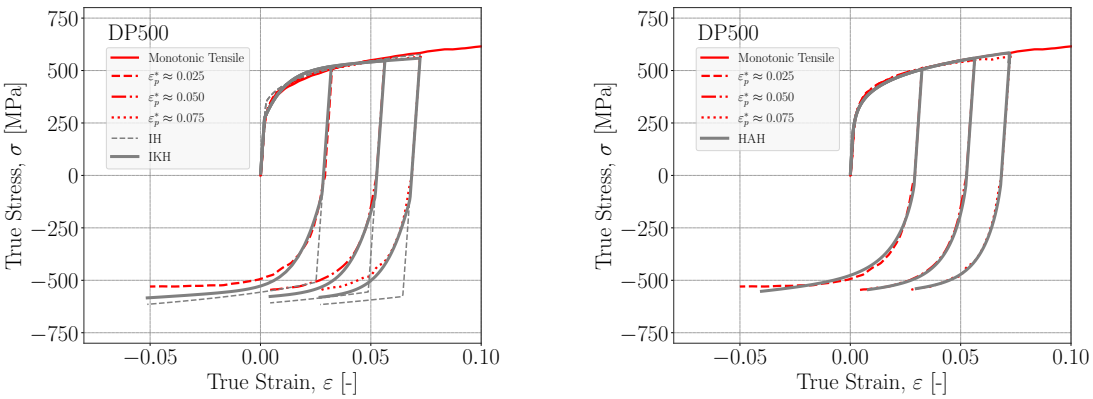
Table 4.4: Identified parameters for the isotropic-kinematic hardening (IKH) model applied to dual-phase steels.

Combined Isotropic Kinematic Hardening (IKH)					
	K [MPa]	ε_0	n	C [MPa]	γ
DP500	632.6	0.082	0.334	27710	124.2
DP600	874.4	0.0725	0.318	22523	113.9
DP780	651.8	0.054	0.191	38850	88.3

Table 4.5: Identified parameters for the homogeneous anisotropic hardening (HAH) model applied to dual-phase steels.

Anisotropic Hardening (HAH)							
	q	k	k_1	k_2	k_3	k_4	k_5
DP500	2	44	110.61	400.00	0.30	0.80	18.96
DP600	2	44	167.3	111.80	0.32	0.80	50
DP780	2	45	87.83	449.91	0.47	0.78	59.92

The tension-compression tests show that the dual-phase steels exhibit a pronounced transient Bauschinger effect immediately after load reversal, together with signs of work-hardening stagnation and permanent softening. In the modeling results, the IH model fails to predict the Bauschinger behavior and consistently predicts higher stresses after load reversal, especially in the early stages of reversal. Conversely, the IKH model successfully captures the transient Bauschinger effect and provides a more accurate representation of the yield stress under reverse loading than the IH model. However, it still falls short in reproducing the observed work hardening stagnation and permanent softening. On the other hand, the HAH model predicts both the monotonic and reverse loading response more accurately. Overall, this model accurately predicts the new yield stress when the loading direction is reversed, as well as the work-hardening stagnation and permanent softening phenomena. The identified IKH model parameters will be used in Section 4.3 for comparison with the parameters calibrated using ML approaches. On the other hand, the HAH model parameters will be used in Chapter 5.



(a) (b)

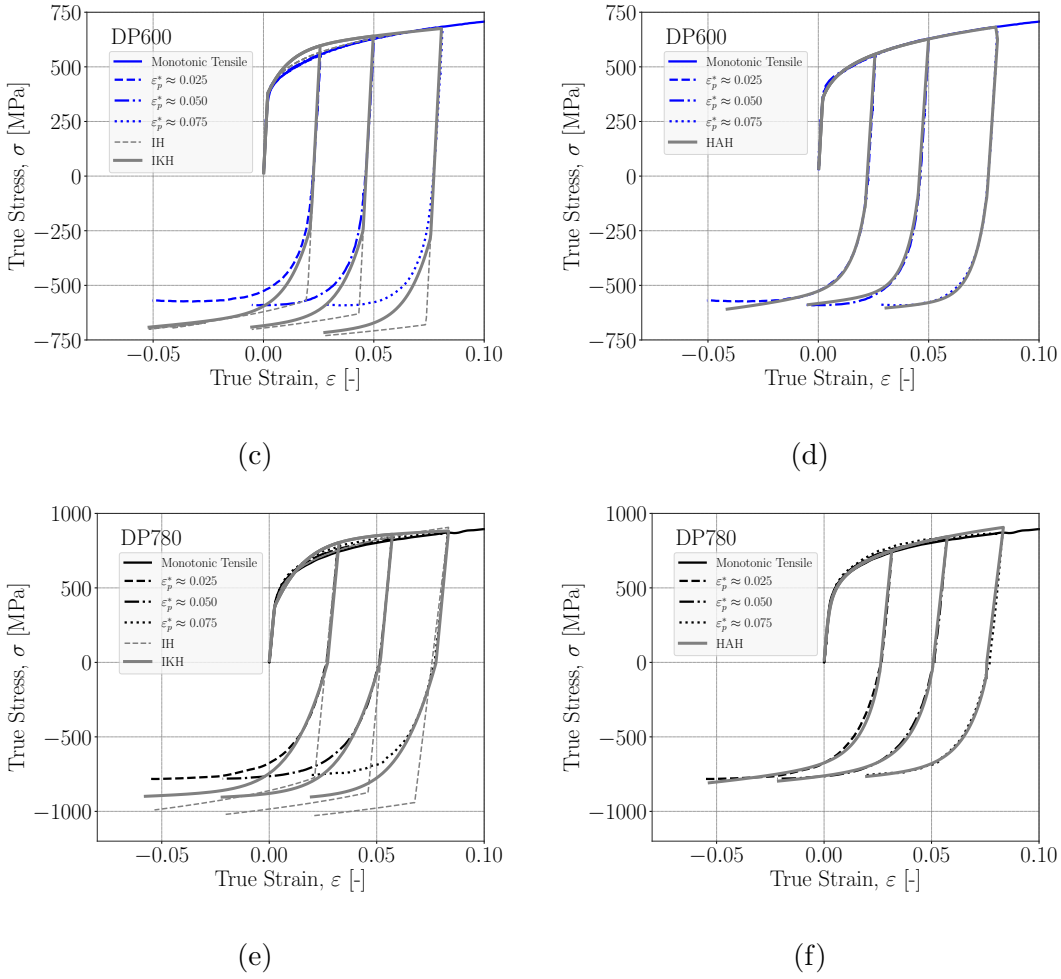


Figure 4.4: Comparison of experimental stress-strain curves with calculated results using the IKH and HAH anisotropic hardening models for (a-b) DP500, (c-d) DP600 and (e-f) DP780.

4.2 Identification of Isotropic Hardening Parameters using Machine Learning and a Three-Point Bending Test

Following the identification of material parameters using traditional optimization algorithms, this section explores the potential of ML models, specifically neural networks, to predict the isotropic hardening behavior of metallic materials based on experimental results from a three-point bending test. The three-point bending test [274] is a classic experiment used to evaluate the behavior of a material when

subjected to bending. This test is relatively simple, as it does not require any prior preparation of the sample (e.g. machining) and can easily be performed on a universal tensile testing machine. The objective of this first study is to leverage the advantages of this test and develop a new methodology based on neural networks to characterize the hardening behavior of a material using the results obtained in a three-point bending test. Accordingly, a new procedure is proposed to replace traditional inverse and analytical fitting methods, offering a more accessible approach for characterizing the hardening behavior of materials.

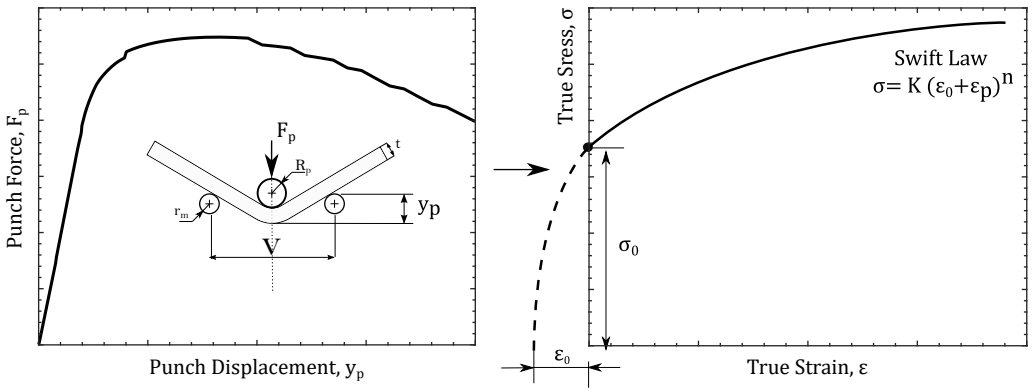


Figure 4.5: Schematic illustration of the three-point bending test and definition of the main problem objectives.

As represented in Figure 4.5, the developed neural networks take as input the punch force–displacement curve obtained from a three-point bending test and output the characteristic parameters (K, ε_0 and n) of the Swift hardening law, as defined in Equation 2.35. The methodology is designed to characterize steel materials with K values ranging from 400 to 1600 MPa, ε_0 values between 0.0001 and 0.1 and n values between 0.05 and 0.35. These ranges are aligned with the objective of characterizing sheet steel materials commonly used in industrial applications, ranging from mild steels to advanced high-strength steels.

4.2.1 Methodology

The methodology that combines neural networks with bending test results is presented in Figure 4.6. This approach is applicable not only to the identification of isotropic parameters discussed in this section, but also to the identification of anisotropic parameters as presented in Section 4.3. The main differences between these applications lie in the nature of the input data, i.e. the type of bending test used and the corresponding output parameters.

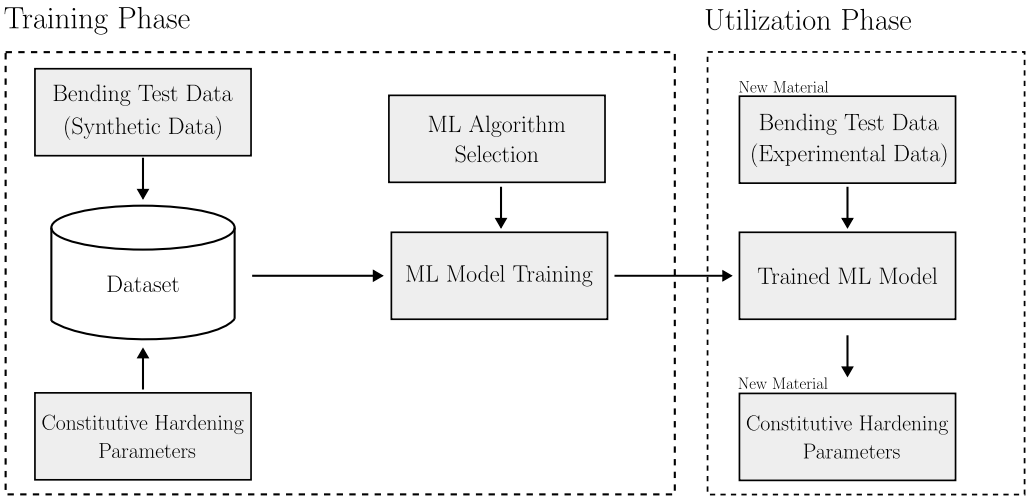


Figure 4.6: Overview of the proposed methodology combining machine learning and bending tests for material parameter identification.

The methodology is divided into two main phases: the training phase and the utilization phase. In the training phase, a synthetic dataset of bending test results is generated using finite element analysis. The numerical model used for this data generation is first validated by experimental tests on DP500, DP600 and DP780 materials. Once the numerical model is validated, multiple numerical simulations are performed using different combinations of material parameters. This process generates a comprehensive dataset covering a wide range of materials and their corresponding bending test results, represented by force-displacement curves. An appropriate machine learning algorithm is then selected based on factors such as the nature of the input data and the type of problem being addressed, in this case a regression problem. The selected ML algorithm is trained on the synthetic dataset, learning how to relate the bending test data to the corresponding constitutive hardening parameters. In the training phase of the machine learning model, several key steps are taken to ensure robust performance and generalization to unseen cases. First, feature identification is performed to select the most relevant input variables from the bending test that effectively capture the underlying material behavior. The synthetic dataset is then divided into distinct subsets, typically training, validation and test, to facilitate model learning and to evaluate performance on data that the model has not previously encountered. Throughout the training process, visualization techniques are used to analyze data distributions and monitor the model's predictions, helping to detect potential biases or overfitting. In addition, regularization strategies and hyperparameter tuning are integrated into the training process

to further enhance the model's ability to generalize and ensure accurate parameter extraction even when presented with new and unseen cases. Once training is complete, the model is considered ready for use. In the utilization phase, the trained ML model is used to predict the constitutive hardening parameters of new materials using real, experimentally collected bending test data (Sections 4.2.4.4 and 4.3.3.2). By processing this new input, the model estimates the hardening behavior of the material efficiently without the need for extensive and time-consuming numerical simulations and optimization loops.

4.2.1.1 FE Model - Three-Point Bending Test

Finite element modeling plays a key role in the proposed methodology, acting as a tool to generate the dataset needed to develop and train the artificial neural networks. By simulating the three-point bending test, FEM accurately replicates the mechanical response of the material under controlled conditions, allowing for the systematic exploration of multiple material parameters. As a result, FEM is able to generate a large amount of data, including punch force-displacement curves, which are used to train the neural network. This approach eliminates the need for extensive physical experimental campaigns, while allowing the exploration of challenging test conditions and materials.

The three-point bending test can be defined as a plane strain problem in which the blank width is much larger than the blank thickness. Due to the symmetry of this test, only half of the real experimental setup was considered in the 2D FE model, as represented in Figure 4.7. The numerical model was developed using ABAQUS with implicit analysis (ABAQUS/Standard) [275]. The punch and die were modeled as fully analytical rigid surfaces. The blank material is considered isotropic elastic, described by the generalized Hooke's law, which has two parameters: the Young's modulus, E and the Poisson's ratio, ν. Additionally, it is described as orthotropic plastic, defined by the Swift hardening law. The sheet blank was discretized using 819 deformable four-node solid elements (CPE4R type from the ABAQUS Library) and nine layers through the thickness. For the mesh discretization, a regular spacing was used in both the thickness and length directions [276]. The frictional interaction between the supports and the blank was modelled using Coulomb's law, assuming a constant friction coefficient, μ. Using this numerical model, a punch force-displacement (F_p-y_p) curve and the variation of the bending angle during the test are obtained.

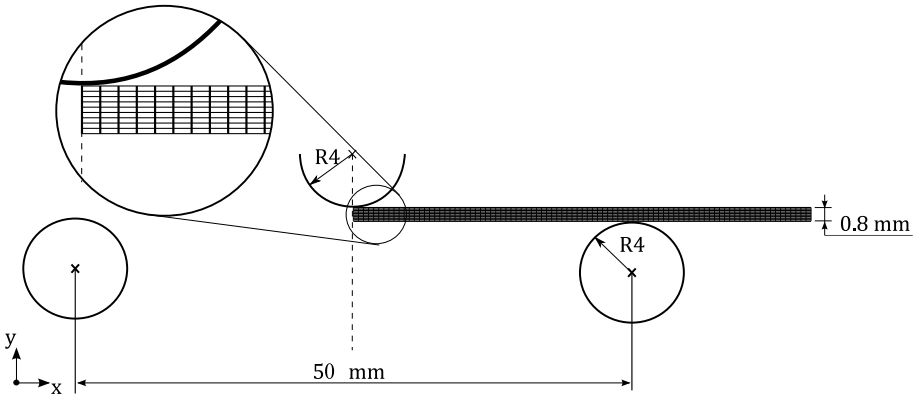


Figure 4.7: Three-point bending test geometry and variables defined.

The experimental validation of the FE model for the three-point bending test is shown in Figure 4.8, which compares the numerical and experimental results for the selected dual-phase steels (DP500, DP600 and DP780). The parameters listed in Table 4.3 were used to model the plastic behavior of these dual-phase steels, while the elastic behavior was defined with a Young's modulus of $E = 210$ GPa and a Poisson's ratio of $\nu = 0.3$. As suggested in Section 3.3.5, the friction coefficient between supports and blank was set as a constant value of $\mu = 0.1$. The numerical results are in good agreement with the experimental data for the selected materials both in the elastic and in the plastic domain, validating the proposed FE model. Furthermore, the estimated friction coefficient in Section 3.3.5 accurately represents the experimental conditions.

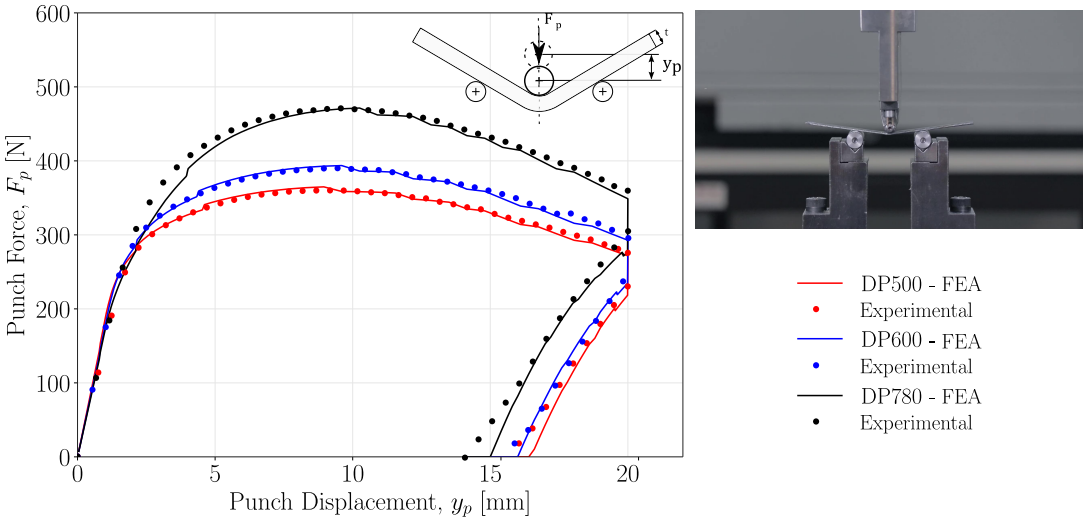


Figure 4.8: Three-point bending force–displacement curves (F_p-y_p) for the selected dual-phase steels (DP500, DP600, DP780) obtained by FEA, with comparison to experimental results.

4.2.1.2 Sensitivity Analysis for Key Variables

To establish a reliable methodology for accurate data generation, the influence of several key variables on the results of the three-point bending test are evaluated through a sensitivity analysis. This analysis is conducted primarily through virtual experiments using the FE model of the three-point bending test. The objective is not only to assess how small variations in different parameters affect the test results, but also to identify the most influential variables, which can later be tuned to improve the agreement between numerical predictions and experimental measurements. These parameters include material properties, such as Young's modulus (E) and plasticity parameters (K, ε_0 and n), as well as geometric and experimental factors such as material thickness (t) and friction coefficient (μ). This preliminary study is an important step in the overall methodology, supporting the creation of a representative and meaningful dataset, as well as the informed selection of relevant inputs and outputs for the neural network framework.

Effect of Young's Modulus

The methodology developed in this work is specifically designed for steel materials, with a particular focus on AHSS. Elastic properties, particularly Young's modulus, can vary across different steel grades, typically ranging between 200 and 210 GPa. Moreover, as demonstrated by Deng et al. [277], Young's modulus can also vary depending on the orientation relative to the material's rolling direction.

In order to assess the impact of Young's modulus variations on the three-point bending curves, a sensitivity analysis was performed using DP500 and DP780 steels. Numerical simulations were performed adjusting the Young's modulus in the range of 190 and 220 GPa while keeping the plastic components constant as specified in Table 4.3. The resulting force-displacement curves for both materials are shown in Figure 4.9a. Despite uncertainties in the elastic material properties, it was observed that variations in Young's modulus have a minimal effect on the punch force-displacement curves in three-point bending tests. The curves closely match throughout the test, diverging only in the elastic regions.

Although the modulus of elasticity may not significantly affect the curves obtained from the three-point bending test, a detailed understanding of the elastic properties of the material is essential to ensure accuracy in the determination of its plastic parameters. Therefore, in addition to determining the material's hardening parameters, the methodology developed next should include a preliminary check to

confirm its classification as a steel, by verifying that its Young's modulus is within the typical range for steels (approximately 190-210 GPa). This verification can be carried out directly from the elastic portion of the bending curves by applying Euler–Bernoulli beam theory in a plane strain analysis. Treating the initial flat sheet as a beam, the deflection of the sheet, δ, in the elastic region in response to the punch force can be determined as:

$$\delta = \frac{F_p V^3}{48 E' I}, \tag{4.1}$$

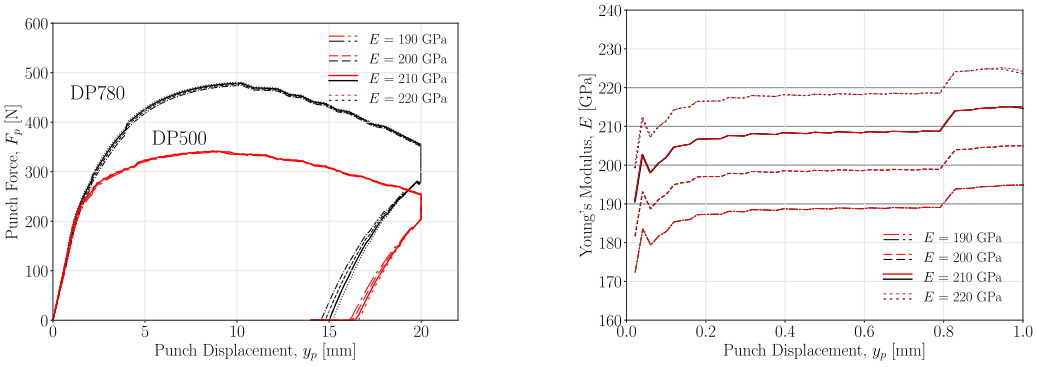
where I is the moment of inertia of the specimen and V is the support span (see Figure A.8). The modulus of elasticity, E', is slightly different from the uniaxial Young's modulus, E and can be expressed as follows:

$$E' = \frac{E}{1-\nu^2}, \tag{4.2}$$

where ν is the Poisson's ratio. Considering the sheet deflection equal to the punch displacement, $\delta = y_p$, the material Young's modulus can be calculated using the punch force-displacement curve by:

$$E = \frac{F_p V^3 (1-\nu^2)}{(48 y_p I)}. \tag{4.3}$$

Based on the three-point bending results for DP500 and DP780 shown in Figure 4.9a, the corresponding Young's modulus, calculated using Equation 4.3 for punch displacements, y_p, less than 1 mm, is shown in Figure 4.9b. As seen, the modulus obtained from the theoretical approach tends to converge to a constant value that is close to the expected value.



(a) (b)

Figure 4.9: Representation of (a) the effect of Young's modulus variations on DP500 and DP780 three-point bending curves and (b) the corresponding analytical estimation of Young's modulus using Equation 4.3.

Effect of Swift Hardening Law Parameters

Following the analysis of Young's modulus, the influence of the Swift hardening parameters (K, ε_0 and n) is evaluated next. To assess the sensitivity of the three-point bending response to each of these parameters a one-at-a-time sensitivity analysis is performed. In this approach, one parameter is varied within a predefined range while the others are held constant. This allows the effect of each parameter on the response to be clearly isolated and interpreted. The sensitivity analysis is performed by fixing two of the Swift hardening parameters and varying the third within its predefined range: K from 400 to 1600 MPa, ε_0 from 0.0001 to 0.1 MPa and n from 0.05 to 0.35.

The results are shown in Figure 4.10: the influence of parameter K is shown in subfigures (a-b), ε_0 in (c-d) and n in (e-f). For each parameter, the left plot shows its effect on the three-point bending force-displacement curve, while the right plot shows the corresponding evolution of the Swift hardening curve (σ–ε_p) for plastic strain values between 0 and 0.2. The common reference parameter set used is $K = 1000$ MPa, $\varepsilon_0 = 0.001$ and $n = 0.2$. For this reference parameter set, Figure 4.11 shows both the equivalent plastic strain (PEEQ) and the stress distribution through the thickness of the material in the three-point bending test for a punch displacement $y_p = 7$ mm. As shown in Figure 4.11b, the levels of equivalent plastic strain developed during the bending test are relatively low. In this case, the maximum plastic strain is about 0.03 meaning that even small variations in the strain hardening curve, especially in the low strain region, can have a significant effect on the resulting force-displacement response. As seen in Figures 4.10b,f, parameters K and n are particularly influential and they affect the overall shape and slope of the strain hardening curve over a wide plastic strain range. Parameter K controls the overall stress level of the curve, while n determines the rate of strain hardening. Consequently, they have the strongest effect on the overall shape of the bending force–displacement curve. In contrast, ε_0 has its strongest influence at low plastic strain values, smoothing the curve near the origin and significantly affecting the initial yield stress. For plastic strains above 0.1, variations in ε_0 become negligible in terms of their effect on the strain hardening behavior. However, since the plastic strains involved in the three-point bend test are small, this parameter still has a significant effect on the three-point bending test response.

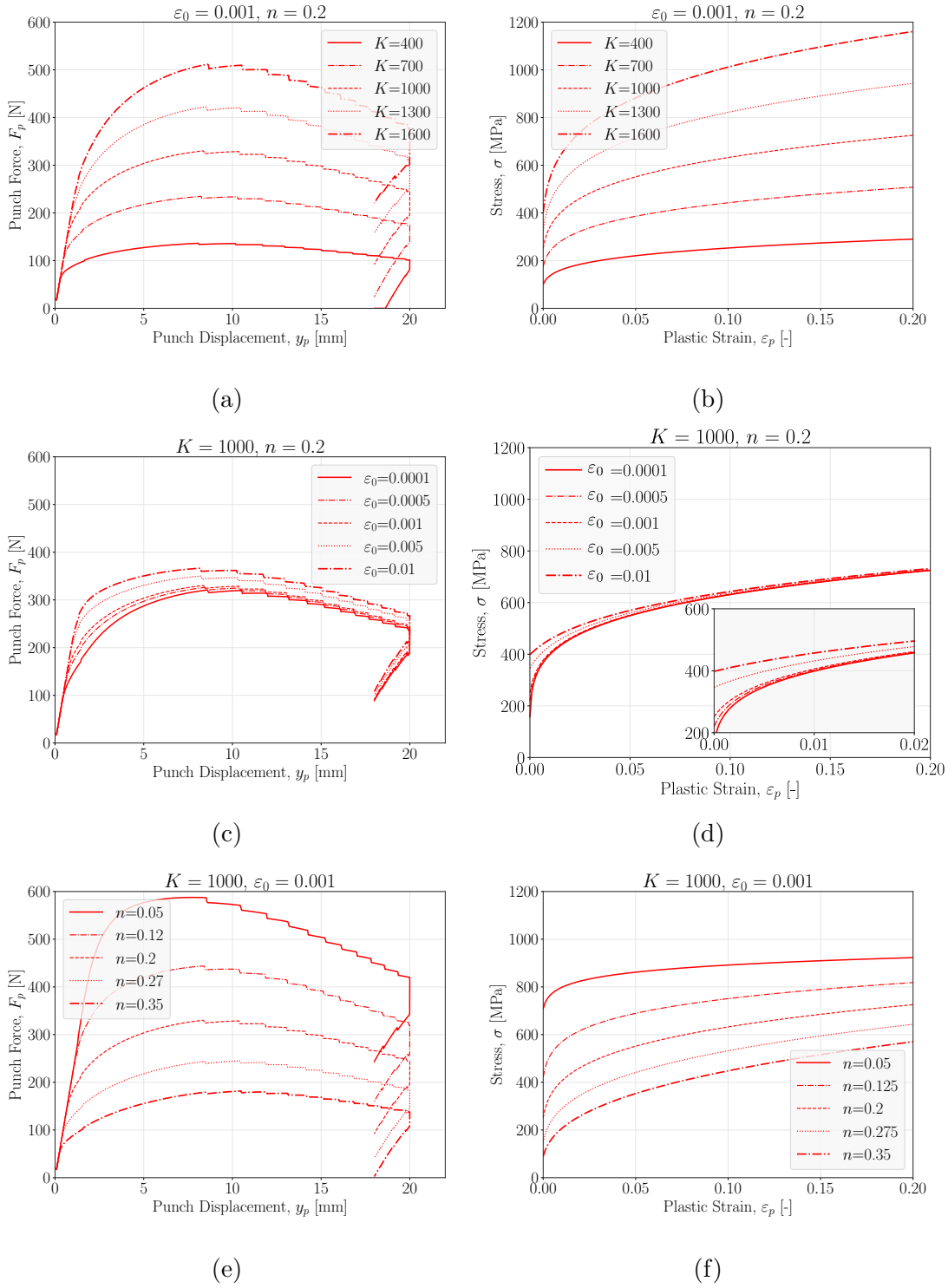
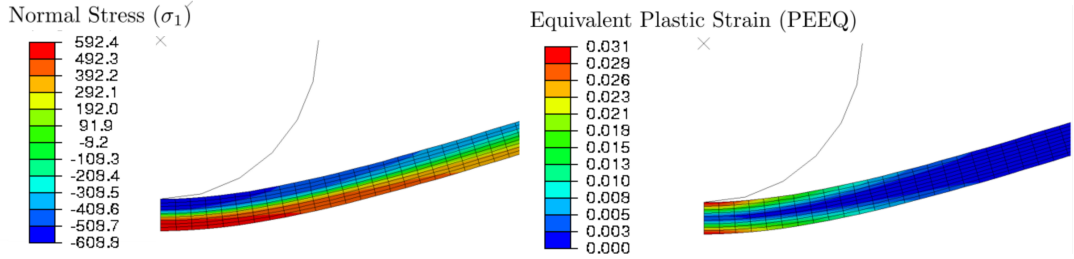


Figure 4.10: Influence of the Swift hardening law parameters on (left) the force –displacement response in the three-point bending test and (right) the corresponding Swift hardening curves: (a, b) parameter K, (c, d) parameter ε_0 and (e, f) parameter n; the reference combination is $K = 1000$ MPa, $\varepsilon_0 = 0.001$ and $n = 0.2$.



(a) (b)

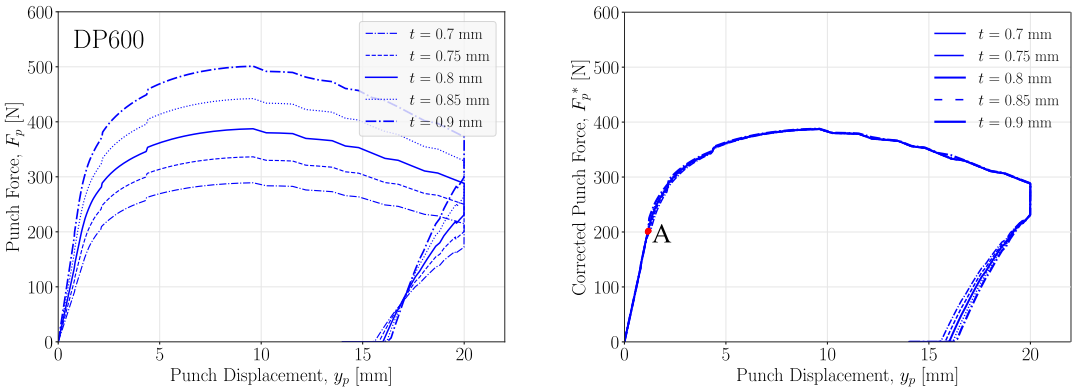
Figure 4.11: Distribution of (a) stress and (b) equivalent plastic strain (PEEQ) through the thickness of the material for the reference Swift hardening parameters ($K = 1000$ MPa, $\varepsilon_0 = 0.001$, $n = 0.2$) during a three-point bending test with a punch displacement of $y_p = 7$ mm.

In summary, the one-at-a-time sensitivity analysis confirms that the three Swift hardening parameters influence the three-point bending response to varying degrees. While K and n govern the overall hardening behavior, ε_0 plays a key role in the initial yielding regime, which is particularly relevant given the low levels of plastic strain induced in the test. These findings highlight not only the importance of accurate parameter identification for reliable predictions of plastic response, but also that, once identified, these parameters provide a robust and precise description of the material's behavior.

Effect of Material Thickness

An important source of variability to consider is related to material thickness. In the context of sheet metal materials, thickness variations are common due to the manufacturing process, resulting in differences from coil to coil and from head to tail [278]. These variations can significantly affect the resulting force-displacement curve and lead to inaccuracy in predicting parameters using neural networks. To evaluate this effect, a sensitivity analysis was performed using DP600 material as a representative case. The analysis focused on evaluating how small variations in thickness affect the three-point bending force displacement curve (F_p-y_p). Numerical simulations were performed for thickness values ranging from 0.7 to 0.9 mm, corresponding to a variation of ± 0.1 mm around the nominal thickness ($t_{nom} = 0.8$ mm). The corresponding curves for each case are shown in Figure 4.12a. The figure shows that even small variations in material thickness can have a significant effect on the force-displacement curve. Therefore, it is important to account for material thickness in the methodology to avoid the potential impact of small variations on

the predictions made by the developed neural networks. To overcome the need to generate a large number of simulations for different thickness values, a normalization procedure is proposed next. This approach transforms the force-displacement curves corresponding to different thicknesses into an equivalent form that corresponds to the curve obtained for the nominal thickness considered in the FE model, i.e. $t_{nom} = 0.8$ mm.



(a) (b)

Figure 4.12: Influence of material thickness in three-point bending curves in the case of DP600: (a) original punch force–displacement curves ($F_p - y_p$); (b) corrected punch force–displacement curves ($F_p^* - y_p$).

Analyzing the stress distribution on the normal section of a bent sheet profile and assuming that the material is strain hardening according to a Swift law, the equilibrium equation is derived using the moment M (see Figure 4.13) as follows [279]:

$$M = \int_{-\frac{t}{2}}^{\frac{t}{2}} \sigma_1 \, y \, dy. \tag{4.4}$$

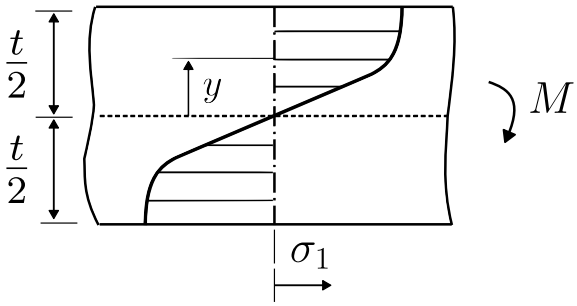


Figure 4.13: Stress distribution on a normal section in bending, considering a strain-hardening material.

The entire section is assumed to behave under elastoplastic deformation and stress, σ_1, at some distance, y, from the middle surface is given by:

$$\sigma_1 = K(\varepsilon_0 + \varepsilon_1)^n = K\left(\varepsilon_0 + \frac{y}{\rho}\right)^n, \tag{4.5}$$

where ρ is the radius of curvature of the bending sheet. This equation reduces to the linear elastic model considering $n = 1$, $K = E'$ and $\varepsilon_0 = 0$. Therefore, the equilibrium equation can be written as:

$$M = 2K\int_0^{\frac{t}{2}} \left(\varepsilon_0 + \frac{y}{\rho}\right)^n y\, dy = 2K\rho^{-n}\left[\frac{t^{n+2}}{2^{n+2}(n+2)} - \frac{\varepsilon_0 t^{n+1}}{2^{n+1}(n+1)}\right]. \tag{4.6}$$

Simplifying the terms, the following equation can be defined for bending a non-linear material:

$$\frac{M}{I_n} = 2K\rho^{-n}, \tag{4.7}$$

where I_n represents the second moment of area for a unit width of sheet, which is given by:

$$I_n = \frac{t^{n+2} - 2\varepsilon_0 t^{n+1}}{2^{n+2}(n+2)(n+1)}. \tag{4.8}$$

Based on these considerations, it is possible to normalize the force–displacement curves for different material thicknesses relative to the nominal material thickness (t_{nom}) using a new variable, the corrected punch force (F_p^*), which can be calculated as follows:

$$F_p^* = F_p \cdot \left(\frac{I_n^t}{I_n^{t_{nom}}}\right), \tag{4.9}$$

where I_n^t and $I_n^{t_{nom}}$ represent the second moment of area for the case of thickness t (different from t_{nom}) and nominal thickness, respectively. Therefore, the normalized curve depends not only on the material thickness t, but also on the hardening parameters n and ε_0 of the material.

For the DP600 material, the normalized curves corresponding to thicknesses within the range of 0.8 ± 0.1 mm are shown in Figure 4.12b. The normalization procedure takes into account two different conditions. For points in the elastic region, up to the point represented by the letter A, the second moment of area was calculated considering the linear elastic model with $n = 1$ and $\varepsilon_0 = 0$. On the other hand, for points in the plastic regime (i.e. points after point A, see Figure 4.12b), the parameters n and ε_0 from Table 4.3 were considered. As seen, the normalization brings the normalized curves for each thickness closer to the nominal curve ($t_{nom} =$ 0.8 mm) in both the elastic and plastic zones. This is a significant advantage in this study as it allows the methodology to be applied to materials with small deviations

from the nominal thickness. In addition, it reduces the number of virtual cases needed for the numerical simulation, since the generated dataset will only consider material thicknesses of 0.8 mm.

Effect of Friction

In order to analyze the effect of the friction coefficient on the three-point bending test results, a numerical sensitivity analysis was conducted using the dual-phase steels (DP500, DP600 and DP780). Different Coulomb friction coefficients, μ, ranging from 0.02 to 0.4 were considered to characterize the friction between the sheet and the tools. The elastic behavior was defined by a constant Young's modulus, E, of 210 GPa and a Poisson coefficient, ν, of 0.3. The plastic behavior was described using the Swift parameters presented in Table 4.3. The results for the selected materials, shown in Figure 4.14, highlight a significant influence of the friction coefficient on the punch force values obtained during the test. As expected, a higher friction coefficient corresponds to a higher punch force for a fixed displacement value. An interesting point to analyze is related to the moment when the punch stops its downward movement and starts an upward movement — denoted as point A in Figure 4.14a.

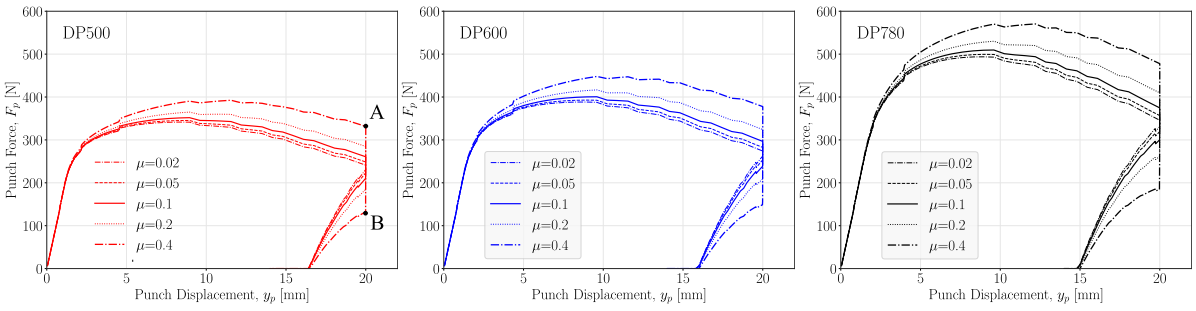


Figure 4.14: Influence of the friction coefficient, μ, on the force–displacement curves of the three-point bending for (a) DP500, (b) DP600 and (c) DP780;

At this point, the frictional force at the points where the plate touches the supports changes sign and as can be seen for all materials, the difference between the force at points A and B is strongly influenced by the existing coefficient of friction. Based on the work of Mentink et al. [280], the coefficient of friction can be estimated according to the Equation A.16, where ΔF is the drop in punch force between points A and B, F_m is the mean value between F_A and F_B and α is half

the bending angle at position A. Using the DP500 as an example, with an expected friction value of $\mu = 0.04$, the bend angle at point A is $\alpha = 83.83°$, F_m is equal to 232 N and ΔF is equal to 199 N. These values lead to an estimated friction value of $\mu = 0.046$, which is close to the expected value. Although the coefficient of friction has a significant influence on the force-displacement curve in three-point bending tests, the experimental setup detailed in Section 3.3.5 does not allow for controlled variation of friction conditions. The use of either lubricant or dry contact does not result in significant changes in the measured force. Therefore, the friction coefficient will not be treated as a variable of interest in the ML model and a constant friction coefficient of $\mu = 0.1$ will be assumed in the FE model, as this value provides the best agreement between the numerical and experimental curve.

4.2.1.3 Dataset Generation

Based on the previous analysis, the methodology for the utilization phase of the ML model is schematically illustrated in Figure 4.15. The process begins with the acquisition of an experimental force-displacement curve from a standardized three-point bending test performed under the conditions described in Section 3.3.5. The raw experimental data is then processed and the force values are normalized using Equation 4.9. This correction ensures that the force values become independent of small variations in material thickness relative to a nominal thickness (t_{nom} = 0.8 mm). Next, the normalized curve is analyzed by a first machine learning model (ML Model - Elasticity), which identifies the elastic portion of the curve and predicts the corresponding Young's modulus (E) of the material. Since this methodology is specifically designed for steel materials, whose plastic behavior is well described by a Swift hardening law, a conditional check is applied. If the predicted Young's modulus is within the expected range for steel (190-220 GPa), a second machine learning model is activated. This model predicts the work hardening parameters (K, ε_0 and n), completing the mechanical characterization of the material. However, if the predicted modulus falls outside the specified range, the second model is bypassed. In this case, only the elastic parameters are reported and the user is notified that the material is not classified as steel under the assumptions of this methodology and therefore the plastic parameters are not evaluated. This two-step approach ensures a systematic and reliable characterization pipeline tailored to steel materials, allowing accurate prediction of both elastic and plastic behavior while avoiding unnecessary computation when the material falls outside the intended scope.

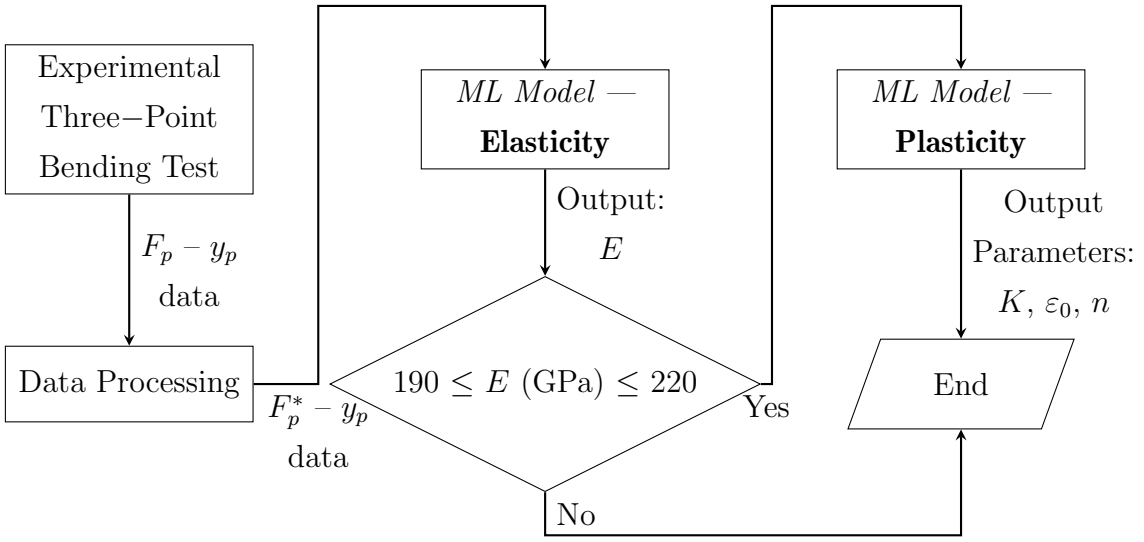


Figure 4.15: Flowchart illustrating the proposed methodology for predicting elastic and plastic parameters of sheet metal materials using experimental three-point bending test curves and neural networks.

The data required to train the ML models was obtained using the numerical model shown in Figure 4.7. As concluded in the previous analysis, the sheet thickness was set to 0.8 mm and the friction coefficient was set to $\mu = 0.1$, as variations in these parameters were shown to either have a negligible effect or were normalized to avoid their influence on the model predictions. To efficiently generate the training data, Python scripts were developed to automatically generate and modify the finite element model by varying the relevant material parameters. These scripts also manage the submission of the simulations. In addition, a post-processing script was implemented to extract key results from each numerical simulation, including punch displacement, punch force, bend angle and corresponding material parameters thus providing the necessary inputs and outputs for neural network training.

Two different datasets were considered, one for training the *ML Model — Elasticity* and the other for training the *ML Model — Plasticity*. The main properties of both datasets are summarized in Table 4.6. For the ML model predicting the Young's modulus of the tested material, 20 different Young's modulus values were numerically considered, equally spaced within $E = [50, 240]$ GPa. For each value, three different sets of strain hardening parameters (K, n and ε_0) were randomly selected within the intervals specified in the table, resulting in 60 different virtual materials. This approach ensures that the ML model learns to identify elastic be-

havior independently of the plastic response. The second dataset was created to have enough data to train the ML model responsible for predicting the hardening parameters of steels. In this case, the elastic properties were fixed at $E = 210$ GPa and $\nu = 0.3$, while the plastic parameters were systematically varied. Specifically, 13 values of K were selected uniformly within the range $K = [400, 1600]$ MPa, 7 values of n were distributed uniformly across $n = [0.05, 0.35]$ and 7 values of ε_0 were chosen within the range $\varepsilon_0 = [0.0001, 0.01]$. The plastic parameters were considered variable, with the combinations shown in Figure 4.16, resulting in a total of 637 cases.

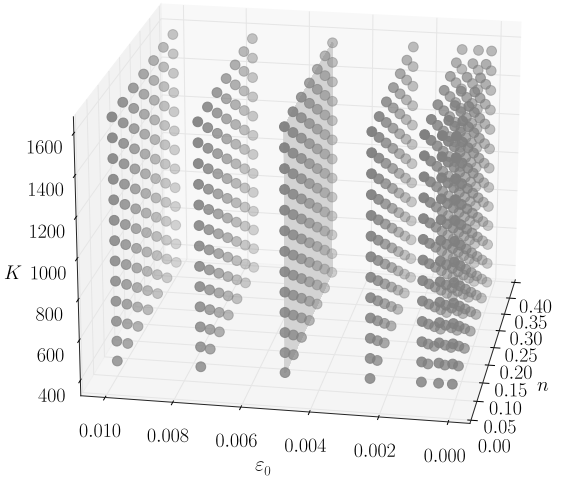


Figure 4.16: Combinations of Swift hardening parameters (K, n, ε_0) selected to generate the dataset for training the *ML Model — Plasticity* consist of 13 values for the K variable ranging between 400 and 1600 MPa with increments of 100 MPa, 7 values for the n variable ranging between 0.05 and 0.35 with increments of 0.05 and 7 values for ε_0 {0.0001, 0.0005, 0.001, 0.0025, 0.005, 0.0075, 0.01}.

Table 4.6: Elastic properties and Swift law hardening parameters considered to develop the ML models.

Properties		**ML Model — Elasticity**	**ML Model — Plasticity**
Elastic Modulus	E	50–240 GPa	210 GPa
Poisson Coefficient	ν	0.3	0.3
Swift Parameter	K [MPa]	400–1600	400–1600
	ε_0	0.0001–0.01	0.0001–0.01
	n	0.05–0.35	0.05–0.35

The combination of these three parameters covers the characterization of the hardening behavior of different types of steel materials, ranging from mild steels to advanced high-strength steels. Each numerical simulation resulted in a force-displacement curve sampled with 500 discrete points, which were used as input feature to train the neural networks.

4.2.2 Neural Network Implementation: ML Model — Plasticity

Considering the dataset shown in Figure 4.16, which consists of 637 cases, three different datasets were created. Following recommended practices for machine learning model development (see Section 2.1.5), the data was randomly divided into training, validation and test sets with distributions of 70%, 15% and 15%, respectively. This division resulted in 446 cases for the training dataset and 95 cases each for the validation and test datasets, as shown in Figure 4.17. For visual clarity, the figure uses a color scheme based on shades of gray, black and red: gray represents cases from the training dataset, black represents cases from the validation dataset and red represents cases from the test dataset. This color scheme will be used consistently throughout the document whenever the division of datasets needs to be illustrated.

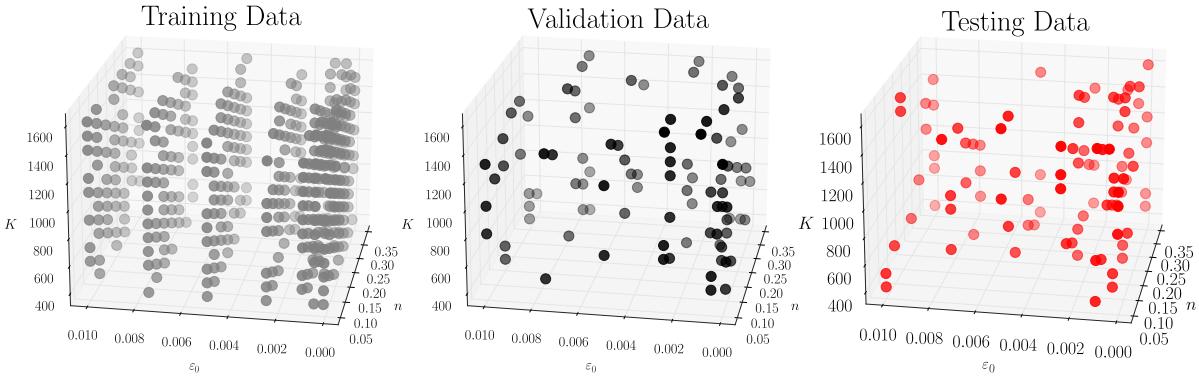


Figure 4.17: Distribution of cases in (a) training dataset (shades of grey), (b) validation dataset (shades of black) and (c) testing dataset (shades of red color), resulting from the random division of the complete dataset (637 cases).

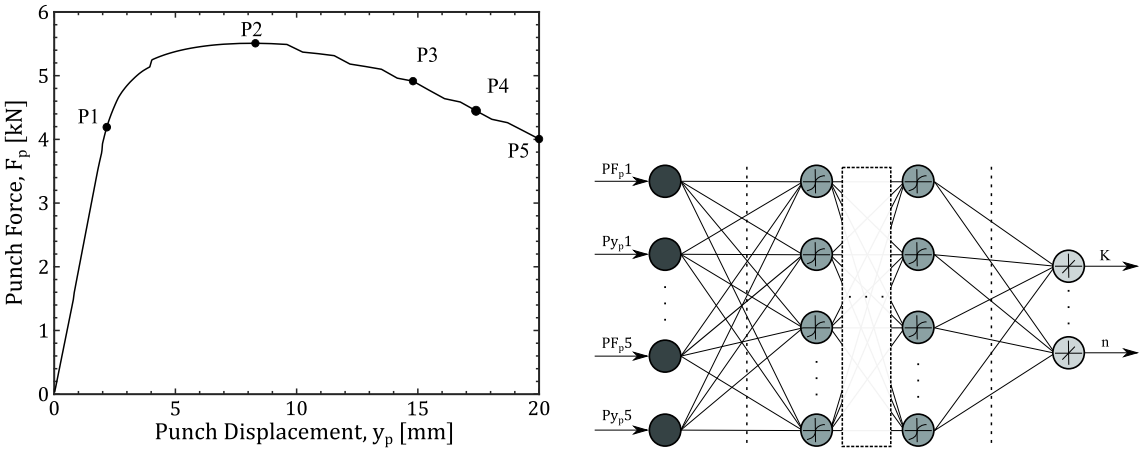
Once the data was split, the next step was to select the most appropriate type of ML model to solve the problem. Two different types of neural networks were tested: one based on shallow conventional feedfoward neural networks and the other based on recurrent neural networks. FNNs process each input independently, without regard to the sequence or context of previous data points. These networks are typically well

suited to static tasks where the relationship between input and output can be treated as discrete and non-sequential. In contrast, RNNs are able to analyze the force-displacement curve as a sequence, taking into account the temporal dependencies and relationships between successive points. This feature allows RNNs to capture more complex patterns in the data that may not be fully represented by discrete point analysis alone. By incorporating feedback loops, RNNs can maintain a memory of past states in the curve, allowing them to model the dynamic evolution of the material's response throughout the bending process.

4.2.2.1 Feedforward Neural Networks

The three-point bending data provided by FEA consists of a punch force displacement curve, F_p-y_p, containing 500 discrete pairs of data points. In an FNN, each layer is fully connected to the next, making it impractical to use all 1000 points as elements in the input layer. To simplify the FNN structure and reduce the number of parameters to be tuned, a guided selection of points is performed. Based on a previous work [238], five pairs of points were selected based on their representativeness, as shown in Figure 4.18a. This approach ensures that the most relevant features of the force-displacement curve are captured while minimizing the complexity of the model. P1 corresponds to the point that separates the elastic deformation zone, characterized by a linear $F_p - y_p$ trend, from the plastic deformation zone on the test curve. On the other hand, P2 represents the point of maximum force in each test. Similarly, P3, P4 and P5 are points with arbitrarily selected fixed displacement values (15 mm, 17 mm, 20 mm) used in each curve. Therefore, as shown in Figure 4.18b, the feedforward FNN is characterized by ten processing elements corresponding to the five pairs of punch force-displacement values in the input layer and three output values corresponding to the K, ε_0 and n parameters of the Swift law.

The ML models were implemented using the Python programming language due to its flexibility and the extensive libraries available for data analysis and machine learning. In particular, the feedforward neural networks were developed using the Keras API [281], a high-level neural network library running on top of TensorFlow [282]. The Adaptive Moment Estimation (*Adam*) optimization algorithm was used throughout the training, with mean squared error as the performance metric. *Adam* is an adaptive optimization method that can incorporate exponential decay for the learning rate, ensuring efficient convergence during training. Hyper-



(a) (b)

Figure 4.18: Implementation of material characterization problem: (a) punch force-displacement curve and the selected five pairs of values (P1-P5); (b) structure of the neural network with ten processing elements in the input layer corresponding to the five pairs of punch force-displacement values and three nodes in the output layer (Swift parameters — K, ε_0 and n).

parameter tuning was systematically performed to improve model performance and generalization. Key hyperparameters, such as number of hidden layers, number of neurons per layer, batch size and decay steps were evaluated across multiple configurations. The decay steps refer to the interval at which the learning rate is reduced during training, facilitating convergence by gradually decreasing the step size as the optimization progresses. A summary of the hyperparameters are presented in Table 4.7. A Bayesian optimization strategy [283] guided the search for optimal hyperparameter values. For the best performing configurations, three independent runs with different random initializations were performed to assess model stability and robustness. Training was performed in batch mode, where model weights were updated after processing a defined number of cases. To avoid overfitting and ensure efficient learning, early stopping was applied based on the performance of the validation set. As a standard preprocessing step, both input and output features were normalized to the range $[-1, 1]$. This normalization improved training stability and ensured that the model was not biased by the scale of the features. To support experiment visualization and comparison between model runs, *Weights & Biases (wandb)* [284] was integrated into the workflow. *Wandb* enabled real-time monitoring of training metrics, automated logging of hyperparameters and results and seamless comparison between different model configurations, increasing the re-

producibility and transparency of the model development process.

The best model was obtained with two hidden layers and 20 neurons per layer, combined with a batch size of 128. A learning rate decay strategy was applied using a decay step of 3000 iterations, which helped improve convergence and model stability during training. This architecture resulted in 703 trainable parameters. The results for this optimized model are shown in Figure 4.19, which provides an analysis of the coefficient of determination (R^2) for each dataset and variable. The first row shows the comparison between the true values and the predictions for the training dataset, with all values normalized to the range $[-1, 1]$. The R^2 results show that the three variables - K, ε_0 and n - are predicted with comparable accuracy, achieving coefficients of determination close to 0.9. However, the variable ε_0 has slightly lower R^2 values compared to the others. The validation and test datasets, shown in the second and third rows, respectively, show a different trend. The R^2 values for the variables K and n are consistent with those in the training dataset, indicating that the model effectively generalizes to the unseen data and does not overfit. On the other hand, the R^2 score for the variable ε_0 is significantly lower, around 0.7, highlighting a limitation in the model's ability to generalize for this particular variable. This discrepancy suggests that the model may be struggling to capture the underlying patterns or relationships specific to ε_0.

Based on these results, it can be concluded that the use of feedforward neural networks combined with the adopted strategy of selecting the most significant features from the force-displacement curves did not produce acceptable results. Although the variables K and n were predicted with relative errors below 20%, as shown in Figure 4.20, the predictions for ε_0 showed significant inaccuracies, with both maximum and minimum relative errors exceeding 100%. These results highlight the need for an alternative modeling strategy that can better capture the underlying patterns associated with ε_0.

Table 4.7: Summary of hyperparameter ranges and fixed training parameters used for the FNN model.

Training Parameters	
Parameter	**Value/Range**
Number of Layers	[2, 10]
Number of Neurons	[5, 50]
Optimizer	Adams
Learning Rate	0.01
Decay Steps	[500, 5000]
Decay Rate	0.96
Batch Size	[32, 64, 128]
Epochs	50,000
Hyperparameter Tuner	Bayesian Optimization

One possible direction is to expand the dataset by including more cases with different ε_0 values, thereby improving the model's ability to generalize. In addition, enriching the input space by including more features from the $F_p - y_p$ curves could provide the model with more informative patterns. Instead of limiting the input representation to five selected force-displacement point pairs, a more comprehensive approach would be to use the full set of 500 points generated by the FE simulations or a suitably representative subset of them. While this would allow for a richer and more accurate description of the mechanical behavior, it would also result in a significant increase in the number of input features and, consequently, the number of trainable parameters, posing computational and optimization challenges. In this context, recurrent neural networks emerge as a promising alternative. Designed to handle sequential data, RNNs can effectively process the entire force-displacement curve while capturing temporal dependencies across the sequence without scaling the number of trainable parameters with the sequence length. This capability makes them particularly well suited to modeling the full behavior of the $F_p - y_p$ curves without the need for extensive feature reduction.

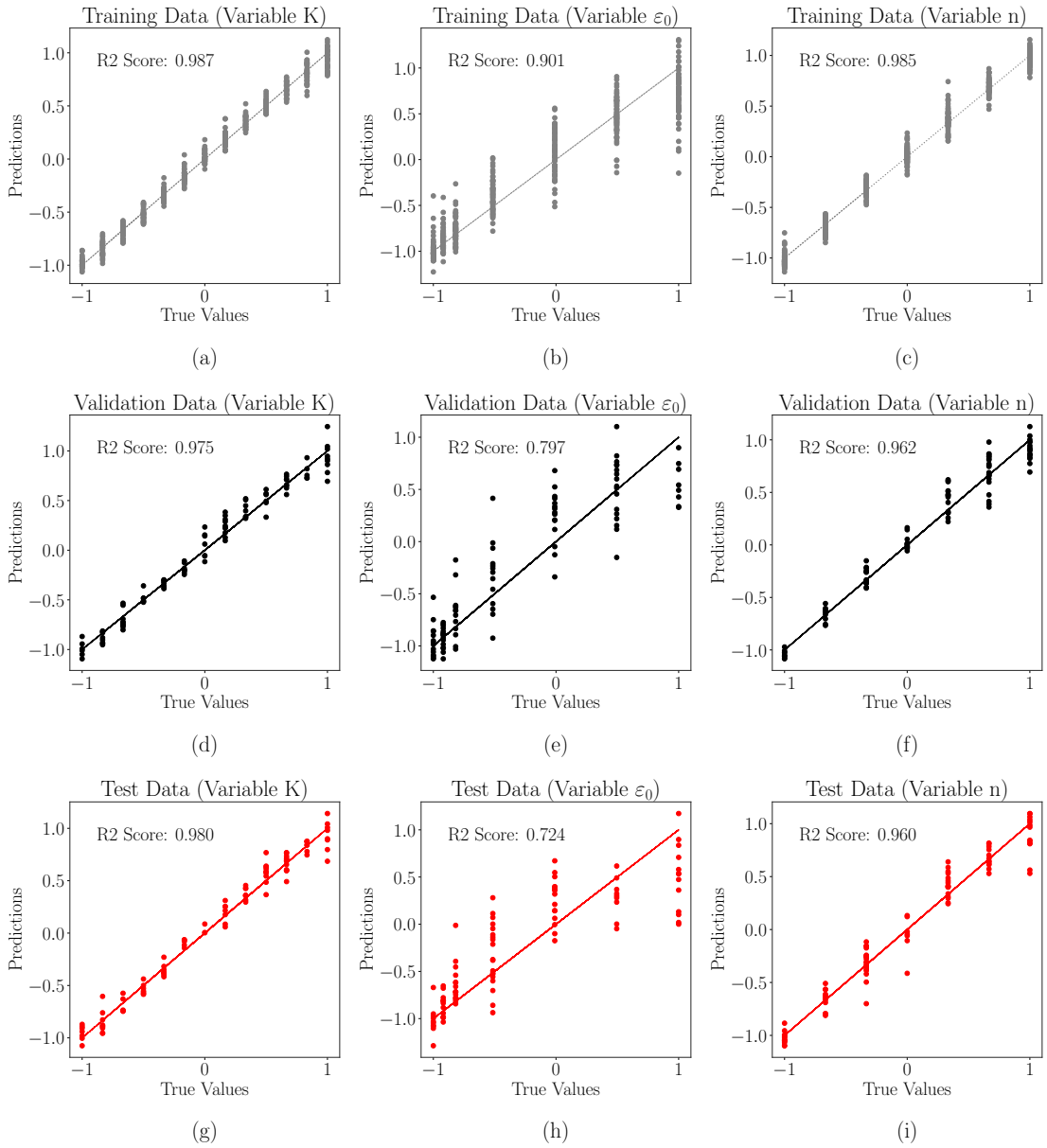


Figure 4.19: Coefficient of determination (R^2) for each dataset—training (gray), validation (black) and testing (red) across the variables K, ε_0 and n obtained considering FNNs.

4.2.2.2 Recurrent Neural Networks

Given the nature of the results obtained from a three-point bending test, expressed as a sequence of force and displacement points, a more comprehensive approach involves the use of deep learning methods based on recurrent neural networks, specifically LSTM networks. As described in Section 2.1.3, LSTM networks

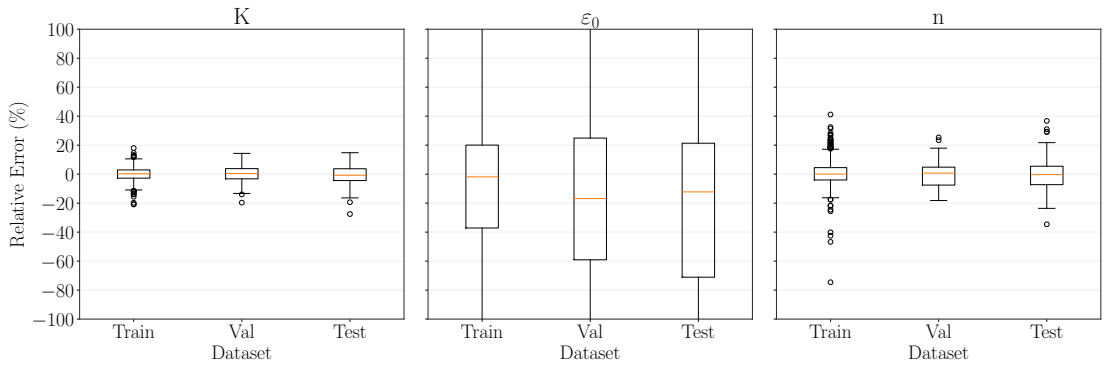


Figure 4.20: Boxplots of relative error percentages for the variables K, ε_0 and n across the training, validation and test datasets, obtained considering FNNs; (Relative Error (%) $= (y_{\text{pred}} - y_{\text{true}})/y_{\text{true}} \times 100$).

are specifically designed to effectively address sequence-related challenges. In this study, they are used to solve a "sequence-to-one" problem, where the model analyzes an input sequence in its entirety and generates a single output, taking advantage of its ability to capture dependencies and patterns throughout the sequence. The following sections describe the implementation of the LSTM-based model and provide a detailed analysis of the training process and its results. The development of the ML model and the subsequent training process were implemented using Python code, making use of the robust deep learning library Keras [281] for LSTM networks. In configuring the LSTM model, a crucial parameter to account for is the number of hidden units in the LSTM layer. This value corresponds to the dimensionality of the output space, i.e., the size of the hidden state at a given time step, $\boldsymbol{h}_t$ in Equation 2.10 and determines the capacity of the model to capture patterns in the sequential data.

For the identification of the parameters of a Swift hardening law, an alternative LSTM variant was explored, namely the Bidirectional LSTM. This choice is justified by the availability of the complete sequence of curves (F_p-y_p) during the prediction phase. This particular recurrent neural network architecture processes the input data bidirectionally, considering both forward and backward directions. Unlike simpler LSTM models that focus only on past context, bidirectional LSTM cover both past and future context, allowing them to capture more detailed patterns in sequential data. In the context of a three-point bend test, the punch force-displacement sequence is processed by the bidirectional LSTM in two passes: one from the beginning of the test ($y_p = 0$ mm) to the end (forward pass) and another from the end to

the beginning (backward pass). The outputs from both passes are then combined to provide a comprehensive representation of the input sequence.

Table 4.8: Summary of hyperparameter ranges and fixed training parameters used for the bidirectional LSTM model.

Training Parameters	
Parameter	**Value/Range**
Number of Units	[10, 80]
Optimizer	Adams
Learning Rate	0.1
Decay Steps	[500, 5000]
Batch Size	64
Decay Rate	0.96
Epochs	50,000
Hyperparameter Tuner	Bayesian Optimization

The training process uses the *Adam* optimization algorithm to minimize the MSE loss on the training dataset. Two different hyperparameters were considered for this model: the number of units of the bidirectional LSTM and the decay steps. The range of variability for these hyperparameters is shown in Table 4.8, along with the fixed training parameters. Multiple runs were considered and the best performance was achieved with a total of 40 hidden units in the bidirectional LSTM and 3670 decay steps, resulting in a total of 3803 trained parameters. Although each run was trained for 50000 epochs, the final model prioritizes the network weights associated with the lowest error in the validation dataset.

The results for the best model are shown in Figure 4.21. This figure shows the coefficient of determination, R^2, for each variable (K, ε_0 and n) split in each dataset (training, validation and test). Both the true values and the predictions are shown as normalized values. Similar to the previous model, both inputs and outputs have been normalized within the range $[-1, 1]$. By analyzing the results, it can be observed that the values for all variables are close to 1 across the three datasets, indicating strong model performance.

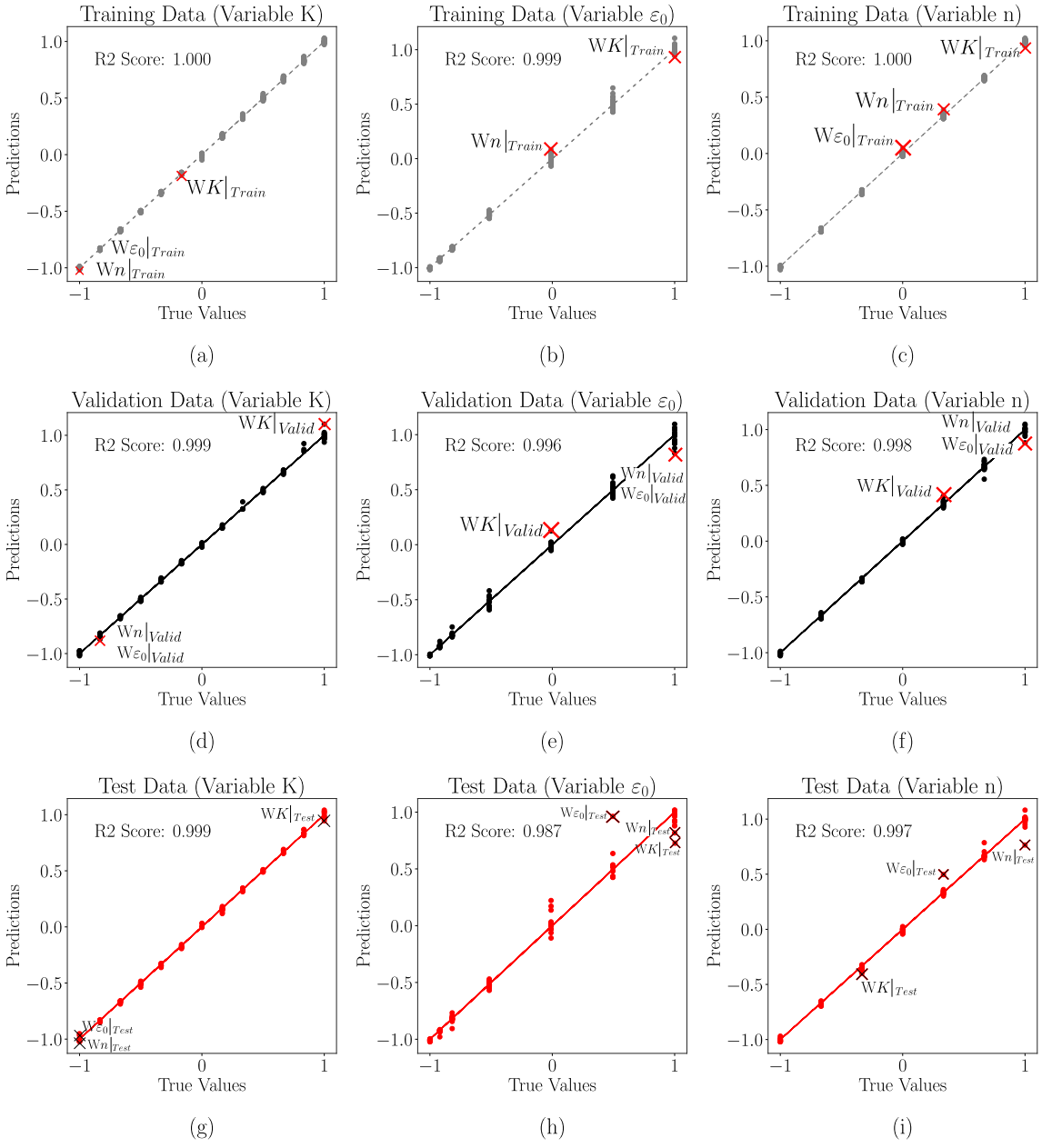


Figure 4.21: Coefficient of determination (R^2) for each dataset - training (grey), validation (black) and testing (red) across the variables K, ε_0 and n obtained using recurrent neural networks.

When comparing the prediction performance for the three variables, it is evident that the parameter ε_0 has the lowest R^2, as was also observed in the FNN-based model, with the test dataset having a R^2 value of 0.987 (Figure 4.21h). This may be related to the limited number of cases in the original dataset, as only seven values for ε_0 in the range [0.01 to 0.0001] were considered. Improving the prediction performance may require generating more data distributed over the specified range.

The variable n also shows some values outside the expected range, especially in the test dataset (Figure 4.21i). In each dataset, three different cases are highlighted, denoted by the letter W. For example, in the training dataset (Figure 4.21a,b,c), the cases W_K, W_{ε_0} and W_n represent the instances with the worst performance for the variables K, ε_0 and n, respectively. These instances are characterized by higher absolute errors between the predicted values and the true values. It is noteworthy that for the validation dataset, the worst cases for n and ε_0 correspond to the same instance. These specific cases will be further examined in the next section to provide a more detailed analysis of the performance of the model and the influence of the prediction errors on the final stress-strain response.

Figure 4.22 shows the box plot with the relative errors for each variable. As seen, the use of LSTMs shows a clear improvement compared to the model based on FNNs, with RNNs providing significantly lower relative errors for all variables. Specifically, regarding the variable ε_0, which previously showed the worst performance, it is evident that with RNNs, the maximum relative errors for this variable are now in the same order of magnitude as the other variables. However, some outliers are still noticeable, with extreme errors close to 100% in some cases. Although this value is high, it is isolated and significantly lower than the extreme limits observed with FNNs, as confirmed by the histograms in Figure 4.23.

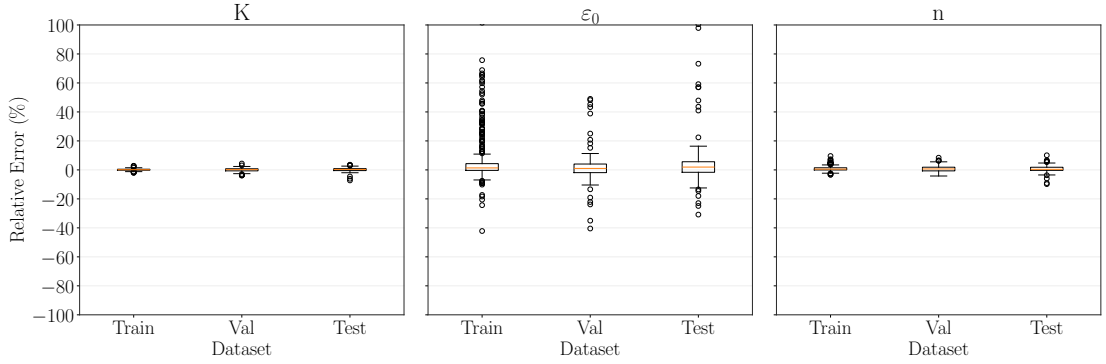


Figure 4.22: Boxplots of relative error percentages for the variables K, ε_0 and n across the training, validation and test datasets, obtained considering RNNs; (Relative Error (%) $= (y_{\text{pred}} - y_{\text{true}})/y_{\text{true}} \times 100$).

In this figure, the histograms of the relative errors for the three variables obtained with FNNs are shown on the left, while the histograms of the relative errors obtained with LSTMs are shown on the right. As mentioned before, the results are significantly better when LSTMs are used for all variables. For the variables

K and n, LSTMs show a maximum and minimum relative error below about 10% and 15%, respectively. In contrast, for FNNs, these values increase to 25% and 50%, respectively. For the variable ε_0, the relative error is one order of magnitude higher than for the variables K and n. For the LSTMs, the extreme relative error is less than 100%, while the error obtained with the FNN-based model is an order of magnitude higher, exceeding 2000%. The influence of these excessive relative errors, especially the parameter ε_0, on the strain hardening curve will be further analyzed in the results section.

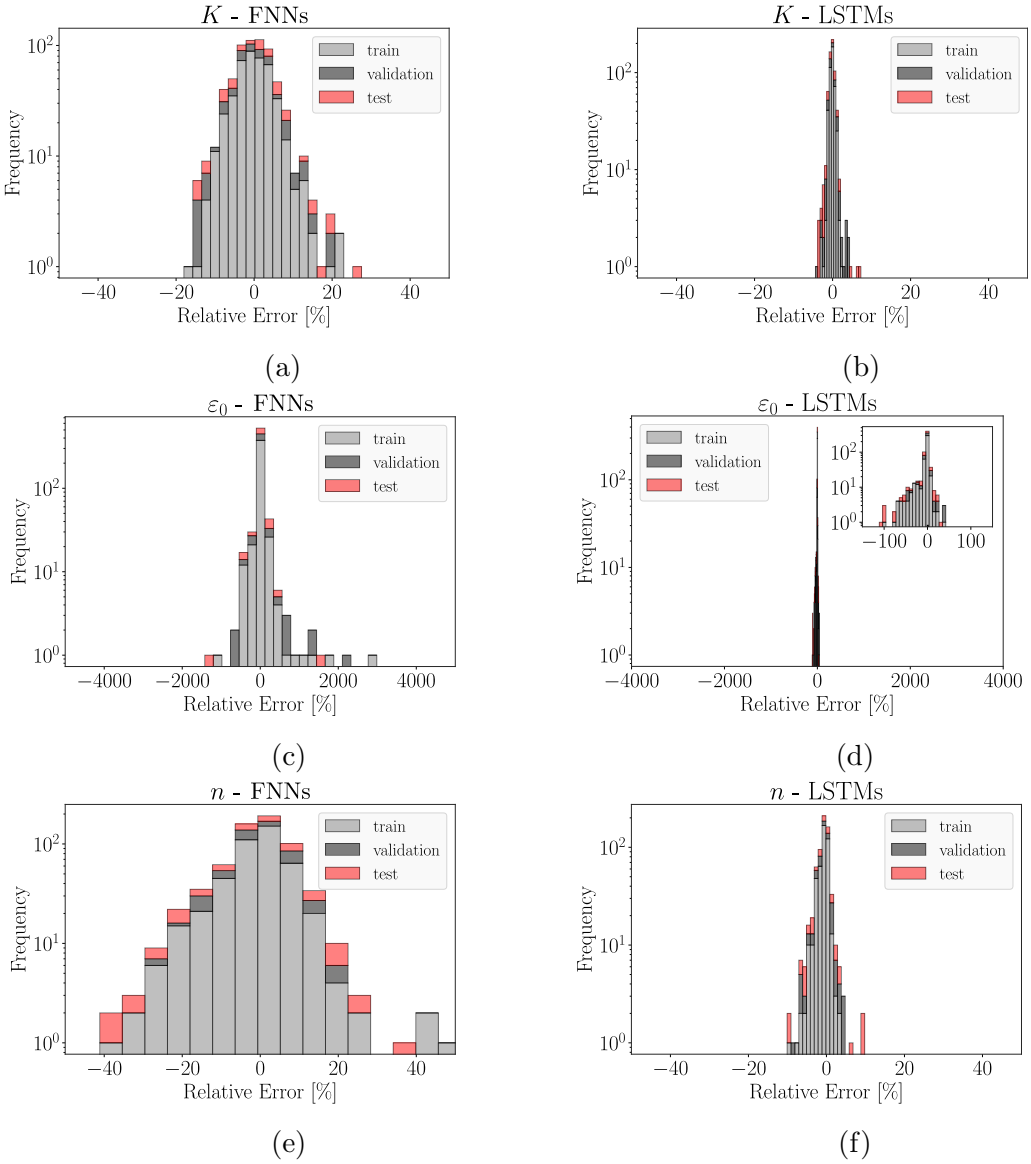


Figure 4.23: Histograms of the relative errors for the three variables (K, n and ε_0) obtained using FNNs (left side) and LSTMs (right side);(Relative Error (%) = $(y_{\text{pred}} - y_{\text{true}})/y_{\text{true}} \times 100$).

Based on this comparison, it can be concluded that the approach based on recurrent neural networks, specifically LSTMs, has greater potential for solving the problem at hand. This is because LSTMs not only take into account more information from the experiment, but also the order in which the data is presented. This allows them to better capture the underlying patterns in the force-displacement relationship, which is critical for accurate predictions. It is important to recognize the computational requirements associated with the LSTM-based approach. The extended training time required for hyperparameter tuning in LSTMs is challenging, especially as the dataset size increases. This computational demand is a trade-off for the improved predictive capabilities and ability to capture temporal patterns offered by LSTMs compared to conventional FNNs.

4.2.3 Neural Network Implementation: ML Model — Elasticity

The data used to train the model for predicting the modulus of elasticity of a material based on a three-point bend test was divided into three separate datasets: training, validation and test. Proportions of 70%, 15% and 15% were used, resulting in 42 cases for training, 9 for validation and 9 for testing. Figure 4.24 shows examples of punch force-displacement curves selected from the original dataset. The selection is limited to cases with Young's moduli of 100 and 220 GPa.

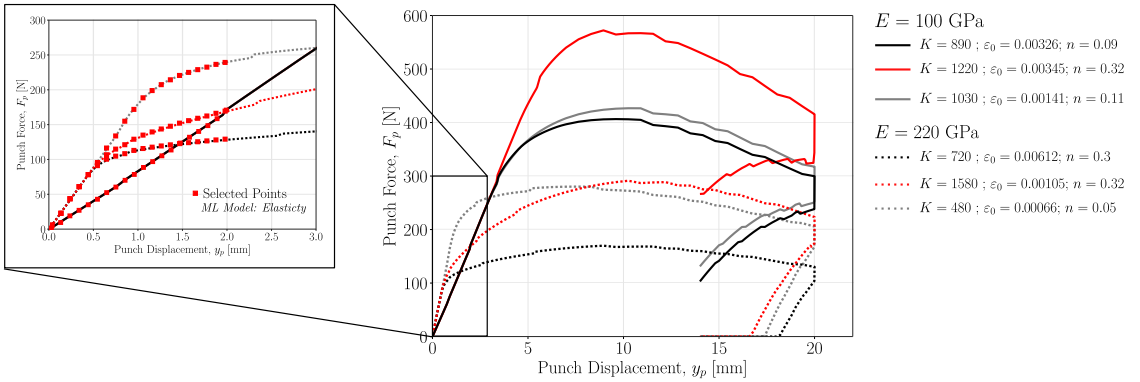
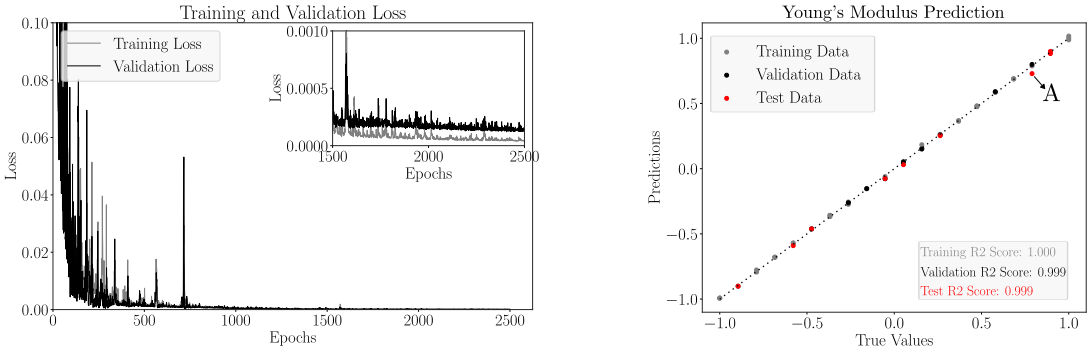


Figure 4.24: Punch force–displacement curves for cases in the training (grey), validation (black) and testing (red) datasets, illustrating selected points for ML development within the $y_p = 0$ mm to $y_p = 2$ mm range.

The main objective of this ML model is to determine the Young's modulus of the tested material. Therefore, it is reasonable to consider only the data points from the initial phase of the test, where the relationship between force and displacement follows a linear pattern. Specifically, for each curve derived from the numerical

simulation, which originally included a total of 500 points, 20 points were selected within the punch displacement range of $y_p = 0$ mm to $y_p = 2$ mm. It is worth noting that in some cases these selected points may contain data from the plastic component, as shown visually in Figure 4.24.

For this ML model developed, since the relationship between variables is essentially linear, only five hidden units were considered in a single LSTM layer. After the LSTM layer, a dense layer was incorporated to aggregate the output of each hidden unit into a single output representing the value of Young's modulus. Both input and output variables were normalized to a standardized range between -1 and 1. The training process used the *Adam* optimization algorithm to minimize the mean square error loss function. In this case, an initial learning rate of 0.1 is applied and reduced by 0.96 every 100 epochs. The model was trained for a total of 2500 epochs and the best performing epoch was selected from the validation set.



(a) (b)

Figure 4.25: Training and performance evaluation figures illustrating (a) the convergence of error curves and (b) coefficient of determination (R^2) in the training, validation and testing datasets.

The training curves in Figure 4.25a show the convergence of both the training and validation errors over 2500 epochs. Both error curves converge to a minimized error value with an MSE on the order of 1×10^{-4}. This value was obtained with the input and output normalized. Such convergence is indicative of robust learning of the model without signs of overfitting. More information about the model's performance can be found in Figure 4.25b, which shows the coefficient of determination, R^2, for the prediction of Young's modulus. It is noteworthy that the coefficient R^2 is approximately one for all three datasets, indicating a high degree of accuracy in the predictions. In the most challenging case, denoted by the letter A, the relative error obtained is 2.5%. For this specific case, the expected Young's modulus is 220 GPa

and the ML model predicted 214 GPa, which is an acceptable deviation. Despite a difference of 6 GPa, this material is still classified as steel since the obtained Young's modulus falls within the acceptable range ($190 \leq E(\text{GPa}) \leq 220$).

4.2.4 Results and Validation of Developed ML models

4.2.4.1 ML Model — Elasticity

Based on the best model presented in Section 4.2.2.2, this section provides additional results with three new virtual materials to complement the analysis of the predictive capabilities of the *ML Model — Elasticity*. To do this, the three-point bending test was numerically simulated for the three new virtual materials, designated *VM1, VM2, VM3*, with Young's modulus values of 75, 215 and 225 GPa, respectively. These elastic parameter values were not included in the original dataset used to develop the ML model, meaning that the trained model was not exposed to such values during its training and testing phases. For each virtual material (*VM1, VM2, VM3*), the plastic parameters (K, ε_0 and n) were randomly selected from the allowed range presented in Table 4.6. The corresponding values for each virtual material are summarized in Table 4.9. Based on these elastic and plastic parameters, the three-point punch force-displacement curves shown in Figure 4.26 were obtained by FEA. For each curve, twenty points up to a punch displacement of $y_p = 2$ mm were considered as input to the trained ML model and are also shown in Figure 4.26. The Young's modulus predicted by the trained LSTM is summarized in Table 4.9. The results show good accuracy, as the predicted values closely match the true values, with a relative error consistently below 3% for the additional virtual materials. This high level of accuracy is indicative of the robust generalization capability of the model, which performs well not only on materials from the original dataset, but also on new randomly generated materials. Furthermore, it can be concluded that the prediction is independent of the plastic parameters of the material, since these values were randomly chosen both in the training dataset and in these additional cases. Even though for some materials the selected 20 points include points outside the elastic regime, the ML model can effectively predict the corresponding modulus of elasticity of the material. Following the intended approach of using ML presented in Figure 4.15, in this case only the virtual material *VM2* would be considered as steel and thus it would proceed to the next stage of identification of plastic parameters.

Table 4.9: Plastic parameters (K, ε_0, n) and corresponding Young's modulus (E) predictions for virtual materials (*VM1*, *VM2*, *VM3*), compared with true values.

	Swift Parameters			**Young's Modulus (E)**		
Material	$\boldsymbol{K}$ **[MPa]**	$\boldsymbol{\varepsilon_0}$	$\boldsymbol{n}$	**True [GPa]**	**Predicted [GPa]**	**Error [%]**
VM1	1020	0.007	0.23	75.00	75.91	1.21
VM2	1011	0.0019	0.16	215.00	215.07	0.03
VM3	1150	0.0032	0.32	225.00	221.68	1.48

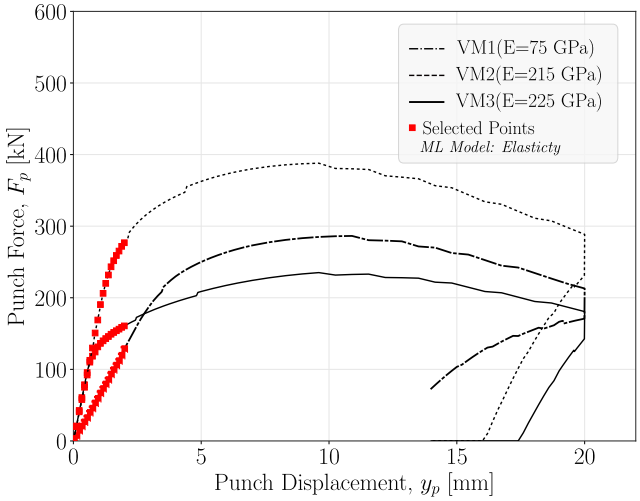


Figure 4.26: Three-point bending punch force–displacement curves obtained by FEA for virtual materials *VM1*, *VM2* and *VM3* with Young's modulus (E) values of 75, 215 and 225 GPa, respectively.

4.2.4.2 ML Model — Plasticity

Based on the best model presented in Section 4.2.2.2, this section provides additional results to complement the analysis of the predicted capabilities of the *ML Model — Plasticity*. Figure 4.27 illustrates the overall relationship between the three targets (K, ε_0 and n) and the obtained predictions for the entire dataset (637 cases) used in the development of this model. In each graph, the points marked with a blue star represent the predictions obtained by the developed model and the circles represent the true/expected values. In this plot, the Swift parameters (K, ε_0 and n) are shown in non-normalised values. It can be seen that in the majority of cases

there is a close match between the predictions and the true values, which is particularly evident in the training dataset. However, in some cases within the validation and test datasets there is a slight deviation between predictions and true values.

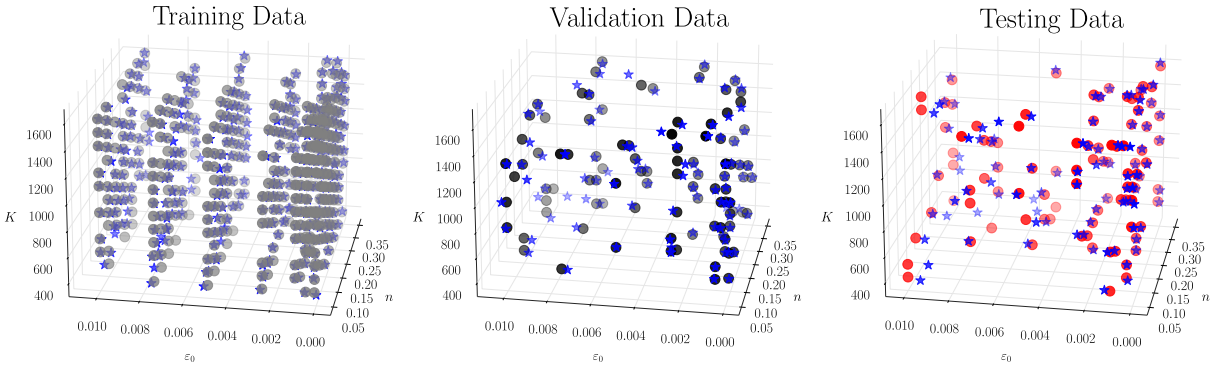


Figure 4.27: Schematic representation of the comparison between the target (circles) and the prediction (blue stars) for (a) the training dataset (grey color), (b) the validation dataset (black color) and (c) the testing dataset (red color).

In order to quantify the worst cases and assess the influence of the prediction on the resultant Swift curve, the instances labeled as W introduced in Figure 4.21 were analyzed and they are represented in Figure 4.28. The corresponding true stress–strain ($\sigma - \varepsilon_p$) curve for each worst case, within a true strain range of $\varepsilon_p = [0, 0.2]$, is presented in Figure 4.28a–c for the training, validation and testing datasets, respectively. Additionally, an example of a case with an accurate prediction result is shown for each dataset ($Best|_{Train}$, $Best|_{Valid}$ and $Best|_{Test}$). For each case, two different stress–strain curves are presented: one obtained considering the true parameter values (solid line) and the other using the parameters predicted by the developed ML model (dashed/dotted lines). To better quantify the errors between the stress values calculated using Swift parameters predicted by the ML model and the true values, Figure 4.28d–f display the true stress error, $\Delta\sigma$, for the cases belonging to the training, validation and testing datasets, respectively. The true stress error is determined by the difference between the stress calculated by the ML model and the target value of stress ($\Delta\sigma = \sigma_{LSTM} - \sigma_{target}$) for each value of plastic strain, ε_p.

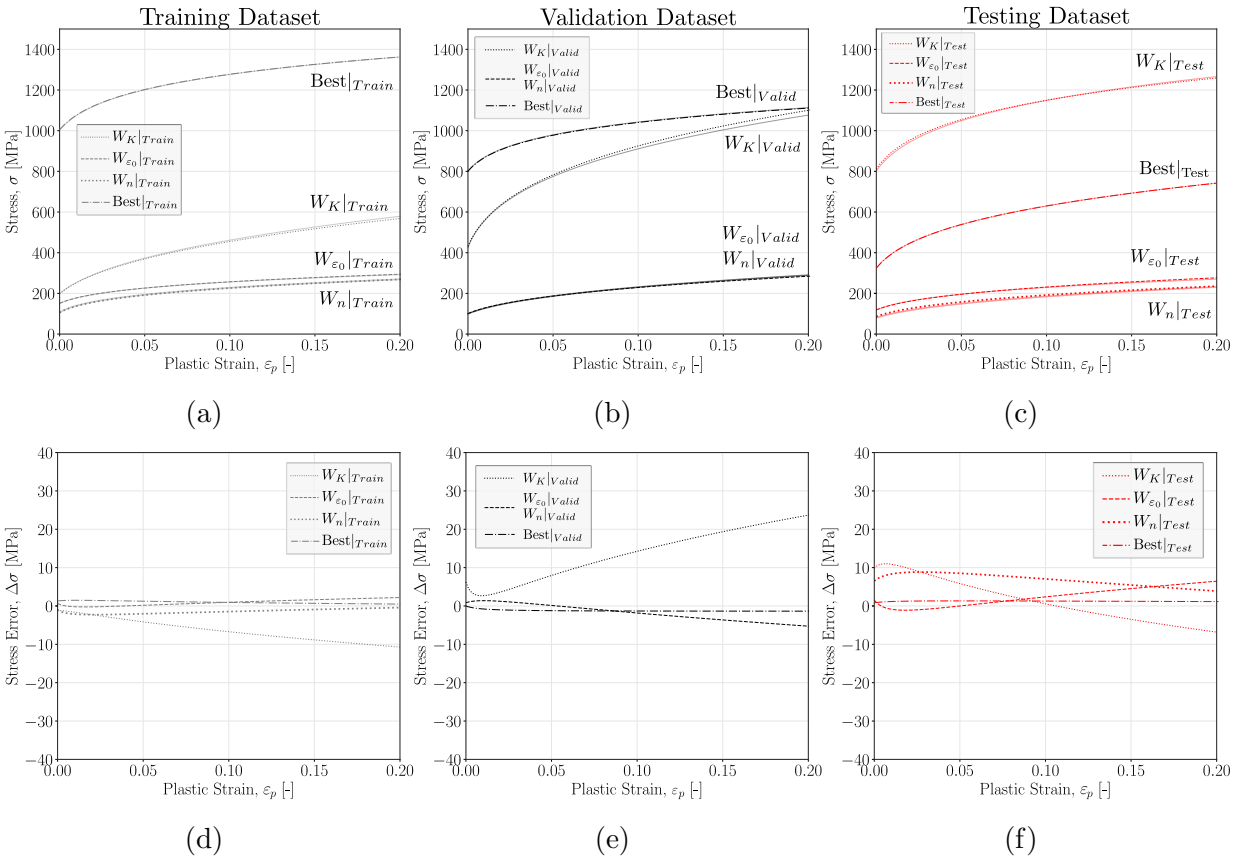


Figure 4.28: Comparison of predicted (dashed/dotted line) and expected (solid line) true stress–strain curves ($\sigma - \varepsilon_p$) for cases W_K, W_{ε_0} and W_n for the training (a), validation (b) and testing (c) datasets and respective true stress errors, $\Delta\sigma$, for the training (d), validation (e) and testing (f) datasets; $Best|_{Train}$, $Best|_{Valid}$ and $Best|_{Test}$ $Best|_{Train}$ are examples of cases with an accurate prediction result.

Analysis of the best cases in the three datasets ($Best|_{Train}$, $Best|_{Valid}$ and $Best|_{Test}$) shows that the predicted curves closely match the target curve for the range of plastic strain considered, with a stress error of less than approximately 5 MPa in all datasets. This error value may be representative of the majority of the total number of cases, as shown in Figure 4.29. This figure includes both the histogram of the maximum absolute stress error, $|\Delta\sigma|_{\max}$, (Figure 4.29a) and the corresponding quartile analysis of the maximum relative stress error (Figure 4.29b). The maximum absolute stress error, $|\Delta\sigma|_{\max}$, corresponds for each case to the maximum absolute difference in stress values determined between a plastic strain, ε_p, of 0 and 0.2. The quartile analysis shows that 75% of the total number of cases (75th percentile Q3) have a maximum relative stress error less than 1%. In addition, 97% of the cases have a maximum absolute stress error less than 9.3 MPa, which corresponds to a

relative stress error less than 2%, which can be considered perfectly acceptable in this context. As seen from the analysis, some outliers have been identified, with the histogram showing that these cases are mainly from the validation and test datasets. Despite the existence of these outliers, they represent only 3% of all cases, with the maximum relative error never exceeding 10%. This result suggests that the proposed ML model based on LSTMs is capable of accurately determining the Swift parameters for the majority of cases in the dataset. Furthermore, the chosen LSTM structure, specifically a bidirectional LSTM layer with 40 hidden units, seems to be adequate to capture the patterns in the sequential data and to establish correlations between these patterns and the corresponding hardening parameters.

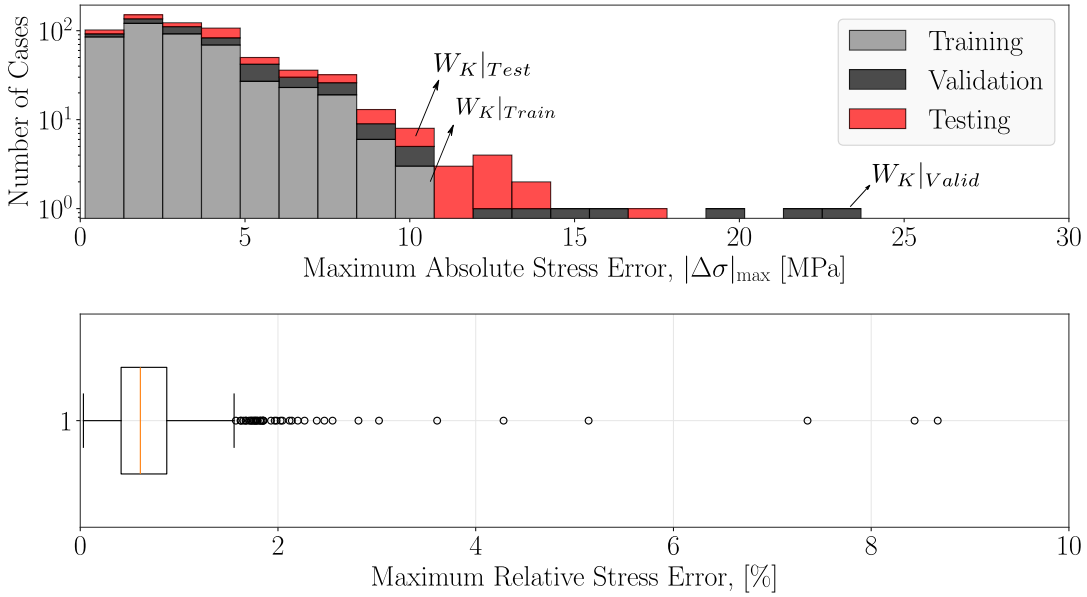


Figure 4.29: Representation of (a) histogram of maximum absolute stress errors $|\Delta\sigma|_{max}$ and (b) respective quartile analysis.

The worst cases (W_K, W_n and W_{ε_0}) across the three datasets reveal potential outliers in the predictions. In the training dataset, the highest stress error, Figure 4.28a,d, occurs for the case $W_K|_{Train}$ at a plastic strain value of $\varepsilon_p = 0.2$, representing a maximum absolute stress error of approximately 10 MPa. Therefore, as indicated in Figure 4.29b, this case is considered an outlier. The expected K value for this case is 1000 MPa and the predicted value is 971.56 MPa, resulting in a relative error of less than 3%. On the other hand, the worst cases, $W_n|_{Train}$ and $W\varepsilon_0|_{Train}$, can be considered as accurate results, as the maximum absolute stress error is below 5 MPa.

For the validation dataset, as shown in Figure 4.28b,e, the worst case is again the one which considers the maximum absolute error in the prediction of the K parameter, $W_K|_{Valid}$. The expected K value for this case is 1600 MPa and the predicted value is 1661.31 MPa, giving a relative error in prediction of about 3%. This difference leads to a maximum absolute stress error value of 23 MPa for a plastic strain value of $\varepsilon_p = 0.2$. Consequently, as shown in Figure 4.29, this case stands out as the most extreme outlier in the prediction, meaning that all other cases show superior performance. As mentioned earlier, for the validation dataset, the worst cases, $W_n|_{Valid}$ and $W_{\varepsilon_0}|_{Valid}$, are the same, meaning they have the same hardening parameters. Similar to the training dataset, this case can be considered a good result as the stress error is within the acceptable range of ± 5 MPa.

Finally, for the test dataset, as shown in Figure 4.28c,f, the maximum stress errors for the cases $W_K|_{Test}$, $W_n|_{Test}$ and $W_{\varepsilon_0}|_{Test}$ are similar and closer to 10 MPa. Once again, the parameter K is the largest contributor to the increase in stress error, which in this case is an outlier, as shown in Figure 4.29b. From this analysis it can be concluded that the parameter K has the greatest influence on the maximum stress error obtained. It should therefore be the parameter with the lowest prediction error in order to minimise stress errors. An analysis of the performance curves shown in Figure 4.21 confirms that this variable is indeed the best performer in this method, with an R^2 very close to one.

Although the prediction of the parameters ε_0 and n is not as accurate as for the parameter K, it can be concluded that the influence of the prediction errors obtained for these parameters does not have a significant impact on the final stress-strain curve. The worst cases for these two variables (W_{ε_0} and W_n) show errors of less than 10 MPa for the three datasets, corresponding to relative stress errors of about 3% and 8%, respectively, which are comparable to majority of the total cases. An important aspect to highlight is the value of the stress for zero plastic deformation, i.e. the yield stress, obtained by the ML approach. This value is generally well determined for the cases analysed, with errors below 10 MPa ($\approx 5\%$). Assuming that the outliers presented represent the worst cases, it can be concluded that the proposed ML model has a high degree of accuracy in predicting the stress-strain relationship, with maximum relative errors never exceeding 10%.

4.2.4.3 Results for Materials with Thickness Variations

As mentioned in Section 4.2.1.3, the proposed methodology should be prepared to be applied to materials with thicknesses in the range $t = 0.8 \pm 0.1$ mm. Therefore, in Section 4.2.1.2, a new approach was proposed to transform the punch force sequence, F_p, into a corrected punch force, F_p^*. This variable standardizes the force values with respect to the nominal thickness, t_{nom}, as given in Equation 4.9, using not only the material thickness but also the material hardening parameters (n and ε_0). However, these two variables are among the main outputs to be predicted by the developed machine learning model. Consequently, they are unknown before the three-point bending tests are performed. To address this issue, a compromise solution is to consider average values for both variables. Since the admissible range of values for n and ε_0 is $[0.05, 0.35]$ and $[0.0001, 0.01]$, respectively, the following analysis will consider the use of arbitrary intermediate values of $n = 0.15$ and $\varepsilon_0 = 0.001$. To validate this simplification, two new virtual materials, denoted *VM4* and *VM5*, were considered and their parameters are presented in Table 4.10. Both materials have a K parameter of 600 MPa, but have different values for the remaining parameters. Specifically, *VM4* represents the lower parameter combination with $n = 0.05$ and $\varepsilon_0 = 0.0001$, while *VM5* represents the higher parameter combination with $n = 0.35$ and $\varepsilon_0 = 0.01$. For each material, three numerical simulations were performed considering different values of thickness $t = \{0.7, 0.8, 0.9\}$, corresponding to the limits of applicability of the proposed methodology. The resulting punch force-displacement curves for each material and thickness are shown in Figure 4.30a. It is evident from this graph that materials with the same Young's modulus and identical thickness exhibit a similar punch force relationship in the elastic regime.

Table 4.10: Swift parameters and Young's modulus of virtual materials *VM4* and *VM5*.

	Swift Parameters			**Young's Modulus**
Material	$\boldsymbol{K}$ **[MPa]**	$\boldsymbol{\varepsilon_0}$	$\boldsymbol{n}$	$\boldsymbol{E}$ **[GPa]**
VM4	600	0.0001	0.05	210
VM5	600	0.01	0.35	

The corrected punch force-displacement curves for these materials are shown in Figure 4.30b. Using Equation 4.9, two sets of parameters were considered: $n = 1$

and $\varepsilon_0 = 0$ for the elastic portion and the parameters $n = 0.15$ and $\varepsilon = 0.001$ for the plastic portion of the curve. It can be seen that, even assuming average parameter values, the curves for thicknesses of 0.7 and 0.9 mm tend to be close to the curve for the nominal thickness, $t_{\text{nom}} = 0.8$ mm, in both the elastic and plastic zones.

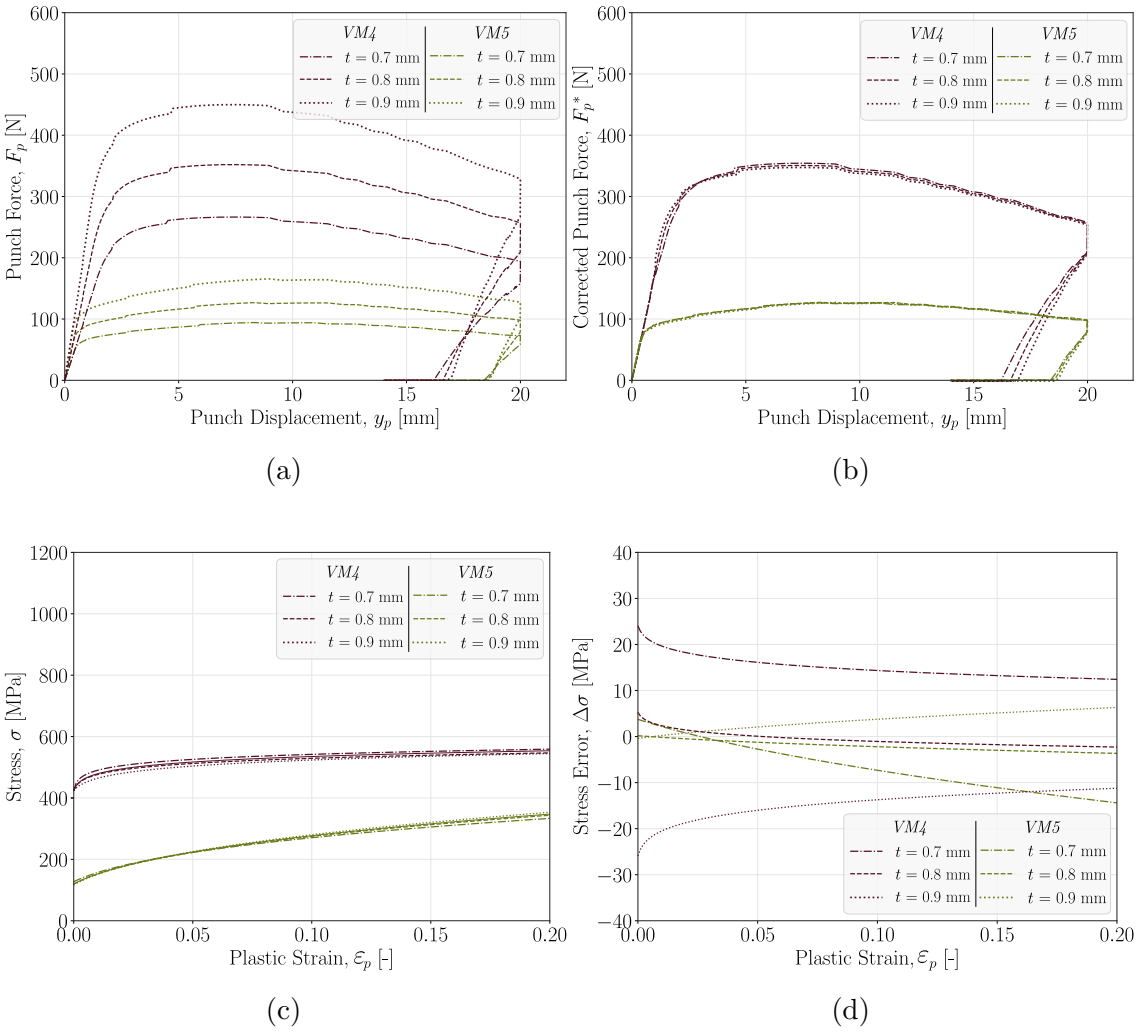


Figure 4.30: Influence of material thickness for *VM4* and *VM5* on (a) punch force–displacement curve, (b) corrected punch displacement curve, (c) true stress–strain curves predicted by the trained LSTM and (d) stress error.

The true stress-strain curves corresponding to the parameters predicted by the trained ML model using the corrected punch displacement curves for each case are shown in Figure 4.30c. Comparison with the target curve shows that, as expected, the predictions are very accurate for cases where the material thickness is equal to the nominal thickness, with the curves matching the target. For these cases, the stress error, $\Delta\sigma$, is approximately 0, as shown in Figure 4.30d. On the other hand,

for thicknesses different from the nominal thickness, there is an observable increase in prediction errors. The resulting stress-strain curves deviate slightly from the target curve, resulting in higher stress errors. Nevertheless, for the cases analyzed, these errors remain below 30 MPa, which can be considered acceptable, corresponding to a relative error of less than 10%. It is important to note that this methodology is designed to be applied to small thickness variations and the specified thickness range of ±0.1 mm was intentionally overestimated. In reality, variations around the nominal thickness are not expected to be of this magnitude. Therefore, the consideration of intermediate parameters for n and ε_0 results in an acceptable solution with relative stress errors much less than 10%.

4.2.4.4 Experimental Validation

After validating the two implemented ML models, this section focuses on evaluating their performance using experimental three-point bending results of the selected dual-phase steels (DP500, DP600 and DP780). The experimental punch force-displacement curves shown in Figure 4.8 have been replaced by the corrected punch force-displacement curves, taking into account the measured thickness of each material (Table 3.2) and the average values of n and ε_0, set to 0.15 and 0.001, respectively.

Table 4.11: Comparison of Young's modulus predicted by the *ML model — Elasticity* with the analytical approach (Equation 4.3) and comparison of Swift parameters predicted by the *ML model — Plasticity* with the parameters obtained from experimental tensile test curves.

	Young's Modulus		**Swift Parameters**					
	***E* [GPa]**		***K* [MPa]**		**ε_0**		***n***	
Material	**Analytical**	**Ml Elasticity**	**Tensile**	**3Point Bend**	**Tensile**	**3Point Bend**	**Tensile**	**3Point Bend**
DP500	192	191	865.32	835.56	0.0026	0.0035	0.1530	0.1421
DP600	208	209	1011.01	1063.21	0.0019	0.0039	0.1563	0.1805
DP780	196	194	1253.72	1281.27	0.0001	0.0010	0.1431	0.1559

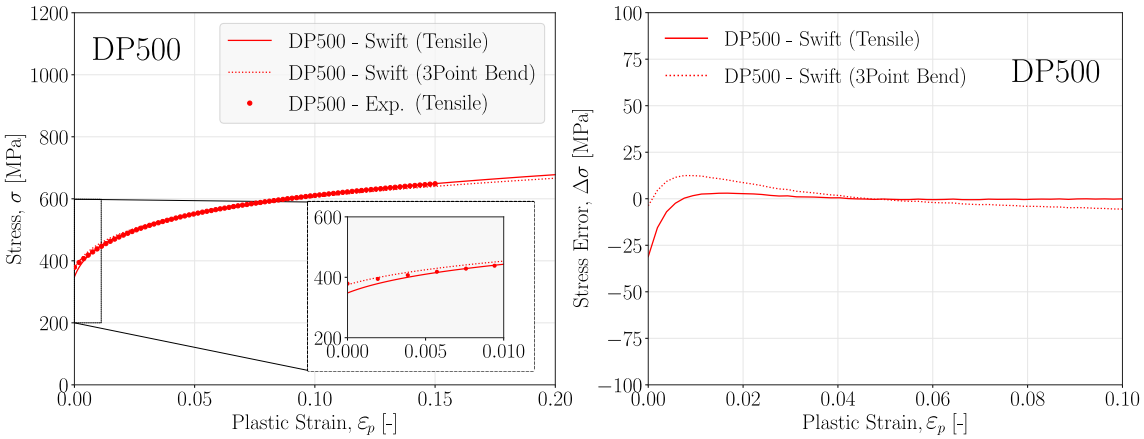
For the first ML model, which evaluates the elastic behavior and determines the Young's modulus of the material, twenty points were considered in the initial part

of the curve between a punch displacement of 0 and 2 mm. The predicted Young's modulus for each material is summarized in Table 4.11. As expected, the Young's modulus of the three materials is closer to the reference modulus of steel and the predicted values are also similar to those obtained using the analytical expression, Equation 4.3, with deviations below 1% in all cases. Since the obtained modulus of elasticity falls within the limits allowed by the algorithm, i.e., [190, 220], the ML model predicting the Swift hardening parameters for steels can be applied.

Starting with the corrected experimental curve, 500 discrete points were selected across the curve to format the data for application of the *ML Model — Plasticity*. The Swift hardening parameters (K, n and ε_0) predicted by this model are summarized in Table 4.11. In addition, they are compared with the Swift parameters obtained using the experimental tensile test and the optimization algorithm presented in Section 4.1.2.1. As seen, the two methods provide different sets of hardening parameters, with the parameter ε_0 showing the most significant differences. For DP780, the predicted ε_0 from the three-point bend test is 10 times higher than that obtained from the tensile test. However, as shown next, this discrepancy does not have a significant impact on the resulting hardening curve.

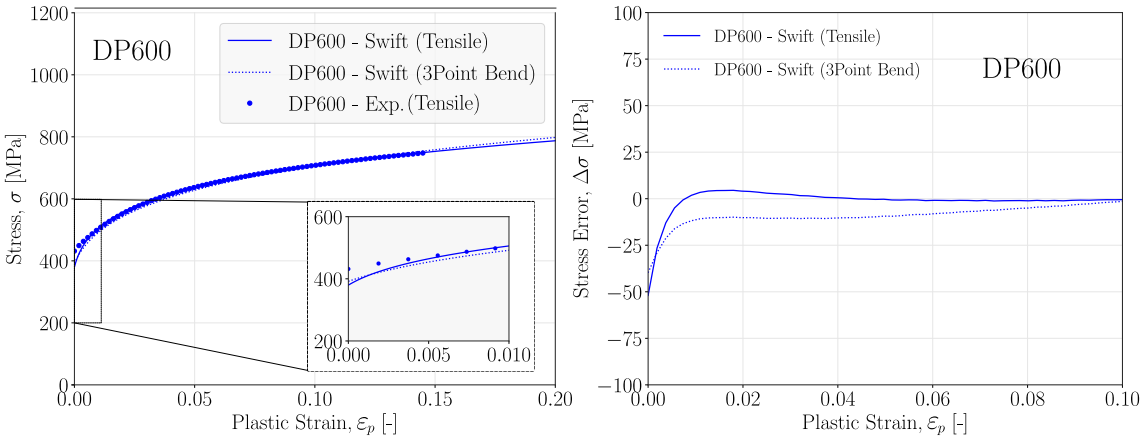
To evaluate the effect of different parameter sets on the resulting true stress–strain (σ-ε_p) curves, the results for each material are systematized in Figures 4.31–4.33 for the DP500, DP600 and DP780, respectively. For each material, the left figure represents the corresponding true stress-strain curve considering the set of Swift law parameters obtained from the three-point test and the parameters obtained based on the experimental tensile test. The reference hardening curve obtained experimentally from the experimental tensile test is also shown. On the right, the stress error, $\Delta\sigma$, for each Swift approximation is shown. In this case, the stress error is calculated as the difference in stress between each Swift curve and the experimental reference. A zero error indicates that for a given value of plastic strain, ε_p, the stress obtained from the Swift equation and the stress obtained experimentally are approximately equal. In the overall analysis, the Swift hardening law obtained by three-point bending can approximate the stress-strain relationship very well for all the materials considered, with an accuracy similar to that obtained using traditional optimization algorithms based on tensile testing. The stress error does not exceed 10% for the range of plastic strain considered, a value that is in agreement with the analysis performed in Section 4.2.4.2. Analyzing the results in detail for small values of plastic strain, especially below $\varepsilon_p < 0.01$, it becomes clear that the Swift curve with parameters obtained by three-point bending tends to improve the characteri-

zation of the material behavior in some cases. The error curves for $\varepsilon_p = 0$ tend to show a significantly smaller error when considering the Swift curve with parameters obtained by three-point bending than the one obtained by tensile testing.



(a) (b)

Figure 4.31: Influence of Swift hardening parameters obtained based on the experimental tensile test and three-point bending Test on (a) true stress–strain curves and (b) respective stress error, $\Delta\sigma$, analysis for DP500 dual-phase steel.

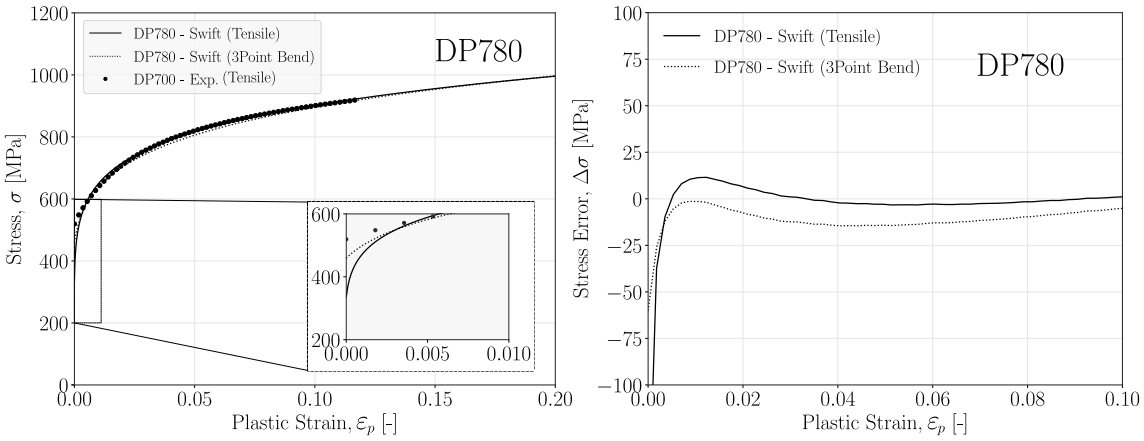


(a) (b)

Figure 4.32: Influence of Swift hardening parameters obtained based on experimental tensile test and three-point bending test on (a) true stress–strain curves and (b) respective stress error, $\Delta\sigma$, analysis for DP600 dual-phase steel.

In conclusion, the application of the developed ML models to experimental three-point bending tests on three grades of dual-phase steels (DP500, DP600, DP780) yielded promising results. The *ML Model — Elasticity* accurately predicted Young's

modulus values consistent with steel materials. In addition, the *ML Model — Plasticity* successfully approximated Swift hardening parameters for dual phase steels, providing a viable alternative to traditional optimization algorithms.



(a) (b)

Figure 4.33: Influence of Swift hardening parameters obtained based on experimental tensile test and three-point bending test on (a) true stress–strain curves and (b) respective stress error, $\Delta\sigma$, analysis for DP780 dual-phase steel.

4.3 Identification of Isotropic and Anisotropic Hardening Parameters using Machine Learning and a Reverse Bending Test

After developing a machine learning model based on RNNs to identify isotropic parameters from three-point bending tests, this section extends the approach to identify hardening parameters using reverse bending tests. As described in Section 3.4.3, the developed experimental setup allows sheet metal to be successively bent in opposite directions, capturing its behavior under cyclic loading conditions. Figure 4.34 schematically illustrates the methodology that is used to identify hardening parameters from the reverse bending test, allowing two different sets of parameters to be determined from the same experimental data. Using only the first load cycle, the isotropic hardening parameters, represented by the Swift curve parameters (K, ε_0 and n), can be determined using a methodology similar to that presented in the previous section. In contrast, the anisotropic hardening parameters can be determined by considering the complete curve, which includes the bending, unbending

and rebending phases. In this work, a mixed hardening model is adopted that combines both isotropic and kinematic hardening components. The isotropic part is described by the three Swift parameters, while the kinematic component is characterized by two parameters (C and γ) from the Frederick-Armstrong model (see Equation 2.43).

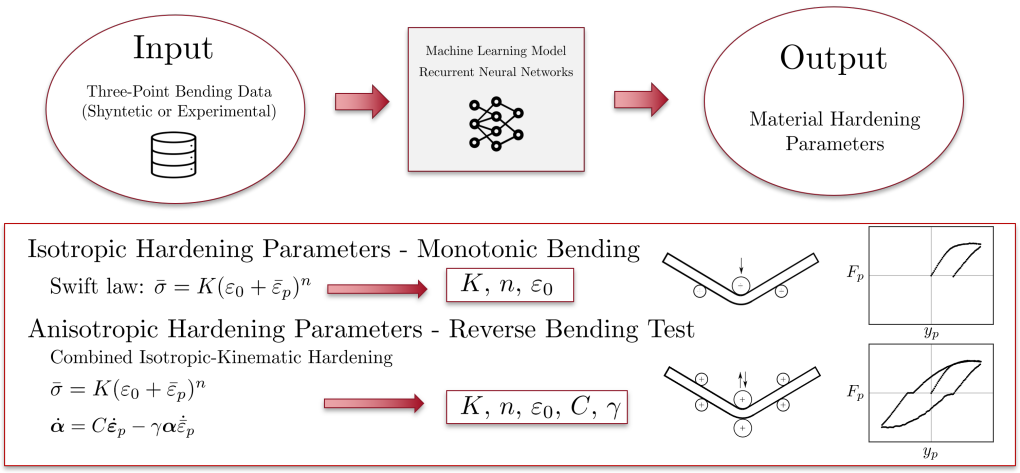


Figure 4.34: Schematic representation of the methodology for identifying hardening parameters using reverse bending tests.

4.3.1 Methodology

4.3.1.1 FE Model - Reverse Bending Test

The data required to train and develop the machine learning models is obtained from FEA, with the ultimate goal of applying the trained model to real experimental data. To achieve this, the first step is to develop and validate the finite element model of the reverse bending tests based on experimental results. Figure 4.35 schematically illustrates the finite element model considered for the reverse bending test, highlighting its key variables of interest. The model was developed using the Abaqus finite element code v.2024. The tools were modeled as fully rigid analytical surfaces and the analysis was performed under plane strain conditions. The blank was discretized with 9 layers through thickness using 912 deformable four-node solid elements (type CPE4R from the ABAQUS library). The Coulomb friction coefficient was set to 0.1 and the material behavior of the blank was modeled as elastoplastic. The elastic constants of the material were defined as $E = 210\,\text{GPa}$ and $\nu = 0.3$. The boundary conditions fixed the left side of the blank while applying displacement to

the rollers on the right side. As in the previous model, the material thickness was set to 0.8 mm.

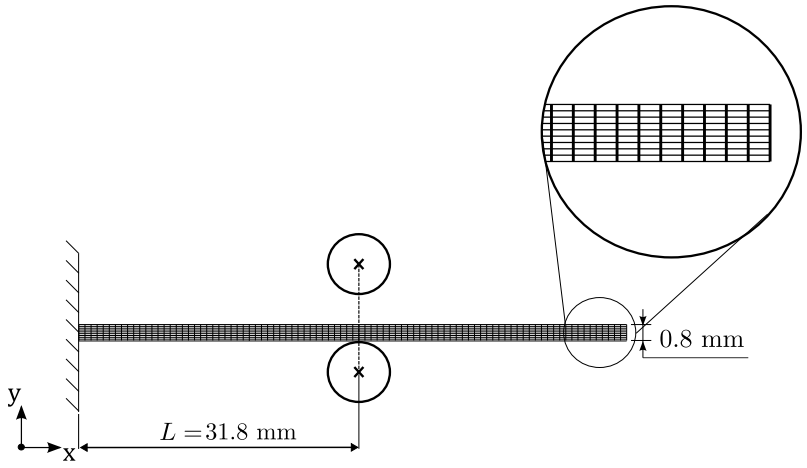


Figure 4.35: Schematic representation of the finite element model used for the reverse bending test.

In this numerical model, in addition to the material parameters, the length L must be adjusted coherently so that the numerical results agree with the experimental results. To validate the FE model for the reverse bending test, the experimental results for DP500, DP600 and DP780 steels, as presented in Section 3.4.3.3, were used. Figure 4.36 shows a comparison between the experimental and FEA force-displacement (F_p-y_p) curves for the three materials. For this validation, only the isotropic hardening parameters (listed in Table 4.3) were considered to represent the plastic behavior of the material. The results considering an isotropic hardening (IH) model are shown in Figure 4.36a,c,e for DP500, DP600 and DP780 respectively. After several iterations, an equivalent length L of 31.8 mm was found to best fit the experimental conditions. As expected, the isotropic hardening model accurately captures the bending behavior only prior to the onset of inversion. Once inversion occurs (steps 2 and 3), the finite element model is unable to accurately reproduce the experimental behavior and tends to overestimate the force values.

On the other hand, when considering an anisotropic hardening model, such as the combined isotropic-kinematic model, the experimental and numerical curves tend to converge, as observed in Figure 4.36b,d,f for DP500, DP600 and DP780, respectively. In this case, the anisotropic parameters (IKH) shown in Table 4.4 were used. However, the agreement is still not perfect, indicating that the set of parameters identified from the tension-compression test may not fully capture the material behavior under bending loads.

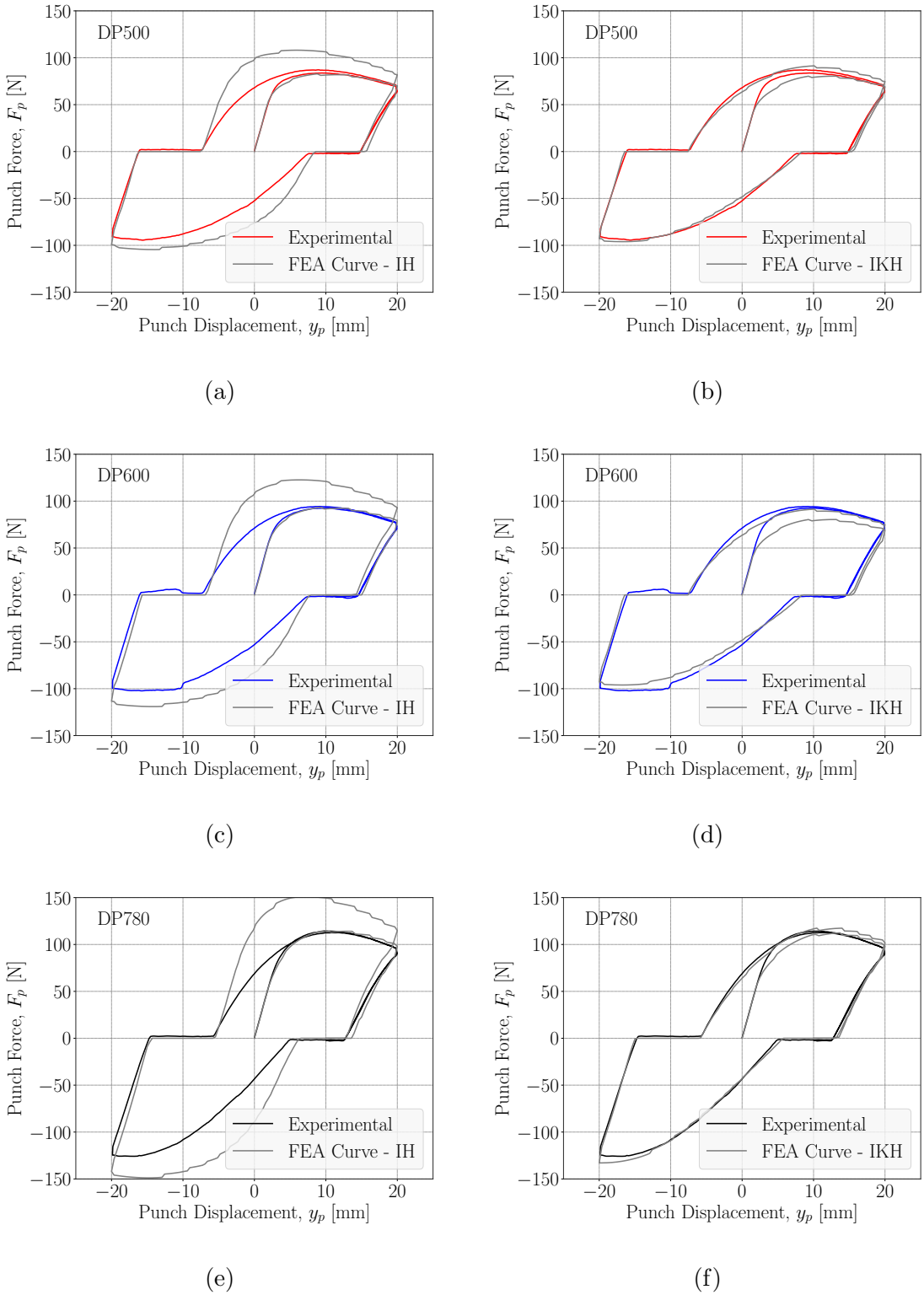


Figure 4.36: Comparison between experimental and numerical force-displacement curves for DP500, DP600 and DP780 steels; the left subfigures illustrate the results using a pure isotropic hardening (IH) model, while the right subfigures show the results with a combined isotropic-kinematic hardening (IKH) model.

Figure 4.37 shows the springback angles α_1, α_2 and α_3 (see Section 3.4.3) obtained numerically by considering both the pure isotropic model and the combined isotropic+kinematic model, along with a comparison with the values obtained experimentally for the three materials. As observed, the use of an anisotropic hardening model allows a more accurate prediction of the springback angle throughout the test compared to using only the isotropic model. Nevertheless, the identification carried out using the experimental tensile-compression tests still results in some prediction errors, especially for the springback angles α_2 and α_3.

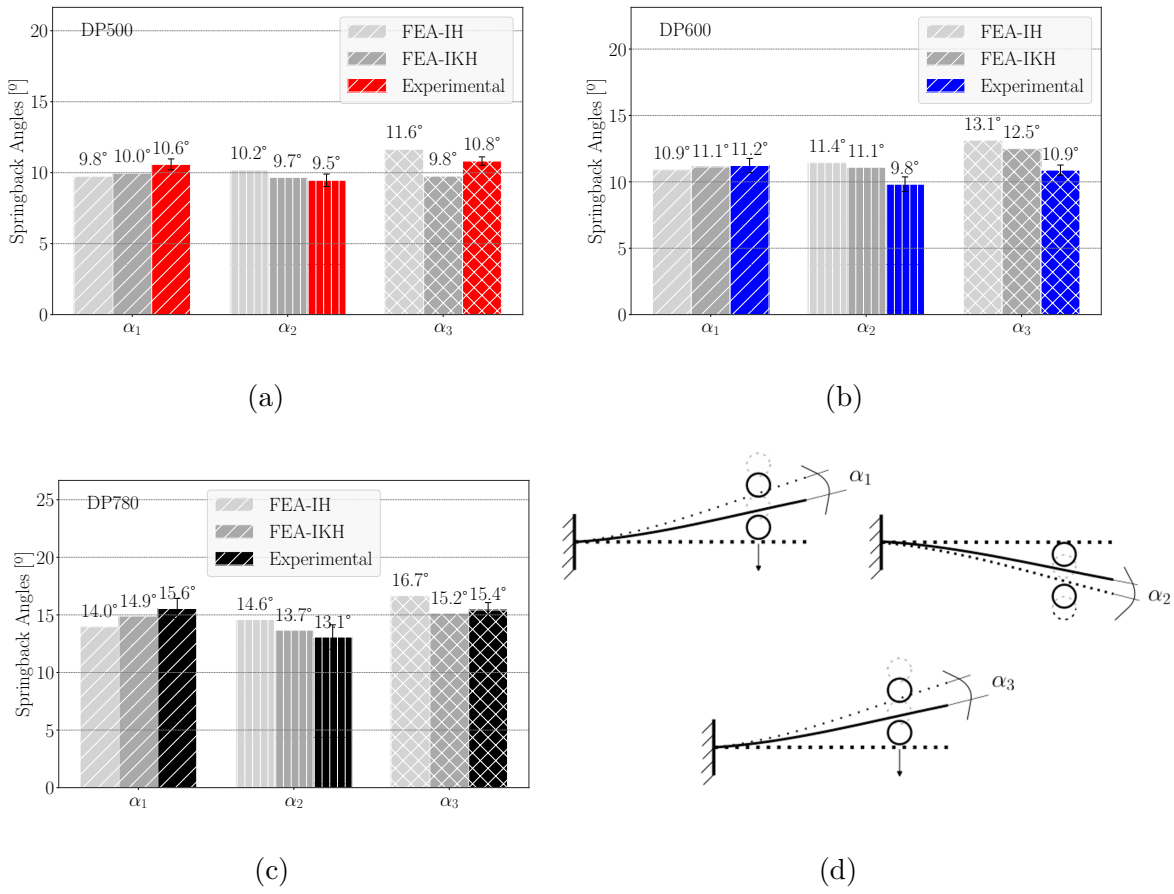


Figure 4.37: Comparison of experimental and numerical springback angles α_1, α_2 and α_3 for (a) DP500, (b) DP600 and (c) DP780 steels and (d) schematic definition of the springback angles (α_1, α_2 and α_3).

4.3.1.2 Dataset Generation

The reverse bending test allows the identification of two different sets of parameters. If only the initial part of the curve is considered, the isotropic strain hardening parameters can be determined using a similar methodology as described in the pre-

vious section. On the other hand, analysis of the entire curve, including the bend, unbend and rebend, allows the determination of anisotropic hardening parameters. Consequently, separate datasets must be generated for each case, hereafter referred to as *RB–IsoDataset* and *RB–AnisoDataset*, where "RB" stands for "Reverse Bending", "Iso" refers to the isotropic model and "Aniso" refers to the anisotropic (combined isotropic-kinematic) model. These datasets must remain independent because there is no direct match between the parameters K, ε_0 and n of the pure isotropic model and those of the combined isotropic-kinematic hardening model. As a result, the same material will have different Swift parameters depending on whether a pure isotropic model or a combined model is considered. The combinations of hardening parameters for *RB - IsoDataset* and *RB - AnisoDataset* are shown in Figure 4.38 and Figure 4.39, respectively.

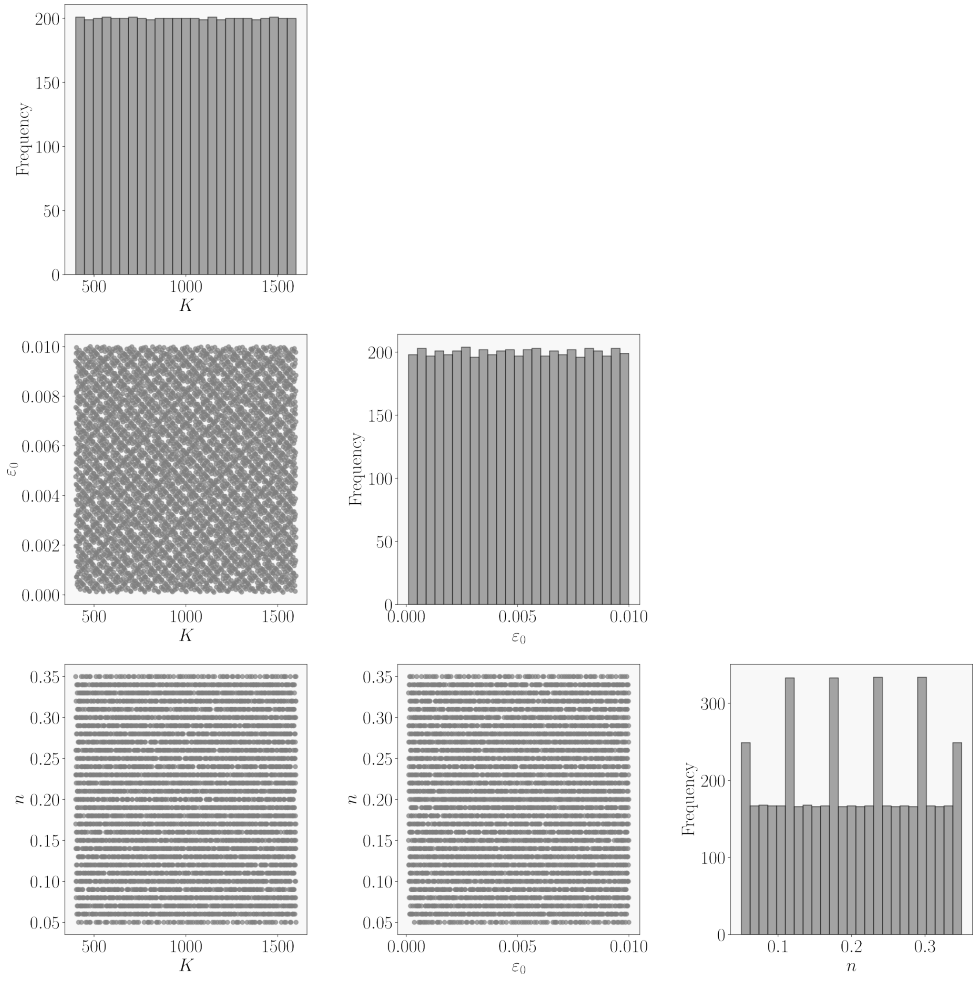


Figure 4.38: Parameter distributions for the *RB - IsoDataset*; the diagonal subplots show histograms of individual parameters, while the off-diagonal subplots display scatter plots of parameter pairs.

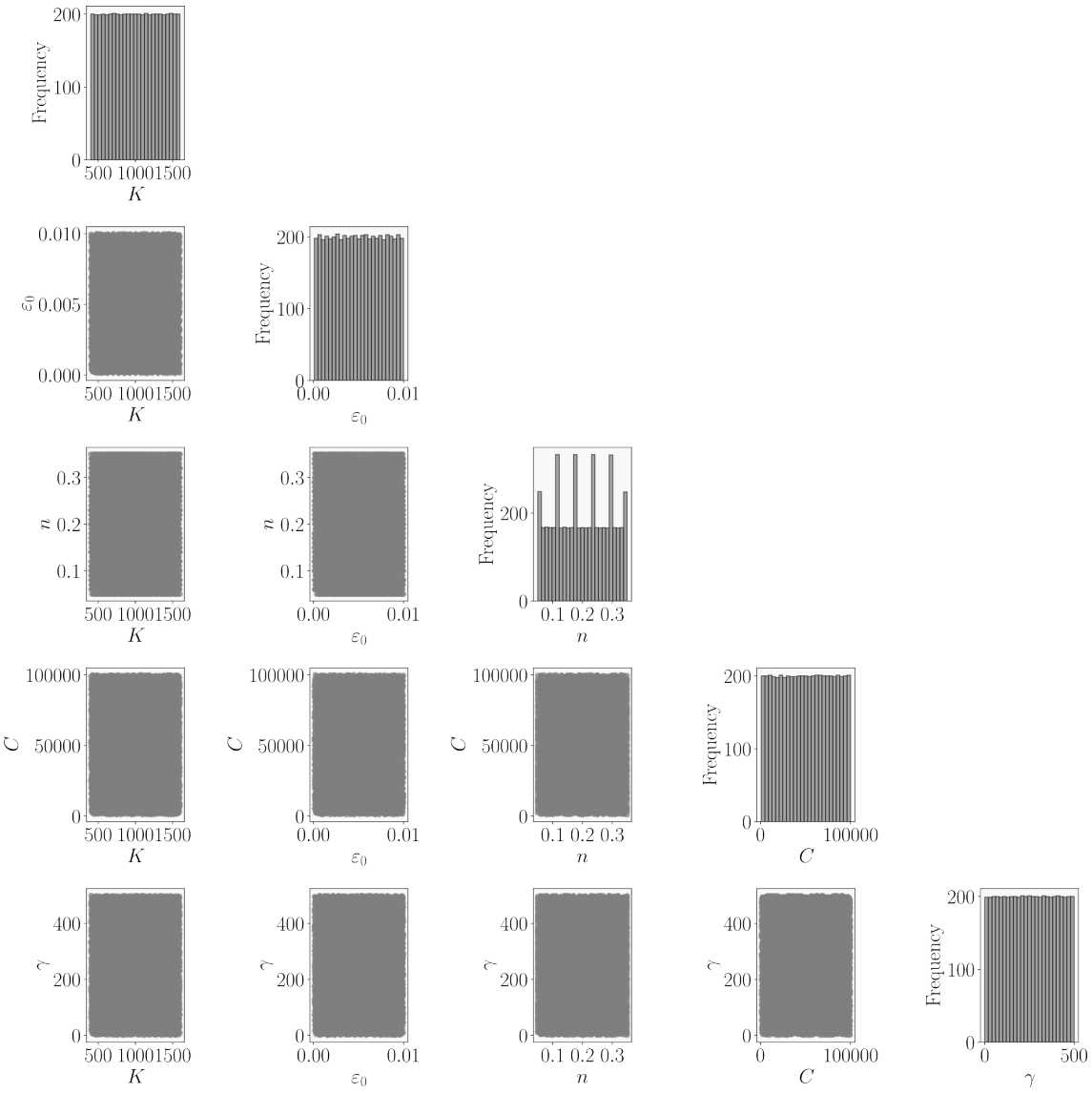
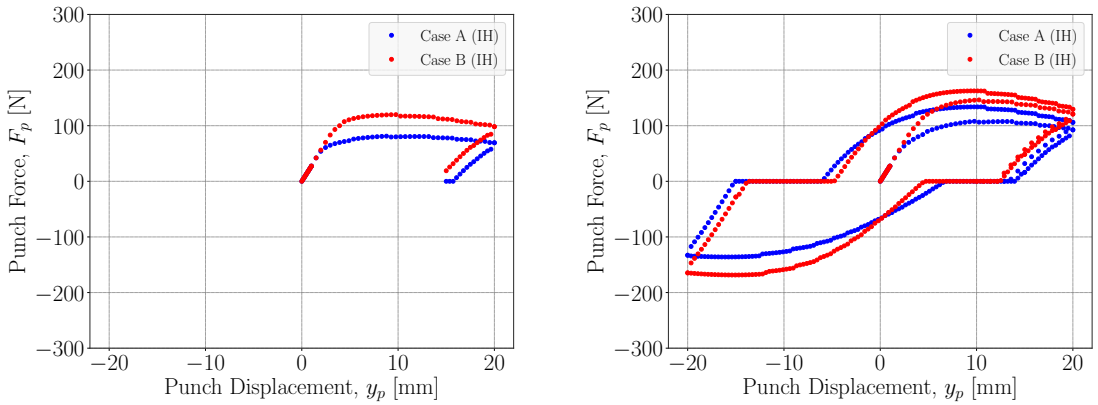


Figure 4.39: Parameter distributions for the *RB - AnisoDataset*; the diagonal subplots show histograms of individual parameters, while the off-diagonal subplots show scatter plots of parameter pairs.

For each dataset, 5000 parameter combinations were generated using Sobel sampling [69]. This technique ensures efficient and representative coverage of the parameter space, reducing sampling bias and the number of samples required compared to random sampling. In each figure, the diagonal subplots show histograms of individual parameters, providing information about the distribution of each parameter in the dataset and illustrating the frequency of different values within specified bounds. The off-diagonal plots show scatterplots of pairs of parameters, revealing possible relationships between them. As shown, the parameters K, ε_0 and n were constrained within the following ranges: K varied between 400 and 1600, ε_0 between 0.0001 and

0.01 and n between 0.05 and 0.35 for both datasets. Regarding the parameters for the *RB-AnisoDataset*, the parameter C was set between 1000 and 100000 [MPa], while the parameter γ was set between 0 and 500. These parameter ranges were defined based on different studies in the literature, such as the work of Silvestre et al. [285], which characterized the combined isotropic kinematic hardening parameters of different materials ranging from mild steels to advanced high strength steels. Python scripts were developed to streamline the numerical simulation of 5000 cases by automating model creation, parameterization, simulation submission and post-processing data extraction (e.g., punch force and displacement), thereby reducing manual intervention and errors.

Figure 4.40 shows examples of force-displacement curves from the considered datasets, with the corresponding parameters for each case summarized in Table 4.12. Figure 4.40a shows two representative cases (A and B) from the *RB–IsoDataset*, while Figure 4.40b shows two representative cases (A and B) from the *RB–AnisoData set*. Note that the parameters K, ε_0 and n were intentionally kept the same for cases A and B in both datasets to highlight that identical Swift parameters in isotropic and anisotropic models do not yield the same monotonic curve.



(a) (b)

Figure 4.40: Example Punch Force Displacement (F_p-y_p) curves for (a) the *RB - IsoDataset* and (b) the *RB - AnisoDataset*.

Table 4.12: Isotropic and kinematic hardening parameters for representative cases (A and B) from the *RB-IsoDataset* and *RB-AnisoDataset*.

Case	K [MPa]	ε_0	n	C [MPa]	γ
Case A (IH)	1000	0.00505	0.20	0	0
Case B (IH)	988	0.00673	0.10	0	0
Case A (IKH)	1000	0.00505	0.20	50500	250
Case B (IKH)	988	0.00673	0.10	67708	346

The curves for the *RB–IsoDataset* consists of 100 uniformly distributed points of force and displacement. In contrast, the curves for the *RB–AnisoDataset* contain 300 discrete points covering the three stages of the test (bending, unbending and rebending). Figure 4.41 shows how these 300 points evolve for cases A and B under the IKH model, detailing the progression of punch force and displacement. For the *RB–IsoDataset*, a similar evolution is observed, although only the first 100 points of force and displacement are included.

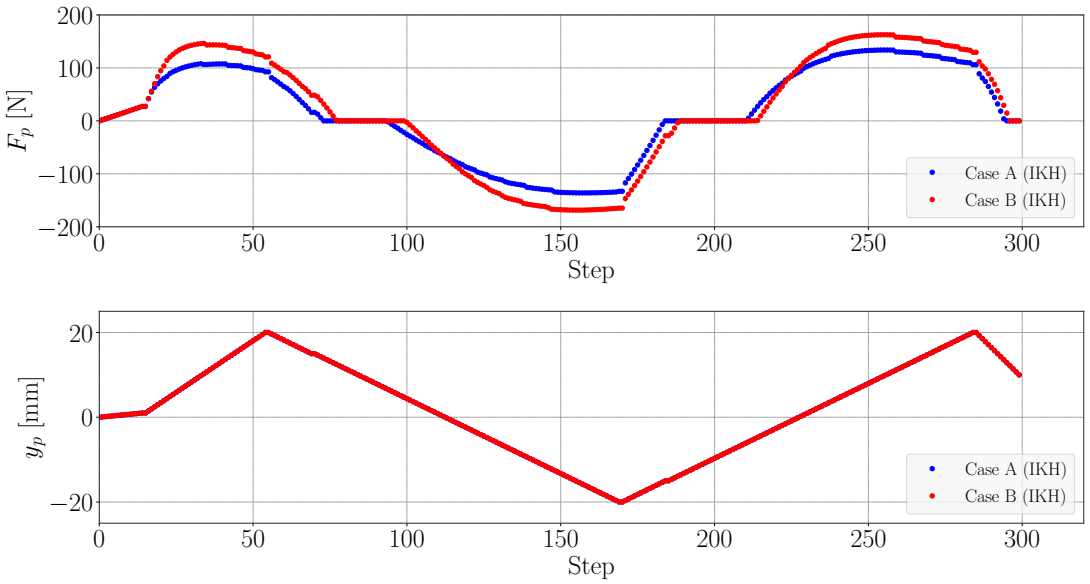
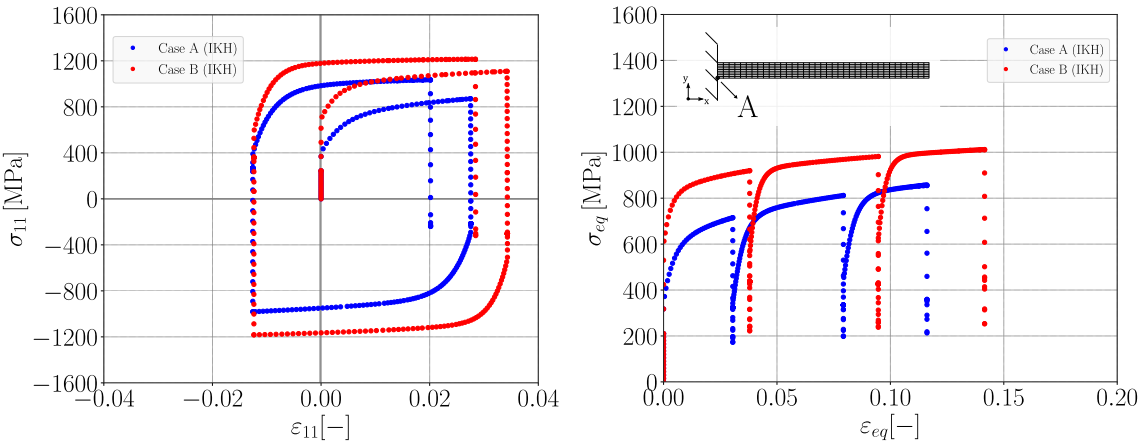


Figure 4.41: Evolution of force and displacement during the test for cases A and B under the IKH model.

In addition, Figure 4.42a shows the evolution of normal stress σ_{11} versus normal strain ε_{11} at point A (located on the bottom of the sheet near the clamp) for both cases. Figure 4.42b shows the corresponding equivalent stress-strain behavior based

on the von Mises yield criterion. From these figures it is possible to observe the levels of plastic deformation throughout the test. In the first stage, the maximum plastic strain value at point A is between 0.03 and 0.05 and the material is in tension. At the end of the second stage, the equivalent strain is about 0.1 and point A shifts to compression. Finally, during the third stage, point A returns to tension and reaches an equivalent strain of about 0.15. Therefore, with this test, it is possible to deform the material alternately with a cumulative deformation value of about 0.2 after three phases.



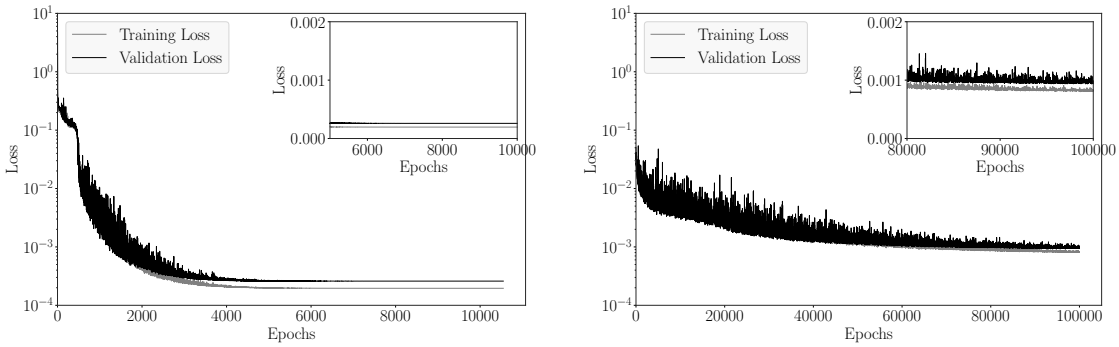
(a) (b)

Figure 4.42: Evolution of (a) normal stress σ_{11} versus normal strain ε_{11} for cases A and B and (b) von Mises equivalent stress-strain behavior for the same cases at point (A).

4.3.2 Neural Network Implementation: Isotropic Parameters

In this section, an ML model is developed to determine the isotropic parameters of a material based on the monotonic force-displacement curve obtained from the reverse bending test. Since the monotonic stage of this test produces curves with a similar overall shape to those from the three-point bending tests presented in the previous section, the previously trained model can be leveraged. However, since the two tests do not yield the same behavior for the same material, direct reuse of the network is not possible. Instead, the pre-trained model can be used as an initial baseline and its weights can be adjusted to fit the new data. This strategy, known as transfer learning, involves reusing a model pre-trained on one task for a different but related task, using its learned features. The main advantage of this approach is that it significantly reduces training time because the model has already learned key

features, minimizing the need for extensive retraining [77]. This can be confirmed in Figure 4.43, which shows two sets of error curves. In Figure 4.43a, the error curves for the training and validation datasets are shown for a model developed using the *RB - IsoDataset* containing 5000 cases, along with the pretrained model. Conversely, Figure 4.43b shows the error curves for the training and validation datasets for a model implemented and trained from scratch, with weights and biases initialized to zero. Both models use exactly the same network architecture, a 40 unit bidirectional LSTM. The same data split and hyperparameters were used in both cases. Comparing the results, it can be observed that for the pre-trained model, 6000 epochs were sufficient for the MSE in the training and validation datasets to stabilize at approximately 10^{-4}. On the other hand, for the model initialized from scratch, this order of magnitude in MSE was achieved only after about 10 times more epochs, i.e., about 60000 epochs. In terms of computation, using the pre-trained network took about 1 hour and 35 seconds, while the model initialized from scratch took 9 hours and 10 minutes, resulting in a significant improvement in computational efficiency of about 88%. The training process was conducted on a computer with an Intel(R) Core(TM) i9-9900K CPU @ 3.60GHz, 64.0 GB of RAM and an NVIDIA Quadro P620 graphics card.

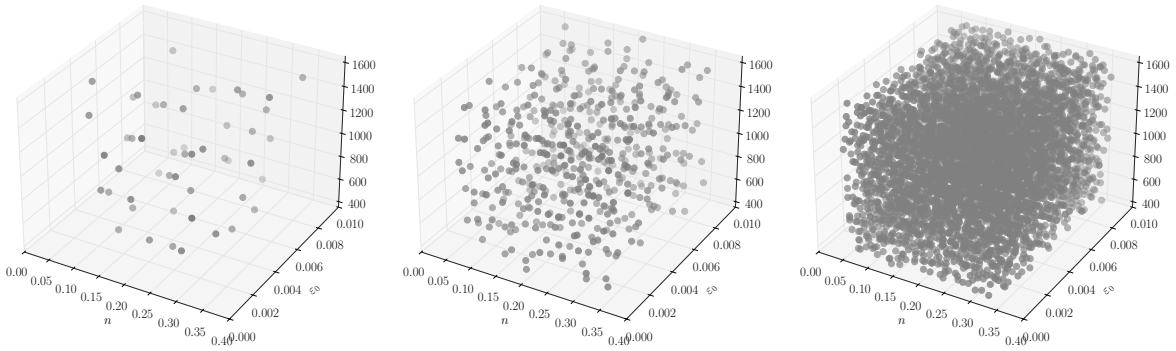


(a) (b)

Figure 4.43: Error curves for the training and validation datasets using the *RB - IsoDataset*: (a) pre-trained model and (b) model trained from scratch.

This improvement in computational efficiency can be very beneficial when using the trained model under test conditions that differ from the original ones. In addition, the model can be adapted to handle data from other material classes, such as aluminum alloys or steel with thicknesses different to the nominal 0.8 mm considered. Another advantage of using pre-trained models is their ability to perform well

with less data. When the new dataset is significantly smaller than the base dataset, transfer learning becomes a powerful tool for training a large target network without the risk of overfitting. Since the model has already learned significant patterns during the initial training, the new model may need less data to adapt to new but similar datasets [286]. To confirm this, an analysis is performed to evaluate the amount of data required to effectively fine-tune the pre-trained model. For this purpose, the number of cases used for fine-tuning will vary from 50 to 5000, as represented by the variable n_{cases}. Figure 4.44 shows the combinations of the parameters K, ε_0 and n for three different values of n_{cases}: 50, 500 and 5000. It is important to note that the cases were sampled using the Sobel operator, which ensures that the selected cases are uniformly distributed over the parameter space. Consequently, the n_{cases} correspond to the first n uniformly distributed cases of the *RB–IsoDataset*.



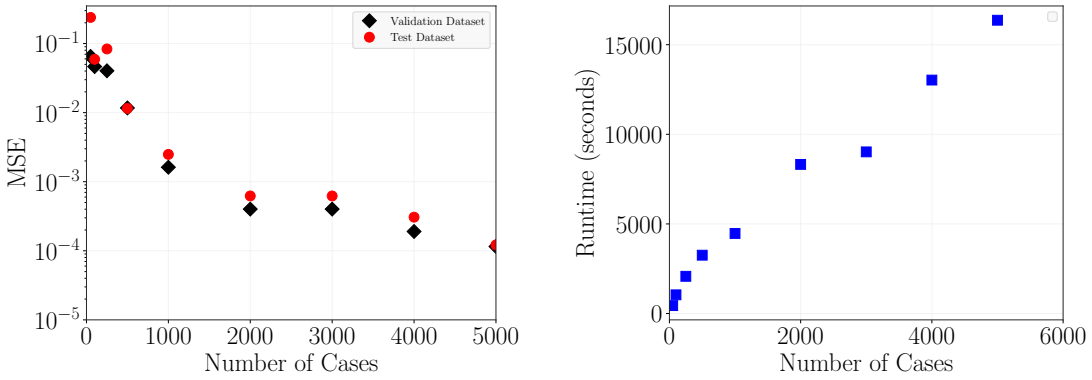
(a) (b) (c)

Figure 4.44: Combinations of the parameters K, ε_0 and n for three different values of n_{cases}: (a) 50, (b) 500 and (c) 5000.

Starting from the pre-trained model for the three-point bending problem, multiple models were trained to evaluate the influence of n_{cases} on the obtained MSE. These models were fine-tuned using different amounts of data, ranging from 50 to 5000 cases, while keeping the hyperparameters constant. The *Adam* optimizer was used with an initial learning rate of 0.001, without an exponential decay schedule. This learning rate was chosen because pre-trained models typically show smaller gradients during fine-tuning, as they are already initialized in a well-optimized region of the parameter space.

Training was performed for 20000 epochs with an early stopping mechanism and a patience of 5000 epochs to prevent overfitting. The objective is to evaluate how the number of cases used for fine-tuning affects the generalization ability of the model

and the rate at which the MSE converges to an acceptable value. For each n_{cases}, the dataset was divided into training, validation and test subsets, maintaining a consistent proportion of 70%-15%-15%. For example, if $n_{\text{cases}} = 500$, 350 cases were assigned to training, 75 cases to validation and 75 cases to testing. Additionally, the remaining 4500 cases not included in the $n_{\text{cases}} = 500$ subset were added to the test dataset, resulting in a total of 4575 cases for testing.



(a) (b)

Figure 4.45: Influence of n_{cases} on (a) MSE and (b) runtime, demonstrating how the amount of data used for fine-tuning influences model accuracy and computational efficiency.

Figure 4.45 shows the MSE on the validation and test datasets for different values of n_{cases}, along with the corresponding runtime for each case. Each data point represents the average MSE from five independent runs, performed with different seed values to account for variability in model training and to ensure that the results are not biased by specific random initializations. The results clearly demonstrate the influence of n_{cases} on both model performance and computational cost. As shown in Figure 4.45a, the MSE decreases with increasing number of cases, indicating improved model performance with more data. A significant reduction in MSE is observed between 100 and 1000 cases, suggesting that this range is critical for effective model training. Beyond approximately 1000 to 2000 cases, the rate of improvement decreases, reflecting diminishing returns to additional data. In addition, the close match between the MSE values for the validation and test datasets indicates good generalization and the absence of overfitting. Figure 4.45b shows that the runtime increases approximately linearly with n_{cases}, highlighting the increasing computational cost associated with larger datasets. From this analysis, it can be concluded

that about 1000/2000 cases is the minimum threshold required to achieve satisfactory performance, with MSE values on the order of 10^{-3}. In this context, the use of a pre-trained network did not significantly reduce the required data size, as at least 1000 cases were still needed to achieve acceptable performance. One possible explanation for these observations is related with the sampling strategy used. For the three-point bending test, a uniform grid sampling method was used (see Figure 4.16), where samples are taken at regular intervals across the data space. While this approach is straightforward, it may not fully capture regions where the system response is highly sensitive to parameter variations if the grid spacing is not fine enough, as is the case for the ε_0 parameter. In contrast, the reverse bending test uses a Sobel-based sampling approach (see Figure 4.44). This method concentrates samples in regions with significant gradients in parameter values. While this targeted sampling can provide a more detailed characterization of these critical regions, it may also require a larger number of samples for the pre-trained network to adequately adapt. This is because the network, initially trained on uniformly sampled data, may require additional examples from high-gradient regions to capture the sensitivities of the new sampling distribution.

4.3.2.1 Results

The results for the pre-trained network with $n_{\text{cases}} = 2000$ and $n_{\text{cases}} = 5000$ are shown in Figure 4.46. The figure shows histograms of the relative errors for each of the three variables (K, ε_0 and n), allowing a direct comparison between the two dataset sizes. For the variable K, the relative prediction errors remain low in both cases, with most errors below 10%. Similarly, the variable n shows consistently low relative errors, also below 10%, for both 2000 and 5000 cases. These results confirm that increasing the number of cases from 2000 to 5000 does not significantly improve the predictions for K and n, since the errors are already minimal. In contrast, the variable ε_0 shows higher relative errors, with some extreme values approaching 100%, especially in the $n_{\text{cases}} = 2000$ scenario. Note that ε_0 typically has values less than 1, in this case between 0.0001 and 0.01. For example, a relative error of 100% for $\varepsilon_0 = 0.001$ results in a prediction of $\varepsilon_0 = 0.002$, which, as seen in the previous problem, is not necessarily a critical problem. Increasing the dataset to 5000 cases results in a slight decrease in the relative errors, indicating a modest improvement in prediction accuracy with a larger dataset, although some high relative errors for ε_0 remain.

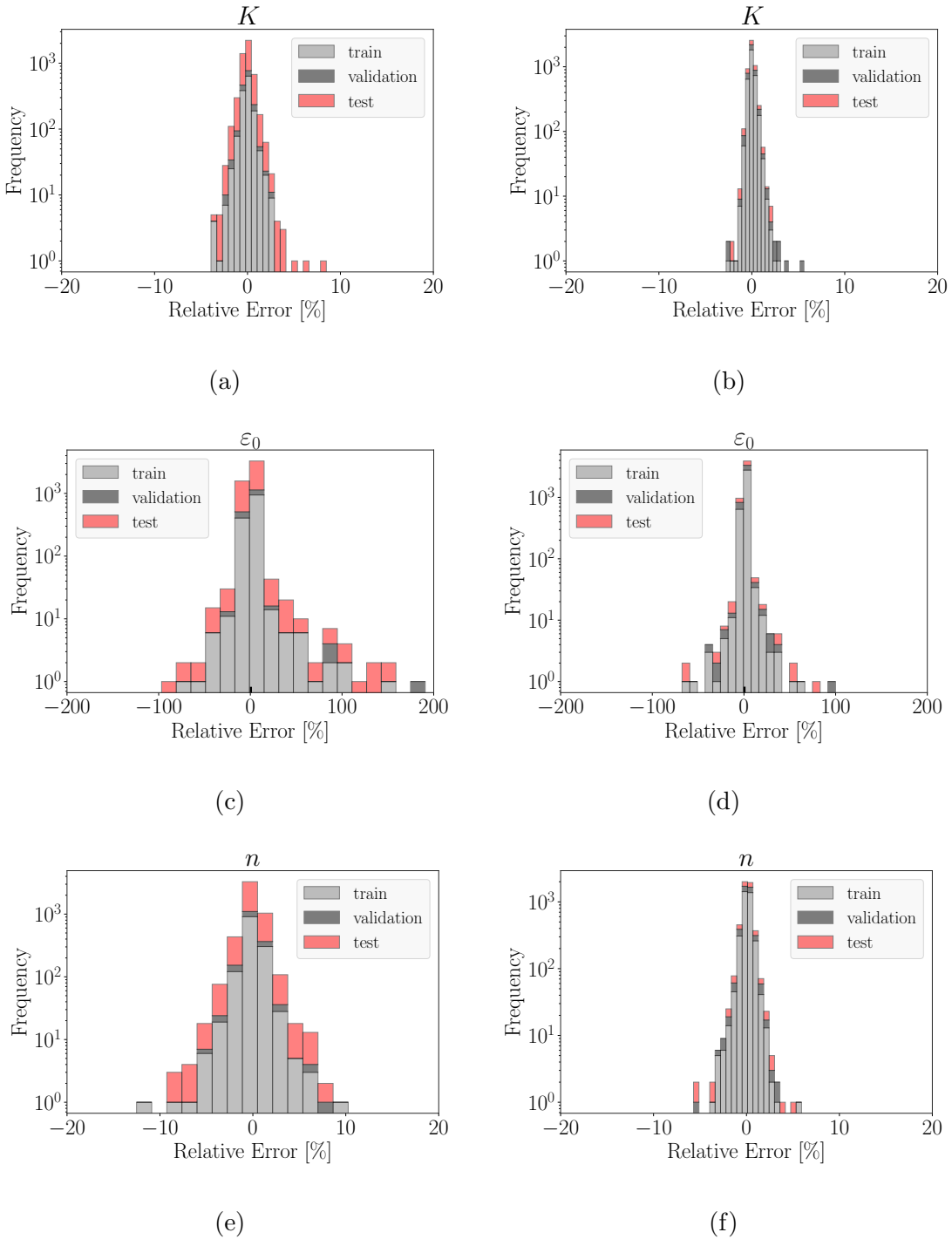
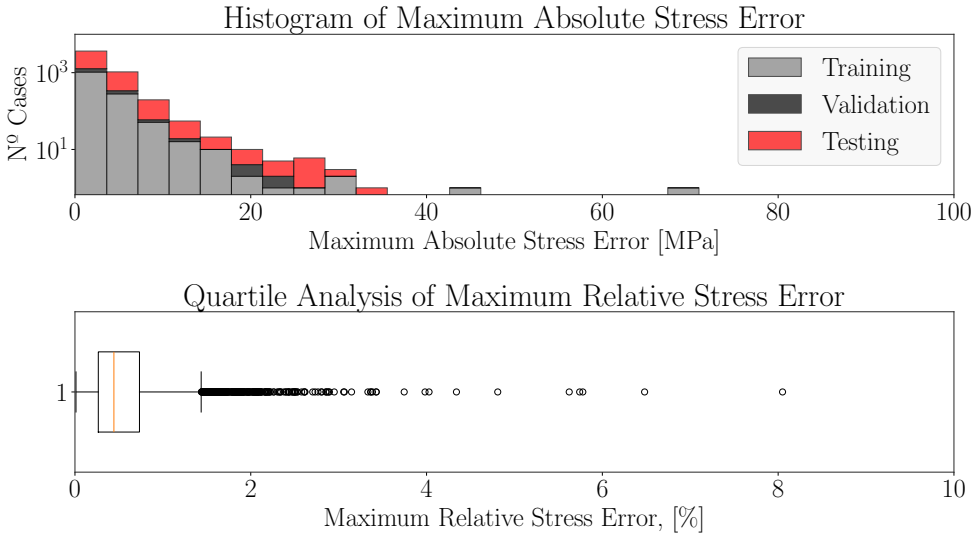


Figure 4.46: Histograms of the relative errors for the three variables (K, n and ε_0) obtained considering 2000 and 5000 cases.

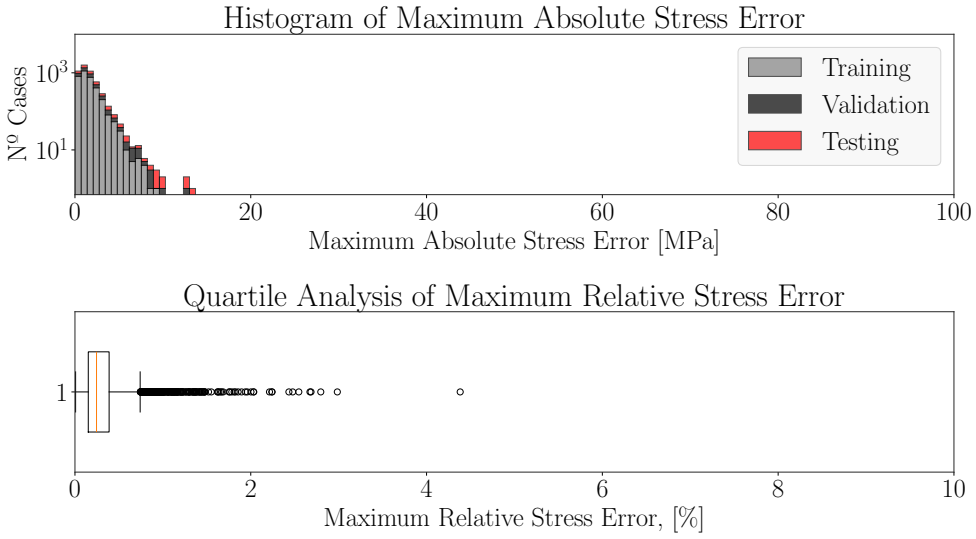
Despite the higher relative errors for ε_0, these errors do not significantly affect the resulting stress-strain curve, as shown in Figure 4.47. This figure shows the histogram of the maximum absolute stress errors and the corresponding quartile analysis for the maximum relative stress errors, for $n_{\text{cases}} = 2000$ and $n_{\text{cases}} = 5000$. For both datasets, the histograms show that the maximum absolute stress errors are predominantly below 40 MPa, with very few cases exceeding this threshold. In these cases, the corresponding relative errors remain below 10%. Comparing the two cases, increasing n_{cases} from 2000 to 5000 does not significantly change the overall error distribution. While there is a slight improvement in the reduction of extreme values, the errors remain consistently low, confirming that the model performs well even with 2000 cases. These results are consistent with the previous analysis and confirm that the network can accurately predict stress values with minimal absolute and relative errors for most scenarios.

4.3.2.2 Transfer Learning Approach for different Test Conditions

The proposed methodology was designed to identify hardening parameters for steels with a nominal thickness of 0.8 mm, such as the dual-phase materials analyzed in this thesis. Although small thickness variations of ±0.1 mm are allowed, as described in Section 4.2.1, the neural network developed for this study cannot be directly applied to steels with nominal thicknesses other than 0.8 mm. For materials with different nominal thicknesses, a new network must be trained using datasets specific to the intended nominal value. Consequently, each nominal thickness would require a dedicated network trained on its corresponding data. This approach has a potential disadvantage due to its lack of generality. However, the incorporation of thickness as an input variable into the neural network was evaluated, but it was not considered advantageous or practical in the LSTM architecture used in this study, which is designed to handle sequential rather than discrete data. In addition, such an implementation would require a significantly larger dataset to accurately represent thickness variability, further increasing computational complexity and training times. Therefore, the authors concluded that developing a dedicated network for each specific material thickness is the most appropriate and efficient solution within the scope of this methodology.



(a)

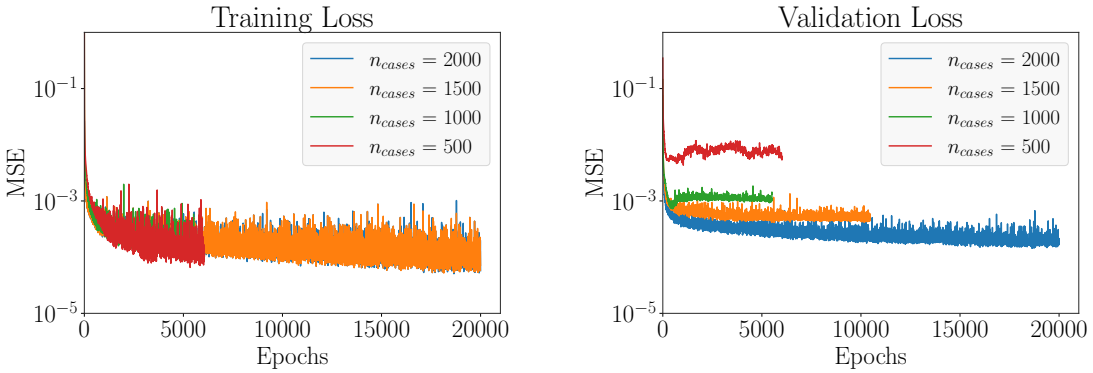


(b)

Figure 4.47: Analysis of stress prediction errors for the the pre-trained network considering (a) 2000 cases and (b) 5000 cases.

As pointed out before, developing a new network for different nominal thicknesses does not have to start from scratch. Instead, transfer learning can be used, using a pre-trained model as a starting point, taking the network trained for a nominal thickness of 0.8 mm with 2000 cases. This transfer learning approach leverages existing knowledge and reduces the computational effort required to train new networks for different thicknesses. To evaluate this approach, virtual data was generated for

steel materials with a nominal thickness of 1.2 mm. The same range of Swift parameters considered for a thickness of 0.8 mm, as presented in Table 4.6, was used and 2000 combinations were generated. The goal is to determine whether a network trained for a nominal thickness of 0.8 mm can effectively adapt to these new materials and whether 2000 cases are sufficient to fine-tune the network. The training process started with the pre-trained network for a nominal thickness of 0.8 mm. The learning rate was set to 0.001 and both input and output were normalized between -1 and 1 to ensure stability during training. The dataset was divided into 70% for training, 15% for validation and 15% for testing. The model was trained for 20000 epochs, with an early stopping criterion set to stop training if no improvement in the validation set was observed for 5000 epochs. Additionally, the effect of dataset size on model performance was evaluated. Virtual datasets of different sizes, including 2000, 1500, 1000 and 500 cases, were used to fine-tune the model. The goal of this analysis was to determine the minimum amount of data required to achieve satisfactory performance while utilizing transfer learning. The training and validation processes were evaluated using the MSE as a performance metric. Figure 4.48 illustrates the evolution of the MSE during training and validation for different dataset sizes. Figure 4.48a shows the MSE for the training dataset, while subfigure Figure 4.48b shows the MSE for the validation dataset.

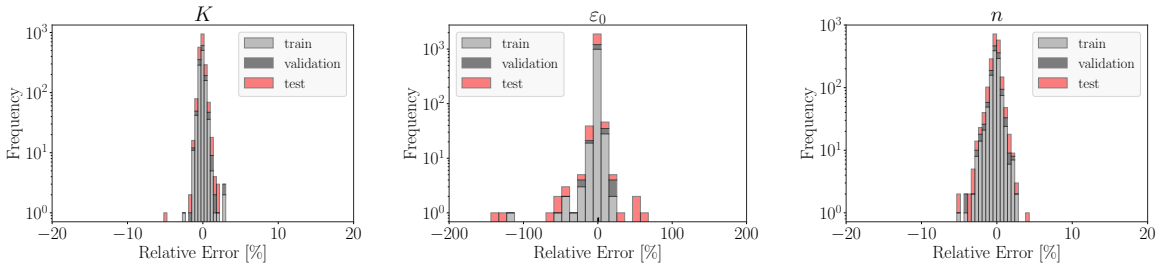


(a) (b)

Figure 4.48: Evolution of the Mean Squared Error (MSE) over the epochs for different numbers of cases: (a) training dataset, (b) validation dataset,

As shown in Figure 4.48a, the training loss decreases consistently over epochs for all dataset sizes. Larger datasets (e.g., $n_{\text{cases}} = 2000$) exhibit smoother convergence and lower final MSE compared to smaller datasets (e.g., $n_{\text{cases}} = 500$), suggesting

that larger datasets provide more robust training. In Figure 4.48b, the validation loss also decreases initially for all cases, but smaller datasets exhibit significantly higher variability and, in some cases, an eventual increase in validation error after certain epochs. This pattern suggests overfitting for smaller datasets (e.g., $n_{\text{cases}} = 500$ and $n_{\text{cases}} = 1000$), where the network performs well on the training data but fails to generalize to the validation dataset. The network trained with $n_{\text{cases}} = 2000$ achieves the lowest validation error, demonstrating a better balance between minimizing training loss and maintaining generalization. Acceptable performance is still observed with $n_{\text{cases}} = 1500$, although the MSE in validation loss is slightly higher. The results suggest that even with transfer learning, datasets containing between 1000 and 2000 cases are required to achieve satisfactory performance, as smaller datasets may lead to overfitting and insufficient generalization.



(a) (b) (c)

Figure 4.49: Histograms of relative errors for (a) K, (b) ε_0 and (c) n using the model trained with $n_{\text{cases}} = 2000$ for $t = 1.2\,\text{mm}$.

In addition to general observations about the effect of dataset size, Figures 4.49 and 4.50 provide a detailed analysis of the model's performance. Figure 4.49 shows histograms of the relative errors for the variables K, ε_0 and n for the model trained with $n_{\text{cases}} = 2000$ at a nominal thickness of $t = 1.2\,\text{mm}$. The results show that the relative errors for K and n are strongly concentrated around 0%, with most errors falling below 5%. This indicates good performance and generalization for these variables. However, for ε_0, a larger distribution of errors is observed, particularly in the validation and test sets, mirroring the trend seen for the model trained with $t = 0.8\,\text{mm}$. Comparing these histograms with those in Figure 4.46 (obtained with $n_{\text{cases}} = 5000$), it can be seen that the relative error distributions for the $t = 1.2\,\text{mm}$ model are very similar to those obtained with 5000 cases. Although this model for $t = 1.2\,\text{mm}$ was fine-tuned using a pre-trained model with $n_{\text{cases}} = 2000$ for $t = 0.8\,\text{mm}$, the transfer learning approach enabled the network to achieve a relative

error distribution similar to that obtained with 5000 cases.

This conclusion is further supported by the analysis in Figure 4.50. The histogram shows the distribution of the maximum absolute errors, while the lower figure shows the quartile analysis of the maximum relative errors. Most of the maximum errors are below 20 MPa, corresponding to relative deviations of about 1%, with only a few outliers exceeding 5%. These results closely mirror those observed for the $t = 0.8$ mm case trained with 5000 cases, illustrating the advantage of transfer learning in achieving comparable performance with significantly fewer training cases. In this case, transfer learning proves beneficial by reducing the amount of data required while maintaining high accuracy, which ultimately reduces computational cost.

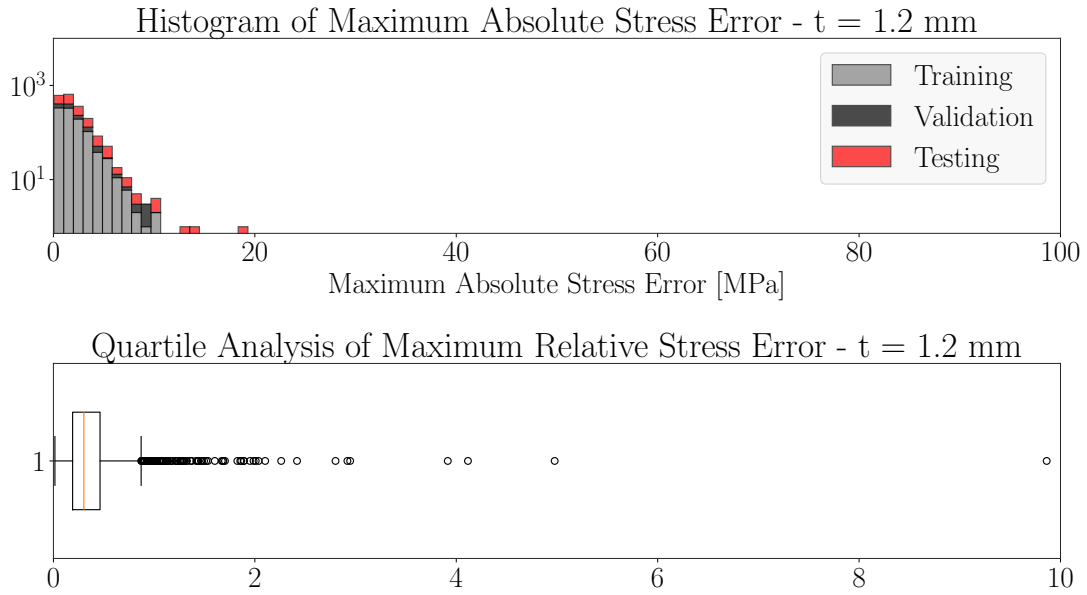


Figure 4.50: Histogram of the maximum absolute stress error and corresponding quartile analysis of the maximum relative stress error for the ML model for materials with t=1.2 mm, trained with 2000 cases.

4.3.3 Neural Network Implementation: Anisotropic Parameters

After identifying the isotropic parameters based on the first segment of the force-displacement curve from the reverse bending test, this section focuses on determining the anisotropic parameters of a combined isotropic-kinematic hardening law using the complete force-displacement curve (Figure 4.41). This hardening law includes five parameters that require calibration: K, ε_0, n, C and γ. To improve prediction

accuracy, the variable ε_0, which had the highest error in the previous section, was replaced with the yield stress variable σ_0. This substitution ensures that all variables remain within the same order of magnitude. The yield stress, σ_0, is defined by the following equation:

$$\sigma_0 = K(\varepsilon_0)^n. \tag{4.10}$$

As a result, the dataset comprises four independent parameters and one dependent parameter, σ_0, which is determined by K, ε_0 and n. Therefore the isotropic hardening component is now given by:

$$\sigma = K\left(\left(\frac{\sigma_0}{K}\right)^{1/n} + \varepsilon_p\right)^n. \tag{4.11}$$

The five parameter combinations, 5000 cases in total, are shown in Figure 4.51. The original dataset was divided into three subsets: training (70%), validation (15%) and testing (15%). The histograms along the diagonal of Figure 4.51 confirm a uniform distribution of cases across the three subsets, ensuring a well-balanced partitioning of the data. The histogram for yield stress (σ_0) shows values ranging from 50 MPa to 1200 MPa. To ensure that all variables are on the same scale, all input and output variables have been normalized to a range between -1 and 1.

Considering that 5000 cases are sufficient to cover the entire solution space, a preliminary analysis was performed to determine the optimal number of LSTM units in the bidirectional architecture for this problem. Experiments were performed with Bi-LSTM unit sizes of 10, 20, 40, 80 and 160, while maintaining a fixed learning rate of 0.001 to ensure stable and gradual convergence during training. The results of this analysis are presented in Figure 4.52, which shows the evolution of the MSE for different LSTM unit configurations. Figures 4.52a and 4.52b show the MSE over epochs for the training and validation datasets, respectively and Figure 4.52c summarizes the best validation and test losses obtained for each LSTM unit configuration.

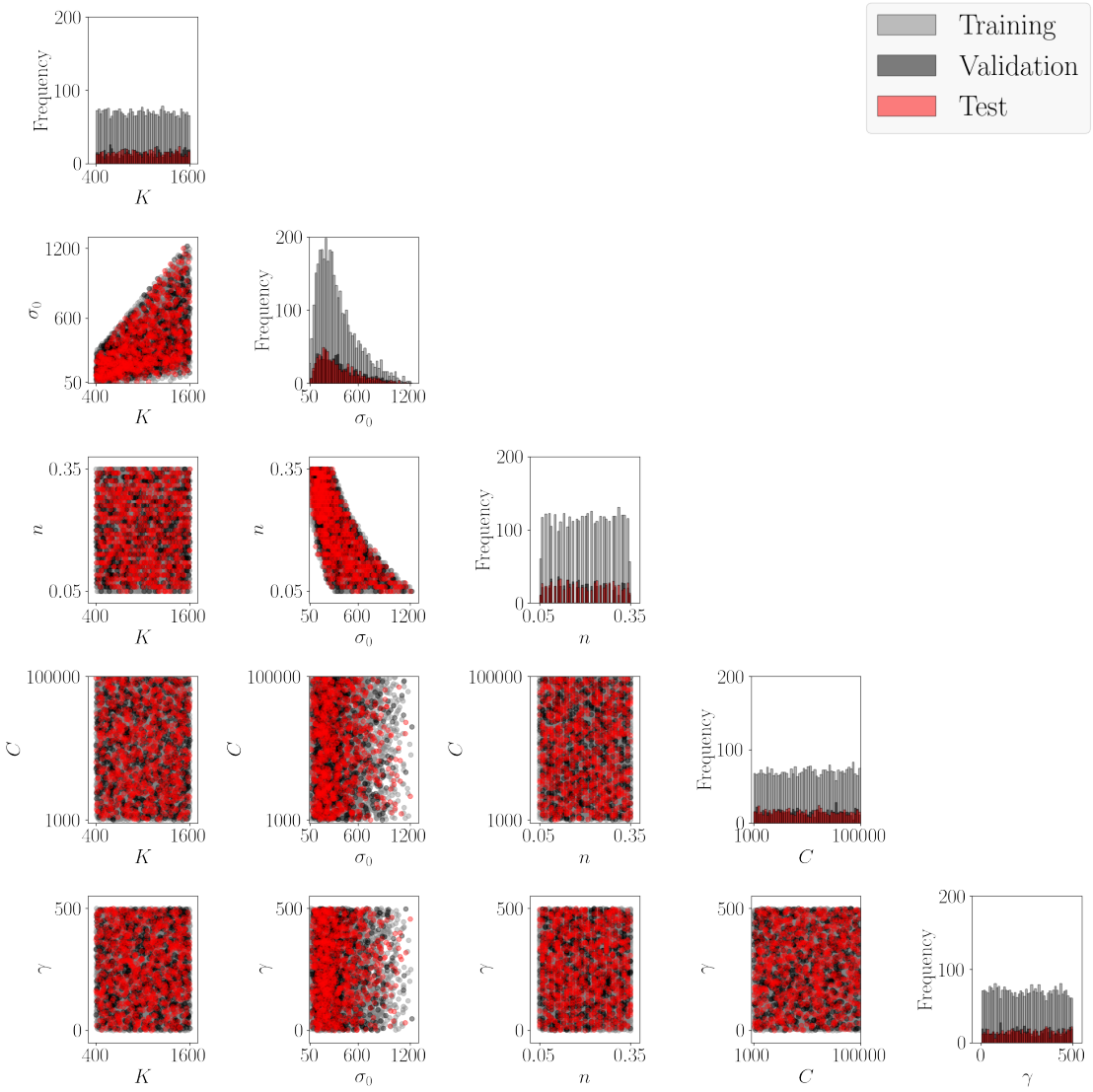


Figure 4.51: Dataset visualization with 5000 parameter combinations, divided into training (grey, 70%), validation (black, 15%) and testing (red, 15%) subsets.

Increasing the number of LSTM units leads to a significant reduction in the MSE on the training dataset, indicating improved model performance. This suggests that as the number of LSTM units increases, the model's ability to fit the training data increases. A similar trend is observed in the MSE on the validation dataset, indicating that a higher number of units contributes to improved generalization to unseen data. However, beyond approximately 40 Bi-LSTM units, further increases in the number of units do not result in significant improvements, indicating diminishing returns in model performance beyond this threshold. As shown in Figure 4.52c, the model with 40 Bi-LSTM units achieves the lowest MSE on both the validation and test datasets, highlighting this configuration as the optimal balance between model

complexity and generalization performance for the given problem. Beyond 40 units, the increase in model complexity does not correspond to a significant improvement in performance, suggesting that the model does not effectively utilize the additional capacity.

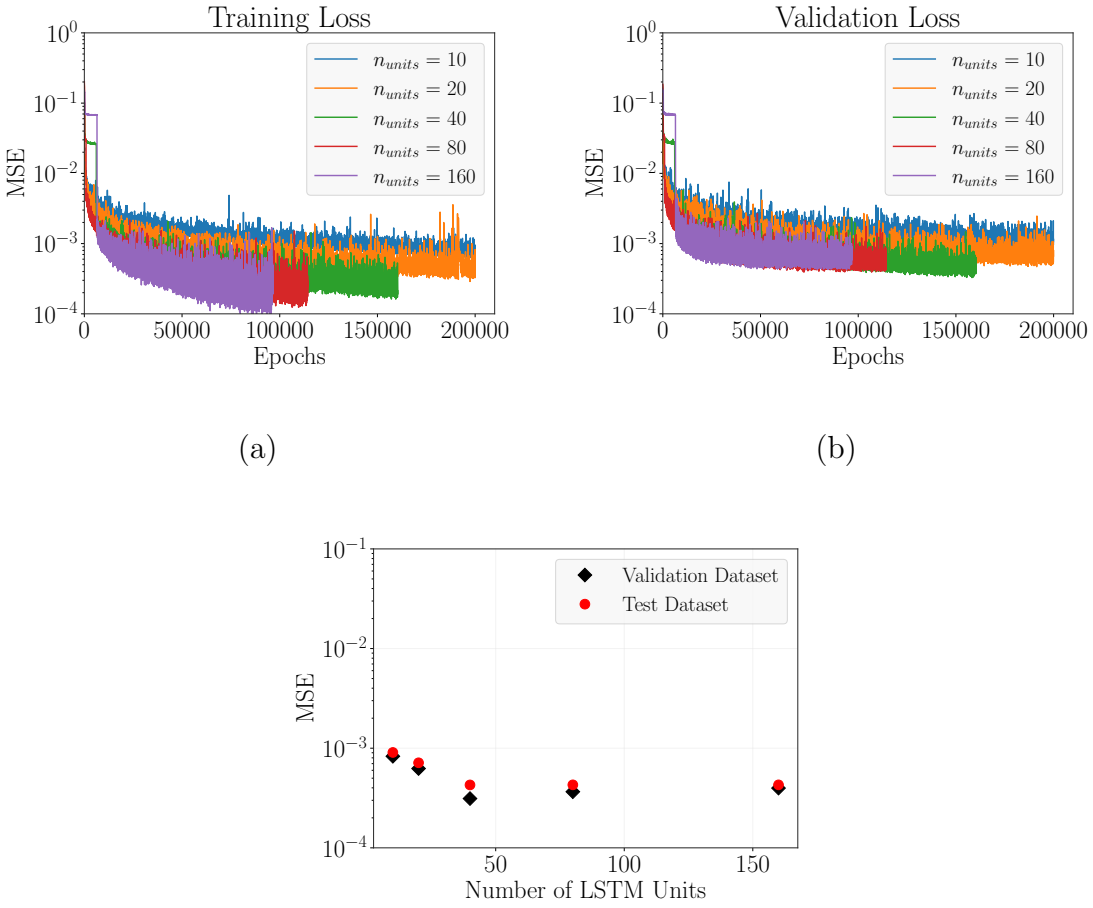


Figure 4.52: Evolution of the Mean Squared Error (MSE) over the epochs for different numbers of Bi-LSTM units: (a) Training dataset, (b) Validation dataset, (c) Best validation loss and test loss for the different numbers of LSTM units.

An extended hyperparameter search was performed on the network with 40 Bi-LSTM units to explore additional configurations and further optimize the performance of the model. The prediction results for the best configuration are shown in Figure 4.53 and can be analyzed in more detail in Appendix C. This figure shows the performance of the network in predicting the parameters K, σ_0, n, C and γ. Each row corresponds to a different dataset: the first row represents the training dataset,

the second row represents the validation dataset and the third row represents the test dataset. For the training dataset, R^2 values close to 1.0 indicate strong agreement between predicted and actual values, demonstrating the model's ability to effectively capture the underlying relationships. Similarly, the validation dataset shows high R^2 values, indicating strong generalization of the model to unseen data. While most parameters are predicted with high accuracy, some variation is observed for C and γ, especially at larger values. The test dataset shows consistent performance with high R^2 values for all parameters. However, a slight drop in performance is observed for C ($R^2 = 0.99$) and γ ($R^2 = 0.98$), with the scatter plot for γ showing some outliers. This suggests that the model may have difficulty accurately predicting γ in unseen data, indicating a potential area for improvement.

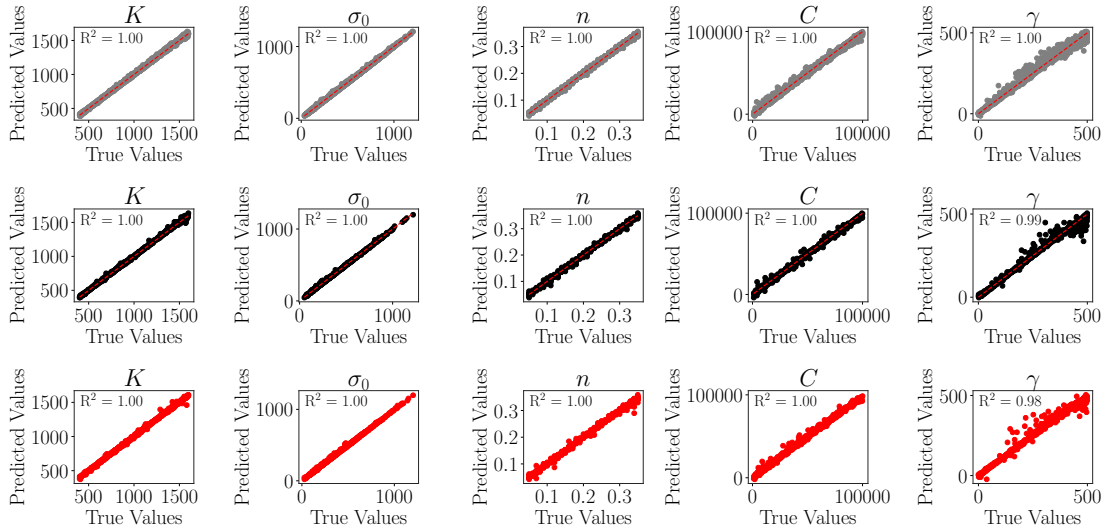
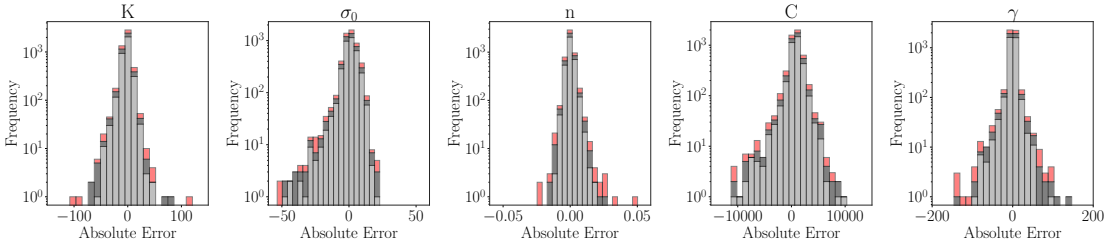


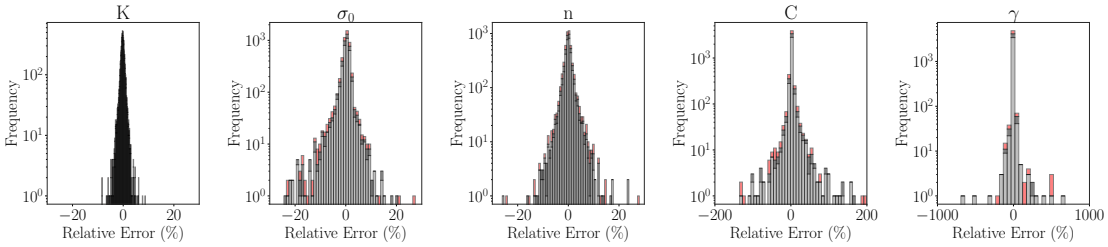
Figure 4.53: Prediction results for the network with 40 Bi-LSTM units. The rows represent the training (top), validation (middle) and test (bottom) datasets, showing the alignment between predicted and true values for K, σ_0, n, C and γ, along with their R^2 values.

Figure 4.54 shows the histograms of both the absolute and relative errors for the five variables. Figure 4.54a shows the absolute errors of the predicted values from the true values, considering non-normalized values. In general, the absolute errors for all variables follow a normal distribution with an average error close to zero and extreme error values occur only in a small number of cases. One variable of note in the analysis is σ_0, which represents the yield stress of the material and replaces the original variable ε_0 (as defined in Equation 4.10). The results show that the yield stress is estimated with an absolute error within ± 50 MPa. In addition, the

relative errors associated with this variable are around 20%, which is considered acceptable for the scope of this analysis. The remaining histograms of relative errors, Figure 4.54b, show that the model predicts the variables K and n quite accurately, with relative errors well below 20%. These predictions indicate good model performance and are consistent with the results from the previous problem. However, as suggested by the analysis in Figure 4.53, the variables C and γ have larger relative errors, highlighting the need for further model improvements to predict these parameters more accurately.



(a)



(b)

Figure 4.54: Histograms of (a) absolute and (b) relative errors across training (grey), validation (black) and test (red) datasets for variables K, σ_0, n, C and γ.

Figure 4.55 clearly shows the difference between the predictions of the isotropic parameters (K, σ_0 and n) and the kinematic parameters (C and γ). This figure illustrates the relationship between the absolute relative error of each variable and its corresponding true value for each case, allowing the identification of regions within the variable range where higher relative errors occur. While the isotropic parameters K, σ_0 and n exhibit similar uniform relative errors over their entire range, the kinematic parameters C and γ exhibit significant variability in their errors. In particular, the relative errors for C and γ tend to be more pronounced at the lower end of their respective ranges, 1000 for C and 0 for γ. This effect is particularly evident for C, where the relative errors increase significantly as the values approach

the lower limit. For variable γ, the distribution shows a greater occurrence of outliers all across the range, further indicating the challenges the model faces in accurately predicting this parameter. This discrepancy is partly due to the large differences in the magnitudes of the parameters. The ranges for K (400-1600 [MPa]), σ_0 (50-1200 [MPa]) and n (0.05-0.35) span below two orders of magnitude, while the ranges for C (1000-100000 [MPa]) and γ (0-500) span or above orders of magnitude, respectively. This considerable difference in scale has a direct impact on the sensitivity of the model, making the calibration of C and γ more difficult. Since these parameters vary over much larger scales, small absolute variations correspond to substantial relative changes, resulting in higher relative errors, especially at lower values.

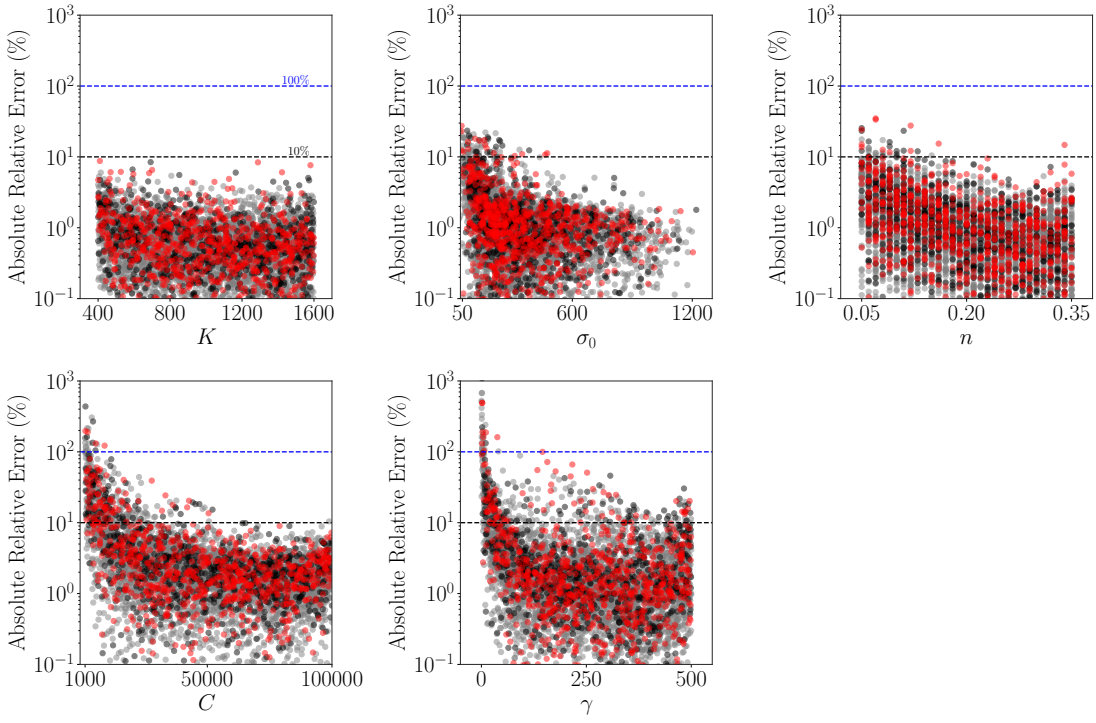


Figure 4.55: Correlation between true values and absolute relative errors on a logarithmic scale with error lines at 10% (black) and 100% (blue).

4.3.3.1 Results

Next, specific cases are presented to evaluate how the prediction errors affect the final response of the hardening model. Figure 4.56 shows the distribution of the MSE for the normalized outputs of the model, considering the five variables under analysis. The box plots are organized by data subsets: training, validation and test. In addition, the MSE loss function distribution is shown for the entire dataset, which

includes all 5000 cases. Each box plot shows the interquartile range (IQR), with the median (Q2) indicated by the central line and the first (Q1) and third (Q3) quartiles by the edges of the boxes. The whiskers extend to the most extreme data points within 1.5 times the IQR of the quartiles, with outliers beyond this range marked as single black circles. Three representative cases are selected from this plot: the Q2 case (median), the Q3 case (third quartile) and the Max case (maximum MSE). These cases, of the test dataset, provide insight into the performance of the model over different MSE distributions.

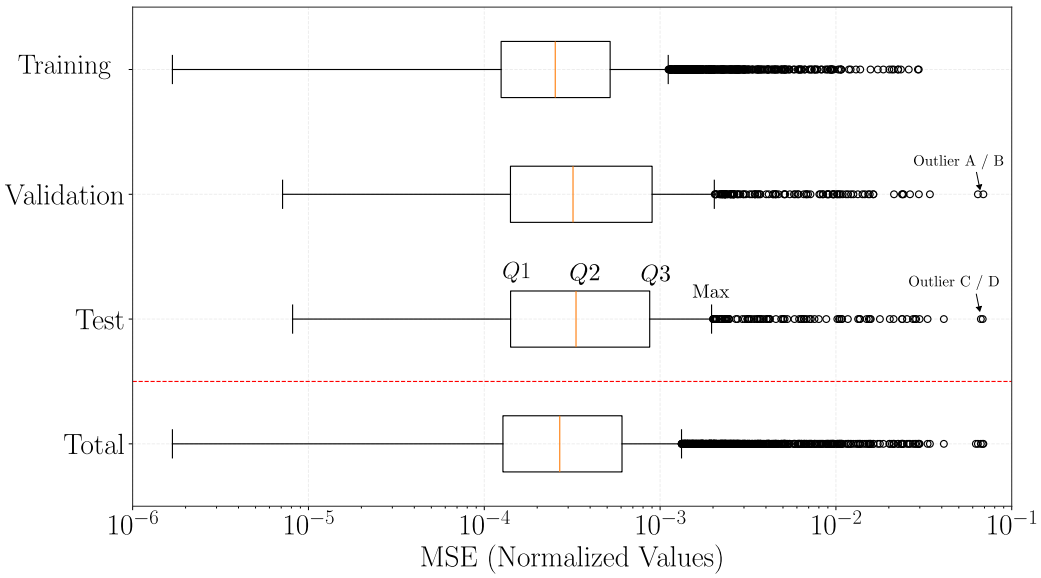


Figure 4.56: Boxplot representation of the Mean Squared Error (MSE) distribution for normalized output values across the Training, Validation, Test and Total datasets.

The corresponding expected (true) and predicted values for these representative cases are detailed in Table 4.13, along with the relative prediction errors for each variable. It is evident that the isotropic hardening variables are predicted with low relative errors (less than 2%), indicating good accuracy. On the other hand, the kinematic hardening variables have higher relative errors, about 2% for the Q2 case, 10% for the Q3 case and about 40% for the Max case. As expected, the variables C and γ contribute the most to the total error. In the test dataset, 75% of cases (563 out of 750) perform as well as or better than the Q3 case and 87% (655 cases) perform as well as or better than the Max case. While the overall performance appears promising, there are some outliers, i.e., predictions well outside the expected

or acceptable value. A total of 95 cases (13%) are identified as outliers and will be analyzed further.

Table 4.13: Expected and predicted parameters for Cases Q2, Q3 and Max, along with the relative prediction error for each variable.

	Case	K [MPa]	σ_0 [MPa]	n	C [MPa]	γ
Q2	**Expected**	837.11	220.55	0.23	42088.87	478.03
	Predicted	842.06	216.87	0.23	40425.30	472.88
	Relative Error	0.59%	1.67%	0.00%	3.95%	1.08%
Q3	**Expected**	600.83	367.35	0.10	10849.24	213.32
	Predicted	602.28	368.31	0.10	9755.39	202.24
	Relative Error	0.24%	0.26%	0.00%	10.10%	5.20%
Max	**Expected**	817.48	499.20	0.10	3586.18	484.25
	Predicted	823.18	496.74	0.10	2283.24	388.40
	Relative Error	0.70%	0.49%	0.00%	36.32%	19.79%

To evaluate how prediction errors in the five parameters can affect the final response of the constitutive hardening model, uniaxial loading conditions are simulated with a single element numerical model. This simplified model makes it possible to verify whether small variations in the constitutive parameters lead to coherent and physically meaningful changes in the stress–strain response under well-defined loading paths. Shell elements (element type S4R) are used for this analysis. The material is modeled with elastoplastic behavior, using a Young's modulus of 210 GPa and assuming a combined isotropic-kinematic hardening model. An isotropic yield criterion is also assumed. As represented in Figure 4.57, three different uniaxial steps are considered: tension, compression and subsequent tension. The displacements x_1, x_2 and x_3 are applied to induce a equivalent strain of approximately 0.05 in the material at each stage. This plastic strain value is consistent with the strain values imposed during the reverse bending test.

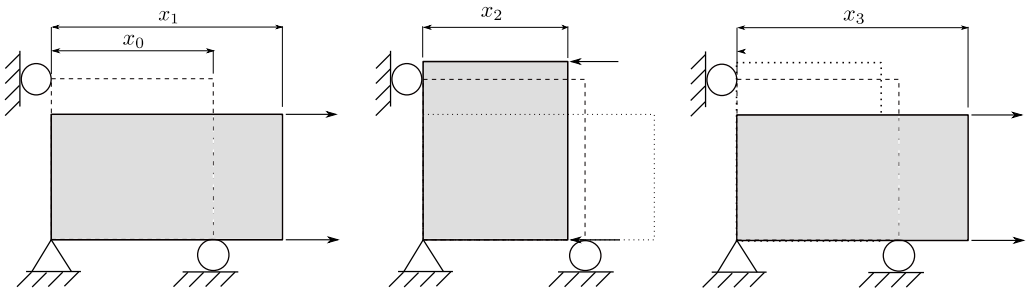
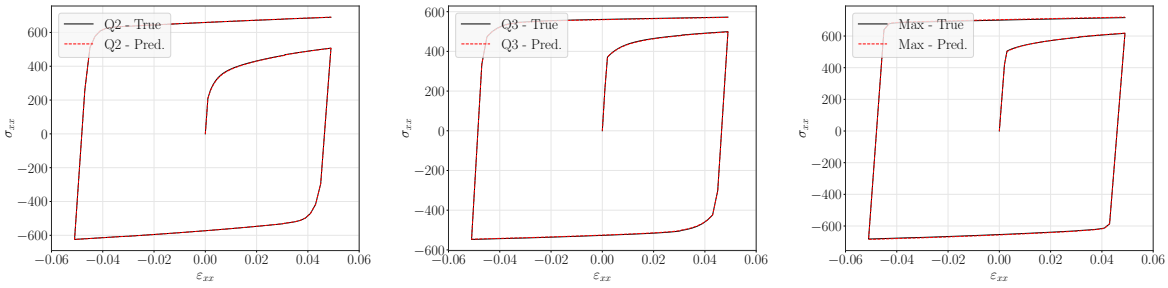


Figure 4.57: Schematic representation of uniaxial loading conditions applied to a single element, illustrating the three distinct stages: initial tension, compression and subsequent tension.

Figure 4.58 shows the tension-compression-tension (TCT) stress-strain (σ_{xx}-ε_{xx}) curves for the Q2, Q3 and Max cases. For each case, two curves are shown: the target curve derived using the five true hardening parameters and the predicted curve obtained using the parameters predicted by the ML model. As seen, for the three cases, parameter prediction directly resulted in excellent agreement between the true and predicted stress-strain curves. Despite some higher errors in the prediction of the kinematic parameters, e.g. for the Max case, these do not necessarily translate into significant discrepancies in the resulting stress-strain curve.



(a) (b) (c)

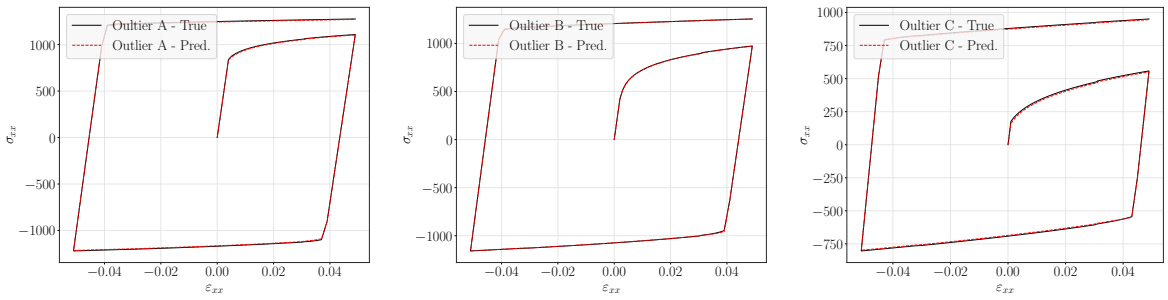
Figure 4.58: Tension-compression-tension (TCT) stress-strain (σ_{xx}-ε_{xx}) curves for three distinct cases: (a) Case Q2, (b) Case Q3 and (c) Case Max.

Next, some outliers are analyzed, referred to as outliers A, B, C and D. As shown in Figure 4.56, these cases have the highest MSE values. Outliers A and B belong to the validation dataset, while outliers C and D belong to the test dataset. The true parameters and predicted values for these four outliers are presented in Table 4.14, along with their corresponding relative errors. It can be observed that the isotropic parameters are well predicted, even for the worst outliers, with relative errors below

20%. On the other hand, the kinematic parameters have higher relative errors. Of particular concern is outlier D, which has a negative value for the kinematic variable C. Instead of predicting a value of 1120.85, the model predicts a value of -1087.02, resulting in a relative error close to 200%. This problem is not exclusive to outlier D, as 12 cases show negative predictions for the C variable and 16 cases for the γ variable. Notably, no negative values were predicted for the isotropic variables. As shown in Figure C.1, these negative predictions occur primarily for true values close to the lower bound of the variables: 1000 for C and 0 for γ. The stress-strain curves for the outlier cases A, B and C are shown in Figure 4.59. Although these are the worst cases, the predicted and true curves show a very reasonable overlap, demonstrating that the model still effectively captures the underlying trends even in challenging scenarios.

Table 4.14: Expected and predicted parameters for Outliers A, B, C and D, along with the relative prediction error for each variable.

	Outlier	K [MPa]	σ_0 [MPa]	n	C [MPa]	γ
A	**Expected**	1449.41	849.73	0.09	4528.81	482.67
	Predicted	1440.60	837.10	0.09	4021.61	336.09
	Relative Error	0.61%	1.48%	0.00%	11.20%	30.40%
B	**Expected**	1575.83	467.03	0.16	4661.74	307.07
	Predicted	1581.88	461.20	0.16	4390.25	448.54
	Relative Error	0.38%	1.25%	0.00%	5.82%	46.08%
C	**Expected**	1546.53	170.67	0.34	1858.03	216.74
	Predicted	1549.50	147.87	0.34	878.87	360.52
	Relative Error	0.19%	13.36%	0.00%	52.70%	66.32%
D	**Expected**	1211.82	747.36	0.10	1120.85	145.63
	Predicted	1214.34	746.12	0.10	-1087.02	291.34
	Relative Error	0.21%	0.17%	0.00 %	196.91%	100.05%



(a) (b) (c)

Figure 4.59: Tension-compression-tension (TCT) stress-strain (σ_{xx}-ε_{xx}) curves for three distinct cases: (a) Outlier A, (b) Outlier B and (c) Outlier C.

4.3.3.2 Penalty in Loss Function based on Kinematic Parameters Analysis

Although the results presented in the previous sections demonstrate strong predictive capability of the ML model for most cases, approximately 30 cases yield negative values for the kinematic hardening parameters, C and γ. These results expose specific limitations of the model, particularly regarding the enforcement of the underlying physical laws governing the constitutive behavior. According to the thermodynamic framework described by Yang et al. [287], in the energy analysis of elastic–plastic materials undergoing an isothermal process, the work per unit volume, $\widehat{W}$, can be decomposed into two contributions: the rate of free energy storage and the rate of dissipation. This is expressed by the internal dissipation balance, subject to the thermodynamic inequality:

$$\widehat{W} = \boldsymbol{\sigma}_{ij}\dot{\varepsilon}_{ij} = \dot{\Psi} + \Phi, \quad \text{with } \Phi \geq 0, \tag{4.12}$$

where Ψ denotes the Helmholtz free energy and Φ represents the intrinsic dissipation, which must satisfy the second law of thermodynamics by remaining non-negative at all times. In rate-independent plasticity, the dissipation arises primarily from irreversible mechanisms such as plastic slip and must therefore be formulated in a way that precludes energy generation within the material.

With the decoupling assumption between elastic and plastic contributions to free energy, the dissipation inequality can be written more explicitly as:

$$\Phi = \sigma_{ij}\dot{\varepsilon}^{pl}_{ij} - \dot{\Psi}_{pl} = \sigma_{ij}\dot{\varepsilon}^{pl}_{ij} - \rho\dot{\psi}_{pl} \geq 0, \tag{4.13}$$

where $\dot{\varepsilon}^{pl}_{ij}$ is the plastic strain rate, ψ_{pl} is the plastic free energy per unit mass and ρ is the mass density.

For constitutive models that incorporate kinematic hardening, the total Helmholtz free energy is typically decomposed into elastic, isotropic plastic and kinematic plastic components. In the case of the nonlinear kinematic hardening model proposed by Armstrong and Frederick [107], the stored energy associated with the kinematic hardening mechanism is given by:

$$\Psi^{\text{pl, kin}} = \frac{1}{2\rho C}\alpha_{ij}\alpha_{ij}, \tag{4.14}$$

where α_{ij} denotes the backstress tensor and C is the kinematic hardening modulus. As shown in Equation 2.43, the evolution of the backstress follows a nonlinear saturation-type law of the form:

$$\dot{\alpha}_{ij} = C\dot{\varepsilon}^{pl}_{ij} - \gamma\dot{\lambda}\alpha_{ij}, \tag{4.15}$$

where γ is a recovery parameter that controls the rate at which the backstress saturates and $\dot{\lambda} \geq 0$ is the plastic multiplier. This evolution equation introduces a dissipative mechanism associated with dynamic recovery. By substituting the stress decomposition and the kinematic evolution into the thermodynamic balance, the plastic dissipation rate becomes:

$$\Phi = s_{ij}\dot{\varepsilon}^{pl}_{ij} - \alpha_{ij}\dot{\varepsilon}^{pl}_{ij} + \frac{\gamma}{C}\dot{\lambda}\alpha_{ij}\alpha_{ij}. \tag{4.16}$$

This expression can be reformulated using the yield stress magnitude k and the normalized plastic flow direction m_{ij}, resulting in:

$$\Phi = km_{ij}\dot{\varepsilon}^{pl}_{ij} + \frac{\gamma}{C}\dot{\lambda}\alpha_{ij}\alpha_{ij}. \tag{4.17}$$

The first term corresponds to the dissipation associated with plastic flow. The second term accounts for the energy dissipated during the evolution of the backstress. The condition, required by the second law of thermodynamics, is satisfied only if $C > 0$ and $\gamma > 0$. This ensures that the kinematic hardening behavior is physically admissible. Negative values for either parameter imply that energy could be artificially introduced into the system, which would violate the principle of irreversibility. This theoretical insight underscores the importance of explicitly enforcing positivity constraints on the kinematic hardening parameters when developing and training predictive models, especially in machine learning frameworks that do not inherently consider such physical constraints.

One possible strategy to prevent negative predictions is to apply a ReLU activation function to the final dense layer of the neural network. The ReLU function

restricts outputs to non-negative values, which may initially appear consistent with the physical requirement that parameters such as C and γ must not be negative. Since the outputs in this study were normalized to the interval $[-1, 1]$, applying ReLU would artificially clip valid negative values, making it incompatible with the intended output space and disrupting the denormalization process. If the outputs had instead been normalized to the interval $[0, 1]$, ReLU would be applicable in principle. In particular, for the kinematic recovery parameter γ, whose valid physical domain starts at zero ($\gamma \geq 0$), the use of ReLU could effectively enforce physical admissibility by eliminating negative predictions. However, the remaining parameters predicted by the model, including C, K, σ_0 and n, may assume values below those represented in the training dataset while still being physically meaningful. The use of ReLU would prevent the network from extrapolating to these admissible lower values and reduce its generalization capability. While ReLU enforces non-negativity, it imposes a hard lower bound that could exclude valid physical outcomes for parameters whose minimum value is greater than zero but not necessarily zero itself. For these reasons and to preserve both physical plausibility and the ability to generalize beyond the training range, the ReLU activation function was not adopted in this work.

As an alternative to architectural constraints, a more flexible approach consists in embedding the physical admissibility requirements directly into the loss function used during training. This is achieved by introducing a physics-based penalty term that explicitly penalizes violations of the thermodynamic condition $\Phi \geq 0$, without restricting the model's ability to extrapolate. In this context, a custom loss function is defined as the weighted combination of a standard regression term, the MSE between predicted and true normalized values and a penalty term associated with physical violations. The total loss function is expressed as:

$$\mathcal{L}_{\text{total}} = (1 - \lambda) \cdot \text{MSE} + \lambda \cdot \text{Penalty}_{\text{physics}}, \tag{4.18}$$

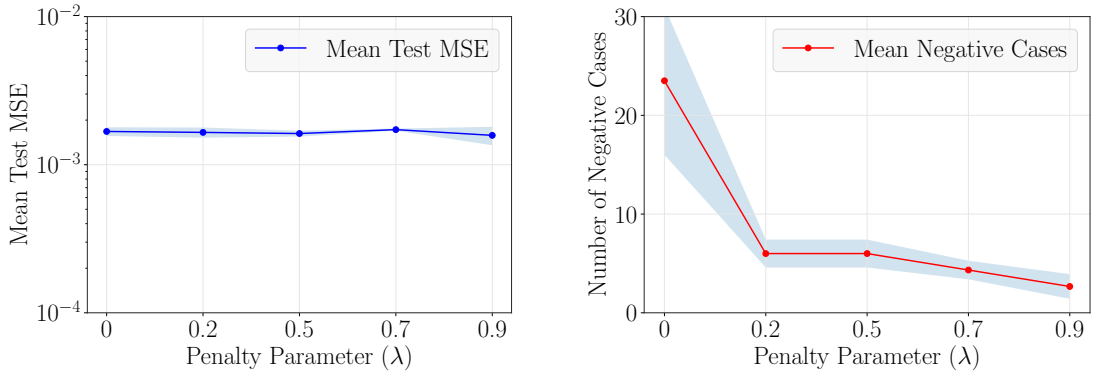
where the scalar parameter $\lambda \in [0, 1]$ controls the trade-off between data fidelity and physical admissibility. The penalty term is constructed to penalize negative predictions of the kinematic parameters C and γ and is defined as:

$$\text{Penalty}_{\text{physics}} = \frac{\text{ReLU}(-C)}{C_{\max} - C_{\min}} + \frac{\text{ReLU}(-\gamma)}{\gamma_{\max} - \gamma_{\min}}, \tag{4.19}$$

where the ReLU operator ensures that only negative values are penalized, while the normalization by the parameter ranges prevents the penalty from dominating the

loss due to scale differences. This formulation retains gradient flow during training and allows the model to learn both accurate and physically consistent parameters, preserving compliance with the dissipation inequality.

Figure 4.60 illustrates the impact of the penalty weight λ in the physics-based loss function on both prediction accuracy and physical admissibility. Figure 4.60a shows the variation of the mean test MSE with increasing values of λ, while Figure 4.60b shows the corresponding evolution of the mean number of predicted negative values for the kinematic parameters C and γ. As seen, the inclusion of the physics-based penalty does not significantly affect the prediction accuracy, as the mean squared error remains approximately constant across the entire range of λ. This indicates that incorporating physical constraints into the loss function does not compromise the model's ability to fit the data. However, the number of negative cases is substantially reduced as λ increases, dropping from more than 20 cases when $\lambda = 0$ (i.e., no physical penalization) to fewer than 5 cases for $\lambda \geq 0.5$. This result demonstrates the effectiveness of the penalty term in promoting thermodynamically admissible predictions. The diminishing marginal effect beyond $\lambda = 0.2$ also suggests that moderate penalization is sufficient to eliminate most of the unphysical outputs, allowing a balance between learning flexibility and constraint enforcement. These findings validate the proposed loss formulation and support the adoption of physics-based terms in machine learning workflows for constitutive modeling, especially when physical consistency is critical.



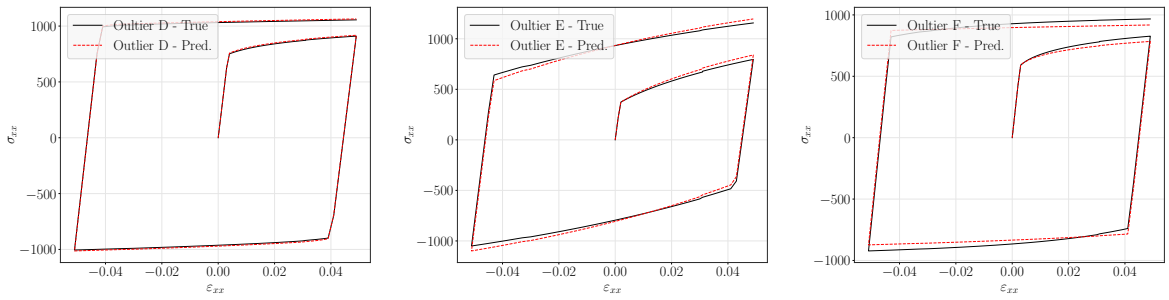
(a) (b)

Figure 4.60: Influence of the penalty parameter λ on (a) test mean squared error and (b) number of predicted negative values for C and γ.

Table 4.15 compares the expected and predicted material parameters for three representative outlier cases: D, E and F. These cases were initially identified as producing negative values for the kinematic parameters C or γ when no physical constraint ($\lambda = 0$) was applied. Predictions are shown for both the unconstrained model and the best-performing physics-informed model with $\lambda = 0.9$, which yielded only one violation among 5000 cases. For cases D and E, the inclusion of the physical penalty term successfully eliminated the negative predictions, resulting in physically consistent values for all parameters. In case F, however, a slightly negative value of C was still predicted. This highlights that although the proposed approach significantly reduces the occurrence of unphysical predictions, it does not guarantee full compliance with the thermodynamic constraints in all situations. For this case and any similar new scenarios the adopted strategy was to set negative values to zero. The tension-compression curves presented in Figure 4.61 confirm that the predicted parameters yield mechanically consistent behavior, even for these difficult edge cases, including the outlier F.

Table 4.15: Comparison of expected and predicted material parameters for outliers D, E and F. Predicted values are shown for two regularization levels: $\lambda = 0$ and $\lambda = 0.9$.

	Outlier	K [MPa]	σ_0 [MPa]	n	C [MPa]	γ
D	**Expected**	1211.82	747.36	0.10	1120.85	145.63
	Predicted ($\lambda = 0$)	1214.34	746.12	0.10	-1087.02	291.34
	Predicted ($\lambda = 0.9$)	1219.32	753.57	0.10	2710.83	286.16
E	**Expected**	1479.00	369.71	0.29	4601.32	10.86
	Predicted ($\lambda = 0$)	1475.50	367.08	0.29	5114.64	-9.56
	Predicted ($\lambda = 0.9$)	1448.00	369.26	0.28	5831.57	11.11
F	**Expected**	1061.38	587.72	0.10	2051.39	38.02
	Predicted ($\lambda = 0$)	1075.61	584.87	0.10	-1848.21	-23.23
	Predicted ($\lambda = 0.9$)	1062.71	590.00	0.10	-85.68	15.36



(a) (b) (c)

Figure 4.61: Tension-compression-tension (TCT) stress-strain (σ_{xx}-ε_{xx}) curves for (a) Outlier D, (b) Outlier E and (c) Outlier F.

Finally, for a more comprehensive analysis of the results, two equivalent quantities are defined to evaluate the isotropic and kinematic components of the hardening model separately. For the isotropic component, the evolution of the equivalent stress, σ, with the equivalent plastic strain, ε_p, is described by the Swift hardening law, using both the predicted and true parameters:

$$\sigma^{\text{pred}} = \hat{K}\left(\left(\frac{\hat{\sigma}_0}{\hat{K}}\right)^{1/\hat{n}} + \varepsilon_p\right)^{\hat{n}}, \tag{4.20}$$

$$\sigma^{\text{true}} = K\left(\left(\frac{\sigma_0}{K}\right)^{1/n} + \varepsilon_p\right)^{n}, \tag{4.21}$$

where σ^{pred} and σ^{true} are the predicted and true equivalent stresses, respectively. The parameters $\hat{K}$, $\hat{\sigma}_0$ and $\hat{n}$ represent the predicted isotropic hardening parameters, while K, σ_0 and n denote the corresponding true values.

Similarly, for the kinematic component, the evolution of the backstress, α, as a function of the equivalent plastic strain is evaluated using the Frederick-Armstrong hardening rule:

$$\alpha^{\text{pred}} = \frac{\hat{C}}{\hat{\gamma}} \cdot \left(1 - e^{-\hat{\gamma}\varepsilon_p}\right), \tag{4.22}$$

$$\alpha^{\text{true}} = \frac{C}{\gamma} \cdot \left(1 - e^{-\gamma\varepsilon_p}\right), \tag{4.23}$$

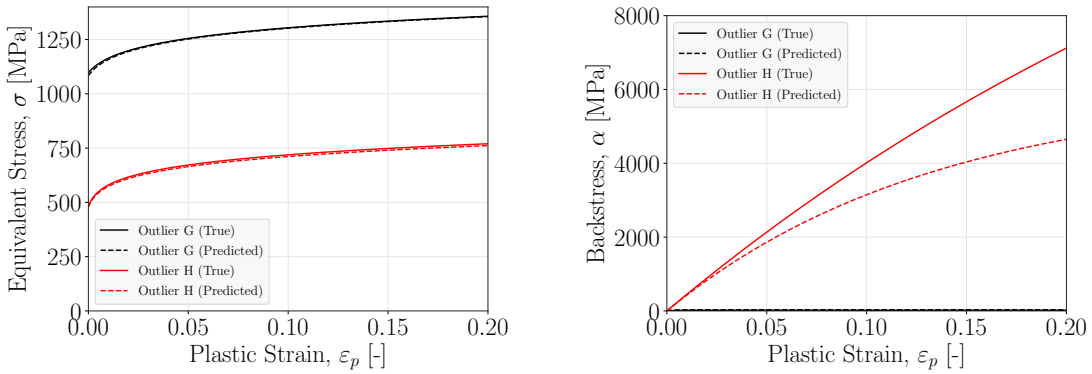
where α^{pred} and α^{true} are the predicted and true backstress values, respectively. The parameters $\hat{C}$ and $\hat{\gamma}$ refer to the predicted kinematic hardening coefficients, C and γ are the corresponding true values.

The evolution of the equivalent stress, σ and the backstress, α, for two additional outliers, G and H, is shown in Figure 4.62. Only plastic strain values, ε_p, between 0 and 0.2 are considered. The respective true and predicted hardening parameters are summarized in Table 4.16, along with the relative errors associated with each variable. Outliers G and H correspond to the test dataset cases with the highest relative errors in predicting the variables C (131.43%) and γ (189.06%), respectively. As shown in Figure 4.62a, the evolution of the isotropic equivalent stress, calculated using both the true and predicted isotropic parameters, shows excellent agreement. This behavior was expected since the predicted and true isotropic parameters are very close for both outliers, with relative errors below 2%. On the other hand, the evolution of the kinematic backstress, shown in Figure 4.62b, shows more pronounced differences. This divergence is particularly noticeable for outlier H, where the predicted backstress evolution is consistently different from the true one over the relevant range of plastic strains.

Figure 4.63 shows the predicted and expected stress-strain curves for the TCT loading condition for both outliers. For outlier G, the observed differences in backstress evolution do not visibly translate into a significant difference in the resulting TCT curve. However, for outlier H, the discrepancy in backstress significantly affects the resulting TCT curve. A maximum absolute error of 195 MPa (about 55%) is observed between the predicted and true stress-strain curves.

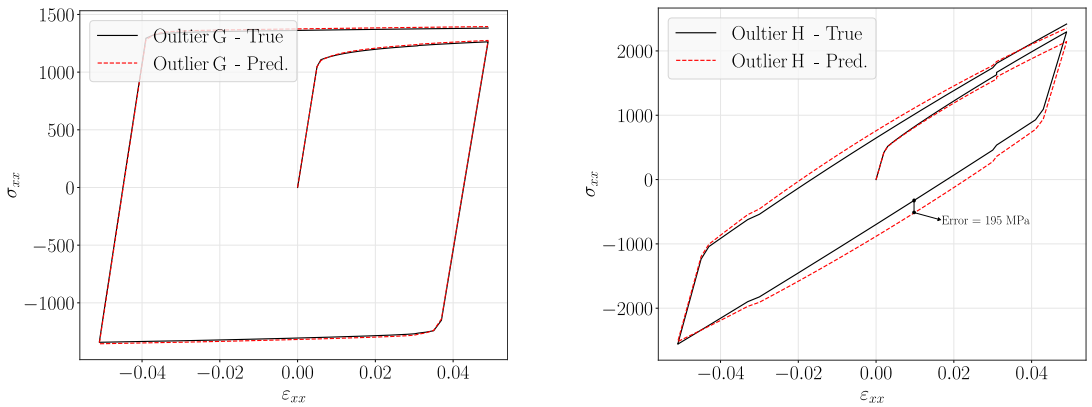
Table 4.16: Expected and predicted parameters for Outliers G and H, along with the relative prediction error for each variable.

	Outlier	K [MPa]	σ_0 [MPa]	n	C [MPa]	γ
G	**Expected**	1492.19	1097.11	0.06	5253.91	291.02
	Predicted	1490.64	1083.54	0.06	12158.02	369.35
	Relative Error	0.10%	1.24%	0.00%	131.43%	26.96%
H	**Expected**	903.61	481.87	0.10	45496.83	2.56
	Predicted	893.64	477.37	0.10	44552.06	7.40
	Relative Error	1.10%	0.94%	0.00%	2.08%	189.06%



(a) (b)

Figure 4.62: Comparison of (a) equivalent stress and (b) backstress evolution for Outliers G and H as a function of plastic strain (ε_p).



(a) (b)

Figure 4.63: Tension-compression-tension (TCT) stress-strain (σ_{xx}-ε_{xx}) curves for (a) Outlier G, (b) Outlier H.

Considering all 5000 cases in the original dataset, Figure 4.64 illustrates the prediction accuracy of the machine learning model for the isotropic and kinematic hardening components. Figure 4.64a and b show histograms of the maximum absolute errors in equivalent stress σ (associated with isotropic hardening) and backstress α (associated with kinematic hardening), respectively. These errors were computed for each case over 50 equally spaced plastic strain levels ranging from 0 to 0.2, across the training, validation and test sets. As shown in Figure 4.64a, most predictions of equivalent stress exhibit maximum absolute errors below 20 MPa, corresponding to relative deviations typically under 10%, with only a small number of outliers exceeding 30 MPa. A similar pattern is observed for the backstress in Figure 4.64b,

although its error distribution is broader, reflecting the greater sensitivity of the kinematic hardening model to variations in the predicted parameters C and γ. Figure 4.64c complements this analysis by presenting boxplots of the maximum relative errors (in %) for both quantities on a logarithmic scale. For equivalent stress, the interquartile range remains below 10%, with only a few high-error cases. The relative errors for the backstress are generally higher and more dispersed, confirming that the kinematic component is more difficult to predict accurately. Overall, these results confirm that the model captures the isotropic hardening behavior with high fidelity, while also providing physically meaningful and consistent predictions for the kinematic component, despite its increased complexity.

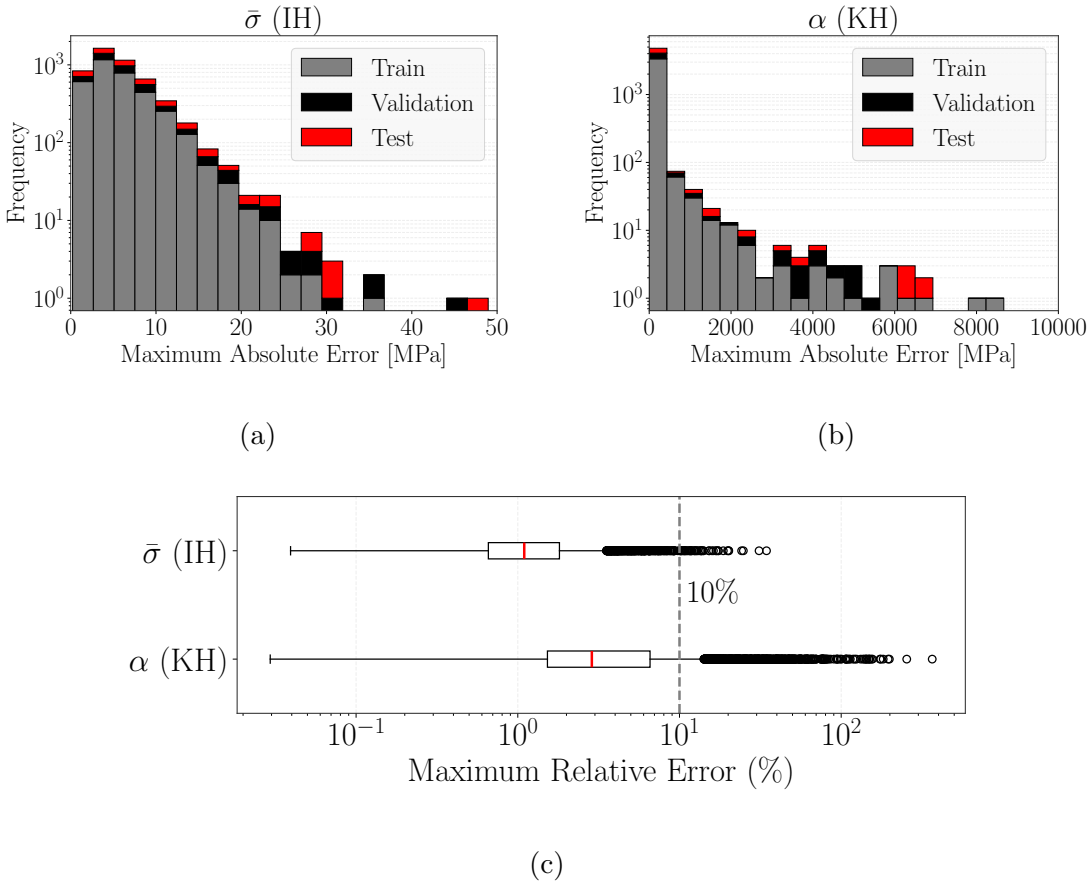


Figure 4.64: Error analysis for isotropic (σ) and kinematic (α) hardening components. (a) Maximum absolute error distribution for σ; (b) maximum absolute error for α; (c) boxplot of the maximum relative error (%).

Experimental Validation

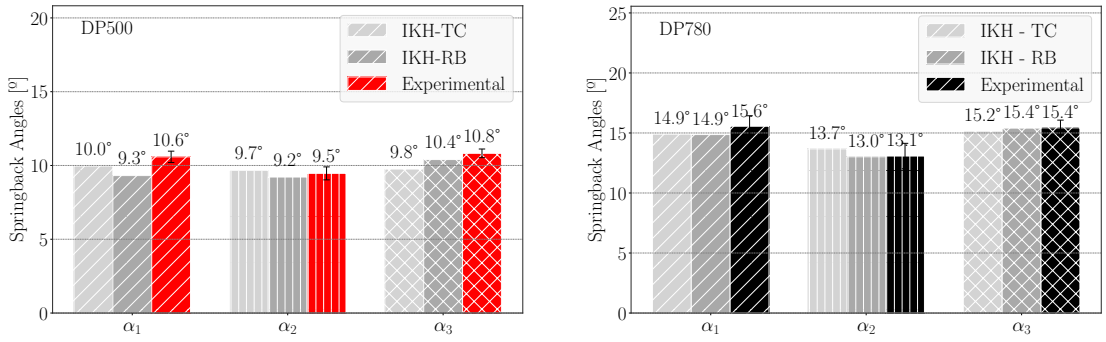
To validate this methodology and framework in a real application, the experimental reverse bending (RB) results obtained in Section 3.4.3.3 for the DP500 and DP780 steels are considered. The original experimental data, consisting of a sequence of force-displacement points, were formatted to meet the requirements for applying the LSTM-based model. Specifically, each curve was resampled into 300 equally spaced points, with each point containing two features, force and displacement, resulting in a total of 600 different values per sequence. To ensure consistency, both features were normalized using the same scaling scheme applied during training, mapping values to the range $[-1, 1]$. The identified material parameters for the dual-phase steels are summarized in Table 4.17. This table compares the five hardening parameters identified by the ML model using the experimental reverse bending (RB) data with those obtained from the tension-compression (TC) test whose identification was performed in Section 4.1.2.2. Overall, the identified parameters are comparable and of the same order of magnitude, especially the isotropic hardening parameters (K, σ_0 and n). In particular, the yield stress σ_0 shows strong agreement between the TC and RB tests, with a variation of about 12% in MPa for both materials. On the other hand, the kinematic hardening parameters (C and γ) show more pronounced differences, suggesting potential variations in material behavior under different loading conditions.

Table 4.17: Anisotropic hardening parameters of the combined isotropic-kinematic hardening (IKH) model, identified based on tension-compression tests (TC) and reverse bending tests (RB).

	Material	K [MPa]	σ_0 [MPa]	n	C [MPa]	γ
DP500	**Tension - Compression (TC)**	632.6	273.8	0.334	27710	124.2
	Reverse Bending (RB)	616.08	243.3	0.21	67824	374.8
DP780	**Tension - Compression (TC)**	651.8	373.2	0.191	38850.00	88.3
	Reverse Bending (RB)	647.1	326.1	0.27	69941.01	206.1

To understand the impact of these differences, Figure 4.65 shows the corresponding springback angles (α_1, α_2 and α_3) obtained by FEA of a reverse bending test, considering the hardening parameters identified from the TC test and the RB test, along with the corresponding experimentally obtained values. As observed, the pre-

dicted springback angles from both sets of parameters are very close and in good agreement with the experimental results. However, using the parameters calibrated with the RB test results in springback angles that are slightly closer to the experimental values.



(a) (b)

Figure 4.65: Comparison of the springback angles (α_1, α_2 and α_3) obtained from FEA using the hardening parameters identified from the TC and RB tests alongside the corresponding experimental values for (a) DP500 and (b) DP780.

4.4 Final Remarks

This section presents a novel approach using machine learning techniques, specifically long short-term memory networks, to characterize the hardening behavior of sheet metal steels based on bending test results. Given the sequential nature of the data obtained from these tests, namely the punch force-displacement curve, LSTM networks were chosen over traditional feed-forward neural networks to better capture the underlying material behavior.

In a first work, isotropic hardening parameters were determined using a standard three-point bending test. The methodology involved the sequential application of two machine learning models: one to characterize elasticity and another to characterize plasticity. The first model was responsible for estimating the Young's modulus of the tested material and when the predicted Young's modulus fell within the expected range for steels, the second model was applied to determine the Swift hardening parameters (K, n and ε_0). The results showed that the LSTM networks effectively captured the relationships between the sequential data and produced accurate predictions for both models. The elasticity model was able to predict Young's modulus with errors consistently below 3% for a wide range of materials. The plas-

ticity model, based on a bidirectional LSTM architecture, was optimized by Bayesian hyperparameter tuning, with an optimal configuration of 40 LSTM units. The predicted parameters had relative errors within acceptable limits, with the parameter K having the highest prediction accuracy. In contrast, ε_0 had the higher relative errors, but these had minimal impact on the final stress-strain response, influencing only the yield stress of the material. Even in the worst case scenarios, the predicted stress values deviated from the expected stress-strain curve by only about 10%, demonstrating the applicability of the proposed approach. The influence of sheet thickness on the three-point bending results was also evaluated, confirming the reliability of the method in dealing with small thickness variations of ± 0.1 mm in thickness. Application of the trained models to experimental three-point bending tests on DP500, DP600 and DP780 steels demonstrated the potential of this approach. The elasticity model successfully estimated Young's modulus within the expected range for the steels, while the plasticity model provided a viable alternative to traditional optimization-based parameter identification techniques.

In the second study, the same machine learning techniques were applied to a new experimental reverse bending test. This test allows sheet metal to be successively bent in opposite directions, capturing its behavior under cyclic loading conditions. By analyzing only the first loading cycle, the isotropic hardening parameters (K, ε_0 and n) can be identified using a methodology similar to the previous work. On the other hand, the anisotropic hardening parameters (K, ε_0, n, C and γ) are determined by considering the entire bending curve, which includes the bending, unbending and rebending phases. Building on the trained model from the previous study, a transfer learning approach was used to adapt the ML model originally developed for the three-point bending test to the reverse bending test. This approach provided significant computational benefits, reducing the training time by approximately 80% compared to training the model from scratch. While transfer learning accelerated the training process, it did not reduce the amount of data required to achieve satisfactory performance. The model still required between 1000 and 2000 cases to achieve adequate generalization. It was concluded that this result was primarily due to the difference in the sampling technique used in the three-point bending test (grid sampling) and the reverse bending test (Sobel sampling). Transfer learning was also used to train an ML model for a sheet thickness of 1.2 mm, which differs from the original nominal thickness of 0.8 mm. In this case, in addition to the reduction in computation time, less data samples were required to achieve superior performance. This suggests that transfer learning can be particularly beneficial when adapting a

pre-trained model to variations in material properties or test conditions, improving both efficiency and data utilization.

A similar LSTM-based approach was used to identify the anisotropic hardening parameters of sheet metal materials. In this approach, the variable ε_0 was replaced by the yield stress of the material, σ_0, which resulted in a significant reduction in the relative errors associated with this parameter, with maximum errors of about 20%. When analyzing the predictions for the combined isotropic kinematic hardening (IKH) model, the isotropic parameters showed better results than the kinematic parameters, which showed higher relative errors and the presence of extreme outliers. Some of these outliers corresponded to negative values for the variables C and γ, which are not possible in this hardening model. To reduce these outliers, the loss function used in the training process was modified. By incorporating physical constraints associated with the material model into the loss function, the model was encouraged to learn parameter relationships that were not only numerically accurate but also physically meaningful. Specifically, the penalty targeted negative predictions of the kinematic parameters C and γ using a normalized ReLU-based formulation. This strategy significantly reduced the number of physically inconsistent predictions without compromising overall model accuracy.

To further improve predictions, additional training data should be incorporated, particularly in regions where prediction errors are highest. A more targeted distribution of data in these critical areas could significantly improve the model's performance. However, increasing the dataset size comes at a computational cost, so a balance must be struck between improving accuracy and maintaining training efficiency. Another potential improvement is refining the data discretization strategy. In this study, each force-displacement curve was resampled to 300 points to preserve computational efficiency while maintaining representativeness. A finer discretization could capture more complex material behaviors, leading to improved generalization. However, increasing the number of points would inevitably increase the computational cost during training.

In addition to the global force–displacement response, further input features could be considered to improve the model performance. For example, the strain distribution across the sheet thickness and its evolution during the reverse bending, would provide a richer dataset for the characterization of kinematic hardening. Although such data can be easily obtained numerically for the creation of the training dataset, it is very difficult to measure experimentally, since capturing the strain field across the sheet thickness is challenging with techniques such as digital image

correlation, particularly in thin sheets. Another promising direction is to introduce derived features, such as the cumulative force-displacement area, which represents the strain energy density of the material. This variable is calculated as the integral of the force-displacement curve up to a given displacement value. Finally, conducting a more exhaustive hyperparameter search could further refine the model, enhancing its generalization. Future developments should focus on extending this methodology to more complex hardening models, incorporating alternative laws such as the Voce equation, which is particularly relevant for aluminum alloys, as well as more complex kinematic hardening models with additional parameters. Other tests involving reverse loading could also be considered, where full-field data can be more easily obtained using image correlation techniques.

In conclusion, the use of machine learning for parameter identification presents both advantages and limitations compared to classical approaches such as FEMU. One of the key advantages of ML-based methods is their computational efficiency once the model is trained. Unlike traditional methods, where parameter identification often involves iterative optimization procedures requiring multiple finite element simulations, an ML-based model provides instantaneous predictions. The computational effort is concentrated in the development of the training dataset and model training phase. Once trained, the model can quickly predict material parameters for new experimental data, significantly reducing computational costs during application. However, ML-based approaches also have limitations. A major drawback is their dependence on the training data, meaning the models are only reliable for materials with characteristics similar to those represented in the training dataset. In contrast to FEM, which can be applied to a wide range of materials by adjusting optimization constraints, an ML model requires retraining when applied to a new material outside its learning domain. Additionally, ML models are highly sensitive to the quality and diversity of the training data. If the dataset lacks sufficient variability or does not cover certain critical material behaviors, the model may fail to generalize, leading to inaccurate predictions. This highlights the importance of careful dataset selection, preprocessing and augmentation strategies. However, some of these limitations can be mitigated by techniques such as transfer learning. By leveraging knowledge from previously trained models, transfer learning enables faster adaptation to new materials with reduced training requirements, making ML-based approaches more practical for broader applications.

Chapter 5

Data Driven Constitutive Modeling

This chapter explores a different approach to the application of machine learning methods in constitutive modeling. While the previous chapter used artificial neural networks, more specifically recurrent neural networks, to identify parameters in established constitutive models, namely isotropic and anisotropic hardening parameters, this chapter focuses on using machine learning techniques to develop purely data-driven constitutive models. These models are designed to act as surrogate models, reproducing the path-dependent plastic behavior based solely on data. In other words, the stress-strain relationship is learned entirely from input-output data without relying on a predefined mathematical model.

To implement a fully data-driven modeling strategy, this work employs a specific type of recurrent neural network developed by Bonatti et al. [185], known as the linearized minimal state cells, to model the constitutive behavior of the DP780 material. Specifically, this chapter evaluates the ability of LMSCs to capture the anisotropic yielding and hardening behavior of AHSS, including key behaviors typically modeled by classical phenomenological formulations particularly the evolution of anisotropy and the Bauschinger effect under non-proportional loading. In addition, key aspects related to the training process are analyzed, including the type and amount of data required for effective learning, as well as the optimal neural network architecture, such as the number of layers, the size of each layer and other relevant hyperparameters.

A key focus of this study is the evaluation of the model's generalization capability across different types of loading paths in the context of finite element analysis. To this end, the trained neural networks are tested not only on standard monotonic and reverse loading sequences but also on deformation trajectories extracted from numerical simulations of stamping forming processes, such as cylindrical cup

drawing and rail-shaped deep drawing. The goal is to determine whether the neural network model can reproduce the stress response predicted by a conventional constitutive model (YLD2000-2d combined with the HAH model) when subjected to path-dependent loading histories. This evaluation is performed under both quasi-static and dynamic conditions, which introduce substantial variations in time integration schemes. In this context, it is particularly important to assess the self-consistency of the LMSC-based model, i.e., its ability to produce stress histories that are independent of the discretization of the strain path, ensuring reliable predictions across a wide range of time step sizes.

The chapter is structured as follows. Section 5.1 introduces the theoretical foundations and architecture of Linearized Minimal State Cells. Section 5.2 describes the dataset generation procedures, including the design of random and smooth strain paths to capture a wide range of material responses. Section 5.3 presents the training methodology, hyperparameter optimization and strategies to improve the model generalization. Finally, Section 5.4 is dedicated to model validation and performance assessment, including comparisons with conventional constitutive models and discussions on the robustness of the LMSC approach in finite element simulations.

5.1 Linearized Minimal State Cells (LMSCs)

Constitutive material modeling aims to predict the stress response of a material based on its deformation history. The deformation history is typically represented as a sequence of strain increments, denoted as $\Delta\boldsymbol{\varepsilon}(t_1), \ldots, \Delta\boldsymbol{\varepsilon}(t_n)$. Using this information, a constitutive material model predicts both the stress tensor $\boldsymbol{\sigma}(t_n)$ and the internal state variables $\boldsymbol{\chi}(t_n)$ at a given time t_n. These predictions are derived as functions of the current strain increment $\Delta\boldsymbol{\varepsilon}(t_n)$ and the material state at the previous time step, $\boldsymbol{\chi}(t_{n-1})$, according to the following relationship:

$$f : \{\Delta\boldsymbol{\varepsilon}(t_n), \boldsymbol{\chi}(t_{n-1}) \rightarrow \boldsymbol{\sigma}(t_n), \boldsymbol{\chi}(t_n)\} \quad (5.1)$$

This recursive structure aligns naturally with recurrent neural network architectures. However, conventional RNNs such as LSTM or GRU present limitations when applied to constitutive modeling [184]. In particular, their internal state dimension is tightly coupled with the number of trainable parameters, leading to unnecessarily high memory requirements and limited interpretability. Moreover, they do not inherently guarantee consistency of the stress response with respect to the discretization

of the strain path, a crucial property for numerical simulations involving different time step sizes.

To address these issues, Bonatti and Mohr [184] proposed the Minimal State Cells, designed to decouple the number of internal state variables from the number of trainable parameters. Building on this foundation, Bonatti et al. [185] introduced the Linearized Minimal State Cells a variant specifically designed to ensure self-consistency, i.e., the ability of the model to produce converging stress responses as the time increment decreases. This property makes LMSCs particularly well-suited for integration into explicit finite element solvers, where time step sizes may vary significantly depending on mesh resolution and loading rate [288]. Figure 5.1 shows the sequence of mathematical operations in an LMSC network.

The memory state at time t_n is represented as $\boldsymbol{\chi}_n$:

$$\boldsymbol{\chi}_n = \begin{bmatrix} \chi_n^1 \\ \chi_n^2 \\ \dots \\ \chi_n^{n_s} \end{bmatrix} \tag{5.2}$$

where n_s represents the number of state variables. The network input is a vector of strain increments $\Delta\boldsymbol{\varepsilon}_n$ and the state variables $\boldsymbol{\chi}_{n-1}$ at time $t - \Delta t$. The network outputs are the updated state vector $\boldsymbol{\chi}_n$ and the stress vector $\boldsymbol{\sigma}_n$. For a plane stress case (2D) the inputs strain increments, $\Delta\boldsymbol{\varepsilon}_n$ and the normalized stress output, $\boldsymbol{\sigma}_n$, are defined as:

$$\boldsymbol{\Delta\varepsilon}_n = \begin{bmatrix} \Delta\varepsilon_{xx,n} \\ \Delta\varepsilon_{yy,n} \\ \Delta\varepsilon_{xy,n} \end{bmatrix}. \tag{5.3}$$

$$\boldsymbol{\sigma}_n = \begin{bmatrix} \frac{\sigma_{xx,n}+\sigma_{yy,n}}{s_1} \\ \frac{\sigma_{xx,n}-\sigma_{yy,n}}{s_2} \\ \frac{\sigma_{xy,n}}{s_3} \end{bmatrix}. \tag{5.4}$$

The constants s_1, s_2 and s_3 are chosen so that each stress component has approximately unit standard deviation over the training dataset [185]. This normalization ensures that all stress components contribute equally to the loss function during training, regardless of their original scale.

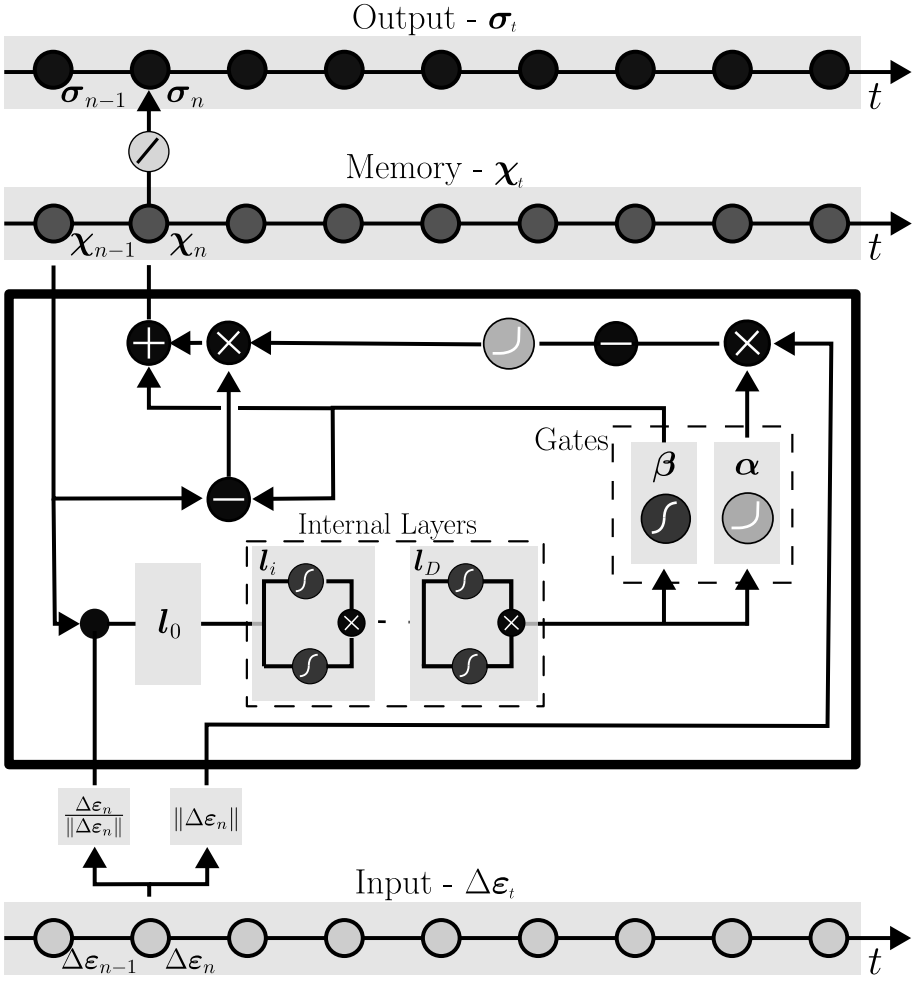


Figure 5.1: Network structure of a Linearized Minimal State Cell (LMSC): $\Delta\boldsymbol{\varepsilon}_t$ represents the input, $\boldsymbol{\chi}_t$ the memory state and $\boldsymbol{\sigma}_t$ the output.

As represented in Figure 5.1, the first layer, $\boldsymbol{l}_0$, concatenates the previous memory state, $\boldsymbol{\chi}_{n-1}$, with the normalized current strain increment, $\Delta\boldsymbol{\varepsilon}_n$:

$$\boldsymbol{l}_0 = \begin{pmatrix} \boldsymbol{\chi}_{n-1} \\ \frac{\Delta\boldsymbol{\varepsilon}_n}{\|\Delta\boldsymbol{\varepsilon}_n\|} \end{pmatrix}. \tag{5.5}$$

The internal layers are defined through two parallel processes: linear transformations followed by hyperbolic tangent activations. The outputs of these processes are then combined using elementwise multiplication, as expressed by:

$$\boldsymbol{l}_i = \tanh(\mathbf{W}_{a,i}\boldsymbol{l}_{i-1} + \mathbf{b}_{a,i}) \odot \tanh(\mathbf{W}_{b,i}\boldsymbol{l}_{i-1} + \mathbf{b}_{b,i}), \tag{5.6}$$

for $i = 1, \ldots, D$. From the last hidden layer $\boldsymbol{l}_D$, two update vectors, $\boldsymbol{\alpha}$ and $\boldsymbol{\beta}$, are defined as follows:

$$\boldsymbol{\alpha} = \exp(\mathbf{W}_{\alpha}\boldsymbol{l}_D + \mathbf{b}_{\alpha}), \tag{5.7}$$

$$\boldsymbol{\beta} = \tanh(\mathbf{W}_{\beta}\boldsymbol{l}_D + \mathbf{b}_{\beta}). \tag{5.8}$$

These two vectors define the trajectory in state-space: $\boldsymbol{\alpha}$ governs the update velocity, while $\boldsymbol{\beta}$ determines the long-term target in state-space. The updated memory state, $\boldsymbol{\chi}_n$, is then calculated using the following update rule:

$$\boldsymbol{\chi}_n = \exp(-\|\Delta\boldsymbol{\varepsilon}_n\|\boldsymbol{\alpha}) \odot (\boldsymbol{\chi}_{n-1} - \boldsymbol{\beta}) + \boldsymbol{\beta}. \tag{5.9}$$

The stress output at time t_n is a linear transformation of the memory state $\boldsymbol{\chi}_n$, expressed as:

$$\boldsymbol{\sigma}_n = \mathbf{W}_{\text{out}}\boldsymbol{\chi}_n. \tag{5.10}$$

In total, the model includes nine groups of trainable parameters, corresponding to the weights and biases of the various layers in the network:

$$\{\boldsymbol{W}_{a,i}, \boldsymbol{b}_{a,i}, \boldsymbol{W}_{b,i}, \boldsymbol{b}_{b,i}, \boldsymbol{W}_{\alpha}, \boldsymbol{b}_{\alpha}, \boldsymbol{W}_{\beta}, \boldsymbol{b}_{\beta}, \boldsymbol{W}_{\text{out}}\}$$

The structure of the LMSC model is defined by a set of architectural hyperparameters, which are fixed prior to training. These include the number of internal state variables n_s, which determines the size of the memory state vector $\boldsymbol{\chi}_n$, the number of hidden layers d used in each of the two parallel branches and the layer width w, corresponding to the number of neurons per hidden layer. These hyperparameters control the model's complexity and represent a trade-off between learning capacity and computational efficiency.

5.2 Data Generation

The dataset used to train and evaluate the surrogate LMSC model is entirely synthetic, generated through controlled finite-element simulations. To construct the dataset a series of finite element simulations is performed using the DP780 advanced high-strength steel. A single-element model with reduced integration (S4R) is used to impose a variety of strain paths under controlled conditions. The simulations are carried out using the *Abaqus/Standard* solver and the stress-strain responses are obtained via a user-defined material subroutine (UMAT) [289] implementing

the YLD2000-2d yield criterion combined with the homogeneous anisotropic hardening model. The material parameters used in the UMAT implementation of the YLD2000-2d and HAH models are listed in Table 4.2 and Table 4.5, respectively.

To build a dataset that accurately reflects the anisotropic and path-dependent plastic behavior of the material, a variety of physically meaningful strain paths is generated. To this end, two types of strain paths are considered, following the work of Bonatti et al. [185]:

- **Random walk paths**, composed of piecewise-linear segments with abrupt changes in direction;
- **Smooth walk paths**, defined by continuously varying strain directions.

All strain paths are defined in a two-dimensional strain space and are expressed in terms of three components: the normal strains ε_{xx}, ε_{yy} and the shear strain ε_{xy}. Throughout this chapter, the strain components are consistently color-coded for clarity: black is used for ε_{xx}, blue for ε_{yy} and red for ε_{xy}. The strain histories are imposed directly on the finite element model by prescribing their evolution over time. The corresponding stress and strain values are extracted at each increment and organized into input-output sequences for supervised training of the neural network. To ensure balanced learning across all output components, the stress values are normalized using the scale factors $s_1 = 1530.09$, $s_2 = 605.96$ and $s_3 = 239.25$, as defined in Equation 5.4. This normalization ensures that each stress component contributes equally to the loss function, regardless of differences in magnitude or units.

5.2.1 Random Walks

For the random walks, as represented in Figure 5.2, the strain path used for dataset construction is defined as the sum of a piecewise-linear main path and a superimposed random perturbation:

$$\boldsymbol{\varepsilon}_{\mathrm{RW}}(s) = \boldsymbol{\varepsilon}_m(s) + \boldsymbol{\varepsilon}_r(s), \tag{5.11}$$

where $s \in [0, 1]$ is a normalized parameter describing the progression along the strain path. The main path, $\boldsymbol{\varepsilon}_m(s)$, starts at the origin, $\hat{\varepsilon}_0 = 0$ and proceeds through a sequence of randomly sampled "corner" points $\hat{\varepsilon}_i$, drawn uniformly from a ball of radius $R = 0.3$ in the three-dimensional strain space:

$$\hat{\boldsymbol{\varepsilon}}_i \sim \mathcal{U}(\mathbb{B}_3(0.3)), \quad \text{for } i \geq 1 \tag{5.12}$$

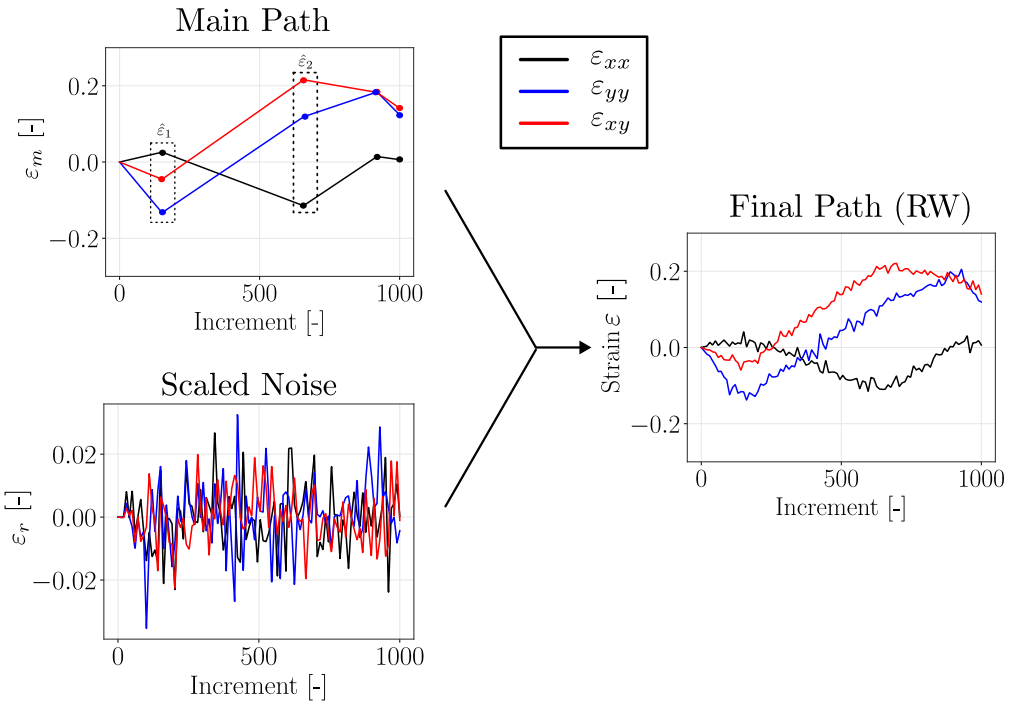


Figure 5.2: Random walk strain path generated by adding scaled noise to a piecewise-linear main path.

Each segment connecting two consecutive corner points $(\hat{\boldsymbol{\varepsilon}}_{i-1}, \hat{\boldsymbol{\varepsilon}}_i)$ is subdivided into n_i steps based on the local step size ℓ_i, sampled from a log-uniform distribution:

$$\ell_i \sim \text{LogUniform}(0.005,\ 0.01) \tag{5.13}$$

$$n_i = \left\lfloor \frac{\|\hat{\varepsilon}_i - \hat{\varepsilon}_{i-1}\|}{\ell_i} \right\rfloor \tag{5.14}$$

To introduce local variability, random noise is added to each substep. The perturbation at substep (i, j) is defined as:

$$\boldsymbol{\varepsilon}_r^{(i,j)} = \ell_i \cdot m_{i,j} \cdot \boldsymbol{v}_{i,j} \tag{5.15}$$

where

$$m_{i,j} \sim \mathcal{U}(0, 1) \tag{5.16}$$

$$\boldsymbol{v}_{i,j} \sim \mathcal{U}(\mathbb{B}_3(\rho)), \quad \rho = 2.0 \tag{5.17}$$

The final strain value at each substep is given by:

$$\boldsymbol{\varepsilon}_{\text{RW}}^{(i,j)} = \boldsymbol{\varepsilon}_m^{(i,j)} + \boldsymbol{\varepsilon}_r^{(i,j)} \tag{5.18}$$

The path generation process terminates when a fixed total number of points is reached (e.g., $N = 100$) or when the number of corner points exceeds a predefined

maximum (e.g., 50). To obtain a consistent time discretization, the resulting path is resampled over a uniform time grid using linear interpolation, typically to 1000 points:

$$s_k = \frac{k}{N-1}, \quad k = 0, \ldots, N-1 \tag{5.19}$$

$$\boldsymbol{\varepsilon}_{\mathrm{RW}}(s_k) \approx \mathrm{Interp}\left(\left\{\boldsymbol{\varepsilon}_{\mathrm{RW}}^{(i,j)}\right\}, s_k\right) \tag{5.20}$$

Figure 5.3 presents an example of a single random walk simulation, showing the evolution of the strain components (ε_{xx}, ε_{yy}, ε_{xy}) and the corresponding stress response (σ_{xx}, σ_{yy}, σ_{xy}). For the same case, Figure 5.4 shows the processed data used for model training, including the original strain history and stress outputs, as well as the derived inputs (strain increments) and normalized outputs required by the LMSC architecture.

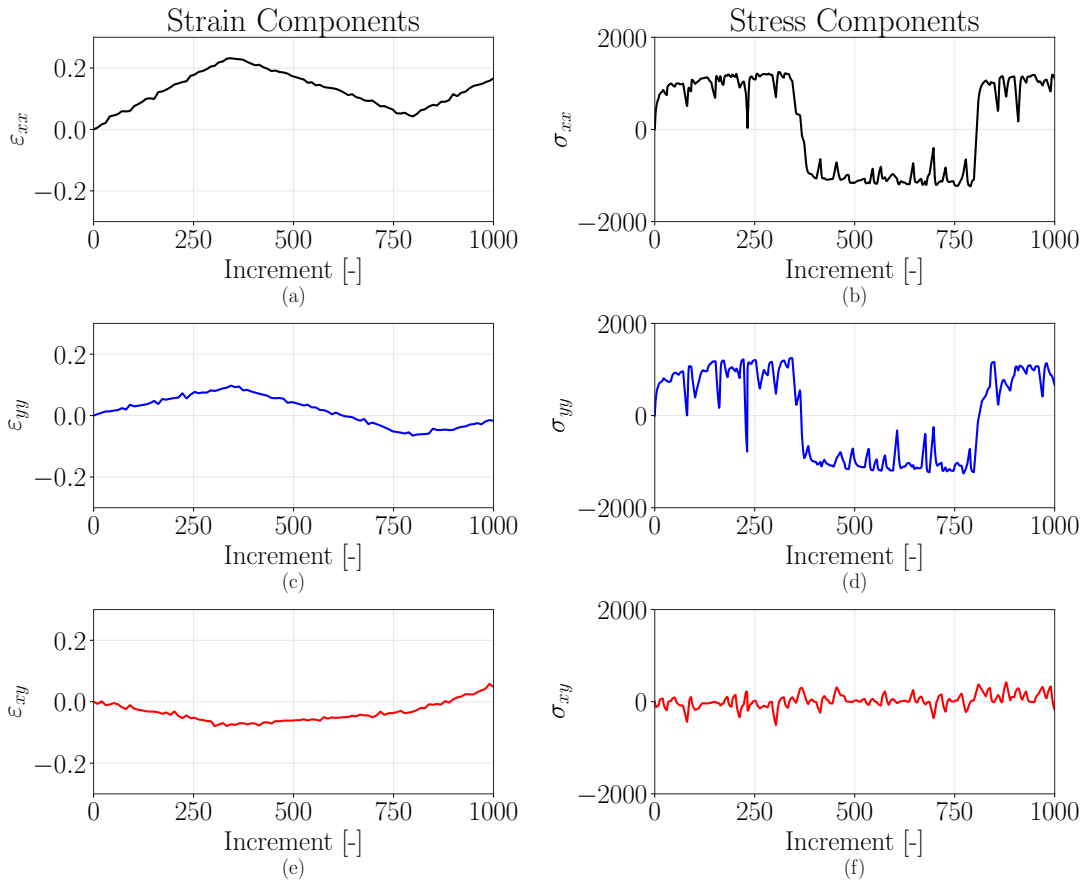


Figure 5.3: Stress and strain components over time for a single random walk simulation; (a,c,e): strain components ε_{xx}, ε_{yy}, ε_{xy}; (b,d,f): corresponding stress components σ_{xx}, σ_{yy}, σ_{xy}.

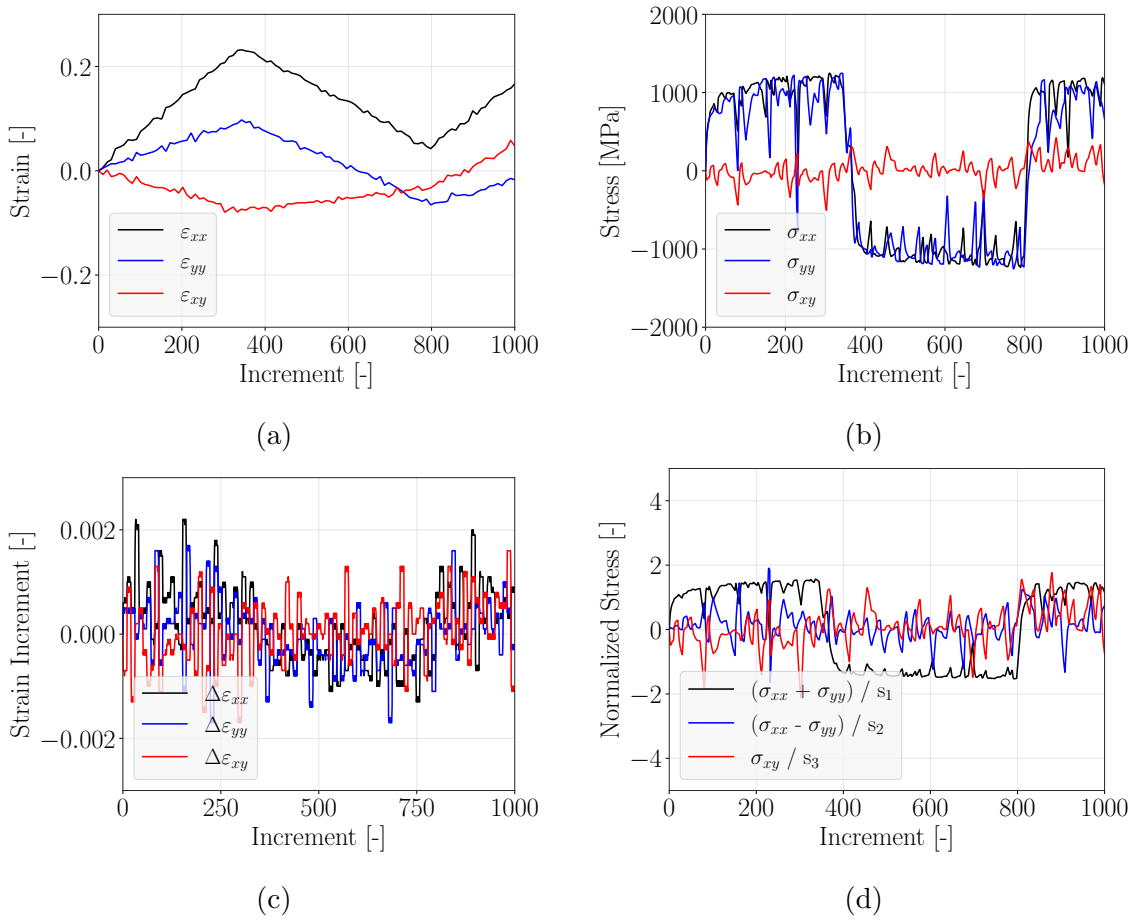


Figure 5.4: Processed input-output data used for model training. (a) strain history; (b) raw stress outputs; (c) strain increments $\Delta\varepsilon$; (d) normalized stress outputs used for LMSC training.

5.2.2 Smooth Walks

Smooth strain paths are constructed to simulate continuous loading conditions. For each path, a target arc length ℓ is sampled from a uniform distribution:

$$\ell \sim \mathcal{U}(0.1,\ 1.0) \tag{5.21}$$

The path generation starts at the origin with

$$\hat{\varepsilon}_0 = 0, \quad t_0 = 0 \tag{5.22}$$

While the total time remains below unity ($t_i < 1$), new strain points $\hat{\varepsilon}_i$ are sampled uniformly from a ball of radius 0.3 in three-dimensional strain space:

$$\hat{\boldsymbol{\varepsilon}}_i \sim \mathcal{U}(\mathbb{B}_3(0.3)) \tag{5.23}$$

The corresponding time values are computed as:

$$t_i = t_{i-1} + \frac{\|\hat{\boldsymbol{\varepsilon}}_i - \hat{\boldsymbol{\varepsilon}}_{i-1}\|}{\ell} \tag{5.24}$$

The process is repeated until $t_i > 1$, at which point a component-wise cubic spline interpolation is applied over the sequence $\{(t_i, \hat{\varepsilon}_i)\}$ to obtain a smooth strain trajectory. The final path is then resampled uniformly over 1001 time steps:

$$s_k = \frac{k}{1000}, \quad k = 0, \ldots, 1000 \tag{5.25}$$

$$\boldsymbol{\varepsilon}(s_k) = \text{Interp}\left(\{(t_i, \hat{\boldsymbol{\varepsilon}}_i)\}, \boldsymbol{s}_k\right) \tag{5.26}$$

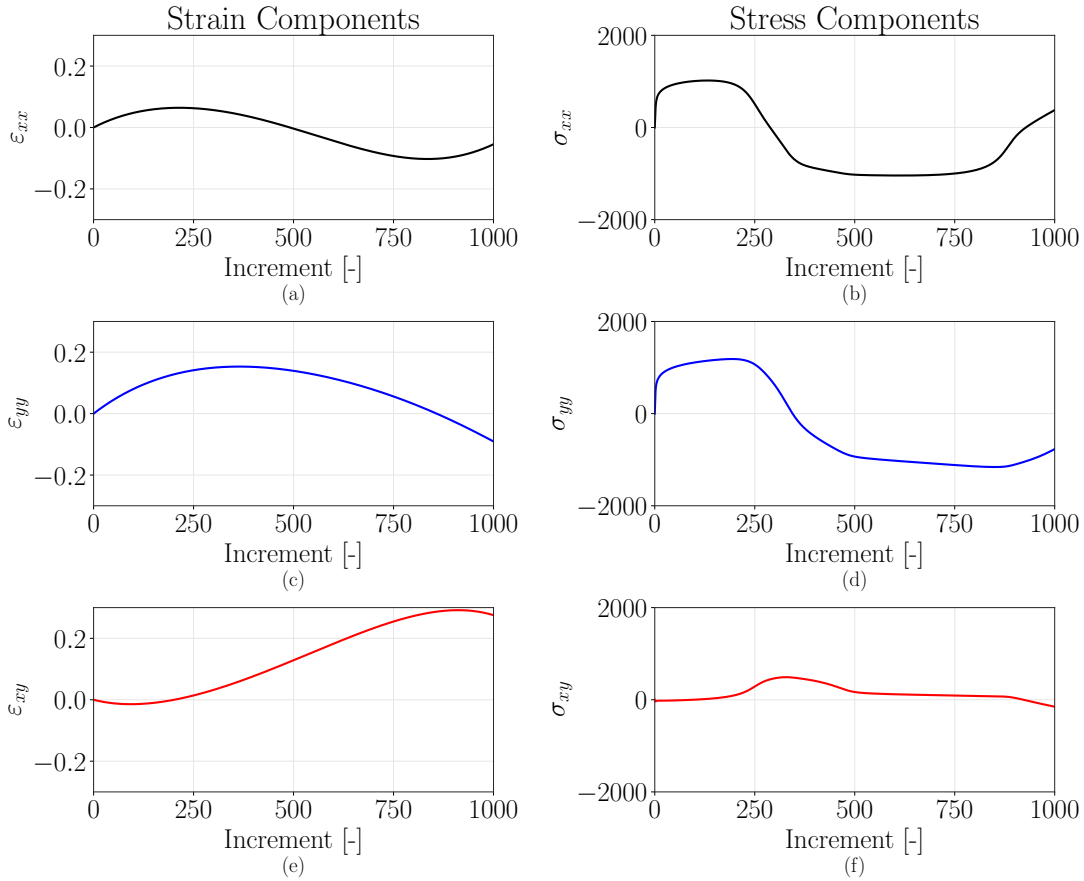


Figure 5.5: Strain and stress components along a smooth path; left plots: ε_{xx}, ε_{yy}, ε_{xy}; right plots: σ_{xx}, σ_{yy}, σ_{xy}.

Figure 5.5 presents an example of a single smooth walk simulation, showing the evolution of the strain components (ε_{xx}, ε_{yy}, ε_{xy}) and the corresponding stress response (σ_{xx}, σ_{yy}, σ_{xy}). For the same smooth case, Figure 5.6 shows the processed data used for model training, including the original strain history and stress outputs, as well as the derived inputs (strain increments) and normalized outputs.

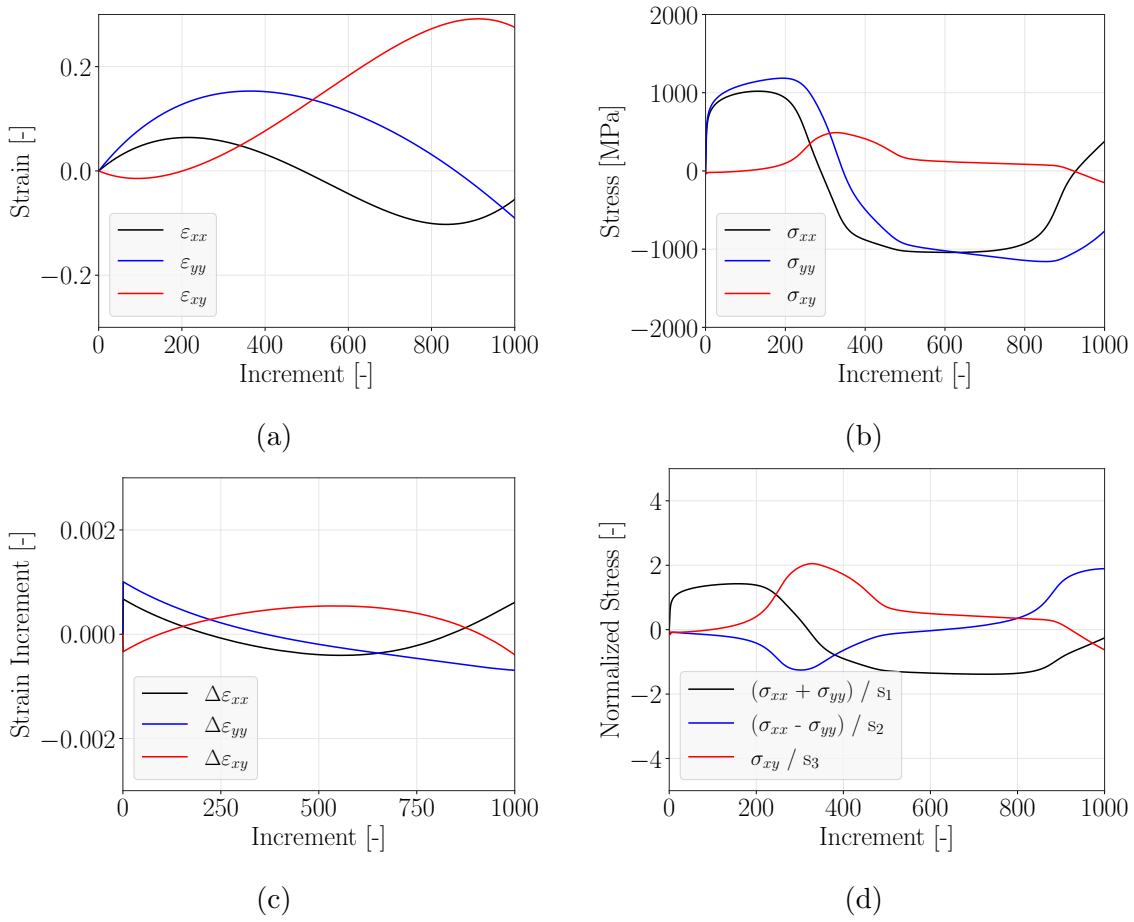
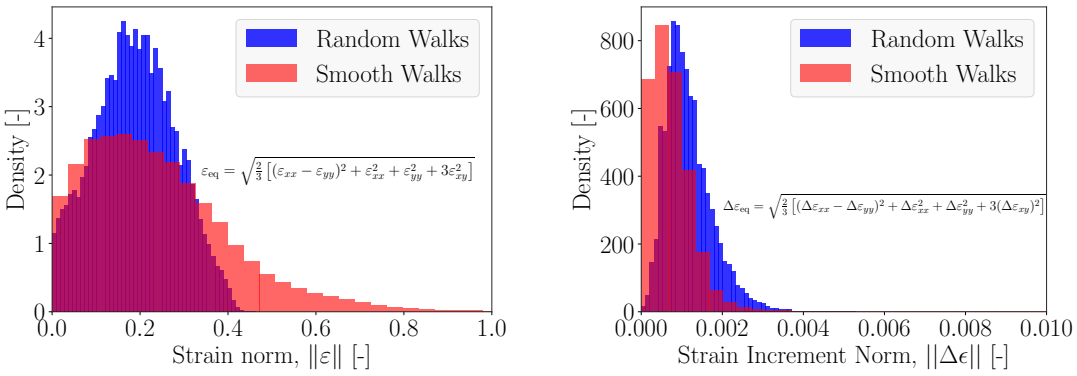


Figure 5.6: Smooth path data used for model training: (a) strain history, (b) stress response, (c) strain increments, (d) normalized outputs.

A total of 4822 random walk cases and 2493 smooth path cases were considered. Figure 5.7 shows a statistical comparison of the strain path characteristics for random and smooth paths. Figure 5.7a shows the distribution of the total strain norm $\|\boldsymbol{\varepsilon}\|$, while Figure 5.7b presents the distribution of the strain increment norm $\|\Delta\boldsymbol{\varepsilon}\|$. Smooth paths reach higher total strain values, with a broader distribution and heavier tail, whereas random walks are more concentrated at lower norms. In contrast, random walks exhibit significantly larger and more scattered strain increments, consistent with their irregular nature. These patterns reflect the expected

behavior of smooth versus random trajectories in deformation space.



(a) (b)

Figure 5.7: Comparison of strain path characteristics between random and smooth paths: (a) strain norm, (b) strain increment norm.

5.2.3 Dataset Division

The complete dataset, which includes random and smooth paths, is divided into three subsets: training, validation and test. The split follows a 70/15/15 ratio and is applied uniformly across both types of paths to ensure diversity and balance in all subsets. Out of the total 4822 random walk cases and 2493 smooth walk cases, 70% are used for training, while the remaining 30% is equally divided between validation and test sets. This results in 5120 training cases (3375 random and 1745 smooth paths), 1096 validation cases (723 random and 373 smooth paths) and 1099 test cases (724 random and 375 smooth paths).

In addition to the three main subsets, an extra dataset comprising 20 loading paths is used to evaluate the generalization capability of the trained models. These 20 loading paths correspond to the same strain trajectories tested experimentally in Chapter 3 and are therefore used to verify whether the LMSC-based model can accurately reproduce anisotropic hardening and path-dependent behavior. They are excluded from both the training and hyperparameter optimization processes and are used only for the physical validation of the surrogate model. The extra dataset includes monotonic uniaxial tension tests in the rolling direction and transverse direction, as well as biaxial tension and monotonic shear cases. It also contains tension-compression tests and reverse shear tests. For the reversal loading cases, three levels of pre-strain were considered. In the uniaxial tension-compression tests,

reversals occur after reaching plastic strain levels of $\varepsilon^*_{xx} \approx 0.025$, 0.050 and 0.075. For reverse shear tests, reversals are applied at shear strain levels of $\varepsilon^*_{xy} \approx 0.1$, 0.2 and 0.3. The full evolution of these strain paths and their corresponding stress responses is provided in Appendix D.

5.3 Training Methodology

5.3.1 Training Strategy

The training of LMSC models was carried out using a progressive learning approach, in which the strain increment size is gradually reduced over successive training phases. This strategy facilitates the learning of long-term dependencies while improving numerical stability, particularly in the initial stages of training. According to Bonatti et al. [185], progressive learning significantly enhances training efficiency compared to direct learning strategies, where the model is exposed from the outset to finely resolved loading sequences. In contrast, the progressive method allows the network to first learn the coarse structure of the stress response before dealing with fine-scale variations, leading to faster convergence and more stable optimization.

In this work, training was performed over a total of 1000 epochs, divided into five phases of 200 epochs each, with progressively smaller strain increments (corresponding to sampling periods of 16, 8, 4, 2 and 1). The LMSC models were trained using the *Adam* optimizer. The initial learning rate was set to 1×10^{-2} and a gradient clipping threshold of 10^{-3} was applied to prevent gradient explosion and improve training stability. A batch size of 128 was used throughout all training phases. To further stabilize and accelerate convergence, a custom learning rate scheduler was employed, progressively reducing the learning rate over epochs following a power decay schedule, with a lower bound of 1×10^{-6}. Model checkpoints and training logs were recorded at each epoch and additional callbacks were used to reload weights with adjusted optimizer states in case of stagnation, ensuring robust learning throughout the progressive training process.

To explore the influence of model architecture on performance, a systematic study was conducted by varying three key hyperparameters: the number of internal state variables, n_s, the number of hidden layers, d and the number of neurons per layer, w. The internal state size, n_s, which defines the dimensionality of the memory vector $\boldsymbol{\chi}_n$, was varied between 5 and 80. The number of hidden layers d in each of the two parallel branches ranged from 1 to 4, while the width w, representing the

number of neurons per hidden layer, was varied from 10 to 100. These architectural choices govern the model's capacity to represent the path-dependent behavior of the material and their effects are analyzed in the following section.

5.3.2 Models Performance

The performance of the LMSC model is evaluated based on its ability to accurately reproduce the stress response of the reference material model under both random and smooth strain path conditions. To explore the impact of architectural complexity on predictive accuracy, a comprehensive hyperparameter search was conducted, considering variations in the number of internal state variables (n_s), the number of hidden layers (d) and the layer width (w). To account for differences in data complexity, the analysis is performed separately for random walk (RW) and smooth walk (SW) trajectories. As shown in Figure 5.8, the mean squared error is computed on the training, validation and test datasets for all model configurations. This metric provides a global assessment of both the model's ability to learn from data and its generalization capability to unseen strain paths. Each subplot in Figure 5.8 presents the variation of the MSE as a function of the total number of trainable parameters in the model, for different values of the internal state size n_s. The x-axis, shown on a logarithmic scale, represents the number of trainable parameters in each LMSC configuration. This number increases with the depth (d) and width (w) of the internal network layers. The y-axis shows the corresponding MSE, also in logarithmic scale, computed for training, validation and test datasets.

A consistent trend is observed across all subplots: increasing the model complexity leads to a systematic reduction in MSE. This effect is particularly evident for the training dataset, as represented in Figure 5.8a-b where larger models show clear improvements in fitting both the RW and SW training data. Both RW and SW cases exhibit similar training errors for a given set of hyperparameters, with MSE decreasing for both as model capacity grows. However, the generalization behavior differs between the two datasets, as represented in Figure 5.8c-d for the validation dataset and Figure 5.8e-f for the test dataset. For RW data, validation and test errors consistently decrease with model size, indicating that additional capacity improves generalization. Signs of overfitting only become apparent for models with a number of parameter close to 10^5, where the error on the validation and test sets stop decreasing compared to the training error. In contrast, for SW data, validation and test errors remain relatively constant across all configurations, showing

no benefit from increased complexity. Signs of overfitting appear earlier than in RW, becoming noticeable for models with approximately 10^4 trainable parameters. Additionally, models trained on RW data consistently achieve lower validation and test errors than their SW counterparts. Although the training MSE are comparable, the smooth walk paths appear to be more difficult to generalize. This becomes clear when examining the loss curves presented in Appendix E. Figure E.1a shows the training and validation loss curves for a model trained exclusively on RW data. Both loss curves gradually decrease across the five progressive learning phases, indicating continuous generalization improvement. In contrast, Figure E.1b shows the corresponding curves for a model trained using only SW data. In this case, the training loss decreases rapidly to values much lower than those in the RW case. However, despite ongoing reductions in training loss, the validation loss stops improving after just a few epochs. This behavior suggests that while the network can fit smooth trajectories with low training error, its ability to generalize quickly saturates. Furthermore, progressive learning offers no additional benefit: the model captures the coarser discretizations in the early phases and further refining the sampling resolution does not lower the validation loss. This suggests that increasing network complexity does not equally improve performance for both data types. For smooth-walk trajectories, a simple model achieves very low training error and adding more capacity results in only marginal improvements on the validation set. In contrast, random-walk data continuously benefit from larger models because their irregular features require greater representational capacity to reduce training and validation loss.

Among the different configurations, models with $n_s = 20$ and $n_s = 40$ tend to achieve the best trade-off between performance and model size, consistently yielding low MSE values across all datasets. Increasing the state dimension beyond $n_s = 40$ does not lead to noticeable improvements. In contrast, models with a small state size ($n_s = 5$) exhibit significantly higher errors, particularly on the test set, suggesting limited capacity to capture history-dependent behavior.

To further evaluate the influence of architectural hyperparameters, Figure 5.9 shows surface plots of the MSE, as a function of the internal layer width (w) and network depth (d) for two representative values of memory sizes: $n_s = 20$ and $n_s = 40$. Unlike the broader MSE analysis in Figure 5.8, which includes training, validation and test sets, this analysis focuses exclusively on test performance in order to evaluate the model's generalization ability.

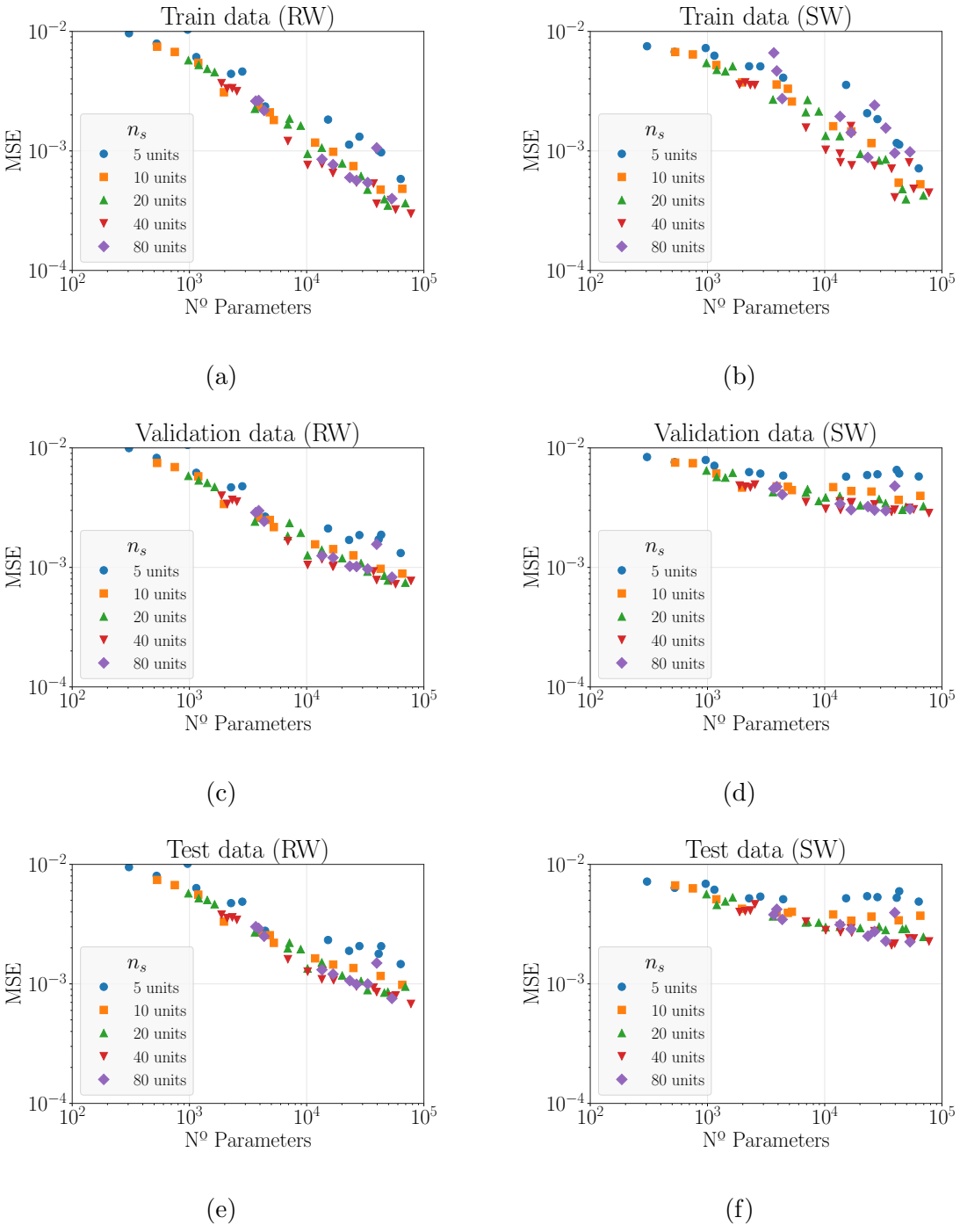


Figure 5.8: Test, validation and training MSE as a function of the total number of trainable parameters for different memory sizes n_s; left plots: random walks (RW); right plots: smooth walks (SW).

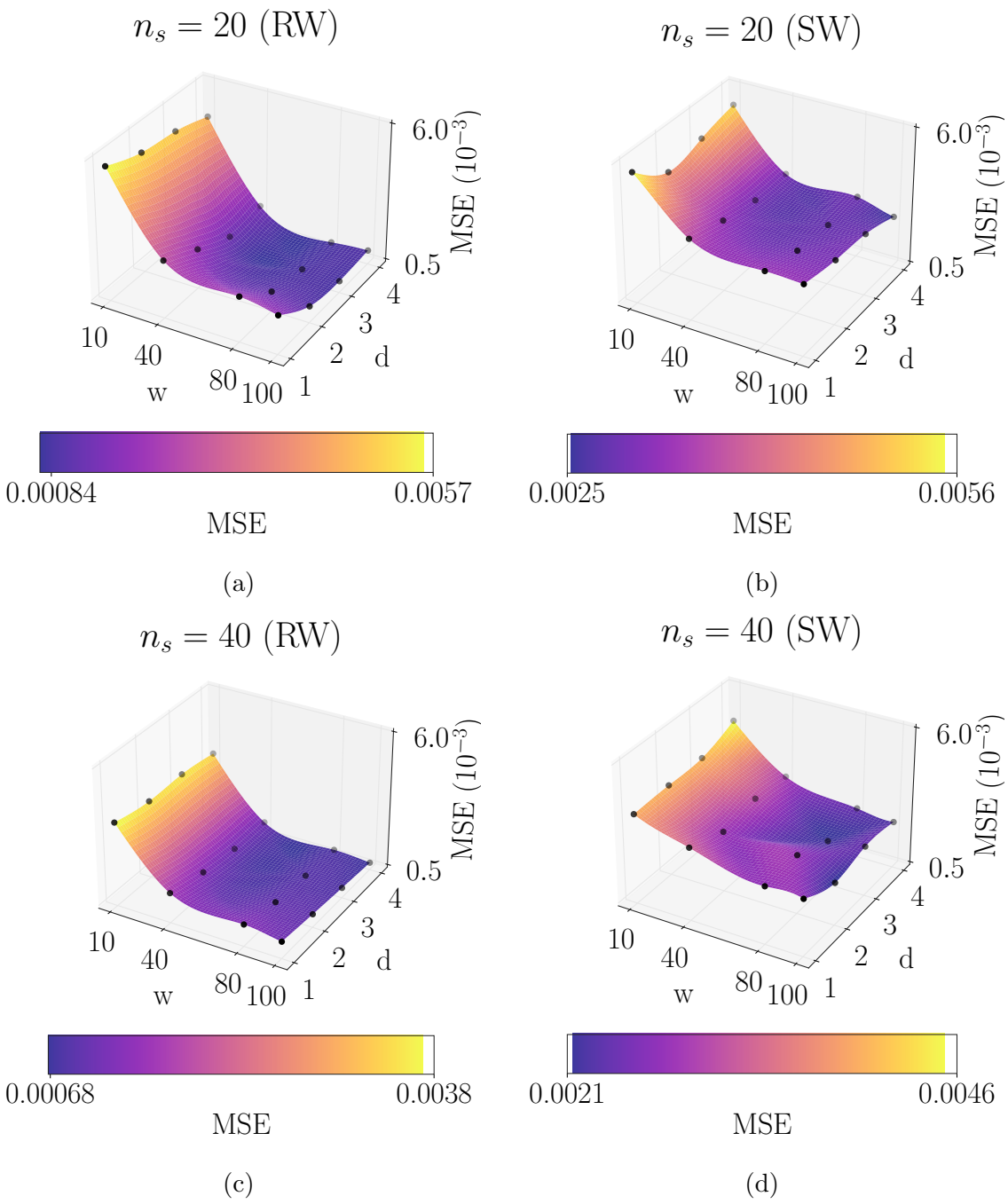


Figure 5.9: Test set MSE as a function of network depth d and width w, for memory sizes $n_s = 20$ (top) and $n_s = 40$ (bottom); left plots: random walks; right plots: smooth walks.

The results confirm the trends previously observed. In general, the test error decreases as model capacity increases. However, the reduction in MSE is more sensitive to changes in the layer width than to network depth. This effect is particularly pronounced for random walk data, where increasing w leads to clear and consistent

improvements across both memory sizes. For smooth paths, the influence of w is also present but less dominant and increasing d provides some additional benefits, especially at smaller widths. Overall, models with a larger memory size, $n_s = 40$, achieve lower test errors than those with $n_s = 20$, confirming the advantage of a more expressive internal state. These findings suggest that while both architectural dimensions contribute to model performance, the layer width plays a more significant role, particularly for capturing the variability present in irregular strain paths such as random walks.

To complete the analysis of the influence of architectural hyperparameters on generalization, Figure 5.10 shows the absolute error boxplots, considering normalized values, for different architectural configurations, considering memory sizes $n_s = 20$ and $n_s = 40$. For the layer width w and depth d, only the extreme values were selected, specifically, $d = 1$, $d = 4$, $w = 10$ and $w = 100$, in order to highlight the impact of minimal and maximal architectural complexity. As expected, models with greater capacity generally exhibit more compact error distributions, indicating improved prediction performance. In every subplot, increasing the layer width from $w = 10$ to $w = 100$ yields a tighter error distribution and a lower median error. In contrast, increasing the depth from $d = 1$ to $d = 4$ produces relatively smaller gains. This trend holds for both random walks, Figures 5.10a,c and smooth walks, Figures 5.10b,d and for both memory sizes.

In addition to the trends seen in the boxplots, Table 5.1 quantifies key error metrics for four representative LMSC architectures with $n_s = 40$. As shown in the table, the model u40_d4_w100 (deepest and widest) achieves the lowest test MSE for both random walks (0.0007) and smooth walks (0.0023). Across all configurations, the percentage of outliers remains below 12%, indicating that cases with large errors are relatively insensitive to network size. Similarly, the maximum absolute error only varies slightly, between 3.73 and 3.87 for random walks and between 4.25 and 4.51 for smooth walks. These results suggest that wider and deeper networks improve overall performance but do not eliminate the most challenging edge cases. The impact of error magnitudes on these cases will be analyzed in the following section.

Table 5.1: Test MSE, outlier percentage and maximum error for models with $n_s = 40$, comparing random walk (RW) and smooth walk (SW) data across different network depths and widths.

Model	Random Walks (RW)			Smooth Walks (SW)		
	MSE [-]	Outlier [%]	Max Error [-]	MSE [-]	Outlier [%]	Max Error [-]
u40_d1_w10	0.0038	5.2	3.73	0.0040	7.2	4.51
u40_d4_w10	0.0034	5.0	3.74	0.0046	8.1	4.45
u40_d1_w100	0.0011	5.5	3.79	0.0027	10.7	4.25
u40_d4_w100	0.0007	5.4	3.87	0.0023	11.5	4.44

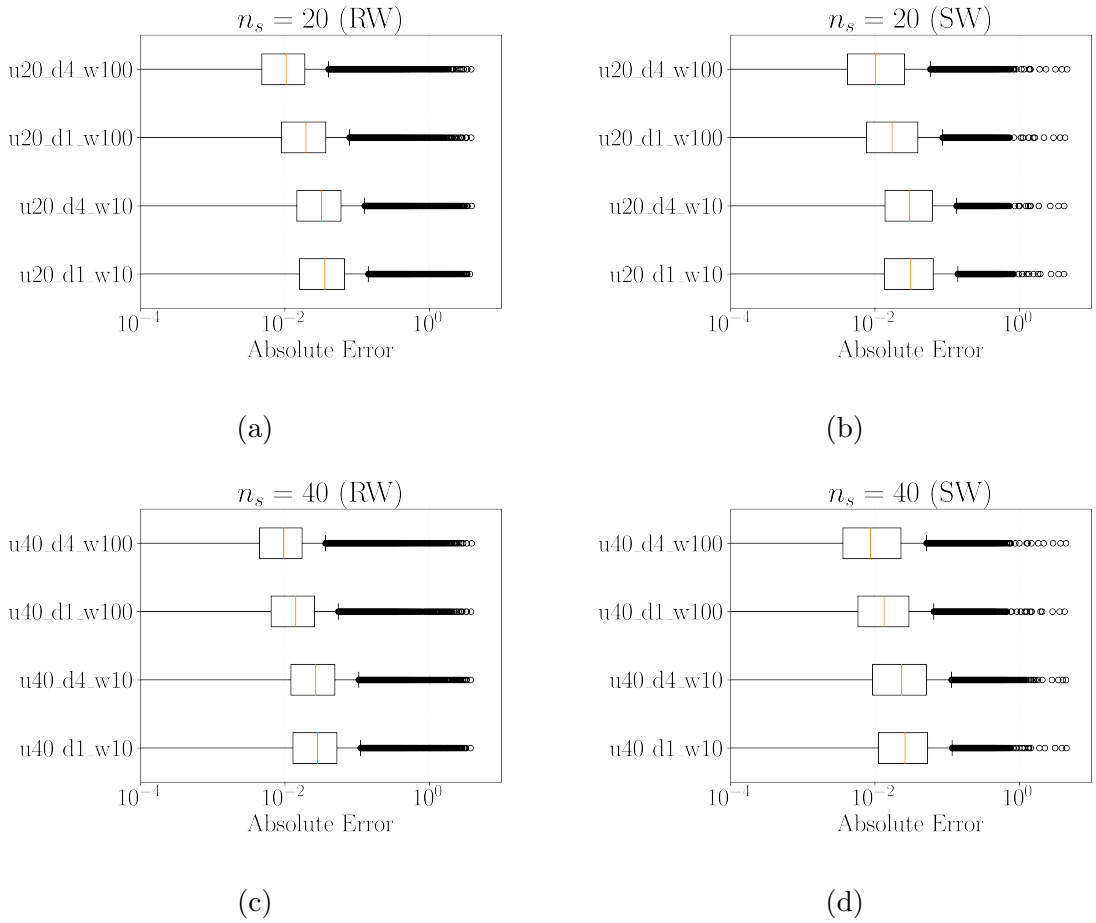


Figure 5.10: Distribution of absolute errors on the test dataset for selected LMSC architectures with $n_s = 20$ (top) and $n_s = 40$ (bottom); left plots: random walks; right plots: smooth walks.

5.4 Results

This section presents a detailed evaluation of the trained LMSC model with architecture $n_s = 40$, $d = 4$ and $w = 100$, chosen based on the hyperparameter study. The analysis that follows assesses prediction performance and error metrics on loading conditions loading conditions that were not seen during the training process. All results refer to denormalized stress outputs obtained on the test dataset, which includes both random-walk and smooth-walk strain paths.

To evaluate the stability of the training process and the sensitivity of the model to stochastic variation, the same model architecture was trained three times using different random seeds. In this context, each seed determines the initial point of random number generation, which affects the initial weight values. Figure 5.11 shows the evolution of the training and validation MSE across epochs for each run. Despite minor fluctuations in the early stages, all three runs converge towards similar loss values, demonstrating the robustness of the training strategy and the absence of significant sensitivity to random initialization.

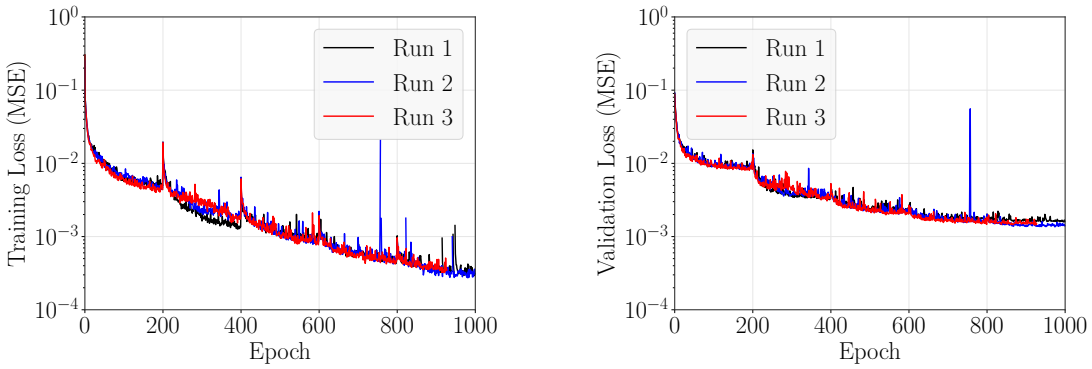


Figure 5.11: Evolution of: (a) training and (b) validation loss across three independent training runs with different random seeds for the u40_d4_w100 model.

Figure 5.12 show the distribution of the absolute (Figure 5.12a,b) and relative errors (Figure 5.12c,d) for the predictions of each stress component in the test dataset for random and smooth walks, respectively. The distributions are strongly right-skewed for both the RW and SW cases, with a small number of large outliers extending into higher error regions. This is particularly evident in the relative error plots, where most predictions remain below 10% error, though outliers occasionally exceed 100%. These large relative errors typically correspond to stress values close to

zero in the reference data, where even small absolute deviations can produce disproportionately high relative percentages. Across all components, σ_{xx} and σ_{yy} exhibit similar error profiles. Although σ_{xy} generally shows lower absolute errors, its relative error tends to be of the same order of magnitude as the other two components and in some cas even slightly higher. This is primarily due to the lower magnitude of σ_{xy} values in the dataset, which amplifies the impact of absolute deviations when computing relative errors.

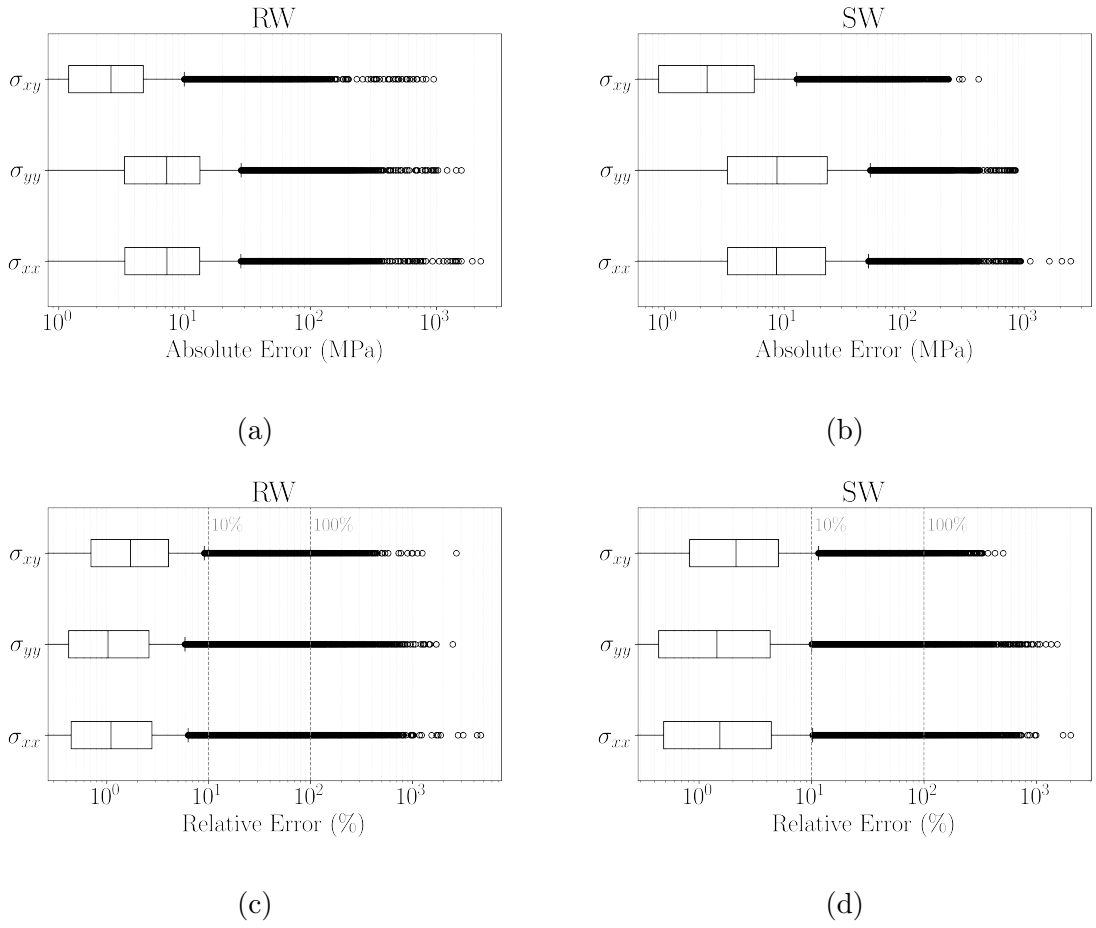


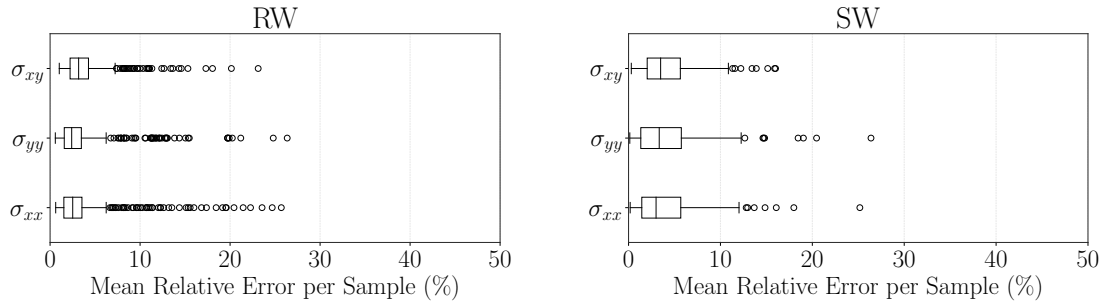
Figure 5.12: Distribution of absolute (top) and relative (bottom) errors for each stress component in the test set; left plots: random walks; right plot: smooth walks; (Relative Error (%) $= |\sigma_{\text{pred}} - \sigma_{\text{true}}| / \sigma_{\text{true}} \times 100$).

To evaluate the model´s predictions more effectively across entire strain sequences, Figure 5.13 shows the distribution of mean relative error per sample, calculated for each stress component separately. This metric captures how accurately the model reproduces the full stress response over time for individual trajectories, providing a complement to the previous pointwise error analysis. For each path in

the test dataset, the mean relative error is determined by averaging the relative error over all increments:

$$\text{Mean Relative Error (MRE)} = \frac{1}{T}\sum_{t=1}^{T}\frac{|\hat{\sigma}_t - \sigma_t|}{|\sigma_t|} \times 100\% \tag{5.27}$$

where $\hat{\sigma}_t$ and σ_t are the predicted and true stress values at increment t, respectively. In this case, each test sequence contains $T = 1000$ increments. Results are shown for both random walk and smooth walk on Figure 5.13a and b, respectively. Overall, the maximum mean relative errors, excluding outliers, remain relatively low for both types of loading path. For random walks (RW), these values range from 6% to 7%, while for smooth walks (SW) they range from 11% to 12%. For both cases, these limits cover approximately 90% of the test dataset, indicating that the model delivers accurate predictions for the vast majority of test cases. When examining the outliers, defined as samples with a mean relative error exceeding $Q_3 + 1.5 \cdot \text{IQR}$, a clear difference emerges between the two loading types. For RW, about 50 samples (around 5-7% of the cases) fall into this category. In these cases, the mean error can reach values up to 25%, reflecting isolated but significant deviations. In contrast, the number of outliers for SW is much lower, with only around 10 samples, corresponding to approximately 2% of the dataset. Nevertheless, the maximum error in these cases is also about 25%, similar to that observed in the RW case.

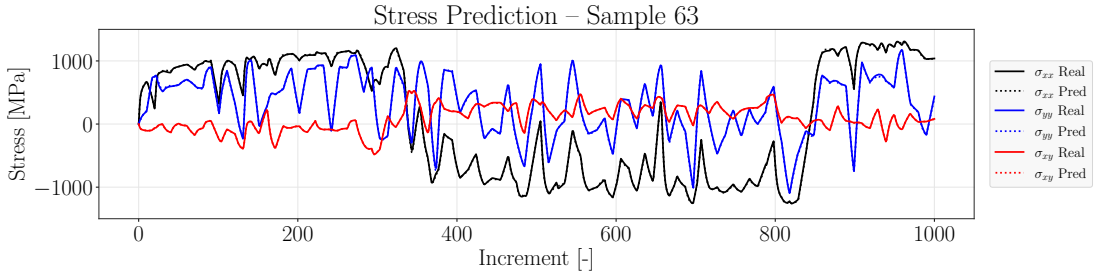


(a) (b)

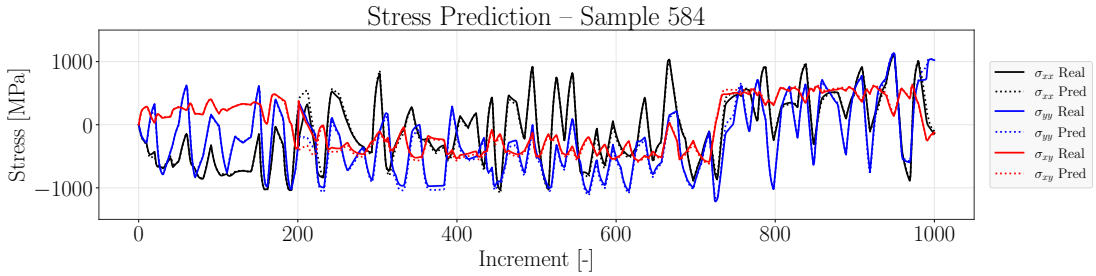
Figure 5.13: Boxplots of mean relative error per test sample for each stress component for (a) random walks and (b) smooth walks.

To further illustrate the model's predictive capabilities, Figure 5.14 compares the predicted and true stress histories for selected cases from the test dataset. These include both typical and worst-case scenarios, based on the mean relative error per sample. Figures 5.14a,c show representative median-error responses, corresponding

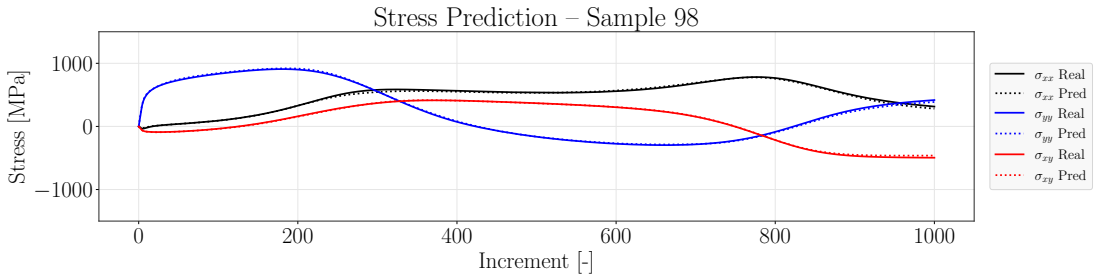
to typical prediction behavior observed across the test dataset, for RW and SW trajectories, respectively. In both cases, the model accurately reproduces the full stress response, with predictions closely matching the reference curves across all stress components. In contrast, Figures 5.14b,d present the worst-case samples for RW and SW data, corresponding to cases with the highest mean relative errors across components. Overall, even in these challenging cases, the predicted stress curves generally follow the correct trends. However, in segments with abrupt strain transitions, the model's performance tends to decrease, highlighting the increased difficulty in generalizing to such conditions.



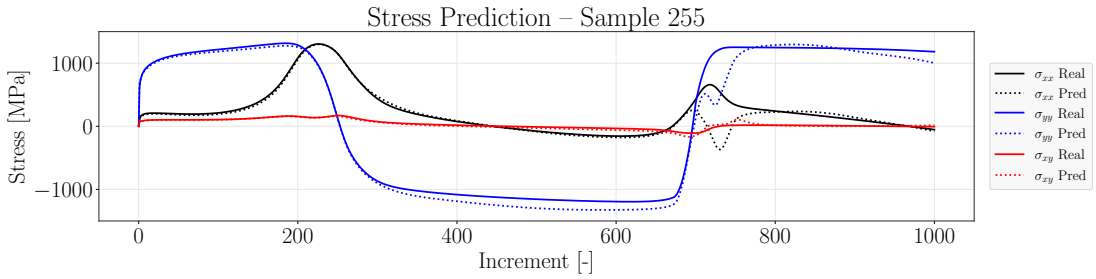
(a)



(b)



(c)



(d)

Figure 5.14: Comparison between predicted and true stress histories: (a, c) representative median-error cases for random walk (RW) and smooth walk (SW); (b, d) worst-case examples based on mean relative error for RW and SW.

5.4.1 Evaluation on Standard Experimental Loading Paths

In addition to the random and smooth strain trajectories used during training and testing, this section evaluates the predictive capabilities of the trained model on additional unseen loading cases, representative of standard experimental tests. As shown in Appendix D, these cases include monotonic and reverse loading paths, corresponding to the stablished mechanical tests for material characterization introduced in Chapter 3. The objective of this additional evaluation is to assess the model's ability to generalize to structured and interpretable loading patterns that were not explicitly included in the training set.

5.4.1.1 Monotonic Loading Cases

Figure 5.15 shows the model's performance under the four standard monotonic loading scenarios: (a) uniaxial tension in the rolling direction, (b) uniaxial tension in the transverse direction, (c) biaxial tension and (d) simple shear. The corresponding strain evolution for these cases is shown in Figure D.1 and D.2. In each figure, the predicted stress components (dotted lines) are compared to the reference values (solid lines) over the full loading history, comprising 1000 increments.

Overall, the model demonstrates strong predictive performance across all monotonic loading cases, accurately reproducing the stress evolution throughout the full deformation histories. The predicted curves show close agreement with the reference data, with only minor deviations, especially for the dominant stress components. Notably, the model captures the anisotropic behavior of the material, evident by the

distinct behavior in the rolling (Figure 5.15a) and transverse (Figure 5.15b) directions, correctly predicting a higher stress response in the TD compared to the RD. In the case of biaxial loading (Figure 5.15c), the predicted normal stresses σ_{xx} and σ_{yy} align very closely with the reference values throughout the entire loading path, while the shear stress σ_{xy} remains nearly zero as expected. Similarly, in the simple shear scenario (Figure 5.15d), the model accurately predicts the increasing shear stress σ_{xy}, while maintaining the near-zero behavior for the normal components.

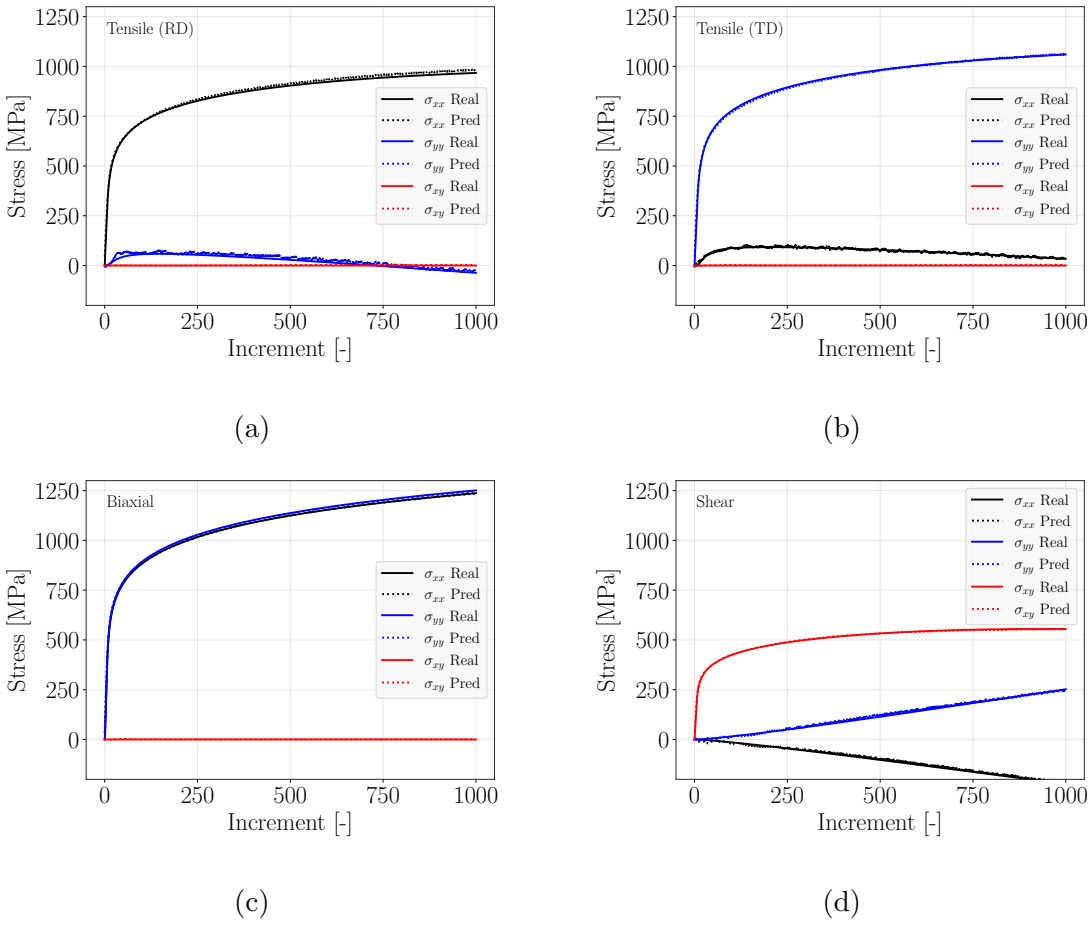


Figure 5.15: Predicted vs. reference stress responses for standard monotonic loading cases: (a) uniaxial tension in the rolling direction (RD), (b) uniaxial tension in the transverse direction (TD), (c) biaxial tension and (d) simple shear.

Over the 1000 increments, uniaxial tension in the rolling direction shows a mean relative error of 0.97% in σ_{xx}, while uniaxial tension in the transverse direction yields an MRE of 0.38% in σ_{yy}. For biaxial tension, the MREs for both σ_{xx} and σ_{yy} are 0.50% and for simple shear, the shear stress σ_{xy} reaches an MRE of 0.32%. These values demonstrate that the surrogate model reproduces each monotonic loading

path with errors in the dominant stress component below 1%. These results are in line with the performance observed in the previous section, confirming the robustness and generalization capability of the surrogate model on loading cases not seen during training.

5.4.1.2 Reverse Loading Cases

To evaluate the model's performance under strain path reversals, Figure 5.16 presents the predicted stress responses for two reverse loading scenarios: tension – compression (Figures 5.16a,c and e) and reverse shear tests (Figures 5.16b, d and f). These cases were selected to evaluate the model's ability to capture the material behavior under load reversals, including phenomena such as the Bauschinger effect. In each subfigure of Figure 5.16, the predicted stress components (dotted lines) are plotted alongside the reference values (solid lines) over the full loading sequence of 1000 increments. The corresponding strain paths for the TC and RS cases, are shown in Figures D.3 and D.4, respectively.

Overall, the model accurately reproduces the monotonic segments of the loading paths and closely matches the reference stress evolution across all components. This confirms the robustness of the model in handling unidirectional loading, as confirmed in the previous section. However, during the unloading and reverse loading phases, particularly after the strain path inversion, the predicted stresses tend to be slightly overestimated in magnitude when compared to the reference curves. This overestimation is most evident in the dominant stress components for each loading type, namely σ_{xx} for tension–compression paths and σ_{xy} for reverse shear paths. In these cases, the model typically overshoots the stress amplitude immediately after reversal and exhibits a delayed realignment with the target trajectory, suggesting difficulty in capturing the abrupt change in loading direction, as was previously observed in the analysis of Figure 5.14d. These predictive behaviors suggest that transitions to reverse loading remain challenging for the current LMSC model, possibly due to the limited presence of such cases in the original training data.

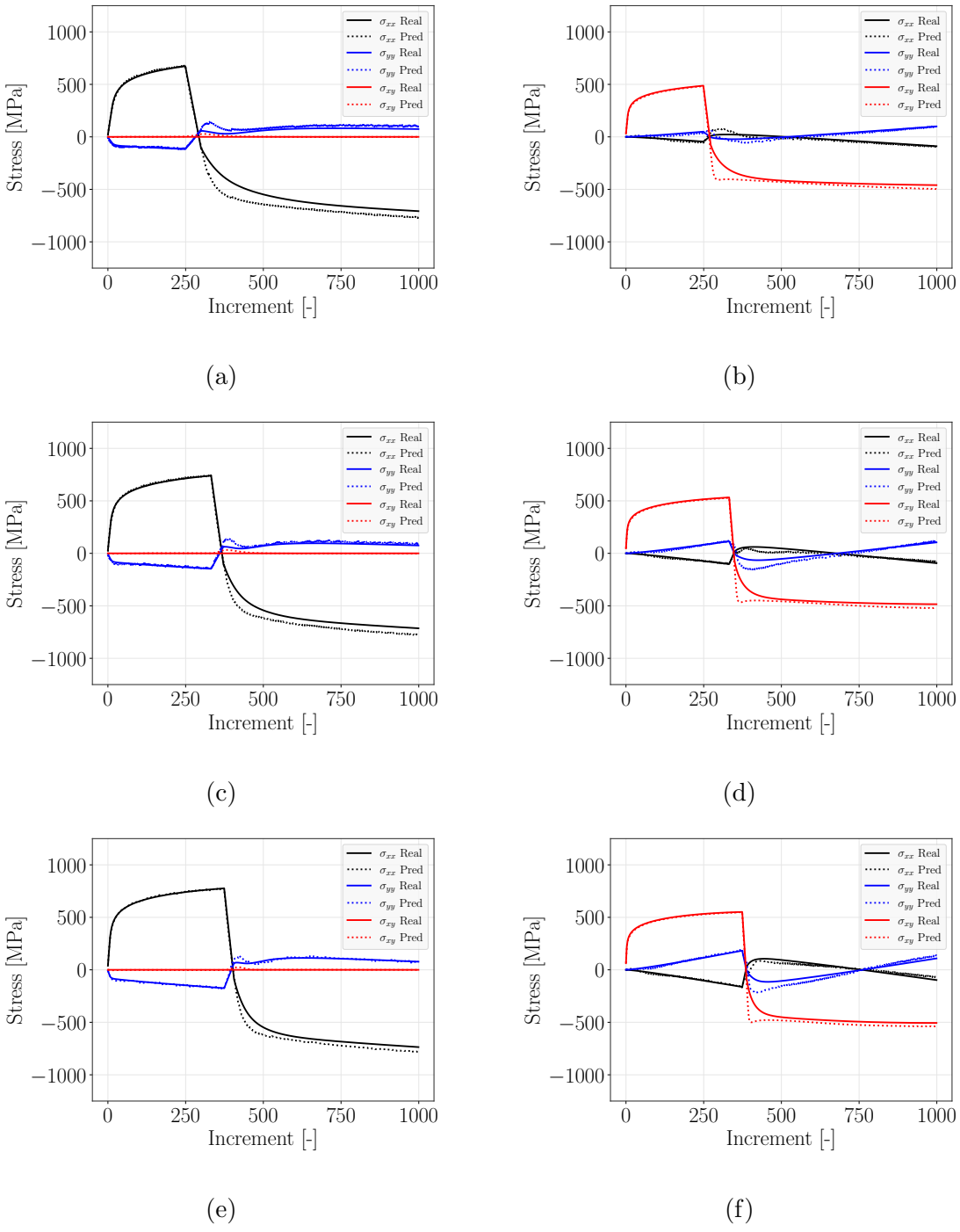


Figure 5.16: Stress predictions for reverse loading scenarios; left plots: TC paths with strain reversal applied at different strain levels ($\varepsilon^*_{xx} = 0.025$, 0.05 and 0.075); right plots: RS paths with reversal applied at different strain levels ($\varepsilon^*_{xy} = 0.1$, 0.2 and 0.3).

To improve the model's performance during strain-path reversals, two additional sequence types were added to the original dataset. First, new random-walk trajec-

tories were generated using the procedure of Section 5.2.1, but without local noise perturbations. It is expected that removing noise will help the model to capture sharp transitions and strain reversals more effectively, since noisy trajectories tend to distort the true shape of the stress behavior after reversal. Second, simplified loading cases were introduced in which only a single strain component varies while the others remain fixed, thereby isolating the material response to each individual mode. Figure 5.17 shows examples of these complementary sequences. Figures 5.17a,b show a representative noise-free RW sequence and its predicted stress response, respectively. Figures 5.17c,d show a case with only uniaxial deformation along the ε_{xx} direction. In total, 1000 noise-free random walks and 150 single-component loading sequences (50 per strain component) were added.

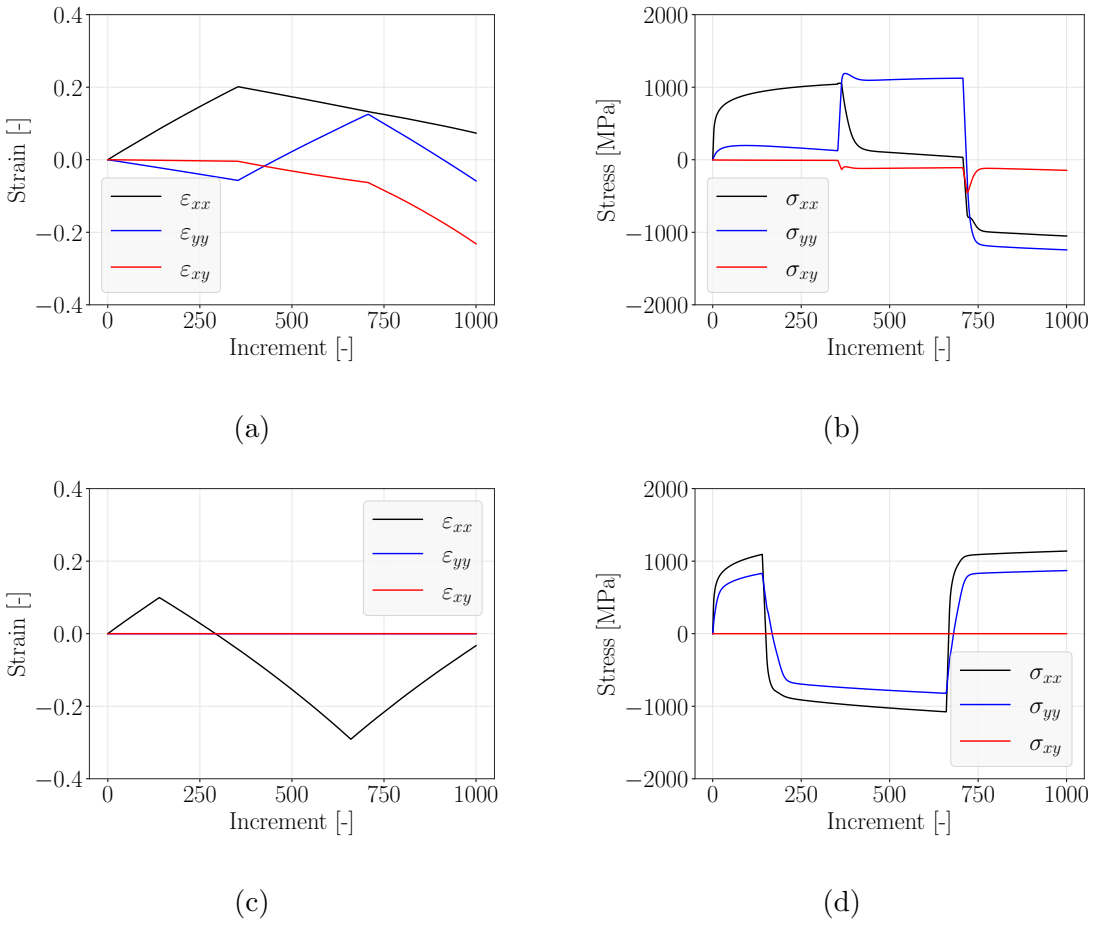


Figure 5.17: Additional training examples for strain-path reversals: (a–b) noise-free random walk and its stress response; (c–d) uniaxial ε_{xx} trajectory and response.

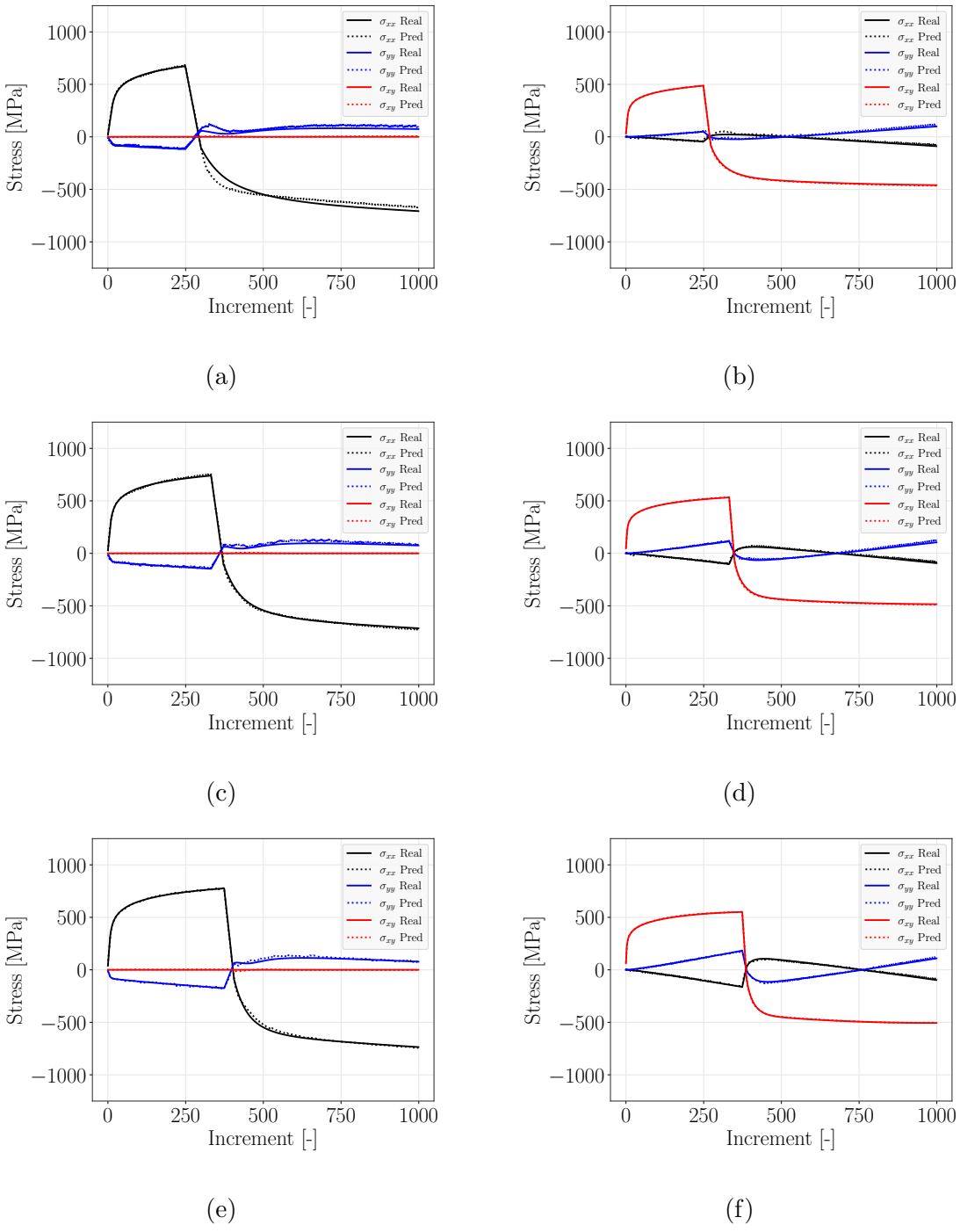


Figure 5.18: Stress predictions for reverse loading scenarios using the retrained LMSC model; left plots: TC paths with strain reversal applied at different strain levels ($\varepsilon^*_{xx} = 0.025, 0.05$ and 0.075); right plots: RS paths with reversal applied at different shear strain levels ($\varepsilon^*_{xy} = 0.1, 0.2$ and 0.3).

Following the original proportions, the dataset was split into training (70%), validation (15%) and test (15%) subset and the LMSC model was retrained on this

expanded dataset. Figure 5.18 shows the stress predictions for reverse loading cases after retraining the model with the expanded dataset.

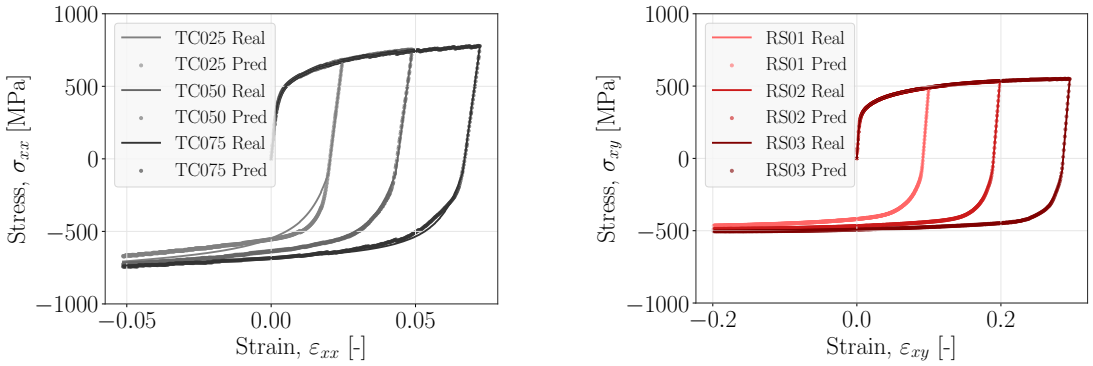
Overall, the model continues to accurately reproduce the monotonic part. Additionally, the stress amplitudes after reversal are better captured and the predicted curves converge more rapidly toward the reference responses. This effect is noticeable in the tension–compression (TC) tests shown in Figures 5.18a, c and e, where the previously observed overestimation in σ_{xx} has been substantially reduced. Similarly, for the reverse shear (RS) cases (Figures 5.18b, d and f), the predicted σ_{xy} values more accurately reflect the reference behavior across the full loading path. Table 5.2 shows that adding noise-free and single-mode paths reduces the mean relative error by at least half for every reverse-loading scenario. In TC scenarios, the MRE in σ_{xx} drops from 14.4% to 7.2% at $\varepsilon^*_{xx} = 0.025$, from 7.8% to 3.2% at $\varepsilon^*_{xx} = 0.050$ and from 2.3% to 1.7% at $\varepsilon^*_{xx} = 0.075$. Reverse-shear cases see similarly large gains, with the MRE in σ_{xy} falling from 12.7% to 1.1% at $\varepsilon^*_{xy} = 0.10$, from 7.6% to 1.2% at $\varepsilon^*_{xy} = 0.20$ and from 5.8% to 1.4% at $\varepsilon^*_{xy} = 0.30$. Overall, the expanded dataset delivers significant error reductions in the dominant stress components for all selected reversals. The first TC case ($\varepsilon^*_{xx} = 0.025$) remains the highest MRE but still falls within the maximum error observed in earlier performance analyses. Further improvement would require additional noise-free training paths. By removing artificial noise and introducing clean, uniaxial loading paths, the model learns more consistent stress–strain mappings and is better able to capture the transition mechanisms associated with strain-path reversals.

Table 5.2: Mean relative error (%) in σ_{xx} for tension–compression (TC) cases and in σ_{xy} for reverse-shear (RS) cases, comparing baseline and expanded datasets.

Reversal Strain	**MRE (%) - Baseline dataset**	**MRE (%) - Expanded dataset**
TC, $\varepsilon^*_{xx} = 0.025$	14.39	7.22
TC, $\varepsilon^*_{xx} = 0.050$	7.81	3.19
TC, $\varepsilon^*_{xx} = 0.075$	2.32	1.70
RS, $\varepsilon^*_{xy} = 0.10$	12.71	1.06
RS, $\varepsilon^*_{xy} = 0.20$	7.58	1.20
RS, $\varepsilon^*_{xy} = 0.30$	5.75	1.40

To better illustrate the model's ability to reproduce the full stress–strain behavior, Figure 5.19 shows the predicted versus reference stress–strain curves for both

tension–compression (TC) and reverse shear (RS) loading paths. Each curve represents one of the cases previously shown in Figures 5.18a–f, plotted with respect to the primary strain component. Figure 5.19a presents the axial stress σ_{xx} as a function of the axial strain ε_{xx} for three TC cases, while Figure 5.19b shows the shear stress σ_{xy} against the shear strain ε_{xy} for the corresponding RS paths. The results demonstrate that the retrained model captures not only the correct amplitude and shape of the loading curves but also the transition behavior during strain path inversion. The predicted stress-strain behavior align closely with the reference data across the different reversal levels, confirming the model's improved performance in reproducing Bauschinger behavior.



(a) (b)

Figure 5.19: Comparison between predicted and reference stress–strain curves for reverse loading paths using the retrained model: (a) TC paths at reversal strains $\varepsilon^*_{xx} = 0.025$, 0.05 and 0.075; (b) RS paths at reversal strains $\varepsilon^*_{xy} = 0.1$, 0.2 and 0.3.

5.4.2 Evaluation on FEA-Based Strain Histories

To further evaluate the performance of the trained LMSC model, this section tests its behavior under FEA-based strain histories. Therefore, two different FE simulation modes are considered: an implicit static analysis with displacement controlled boundary conditions and coarse time increments and an explicit dynamic analysis with velocity controlled boundary conditions and with fine time steps (in some cases hundreds of thousands of increments) to replicate industrial forming and analyze long–sequence stability and generalization. The objective of this analysis is to evaluate the generalization capability of the model to new FEA derived strain trajectories in both static and dynamic simulations and consequently evaluate the

self-consistency of the trained model, i.e, its ability to produce consistent stress responses regardless of time-step size or integration scheme.

Four case studies of increasing complexity are evaluated: a uniaxial tensile test, a reverse bending test, a cylindrical cup deep drawing [290] and the 3DS (Digital Die Design System) rail-forming benchmark [291], each representative of different sheet metal forming operations. The DP780 constitutive behavior is implemented via the publicly available UMAT and VUMAT subroutines [289] for implicit static and explicit dynamic analyses, respectively. All numerical models use four-node shell elements with reduced integration (S4R) to capture in-plane stresses σ_{xx}, σ_{yy} and σ_{xy} at each integration point. For each simulation, selected integration points are analyzed by importing their strain histories into the LMSC surrogate model. The resulting stress predictions are then compared directly against the reference FEA outputs.

Before embedding the LMSC surrogate, consistency between the UMAT and VUMAT implementations of the baseline constitutive model is confirmed using a single-element S4R shell simulation. Figure 5.20 compares the σ_{xx}–ε_{xx} curves for a tension–compression–tension path from UMAT (solid red) and VUMAT (dashed black), showing near-perfect agreement. The UMAT uses a closest-point projection algorithm for the stress update, while the VUMAT employs a non-iterative stress projection method with the continuum tangent operator. This ensures that any discrepancies in subsequent results are due to surrogate model rather than differences in the underlying finite-element formulations.

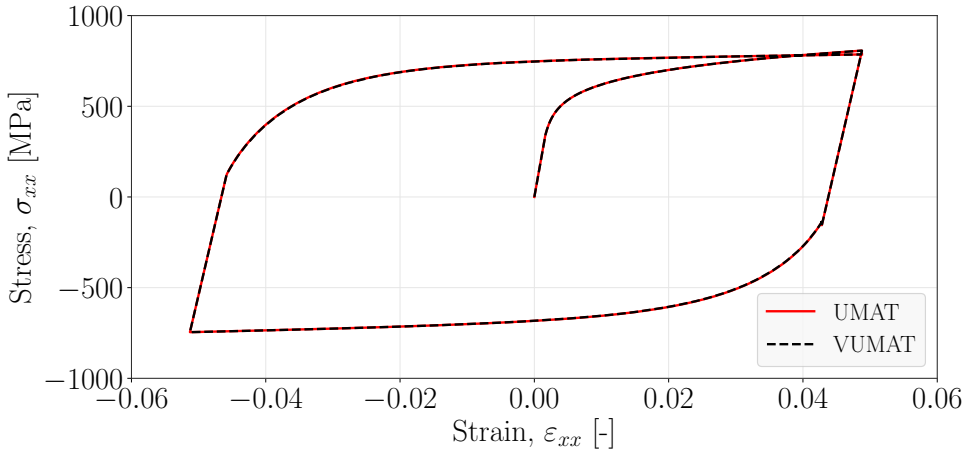


Figure 5.20: Comparison between UMAT and VUMAT implementations of the constitutive model under a tension-compression-tension (TCT) path.

5.4.2.1 Tensile Test

The tensile test follows the ASTM E8 [292] standard and is simulated consider a quarter-model dog-bone specimen. The finite-element mesh and contour plot of the equivalent stress distribution are shown in Figure 5.21. Displacement is applied incrementally along the rolling direction (x-axis) on the free edge, while the opposite edges are constrained to enforce symmetry and prevent rigid-body motion. The methodology adopted follows a direct and offline validation strategy. First, uniaxial tensile tests are simulated with the FE model, from which strain paths are extracted at selected integration points. These strain paths are then imported into the trained LMSC network, which predicts the corresponding stress response. Finally, the predicted stress histories are compared with the FE reference results to evaluate the capability of the neural network to reproduce the constitutive behavior. Two integration points are selected for detailed analysis: IntPtA, located at the center of the gauge section and IntPtB, positioned 25 mm from IntPtA along the specimen length.

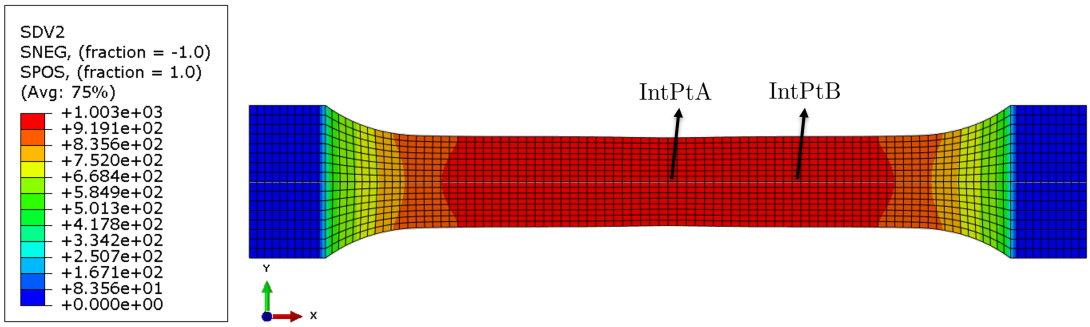


Figure 5.21: Finite element mesh and contour plot of the equivalent stress distribution (`SDV2`) for the tensile test simulation.

Figure 5.22 shows the evolution of the in-plane strain components ε_{xx}, ε_{yy} and ε_{xy}, for both IntPtA and IntPtB, together with the corresponding increments $\Delta\varepsilon$, as extracted from the static/implicit simulation. Both points follow a nearly identical, predominantly uniaxial tension in ε_{xx} until the final increments, where IntPtA deviates due to the onset of necking. Figure 5.23 compares the stresses predicted by the LMSC network ('Pred') with the reference FE results obtained from the UMAT implementation ('Real') at IntPtA and IntPtB. The surrogate accurately reproduces the monotonic increase in σ_{xx} and the negligible transverse stresses σ_{yy} and σ_{xy}, maintaining errors below 1% throughout the loading history.

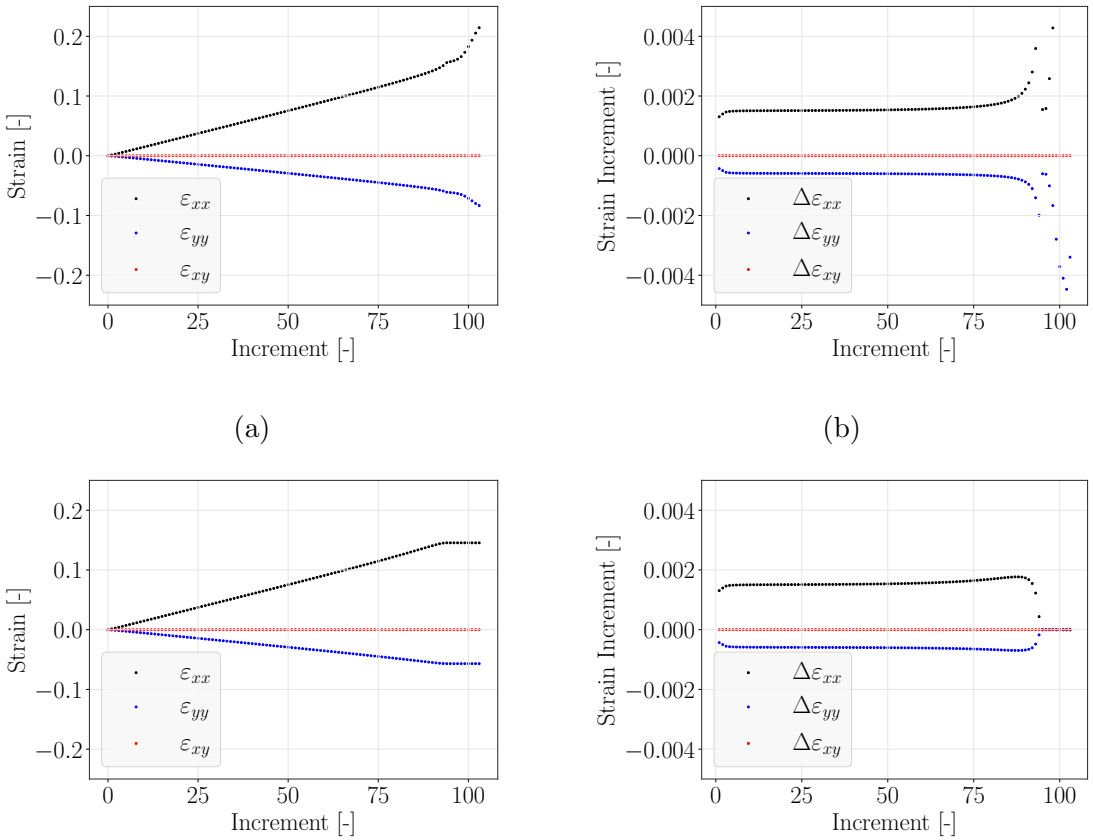


Figure 5.22: Strain paths and corresponding increments extracted from the static/implicit tensile simulation: (a)–(b) IntPtA, (c)–(d) IntPtB.

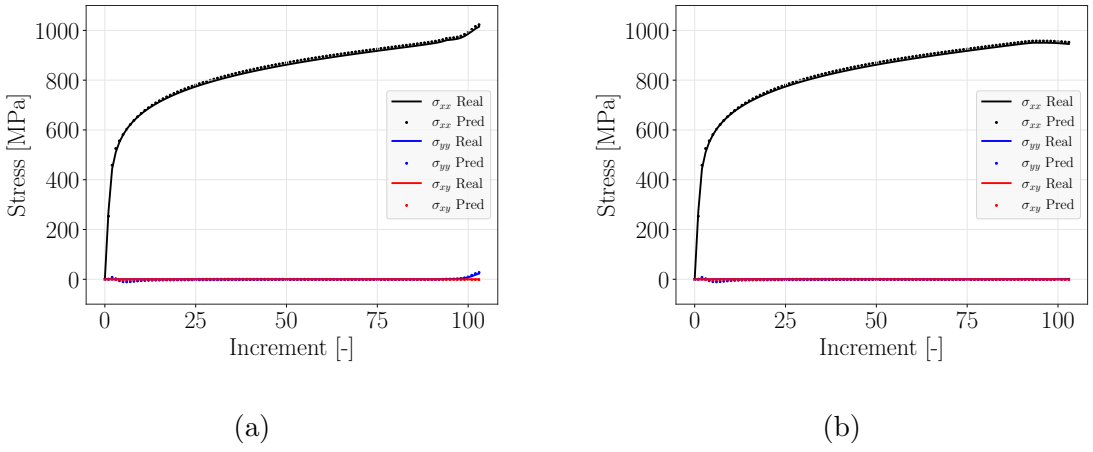
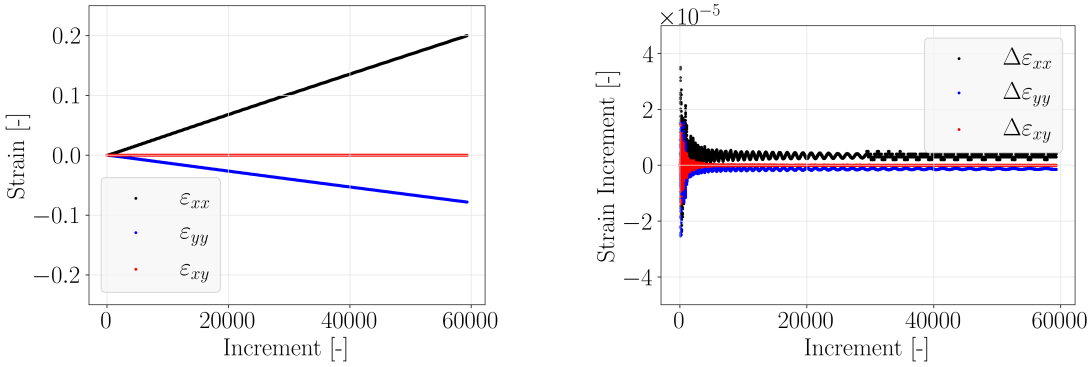


Figure 5.23: Comparison between LMSC predictions ('Pred') and UMAT reference ('Real') at selected integration points in the static/implicit tensile test: (a) IntPtA; (b) IntPtB.

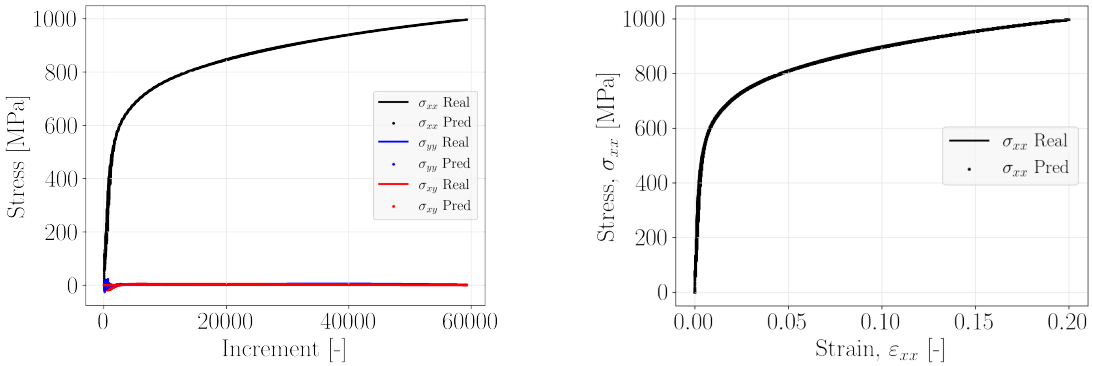
To further evaluate the stability and self-consistency of the LMSC surrogate model, the same tensile test was simulated in a dynamic/explicit approach considering the VUMAT subrotine. Figure 5.24 shows the resulting strain path and increment evolution for the representative integration point A (IntPtA). The dynamic simulation uses over 60000 increments, resulting in strain increment sizes approximately two orders of magnitude smaller than in the static run and thus providing a much finer resolution of the tensile strain path.



(a) (b)

Figure 5.24: Strain evolution for IntPtA in the dynamic/explicit tensile simulation: (a) strain components and (b) corresponding incremental strain steps.

Figure 5.25 confirms that the LMSC surrogate model remains both accurate and self-consistent under the fine time stepping of an dynamic/explicit simulation. In Figure 5.25a, the predicted stress components nearly match the reference curve almost exactly over all 60000 increments. The prediction error for σ_{xx} remains below 1% throughout the simulation. The transverse stresses σ_{yy} and σ_{xy} remain essentially zero, as expected for a uniaxial tensile path, with only imperceptible deviations at the start of loading. Figure 5.25b presents the same data as a stress–strain plot (σ_{xx} vs. ε_{xx}), where the predicted and reference curves are almost indistinguishable. These results highlights that the surrogate's integration of the stress update is independent of increment size.



(a) (b)

Figure 5.25: Comparison between VUMAT reference ('Real') and LMSC prediction ('Pred') at IntPtA in the dynamic explicit tensile test: (a) stress components versus increments; (b) σ_{xx} versus ε_{xx}.

To further evaluate path dependence, the standard tensile sequence was extended with a compression reversal, taking the axial strain from $\varepsilon_{xx} = 0.05$ down to $\varepsilon_{xx} = -0.05$. The resulting strain histories and corresponding strain-increment evolutions at IntPtA are presented in Figure 5.26 for both static and dynamic simulations. The static simulation uses about 2000 increments, whereas the dynamic simulation uses over 150000 increments, which is nearly two orders of magnitude finer resolution. Figures 5.27 compare the LMSC-predicted stresses against the reference in both static and dynamic simulations. In each case, the surrogate not only reproduces the monotonic tensile loading curve but also maintains accuracy through the compression reversal. The predicted σ_{xx} stress deviates by less than 1% from both UMAT and VUMAT references, demonstrating excellent agreement. Furthermore, no unexpected variation is observed, even after long simulation sequences. These results show that the LMSC surrogate has successfully learned the full path-dependent behavior, including sharp load inversions and can be reliably embedded in both implicit and explicit FEA workflows.

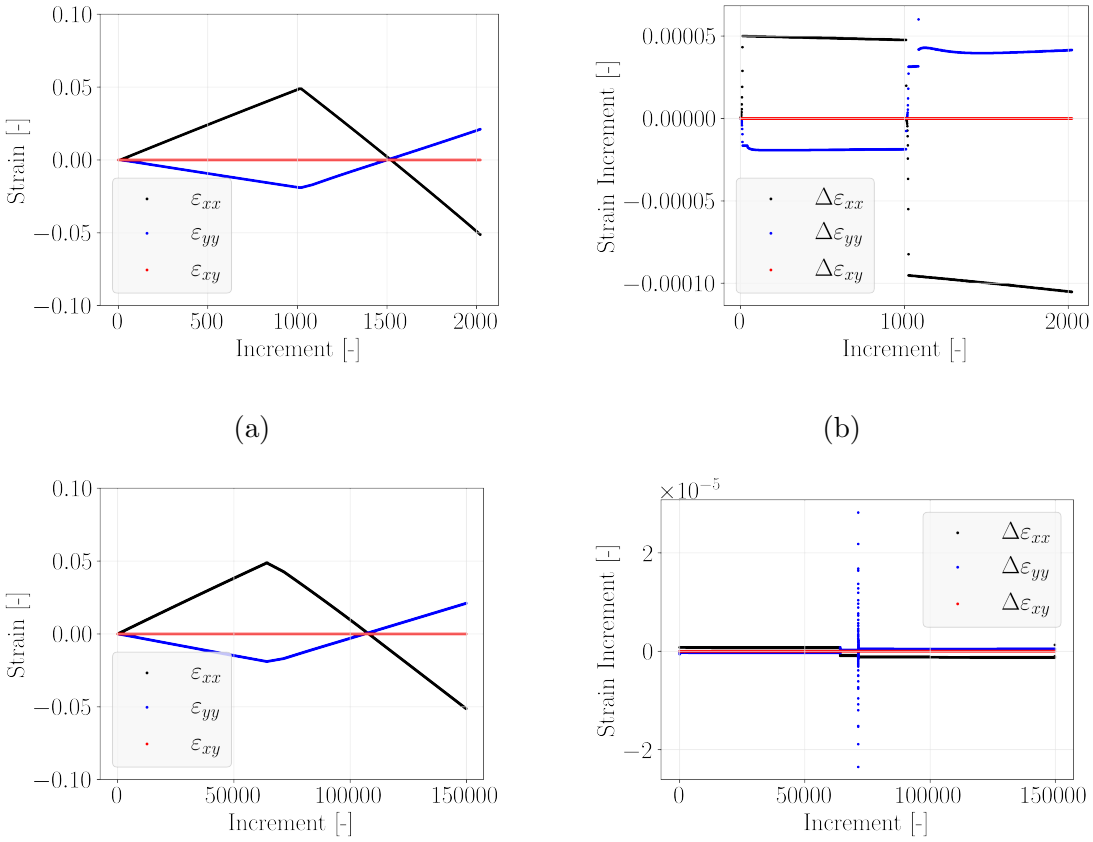


Figure 5.26: Strain paths and corresponding increments for the (a-b) static and (c-d) dynamic tension-compression simulation.

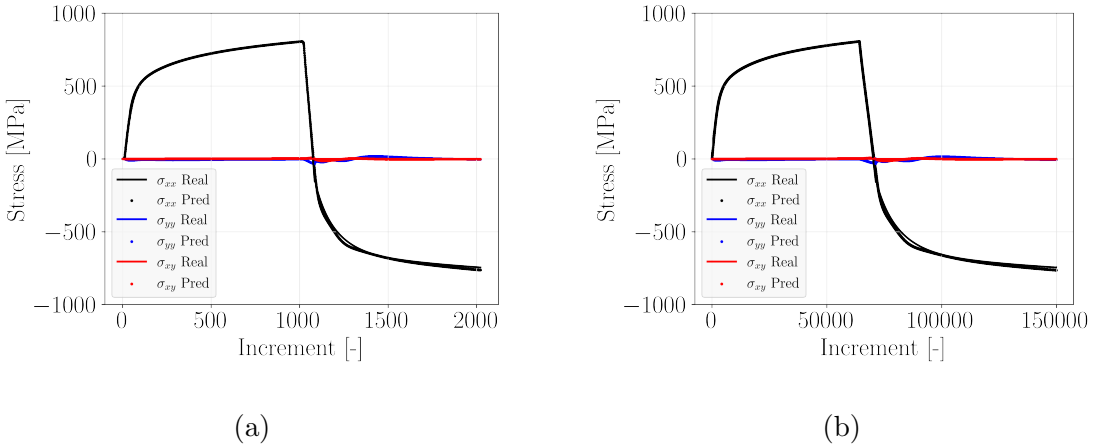
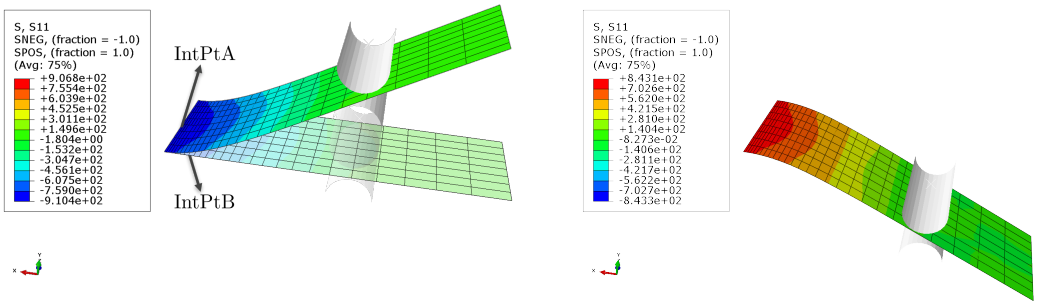


Figure 5.27: Comparison between reference ('Real') and LMSC prediction ('Pred') for the tension–compression simulation: (a) static and (b) dynamic case.

5.4.2.2 Reverse Bending Test

This case study evaluates the performance of the trained LMSC surrogate model under reversed bending conditions, based on the experimental reverse bending test presented in Section 3.4.3. For this case, only the static implementation is considered, since the load reversal involves elastic recovery of the material (springback), a phenomenon that is not well captured by dynamic explicit analysis due to its sensitivity to inertial effects, particularly during the unloading phase. Figure 5.28 shows the numerical model using 3D shell elements, with the principal stress distribution displayed at the end of the first and second loading steps. Two integration points, symmetrically positioned through the thickness of the same shell element, are selected for detailed analysis: IntPtA is on the top surface and IntPtB is on the bottom surface. These points undergo opposite strain-path histories during the test.



(a) (b)

Figure 5.28: Finite element model of the reverse bending test using 3D shell elements and the distribution of principal stress (S11) at the end of the (a) first step (bending) and (b) second loading step (unbending).

The strain paths extracted from the numerical simulation are shown in Figure 5.29 for both integration points. Figure 5.29a,b show, for the top integration point (IntPtA), the strains ε_{xx}, ε_{yy}, ε_{xy} and their corresponding increments, $\Delta\varepsilon$, showing compression–tension loading. Figure 5.29c,d show the same for the bottom integration point (IntPtB), showing tension–compression loading. As expected, the strain paths and their corresponding increments have similar shapes, but they evolve in opposite directions.

Figure 5.30 compares the stress histories predicted by the LMSC surrogate model with the reference UMAT results at each integration point. Figure 5.30a corresponds to IntPtA, located on the top surface and subjected to compression–tension (CT) loading, while Figure 5.30b corresponds to IntPtB, located on the bottom surface

and subjected to tension–compression (TC) loading. The initial loading phase is well predicted in both cases, with accurate predictions of the stress components σ_{xx}, σ_{yy} and σ_{xy}. After load reversal, however, the TC case shows better agreement with the reference, particularly during the transition through unloading and reloading. In contrast, the CT case exhibits slightly larger deviations in the post-reversal regime, especially for σ_{xx}, suggesting reduced generalization accuracy for strain paths starting in compression. Over the entire loading sequence, the mean stress prediction error is approximately 20% for the CT case and 13% for the TC case.

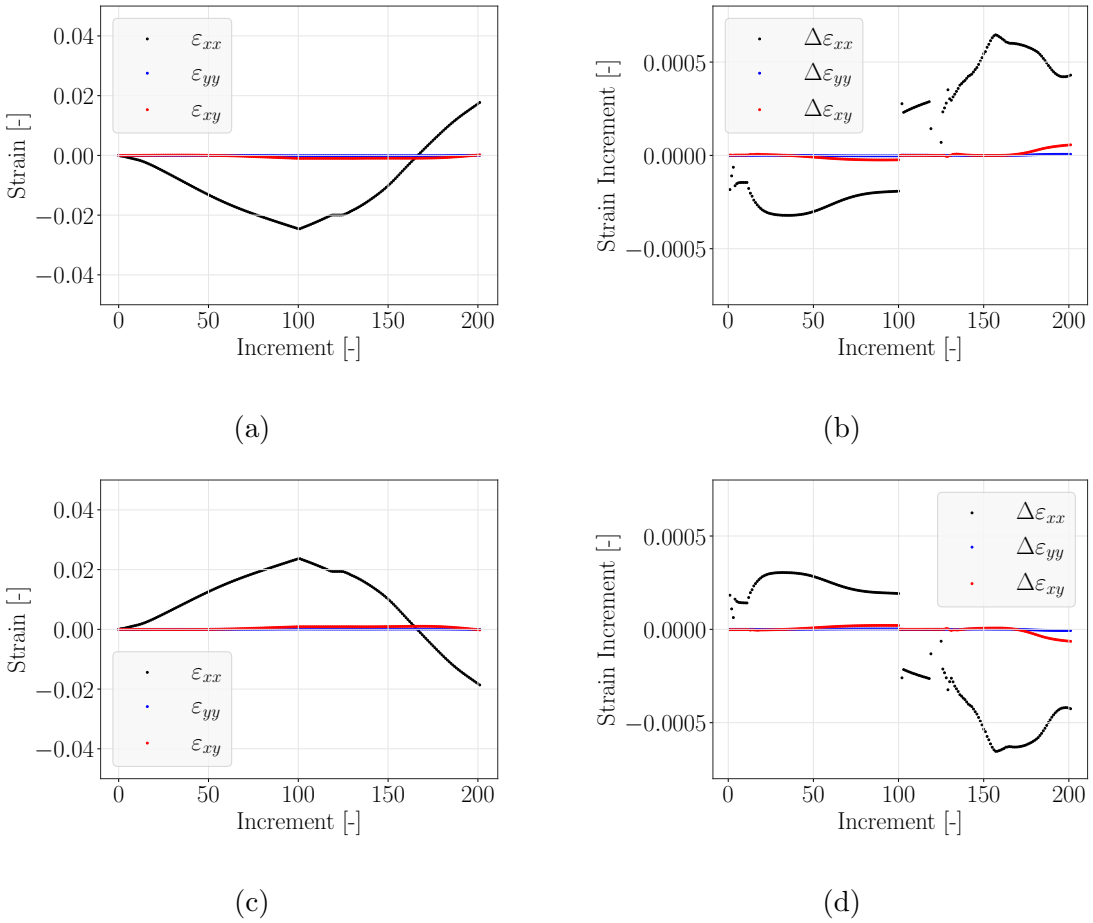
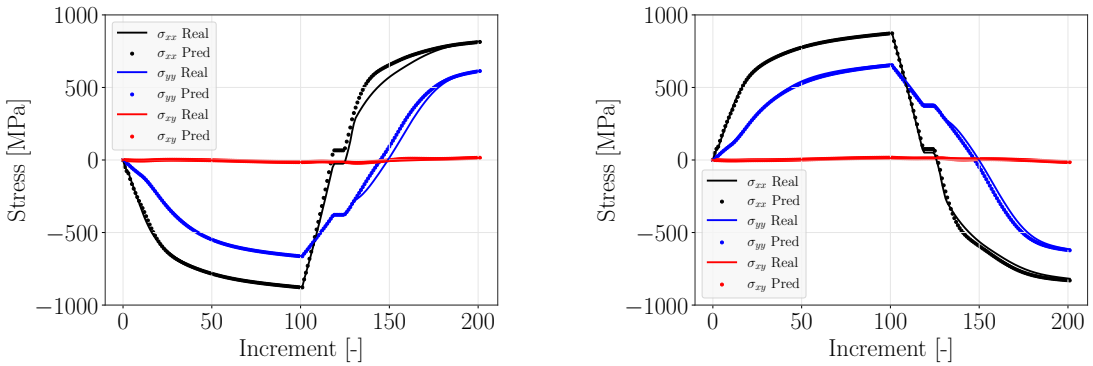


Figure 5.29: Strain components ε_{xx}, ε_{yy}, ε_{xy} and their increments $\Delta\varepsilon$ during the reverse bending test: (a–b) correspond to top integration point (IntPtA) and (c–d) to bottom integration point (IntPtB).

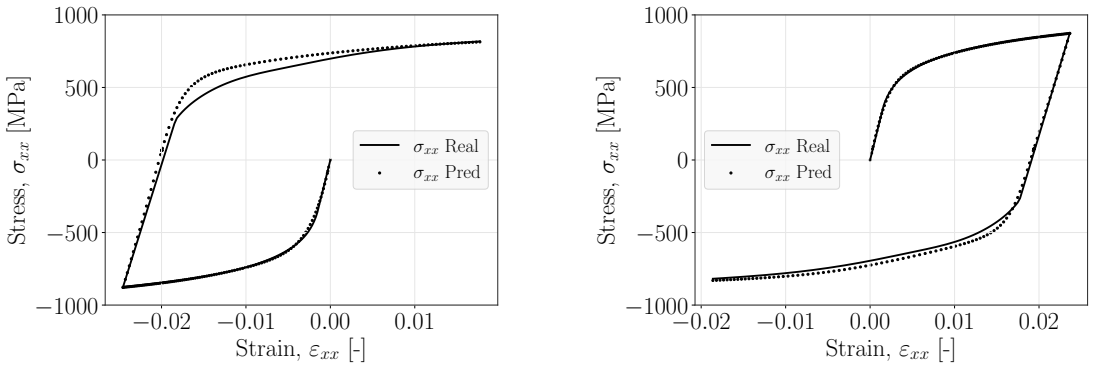


(a) (b)

Figure 5.30: Comparison between the LMSC-predicted ('Pred') and reference ('Real') stress components during the reverse bending test for: (a) top integration point (IntPtA) and (b) bottom integration point (IntPtB).

Finally, Figure 5.31 shows the predicted and reference stress–strain curves for both integration points in the reverse bending test. The plots show the normal stress σ_{xx} as a function of the axial strain ε_{xx}, enabling a direct assessment of the surrogate model's ability to capture the material behavior under reversed loading. The general shape is well reproduced by the LMSC model in both cases. As observed previously, the agreement is slightly better for the tension–compression (TC) path, Figure 5.31b with the surrogate more accurately following the unloading and reloading steps. In the compression–tension (CT) case, Figure 5.31a, small deviations appear near the strain reversal point, though the overall response remains consistent with the reference solution.

Overall, the reverse bending test demonstrates the ability of the LMSC surrogate model to generalize well to non-monotonic loading paths involving strain reversals and elastic recovery. Despite minor deviations around the reversal points, more pronounced in the compression–tension case, the model captures the overall stress–strain behavior, including path dependency, with good accuracy. These results confirm the robustness of the surrogate in predicting cyclic loading responses beyond the conditions seen during training.



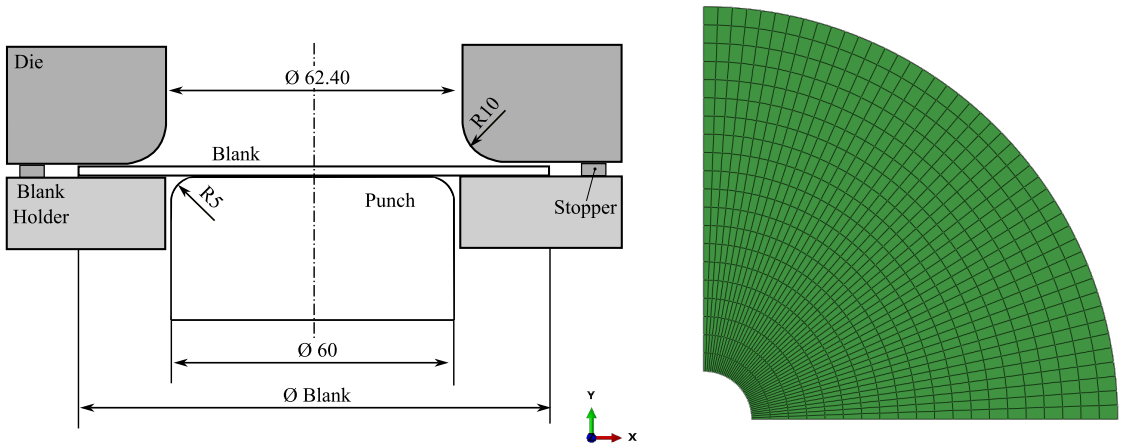
(a) (b)

Figure 5.31: Comparison of LMSC-predicted ('Pred') and reference ('Real') stress–strain curves (σ_{xx} vs. ε_{xx}) for the reverse bending test for: top integration point (IntPtA) and (b) bottom integration point (IntPtB).

5.4.2.3 Cylindrical Cup Forming

The third case study evaluates the performance of the LMSC surrogate model in a deep drawing scenario involving a cylindrical cup forming process, as presented in the ESAFORM 2021 benchmark [290]. The plastic deformation levels in this test are significantly more severe than in the previous cases, making it a more challenging benchmark for model evaluation. Additionally, this benchmark introduces more complex deformation patterns, including through-thickness thinning, strain-path changes and contact with rigid tools.

The numerical model of this forming process includes three main tools: the punch, the blank holder and the die, whose respective geometries and dimensions are shown in Figure 5.32a. The circular blank has an average thickness of 0.8 mm and a diameter of 106 mm. As shown in Figure 5.32b, the blank is discretized with 900 linear quadrilateral shell elements (S4R). On the other hand the tools were modelled as analytical rigid bodies. The numerical simulation is performed considering a constant gap between the die and blankholder equal to 10% of thickness. The punch descends 54 mm, drawing the blank completely into the die. Frictional interaction between the tools and the blank is modeled using Coulomb's law with a constant coefficient of 0.1.



(a) (b)

Figure 5.32: Cylindrical cup forming setup: (a) tooling geometry and main dimensions and (b) finite element mesh of the blank.

To evaluate the LMSC surrogate model throughout the cup forming process, three integration points were selected (Figure 5.33). IntPtA is located near the shoulder radius and IntPtB lies at the at the midpoint of the cup wall in the rolling direction. IntPtC is also at the mid-height, but it is oriented at a 45° angle to the RD. The strain paths (ε_{xx}, ε_{yy} and ε_{xy}) for the static/implicit simulation and their corresponding increments, $\Delta\varepsilon$, at the selected integration points are shown in Figure 5.34.

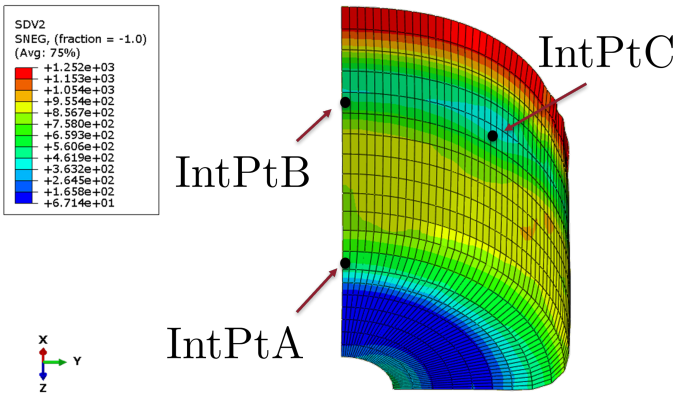


Figure 5.33: Equivalent stress distribution (`SDV2`) in the final formed cup, showing the selected integration points for analysis.

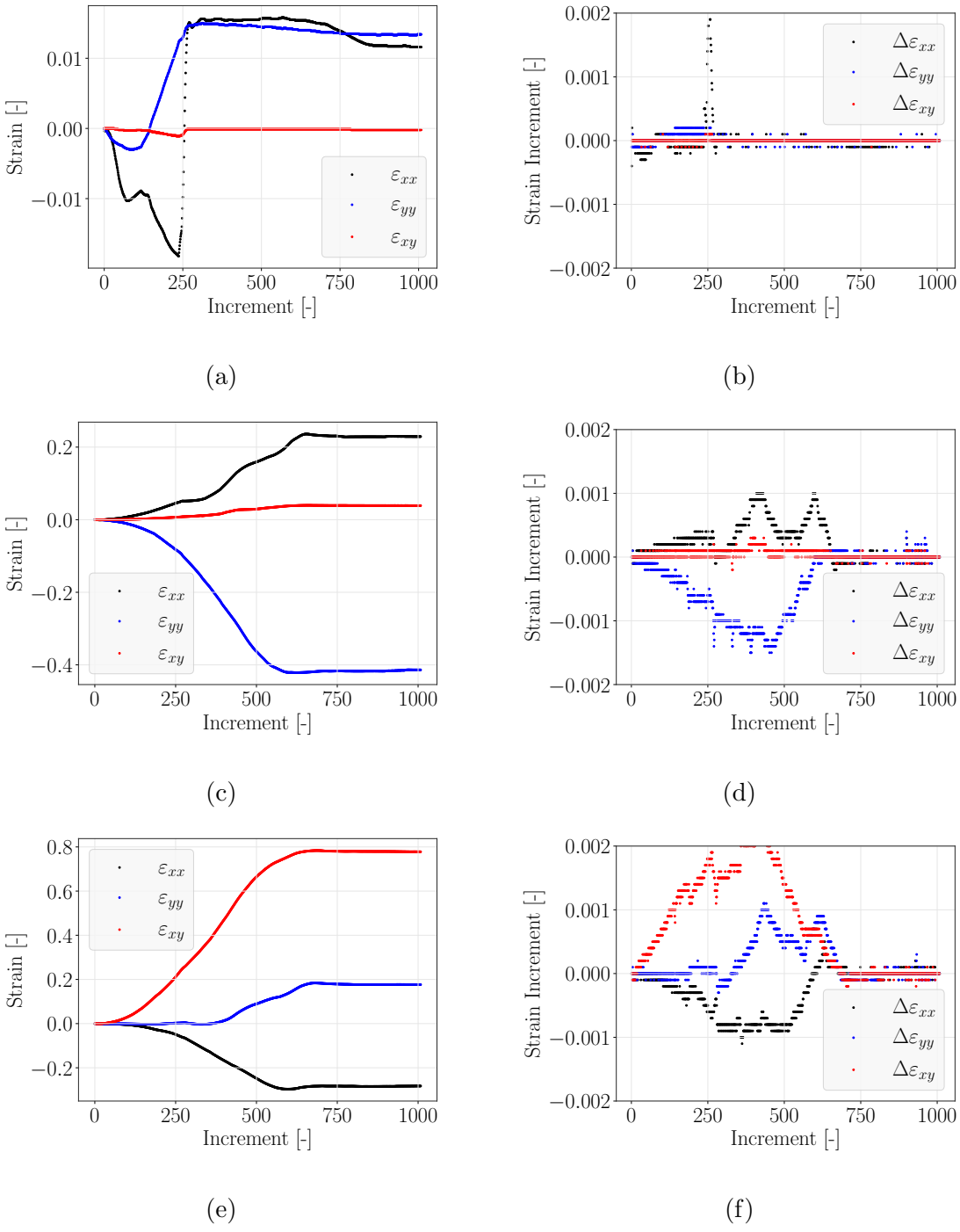


Figure 5.34: Strain components (ε_{xx}, ε_{yy} and ε_{xy}) and corresponding strain increments ($\Delta\varepsilon$) for the selected integration points during the cup forming static/implicit simulation: (a–b) IntPtA, (c–d) IntPtB and (e–f) IntPtC.

Figure 5.35 compares the predicted and reference stress components at the three selected integration points during the cup forming static/implicit simulation. At IntPtA (Figure 5.35a), located near the shoulder radius, the stress histories reflect

the bending–unbending sequence, with reversals in σ_{xx} and σ_{yy}. This region experiences relatively small strains (below approximately 0.02 in both ε_{xx} and ε_{yy}), while the shear component remains near zero. The surrogate model captures the overall trends and reversal amplitudes. The mean relative error per sample is 22.14% for σ_{xx} and 4.39% for σ_{yy}, with the largest deviations occurring around the stress reversals transition near increment 250.

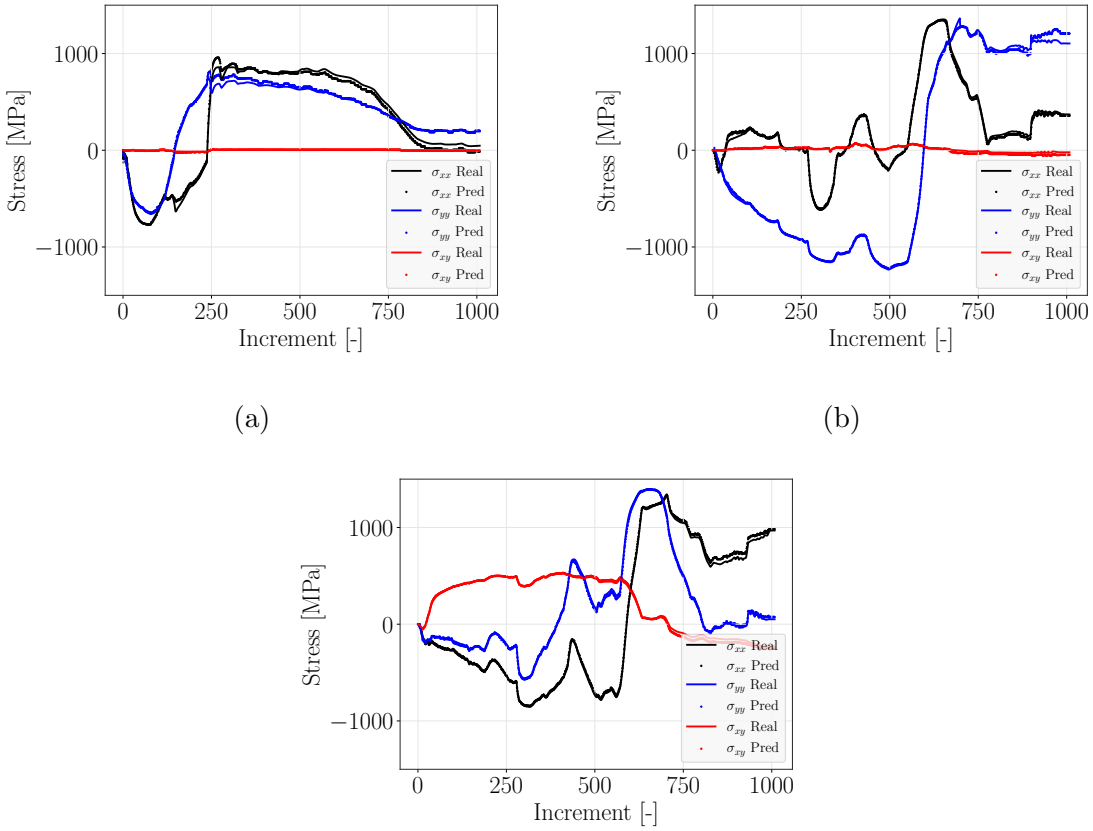


Figure 5.35: Comparison between LMSC-predicted ('Pred') and reference ('Real') stress components (σ_{xx}, σ_{yy} and σ_{xy}) at the selected integration points during the cup forming static/implicit simulation: (a) IntPtA, (b) IntPtB and (c) IntPtC.

At IntPtB, located on the mid-wall in the rolling direction, the strain evolution is smoother and essentially monotonic, as represented in Figure 5.34b. The local deformation is dominated by ε_{xx} and ε_{yy}, reaching approximately 0.2 and -0.4, respectively, while ε_{xy} remains near zero. As shown in Figure 5.35b, the surrogate model closely follows the reference trajectory, with mean relative errors per sample of 16.50% for σ_{xx} and 16.07% for σ_{yy}. The largest discrepancies appear between

increments 750 and 1000, especially for σ_{yy}.

At IntPtC, which is oriented 45° to the rolling direction, the local state combines shear and normal strain with $\varepsilon_{xy} \approx 0.8$, $\varepsilon_{xx} \approx -0.2$ and $\varepsilon_{yy} \approx 0.2$, as shown in Figure 5.34c. However, although the global strain state contains a substantial shear component, the local condition does not correspond to pure shear since the principal stress directions are rotated relative to the global axes. In contrast, IntPtA and B are aligned with the rolling direction, so their principal directions are directly correlated with the global strain components. For IntPtC, the surrogate model reproduces the general behavior with mean relative errors per sample of 7.62% for σ_{xx}, 25.62% for σ_{yy} and 13.47% for σ_{xy}. Overall, the results demonstrate that the LMSC surrogate generalizes across distinct local deformation modes, with the most challenging behavior arising in mixed loading states and regions exhibiting strain reversals.

Figure 5.36 presents the predicted and reference stress–strain curves at IntPtB, located on the mid-wall and aligned with the rolling direction. The predicted and true curves nearly overlap, indicating strong agreement. The corresponding stress–strain evolutions for IntPtA and IntPtC are provided in Appendix F.

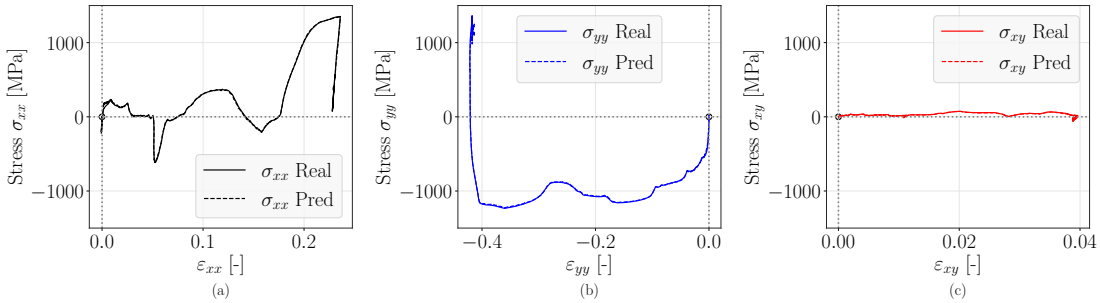


Figure 5.36: Comparison of LMSC-predicted ('Pred') and reference ('Real') stress–strain evolution at IntPtB during cylindrical cup forming static/implicit simulation.

To evaluate the self-consistency of the surrogate LMSC model, the selected integration points are evaluated in an explicit dynamic simulation of the cylindrical cup forming. The strain histories and corresponding strain increments for each integration point are provided in Appendix F. The number of increments increases from about 1000 in the static runs to over 2 million in the dynamic simulation, reducing the strain increment magnitude by roughly three orders of magnitude and yielding a much finer resolution of the deformation paths. Despite the significant change in the

size of the increments, the model response remains stable, as shown in Figure 5.37, which compares stress versus increment for the three integration points. Overall, the surrogate model show good self-consistency, accurately predicting the stress histories across the different deformation states. The largest deviations occur in regions that were also challenging in the implicit static simulation: IntPtA around the reversal transition near 1.0×10^6 increments, IntPtB in the later part of its trajectory around 0.5×10^6 and IntPtC toward the end of the load history. Although some discrepancies are present, the final stress–strain curves remain very similar, as shown in Figure 5.38, which compares predicted and reference responses at IntPtB for the explicit dynamic analysis. The evolution closely matches the static result (see Figure 5.36), with strong overlap between predicted and true curves. The corresponding stress–strain histories for IntPtA and IntPtC are provided in Appendix G.

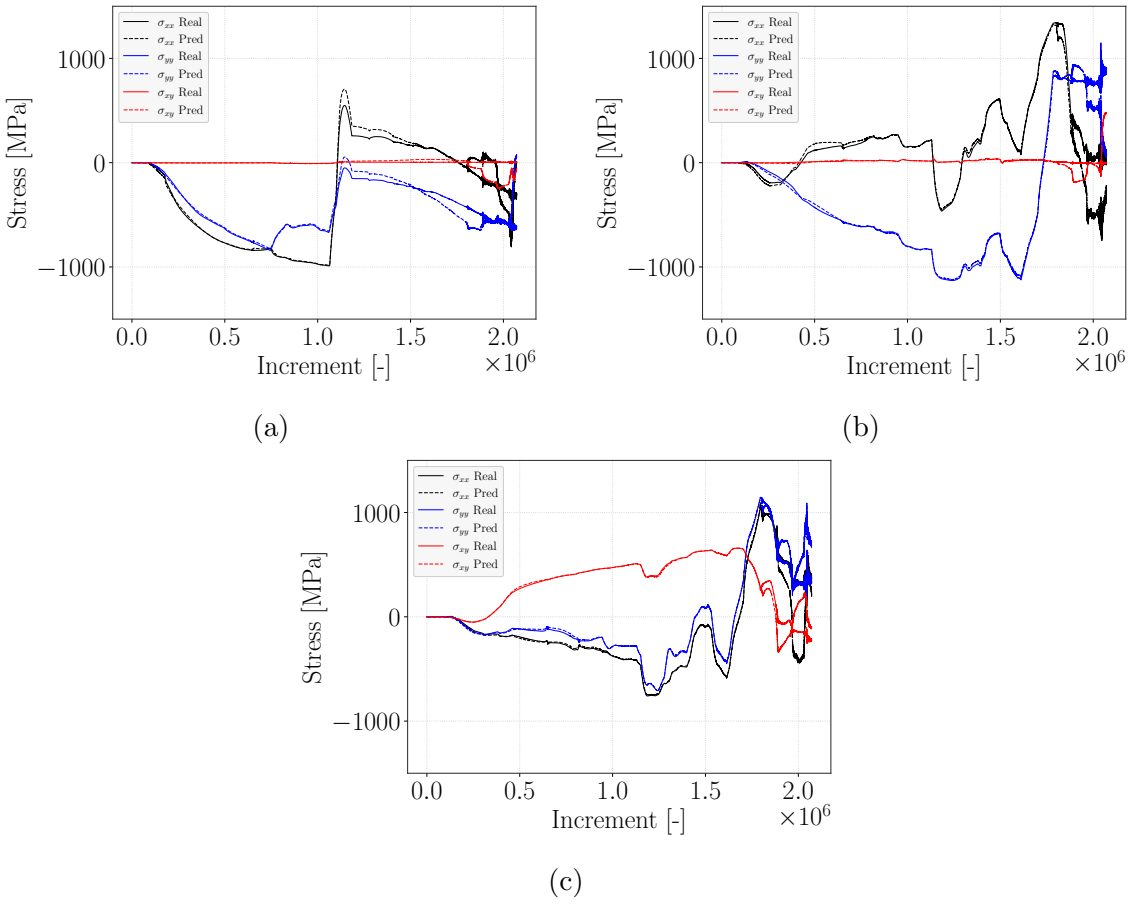


Figure 5.37: Comparison between LMSC-predicted ('Pred') and reference ('Real') stress components (σ_{xx}, σ_{yy} and σ_{xy}) at the selected integration points during the cup forming dynamic/explicit simulation: (a) IntPtA, (b) IntPtB and (c) IntPtC.

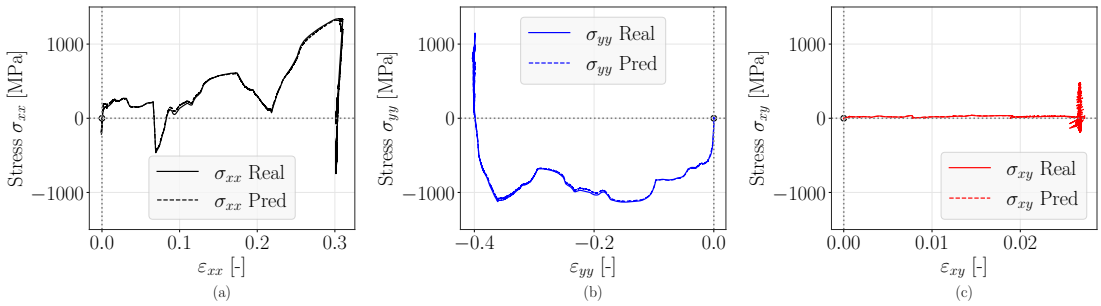


Figure 5.38: Comparison of LMSC-predicted ('Pred') and reference ('Real') stress–strain evolution at IntPtB during cylindrical cup forming dynamic/explicit simulation.

5.4.2.4 3DS Benchmark – Rail Forming

This subsection presents the final validation of the LMSC model using the 3DS (Digital Die Design System) rail-forming benchmark [291]. This benchmark is part of an international project aimed at improving the predictive capability of sheet-metal forming simulations, with particular emphasis on typical forming defects and material behaviors resulting from plastic deformation. To support this objective, the 3DS project established a rigorous experimental program to supply high-fidelity reference data, paying careful attention to material characterization, test procedure definition and precise measurement of key outputs such as final geometries along representative profiles. Figure 5.39 shows one of the 3DS project geometries considered in this case. The simulation takes advantage of symmetry by modeling only one-quarter of the full rail. The corresponding dimensions of the quarter blank are shown in Figure 5.39b. The blank is discretized with 3600 four-node shell elements with reduced integration (S4R).

Figure 5.40 shows the selected integration point, IntPtA, located at the center of the wall analyzed in this final case study. The corresponding strain component paths (ε_{xx}, ε_{yy} and ε_{xy}) from the static/implicit simulation are shown in Figure 5.41a, while Figure 5.41b shows the associated strain increments $\Delta\varepsilon$. The deformation at IntPtA is dominated primarily by deformation in the ε_{yy} direction, reaching a maximum of approximately 0.05, while ε_{xx} and ε_{xy} remain near zero. After this peak, ε_{yy} begins to decrease, indicating a reversal in the local deformation.

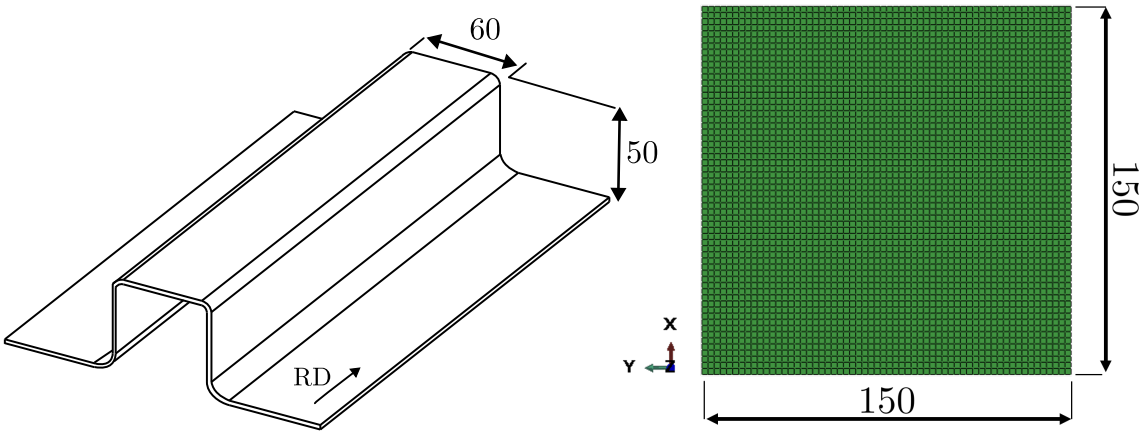


Figure 5.39: 3DS 2D-Rail forming (a) geometry and (b) blank finite-element discretization used in the 3DS benchmark

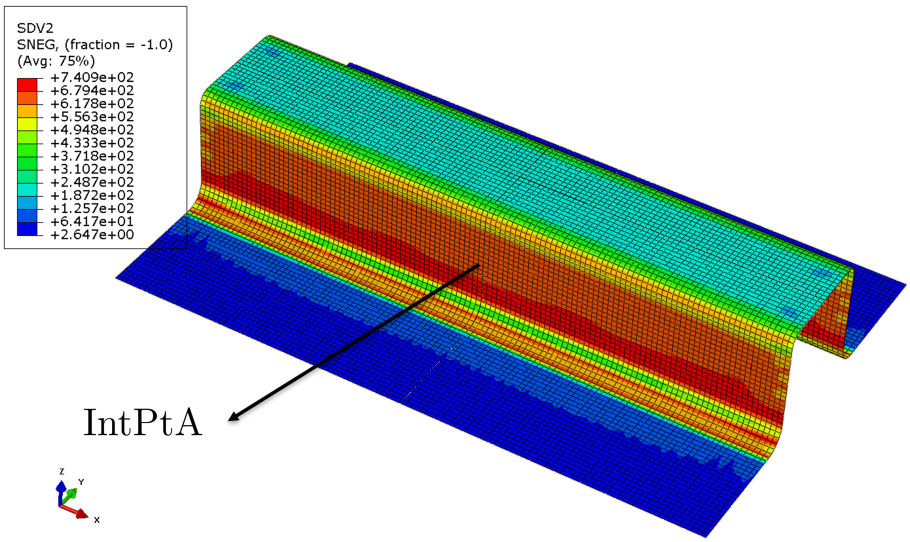
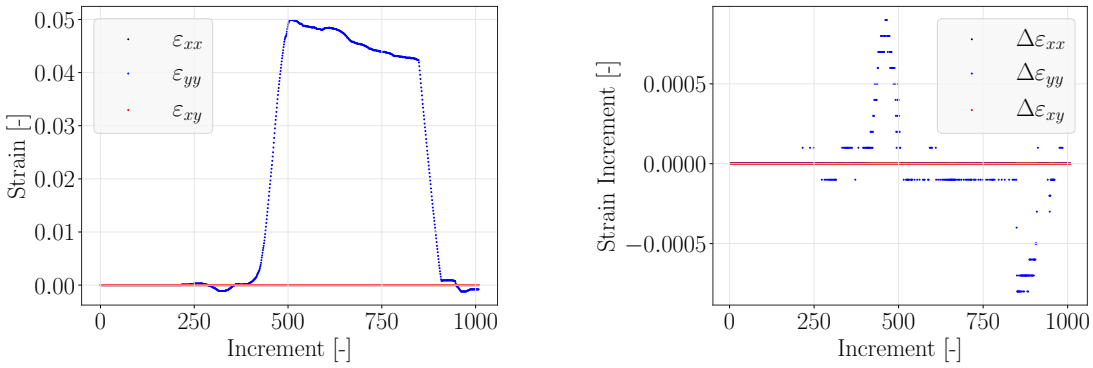


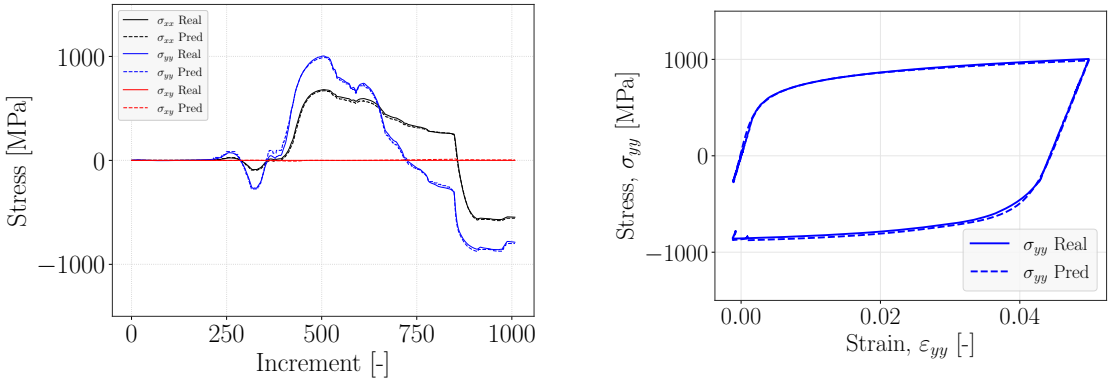
Figure 5.40: Equivalent stress distribution (`SDV2`) in the final formed cup, showing the selected integration points for analysis.

Figure 5.42a shows the full stress component history at IntPtA. The surrogate model captures the overall evolution of σ_{xx}, σ_{yy} and σ_{xy}, including the monotonic increase and subsequent behavior in the strain reversal in σ_{yy} and σ_{xx} around increment 500. The mean relative errors per sample are low for the dominant components, with σ_{xx} exhibiting an MRE of 3.91% and σ_{yy} an MRE of 4.07%. Figure 5.42b isolates the dominant stress–strain relation (σ_{yy}-ε_{yy}) at IntPtA. The predicted and reference curves almost overlap, indicating that the surrogate model reproduces the local constitutive behavior in this integration point with high fidelity.



(a) (b)

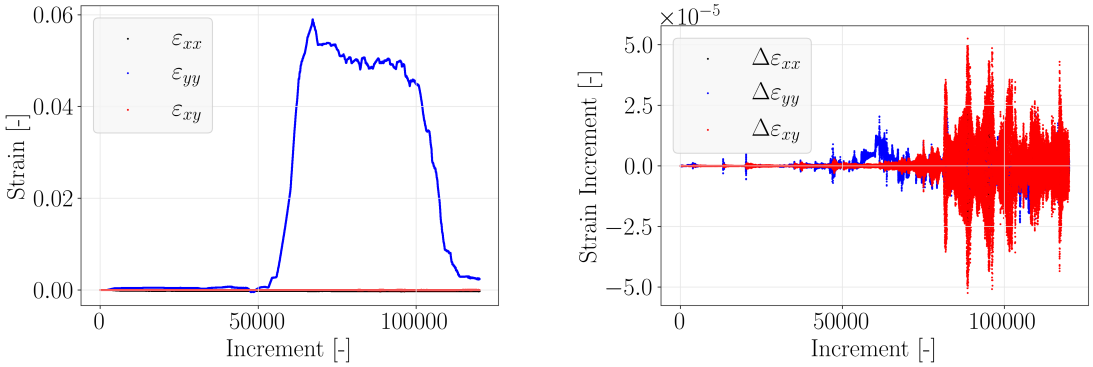
Figure 5.41: Strain components (ε_{xx}, ε_{yy} and ε_{xy}) and corresponding strain increments ($\Delta\varepsilon$) for the selected integration points during the 3DS Rail Forming static/implicit simulation at IntPtA.



(a) (b)

Figure 5.42: Comparison between (a) LMSC-predicted ('Pred') and reference ('Real') stress components (σ_{xx}, σ_{yy} and σ_{xy}) at IntPtA and (b) LMSC-predicted ('Pred') and reference ('Real') stress–strain evolution ($\sigma_{yy} - \varepsilon_{yy}$) at IntPtA points during the 3DS rail forming static/implicit simulation.

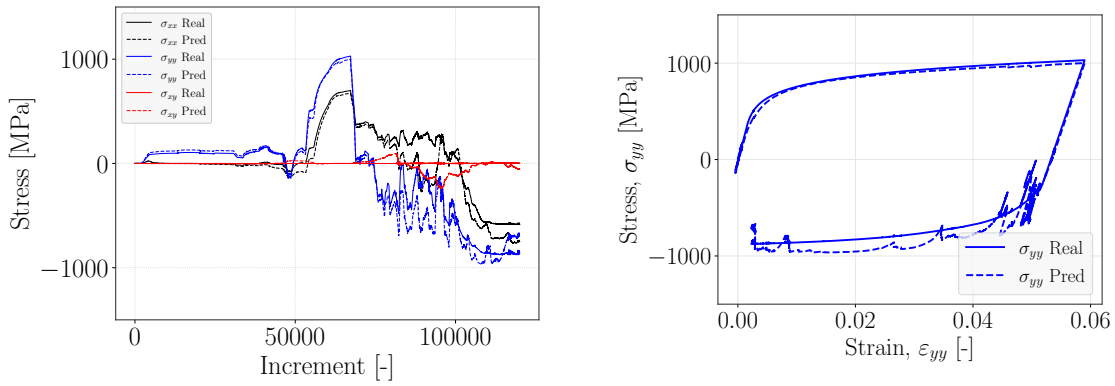
The dynamic/explicit simulation of the 3DS rail forming case uses a substantially larger number of increments than the static runs (approximately 10^4 rather than $\sim 10^2$), resulting in strain increment magnitudes that are approximately two orders of magnitude smaller. Figure 5.43 shows the strain history at IntPtA under these conditions.



(a) (b)

Figure 5.43: Strain components (ε_{xx}, ε_{yy} and ε_{xy}) and corresponding strain increments ($\Delta\varepsilon$) for the selected integration points during the 3DS rail forming dynamic/explicit simulation at IntPtA.

Despite the drastic change in time discretization, the surrogate model remains stable and consistent. As shown in Figure 5.44, the extracted stress histories follow the expected trends and are comparable to those from the static run (Figure 5.41). The finer resolution exposes local fluctuations in the increments, especially during the plateau and reversal phases, yet the LMSC surrogate continues to reproduce the underlying constitutive behavior, confirming self-consistency across very different increment sizes. The mean relative errors per sample are higher than in the static case for the dominant components, with σ_{xx} at 35.76% and σ_{yy} at 37.32% this reflects the increased sensitivity introduced by the much smaller strain increments, especially following strain-path changes. Figure 5.44(b) isolates the primary relation σ_{yy}-ε_{yy} at IntPtB. The monotonic portion of the curve is well captured by the surrogate model, with predicted and reference paths closely overlapping. Deviations become more pronounced after the strain-path inversion, where the nonlinearity and subtle reversal effects introduce differences. However, the predicted and reference curves remain similar in shape, indicating that the underlying constitutive trend is preserved. Overall, the results indicate that the LMSC surrogate maintains qualitative fidelity under dynamic/explicit conditions, while localized transitions and reversals are the dominant sources of increased quantitative error.



(a) (b)

Figure 5.44: Comparison between (a) LMSC-predicted ('Pred') and reference ('Real') stress components (σ_{xx}, σ_{yy} and σ_{xy}) at IntPtA and (b) LMSC-predicted ('Pred') and reference ('Real') stress–strain evolution ($\sigma_{yy} - \varepsilon_{yy}$) at IntPtA points during the 3DS rail forming dynamic/explicit simulation.

5.5 Discussion and Final Remarks

The results presented in this chapter demonstrate that the Linearized Minimal State Cell framework provides a robust, purely data-driven surrogate for path-dependent plasticity, with the capacity to capture Bauschinger effects in advanced high-strength steels such as DP780. While prior studies mainly demonstrated the applicability of this class of models as surrogates for J2 plasticity with isotropic hardening [185; 186], the present work extends their use to more complex constitutive behavior, including anisotropic yield and hardening models (e.g., YLD2000-2d coupled with HAH).

To enable direct comparison with prior work, the numerically generated datasets followed the types and generation procedures of random-walk (RW) and smooth-walk (SW) trajectories as described in the literature. Different generalization behaviors emerged between RW and SW trajectories. RW paths continue to present new features as the model's capacity increases due to their abrupt directional changes and local noise. This yields consistently lower validation and test errors up to approximately 10^5 parameters. In contrast, SW trajectories have low complexity and therefore a model with $\sim 10^4$ parameters is sufficient and additional capacity offers little benefit. Hyperparameter tuning revealed that an internal state dimension (n_s) between 20 and 40 is sufficient to capture history effects of the traing dataset

considering both RW and SW. Larger values produce negligible benefit, while smaller values (e.g., $n_s = 5$) lead to overfitting. Layer width (w) has a stronger influence on predictive performance than network depth (d), suggesting that, for LMSC surrogate model, widening internal layers should be prioritized over deepening them.

After hyperparameter tuning, the optimized architecture ($n_s = 40$, d = 4, w = 100) was evaluated. For this network structure, the training and validation mean squared error fall within the range of 10^{-3}, consistent with the values presented in the literature. Additionally, the surrogate model accurately predicts all three local stress components on the test dataset, which contains 724 RW and 375 SW cases. The MSE for RW is approximately 7×10^{-4} and for SW is approximately 2.3×10^{-3}. For all three stress components at least 90% of the predictions present a stress relative error below 10%. Only a very small fraction (less than 1–2%) exceeds stress relative error of 100%, almost exclusively when $|\sigma_{\text{true}}|$ is near zero, where small absolute deviations produce large relative percentages. On average, the mean relative error remains low for the majority of paths. Excluding outliers, RW sequences typically lie within a 6-7% MRE, while SW sequences lie within an 11-12% MRE. Outliers are limited to approximately 2-7% of the cases and reach a mean relative error of approximately 25%.

With approximately 5000 RW and 2500 SW training cases, the trained LMSC model reproduces stress–strain histories with acceptable performance. The main limitation arises at strain-path reversals, particularly tension–compression and reverse shear loading paths. In these cases loading and unloading segments are well captured, but the immediate post-reversal response is typically overestimated. To address this, the training set was expanded with two specific types of new trajectories: (i) noise-free random-walk trajectories in order to capture with more detail the Bauschinger behavior without being influenced by noise and (ii) single-mode sequences, where only one strain component varies. After retraining the LMSC model on the expanded dataset, reversal accuracy improved significantly: the mean relative error in the dominant stress component decreased by at least half for all the evaluated cases, the post-reversal overshoot was reduced and predicted curves realigned more rapidly with the reference responses.

An additional contribution of this work was the evaluation of the LMSC surrogate model on finite-element based strain trajectories ranging from uniaxial tensile test and near industrial forming cases such as the rail forming of 3DS benchmark. This evaluation prove the excellent self-consistency of the trained model under both implicit/static and explicit/dynamic integration schemes. Even when using time

steps two to three orders of magnitude smaller than in the static runs, the surrogate closely reproduced the YLD2000-2d + HAH stress histories. This offline evaluation strategy, which involves generating strain histories using the FE solver and querying the surrogate externally, is a key intermediate step before embedding the LMSC in a UMAT/VUMAT subroutine of Abaqus FE code.

Overall, the LMSC surrogate achieves high performance and strong generalization capabilities across heterogeneous loading paths, capturing anisotropy and Bauschinger effects and remaining stable under large changes in time discretization. The remaining difficulties concentrate around sharp path inversions and mixed loading states. These can be mitigated through targeted data enrichment (e.g., adding specific reversal sequences) and physics-guided regularization (e.g., enforcing dissipation consistency). Future work will extend the LMSC surrogate beyond DP780 using transfer learning. The plan is to first pretrain a model using large synthetic RW/SW datasets and then fine-tune using small, targeted experimental campaigns for other AHSS grades. Since the underlying deformation mechanisms are similar across these materials, only modest fine-tuning will be necessary, which will reduce the scope of new testing. Recent preliminary studies have explored this concept. Heidenreich et al. [186] showed that pretraining sequence-based plasticity surrogates on broad synthetic histories and fine-tuning them on small, targeted experimental sets can reduce data requirements and training time while preserving path-dependence fidelity. A parallel direction is full finite-element integration of the LMSC via UMAT/VUMAT-style user subroutines. This implementation should be designed to be efficient by taking advantage of recurrent and closed-form updates instead of conventional return-mapping schemes. Integrating the LMSC at element integration points leverages its low inference cost, delivering competitive runtime performance compared to traditional constitutive updates while maintaining the self-consistency demonstrated in offline evaluations.

Chapter 6

Conclusions

This thesis explored the potential of machine learning for constitutive modeling of advanced high-strength steels, with a particular focus on their anisotropic and path-dependent behavior in sheet metal forming processes. The work combined experimental characterization, parameter identification and the development of fully data-driven constitutive models, aiming to bridge the gap between classical phenomenological formulations and modern data-driven strategies.

The experimental campaign carried out on three dual-phase steels (DP500, DP600, DP780) provided a reliable basis for constitutive model calibration. It included both monotonic and reverse loading tests, supported by novel testing devices such as the Miniaturized Specimen Tester Device (MSTD). These tests enabled the assessment of key features including anisotropy, the Bauschinger effect and degradation of Young's modulus, while demonstrating the efficiency of miniaturized testing strategies. A particularly relevant result was the ability of miniaturized compression specimens to reach plastic strains of approximately 7% without buckling, eliminating the need for lateral supports. Reverse shear tests conducted with miniaturized specimens adapted from the ASTM B831-05 standard geometry showed good agreement with reference single-gauge specimens from the literature and allowed stable characterization at higher strain levels after inversion ($\varepsilon_{xy} = -0.2$), without instabilities. These results confirmed the suitability of the MSTD for investigating anisotropic and kinematic hardening effects. The same device was also used to study the degradation of Young's modulus with plastic strain, showing a reduction of approximately 19% for DP500 and about 24% for both DP600 and DP780. In parallel, a reverse bending experimental setup was developed to characterize cyclic bending behavior of sheet metal materials, representative of industrial sheet forming operations. A key advantage of this setup is its ability to evaluate elastic recovery at the end of

each loading phase, offering direct insights into cyclic hardening and springback.

Building on this foundation, machine learning was applied to the identification of isotropic and anisotropic hardening laws using Long Short-Term Memory (LSTM) networks trained on bending and reverse bending curves. For isotropic hardening, the network received as input the punch force–displacement curves obtained from monotonic bending tests, with the Swift parameters (K, n, ε_0) and the Young's modulus (E) as outputs. In the case of anisotropic hardening, reverse bending tests were used, where the complete bending–unbending–rebending sequence served as input and the corresponding hardening parameters $(K, n, \varepsilon_0, C, \gamma)$ were predicted, capturing both isotropic and kinematic contributions. The use of LSTMs proved effective in exploiting the sequential nature of the data, enabling a direct mapping between experimental curves and constitutive parameters. The trained models achieved high predictive accuracy: Young's modulus was estimated with errors consistently below 3%, while isotropic hardening parameters were identified with mean relative errors between 0.7% and 1.5%, with more than 90% of the predictions below 4% and only 6–9% classified as outliers. In contrast, the kinematic hardening parameters exhibited greater variability, with mean relative errors of about 7% and the majority of cases below 10%. Approximately 11% of the predictions were identified as outliers, including some extreme deviations and occasional non-physical results. This issue was largely resolved by incorporating physical constraints into the loss function, which reduced the occurrence of negative predictions for C and γ. In addition, a force–displacement normalization procedure was introduced, which proved effective in mitigating the effect of small thickness variations (± 0.1 mm) while maintaining low stress errors, further validating the methodology. Transfer learning strategies significantly improved computational efficiency, reducing training time by up to 80% and enhancing the adaptability of the models to variations in material thickness and test conditions. Experimental validation with DP500, DP600 and DP780 steels confirmed the robustness of the proposed methodology, demonstrating that ML-based identification not only reproduces the results of conventional parameter calibration but also provides a viable and efficient alternative for the characterization of advanced high-strength steels.

The thesis also explored the development of fully data-driven constitutive models by applying the Linearized Minimal State Cells (LMSC) recurrent architecture, to advanced high-strength steels, specifically DP780, incorporating anisotropic yield and hardening laws. Through systematic hyperparameter tuning, it was found that an internal state dimension between 20 and 40 provided the best balance between

accuracy and generalization. Moreover, the width of the hidden layers had a stronger influence on predictive performance than network depth, indicating that widening the architecture is more beneficial than deepening it for this class of surrogate models. With this optimized configuration, the models accurately reproduced nonlinear and path-dependent stress–strain responses, achieving mean squared errors on the order of 10^{-3}, with more than 90% of predictions within 10% relative stress error. Although outliers persisted in 2–7% of the cases, particularly in post-reversal segments, targeted data enrichment strategies substantially reduced these deviations and improved post-reversal performance. Validation against FE–based strain paths, including benchmark forming cases, further confirmed the robustness of the approach across static and dynamic formulations and under different time increment sizes, demonstrating its potential as a reliable surrogate for industrial applications.

A central role throughout this work was played by recurrent neural architectures, whose ability to capture sequential dependencies proved particularly effective in mapping experimental curves to constitutive parameters and in reproducing nonlinear stress–strain histories with path dependence and reversals. This recurrent framework, explored here for constitutive modeling, also finds application at the process level, as illustrated by the complementary study included in the Appendix G, where recurrent neural networks were applied to identify sources of uncertainty in sheet metal forming operations. Together, these contributions demonstrate the potential of machine learning, specifically recurrent neural networks, to advance constitutive modeling of advanced high-strength steels, establishing a solid foundation for future developments and their integration into industrial sheet metal forming simulations.

6.1 Future Work

For a deeper understanding of the topics investigated in this thesis, future work should pursue further developments along different directions. With this perspective in mind, the following outlook is structured according to the three main axes of this work: experimental testing, parameter identification and fully data-driven modeling.

Regarding the experimental contributions, although the dataset generated in Chapter 3 is comprehensive, it still represents a limited subset of the complex strain paths encountered in industrial forming and is therefore insufficient to support the development of fully data-driven ML models. Future experimental efforts should focus on developing methods to generate richer and more diverse data. In this context, robotic testing systems can play a central role in improving efficiency and enabling

automated execution of complex loading sequences. Miniaturized tests would further enhance feasibility by reducing material consumption while still capturing the relevant deformation mechanisms. Combined with full-field measurement techniques, these developments would provide detailed and varied datasets across a broad spectrum of strain histories, ultimately delivering the experimental data needed to fully exploit ML in constitutive modeling.

In the domain of parameter identification, future developments should aim at enriching the data available for training by incorporating full-field measurements, such as strain fields obtained from digital image correlation, which can provide richer input features and improve model robustness. Additionally, transfer learning approaches should be further explored not only as a means of reusing knowledge across different materials and test conditions, but also for adapting models to alternative constitutive formulations, thereby reducing data requirements and enhancing the applicability of ML-based identification methods in industrial settings.

Finally, concerning fully data-driven constitutive models, future research should further explore transfer learning to extend trained surrogates beyond DP780 and adapt them to other Advanced High-Strength Steels (AHSS) grades. By reusing knowledge from one steel and fine-tuning with a smaller set of targeted tests, this strategy can reduce the need for extensive experimental campaigns, shorten training times and improve adaptability across materials, making ML-based constitutive modeling more practical for industrial applications. Equally important is the establishment of standardized benchmark datasets for material behavior, similar to the role played by *MNIST* [293] in computer vision, to ensure reproducibility, comparability and faster progress across the community. In parallel, the direct implementation of LMSC models into commercial finite element solvers via UMAT/VUMAT Abaqus code routines should be explored, enabling efficient integration at the element level and paving the way for real-time application in large-scale forming simulations.

References

[1] Maria E. Mondejar, Ram Avtar, Heyker Lellani Baños Diaz, Rama Kant Dubey, Jesús Esteban, Abigail Gómez-Morales, Brett Hallam, Nsilulu Tresor Mbungu, Chukwuebuka Christopher Okolo, Kumar Arun Prasad, Qianhong She, and Sergi Garcia-Segura. Digitalization to achieve sustainable development goals: Steps towards a smart green planet. *Science of The Total Environment*, 794:148539, November 2021. ISSN 0048-9697. doi: 10.1016/j.scitotenv.2021.148539. URL `http://dx.doi.org/10.1016/j.scitotenv.2021.148539`.

[2] Elias G. Carayannis and Joanna Morawska-Jancelewicz. The futures of europe: Society 5.0 and industry 5.0 as driving forces of future universities. *Journal of the Knowledge Economy*, 13(4):3445–3471, January 2022. ISSN 1868-7873. doi: 10.1007/s13132-021-00854-2. URL `http://dx.doi.org/10.1007/s13132-021-00854-2`.

[3] Klaus Schwab. *The Fourth Industrial Revolution*. Crown Business, 2017.

[4] Violeta Sima, Ileana Georgiana Gheorghe, Jonel Subić, and Dumitru Nancu. Influences of the industry 4.0 revolution on the human capital development and consumer behavior: A systematic review. *Sustainability*, 12(10):4035, May 2020. ISSN 2071-1050. doi: 10.3390/su12104035. URL `http://dx.doi.org/10.3390/su12104035`.

[5] M. C. Bishop. *Pattern Recognition and Machine Learning*. Information Science and Statistics. Springer, New York, NY, 2006.

[6] Pedro Prates and André Pereira. Recent advances and applications of machine learning in metal forming processes. *Metals*, 12(8):1342, 2022. ISSN 2075-4701. doi: 10.3390/met12081342. URL `http://dx.doi.org/10.3390/met12081342`.

[7] Vinod Laxman Hattalli and Shivashankar R. Srivatsa. Sheet metal forming processes – recent technological advances. *Materials Today: Proceedings*, 5: 2564–2574, 2018.

[8] M. A. Dib, N. J. Oliveira, A. E. Marques, M. C. Oliveira, J. V. Fernandes, B. M. Ribeiro, and P. A. Prates. Single and ensemble classifiers for defect prediction in sheet metal forming under variability. *Neural Computing and Applications*, 32(16):12335–12349, 2019. ISSN 1433-3058. doi: 10.1007/s00521-019-04651-6. URL `http://dx.doi.org/10.1007/s00521-019-04651-6`.

[9] Pedro André Dias Prates. *Inverse Methodologies for Identifying Constitutive Parameters of Metal Sheets*. PhD thesis, Universidade de Coimbra (Portugal), 2014.

[10] Joseba Mendiguren, Juan J. Trujillo, Fernando Cortés, and Lander Galdos. An extended elastic law to represent non-linear elastic behaviour: Application in computational metal forming. *International Journal of Mechanical Sciences*, 77:57–64, 2013. ISSN 0020-7403. doi: 10.1016/j.ijmecsci.2013.09.026. URL `http://dx.doi.org/10.1016/j.ijmecsci.2013.09.026`.

[11] Daniele Versino, Alberto Tonda, and Curt A. Bronkhorst. Data driven modeling of plastic deformation. *Computer Methods in Applied Mechanics and Engineering*, 318:981–1004, 2017. ISSN 0045-7825. doi: 10.1016/j.cma.2017.02.016. URL `http://dx.doi.org/10.1016/j.cma.2017.02.016`.

[12] Hamdi Aguir, Hédi BelHadjSalah, and Ridha Hambli. Parameter identification of an elasto-plastic behaviour using artificial neural networks–genetic algorithm method. *Materials amp; Design*, 32(1):48–53, January 2011. ISSN 0261-3069. doi: 10.1016/j.matdes.2010.06.039. URL `http://dx.doi.org/10.1016/j.matdes.2010.06.039`.

[13] Armando E. Marques, Tomás G. Parreira, André F.G. Pereira, Bernardete M. Ribeiro, and Pedro A. Prates. Machine learning applications in sheet metal constitutive modelling: A review. *International Journal of Solids and Structures*, 303:113024, October 2024. ISSN 0020-7683. doi: 10.1016/j.ijsolstr.2024.113024. URL `http://dx.doi.org/10.1016/j.ijsolstr.2024.113024`.

[14] J. Ghaboussi and D.E. Sidarta. New nested adaptive neural networks (nann) for constitutive modeling. *Computers and Geotechnics*, 22(1):29–52, January

1998. ISSN 0266-352X. doi: 10.1016/s0266-352x(97)00034-7. URL http://dx.doi.org/10.1016/S0266-352X(97)00034-7.

[15] Johannes Dornheim, Lukas Morand, Hemanth Janarthanam Nallani, and Dirk Helm. Neural networks for constitutive modeling: From universal function approximators to advanced models and the integration of physics. *Archives of Computational Methods in Engineering*, 31(2):1097–1127, October 2023. ISSN 1886-1784. doi: 10.1007/s11831-023-10009-y. URL http://dx.doi.org/10.1007/s11831-023-10009-y.

[16] Filippo Masi, Ioannis Stefanou, Paolo Vannucci, and Victor Maffi-Berthier. Thermodynamics-based artificial neural networks for constitutive modeling. *Journal of the Mechanics and Physics of Solids*, 147:104277, February 2021. ISSN 0022-5096. doi: 10.1016/j.jmps.2020.104277. URL http://dx.doi.org/10.1016/j.jmps.2020.104277.

[17] Jean Besson, Gilles Cailletaud, Jean-Louis Chaboche, and Samuel Forest. *Non-Linear Mechanics of Materials*. Springer, 2010. ISBN 978-90-481-3355-5. doi: 10.1007/978-90-481-3356-2. URL https://link.springer.com/book/10.1007/978-90-481-3356-2.

[18] G. I. Taylor and C. F. Elam. Bakerian lecture. the distortion of an aluminium crystal during a tensile test. *Proceedings of the Royal Society of London. Series A, Containing Papers of a Mathematical and Physical Character*, 102 (719):643–667, 1923. ISSN 09501207. doi: 10.1098/rspa.1923.0023. URL http://dx.doi.org/10.1098/rspa.1923.0023.

[19] E. Schmid, W. Boas, and F. I. G. Rawlins. Kristallplastizit¨at. *The Journal of Physical Chemistry*, 39, 1934.

[20] Tiago Jordao Grilo. *Development of computational anisotropic hypoelastic-and hyperelastic-based modelsincluding nonlinear kinematic hardening*. PhD thesis, Universidade de Aveiro Departamento de Engenharia Mecanica, 2015.

[21] F. Adzima, T. Balan, P.Y. Manach, N. Bonnet, and L. Tabourot. Crystal plasticity and phenomenological approaches for the simulation of deformation behavior in thin copper alloy sheets. *International Journal of Plasticity*, 94: 171–191, 2017. ISSN 0749-6419. doi: 10.1016/j.ijplas.2016.06.003. URL http://dx.doi.org/10.1016/j.ijplas.2016.06.003.

[22] F. Roters, P. Eisenlohr, L. Hantcherli, D.D. Tjahjanto, T.R. Bieler, and D. Raabe. Overview of constitutive laws, kinematics, homogenization and multiscale methods in crystal plasticity finite-element modeling: Theory, experiments, applications. *Acta Materialia*, 58(4):1152–1211, 2010. ISSN 1359-6454. doi: 10.1016/j.actamat.2009.10.058. URL `http://dx.doi.org/10.1016/j.actamat.2009.10.058`.

[23] Dorel Banabic. *Sheet Metal Forming Processes*. Springer Berlin Heidelberg, 2010. ISBN 9783540881131. doi: 10.1007/978-3-540-88113-1. URL `http://dx.doi.org/10.1007/978-3-540-88113-1`.

[24] P. A. Prates, A. F. G. Pereira, N. A. Sakharova, M. C. Oliveira, and J. V. Fernandes. Inverse strategies for identifying the parameters of constitutive laws of metal sheets. *Advances in Materials Science and Engineering*, 2016: 1–18, 2016. ISSN 1687-8442. doi: 10.1155/2016/4152963. URL `http://dx.doi.org/10.1155/2016/4152963`.

[25] F. Latourte, A. Chrysochoos, S. Pagano, and B. Wattrisse. Elastoplastic behavior identification for heterogeneous loadings and materials. *Experimental Mechanics*, 48(4):435–449, October 2007. ISSN 1741-2765. doi: 10.1007/s11340-007-9088-y. URL `http://dx.doi.org/10.1007/s11340-007-9088-y`.

[26] Jiawei Fu, Frédéric Barlat, Jin-Hwan Kim, and Fabrice Pierron. Application of the virtual fields method to the identification of the homogeneous anisotropic hardening parameters for advanced high strength steels. *International Journal of Plasticity*, 93:229–250, June 2017. ISSN 0749-6419. doi: 10.1016/j.ijplas.2016.07.013. URL `http://dx.doi.org/10.1016/j.ijplas.2016.07.013`.

[27] Jean Noël Périé, Hugo Leclerc, Stéphane Roux, and François Hild. Digital image correlation and biaxial test on composite material for anisotropic damage law identification. *International Journal of Solids and Structures*, 46(11–12): 2388–2396, June 2009. ISSN 0020-7683. doi: 10.1016/j.ijsolstr.2009.01.025. URL `http://dx.doi.org/10.1016/j.ijsolstr.2009.01.025`.

[28] B.M. Chaparro, S. Thuillier, L.F. Menezes, P.Y. Manach, and J.V. Fernandes. Material parameters identification: Gradient-based, genetic and hybrid optimization algorithms. *Computational Materials Science*, 44(2):339–346, De-

cember 2008. ISSN 0927-0256. doi: 10.1016/j.commatsci.2008.03.028. URL http://dx.doi.org/10.1016/j.commatsci.2008.03.028.

[29] MA Sutton, Cheng Mingqi, WH Peters, YJ Chao, and SR McNeill. Application of an optimized digital correlation method to planar deformation analysis. *Image and Vision Computing*, 4(3):143–150, August 1986. ISSN 0262-8856. doi: 10.1016/0262-8856(86)90057-0. URL http://dx.doi.org/10.1016/0262-8856(86)90057-0.

[30] Stéphane Avril, Marc Bonnet, Anne-Sophie Bretelle, Michel Grédiac, François Hild, Patrick Ienny, Félix Latourte, Didier Lemosse, Stéphane Pagano, Emmanuel Pagnacco, and Fabrice Pierron. Overview of identification methods of mechanical parameters based on full-field measurements. *Experimental Mechanics*, 48(4):381–402, 2008. ISSN 1741-2765. doi: 10.1007/s11340-008-9148-y. URL http://dx.doi.org/10.1007/s11340-008-9148-y.

[31] Rubén Ibáñez, Emmanuelle Abisset-Chavanne, David González, Jean-Louis Duval, Elias Cueto, and Francisco Chinesta. Hybrid constitutive modeling: data-driven learning of corrections to plasticity models. *International Journal of Material Forming*, 12(4):717–725, 2018. ISSN 1960-6214. doi: 10.1007/s12289-018-1448-x. URL http://dx.doi.org/10.1007/s12289-018-1448-x.

[32] M.A. Bessa, R. Bostanabad, Z. Liu, A. Hu, Daniel W. Apley, C. Brinson, W. Chen, and Wing Kam Liu. A framework for data-driven analysis of materials under uncertainty: Countering the curse of dimensionality. *Computer Methods in Applied Mechanics and Engineering*, 320:633–667, June 2017. ISSN 0045-7825. doi: 10.1016/j.cma.2017.03.037. URL http://dx.doi.org/10.1016/j.cma.2017.03.037.

[33] Tarek Iraki, Lukas Morand, Johannes Dornheim, Norbert Link, and Dirk Helm. A multi-task learning-based optimization approach for finding diverse sets of microstructures with desired properties. *Journal of Intelligent Manufacturing*, 35(4):1887–1903, May 2023. ISSN 1572-8145. doi: 10.1007/s10845-023-02139-8. URL http://dx.doi.org/10.1007/s10845-023-02139-8.

[34] R. Liu, A. Kumar, Z. Chen, A. Agrawal, V. Sundararaghavan, and A. Choudhary. A predictive machine learning approach for microstructure optimization and materials design. *Scientific Reports*, 5(1):1–12, 2015.

[35] Johannes Dornheim, Norbert Link, and Peter Gumbsch. Model-free adaptive optimal control of episodic fixed-horizon manufacturing processes using reinforcement learning. *International Journal of Control, Automation and Systems*, 18(6):1593–1604, December 2019. ISSN 2005-4092. doi: 10.1007/s12555-019-0120-7. URL `http://dx.doi.org/10.1007/s12555-019-0120-7`.

[36] S. Liu, Z. Shi, J. Lin, and Z. Li. Reinforcement learning in free-form stamping of sheet-metals. *Procedia Manufacturing*, 50:444–449, 2020.

[37] Francisco Chinesta, Elias Cueto, Emmanuelle Abisset-Chavanne, Jean Louis Duval, and Fouad El Khaldi. Virtual, digital and hybrid twins: A new paradigm in data-based engineering and engineered data. *Archives of Computational Methods in Engineering*, 27(1):105–134, November 2018. ISSN 1886-1784. doi: 10.1007/s11831-018-9301-4. URL `http://dx.doi.org/10.1007/s11831-018-9301-4`.

[38] G. Anand, Swarnava Ghosh, Liwei Zhang, Angesh Anupam, Colin L. Freeman, Christoph Ortner, Markus Eisenbach, and James R. Kermode. Exploiting machine learning in multiscale modelling of materials. *Journal of The Institution of Engineers (India): Series D*, 104(2):867–877, November 2022. ISSN 2250-2130. doi: 10.1007/s40033-022-00424-z. URL `http://dx.doi.org/10.1007/s40033-022-00424-z`.

[39] Zeliang Liu, C.T. Wu, and M. Koishi. A deep material network for multiscale topology learning and accelerated nonlinear modeling of heterogeneous materials. *Computer Methods in Applied Mechanics and Engineering*, 345:1138–1168, March 2019. ISSN 0045-7825. doi: 10.1016/j.cma.2018.09.020. URL `http://dx.doi.org/10.1016/j.cma.2018.09.020`.

[40] Y.C. Lin, Jun Zhang, and Jue Zhong. Application of neural networks to predict the elevated temperature flow behavior of a low alloy steel. *Computational Materials Science*, 43(4):752–758, October 2008. ISSN 0927-0256. doi: 10.1016/j.commatsci.2008.01.039. URL `http://dx.doi.org/10.1016/j.commatsci.2008.01.039`.

[41] Kurt Hornik, Maxwell Stinchcombe, and Halbert White. Multilayer feedforward networks are universal approximators. *Neural Networks*, 2(5):359–366, 1989. ISSN 0893-6080. doi: 10.1016/0893-6080(89)90020-8. URL http://dx.doi.org/10.1016/0893-6080(89)90020-8.

[42] Arthur L. Samuel. Some studies in machine learning using the game of checkers. i. In *Computer Games I*, pages 335–365. Springer New York, 1988. doi: 10.1007/978-1-4613-8716-9_14. URL https://doi.org/10.1007/978-1-4613-8716-9_14.

[43] Alberto Diez Oliván. *Machine Learning for Data-driven Prognostics : Methods and Applications*. PhD thesis, Universidad Politecnica de Madrid - University Library, 2017.

[44] Issam El Naqa and Martin J. Murphy. What is machine learning? In *Machine Learning in Radiation Oncology*, pages 3–11. Springer International Publishing, 2015. doi: 10.1007/978-3-319-18305-3_1. URL https://doi.org/10.1007/978-3-319-18305-3_1.

[45] Syed Mohtashim Mian, Mohammad Shuaib Khan, Mohd Shawez, and Amandeep Kaur. Artificial intelligence (ai), machine learning (ml) amp; deep learning (dl): A comprehensive overview on techniques, applications and research directions. In *2024 2nd International Conference on Sustainable Computing and Smart Systems (ICSCSS)*, page 1404–1409. IEEE, 2024. doi: 10.1109/icscss60660.2024.10625198. URL http://dx.doi.org/10.1109/ICSCSS60660.2024.10625198.

[46] Ian Goodfellow, Yoshua Bengio, and Aaron Courville. *Deep Learning*. MIT Press, 2016.

[47] Kevin P. Murphy. *Machine Learning: A Probabilistic Perspective*. MIT Press, 2012.

[48] Richard S. Sutton and Andrew G. Barto. *Reinforcement Learning: An Introduction*. MIT Press, 2nd edition, 2018.

[49] Simon Haykin. *Neural Networks: A Comprehensive Foundation*. Prentice Hall, 1998.

[50] David E. Rumelhart, Geoffrey E. Hinton, and Ronald J. Williams. Learning representations by back-propagating errors. *Nature*, 323(6088):533–536, October 1986. ISSN 1476-4687. doi: 10.1038/323533a0. URL http://dx.doi.org/10.1038/323533a0.

[51] Vinod Nair and Geoffrey E Hinton. Rectified linear units improve restricted boltzmann machines. pages 807–814, 2010.

[52] J. Hertz, A. Krogh, and R. G Palmer. *Introduction To The Theory Of Neural Computation*, volume 44. CRC Press, 1991. doi: 10.1063/1.2810360.

[53] Tianyi Liu, Shuangsang Fang, Yuehui Zhao, Peng Wang, and Jun Zhang. Implementation of training convolutional neural networks, 2015. URL https://arxiv.org/abs/1506.01195.

[54] Keiron O'Shea and Ryan Nash. An introduction to convolutional neural networks. 2015. doi: 10.48550/ARXIV.1511.08458. URL https://arxiv.org/abs/1511.08458.

[55] Robin M. Schmidt. Recurrent neural networks (rnns): A gentle introduction and overview. 2019. doi: 10.48550/ARXIV.1912.05911. URL https://arxiv.org/abs/1912.05911.

[56] Alex Sherstinsky. Fundamentals of recurrent neural network (RNN) and long short-term memory (LSTM) network. *Physica D: Nonlinear Phenomena*, 404: 132306, March 2020. doi: 10.1016/j.physd.2019.132306. URL https://doi.org/10.1016/j.physd.2019.132306.

[57] Sepp Hochreiter and Jürgen Schmidhuber. Long short-term memory. *Neural Computation*, 9(8):1735–1780, November 1997. ISSN 1530-888X. doi: 10.1162/neco.1997.9.8.1735. URL http://dx.doi.org/10.1162/neco.1997.9.8.1735.

[58] Dario Amodei, Rishita Anubhai, Eric Battenberg, Carl Case, Jared Casper, Bryan Catanzaro, Jingdong Chen, Mike Chrzanowski, Adam Coates, Greg Diamos, Erich Elsen, Jesse Engel, Linxi Fan, Christopher Fougner, Tony Han, Awni Hannun, Billy Jun, Patrick LeGresley, Libby Lin, Sharan Narang, Andrew Ng, Sherjil Ozair, Ryan Prenger, Jonathan Raiman, Sanjeev Satheesh, David Seetapun, Shubho Sengupta, Yi Wang, Zhiqian Wang, Chong Wang, Bo Xiao, Dani Yogatama, Jun Zhan, and Zhenyao Zhu. Deep speech

2: End-to-end speech recognition in english and mandarin. 2015. doi: 10.48550/ARXIV.1512.02595. URL https://arxiv.org/abs/1512.02595.

[59] William Chan, Navdeep Jaitly, Quoc V. Le, and Oriol Vinyals. Listen, attend and spell. 2015. doi: 10.48550/ARXIV.1508.01211. URL https://arxiv.org/abs/1508.01211.

[60] Aston Zhang, Zachary C. Lipton, Mu Li, and Alexander J. Smola. Dive into deep learning, 2021. URL https://arxiv.org/abs/2106.11342.

[61] Robert DiPietro and Gregory D. Hager. Deep learning: RNNs and LSTM. In *Handbook of Medical Image Computing and Computer Assisted Intervention*, pages 503–519. Elsevier, 2020. doi: 10.1016/b978-0-12-816176-0.00026-0. URL https://doi.org/10.1016/b978-0-12-816176-0.00026-0.

[62] Arka Daw, Anuj Karpatne, William Watkins, Jordan Read, and Vipin Kumar. Physics-guided neural networks (pgnn): An application in lake temperature modeling, 2017. URL https://arxiv.org/abs/1710.11431.

[63] Chuizheng Meng, Sungyong Seo, Defu Cao, Sam Griesemer, and Yan Liu. When physics meets machine learning: A survey of physics-informed machine learning, 2022. URL https://arxiv.org/abs/2203.16797.

[64] Tobias Pfaff, Meire Fortunato, Alvaro Sanchez-Gonzalez, and Peter W. Battaglia. Learning mesh-based simulation with graph networks. *CoRR*, abs/2010.03409, 2020. URL https://arxiv.org/abs/2010.03409.

[65] Xiaowei Jia, Jared Willard, Anuj Karpatne, Jordan S. Read, Jacob A. Zwart, Michael Steinbach, and Vipin Kumar. Physics-guided machine learning for scientific discovery: An application in simulating lake temperature profiles. *ACM/IMS Transactions on Data Science*, 2(3):1–26, May 2021. ISSN 2691-1922. doi: 10.1145/3447814. URL http://dx.doi.org/10.1145/3447814.

[66] Pongpisit Thanasutives, Masayuki Numao, and Ken-ichi Fukui. Adversarial multi-task learning enhanced physics-informed neural networks for solving partial differential equations. 2021. doi: 10.48550/ARXIV.2104.14320. URL https://arxiv.org/abs/2104.14320.

[67] George Em Karniadakis, Ioannis G. Kevrekidis, Lu Lu, Paris Perdikaris, Sifan Wang, and Liu Yang. Physics-informed machine learning. *Nature Reviews*

Physics, 3(6):422–440, 2021. doi: 10.1038/s42254-021-00314-5. URL https://doi.org/10.1038/s42254-021-00314-5.

[68] Maziar Raissi, Paris Perdikaris, and George Em Karniadakis. Physics informed deep learning (part i): Data-driven solutions of nonlinear partial differential equations. 2017. doi: 10.48550/arxiv.1711.10561. URL https://arxiv.org/abs/1711.10561.

[69] I.M Sobol'. On the distribution of points in a cube and the approximate evaluation of integrals. *USSR Computational Mathematics and Mathematical Physics*, 7(4):86–112, January 1967. ISSN 0041-5553. doi: 10.1016/0041-5553(67)90144-9. URL http://dx.doi.org/10.1016/0041-5553(67)90144-9.

[70] M. D. McKay, R. J. Beckman, and W. J. Conover. A comparison of three methods for selecting values of input variables in the analysis of output from a computer code. *Technometrics*, 21(2):239, May 1979. ISSN 0040-1706. doi: 10.2307/1268522. URL http://dx.doi.org/10.2307/1268522.

[71] Christiane Lemieux. *Monte Carlo and Quasi-Monte Carlo Sampling*. Springer Series in Statistics. Springer, New York, 2009. ISBN 978-0-387-78164-8. doi: 10.1007/978-0-387-78165-5. URL http://dx.doi.org/10.1007/978-0-387-78165-5.

[72] Stephen Joe and Frances Y. Kuo. Constructing sobol sequences with better two-dimensional projections. *SIAM Journal on Scientific Computing*, 30(5):2635–2654, 2008.

[73] Zhi-Hua Zhou. A brief introduction to weakly supervised learning. *National Science Review*, 5(1):44–53, August 2017. ISSN 2053-714X. doi: 10.1093/nsr/nwx106. URL http://dx.doi.org/10.1093/nsr/nwx106.

[74] James Bergstra and Yoshua Bengio. Random search for hyper-parameter optimization. *Journal of Machine Learning Research*, 13(2):281–305, 2012.

[75] Nitish Srivastava, Geoffrey Hinton, Alex Krizhevsky, Ilya Sutskever, and Ruslan Salakhutdinov. Dropout: a simple way to prevent neural networks from overfitting. *J. Mach. Learn. Res.*, 15(1):1929–1958, 2014. ISSN 1532-4435.

[76] Ron Kohavi. A study of cross-validation and bootstrap for accuracy estimation and model selection. In *Proceedings of the 14th International Joint Conference on Artificial Intelligence - Volume 2*, IJCAI'95, page 1137–1143, San Francisco, CA, USA, 1995. Morgan Kaufmann Publishers Inc. ISBN 1558603638.

[77] Sinno Jialin Pan and Qiang Yang. A survey on transfer learning. *IEEE Transactions on Knowledge and Data Engineering*, 22(10):1345–1359, October 2010. ISSN 1041-4347. doi: 10.1109/tkde.2009.191. URL `http://dx.doi.org/10.1109/TKDE.2009.191`.

[78] Tianyi Chai and Roland R Draxler. Root mean square error (rmse) or mean absolute error (mae)?—arguments against avoiding rmse in the literature. *Geoscientific Model Development*, 7(3):1247–1250, 2014.

[79] H.-É. Tresca. *Memoire sur l'ecoulement des corps solides soumis a de fortes pressions*. C. R. Acad. Sci., 1864.

[80] Huber MT. Przyczynek do podstaw wytorymalosci. *Czasopismo Techniczne*, 22:31–82, 1904.

[81] Mises R. Mechanics of solids in plastic state. *Göttinger Nachrichten MathematicalPhysics*, 4:582–592, 1913.

[82] Hencky H. On the theory of plastic deformations. *Zeitschrift für AngewandteMathematik und Mechanik*, 4:323–334, 1924.

[83] Bauscher JA Lankford WI, Snyder SC. New criteria for predicting the pressperformance of deep-drawing sheets. *Transaction ASM*, 42:1196–1232, 1950.

[84] ISO6892-1. Iso 6892-1 - metallic materials - tensile testing - method of test at room temperature. Standard, International Organization for Standardization, Geneva, CH, 2016.

[85] F. Barlat, J.C. Brem, J.W. Yoon, K. Chung, R.E. Dick, D.J. Lege, F. Pourboghrat, S.-H. Choi, and E. Chu. Plane stress yield function for aluminum alloy sheets—part 1: theory. *International Journal of Plasticity*, 19(9): 1297–1319, 2003. ISSN 0749-6419. doi: 10.1016/s0749-6419(02)00019-0. URL `http://dx.doi.org/10.1016/S0749-6419(02)00019-0`.

[86] Rodney Hill. A theory of the yielding and plastic flow of anisotropic metals. *Proceedings of the Royal Society of London. Series A. Mathematical and Physical Sciences*, 193(1033):281–297, 1948. doi: 10.1098/rspa.1948.0045.

[87] Juan Liao, Xin Xue, Myoung-Gyu Lee, Frédéric Barlat, Gabriela Vincze, and António B. Pereira. Constitutive modeling for path-dependent behavior and its influence on twist springback. *International Journal of Plasticity*, 93:64–88, June 2017. ISSN 0749-6419. doi: 10.1016/j.ijplas.2017.02.009. URL `http://dx.doi.org/10.1016/j.ijplas.2017.02.009`.

[88] J.H. Choi, S.L. Zang, M.G. Lee, J.H. Kim, and F. Barlat. Determining the coefficients of a homogeneous anisotropic hardening model for ultrathin steel sheets. *International Journal of Mechanical Sciences*, 157–158:428–438, July 2019. ISSN 0020-7403. doi: 10.1016/j.ijmecsci.2019.04.050. URL `http://dx.doi.org/10.1016/j.ijmecsci.2019.04.050`.

[89] J.L. Chaboche and O. Jung. Application of a kinematic hardening viscoplasticity model with thresholds to the residual stress relaxation. *International Journal of Plasticity*, 13(10):785–807, December 1997. ISSN 0749-6419. doi: 10.1016/s0749-6419(97)00066-1. URL `http://dx.doi.org/10.1016/S0749-6419(97)00066-1`.

[90] Muhammad Junaid Afzal, Fawad Maqbool, Ramin Hajavifard, Johannnes Buhl, Frank Walther, and Markus Bambach. Modeling the residual stresses induced in the metastable austenitic stainless steel disc springs manufactured by incremental sheet forming by a combined hardening model with phase transformation. *Procedia Manufacturing*, 47:1410–1415, 2020. ISSN 2351-9789. doi: 10.1016/j.promfg.2020.04.300. URL `http://dx.doi.org/10.1016/j.promfg.2020.04.300`.

[91] Ji He, Bin Gu, Yongfeng Li, and Shuhui Li. Forming limits under stretch-bending through distortionless and distortional anisotropic hardening. *Journal of Manufacturing Science and Engineering*, 140(12), October 2018. ISSN 1528-8935. doi: 10.1115/1.4041329. URL `http://dx.doi.org/10.1115/1.4041329`.

[92] F. Iob, F. Campanelli, and T. Coppola. Modelling of anisotropic hardening behavior for the fracture prediction in high strength steel line pipes. *Engineering Fracture Mechanics*, 148:363–382, November 2015. ISSN 0013-7944.

doi: 10.1016/j.engfracmech.2015.04.030. URL http://dx.doi.org/10.1016/j.engfracmech.2015.04.030.

[93] Annan Zhang and Dirk Mohr. Using neural networks to represent von mises plasticity with isotropic hardening. *International Journal of Plasticity*, 132: 102732, September 2020. ISSN 0749-6419. doi: 10.1016/j.ijplas.2020.102732. URL http://dx.doi.org/10.1016/j.ijplas.2020.102732.

[94] P. Ludwik. *Elemente der Technologischen Mechanik*. Springer Berlin Heidelberg, 1909. doi: 10.1007/978-3-662-40293-1. URL https://doi.org/10.1007/978-3-662-40293-1.

[95] J. H. Hollomon. Tensile deformation. *Transactions of the Metallurgical Society of AIME*, 162, 1945.

[96] H.W. Swift. Plastic instability under plane stress. *Journal of the Mechanics and Physics of Solids*, 1(1):1–18, October 1952. ISSN 0022-5096. doi: 10.1016/0022-5096(52)90002-1. URL http://dx.doi.org/10.1016/0022-5096(52)90002-1.

[97] E. Voce. The relationship between stress and strain for homogeneous deformations. *Journal of the Institute of Metals*, 1948.

[98] Ji Hyun Sung, Ji Hoon Kim, and R.H. Wagoner. A plastic constitutive equation incorporating strain, strain-rate, and temperature. *International Journal of Plasticity*, 26(12):1746–1771, December 2010. ISSN 0749-6419. doi: 10.1016/j.ijplas.2010.02.005. URL http://dx.doi.org/10.1016/j.ijplas.2010.02.005.

[99] B. Scott Kessler, A. Sherif El-Gizawy, and Douglas E. Smith. Incorporating neural network material models within finite element analysis for rheological behavior prediction. *Journal of Pressure Vessel Technology*, 129 (1):58–65, 2006. ISSN 1528-8978. doi: 10.1115/1.2389004. URL http://dx.doi.org/10.1115/1.2389004.

[100] J.H. Schmitt, E.L. Shen, and J.L. Raphanel. A parameter for measuring the magnitude of a change of strain path: Validation and comparison with experiments on low carbon steel. *International Journal of Plasticity*, 10(5): 535–551, January 1994. ISSN 0749-6419. doi: 10.1016/0749-6419(94)90013-2. URL http://dx.doi.org/10.1016/0749-6419(94)90013-2.

[101] Frédéric Barlat, José J. Gracio, Myoung-Gyu Lee, Edgar F. Rauch, and Gabriela Vincze. An alternative to kinematic hardening in classical plasticity. *International Journal of Plasticity*, 27(9):1309–1327, September 2011. ISSN 0749-6419. doi: 10.1016/j.ijplas.2011.03.003. URL http://dx.doi.org/10.1016/j.ijplas.2011.03.003.

[102] Huachao Yang, Wen Zhang, Xincun Zhuang, and Zhen Zhao. Phenomenological modeling of deformation-induced anisotropic hardening behaviors: A review. *Metals*, 13(2):364, February 2023. ISSN 2075-4701. doi: 10.3390/met13020364. URL http://dx.doi.org/10.3390/met13020364.

[103] Seong-Yong Yoon, Frédéric Barlat, Shin-Yeong Lee, Jin-Hwan Kim, Min-Su Wi, and Dong-Jin Kim. Finite element implementation of hydrostatic pressure-sensitive plasticity and its application to distortional hardening model and sheet metal forming simulations. *Journal of Materials Processing Technology*, 302:117494, April 2022. ISSN 0924-0136. doi: 10.1016/j.jmatprotec.2022.117494. URL http://dx.doi.org/10.1016/j.jmatprotec.2022.117494.

[104] Jisheng Qin, Bjørn Holmedal, and Odd Sture Hopperstad. A combined isotropic, kinematic and distortional hardening model for aluminum and steels under complex strain-path changes. *International Journal of Plasticity*, 101:156–169, February 2018. ISSN 0749-6419. doi: 10.1016/j.ijplas.2017.10.013. URL http://dx.doi.org/10.1016/j.ijplas.2017.10.013.

[105] William Prager. A new method of analyzing stresses and strains in work-hardening plastic solids. *Journal of Applied Mechanics*, 23(4):493–496, December 1956. ISSN 1528-9036. doi: 10.1115/1.4011389. URL http://dx.doi.org/10.1115/1.4011389.

[106] Hans Ziegler. A modification of prager's hardening rule. *Quarterly of Applied Mathematics*, 17(1):55–65, April 1959. ISSN 1552-4485. doi: 10.1090/qam/104405. URL http://dx.doi.org/10.1090/qam/104405.

[107] Peter J Armstrong, Charles O Frederick, et al. *A mathematical representation of the multiaxial Bauschinger effect*, volume 731. Berkeley Nuclear Laboratories Berkeley, CA, 1966.

[108] J. L. Chaboche and G. Rousselier. On the Plastic and Viscoplastic Constitutive Equations—Part I: Rules Developed With Internal Variable Concept. *Journal*

of Pressure Vessel Technology, 105(2):153–158, 05 1983. ISSN 0094-9930. doi: 10.1115/1.3264257. URL https://doi.org/10.1115/1.3264257.

[109] Z. Mróz. On the description of anisotropic workhardening. *Journal of the Mechanics and Physics of Solids*, 15(3):163–175, 1967. ISSN 0022-5096. doi: 10.1016/0022-5096(67)90030-0. URL http://dx.doi.org/10.1016/0022-5096(67)90030-0.

[110] R. D. Krieg. A Practical Two Surface Plasticity Theory. *Journal of Applied Mechanics*, 42(3):641–646, 1975. ISSN 0021-8936. doi: 10.1115/1.3423656. URL https://doi.org/10.1115/1.3423656.

[111] Y. F. Dafalias and E. P. Popov. Plastic Internal Variables Formalism of Cyclic Plasticity. *Journal of Applied Mechanics*, 43(4):645–651, 1976. ISSN 0021-8936. doi: 10.1115/1.3423948. URL https://doi.org/10.1115/1.3423948.

[112] Lumin Geng, Yao Shen, and R.H Wagoner. Anisotropic hardening equations derived from reverse-bend testing. *International Journal of Plasticity*, 18(5–6):743–767, October 2002. ISSN 0749-6419. doi: 10.1016/s0749-6419(01)00048-1. URL http://dx.doi.org/10.1016/S0749-6419(01)00048-1.

[113] F. Yoshida and T. Uemori. A model of large-strain cyclic plasticity and its application to springback simulation. *International Journal of Mechanical Sciences*, 45(10):1687–1702, 2003. ISSN 0020-7403. doi: 10.1016/j.ijmecsci.2003.10.013. URL http://dx.doi.org/10.1016/j.ijmecsci.2003.10.013.

[114] Rui P.R. Cardoso and Jeong Whan Yoon. Stress integration method for a nonlinear kinematic/isotropic hardening model and its characterization based on polycrystal plasticity. *International Journal of Plasticity*, 25(9):1684–1710, September 2009. ISSN 0749-6419. doi: 10.1016/j.ijplas.2008.09.007. URL http://dx.doi.org/10.1016/j.ijplas.2008.09.007.

[115] Dongkeon Kim, Gary F. Dargush, and Cemal Basaran. A cyclic two-surface thermoplastic damage model with application to metallic plate dampers. *Engineering Structures*, 52:608–620, July 2013. ISSN 0141-0296. doi: 10.1016/j.engstruct.2013.02.030. URL http://dx.doi.org/10.1016/j.engstruct.2013.02.030.

[116] Fusahito Yoshida and Takeshi Uemori. A model of large-strain cyclic plasticity describing the bauschinger effect and workhardening stagnation. *Inter-*

national Journal of Plasticity, 18(5–6):661–686, October 2002. ISSN 0749-6419. doi: 10.1016/s0749-6419(01)00050-x. URL http://dx.doi.org/10.1016/S0749-6419(01)00050-X.

[117] M. Yang, Y. Akiyama, and T. Sasaki. Evaluation of change in material properties due to plastic deformation. *Journal of Materials Processing Technology*, 151(1–3):232–236, September 2004. ISSN 0924-0136. doi: 10.1016/j.jmatprotec.2004.04.114. URL http://dx.doi.org/10.1016/j.jmatprotec.2004.04.114.

[118] Toshihiko Kuwabara, Fumitake Yoshida, and Takaji Uemori. Elastic–plastic behavior of aluminum alloy sheet under in-plane cyclic tension–compression at large plastic strain. *International Journal of Plasticity*, 21(1):101–117, 2005.

[119] Fumitake Yoshida and Takaji Uemori. A model of large-strain cyclic plasticity and its application to springback simulation. *International Journal of Mechanical Sciences*, 50(3):428–439, 2008.

[120] Yun Zhang and Xiaojie Xu. Predicting springback radii and angles in air bending of high-strength sheet steel through gaussian process regressions. *International Journal on Interactive Design and Manufacturing (IJIDeM)*, 16 (3):863–870, June 2022. ISSN 1955-2505. doi: 10.1007/s12008-022-00945-7. URL http://dx.doi.org/10.1007/s12008-022-00945-7.

[121] Jiaxin Zhou, Frederic Barlat, and Jeong Whan Yoon. A robust and efficient return mapping algorithm for distortional hardening models with evolving yield surfaces. *Computer Methods in Applied Mechanics and Engineering*, 337:224–244, 2018.

[122] Jinwoo Lee, Myoung-Gyu Lee, Frédéric Barlat, and Ji Hoon Kim. Stress integration schemes for novel homogeneous anisotropic hardening model. *Computer Methods in Applied Mechanics and Engineering*, 247–248:73–92, 2012. ISSN 0045-7825. doi: 10.1016/j.cma.2012.07.013. URL http://dx.doi.org/10.1016/j.cma.2012.07.013.

[123] Haiming Zhang, Martin Diehl, Franz Roters, and Dierk Raabe. A virtual laboratory using high resolution crystal plasticity simulations to determine the initial yield surface for sheet metal forming operations. *International Journal of Plasticity*, 80:111–138, May 2016. ISSN 0749-6419. doi: 10.1016/j.ijplas.2016.01.002. URL http://dx.doi.org/10.1016/j.ijplas.2016.01.002.

[124] Fethi Abbassi, Touhami Belhadj, Sébastien Mistou, and Ali Zghal. Parameter identification of a mechanical ductile damage using artificial neural networks in sheet metal forming. *Materials amp; Design*, 45:605–615, March 2013. ISSN 0261-3069. doi: 10.1016/j.matdes.2012.09.032. URL http://dx.doi.org/10.1016/j.matdes.2012.09.032.

[125] Robin Schulte, Cavid Karca, Richard Ostwald, and Andreas Menzel. Machine learning-assisted parameter identification for constitutive models based on concatenated loading path sequences. *European Journal of Mechanics - A/Solids*, 98:104854, March 2023. ISSN 0997-7538. doi: 10.1016/j.euromechsol.2022.104854. URL http://dx.doi.org/10.1016/j.euromechsol.2022.104854.

[126] Armando Marques, André Pereira, Bernardete Ribeiro, and Pedro A. Prates. On the identification of material constitutive model parameters using machine learning algorithms. *Key Engineering Materials*, 926:2146–2153, July 2022. doi: 10.4028/p-5hf550. URL https://doi.org/10.4028/p-5hf550.

[127] Frederic E. Bock, Roland C. Aydin, Christian J. Cyron, Norbert Huber, Surya R. Kalidindi, and Benjamin Klusemann. A review of the application of machine learning and data mining approaches in continuum materials mechanics. *Frontiers in Materials*, 6, 2019. doi: 10.3389/fmats.2019.00110. URL https://doi.org/10.3389/fmats.2019.00110.

[128] Rúben Lourenço, António Andrade-Campos, and Pétia Georgieva. The use of machine-learning techniques in material constitutive modelling for metal forming processes. *Metals*, 12(3):427, 2022. doi: 10.3390/met12030427. URL https://doi.org/10.3390/met12030427.

[129] Kenneth T. Kavanagh and Ray W. Clough. Finite element applications in the characterization of elastic solids. *International Journal of Solids and Structures*, 7(1):11–23, 1971. ISSN 0020-7683. doi: 10.1016/0020-7683(71)90015-1. URL http://dx.doi.org/10.1016/0020-7683(71)90015-1.

[130] D. Claire, F. Hild, and S. Roux. A finite element formulation to identify damage fields: the equilibrium gap method. *International Journal for Numerical Methods in Engineering*, 61(2):189–208, August 2004. doi: 10.1002/nme.1057. URL https://doi.org/10.1002/nme.1057.

[131] M. Grédiac. Principe des travaux virtuels et identification. *Comptes Rendus de l'Académie des Sciences*, 309(309):1 – 5, 1989. URL

https://www.scopus.com/inward/record.uri?eid=2-s2.0-0001926717&partnerID=40&md5=312a757cb9175dc1fd3067c65aa1460f.

[132] J.M.P. Martins, A. Andrade-Campos, and S. Thuillier. Comparison of inverse identification strategies for constitutive mechanical models using full-field measurements. *International Journal of Mechanical Sciences*, 145:330–345, 2018. ISSN 0020-7403. doi: 10.1016/j.ijmecsci.2018.07.013. URL http://dx.doi.org/10.1016/j.ijmecsci.2018.07.013.

[133] A. Chamekh, H. Bel Hadj Salah, and R. Hambli. Inverse technique identification of material parameters using finite element and neural network computation. *The International Journal of Advanced Manufacturing Technology*, 44(1–2):173–179, November 2008. ISSN 1433-3015. doi: 10.1007/s00170-008-1809-6. URL http://dx.doi.org/10.1007/s00170-008-1809-6.

[134] N. Huber and Ch. Tsakmakis. A neural network tool for identifying the material parameters of a finite deformation viscoplasticity model with static recovery. *Computer Methods in Applied Mechanics and Engineering*, 191 (3-5):353–384, November 2001. doi: 10.1016/s0045-7825(01)00278-x. URL https://doi.org/10.1016/s0045-7825(01)00278-x.

[135] Zied Ktari, Carlos Leitão, Pedro A. Prates, and Ali Khalfallah. Mechanical design of ring tensile specimen via surrogate modelling for inverse material parameter identification. *Mechanics of Materials*, 153:103673, February 2021. doi: 10.1016/j.mechmat.2020.103673. URL https://doi.org/10.1016/j.mechmat.2020.103673.

[136] Pierre-Olivier Bouchard, Ludovic Bourgeon, Sebastien Fayolle, and Katia Mocellin. An enhanced lemaitre model formulation for materials processing damage computation. *International Journal of Material Forming*, 4(3): 299–315, August 2010. ISSN 1960-6214. doi: 10.1007/s12289-010-0996-5. URL http://dx.doi.org/10.1007/s12289-010-0996-5.

[137] A.P. Karafillis and M.C. Boyce. A general anisotropic yield criterion using bounds and a transformation weighting tensor. *Journal of the Mechanics and Physics of Solids*, 41(12):1859–1886, December 1993. ISSN 0022-5096. doi: 10.1016/0022-5096(93)90073-o. URL http://dx.doi.org/10.1016/0022-5096(93)90073-O.

[138] Dan Yao, Yong chuan Duan, Mu yu Li, and Ying ping Guan. Hybrid identification method of coupled viscoplastic-damage constitutive parameters based on BP neural network and genetic algorithm. *Engineering Fracture Mechanics*, 257:108027, 2021. doi: 10.1016/j.engfracmech.2021.108027. URL https://doi.org/10.1016/j.engfracmech.2021.108027.

[139] Lukas Morand and Dirk Helm. A mixture of experts approach to handle ambiguities in parameter identification problems in material modeling. *Computational Materials Science*, 167:85–91, September 2019. doi: 10.1016/j.commatsci.2019.04.003. URL https://doi.org/10.1016/j.commatsci.2019.04.003.

[140] Zhenfei Guo, Ruixiang Bai, Zhenkun Lei, Hao Jiang, Da Liu, Jianchao Zou, and Cheng Yan. CPINet: Parameter identification of path-dependent constitutive model with automatic denoising based on CNN-LSTM. *European Journal of Mechanics - A/Solids*, 90:104327, 2021. doi: 10.1016/j.euromechsol.2021.104327. URL https://doi.org/10.1016/j.euromechsol.2021.104327.

[141] Changwu Huang, Abdelkhalak El Hami, and Bouchaïb Radi. Metamodel-based inverse method for parameter identification: elastic–plastic damage model. *Engineering Optimization*, 49(4):633–653, July 2016. ISSN 1029-0273. doi: 10.1080/0305215x.2016.1206537. URL http://dx.doi.org/10.1080/0305215X.2016.1206537.

[142] Nelson Bastos, Pedro André Prates, and António Andrade-Campos. Material parameter identification of elastoplastic constitutive models using machine learning approaches. *Key Engineering Materials*, 926:2193–2200, July 2022. ISSN 1662-9795. doi: 10.4028/p-zr575d. URL http://dx.doi.org/10.4028/p-zr575d.

[143] Oana Cazacu, Brian Plunkett, and Frédéric Barlat. Orthotropic yield criterion for hexagonal closed packed metals. *International Journal of Plasticity*, 22(7):1171–1194, 2006. ISSN 0749-6419. doi: 10.1016/j.ijplas.2005.06.001. URL http://dx.doi.org/10.1016/j.ijplas.2005.06.001.

[144] Pedro Prates, Dário Mitreiro, and António Andrade-Campos. Limitations of xgboost in predicting material parameters for complex constitutive models. *MATEC Web of Conferences*, 408:01023, 2025. ISSN 2261-236X.

doi: 10.1051/matecconf/202540801023. URL http://dx.doi.org/10.1051/matecconf/202540801023.

[145] Craig M. Hamel, Kevin N. Long, and Sharlotte L. B. Kramer. Calibrating constitutive models with full-field data via physics informed neural networks. *Strain*, 59(2), November 2022. ISSN 1475-1305. doi: 10.1111/str.12431. URL http://dx.doi.org/10.1111/str.12431.

[146] Siyuan Song and Hanxun Jin. Identifying constitutive parameters for complex hyperelastic materials using physics-informed neural networks. *Soft Matter*, 20(30):5915–5926, 2024. ISSN 1744-6848. doi: 10.1039/d4sm00001c. URL http://dx.doi.org/10.1039/d4sm00001c.

[147] Fei Tao, Xin Liu, Haodong Du, and Wenbin Yu. Learning composite constitutive laws via coupling abaqus and deep neural network. *Composite Structures*, 272:114137, September 2021. ISSN 0263-8223. doi: 10.1016/j.compstruct.2021.114137. URL http://dx.doi.org/10.1016/j.compstruct.2021.114137.

[148] Jamshid Ghaboussi, David A. Pecknold, Mingfu Zhang, and Rami M. Haj-Ali. Autoprogressive training of neural network constitutive models. *International Journal for Numerical Methods in Engineering*, 42(1):105–126, May 1998. doi: 10.1002/(sici)1097-0207(19980515)42:1<105::aid-nme356>3.0.co;2-v. URL http://dx.doi.org/10.1002/(SICI)1097-0207(19980515)42:1<105::AID-NME356>3.0.CO;2-V.

[149] J. Ghaboussi, J. H. Garrett, and X. Wu. Knowledge-based modeling of material behavior with neural networks. *Journal of Engineering Mechanics*, 117(1):132–153, January 1991. ISSN 1943-7889. doi: 10.1061/(asce)0733-9399(1991)117:1(132). URL http://dx.doi.org/10.1061/(ASCE)0733-9399(1991)117:1(132).

[150] Tomonari Furukawa and Genki Yagawa. Implicit constitutive modelling for viscoplasticity using neural networks. *International Journal for Numerical Methods in Engineering*, 43(2):195–219, September 1998. ISSN 1097-0207. doi: 10.1002/(sici)1097-0207(19980930)43:2<195::aid-nme418>3.0.co;2-6. URL http://dx.doi.org/10.1002/(SICI)1097-0207(19980930)43:2<195::AID-NME418>3.0.CO;2-6.

[151] Maysam B. Gorji and Dirk Mohr. Towards neural network models for describing the large deformation behavior of sheet metal. *IOP Conference Series:*

Materials Science and Engineering, 651(1):012102, November 2019. ISSN 1757-899X. doi: 10.1088/1757-899x/651/1/012102. URL http://dx.doi.org/10.1088/1757-899X/651/1/012102.

[152] Maxime Lavech du Bos, Fadoua Balabdaoui, and Julian N. Heidenreich. Modeling stress-strain curves with neural networks: a scalable alternative to the return mapping algorithm. *Computational Materials Science*, 178:109629, June 2020. ISSN 0927-0256. doi: 10.1016/j.commatsci.2020.109629. URL http://dx.doi.org/10.1016/j.commatsci.2020.109629.

[153] K.P. Rao and Y.K.D.V. Prasad. Neural network approach to flow stress evaluation in hot deformation. *Journal of Materials Processing Technology*, 53 (3–4):552–566, September 1995. ISSN 0924-0136. doi: 10.1016/0924-0136(94)01744-l. URL http://dx.doi.org/10.1016/0924-0136(94)01744-L.

[154] Amit Kumar Gupta, Hansoge Nitin Krishnamurthy, Yashjeet Singh, Kaushik Manga Prasad, and Swadesh Kumar Singh. Development of constitutive models for dynamic strain aging regime in austenitic stainless steel 304. *Materials amp; Design*, 45:616–627, March 2013. ISSN 0261-3069. doi: 10.1016/j.matdes.2012.09.041. URL http://dx.doi.org/10.1016/j.matdes.2012.09.041.

[155] Sumit Kumar, Anish Karmakar, and Sumeer K. Nath. Construction of hot deformation processing maps for 9cr-1mo steel through conventional and ann approach. *Materials Today Communications*, 26:101903, March 2021. ISSN 2352-4928. doi: 10.1016/j.mtcomm.2020.101903. URL http://dx.doi.org/10.1016/j.mtcomm.2020.101903.

[156] H. R. Rezaei Ashtiani and A. A. Shayanpoor. Hot deformation characterization of pure aluminum using artificial neural network (ann) and processing map considering initial grain size. *Metals and Materials International*, 27(12):5017–5033, March 2021. ISSN 2005-4149. doi: 10.1007/s12540-020-00943-y. URL http://dx.doi.org/10.1007/s12540-020-00943-y.

[157] Y. Sun, W.D. Zeng, Y.Q. Zhao, Y.L. Qi, X. Ma, and Y.F. Han. Development of constitutive relationship model of ti600 alloy using artificial neural network. *Computational Materials Science*, 48(3):686–691, May 2010. ISSN 0927-0256. doi: 10.1016/j.commatsci.2010.03.007. URL http://dx.doi.org/10.1016/j.commatsci.2010.03.007.

[158] S. Aliakbari Sani, G.R. Ebrahimi, H. Vafaeenezhad, and A.R. Kiani-Rashid. Modeling of hot deformation behavior and prediction of flow stress in a magnesium alloy using constitutive equation and artificial neural network (ann) model. *Journal of Magnesium and Alloys*, 6(2):134–144, June 2018. ISSN 2213-9567. doi: 10.1016/j.jma.2018.05.002. URL http://dx.doi.org/10.1016/j.jma.2018.05.002.

[159] Kedar S. Pandya, Christian C. Roth, and Dirk Mohr. Strain rate and temperature dependent fracture of aluminum alloy 7075: Experiments and neural network modeling. *International Journal of Plasticity*, 135:102788, 2020. ISSN 0749-6419. doi: 10.1016/j.ijplas.2020.102788. URL http://dx.doi.org/10.1016/j.ijplas.2020.102788.

[160] L. Borkowski, C. Sorini, and A. Chattopadhyay. Recurrent neural network-based multiaxial plasticity model with regularization for physics-informed constraints. *Computers amp; Structures*, 258:106678, January 2022. ISSN 0045-7949. doi: 10.1016/j.compstruc.2021.106678. URL http://dx.doi.org/10.1016/j.compstruc.2021.106678.

[161] Sungmoon Jung and Jamshid Ghaboussi. Neural network constitutive model for rate-dependent materials. *Computers amp; Structures*, 84(15–16):955–963, June 2006. ISSN 0045-7949. doi: 10.1016/j.compstruc.2006.02.015. URL http://dx.doi.org/10.1016/j.compstruc.2006.02.015.

[162] Gun Jin Yun, Jamshid Ghaboussi, and Amr S. Elnashai. A new neural network-based model for hysteretic behavior of materials. *International Journal for Numerical Methods in Engineering*, 73(4):447–469, May 2007. ISSN 1097-0207. doi: 10.1002/nme.2082. URL http://dx.doi.org/10.1002/nme.2082.

[163] Dong Phill Jang, Piemaan Fazily, and Jeong Whan Yoon. Machine learning-based constitutive model for j2- plasticity. *International Journal of Plasticity*, 138:102919, March 2021. ISSN 0749-6419. doi: 10.1016/j.ijplas.2020.102919. URL http://dx.doi.org/10.1016/j.ijplas.2020.102919.

[164] Dengpeng Huang, Jan Niklas Fuhg, Christian Weißenfels, and Peter Wriggers. A machine learning based plasticity model using proper orthogonal decomposition. *Computer Methods in Applied Mechanics and Engineering*, 365:

113008, June 2020. ISSN 0045-7825. doi: 10.1016/j.cma.2020.113008. URL http://dx.doi.org/10.1016/j.cma.2020.113008.

[165] Marcus Stoffel, Franz Bamer, and Bernd Markert. Artificial neural networks and intelligent finite elements in non-linear structural mechanics. *Thin-Walled Structures*, 131:102–106, October 2018. ISSN 0263-8231. doi: 10.1016/j.tws.2018.06.035. URL http://dx.doi.org/10.1016/j.tws.2018.06.035.

[166] Jaber Rezaei Mianroodi, Nima H. Siboni, and Dierk Raabe. Teaching solid mechanics to artificial intelligence—a fast solver for heterogeneous materials. *npj Computational Materials*, 7(1), July 2021. ISSN 2057-3960. doi: 10.1038/s41524-021-00571-z. URL http://dx.doi.org/10.1038/s41524-021-00571-z.

[167] A.L. Frankel, R.E. Jones, C. Alleman, and J.A. Templeton. Predicting the mechanical response of oligocrystals with deep learning. *Computational Materials Science*, 169:109099, November 2019. ISSN 0927-0256. doi: 10.1016/j.commatsci.2019.109099. URL http://dx.doi.org/10.1016/j.commatsci.2019.109099.

[168] Nikolaos N. Vlassis, Ran Ma, and WaiChing Sun. Geometric deep learning for computational mechanics part i: anisotropic hyperelasticity. *Computer Methods in Applied Mechanics and Engineering*, 371:113299, November 2020. ISSN 0045-7825. doi: 10.1016/j.cma.2020.113299. URL http://dx.doi.org/10.1016/j.cma.2020.113299.

[169] Charles Yang, Youngsoo Kim, Seunghwa Ryu, and Grace X. Gu. Prediction of composite microstructure stress-strain curves using convolutional neural networks. *Materials amp; Design*, 189:108509, April 2020. ISSN 0264-1275. doi: 10.1016/j.matdes.2020.108509. URL http://dx.doi.org/10.1016/j.matdes.2020.108509.

[170] Jaber R. Mianroodi, Sebastian Wulfinghoff, and Thomas Böhlke. U-net based reduced-order modeling of microstructural stresses in elasto-plastic heterogeneous materials. *Computer Methods in Applied Mechanics and Engineering*, 379:113750, 2021. doi: 10.1016/j.cma.2021.113750.

[171] Joel Akeret, Chihway Chang, Aurelien Lucchi, and Alexandre Refregier. Radio frequency interference mitigation using deep convolutional neural networks. *Astronomy and Computing*, 18:35–39, 2017.

[172] Yousef Heider, Kun Wang, and WaiChing Sun. So(3)-invariance of informed-graph-based deep neural network for anisotropic elastoplastic materials. *Computer Methods in Applied Mechanics and Engineering*, 363:112875, May 2020. ISSN 0045-7825. doi: 10.1016/j.cma.2020.112875. URL http://dx.doi.org/10.1016/j.cma.2020.112875.

[173] Diab W. Abueidda, Seid Koric, Nahil A. Sobh, and Huseyin Sehitoglu. Deep learning for plasticity and thermo-viscoplasticity. *International Journal of Plasticity*, 136:102852, January 2021. ISSN 0749-6419. doi: 10.1016/j.ijplas.2020.102852. URL http://dx.doi.org/10.1016/j.ijplas.2020.102852.

[174] F. Ghavamian and A. Simone. Accelerating multiscale finite element simulations of history-dependent materials using a recurrent neural network. *Computer Methods in Applied Mechanics and Engineering*, 357:112594, December 2019. ISSN 0045-7825. doi: 10.1016/j.cma.2019.112594. URL http://dx.doi.org/10.1016/j.cma.2019.112594.

[175] Maysam B. Gorji, Mojtaba Mozaffar, Julian N. Heidenreich, Jian Cao, and Dirk Mohr. On the potential of recurrent neural networks for modeling path dependent plasticity. *Journal of the Mechanics and Physics of Solids*, 143:103972, October 2020. ISSN 0022-5096. doi: 10.1016/j.jmps.2020.103972. URL http://dx.doi.org/10.1016/j.jmps.2020.103972.

[176] M. Mozaffar, R. Bostanabad, W. Chen, K. Ehmann, J. Cao, and M. A. Bessa. Deep learning predicts path-dependent plasticity. *Proceedings of the National Academy of Sciences*, 116(52):26414–26420, December 2019. ISSN 1091-6490. doi: 10.1073/pnas.1911815116. URL http://dx.doi.org/10.1073/pnas.1911815116.

[177] Guang Chen. Recurrent neural networks (rnns) learn the constitutive law of viscoelasticity. *Computational Mechanics*, 67(3):1009–1019, February 2021. ISSN 1432-0924. doi: 10.1007/s00466-021-01981-y. URL http://dx.doi.org/10.1007/s00466-021-01981-y.

[178] Aarohi Shah and Julian J. Rimoli. Data-driven approach for dynamic homogenization using meta learning. *Computer Methods in Applied Mechanics and Engineering*, 401:115672, November 2022. ISSN 0045-7825. doi: 10.1016/j.cma.2022.115672. URL http://dx.doi.org/10.1016/j.cma.2022.115672.

[179] Pin Zhang, Zhen-Yu Yin, Yin-Fu Jin, and Guan-Lin Ye. An ai-based model for describing cyclic characteristics of granular materials. *International Journal for Numerical and Analytical Methods in Geomechanics*, 44 (9):1315–1335, March 2020. ISSN 1096-9853. doi: 10.1002/nag.3063. URL http://dx.doi.org/10.1002/nag.3063.

[180] Tongming Qu, Shaocheng Di, Y.T. Feng, Min Wang, and Tingting Zhao. Towards data-driven constitutive modelling for granular materials via micromechanics-informed deep learning. *International Journal of Plasticity*, 144:103046, September 2021. ISSN 0749-6419. doi: 10.1016/j.ijplas.2021.103046. URL http://dx.doi.org/10.1016/j.ijplas.2021.103046.

[181] Thomas Tancogne-Dejean, Maysam B. Gorji, Juner Zhu, and Dirk Mohr. Recurrent neural network modeling of the large deformation of lithium-ion battery cells. *International Journal of Plasticity*, 146:103072, November 2021. ISSN 0749-6419. doi: 10.1016/j.ijplas.2021.103072. URL http://dx.doi.org/10.1016/j.ijplas.2021.103072.

[182] C. Hu, S. Martin, and R. Dingreville. Accelerating phase-field predictions via recurrent neural networks learning the microstructure evolution in latent space. *Computer Methods in Applied Mechanics and Engineering*, 397:115128, 2022. ISSN 0045-7825. doi: 10.1016/j.cma.2022.115128. URL http://dx.doi.org/10.1016/j.cma.2022.115128.

[183] Kyunghyun Cho, Bart van Merrienboer, Caglar Gulcehre, Dzmitry Bahdanau, Fethi Bougares, Holger Schwenk, and Yoshua Bengio. Learning phrase representations using rnn encoder–decoder for statistical machine translation. In *Proceedings of the 2014 Conference on Empirical Methods in Natural Language Processing (EMNLP)*. Association for Computational Linguistics, 2014. doi: 10.3115/v1/d14-1179. URL http://dx.doi.org/10.3115/v1/d14-1179.

[184] Colin Bonatti and Dirk Mohr. One for all: Universal material model based on minimal state-space neural networks. *Science Advances*, 7(26), 2021. ISSN 2375-2548. doi: 10.1126/sciadv.abf3658. URL http://dx.doi.org/10.1126/sciadv.abf3658.

[185] Colin Bonatti and Dirk Mohr. On the importance of self-consistency in recurrent neural network models representing elasto-plastic solids. *Journal of*

the Mechanics and Physics of Solids, 158:104697, January 2022. ISSN 0022-5096. doi: 10.1016/j.jmps.2021.104697. URL http://dx.doi.org/10.1016/j.jmps.2021.104697.

[186] Julian N. Heidenreich, Colin Bonatti, and Dirk Mohr. Transfer learning of recurrent neural network-based plasticity models. *International Journal for Numerical Methods in Engineering*, 125(1), September 2023. ISSN 1097-0207. doi: 10.1002/nme.7357. URL http://dx.doi.org/10.1002/nme.7357.

[187] M. Raissi, P. Perdikaris, and G.E. Karniadakis. Physics-informed neural networks: A deep learning framework for solving forward and inverse problems involving nonlinear partial differential equations. *Journal of Computational Physics*, 378:686–707, February 2019. ISSN 0021-9991. doi: 10.1016/j.jcp.2018.10.045. URL http://dx.doi.org/10.1016/j.jcp.2018.10.045.

[188] Nikolaos N. Vlassis and WaiChing Sun. Sobolev training of thermodynamic-informed neural networks for interpretable elasto-plasticity models with level set hardening. *Computer Methods in Applied Mechanics and Engineering*, 377:113695, April 2021. ISSN 0045-7825. doi: 10.1016/j.cma.2021.113695. URL http://dx.doi.org/10.1016/j.cma.2021.113695.

[189] Kailai Xu, Daniel Z. Huang, and Eric Darve. Learning constitutive relations using symmetric positive definite neural networks. *Journal of Computational Physics*, 428:110072, March 2021. ISSN 0021-9991. doi: 10.1016/j.jcp.2020.110072. URL http://dx.doi.org/10.1016/j.jcp.2020.110072.

[190] João Henriques, Adewale Hakeem, José Xavier, and António Andrade-Campos. On a novel heterogeneous mechanical test with continuous strain path changes for the inverse calibration of constitutive models. 2025. doi: 10.2139/ssrn.5223536. URL http://dx.doi.org/10.2139/ssrn.5223536.

[191] Rúben Lourenço, Petia Georgieva, Elias Cueto, and A. Andrade-Campos. An indirect training approach for implicit constitutive modelling using recurrent neural networks and the virtual fields method. *Computer Methods in Applied Mechanics and Engineering*, 425:116961, May 2024. ISSN 0045-7825. doi: 10.1016/j.cma.2024.116961. URL http://dx.doi.org/10.1016/j.cma.2024.116961.

[192] Bing Pan, Kemao Qian, Huimin Xie, and Anand Asundi. Two-dimensional digital image correlation for in-plane displacement and strain measurement: a

review. *Measurement Science and Technology*, 20(6):062001, apr 2009. doi: 10.1088/0957-0233/20/6/062001. URL https://doi.org/10.1088/0957-0233/20/6/062001.

[193] Morgan Bertin, François Hild, Stéphane Roux, Florent Mathieu, Hugo Leclerc, and Patrick Aimedieu. Integrated digital image correlation applied to elasto-plastic identification in a biaxial experiment. *The Journal of Strain Analysis for Engineering Design*, 51(2):118–131, February 2016. ISSN 2041-3130. doi: 10.1177/0309324715614759. URL http://dx.doi.org/10.1177/0309324715614759.

[194] N. Souto, S. Thuillier, and A. Andrade-Campos. Design of an indicator to characterize and classify mechanical tests for sheet metals. *International Journal of Mechanical Sciences*, 101–102:252–271, October 2015. ISSN 0020-7403. doi: 10.1016/j.ijmecsci.2015.07.026. URL http://dx.doi.org/10.1016/j.ijmecsci.2015.07.026.

[195] Miguel G Oliveira, Sandrine Thuillier, and António Andrade-Campos. Evaluation of heterogeneous mechanical tests for model calibration of sheet metals. *The Journal of Strain Analysis for Engineering Design*, 57(3):208–224, July 2021. ISSN 2041-3130. doi: 10.1177/03093247211027061. URL http://dx.doi.org/10.1177/03093247211027061.

[196] Fabrice Pierron. Material testing 2.0: A brief review. *Strain*, 59(3), March 2023. ISSN 1475-1305. doi: 10.1111/str.12434. URL http://dx.doi.org/10.1111/str.12434.

[197] T. Pottier, F. Toussaint, and P. Vacher. Contribution of heterogeneous strain field measurements and boundary conditions modelling in inverse identification of material parameters. *European Journal of Mechanics - A/Solids*, 30(3):373–382, May 2011. ISSN 0997-7538. doi: 10.1016/j.euromechsol.2010.10.001. URL http://dx.doi.org/10.1016/j.euromechsol.2010.10.001.

[198] Christian C. Roth, Thomas Tancogne-Dejean, and Dirk Mohr. Plasticity and fracture of cast and slm alsi10mg: High-throughput testing and modeling. *Additive Manufacturing*, 43:101998, July 2021. ISSN 2214-8604. doi: 10.1016/j.addma.2021.101998. URL http://dx.doi.org/10.1016/j.addma.2021.101998.

[199] Maysam B. Gorji, Jevan Furmanski, and Dirk Mohr. From macro- to micro-experiments: Specimen-size independent identification of plasticity and fracture properties. *International Journal of Mechanical Sciences*, 199:106389, June 2021. ISSN 0020-7403. doi: 10.1016/j.ijmecsci.2021.106389. URL http://dx.doi.org/10.1016/j.ijmecsci.2021.106389.

[200] Pengfei Zheng, Ran Chen, Haiting Liu, Jiming Chen, Zhijie Zhang, Xing Liu, and Yao Shen. On the standards and practices for miniaturized tensile test – a review. *Fusion Engineering and Design*, 161:112006, December 2020. ISSN 0920-3796. doi: 10.1016/j.fusengdes.2020.112006. URL http://dx.doi.org/10.1016/j.fusengdes.2020.112006.

[201] E. Lucon. *Testing of Small-Sized Specimens*, page 135–163. Elsevier, 2014. ISBN 9780080965338. doi: 10.1016/b978-0-08-096532-1.00110-2. URL http://dx.doi.org/10.1016/B978-0-08-096532-1.00110-2.

[202] R.L. Klueh. Miniature tensile test specimens for fusion reactor irradiation studies. *Nuclear Engineering and Design. Fusion*, 2(3):407–416, January 1985. ISSN 0167-899X. doi: 10.1016/0167-899x(85)90028-x. URL http://dx.doi.org/10.1016/0167-899X(85)90028-X.

[203] Sümer Şahin and Asim Saeed. Experimental evaluation of surveillance capsule assemblies for life assessment of chasnupp unit-1 reactor pressure vessel. *Annals of Nuclear Energy*, 89:90–98, March 2016. ISSN 0306-4549. doi: 10.1016/j.anucene.2015.11.019. URL http://dx.doi.org/10.1016/j.anucene.2015.11.019.

[204] E. Lucon. Material damage evaluation and residual life assessment of primary power plant components using specimens of non–standard dimensions. *Materials Science and Technology*, 17(7):777–785, July 2001. ISSN 1743-2847. doi: 10.1179/026708301101510717. URL http://dx.doi.org/10.1179/026708301101510717.

[205] K.M. Oluwasegun, C. Cooper, Y.L. Chiu, I.P. Jones, H.Y. Li, and G. Baxter. Micro-tensile strength of a welded turbine disc superalloy. *Materials Science and Engineering: A*, 596:229–235, February 2014. ISSN 0921-5093. doi: 10.1016/j.msea.2013.12.046. URL http://dx.doi.org/10.1016/j.msea.2013.12.046.

[206] Peng Liu, Jiafeng Bao, and Yumei Bao. Mechanical properties and fracture behavior of an ebw t2 copper–45 steel joint. *Materials*, 12(10):1714, May 2019. ISSN 1996-1944. doi: 10.3390/ma12101714. URL http://dx.doi.org/10.3390/ma12101714.

[207] Jorge Gil, Ricardo Seca, Rui Amaral, Omid Emadinia, Ana Reis, and Abílio de Jesus. 18ni300 maraging steel produced via direct energy deposition on h13 tool steel and din ck45. *Key Engineering Materials*, 926:194–205, July 2022. ISSN 1662-9795. doi: 10.4028/p-8134oi. URL http://dx.doi.org/10.4028/p-8134oi.

[208] E. Azinpour, D. J. Cruz, J. M. A. Cesar de Sa, and A. Santos. Phase-field approach in elastoplastic solids: application of an iterative staggered scheme and its experimental validation. *Computational Mechanics*, May 2021. doi: 10.1007/s00466-021-02029-x. URL https://doi.org/10.1007/s00466-021-02029-x.

[209] S.M Spearing. Materials issues in microelectromechanical systems (mems). *Acta Materialia*, 48(1):179–196, January 2000. ISSN 1359-6454. doi: 10.1016/s1359-6454(99)00294-3. URL http://dx.doi.org/10.1016/S1359-6454(99)00294-3.

[210] Jagannathan Rajagopalan. *Microelectromechanical Systems (MEMS)-Based Testing of Materials*, pages 1955–1979. Springer Singapore, Singapore, 2019. ISBN 978-981-10-6884-3. doi: 10.1007/978-981-10-6884-3_45. URL https://doi.org/10.1007/978-981-10-6884-3_45.

[211] Martin Rund, Radek Procházka, Pavel Konopík, Jan Džugan, and Hugo Folgar. Investigation of sample-size influence on tensile test results at different strain rates. *Procedia Engineering*, 114:410–415, 2015. ISSN 1877-7058. doi: 10.1016/j.proeng.2015.08.086. URL http://dx.doi.org/10.1016/j.proeng.2015.08.086.

[212] D T Read, L A Liew, R M White, N Barbosa, and J Geaney. Measuring flow curve and failure conditions for a MEMS-scale electrodeposited nickel alloy. *Materials Research Express*, 6(9):0950a6, July 2019. doi: 10.1088/2053-1591/aae6ad. URL https://doi.org/10.1088/2053-1591/aae6ad.

[213] Hong Chul Hyun, Minsoo Kim, Sungsik Bang, and Hyungyil Lee. On acquiring true stress–strain curves for sheet specimens using tensile test and fe

analysis based on a local necking criterion. *Journal of Materials Research*, 29 (5):695–707, March 2014. ISSN 2044-5326. doi: 10.1557/jmr.2014.24. URL http://dx.doi.org/10.1557/jmr.2014.24.

[214] Masayuki Kamaya, Yuji Kitsunai, and Masato Koshiishi. True stress–strain curve acquisition for irradiated stainless steel including the range exceeding necking strain. *Journal of Nuclear Materials*, 465:316–325, October 2015. ISSN 0022-3115. doi: 10.1016/j.jnucmat.2015.05.027. URL http://dx.doi.org/10.1016/j.jnucmat.2015.05.027.

[215] R.K. Boger, R.H. Wagoner, F. Barlat, M.G. Lee, and K. Chung. Continuous, large strain, tension/compression testing of sheet material. *International Journal of Plasticity*, 21(12):2319–2343, December 2005. ISSN 0749-6419. doi: 10.1016/j.ijplas.2004.12.002. URL http://dx.doi.org/10.1016/j.ijplas.2004.12.002.

[216] Edin Omerspahic, Kjell Mattiasson, and Bertil Enquist. Identification of material hardening parameters by three-point bending of metal sheets. *International Journal of Mechanical Sciences*, 48(12):1525–1532, December 2006. ISSN 0020-7403. doi: 10.1016/j.ijmecsci.2006.05.009. URL http://dx.doi.org/10.1016/j.ijmecsci.2006.05.009.

[217] A. Brosius, Q. Yin, A. Güner, and A.E. Tekkaya. A new shear test for sheet metal characterization. *steel research international*, 82(4):323–328, December 2010. ISSN 1869-344X. doi: 10.1002/srin.201000163. URL http://dx.doi.org/10.1002/srin.201000163.

[218] Bin Gu, Ji He, Shuhui Li, Yuan Chen, and Yongfeng Li. Cyclic sheet metal test comparison and parameter calibration for springback prediction of dual-phase steel sheets. *Journal of Manufacturing Science and Engineering*, 139 (9), July 2017. ISSN 1528-8935. doi: 10.1115/1.4037040. URL http://dx.doi.org/10.1115/1.4037040.

[219] Junying Min, Nan Guo, Yong Hou, Kaiwei Jiang, Xinping Chen, John E. Carsley, and Jianping Lin. Effect of tension-compression testing strategy on kinematic model calibration and springback simulation of advanced high strength steels. *International Journal of Material Forming*, 14(3):435–448, August 2020. ISSN 1960-6214. doi: 10.1007/s12289-020-01583-8. URL http://dx.doi.org/10.1007/s12289-020-01583-8.

[220] Yong Hou, Junying Min, Jianping Lin, Zhimiao Liu, John E. Carsley, and Thomas B. Stoughton. Springback prediction of sheet metals using improved material models. *Procedia Engineering*, 207:173–178, 2017. ISSN 1877-7058. doi: 10.1016/j.proeng.2017.10.757. URL http://dx.doi.org/10.1016/j.proeng.2017.10.757.

[221] S. Sumikawa, A. Ishiwatari, J. Hiramoto, and T. Urabe. Improvement of springback prediction accuracy using material model considering elastoplastic anisotropy and bauschinger effect. *Journal of Materials Processing Technology*, 230:1–7, April 2016. ISSN 0924-0136. doi: 10.1016/j.jmatprotec.2015.11.004. URL http://dx.doi.org/10.1016/j.jmatprotec.2015.11.004.

[222] Geunsu Joo, Hoon Huh, and Junbeom Kwon. Evaluation of rate-dependent hardening behaviors of ahss sheets with novel tension and compression test devices. *Journal of Materials Processing Technology*, 270:365–379, August 2019. ISSN 0924-0136. doi: 10.1016/j.jmatprotec.2019.03.011. URL http://dx.doi.org/10.1016/j.jmatprotec.2019.03.011.

[223] Jianping Lin, Yong Hou, Junying Min, Huijun Tang, John E. Carsley, and Thomas B. Stoughton. Effect of constitutive model on springback prediction of mp980 and aa6022-t4. *International Journal of Material Forming*, 13(1): 1–13, January 2019. ISSN 1960-6214. doi: 10.1007/s12289-018-01468-x. URL http://dx.doi.org/10.1007/s12289-018-01468-x.

[224] J.W. Yoon, F. Barlat, J.J. Gracio, and E. Rauch. Anisotropic strain hardening behavior in simple shear for cube textured aluminum alloy sheets. *International Journal of Plasticity*, 21(12):2426–2447, December 2005. ISSN 0749-6419. doi: 10.1016/j.ijplas.2005.03.014. URL http://dx.doi.org/10.1016/j.ijplas.2005.03.014.

[225] S. Bouvier, H. Haddadi, P. Levée, and C. Teodosiu. Simple shear tests: Experimental techniques and characterization of the plastic anisotropy of rolled sheets at large strains. *Journal of Materials Processing Technology*, 172(1):96–103, February 2006. ISSN 0924-0136. doi: 10.1016/j.jmatprotec.2005.09.003. URL http://dx.doi.org/10.1016/j.jmatprotec.2005.09.003.

[226] Q. Yin, C. Soyarslan, A. Güner, A. Brosius, and A.E. Tekkaya. A cyclic twin bridge shear test for the identification of kinematic hardening parameters. *International Journal of Mechanical Sciences*, 59(1):31–43, June 2012. ISSN

0020-7403. doi: 10.1016/j.ijmecsci.2012.02.008. URL http://dx.doi.org/10.1016/j.ijmecsci.2012.02.008.

[227] M.G. Lee, J.W. Lee, J.J. Gracio, G. Vincze, E.F. Rauch, and F. Barlat. A dislocation-based hardening model incorporated into an anisotropic hardening approach. *Computational Materials Science*, 79:570–583, November 2013. ISSN 0927-0256. doi: 10.1016/j.commatsci.2013.05.056. URL http://dx.doi.org/10.1016/j.commatsci.2013.05.056.

[228] E.F. Rauch, J.J. Gracio, and F. Barlat. Work-hardening model for polycrystalline metals under strain reversal at large strains. *Acta Materialia*, 55(9): 2939–2948, May 2007. ISSN 1359-6454. doi: 10.1016/j.actamat.2007.01.003. URL http://dx.doi.org/10.1016/j.actamat.2007.01.003.

[229] M. Weiss, A. Kupke, P.Y. Manach, L. Galdos, and P.D. Hodgson. On the bauschinger effect in dual phase steel at high levels of strain. *Materials Science and Engineering: A*, 643:127–136, September 2015. ISSN 0921-5093. doi: 10.1016/j.msea.2015.07.037. URL http://dx.doi.org/10.1016/j.msea.2015.07.037.

[230] S. Thuillier and P.Y. Manach. Comparison of the work-hardening of metallic sheets using tensile and shear strain paths. *International Journal of Plasticity*, 25(5):733–751, May 2009. ISSN 0749-6419. doi: 10.1016/j.ijplas.2008.07.002. URL http://dx.doi.org/10.1016/j.ijplas.2008.07.002.

[231] A. F. G. Pereira, P. A. Prates, N. A. Sakharova, M. C. Oliveira, and J. V. Fernandes. On the identification of kinematic hardening with reverse shear test. *Engineering with Computers*, 31(4):681–690, July 2014. doi: 10.1007/s00366-014-0369-7. URL https://doi.org/10.1007/s00366-014-0369-7.

[232] F. Yoshida, M. Urabe, and V.V. Toropov. Identification of material parameters in constitutive model for sheet metals from cyclic bending tests. *International Journal of Mechanical Sciences*, 40(2–3):237–249, February 1998. ISSN 0020-7403. doi: 10.1016/s0020-7403(97)00052-0. URL http://dx.doi.org/10.1016/S0020-7403(97)00052-0.

[233] P.-A. Eggertsen and K. Mattiasson. On the modelling of the bending–unbending behaviour for accurate springback predictions. *International Journal of Mechanical Sciences*, 51(7):547–563, 2009. doi: 10.1016/j.ijmecsci.2009.05.007.

[234] Shun-lai Zang, Myoung-Gyu Lee, Li Sun, and Ji Hoon Kim. Measurement of the bauschinger behavior of sheet metals by three-point bending springback test with pre-strained strips. *International Journal of Plasticity*, 59:84–107, August 2014. ISSN 0749-6419. doi: 10.1016/j.ijplas.2014.03.015. URL `http://dx.doi.org/10.1016/j.ijplas.2014.03.015`.

[235] Abbas Ghaei, Daniel E Green, Sandrine Thuillier, and Fabrice Morestin. On the use of cyclic shear, bending and uniaxial tension–compression tests to reproduce the cyclic response of sheet metals. *Proceedings of the Institution of Mechanical Engineers, Part B: Journal of Engineering Manufacture*, 229 (3):453–462, 2014. ISSN 2041-2975. doi: 10.1177/0954405414529122. URL `http://dx.doi.org/10.1177/0954405414529122`.

[236] Dierk Raabe, Binhan Sun, Alisson Kwiatkowski Da Silva, Baptiste Gault, Hung-Wei Yen, Karo Sedighiani, Prithiv Thoudden Sukumar, Isnaldi R. Souza Filho, Shyam Katnagallu, Eric Jägle, Philipp Kürnsteiner, Navyanth Kusampudi, Leigh Stephenson, Michael Herbig, Christian H. Liebscher, Hauke Springer, Stefan Zaefferer, Vitesh Shah, Su-Leen Wong, Christian Baron, Martin Diehl, Franz Roters, and Dirk Ponge. Current challenges and opportunities in microstructure-related properties of advanced high-strength steels. *Metallurgical and Materials Transactions A*, 51(11):5517–5586, September 2020. ISSN 1543-1940. doi: 10.1007/s11661-020-05947-2. URL `http://dx.doi.org/10.1007/s11661-020-05947-2`.

[237] ISO. Metallic materials — Tensile testing — Part 1: Method of test at room temperature. Standard, International Organization for Standardization, Geneva, CH, nov 2019.

[238] Daniel J. Cruz, Sahand P. Shamchi, Abel D. Santos, Rui L. Amaral, Paulo J. Tavares, and PMGP Moreira. Development of a mini-tensile approach for sheet metal testing using digital image correlation. *Procedia Structural Integrity*, 25:316–323, 2020. ISSN 2452-3216. doi: 10.1016/j.prostr.2020.04.036. URL `http://dx.doi.org/10.1016/j.prostr.2020.04.036`.

[239] M. Grédiac and F. Hild (Eds.). *Full-Field Measurements and Identification in Solid Mechanics*. John Wiley and Sons, 2012.

[240] B. Pan. Digital image correlation for surface deformation measurement: historical developments, recent advances and future goals. *Measurement Science*

and Technology, 29(8):082001, 2018. doi: 10.1088/1361-6501/aac55b. URL http://stacks.iop.org/0957-0233/29/i=8/a=082001.

[241] F.G. Cunha, T.G. Santos, and J. Xavier. In situ monitoring of additive manufacturing using digital image correlation: A review. *Materials*, 14(6), 2021. doi: 10.3390/ma14061511. URL https://www.mdpi.com/1996-1944/14/6/1511.

[242] W. H. Peters and W. F. Ranson. Digital Imaging Techniques In Experimental Stress Analysis. *Optical Engineering*, 21(3):427 – 431, 1982. doi: 10.1117/12.7972925. URL https://doi.org/10.1117/12.7972925.

[243] J. Xavier, A.M.P. de Jesus, J.J.L. Morais, and J.M.T. Pinto. Stereovision measurements on evaluating the modulus of elasticity of wood by compression tests parallel to the grain. *Construction and Building Materials*, 26(1):207–215, 2012. ISSN 0950-0618. doi: 10.1016/j.conbuildmat.2011.06.012. URL http://dx.doi.org/10.1016/j.conbuildmat.2011.06.012.

[244] A. M. R. Sousa, J. Xavier, M. Vaz, J. J. L. Morais, and V. M. J. Filipe. Cross-correlation and differential technique combination to determine displacement fields. *Strain*, 47(s2):87–98, December 2011. ISSN 1475-1305. doi: 10.1111/j.1475-1305.2010.00740.x. URL http://dx.doi.org/10.1111/j.1475-1305.2010.00740.x.

[245] Aleksander Sendrowicz, Aleksander Omholt Myhre, Seweryn Witold Wierdak, and Alexei Vinogradov. Challenges and accomplishments in mechanical testing instrumented by in situ techniques: Infrared thermography, digital image correlation, and acoustic emission. *Applied Sciences*, 11(15), 2021. ISSN 2076-3417. doi: 10.3390/app11156718. URL https://www.mdpi.com/2076-3417/11/15/6718.

[246] Dongsheng Zhang, Miao Luo, and Dwayne Arola. Displacement/strain measurements using an optical microscope and digital image correlation. *Optical Engineering - OPT ENG*, 45, 2006. doi: 10.1117/1.2182108. URL http://dx.doi.org/10.1117/1.2182108.

[247] Zili Sun, Jed S Lyons, and Stephen R McNeill. Measuring microscopic deformations with digital image correlation. *Optics and Lasers in Engineering*, 27 (4):409–428, July 1997. ISSN 0143-8166. doi: 10.1016/s0143-8166(96)00041-3. URL http://dx.doi.org/10.1016/S0143-8166(96)00041-3.

[248] N. Sabaté, D. Vogel, A. Gollhardt, J. Keller, B. Michel, C. Cané, I. Gràcia, and J. R. Morante. Measurement of residual stresses in micromachined structures in a microregion. *Applied Physics Letters*, 88(7):071910, February 2006. doi: 10.1063/1.2177357. URL https://doi.org/10.1063/1.2177357.

[249] Fabienne Lagattu, Florent Bridier, Patrick Villechaise, and Jean Brillaud. In-plane strain measurements on a microscopic scale by coupling digital image correlation and an in situ sem technique. *Materials Characterization*, 56(1): 10–18, January 2006. ISSN 1044-5803. doi: 10.1016/j.matchar.2005.08.004. URL http://dx.doi.org/10.1016/j.matchar.2005.08.004.

[250] G. Vendroux and W. G. Knauss. Submicron deformation field measurements: Part 1. developing a digital scanning tunneling microscope. *Experimental Mechanics*, 38(1):18–23, 1998. ISSN 1741-2765. doi: 10.1007/bf02321262. URL http://dx.doi.org/10.1007/BF02321262.

[251] Y.L. Dong and B. Pan. A review of speckle pattern fabrication and assessment for digital image correlation. *Experimental Mechanics*, 57(8):1161–1181, May 2017. ISSN 1741-2765. doi: 10.1007/s11340-017-0283-1. URL http://dx.doi.org/10.1007/s11340-017-0283-1.

[252] Rory Bigger, Benoît Blaysat, Christofer Boo, Manuel Grewer, Jun Hu, Amanda Jones, Markus Klein, Kavesary Raghavan, Phillip Reu, Timothy Schmidt, Thorsten Siebert, Micah Simenson, Daniel Turner, Alessandro Vieira, and Thorsten Weikert. A good practices guide for digital image correlation. October 2018. doi: 10.32720/idics/gpg.ed1. URL http://dx.doi.org/10.32720/idics/gpg.ed1.

[253] João Luís Pereira, José Xavier, Bahman Ghiassi, José Lousada, and José Morais. On the identification of earlywood and latewood radial elastic modulus of pinus pinaster by digital image correlation: A parametric analysis. *The Journal of Strain Analysis for Engineering Design*, 53(8):566–574, July 2018. ISSN 2041-3130. doi: 10.1177/0309324718786351. URL http://dx.doi.org/10.1177/0309324718786351.

[254] João Henriques, José Xavier, and António Andrade-Campos. Identification of orthotropic elastic properties of wood by a synthetic image approach based on digital image correlation. *Materials*, 15(2):625, 2022. doi: 10.3390/ma15020625. URL https://www.mdpi.com/1996-1944/15/2/625.

[255] Pascal Lava, Elizabeth M. C. Jones, Lukas Wittevrongel, and Fabrice Pierron. Validation of finite-element models using full-field experimental data: Levelling finite-element analysis data through a digital image correlation engine. *Strain*, 56(4), 2020. ISSN 1475-1305. doi: 10.1111/str.12350. URL http://dx.doi.org/10.1111/str.12350.

[256] MatchID. *MatchID Manual*. MatchID: Metrology Beyond Colors, 2017.

[257] W.J. Yuan, Z.L. Zhang, Y.J. Su, L.J. Qiao, and W.Y. Chu. Influence of specimen thickness with rectangular cross-section on the tensile properties of structural steels. *Materials Science and Engineering: A*, 532:601–605, January 2012. ISSN 0921-5093. doi: 10.1016/j.msea.2011.11.021. URL http://dx.doi.org/10.1016/j.msea.2011.11.021.

[258] Marion Merklein and Manfredi Biasutti. Forward and reverse simple shear test experiments for material modeling in forming simulations. *Special Edition: 10th International Conference on Technology of Plasticity, ICTP 2011*, pages 702–707, 01 2011.

[259] A.D. Santos, J. Mendes, F. Gomes de Almeida, P. Teixeira, and J. Bessa Pacheco. Caracterização de materiais em chapa metálica com o ensaio bulge: desenvolvimento de um sistema mecânico experimental. In *Actas do X Congresso Iberoamericano de Engenharia Mecânica - CIBEM 10*, pages 103–114, 2011.

[260] F. Mujika. On the effect of shear and local deformation in three-point bending tests. *Polymer Testing*, 26(7):869–877, October 2007. ISSN 0142-9418. doi: 10.1016/j.polymertesting.2007.06.002. URL http://dx.doi.org/10.1016/j.polymertesting.2007.06.002.

[261] Faustino Mujika. Three-point bending test procedure: Rectangular cross section. *Unknow*, 2020. doi: 10.13140/RG.2.2.30407.52645. URL http://rgdoi.net/10.13140/RG.2.2.30407.52645.

[262] Daniel J. Cruz, André F.G. Pereira, Vasco M. Simões, Rui Amaral, Abel dos Santos, and Marta C. Oliveira. Work hardening of metallic sheets under tension-compression and simple shear reverse loading. *Key Engineering Materials*, 926:2012–2021, July 2022. ISSN 1662-9795. doi: 10.4028/p-73lq3w. URL http://dx.doi.org/10.4028/p-73lq3w.

[263] K.M. Zhao and J.K. Lee. Finite element analysis of the three-point bending of sheet metals. *Journal of Materials Processing Technology*, 122(1):6–11, 2002. ISSN 0924-0136. doi: 10.1016/s0924-0136(01)01064-0. URL http://dx.doi.org/10.1016/S0924-0136(01)01064-0.

[264] Zhong Chen, Umesh Gandhi, Jinwoo Lee, and R.H. Wagoner. Variation and consistency of young's modulus in steel. *Journal of Materials Processing Technology*, 227:227–243, January 2016. doi: 10.1016/j.jmatprotec.2015.08.024. URL https://doi.org/10.1016/j.jmatprotec.2015.08.024.

[265] Mohammad Omar Andar, Toshihiko Kuwabara, Shigeru Yonemura, and Akihiro Uenishi. Elastic–plastic and inelastic characteristics of high strength steel sheets under biaxial loading and unloading. *ISIJ International*, 50(4): 613–619, 2010. ISSN 1347-5460. doi: 10.2355/isijinternational.50.613. URL http://dx.doi.org/10.2355/isijinternational.50.613.

[266] H. Yoshihara and S. Tsunematsu. Feasibility of estimation methods for measuring young's modulus of wood by three-point bending test. *Materials and Structures*, 39(1):29–36, April 2006. ISSN 1871-6873. doi: 10.1617/s11527-005-9015-6. URL http://dx.doi.org/10.1617/s11527-005-9015-6.

[267] P.-A. Eggertsen and K. Mattiasson. An efficient inverse approach for material hardening parameter identification from a three-point bending test. *Engineering with Computers*, 26(2):159–170, 2009. ISSN 1435-5663. doi: 10.1007/s00366-009-0149-y. URL http://dx.doi.org/10.1007/s00366-009-0149-y.

[268] Young-Jin Kim, Chang-Ho Lee, Joung-Hun Kim, and Jae Hyuk Lim. Numerical modeling of shape memory alloy plates considering tension/compression asymmetry and its verification under pure bending. *International Journal of Solids and Structures*, 136–137:77–88, 2018. ISSN 0020-7683. doi: 10.1016/j.ijsolstr.2017.12.004. URL http://dx.doi.org/10.1016/j.ijsolstr.2017.12.004.

[269] Ossama Mamdouh Badr, Bernard Rolfe, Peng Zhang, and Matthias Weiss. Applying a new constitutive model to analyse the springback behaviour of titanium in bending and roll forming. *International Journal of Mechanical*

Sciences, 128–129:389–400, 2017. ISSN 0020-7403. doi: 10.1016/j.ijmecsci.2017.05.025. URL http://dx.doi.org/10.1016/j.ijmecsci.2017.05.025.

[270] Gustavo Capilla, Hiroshi Hamasaki, and Fusahito Yoshida. Determination of uniaxial large-strain workhardening of high-strength steel sheets from in-plane stretch-bending testing. *Journal of Materials Processing Technology*, 243:152–169, 2017. ISSN 0924-0136. doi: 10.1016/j.jmatprotec.2016.12.002. URL http://dx.doi.org/10.1016/j.jmatprotec.2016.12.002.

[271] Á. Nádai, A. M. Wahl, and Eugene C. Bingham. Plasticity, a mechanics of the plastic state of matter. *Journal of Rheology*, 2(4):455–456, 1931. ISSN 0097-0360. doi: 10.1122/1.2116408. URL http://dx.doi.org/10.1122/1.2116408.

[272] Jeffrey C. Lagarias, James A. Reeds, Margaret H. Wright, and Paul E. Wright. Convergence properties of the nelder–mead simplex method in low dimensions. *SIAM Journal on Optimization*, 9(1):112–147, January 1998. doi: 10.1137/s1052623496303470. URL https://doi.org/10.1137/s1052623496303470.

[273] Seong-Yong Yoon. Umat optimization public. https://github.com/theysy/UMAT_optimization_public.git, 2017. [Accessed 13-11-2024].

[274] ASTM. Astm e290 - standard test methods for bend testing of material for ductility. Standard, ASTM International, West Conshohocken, PA, USA„ 2014.

[275] Dassault Systèmes. *Abaqus Analysis User's Manual*. Dassault Systèmes, Providence, RI, 2021. Version 2021.

[276] B. Ferreira. Integração de metodologias de análise do processo de quinagem. Master's thesis, Master's Thesis, Faculdade de Engenharia da Universidade do Porto, Porto, Portugal, 2015.

[277] Nengxiu Deng and Yannis P. Korkolis. Elastic anisotropy of dual-phase steels with varying martensite content. *International Journal of Solids and Structures*, 141-142:264–278, June 2018. doi: 10.1016/j.ijsolstr.2018.02.028. URL https://doi.org/10.1016/j.ijsolstr.2018.02.028.

[278] T. de Souza and B. Rolfe. Multivariate modelling of variability in sheet metal forming. *Journal of Materials Processing Technology*, 203(1-3):1–12, July 2008.

doi: 10.1016/j.jmatprotec.2007.09.075. URL https://doi.org/10.1016/j.jmatprotec.2007.09.075.

[279] Z. Marciniak, J.L. Duncan, and S.J. Hu. *Bending of sheet*, page 82–107. Elsevier, 2002. ISBN 9780750653008. doi: 10.1016/b978-075065300-8/50009-1. URL http://dx.doi.org/10.1016/B978-075065300-8/50009-1.

[280] R.J Mentink, D Lutters, A.H Streppel, and H.J.J Kals. Determining material properties of sheet metal on a press brake. *Journal of Materials Processing Technology*, 141(1):143–154, October 2003. ISSN 0924-0136. doi: 10.1016/s0924-0136(03)00274-7. URL http://dx.doi.org/10.1016/S0924-0136(03)00274-7.

[281] François Chollet et al. Keras. https://keras.io, 2015.

[282] Martín Abadi et al. Tensorflow: Large-scale machine learning on heterogeneous systems. *arXiv preprint arXiv:1603.04467*, 2016.

[283] Jasper Snoek, Hugo Larochelle, and Ryan P Adams. Practical bayesian optimization of machine learning algorithms. *Advances in Neural Information Processing Systems*, 25, 2012.

[284] Lukas Biewald. Experiment tracking with weights and biases. https://www.wandb.com/, 2020.

[285] E. Silvestre, J. Mendiguren, L. Galdos, and E. Sáenz de Argandoña. Comparison of the hardening behaviour of different steel families: From mild and stainless steel to advanced high strength steels. *International Journal of Mechanical Sciences*, 101–102:10–20, October 2015. ISSN 0020-7403. doi: 10.1016/j.ijmecsci.2015.07.013. URL http://dx.doi.org/10.1016/j.ijmecsci.2015.07.013.

[286] Jason Yosinski, Jeff Clune, Yoshua Bengio, and Hod Lipson. How transferable are features in deep neural networks? 2014. doi: 10.48550/ARXIV.1411.1792. URL https://arxiv.org/abs/1411.1792.

[287] Han Yang, Sumeet Kumar Sinha, Yuan Feng, David B. McCallen, and Boris Jeremić. Energy dissipation analysis of elastic–plastic materials. *Computer Methods in Applied Mechanics and Engineering*, 331:309–326, April 2018. ISSN 0045-7825. doi: 10.1016/j.cma.2017.11.009. URL http://dx.doi.org/10.1016/j.cma.2017.11.009.

[288] Colin Bonatti, Bekim Berisha, and Dirk Mohr. From cp-fft to cp-rnn: Recurrent neural network surrogate model of crystal plasticity. *International Journal of Plasticity*, 158:103430, November 2022. ISSN 0749-6419. doi: 10.1016/j.ijplas.2022.103430. URL http://dx.doi.org/10.1016/j.ijplas.2022.103430.

[289] Seongyon Yoon. mml_subroutine_public: Umat subroutine for abaqus. https://github.com/theysy/mml_subroutine_public, 2023. Accessed: 2025-07-16.

[290] Anne Marie Habraken, Toros Arda Aksen, José L. Alves, Rui L. Amaral, Ehssen Betaieb, Nitin Chandola, Luca Corallo, Daniel J. Cruz, Laurent Duchêne, Bernd Engel, Emre Esener, Mehmet Firat, Peter Frohn-Sörensen, Jesús Galán-López, Hadi Ghiabakloo, Leo A. I. Kestens, Junhe Lian, Rakesh Lingam, Wencheng Liu, Jun Ma, Luís F. Menezes, Tuan Nguyen-Minh, Sara S. Miranda, Diogo M. Neto, André F. G. Pereira, Pedro A. Prates, Jonas Reuter, Benoit Revil-Baudard, Carlos Rojas-Ulloa, Bora Sener, Fuhui Shen, Albert Van Bael, Patricia Verleysen, Frederic Barlat, Oana Cazacu, Toshihiko Kuwabara, Augusto Lopes, Marta C. Oliveira, Abel D. Santos, and Gabriela Vincze. Analysis of esaform 2021 cup drawing benchmark of an al alloy, critical factors for accuracy and efficiency of fe simulations. *International Journal of Material Forming*, 15(5), 2022. ISSN 1960-6214. doi: 10.1007/s12289-022-01672-w. URL http://dx.doi.org/10.1007/s12289-022-01672-w.

[291] A. Col and A. Santos. 3DS project results concerning springback experiments. In *Proceedings of the IDDRG'03*, Bled, Slovenia, 2003.

[292] ASTM. Astm e8 / e8m-16ae1 - standard test methods for tension testing of metallic materials. Standard, American Society for Testing and Materials, West Conshohocken, 2016.

[293] Yann LeCun, Corinna Cortes, and Christopher J.C. Burges. MNIST handwritten digit database. http://yann.lecun.com/exdb/mnist/, 2010. Accessed: 2025-09-09.

[294] ISO. Metallic materials — Sheet and strip — Determination of biaxial stress-strain curve by means of bulge test with optical measuring systems. Standard, International Organization for Standardization, Geneva, CH, may 2022.

[295] Abel D. Santos, Pedro Teixeira, A. Barata da Rocha, F. Barlat, F. Barlat, Y. H. Moon, and M. G. Lee. On the determination of flow stress using bulge test and mechanical measurement. In *AIP Conference Proceedings*, page 845–852. AIP, 2010. doi: 10.1063/1.3457644. URL `http://dx.doi.org/10.1063/1.3457644`.

[296] Hugo Campos, Abel Santos, Bruno Martins, K. ITO, N. Mori, and Frederic Barlat. Hydraulic bulge test for stress-strain curve determination and damage calibration for ito-goya model. *11th World Congress on Computational Mechanics*, 07 2014.

[297] A. Chamekh, H. BelHadjSalah, R. Hambli, and A. Gahbiche. Inverse identification using the bulge test and artificial neural networks. *Journal of Materials Processing Technology*, 177(1–3):307–310, 2006. ISSN 0924-0136. doi: 10.1016/j.jmatprotec.2006.03.214. URL `http://dx.doi.org/10.1016/j.jmatprotec.2006.03.214`.

[298] X. Lemoine, S. Sriram, and R. Kergen. Flow curve determination at large plastic strain levels to accurately constitutive equations of ahss in forming simulation. *AIP Conference Proceedings*, 1353(1):1417–1422, 2011. doi: 10.1063/1.3589715. URL `http://dx.doi.org/10.1063/1.3589715`.

[299] A. Mutrux, Bernd Hochholdinger, and Pavel Hora. Procedure for evaluation and validation of hydraulic biaxial experiment. *Numisheet*, pages 67–71, 2008.

[300] M. Sigvant, K. Mattiasson, H. Vegter, and P. Thilderkvist. A viscous pressure bulge test for the determination of a plastic hardening curve and equibiaxial material data. *International Journal of Material Forming*, 2(4):235–242, May 2009. ISSN 1960-6214. doi: 10.1007/s12289-009-0407-y. URL `http://dx.doi.org/10.1007/s12289-009-0407-y`.

[301] Lucian Lăzărescu, Dan-Sorin Comşa, Ioan Nicodim, Ioan Ciobanu, and Dorel Banabic. Characterization of plastic behaviour of sheet metals by hydraulic bulge test. *Transactions of Nonferrous Metals Society of China*, 22:s275–s279, December 2012. ISSN 1003-6326. doi: 10.1016/s1003-6326(12)61719-1. URL `http://dx.doi.org/10.1016/S1003-6326(12)61719-1`.

[302] Oskar Pawelski. Über das stauchen von hohlzylindern und seine eignung zur bestimmung der formänderungsfestigkeit dünner bleche. *Archiv für das Eisen-*

hüttenwesen, 38(6):437–442, June 1967. ISSN 0003-8962. doi: 10.1002/srin.196704204. URL http://dx.doi.org/10.1002/srin.196704204.

[303] L. M. Alves, C. V. Nielsen, and P. A. F. Martins. Revisiting the fundamentals and capabilities of the stack compression test. *Experimental Mechanics*, 51(9): 1565–1572, 2011. doi: 10.1007/s11340-011-9480-5. URL https://doi.org/10.1007/s11340-011-9480-5.

[304] ASTM. Astm e9-09 - standard test methods of compression testing of metallic materials at room temperature. Standard, American Society for Testing and Materials, West Conshohocken, 1195.

[305] M. Merklein and A. Kuppert. A method for the layer compression test considering the anisotropic material behavior. *International Journal of Material Forming*, 2(S1):483–486, 2009. ISSN 1960-6214. doi: 10.1007/s12289-009-0592-8. URL http://dx.doi.org/10.1007/s12289-009-0592-8.

[306] DIN. Testing of metallic materials - compression test at room temperature. Standard, Deutsches Institut fur Normung E.V. (DIN), nov 2016.

[307] Peter Hetz, Martin Kraus, and Marion Merklein. Characterization of sheet metal components by using an upsetting test with miniaturized cylindrical specimen. *CIRP Annals*, 71(1):233–236, 2022. doi: 10.1016/j.cirp.2022.03.010. URL http://dx.doi.org/10.1016/j.cirp.2022.03.010.

[308] C.S. Aitchison and L.B Tuckerman. The pack method for compressive tests of thin specimens of materials used in thin-wall structures, 1939.

[309] K.R. Jackman. Improved methods for determining the compression properties of sheet metal. *Automotive and aviation industries 90*, 11:36–38, 1944.

[310] Y. Tozawa. *Plastic Deformation Behavior under Conditions of Combined Stress*, pages 81–110. Springer US, Boston, MA, 1978. ISBN 978-1-4613-2880-3. doi: 10.1007/978-1-4613-2880-3_4. URL https://doi.org/10.1007/978-1-4613-2880-3_4.

[311] Fusahito Yoshida, Takeshi Uemori, and Kenji Fujiwara. Elastic–plastic behavior of steel sheets under in-plane cyclic tension–compression at large

strain. *International Journal of Plasticity*, 18(5):633–659, 2002. ISSN 0749-6419. doi: https://doi.org/10.1016/S0749-6419(01)00049-3. URL https://www.sciencedirect.com/science/article/pii/S0749641901000493.

[312] Akira Sekine and Toshihiko Kuwabara. Development of in-plane reverse loading test apparatus and measurement of the bauschinger effect of sheet metals. *The Proceedings of Autumn Conference of Tohoku Branch*, 2005.41:251–252, 2005. doi: 10.1299/jsmetohoku.2005.41.251. URL http://dx.doi.org/10.1299/jsmetohoku.2005.41.251.

[313] Jian Cao, Wonoh Lee, Hang Shawn Cheng, Mark Seniw, Hui-Ping Wang, and Kwansoo Chung. Experimental and numerical investigation of combined isotropic-kinematic hardening behavior of sheet metals. *International Journal of Plasticity*, 25(5):942–972, May 2009. ISSN 0749-6419. doi: 10.1016/j.ijplas.2008.04.007. URL http://dx.doi.org/10.1016/j.ijplas.2008.04.007.

[314] M. Tritschler, A. Butz, D. Helm, G. Falkinger, and J. Kiese. Experimental analysis and modeling of the anisotropic response of titanium alloy ti-x for quasi-static loading at room temperature. *International Journal of Material Forming*, 7(3):259–273, 2013. ISSN 1960-6214. doi: 10.1007/s12289-013-1125-z. URL http://dx.doi.org/10.1007/s12289-013-1125-Z.

[315] W. Hußnätter. Yielding of magnesium alloy az31. *Proceedings of ICTP2008*, page 109, 2009.

[316] F. Vollertsen, D. Biermann, H.N. Hansen, I.S. Jawahir, and K. Kuzman. Size effects in manufacturing of metallic components. *CIRP Annals*, 58(2):566–587, 2009. ISSN 0007-8506. doi: 10.1016/j.cirp.2009.09.002. URL http://dx.doi.org/10.1016/j.cirp.2009.09.002.

[317] Christian G'Sell, Serge Boni, and Suresh Shrivastava. Application of the plane simple shear test for determination of the plastic behaviour of solid polymers at large strains. *Journal of Materials Science*, 18(3):903–918, 1983. ISSN 1573-4803. doi: 10.1007/bf00745590. URL http://dx.doi.org/10.1007/BF00745590.

[318] E.F Rauch. Plastic anisotropy of sheet metals determined by simple shear tests. *Materials Science and Engineering: A*, 241(1–2):179–183, January 1998.

ISSN 0921-5093. doi: 10.1016/s0921-5093(97)00486-3. URL http://dx.doi.org/10.1016/S0921-5093(97)00486-3.

[319] Lothar W. Meyer, Shawky Abdel-Malek, and Norman Herzig. Experimental methods for characterizing of sheet metals at high strain rates. *Key Engineering Materials*, 473:474–481, March 2011. ISSN 1662-9795. doi: 10.4028/www.scientific.net/kem.473.474. URL http://dx.doi.org/10.4028/www.scientific.net/KEM.473.474.

[320] Qing Yin, Benjamin Zillmann, Sebastian Suttner, Gregory Gerstein, Manfredi Biasutti, A. Erman Tekkaya, Martin F.-X. Wagner, Marion Merklein, Mirko Schaper, Thorsten Halle, and Alexander Brosius. An experimental and numerical investigation of different shear test configurations for sheet metal characterization. *International Journal of Solids and Structures*, 51 (5):1066–1074. ISSN 0020-7683. doi: 10.1016/j.ijsolstr.2013.12.006. URL http://dx.doi.org/10.1016/j.ijsolstr.2013.12.006.

[321] K Miyauchi. A proposal for a planar simple shear test in sheet metals. *Sci. Pap. Inst. Phys. Chem. Res.(Jpn).*, 78(3):27–40, 1984.

[322] ASTM. Astm b831-05 - standard test method for shear testing of thin aluminum alloy products. Standard, American Society for Testing and Materials, West Conshohocken, 2005.

[323] Z. Marciniak. Influence of the sign change of the load on the strain hardening curve of a copper test subject to torsion. *Archiwum Mechaniki Stosowanej*, 13 (1):743 – 751, 1961.

[324] Mehmet Alper Sofuoğlu, Selim Gürgen, Fatih Hayati Çakır, and Sezan Orak. Springback behavior of AA6082t6 tubes in three-point bending operation. *Procedia Engineering*, 182:658–664, 2017. doi: 10.1016/j.proeng.2017.03.176. URL https://doi.org/10.1016/j.proeng.2017.03.176.

[325] D. Raabe, F. Roters, F. Barlat, and L. Q. Chen. *Continuum Scale Simulation of Engineering Materials: Fundamentals, Microstructures, Process Applications*. Weinheim, Germany, Wiley-VCH, 2004.

[326] L. Wagner, P. Larour, D. Dolzer, F. Leomann, and C. Suppan. Experimental issues in the instrumented 3 point bending VDA238-100 test. *IOP Conference Series: Materials Science and Engineering*, 967(1):012079, November

2020. doi: 10.1088/1757-899x/967/1/012079. URL https://doi.org/10.1088/1757-899x/967/1/012079.

[327] S. Naseem, E. S. Perdahcıoğlu, H. J. M. Geijselaers, and A. H. van den Boogaard. A new in-plane bending test to determine flow curves for materials with low uniform elongation. *Experimental Mechanics*, 60(9):1225–1238, 2020. ISSN 1741-2765. doi: 10.1007/s11340-020-00621-5. URL http://dx.doi.org/10.1007/s11340-020-00621-5.

[328] Xiangguo Zhai, Fu Zhang, Hongwei Zhao, Cong Li, Zhaoxin Xu, Xin Hao, Zhongwei Zhu, and Xiuquan Xu. Research on the effects of friction coefficient on three-point bending by finite element analysis. *Journal of Computational and Theoretical Nanoscience*, 12(12):5139–5143, 2015. doi: 10.1166/jctn.2015.4488. URL https://doi.org/10.1166/jctn.2015.4488.

Appendix A

Classical Monotonic Tests for Material Mechanical Characterization

A.1 Uniaxial Tensile Test

The uniaxial tensile test is the primary test used for material characterization due to its simplicity and standardization [84]. The tensile test is performed by applying a constant extension rate to a tensile specimen until failure. During the test, the axial load, F and the axial extension, ΔL, are measured and recorded using load cells and strain gauges, respectively. Using these values, the uniaxial stress-strain curve, σ-ε, is obtained using the following mathematical expressions:

$$\sigma = \frac{F}{A}, \tag{A.1}$$

$$\varepsilon = ln\left(1 + \frac{\Delta L}{L_0}\right), \tag{A.2}$$

where L_0 is the initial gauge length and A is the cross-sectional area of the specimen during the test, which is evaluated by:

$$A = A_0 e^{-\varepsilon}, \tag{A.3}$$

where A_0 is the initial cross-sectional area.

The plastic anisotropy coefficient, r, can be assessed under plane stress conditions by conducting uniaxial tensile tests on specimens taken at different angles relative to the rolling direction within the sheet plane. As presented in Equation 2.23, the r-value is characterize by the ratio between the true plastic strain in the width (ε_{22}) and the strain in the thickness (ε_{33}). Taking into account the condition of volume

constancy ($\varepsilon_{11} + \varepsilon_{22} + \varepsilon_{33} = 0$), Equation 2.23 can be re-written only using the principal ε_{11} and transverse strains ε_{22}:

$$r = \frac{w/w_0}{t/t_0} = \frac{\varepsilon_{22}}{\varepsilon_{33}} = -\frac{\varepsilon_{22}}{\varepsilon_{11} + \varepsilon_{22}} \tag{A.4}$$

where w_0 and t_0 represent the initial width and thickness of the specimen, w and t represent the width and thickness at the specified moment and finally ε_{11} represents the true plastic strain in the axial direction of the specimen.

A.2 Hydraulic Bulge Test

The biaxial hydraulic bulge test [294] is a standard experiment used to evaluate the plastic behavior of materials under biaxial deformation up to levels of plastic deformation significantly higher than those achieved in uniaxial tensile tests. As shown in Figure A.1, the experimental setup consists of a circular die and a circular blank holder, which restrict the specimen during the test by means of a drawbead. The design and configuration of the bulge test promote the material to be in a biaxial stress state [295]. The first step of the test procedure is clamping a circular sheet along its perimeter between the blank holder and the die to prevent the radial slippage of the sheet. Then, hydraulic pressure is injected into the central underside zone, deforming the sheet into an approximately spherical or ellipsoidal shape, depending on the die geometry. Material parameters are identified using both circular and elliptical dies. Circular dies are normally used to determine the parameters of isotropic hardening laws [296] and elliptical dies are used to identify yield surface parameters [297]. The hydraulic bulge test is characterized by lack of contact and consequently, no friction condition in the area of interest, which makes the analytical solution less complicated [295].

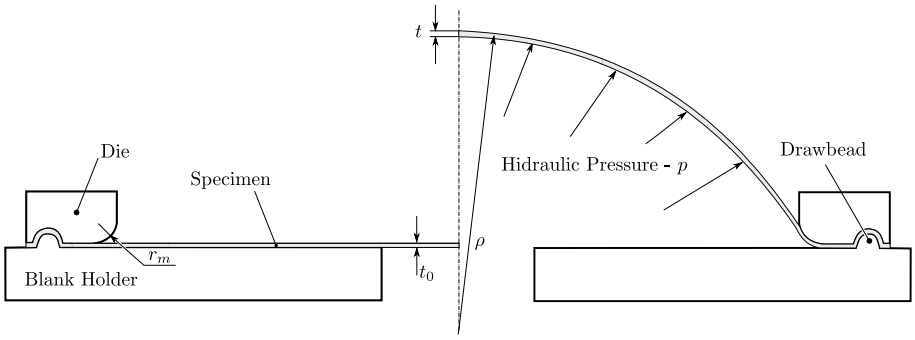


Figure A.1: Schematic representation of the hydraulic bulge test and its key variables; adapted from [295].

The analysis of stresses in the polar region of the bulge test is based on the membrane theory. For circular dies, the stresses in the principal directions ($\sigma_1 = \sigma_2 = \sigma_b$) are assumed to be equal, as are the radii of curvature ($\rho_1 = \rho_2 = \rho$). Therefore, the membrane theory is given by Equation A.5:

$$\sigma_b = \frac{p \cdot \rho}{2 \cdot t}, \tag{A.5}$$

which established a relationship between the hydraulic pressure, p, sheet thickness, t, radius of curvature, ρ and biaxial stress, σ_b, at each instant. The radius of curvature, ρ and the thickness of the specimen, t, at the pole can be determined by a measurement system, represented in Figure A.2, or using the digital image correlation technique [294]. Using the presented measurement system, the external radius of curvature, ρ_{ext}, is calculated by a simple geometric construction, given by:

$$\rho_{ext} = \frac{(D_{cv}/2)^2 + h^2}{2 \cdot h}, \tag{A.6}$$

where D_{cv} is the diameter established by the spherometer and h is the measured distance between the displacement transducer and the support of the spherometer. These variables are measured on the outer surface of the sheet metal. However, since membrane theory is applied to the neutral axis [298; 299], the radius of curvature, ρ, is determined by:

$$\rho = \rho_{ext} - \frac{t}{2}. \tag{A.7}$$

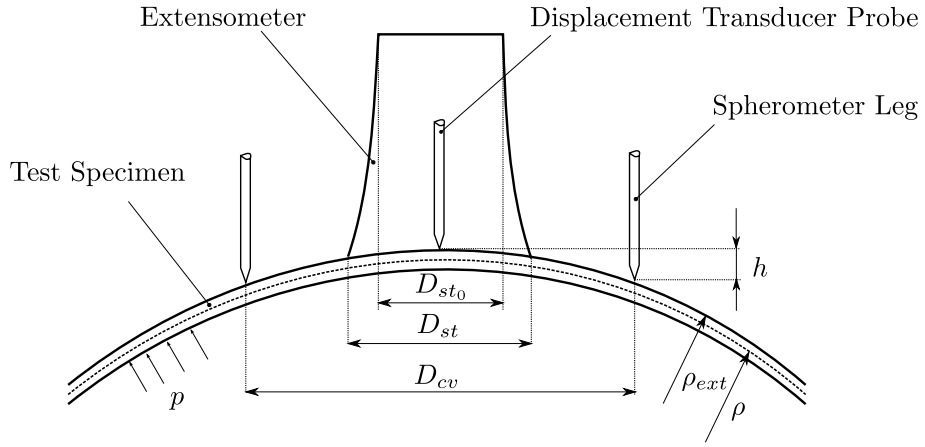


Figure A.2: Scheme of the mechanical measuring system constituted by an extensometer and a spherometer; adapted from [295].

The sheet thickness, t, at the pole of the bulge is evaluated by:

$$t = t_0 \cdot e^{-\varepsilon_t}, \tag{A.8}$$

where t_0 is the sheet's initial thickness and ε_t is the thickness strain (also known as biaxial strain, ε_b). Assuming the material is incompressible, i.e., the sum of all strains is zero and the volume of the material remains constant, the thickness strain, ε_t, can be calculated as follows:

$$\varepsilon_t = -2 \cdot \varepsilon, \tag{A.9}$$

where ε is the membrane strain ($\varepsilon = \varepsilon_1 = \varepsilon_2$).

The value of membrane strain is obtained by measuring the enlargement of the initial diameter, D_{st_0}, which turns into, D_{st} during the test. For the acquisition of such variables, the strain gauge is used in the measurement system, which follows the plastic deformation of the sheet metal throughout the experimental test. Therefore, the strain value, ε, in the sheet plane is given by:

$$\varepsilon = ln\left(\frac{D_{st}}{D_{st_0}}\right). \tag{A.10}$$

The biaxial hydraulic bulge test provides the advantage of obtaining experimental data on material behavior at higher levels of plastic deformation compared to the tensile test allowing the extension of the monotonic material's hardening curve. However, the stress-strain curves from these two tests cannot be directly combined due to the different stress states present in each test. Therefore, it is necessary to

transform the biaxial curve into an equivalent one based on the equivalent plastic work per unit volume (W), a methodology that several researchers have used with satisfactory results [300; 301]. The relationship between the equivalent plastic work and stress-strain data and the methodology for its calculation can be obtained from the integration of $\sigma = f(\varepsilon)$ for the entire plastic domain, being translated by:

$$W(\varepsilon) = \int_{\varepsilon_i}^{\varepsilon_f} \sigma(\varepsilon) \cdot d\varepsilon. \tag{A.11}$$

By defining W_u and W_b as the equivalent plastic work of the uniaxial tensile test and the bulge test, respectively, it is possible to establish a connection between the two curves when both equivalent plastic works are equal ($W_u = W_b$). Assuming the material is incompressible and considering that the stress state at the pole is such that $\sigma_1 = \sigma_2 = \sigma_b$, the stress-strain data from both tests can be related by the following expression:

$$\frac{\sigma}{\sigma_b} = \frac{\varepsilon}{\varepsilon_b} = k, \tag{A.12}$$

where k is a constant.

A.3 Stacked Disc Compression Test

The stacked disc compression test was proposed by Pawelski [302] in 1967 to evaluate the work hardening of sheet metal materials in an equibiaxial stress state. As represented in Figure A.3, the specimen is formed by stacked circular disks that are cut out of a blank with an initial thickness, t_0. Typically, the cylindrical specimen has a diameter/height ratio between $1 < d_0/h_0 < 3$, which is similar to the diameter/height ratio of solid cylinders used in traditional compression tests [303]. The test is performed by axially pressing the cylinder specimen between two flat, parallel, well-lubricated platens [304].

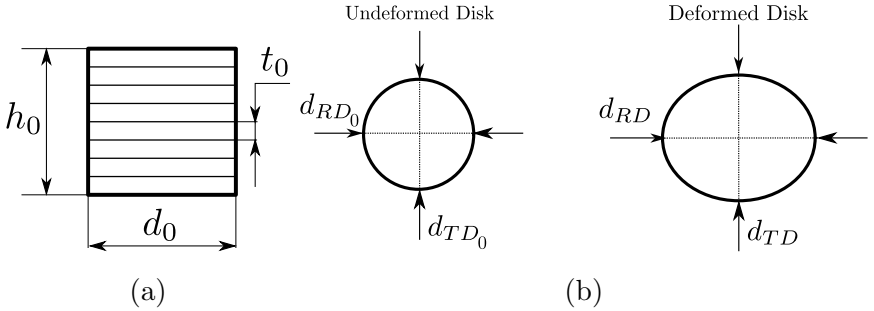


Figure A.3: Stacked disk compression test: (a) specimen; (b) disk diameters before and after deformation.

The test results are greatly influenced by the quality of measurements and frictional conditions at the contact interface between the specimen and the platens. Unlike other mechanical testing procedures, the stack compression test is not standardized. The most comprehensive work in this topic has been performed by Merklein and Kuppert [305], who discussed the utilization of the stack compression test for evaluating the flow curve of anisotropic materials. Additionally, Barlat et al.[101] used this test to measure the biaxial plastic anisotropy coefficient, r_b, of aluminium alloys. This coefficient is defined as:

$$r_b = \frac{\varepsilon^p_{22}}{\varepsilon^p_{11}}. \tag{A.13}$$

The in-plane strain components, ε^p_{11} and ε^p_{22}, are calculated by measuring the diameter of each disk before and after deformation, as shown in Figure A.3b. Furthermore, the through-thickness strain, ε^p_{33}, is calculated with the initial and final thicknesses. All the true plastic strain components can be mathematically described as:

$$\varepsilon^p_{11} = ln\left(\frac{d_{RD}}{d_{RD_0}}\right); \quad \varepsilon^p_{22} = ln\left(\frac{d_{TD}}{d_{TD_0}}\right); \quad \varepsilon^p_{33} = ln\left(\frac{t}{t_0}\right). \tag{A.14}$$

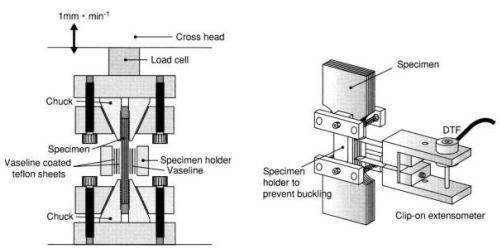
where d_{RD} and d_{TD} are the diameters associated with rolling and transverse direction of the sheet, respectively and t is the sheet thickness.

A.4 In-Plane Compression Test

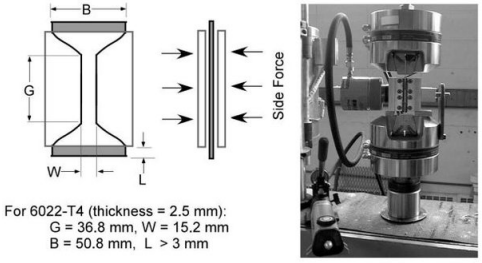
The compression test according to DIN 50106 [306] is a well-established mechanical test used to characterize the material behavior of metallic materials in the uniaxial compression stress state using cylindrical specimens. As presented in Section A.3,

for sheet metal materials, the stacked disc compression test is a valid alternative to evaluate the biaxial compression stress state along the sheet and the uniaxial compression stress state in the sheet thickness direction [307]. However, there is no standardized testing system or methodology in the literature to evaluate the compressive behavior along the sheet plane. The compression of a flat sheet metal test specimen can lead to buckling and thus the test becomes invalid due to a changed stress state. This phenomenon is intensified, especially when the ratio between the reference length and the thickness of the specimen is high. In order to avoid buckling of sheet metal specimens, different solutions have been developed over the years, which can be divided into three groups: (i) pack method, using a set of specimens packed together in the thickness direction; (ii) single sheet with a lateral support system; and (iii) miniaturized test samples with a low gauge-length/thickness ratio.

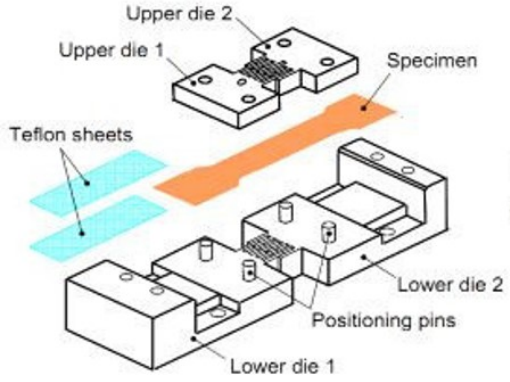
The pack method consists of packing together a set of specimens (in thickness) as a unique specimen. This strategy reduces the length/thickness ratio, reducing the probability of buckling under compression. Aitchison et al. [308] and Jackman [309], joined flat sheet metal tensile specimens in a unique pack and submitted them to compression. In addition to flat tensile test specimens with bone-shaped contours, rectangular sheet metal strips have also been used as specimen geometries [310]. Yoshida et al. [311], Figure A.4a, used a variation of the pack method, where five specimens were glued together and then covered with clamping plates. The pack method requires a large number of specimens and a complex preparation. Therefore, some authors prefer using a single sheet with a lateral support system. Boger et al. [215], Figure A.4b, used two solid support plates to "sandwich" the specimen with a constant restraining side force, generated by a hydraulic cylinder. An exaggerated dog-bone specimen was optimized to suppress buckling in the thickness direction (T-buckling), in the unsupported gap (L-buckling) and in the width direction (W-buckling). Sekine and Kuwabara [312], Figure A.4c, have introduced a device with two sets of fork-shaped supports to eliminate the uncovered area in tensile-compressive relative movements. This design allowed the entire length of the specimen to be supported because, as the sample is compressed, the male and female die slide past each other. Cao et. al [313], Figure A.4d, developed a fixture based on laser extensometers. The specimen was entirely sandwiched between two sets of wedge blocks without any unsupported area.



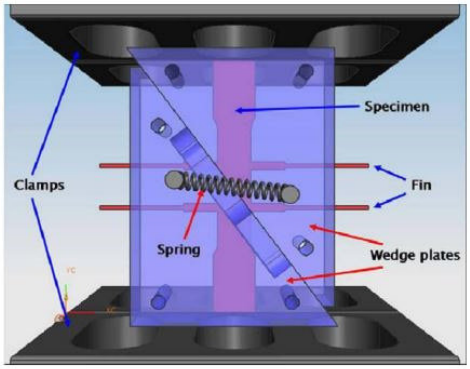
(a) Yoshida et al. [311]



(b) Boger et al. [215]



(c) Kuwabara et al. [312]



(d) Cao et al. [313]

Figure A.4: Different methodologies presented in literature to perform in-plane compression tests.

Buckling in compression is mainly influenced by the ratio between the gauge length and the thickness of the specimen. Therefore, test methods with miniaturized specimens were recently proposed as a powerful solution to study the compression behavior of sheet metal materials. Tritschler et al. [314] tested a 1.2 mm thickness titanium alloy in compression using specimens of 2.5 mm length by 2 mm width, attaining about 2% of compressive strains. Hußnätter [315] used a specimen geometry with a 2 mm length by 2 mm width for the characterization of the magnesium alloy AZ31, achieving about 5% of compressive strains before the specimen buckles. Cruz et al. [238] have analysed the mechanical behavior of sheet materials, comparing miniaturized test samples with macro-standard tensile specimens, concluding that miniaturized test samples can accurately describe the mechanical material behavior and, thus, they can be used to evaluate the mechanical behavior of sheet metal materials during reverse loadings. However, size effects can occur when using a miniaturized specimen geometry [316], which limits the transferability of the results to standardized specimen geometries.

A.5 Shear Test

The in-plane shear test is another common method for measuring the hardening behavior of sheet metals. This test is effective in measuring large plastic deformations while mitigating plastic instability issues such as necking and buckling. Moreover, it can be conveniently conducted using a mechanical tensile testing machine with specialized fixtures. Various versions of the simple shear test can be found in the literature, all of which involve parallel translational displacements to deform a specific shear zone [217]. The one-sided shear test [317] is the simplest approach to implementing a shear test and was adapted for metallic materials by Rauch [318]. As illustrated in Figure A.5, the specimen features two clamping areas that move parallel to each other, deforming a single gauge area. Due to its homogeneous strains and highly simplified geometry, this test is widely employed [85; 318–320]. Despite its simplicity, obtaining accurate results requires significant experimental effort. This effort is primarily attributed to specimen slipping during the test and the reaction moment generated on the specimen [217]. The stress distribution during the test is generally characterized by a homogeneous zone in the center of the gauge area and a heterogeneous zone near the free ends of the specimen [225]. If the stress heterogeneity is restricted to a small zone of the specimen, the shear stress, τ_{xy}, is given by:

$$\tau_{xy} = \frac{F}{L_0 \cdot t_0}, \tag{A.15}$$

where F is the applied axial load and t_0 and L_0 are the initial thickness and initial length of the gauge area.

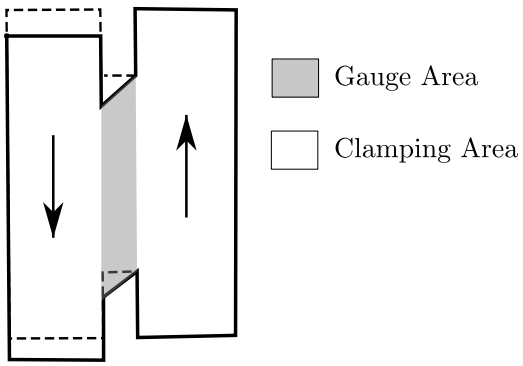
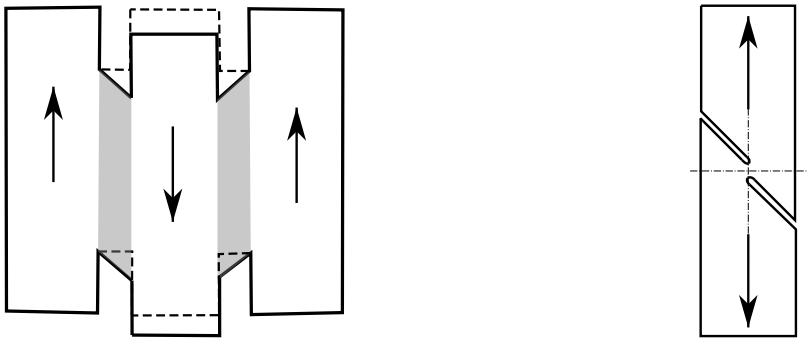


Figure A.5: Shear test specimen with a single gauge area; adapted from [318] .

A different version of the one-side shear test is the symmetrical shear test proposed by Miyauchi [321]. As depicted in Figure A.6a, the shear specimen comprises

three clamping areas and two gauge areas between them. The zones between the clamping areas undergo simple shear due to the parallel displacement of the middle clamp relative to the other ones. In this configuration, the shear forces are balanced, thereby reducing unwanted rotational moments in the specimen [320]. Additionally, the symmetry of the specimen causes the two shear zones to deform in opposite directions. However, the shear zones do not always produce the same shear results depending on factors such as anisotropy, angle in relation to the rolling direction and pre-straining.



(a) (b)

Figure A.6: Shear test specimens according to (a) Miyauchi [321] and (b) ASTM B831-05 [322].

An alternative shear test can be found in the American Standard, ASTM B831-05 [322]. As shown in Figure A.6b, the specimen features a single shear zone and can be easily tested in a universal tensile testing machine without requiring special clamping systems. However, for higher displacements, a rotation of the shear area may occur. This rotation can be minimized by increasing the stiffness of the clamping tool and applying an adequate clamping force. Merklein and Biasutti [258] developed a modified simple shear specimen based on this standard in order to enable the application of cyclic loading.

The in-plane torsion test of sheet metal, first proposed by Marciniak [323], offers a different approach to testing sheet metal materials under shear loadings. The circular specimen, illustrated in Figure A.7a, is initially clamped along the periphery and then a torsional moment, M, is applied through the central clamping area, deforming the gauge area between them. Using this geometry, the unwanted moments observed in previous geometries are suppressed. However, the anisotropy of the materials cannot be investigated with this specimen geometry, as the measured torsional moment is referenced to the complete gauge area. For this reason,

Brosious [217] proposed the twin bridge shear test, in which the shear deformation is confined to two distinct shear bridges, as depicted in Figure A.7a. With this specimen configuration, it becomes possible to evaluate the response of anisotropic materials since the shear regions are deformed in the same orientation. However, this test necessitates specific torsion equipment and is typically not the preferred method for assessing the shear stress state of a sheet metal material.

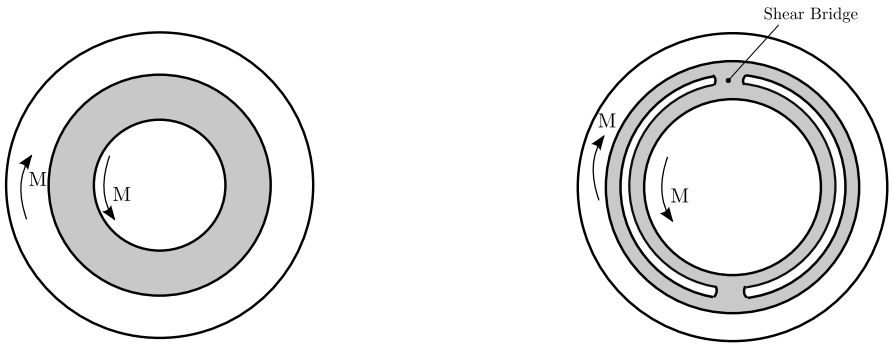


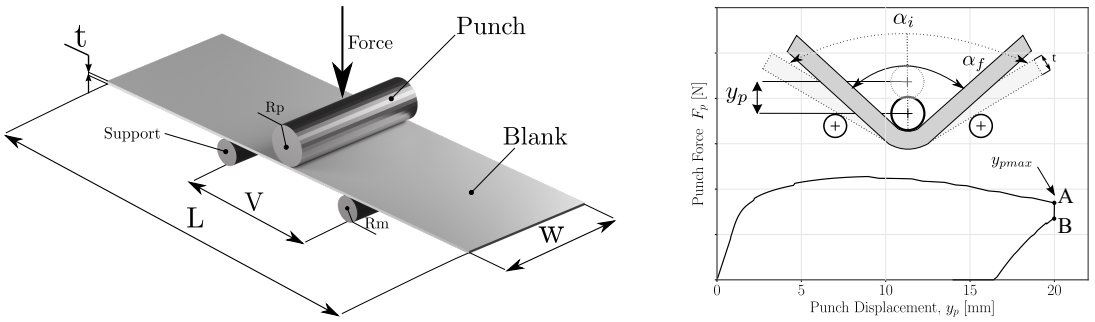
Figure A.7: Representation of torsional shear tests proposed by (a) Marciniak [323] and (b) Brosius [217].

A.6 Three-Point Bending Test

The standard ASTM E290 [274] covers several bending tests used to evaluate the behavior of materials when subjected to bending loads under different boundary conditions. The most common is the guided-bend test, which uses a three-point bending setup (Figure A.8a) without using a female die. The test is conducted by placing a rectangular specimen symmetrically on the support fixture mounted to the testing machine. Load is applied at the specimen's midpoint until either failure occurs or the predefined angle of bend or maximum angle for the fixture is achieved. The bending angle is determined during the test by projecting lines along the specimen's flat surfaces outside the bend region and measuring their intersecting angle. After completing the bending test, the curved surface of the bend is examined to evaluate the presence of cracks or surface irregularities.

For sheet metal materials, the three-point bending test is widely used to evaluate the springback effect of the tested material. As represented in Figure A.8b, the removal of the tools for a punch displacement, y_p, of 20 mm leads to elastic recovery of the material, which results in different bending angles before, α_i and after, α_f,

springback. The springback is entirely intercorrelated with the stress distribution on sheet metal after forming and its magnitude is related to the ratio between the residual stress and the elastic modulus of the material [324]. It is also influenced by material properties such as strain hardening, elastic property evolution, the presence of Bauschinger effects, elastic and plastic anisotropy and tribology between contacting surfaces [325].



(a) (b)

Figure A.8: Schematic illustration of a (**a**) three-point bending test setup and the main variables: support span (V), support radius (Rm), specimen length (L), specimen width (W), specimen thickness (t) and punch radius (Rp); (**b**) example of a punch force–displacement (F_p - y_p) curve of a sheet metal material.

One of the main advantages of the three-point bending test is its simplicity. In fact, this test does not require any special sample preparation, such as machining and can be easily conducted on a universal tensile testing machine. However, despite its simplicity, challenges arise due to the involvement of axial and transverse forces in the bending deformation [326]. Additionally, factors such as friction, local deformation beneath the contact points [327] and the determination of the stiffness of the testing system [261] can affect the results. Interpreting the raw experimental data, normally represented as punch displacement (y_p) and punch force (F_p) and converting it into a stress–strain (σ-ε) response typically involves the use of inverse fitting models [268–270] or analytical approaches [271]. These methods require accurate modeling of the test setup, often involving predetermined hardening models and iterative optimization loops. This strategy can be time-consuming, particularly when multiple experimental tests are performed.

Friction is an inherent aspect of the three-point bending test, with forces emerging at two locations: at the contact points between the sheet and punch and between the sheet and the supports. Friction can be characterized by Coulomb's friction

force model, where the friction force is directly proportional to the normal force and a friction coefficient. While it is improbable for the friction coefficient to remain constant throughout the process, for simplicity, an average coefficient, μ, is assumed [280]. Nevertheless, accurately determining the friction coefficient for the three-point bending test poses challenges due to factors such as the machining quality of the specimen surface and the structure of the supporter during the test [328]. The friction coefficient can be estimated using the punch force displacement curve and is related to the moment when the punch ceases its downward movement and initiates an upward motion — denoted as point A in Figure A.8b. At this point, the friction force at the points where the sheet touches the supports changes sign and the difference between the force at points A and B is strongly influenced by the coefficient of friction. Based on the work of Mentink et al. [280], the friction coefficient can be estimated as:

$$\mu = \frac{\Delta F sin(90 - \alpha)}{2F_m sin(\alpha)}, \tag{A.16}$$

where ΔF represents the drop in punch force between points A and B, F_m is the mean value between F_A and F_B and α represents half of the bending angle at position A.

Appendix B

Article: *"Application of Digital Image Processing Techniques to Detect Through-Thickness Crack in Hole Expansion Test"*

---

metals

MDPI

Article

Application of Digital Image Processing Techniques to Detect Through-Thickness Crack in Hole Expansion Test

Daniel J. Cruz [1,2], Rui L. Amaral [1,2], Abel D. Santos [1,2] and João Manuel R. S. Tavares [1,2,*]

[1] Instituto de Ciência e Inovação em Engenharia Mecânica e Engenharia Industrial, Campus da FEUP, R. Dr. Roberto Frias 400, 4200-465 Porto, Portugal; up201405104@edu.fe.up.pt (D.J.C.); ramaral@inegi.up.pt (R.L.A.); abel@fe.up.pt (A.D.S.)

[2] Faculdade de Engenharia, Universidade do Porto/s/n, R. Dr. Roberto Frias, 4200-465 Porto, Portugal

* Correspondence: tavares@fe.up.pt

Abstract: Advanced high-strength steels (AHSS) have become increasingly popular in the automotive industry due to their high yield and ultimate tensile strengths, enabling the production of lighter car body structures while meeting safety standards. However, they have some setbacks compared to conventional steels, such as edge cracking through sheet thickness caused by forming components with shear-cut edges. When characterizing the formability of sheet metal materials, the hole expansion test is an industry-standard method used to evaluate the stretch-flangeability of their edges. However, accurately visualizing the first cracking is usually tricky and may be subjective, often leading to inconsistent results and low reproducibility with some impact of the operator on both direct and post-processing measurements. To address these issues, a novel digital image processing method is presented to reduce operator reliance and enhance the accuracy and efficiency of the hole expansion test results. By leveraging advanced image processing algorithms, the proposed approach detects the appearance of the first edge cracks, enabling a more precise determination of the hole expansion ratio (HER). Furthermore, it provides valuable insights into the evolution of the hole diameter, allowing for a comprehensive understanding of the material behavior during the test. The proposed method was evaluated for different materials, and the corresponding HER values were compared with the traditional method.

Keywords: edge cracking; hole expansion ratio; adaptive image binarization; circular hough transform; advanced high-strength steels

check for updates

Citation: Cruz, D.J.; Amaral, R.L.; Santos, A.D.; Tavares, J.M.R.S. Application of Digital Image Processing Techniques to Detect Through-Thickness Crack in Hole Expansion Test. *Metals* **2023**, *13*, 1197. https://doi.org/10.3390/met13071197

Academic Editor: Francesco Iacoviello

Received: 9 May 2023
Revised: 22 June 2023
Accepted: 25 June 2023
Published: 28 June 2023

Copyright: © 2023 by the authors. Licensee MDPI, Basel, Switzerland. This article is an open access article distributed under the terms and conditions of the Creative Commons Attribution (CC BY) license (https://creativecommons.org/licenses/by/4.0/).

1. Introduction

The challenge posed to the automotive industry to improve energy efficiency and develop low-consumption vehicles has led to a demand for lighter construction components [1,2]. Using new materials to reduce weight is crucial in addressing these issues. Advanced high-strength steels (AHSS) and aluminum alloys have been employed to achieve this goal instead of using conventional steels [3]. AHSS typically exhibits high yield and ultimate tensile strengths, which are critical to ensure passenger safety. However, their processing poses setbacks and challenges. During the manufacturing forming process, the material undergoes severe loadings such as bending and stretching, which can result in edge cracking through the sheet thickness due to its low resistance to sheared edge cracking. The term "stretch-flangeability" refers to the ability of sheet metal materials to resist edge cracking when exposed to edge stretching deformation. This property is typically evaluated through hole punching and expansion tests [4].

The Hole Expansion Test (HET) is a commonly used method to assess the resistance and stretch-flangeability of sheared edges, and it is defined by the ISO 16630 [5] standard. In this test, a metallic sheet with a specified hole size is expanded by a conical punch until a

visible through-thickness crack appears. The hole expansion ratio ($HER(\%)$), is calculated according to:

$$HER(\%) = \frac{D_f - D_i}{D_f}, \quad (1)$$

where D_f (mm) and D_i (mm) represent the diameter of the expanded hole and the initial diameter on the sheared surface of the pre-punched hole, respectively.

The occurrence of cracks is typically assessed manually through visual inspection and experience. However, in some cases, the operator may not recognize the right moment to stop the test, leading to crack propagation and, consequently, increasing the measurement of the final hole diameter [6]. This human subjectivity can lead to errors and significant deviations in experimental results. Moreover, for certain materials, edge cracks may occur at varying times for each trial, which can increase the scatter of the hole expansion ratio [7].

There are several approaches to experimentally determine the crack initiation during the hole expansion test. Dunckelmeyer et al. [8] and Panich et al. [9] related the appearance of a through-thickness crack to a possible drop in the punch force-displacement curve. This method may be insufficient for some materials and test conditions, as multiple micro-cracks may appear simultaneously, requiring additional approaches. Leonhardt et al. [10] employed an automated pneumatic system to detect the crack. The authors concluded that the developed approach exhibits sufficient sensitivity to accurately determine the HER for different process parameters, e.g., cutting clearance and initial hole diameter.

One effective method for monitoring the development of through-thickness cracks is the implementation of digital image correlation (DIC) techniques. This optical measurement technique is widely used in experimental mechanics to analyze the displacement and strain of an object or surface by comparing images acquired before and after deformation [11]. By acquiring a continuous sequence of images during the hole expansion process, this approach enables the precise determination of the exact time when edge cracks appear and simplifies the analysis of their propagation around the hole [12]. Additionally, DIC techniques provide the capability to measure the strain distribution surrounding the hole during the expansion process. Chen et al. [13] employed a DIC technique to measure the strain field around the expanded hole on the upper surface of the specimen, which was important for understanding the deformation behavior and failure mechanisms of the material under analysis. Li et al. [14] later employed an ARAMIS system to observe the deformation of the specimen and investigate the influence of experimental methods, such as burr direction, hole manufacturing method, blank thickness, and punch shape, on the hole expansion ratio. Krempaszky et al. [15] and Wang et al. [16] used a digital camera system equipped with two charge-coupled device (CCD) cameras to measure the hole expansion ratio and generate precise 3D images of the through-thickness crack. Barlo et al. [17] investigated the boundary conditions of the HET by introducing draw beads to the experimental setup. Additionally, they used images acquired by a 3D DIC system to evaluate the hole expansion ratio, thereby reducing the impact of the operator-reliant post-processing. Digital image correlation systems typically require sophisticated and expensive equipment, including high-resolution cameras, specialized lenses, and complex calibration procedures. The need for such equipment and procedures can make setting up and implementing DIC techniques for hole expansion testing time-consuming.

Due to the disadvantages associated with DIC systems, the use of digital image processing (DIP) techniques has emerged as a simpler and viable alternative for the detection of through-thickness cracks during the hole expansion test [18]. These techniques refer to a broad range of methods and algorithms used to modify and extract information from digital images [19,20]. Chiriac et al. [21] used a Digital Recording and Measurement System (DRMS) to accurately determine the HER for different dual-phase steels resulting in a reduction in the variability of the hole expansion results. During the test operation, the system acquires and displays the edge of the punched hole in real time. After the test, the acquired image sequence is replayed, enabling a frame-by-frame analysis of fracture development. This semi-automatic analysis allows for the selection of the specific image frame of the

occurrence of a single through-thickness crack. By measuring the inside diameter of the hole at the selected frame, the authors accurately calculate the final hole expansion ratio. A similar approach was employed by Kim et al. [22]. In their study, the authors used a visual system for monitoring the edge expansion and investigated the effects of pre-machined processes on the hole expansion ratio. In both studies, the through-thickness crack is manually identified and analyzed using a pre-acquired image sequence, which can still introduce an element of human subjectivity and impact the consistency and reliability of the results. To address the challenges associated with the manual identification of through-thickness cracks, Choi et al. [23] developed an algorithm for smart crack inspection based on image processing techniques, mainly binarization and blob detection. This algorithm can automatically detect the presence of a through-thickness crack and calculate the corresponding HER value. Park et al. [24] developed an integrated analysis system that combines computer vision with punch load analysis to improve the accuracy of the measurements. The system includes an automated image processing algorithm, which reduces the risk of human error and enables more precise prediction of the measurements.

Cruz et al. [25] developed an instrumented device to acquire the real-time evolution of the hole dimensions during the test. They also developed a DIP tool, based on the Circular Hough Transform (CHT), to automatically detect and measure the different hole diameters, enabling a more accurate determination of the final hole expansion ratio. This methodology is suitable for sheet materials with thicknesses between 0.5 and 3 mm. The results were more consistent and accurate when compared to the traditional manual measurement method. Besides these developments, the moment to measure the HER value, i.e., the through-thickness crack occurrence, is still chosen manually using a pre-acquired image sequence. This article aims to give continuity to the work presented above by exploring different digital image processing techniques to automatically detect the occurrence of cracks in the hole expansion test, contributing to the improvement of prediction not only of the HER value, but also of the evolution of the expanded hole diameter during the test.

2. Experimental Setup

The hole expansion tests were conducted according to the ISO 16630 [5] standard using the universal test machine developed by Duarte et al. [26]. Because of its flexible mechanical system, this hydraulic power equipment is commonly used for studying plastic sheet metal forming behavior, and several tests can be performed with this equipment, including Hole Expansion, Erichsen, Nakajima, and Fukui tests, by simply changing the tool setup [27]. A schematic representation of the HET tool setup is represented in Figure 1.

The instrumented device presented in [25] was used to acquire the real-time evolution of the hole expansion throughout the test. The image acquisition system presented in Figure 1 comprises a digital web camera (Microsoft LifeCam Studio Win USB 1080p) with a maximum image resolution of 2560 $\times$ 2048 pixels and a maximum frame rate of 30 fps, and an illumination device installed at the center of the top of the system. It consists of a high-brightness LED strip that distributes light evenly on the sheared surface of the hole. A conical punch with a cone angle of 60º and a diameter of $\phi = 25$ mm was coated with a black PVD layer. This type of coating, as shown in Figure 1, creates a high-contrast region in the acquired image between the inner boundary of the expanded hole and the punch surface, which is critical for the identification of the through-thickness crack and the application of DIP techniques. The implemented image acquisition system is directly synchronized with the universal test machine. Therefore, during each test, an image sequence, i.e., video, is recorded, simultaneously with the displacement and punch force signals. The test stops when the operator sees a macro through-thickness crack. At this point, the test specimen is removed, and the HER value is determined using the acquired image sequence and the proposed digital image processing algorithm.

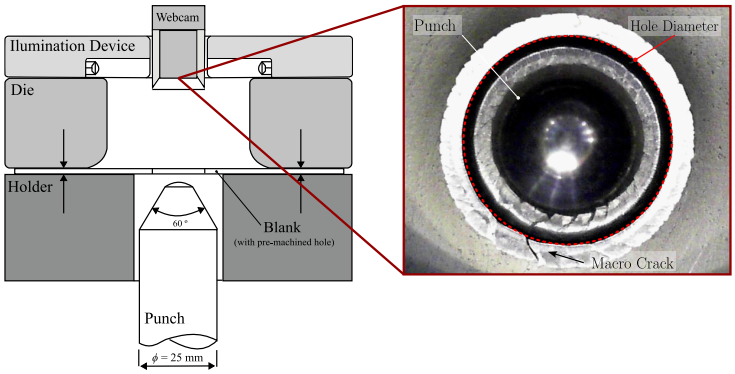


Figure 1. Experimental setup used for the hole expansion test (adapted from [25]).

During the hole expansion test, the punch moves vertically, and the plane where the internal diameter is measured approaches the camera successively. As a result, the system resolution, i.e., the ratio between pixels (px) and millimeters (mm), in the measurement plane varies throughout the test. To accurately account for this variability and address any optical distortions, a calibration procedure was performed for different measurement planes using a calibration gauge, depicted schematically in Figure 2. This gauge has marked circles with well-known diameters, D, in a range between 6 and 30 mm. The measurement plane is defined as the plane where the inner diameter is measured and its vertical displacement is given by $\Delta d_{m.plane}$. In the presented calibration process, the different measurement plane displacements were defined by approaching the gauge into the camera using the punch movement. The calibration results obtained from this procedure are presented in Figure 2, which lets one perceive the relationship between the known diameters of the gauge circles and their corresponding pixel values.

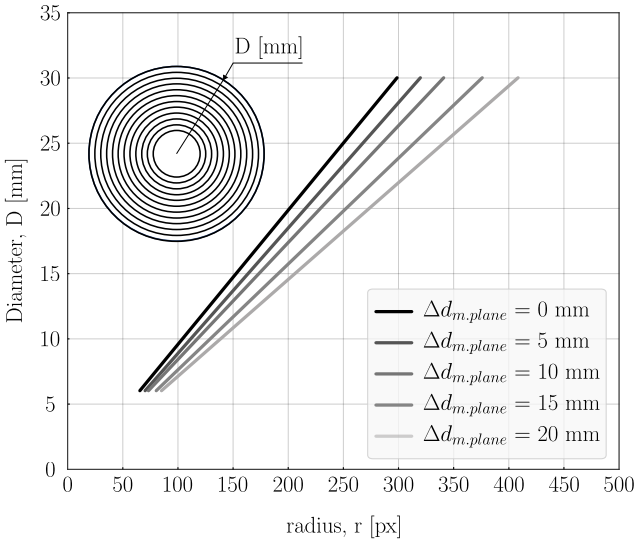


Figure 2. Resolution of the used image acquisition system calibrated for different measurement plane displacements, $\Delta d_{m.plane}$ (adapted from [25]).

3. Digital Image Processing Algorithm

The first step in the proposed methodology is to automatically extract several images from the pre-recorded image sequence for the experimental test under study. These images are the starting point for applying the digital image processing algorithm, and provide the evolution of the hole size and the through-thickness crack during the test. As shown in Figure 3, the DIP algorithm consists of two distinct steps: (a) crack detection and (b) hole diameter measurement. The crack detection step is responsible for detecting the presence of a through-thickness crack on the sheared surface of the specimen, whereas the hole

diameter measurement step is responsible for measuring the corresponding inner hole diameter of the specimen. If the through-thickness crack is identified, the global algorithm determines the corresponding hole expansion ratio using the initial hole diameter (D_i) and the hole diameter determined in the hole diameter measurement step (D_f). If no through-thickness crack is detected, the diameter value from the current image is recorded, and the DIP analysis proceeds to the next image for further evaluation. The sub-algorithms corresponding to the crack detection and hole diameter measurement steps are presented in the following sections.

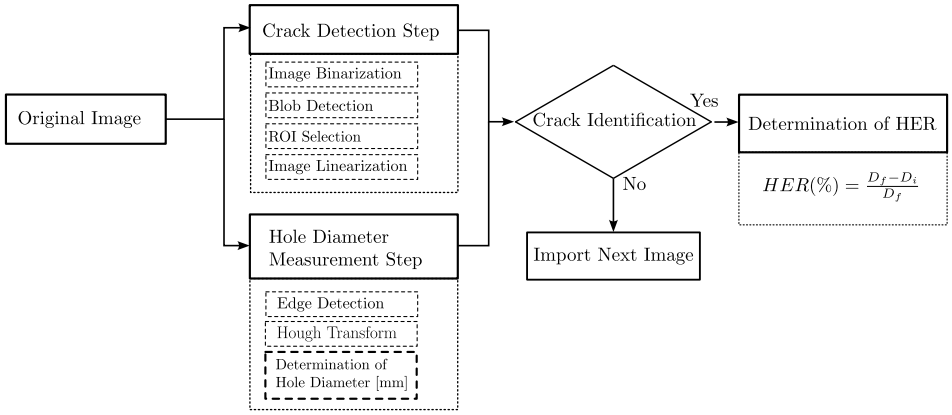


Figure 3. Developed digital image processing algorithm for crack identification and hole diameter measurement.

3.1. Crack Detection Algorithm

The crack detection step consists of four distinct and successive image processing operations, mainly image binarization, blob detection, selection of the region of interest (ROI), and image linearization. Binarization is the process of creating a binary image from a grayscale image using a thresholding method [28]. All pixel values above a globally determined threshold (G_t) are converted to white (a bit value of one), and all other values are set to black (a bit value of zero). Depending on the use of threshold value, the binarization method is divided into global and adaptive binarization. The global binarization method uses a single and constant threshold value for the whole image, whereas the adaptive binarization method uses local threshold values where different threshold values are computed for each pixel in the image. This method offers increased robustness to changes in lighting [29]. The results of both thresholding methods are shown in Figure 4 for an image acquired during the hole expansion test. It is noted that the sheared edge surface is hardly recognized using the global binarization method, as shown in Figure 4b. However, it is possible to obtain a clear binarization image using the adaptive binarization method, as shown in Figure 4c.



(**a**) (**b**) (**c**)

Figure 4. Binarization methods: (**a**) original image, (**b**) binarized image by global binarization, and (**c**) binarized image by adaptive binarization.

In computer vision, blob detection is a technique used to identify and locate regions or "blobs" in an image that differ in properties, such as brightness, color, or texture, from surrounding regions. These regions or blobs may correspond to objects or features of interest in the input image. For the proposed methodology, different operations were considered,

including (a) the suppression of light structures connected to the image border; (b) the combination of adjacent pixels by filling image regions and holes; and (c) morphological operations, such as closing and boundary extraction [30]. These operations are fundamental for correct and efficient ROI selection. An overview of the blob detection step is shown in Figure 5. After this step, the ROI must be defined for the correct identification of the through-thickness crack. The largest closed area is then selected, resulting in a ring-type structure, as shown in Figure 5d. This structure corresponds to the sheared surface of the pre-punched hole and is the region where the crack identification process is then performed. The parameters used for each operation are summarized in Table 1. These parameters were carefully chosen, taking into consideration the specific characteristics of through-thickness cracks, and were tested to robustly identify macro through-thickness cracks rather than small cracks with a resolution of ±0.1 mm.



(**a**) (**b**) (**c**) (**d**)

Figure 5. Blob detection and ROI selection steps: (**a**) original image, (**b**) binarized image, (**c**) resultant image after the morphological operations (clear borders and close mask and fill holes), and (**d**) final selected ROI.

Table 1. Parameters used in the crack detection algorithm.

Image Binarization	Method Sensitivity Foreground Polarity	Adaptive 0.51 'bright'
Blob detection	Method Pixel connectivity	Clear Borders 8
	Method Structuring element Size	Close Mask Disk 1 px
	Method Pixel connectivity	Fill Holes 4
ROI Selection	Method Number of returned objects Property to filter Criterium	Image Filtering 1 Area 'largest'

The final step of the crack detection algorithm is the so-called image linearization step, which consists of linearizing the sheared edge, as represented in Figure 6, to simplify the through-thickness crack detection. In this step, a new image is built considering a transposition of coordinates for polar coordinates with angles between 0 and 360º. Using this transformation, it is possible to transform the circumferential profile (Figure 6a) of the sheared edge surface into a linear profile (Figure 6b). The center of the desired ROI is determined using the Hough transform [31,32], which is presented in detail in the next section. Analyzing the represented image, it is possible to clearly differentiate the inner and outer boundaries of the shear edge. Furthermore, this type of linear representation is advantageous in identifying whether the through-thickness crack is present. As shown in Figure 6c, the crack is automatically identified when the original image's single ROI blob is divided into two or more independent blobs. In this example, two distinct blobs are marked with different colors (orange and blue), indicating the presence of a crack that extends through the thickness of the material. On the other hand, if the analysis of the linearized image reveals only a single blob within the ROI, it signifies that a crack has not

propagated completely through the material's entire thickness. In such cases, the presence of a single blob suggests that the crack may be localized or partial, rather than extending fully through the material's thickness.

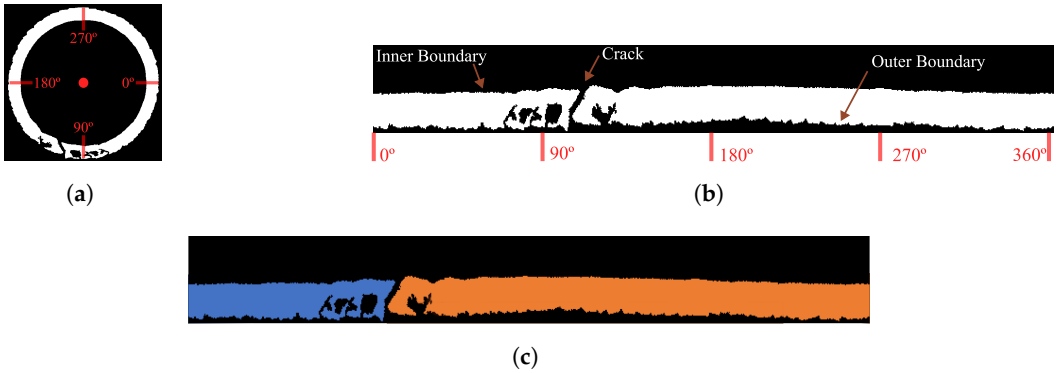


Figure 6. Schematic representation of the image linearization procedure: (**a**) original image (ROI), (**b**) linearized image and identification of inner/outer boundaries and through-thickness crack, and (**c**) linearized image and selection of two different blobs.

3.2. Hole Diameter Measurement Algorithm

The main objective of the algorithm presented in this section is to identify and measure the hole diameter evolution during the hole expansion test. Figure 7 depicts the different steps of the developed methodology applied to the reference image used in Section 3.1. To detect and measure the diameter value in each image, a Hough Transform (HT)-based algorithm is used. The HT is a popular image processing technique for detecting simple shapes in an image, such as lines, circles, and ellipses. It was first proposed by Paul Hough [33] in 1962 to detect straight lines. Essentially, it works by transforming the image from the original spatial domain to the parameter space, where the shape parameters are represented as points.

The Circular Hough Transform (CHT) is a variation of the HT and is a robust technique used to detect circular shapes, such as circles or arcs, in noisy or distorted images. Duda and Hart introduced it in 1972 [34] as an extension of the original Hough Transform. The CHT transforms the image data from the spatial domain to a parameter space, where circles are represented by their center coordinates (x, y) and radius (r). Each point in the image is represented as a circle in the parameter space, and the accumulation of these circles results in a two-dimensional array called the Hough accumulator, which contains the parameter combinations that receive the most votes. To detect circles using the CHT, the maximum peaks in the Hough accumulator correspond to the center coordinates and radius of the circles in the image. The number of peaks detected corresponds to the number of circles present in the image [35].

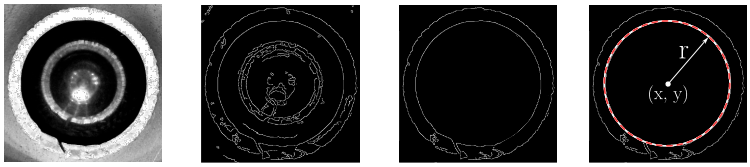


Figure 7. Hole diameter measurement algorithm: (**a**) original gray image, (**b**) edge detection using the Canny edge detector, (**c**) selection of the ROI, and (**d**) application of the Circle Hough Transform.

A preliminary edge detection operation must be performed to apply the CHT to an image properly. Edge detection is a digital image processing technique used to identify and highlight an image's edges, defined as the boundaries between two regions with different intensities or color values. The most commonly used edge detection methods are the Sobel operator, the Canny edge detector, and the Laplacian of the Gaussian method. In this work,

the Canny edge detection method [36] is used, which involves multiple steps, such as noise reduction, gradient calculation, non-maximum suppression, and hysteresis thresholding. A threshold value of 0.5 was adopted, resulting in a binary image as the one represented in Figure 7b with a clear and sharp edge highlighted in white [37].

After the edge detection step, several morphological intermediate operations (Figure 7c) are applied to simplify the selection of the region of interest. The CHT is then applied to the selected ROI, as shown in Figure 7d, to obtain each image's inner and outer diameters in pixels. The parameters considered for the edge detection step and Hough Transform are summarized in Table 2. The final inner diameter, $2r$, is converted from pixels to millimeters using a conversion factor that takes into account multiple factors, including the resolution of the acquisition image system, as discussed in Section 2; the thickness of the material; and the displacement of the punch at the time the image was acquired [25]. The methodology described can be applied to sheet materials with thicknesses ranging from 0.5 to 3 mm, and can measure hole diameters with a maximum accuracy of ±0.1 mm.

Table 2. Parameters used in the hole diameter measurement algorithm.

Edge Detection Step	Method	'Canny Edge'
	Threshold Value	0.5
Hough Transform	Method	'Phase Code'
	Edge Threshold	0.23
	Sensivity	0.93
	Object Polarity	Bright

4. Application of the DIP Algorithm

The developed DIP algorithm was tested and validated using experimental data from hole expansion tests performed on three distinct ferritic carbon steels [38] with different thicknesses and mechanical properties. Table 3 shows the mechanical tensile properties for each studied material in the rolling direction (RD), according to ISO 6892 [39] and the corresponding thickness value. The holes were produced in each specimen by punching, considering a cutting clearance of 15%. Two samples for each material permit testing results for different materials, thicknesses, and any variability for the current proposed automated procedure. The initial hole diameter, also presented in Table 3, was measured using a Mitutoyo digital three-point internal micrometer with a digital step of 0.001 mm. For each material, the hole expansion test was performed considering a constant punch speed of 0.5 mm/min under a blank holding force of 25 kN. The images were acquired at a rate of 5 fps. In this experimental work, the excessively expanded crack morphology (macro fracture) defined by Li et al. [40] was adopted as the criterion to stop the hole expansion test.

Table 3. Tensile properties (RD) and additional information for the studied sheet metal materials.

Material ID	Thickness t (mm)	Yield Strength Re (MPa)	Ultimate Strength Rm (MPa)	Uniform Elongation A (50%)	Initial Diameter d_i (mm)
#1	2.514	480.28	548.82	26.5	10.031
#2	2.319	517.83	581.20	23.5	10.029
#3	1.997	577.93	611.54	24.0	10.028

Results

The force-displacement data obtained for the studied materials during hole expansion are shown in Figure 8. Each curve represents the force–displacement relationship during the hole expansion, with the point of crack identified by the DIP algorithm also indicated. The dotted line on each curve indicates the experimental data acquired between the crack point and the end of the test. The evolution of the punch displacement-force relation exhibits a similar trend for all the studied samples, and the point identified by the DIP

algorithm is consistent across the different materials. Nevertheless, it is important to recognize that the stochastic nature of fracture introduces uncertainty in the observation of the first through-thickness crack and overall fracture behavior.

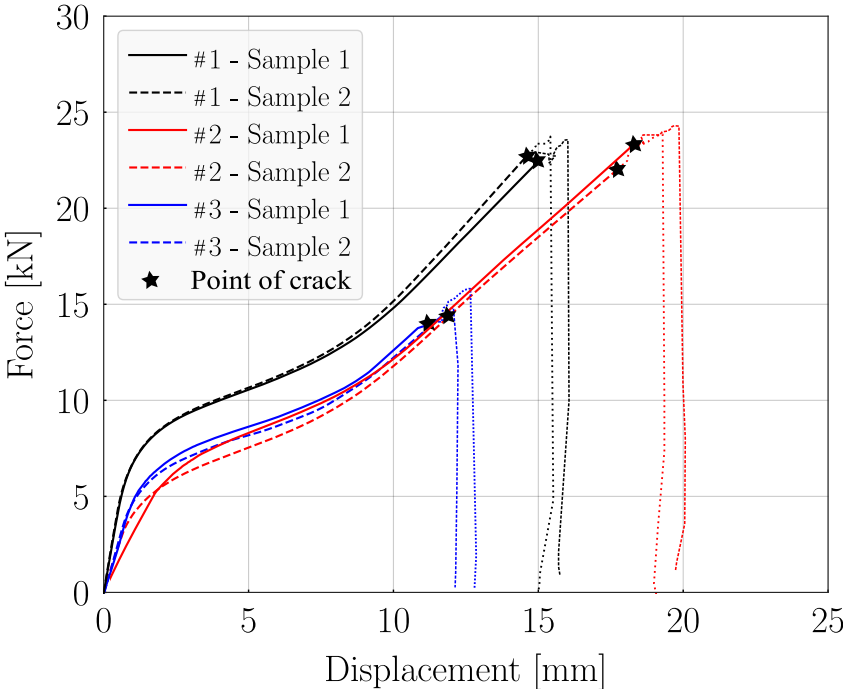


Figure 8. HET punch force–displacement curves obtained for the performed hole expansion tests.

As mentioned earlier, the DIP algorithm was developed to detect cracks and measure hole diameters accurately during hole expansion tests. Figures 9–11 show the evolution of the hole diameter during the tests for materials #1, #2, and #3, respectively. Each material has a representative curve of the hole diameter plotted against punch displacement until the point of cracking through the thickness. At this point, the measured diameter corresponds to the final diameter, D_f, which is used to calculate the final HER using Equation (1). As can be noted in the analysis of Figure 8, the dotted points beyond the crack point indicate excessive expansion of the hole diameter following crack detection. Unlike the traditional method [39], which evaluates the final diameter after the test has stopped and the punch has been removed, the developed method calculates the HER value using the image acquired when the first macro crack appears. Thus, the HER values obtained using the developed method tend to be lower and more conservative than those obtained by manual measurement, as confirmed by the results presented in Table 4. The table presents the hole-expanded diameter values obtained using the developed DIP algorithm and those measured using a Mitutoyo digital three-point internal micrometer (direct measurement). The corresponding HER values are also presented for each sample. Material #2 has a higher edge crack resistance, presenting a HER value of approximately 73%, in contrast to material #3, which has a lower edge crack resistance (HER $\approx$ 33%). Note that these values are overestimated when direct measurement is used, with HER values of 81.0% for material #2 and 42.5% for material #3. The relative error between samples is below 0.5% for materials #1 and #2, and below 3% for material #3. These values are higher when direct measurement is used, with relative errors of 2.5% for materials #1 and #2, and 6.5% for material #3.

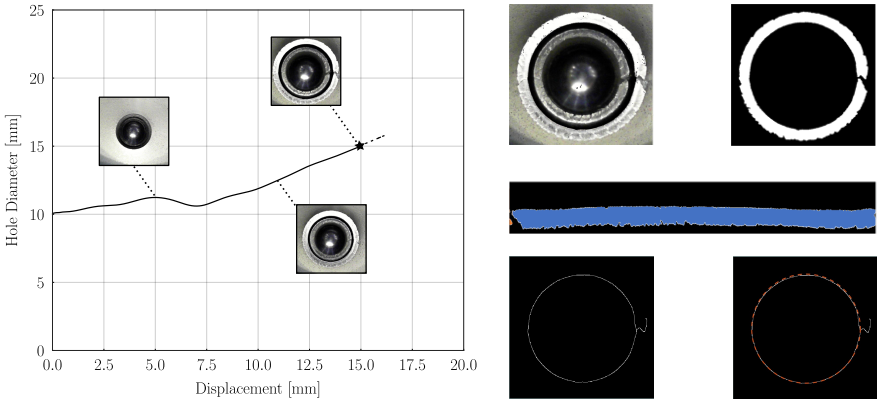
Table 4. The HER values obtained by the DIP algorithm and direct measurement.

Material ID			DIP Algorithm	Direct Measurement
#1	Sample 1	D_f (mm)	14.98	15.26
		HER (%)	49.4	52.1
	Sample 2	D_f (mm)	15.03	15.50
		HER (%)	49.8	54.5
	Error (%)	HER	0.4%	2.4%
#2	Sample 1	D_f (mm)	17.42	18.12
		HER (%)	73.7	80.7
	Sample 2	D_f (mm)	17.36	18.18
		HER (%)	73.2	81.3
	Error (%)	HER	0.5%	0.6%
#3	Sample 1	D (mm)	13.20	14.61
		HER (%)	31.6	45.6
	Sample 2	D (mm)	13.47	13.97
		HER (%)	34.4	39.4
	Error (%)	HER	2.8%	6.2%

Upon analyzing the evolution of the hole diameter with punch displacement in greater detail, it can be realized that the curves for all three materials follow a similar trend. Furthermore, two distinct zones can be identified in the curves. For punch displacements lower than 7.5 mm for materials #1 and #2, and 5 mm for material #3, the hole diameter remains almost constant, with a value equal to the initial diameter ($D_i = 10$ mm), and does not significantly increase with punch displacement. After reaching this point, the evolution of the hole diameter changes significantly, and the relationship between punch displacement and hole diameter becomes linear with a well-defined slope.

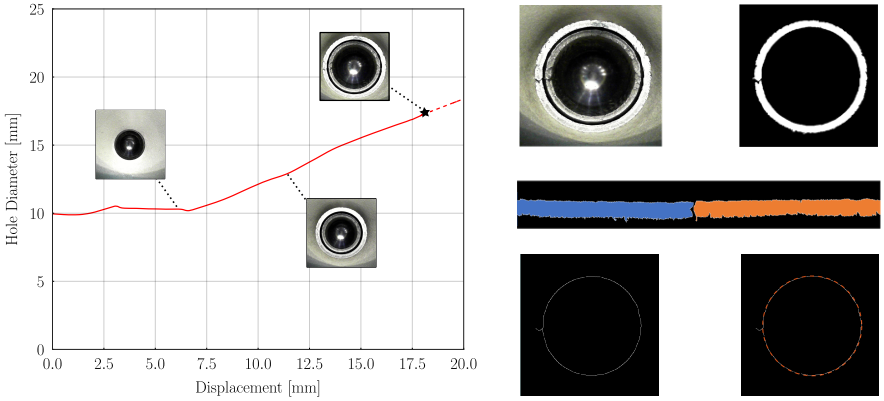
At the beginning of the test, the blank is flat, and the inner and outer diameters are coincident. However, as the punch moves, the blank thickness tilts and becomes visible in the acquired image. Therefore, at the start of the test, the DIP algorithm can only detect the outer diameter and begins to detect the inner diameter when the thickness becomes visible in the image. This phenomenon is evident in the results for material #1, where the DIP algorithm only detects and measures the outer hole diameter between 0 (zero) and 5 mm, as it is associated with the tilt of the thickness. In this specific case, an increase in the outer diameter can be observed with punch displacement. After 5 mm displacement, the inner diameter becomes visible in the acquired image and is measured by the proposed algorithm, resulting in a reduction of the estimated value. As the punch advances, the internal diameter is progressively measured, resulting in a linear evolution. A similar analysis can be conducted for the remaining materials.

Figures 9b, 10b, and 11b show, sequentially, the application of the developed DIP algorithm to detect the through-thickness crack and measure the final hole diameter, D_f, for materials #1, #2, and #3, respectively. The first image represents the original image, and the second represents the binarized image with the selected ROI. The third represents the linearized image and the identification of the number of blobs. The fourth image shows the result of the edge detection algorithm used to estimate the final hole diameter. The red line in the fifth image represents the estimated diameter. As can be seen, the DIP algorithm was successfully applied to the selected materials, all of which present a single through-thickness crack that generates two independent blobs in the linearized image.



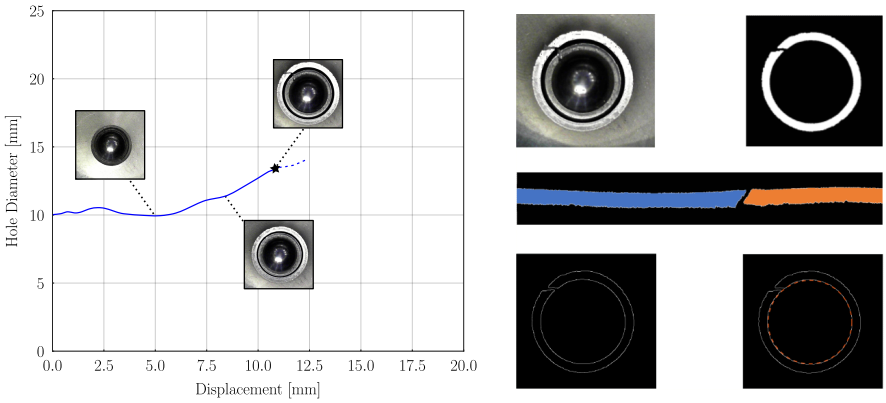
(**a**) (**b**)

Figure 9. Representation of the (**a**) evolution of the hole diameter during the test and the (**b**) application of the developed DIP algorithm to the image with a through-thickness crack for material ID #1.



(**a**) (**b**)

Figure 10. Representation of the (**a**) evolution of the hole diameter during the test and the (**b**) application of the developed DIP algorithm to the image with a through-thickness crack for material ID #2.



(**a**) (**b**)

Figure 11. Representation of the (**a**) evolution of the hole diameter during the test and the (**b**) application of the developed DIP algorithm to the image with a through-thickness crack for material ID #3.

5. Conclusions

This work describes a new method based on digital image processing techniques aimed at improving and automating crack detection and final diameter measurement in hole expansion tests. A new experimental image acquisition system was designed to acquire the evolution of the hole during the test, synchronized with the punch displacement and force signals. After the test, a post-processing image processing algorithm is applied to the acquired image sequence to detect the through-thickness crack and measure the different hole diameters.

The developed digital image processing algorithm comprises two sub-procedures: crack detection and hole diameter measurement. The first involves image binarization, blob detection, ROI selection, image linearization, and crack identification. Adaptive binarization is proposed to enhance the versatility of the algorithm, enabling its application to different sheet metal materials and varying thickness values. The algorithm identifies the through-thickness crack when the single ROI blob is separated into several independent blobs in the linearized image. The second uses the Hough transform to identify and measure the inner diameter of the expanded hole during the test. Additionally, the HER value is determined when the through-thickness crack is identified in the crack detection step. The complexity of the developed algorithms is relatively low, as they involve a series of simple operations that do not require high computational costs. Therefore, the simplicity of the operations allows for efficient execution and analysis of the acquired images, making the proposed method practical and accessible for implementation in various experimental settings.

The proposed method was validated using HER tests with three different sheet metals and different thickness values. The results show an excellent accuracy of the automated procedure when compared with manual image sequence analysis of the first thought thickness crack detection. Additionally, the repeatability of the obtained results shows an improvement achieved by the developed methodology due to its superior accuracy. It must be noted that being experimental tests means that material may behave with some uncertainty for fracture and first through-thickness crack observation as a result of the stochastic behavior of fracture. The proposed method with its automated procedure shows a more reliable determination of the Hole Expansion Ratio, being more suited for industrial applications and not dependent on the experience and skills of the test operator.

Future work will focus on experimental validation of the DIP algorithm for materials with different surface treatments, which may have distinct reflectance properties. Furthermore, the algorithm's performance will be assessed in the presence of double cracks, which may exhibit multiple independent blobs. These test conditions may require a more detailed calibration of the algorithm parameters. The effectiveness of the developed algorithm for fully automating the HET test will be evaluated using it during the test rather than just as a post-processing tool. This improvement in the testing methodology will help prevent further crack propagation, as the test will automatically stop once the DIP algorithm detects the presence of a crack, ensuring a more accurate assessment of the hole expansion ratio.

Author Contributions: Conceptualization and supervision by A.D.S. and J.M.R.S.T.; data collection, formal analysis, and writing—original draft preparation by D.J.C. and R.L.A.; writing—review and editing by and A.D.S. and J.M.R.S.T. All authors have read and agreed to the published version of the manuscript

Funding: The first author gratefully acknowledges the financial support of the Portuguese Foundation for Science and Technology (FCT) for the Doctoral grant 2022.12657.BD provided under the program POCH, co-financed by the European Social Fund (FSE) and Portuguese National Funds from MCTES.

Data Availability Statement: The data presented in this study are available on request from the corresponding author. The data are not publicly available due to privacy.

Conflicts of Interest: The authors declare no conflict of interest.

Abbreviations

The following abbreviations are used in this manuscript:

AHSS	Advanced High-Strength Steels
CCD	Charge-Coupled Device
CHT	Circular Hough Transform
DIC	Digital Image Correlation
DIP	Digital Image Processing
DRMS	Digital Recording and Measurement System
HER	Hole Expansion Ratio
HET	Hole Expansion Test
HT	Hough Transform
PVD	Physical Vapor Deposition
ROI	Region of Interest

References

1. Hovorun, T.P.; Berladir, K.V.; Pererva, V.I.; Rudenko, S.G.; Martynov, A.I. Modern materials for automotive industry. *J. Eng. Sci.* **2017**, *4*, f8–f18. [CrossRef]
2. Ghosh, A.G.M.; Roy, A. Chapter Renewable and Sustainable Materials in Automotive Industry. In *Encyclopedia of Renewable and Sustainable Materials*; Elsevier: Amsterdam, The Netherlands, 2019; pp. 162–179.
3. Hilditch, T.; Souza, T.; Hodgson, P. Chapter 2—Properties and automotive applications of advanced high-strength steels (AHSS). In *Welding and Joining of Advanced High Strength Steels (AHSS)*; Woodhead Publishing: Sawston, UK, 2015; pp. 9–28.
4. Santos, R.; Pereira, A.; Butuc, M.C.; Vincze, G.; Festas, A.; Moreira, L. Development of a Device Compatible with Universal Testing Machine to Perform Hole Expansion and Erichsen Cupping Tests. *Machines* **2019**, *8*, 2. [CrossRef]
5. *ISO 16630:2009*; Metallic Materials-Sheet and Strip-Hole Expanding Test. International Organization for Standardization: Geneva, Switzerland, 2009.
6. Hance, B. Practical Application of the Hole Expansion Test. *SAE Int. J. Engines* **2017**, *10*, 247–257. [CrossRef]
7. Yoon, J.I.; Jung, J.; Joo, S.H.; Song, T.J.; Chin, K.G.; Seo, M.H.; Kim, S.J.; Lee, S.; Kim, H.S. Correlation between fracture toughness and stretch-flangeability of advanced high strength steels. *Mater. Lett.* **2016**, *180*, 322–326. [CrossRef]
8. Dünckelmeyer, M.; Krempaszky, C.; Werner, E.; Doppler, C. Instrumented hole expansion test. *Mater. Sci.* **2009**, *8*, 50–57.
9. Panich, S.; Chongbunwatana, K. Influence of anisotropic yield criteria on simulation accuracy of the hole-expansion test. *IOP Conf. Ser. Mater. Sci. Eng.* **2020**, *967*, 012037. [CrossRef]
10. Leonhardt, A.; Kräusel, V.; Paar, U. Automated hole expansion test with pneumatic crack detection. *IOP Conf. Ser. Mater. Sci. Eng.* **2019**, *480*, 012026. [CrossRef]
11. Schreier, H.; Orteu, J.J.; Sutton, M.A. *Image Correlation for Shape, Motion and Deformation Measurements*; Springer US: New York, NY, USA, 2009. [CrossRef]
12. Behrens, B.A.; Diaz-Infante, D.; Altan, T.; Yilkiran, D.; Wölki, K.; Hübner, S. Improving Hole Expansion Ratio by Parameter Adjustment in Abrasive Water Jet Operations for DP800. *SAE Int. J. Mater. Manuf.* **2018**, *11*, 241–252. [CrossRef]
13. Chen, X.; Yang, L.; Chirac, C.; Du, C.; Zhou, D. *Measurement of Strain Distribution for Hole Expansion with Digital Image Correlation (DIC) System*; SAE: Warrendale, PA, USA , 2011. [CrossRef]
14. Li, J.; Wang, H.; Yan, D.W. Influence of Experiment Methods on Limit Hole Expansion Ratio. *DEStech Trans. Eng. Technol. Res.* **2016** . [CrossRef]
15. Krempaszky, C.; Larour, P.; Freudenthaler, J.; Werner, E. Towards More Efficient Hole Expansion Testing. In Proceedings of the IDDRG 2014 Conference, Paris, France, 1–4 June 2014 .
16. Wang, K.; Luo, M.; Wierzbicki, T. Experiments and modeling of edge fracture for an AHSS sheet. *Int. J. Fract.* **2014**, *187*, 245–268. [CrossRef]
17. Barlo, A.; Sigvant, M.; Pérez, L.; Islam, M.S.; Pilthammar, J. A Study of the Boundary Conditions in the ISO-16630 Hole Expansion Test. *IOP Conf. Ser. Mater. Sci. Eng.* **2022**, *1238*, 012031. [CrossRef]
18. Oh, S.H.; Yang, S.H.; Kim, Y.S. Chapter A study of image processing based hole expansion test. In *Testing and Measurement: Techniques and Applications*; CRC Press: London, UK, 2015; p. 8.
19. Pratt, W.K. *Digital Image Processing*; John Wiley & Sons, Inc.: Hoboken, NJ, USA, 2007. [CrossRef]
20. Gonzalez, R.C.; Woods, R.E. *Digital Image Processing*, 2nd ed.; Pearson: Upper Saddle River, NJ, USA, 2001.
21. Chiriac, C.; Chen, G. Formability Characterization of AHSS-Digital Camera Based Hole Expansion Test Development. In Proceedings of the International Deep Drawing Research Group IDDRG 2008 International Conference, Olofström, Sweden. 16–18 June 2008; pp. 16–18.
22. Kim, H.; Shang, J.; Beam, K.; Samant, A.; Hoschouer, C.; Dykeman, J. Development of new hole expansion testing method. *J. Phys. Conf. Ser.* **2016**, *734*, 032025. [CrossRef]
23. Choi, S.; Kim, K.; Lee, J.; Park, S.H.; Lee, H.J.; Yoon, J. Image Processing Algorithm for Real-Time Crack Inspection in Hole Expansion Test. *Int. J. Precis. Eng. Manuf.* **2019**, *20*, 1139–1148. [CrossRef]

24. Park, J.; Won, C.; Lee, H.J.; Yoon, J. Integrated Machine Vision System for Evaluating Hole Expansion Ratio of Advanced High-Strength Steels. *Materials* **2022**, *15*, 553. [CrossRef]
25. Cruz, D.J.; Santos, A.D.; Amaral, R.L.; Mendes, J.G.; Miranda, S.S.; Fernandes, J.V. Chapter An integrated methodology for HER determination in hole expansion test. In *Materials Design and Applications III*; Advanced Structured Materials; Springer International Publishing: Berlin/Heidelberg, Germany, 2021; pp. 243–256.
26. Duarte, J.F.; Santos, A.D.d.; da Rocha, A.B. Development of Testing Equipment for Sheet Metal Forming Analysis. In Proceedings of the IDDRG'94-International Deep Drawing Research Group 18th Biennial Congress, Conference Proceedings, Lisbon, Portugal, 16–20 May 1994; pp. 259–272.
27. Sousa, J. P. Desenvolvimento de um Sistema de Controlo e Aquisição de Dados para Máquina Universal de Ensaios de Chapas Metálicas. Master's Thesis, Faculdade de Engenharia da Universidade do Porto, Porto, Portugal, 2019.
28. Otsu, N. A Threshold Selection Method from Gray-Level Histograms. *IEEE Trans. Syst. Man Cybern.* **1979**, *9*, 62–66. [CrossRef]
29. Bradley, D.; Roth, G. Adaptive Thresholding using the Integral Image. *J. Graph. Tools* **2007**, *12*, 13–21. [CrossRef]
30. Soille, P. *Morphological Image Analysis*; Springer: Berlin/Heidelberg, Germany, 1999. [CrossRef]
31. Atherton, T.; Kerbyson, D. Size invariant circle detection. *Image Vis. Comput.* **1999**, *17*, 795–803. [CrossRef]
32. Yuen, H.; Princen, J.; Illingworth, J.; Kittler, J. Comparative study of Hough Transform methods for circle finding. *Image Vis. Comput.* **1990**, *8*, 71–77. [CrossRef]
33. Hough, P.V. Method and Means for Recognizing Complex Patterns. U.S. Patent 3,069,654, 18 December 1962
34. Duda, R.O.; Hart, P.E. Use of the Hough transformation to detect lines and curves in pictures. *Commun. ACM* **1972**, *15*, 11–15. [CrossRef]
35. Smereka, M.; Duleba, I. Circular Object Detection Using a Modified Hough Transform. *Appl. Math. Comput. Sci.* **2008**, *18*, 85–91. [CrossRef]
36. Canny, J. A Computational Approach to Edge Detection. *IEEE Trans. Pattern Anal. Mach. Intell.* **1986**, *PAMI-8*, 679–698. [CrossRef]
37. Parker, J.R. *Algorithms for Image Processing and Computer Vision*, 2nd ed.; John Wiley & Sons: Chichester, UK, 2010.
38. Marques, A.E.; Dib, M.A.; Khalfallah, A.; Soares, M.S.; Oliveira, M.C.; Fernandes, J.V.; Ribeiro, B.M.; Prates, P.A. Machine Learning for Predicting Fracture Strain in Sheet Metal Forming. *Metals* **2022**, *12*, 1799. [CrossRef]
39. *ISO 6892-1*; Metallic Materials-Tensile Testing-Method of Test at Room Temperature. International Organization for Standardization: Geneva, Switzerland, 2016.
40. Li, W.; Xia, M.; Peng, P.; Jia, Q.; Wan, Z.; Zhu, Y.; Guo, W. Microstructural evolution and deformation behavior of fiber laser welded QP980 steel joint. *Mater. Sci. Eng. A* **2018**, *717*, 124–133. [CrossRef]

Disclaimer/Publisher's Note: The statements, opinions and data contained in all publications are solely those of the individual author(s) and contributor(s) and not of MDPI and/or the editor(s). MDPI and/or the editor(s) disclaim responsibility for any injury to people or property resulting from any ideas, methods, instructions or products referred to in the content.

Appendix C

R^2 Analysis for the Prediction of Hardening Parameters

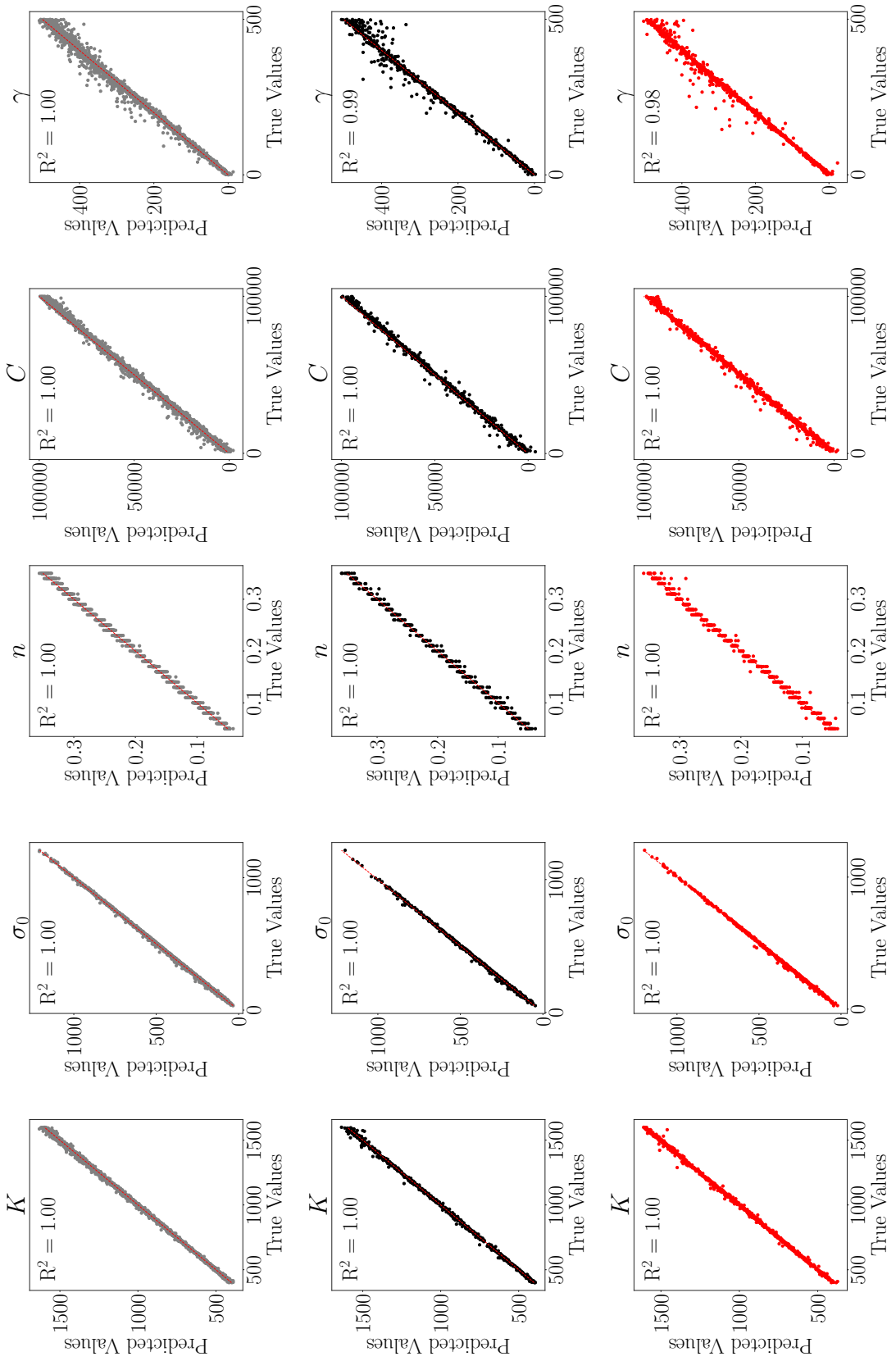


Figure C.1: Prediction results for the network with 40 Bi-LSTM units.

Appendix D

Evaluation Cases for Standard Experimental Loading Paths

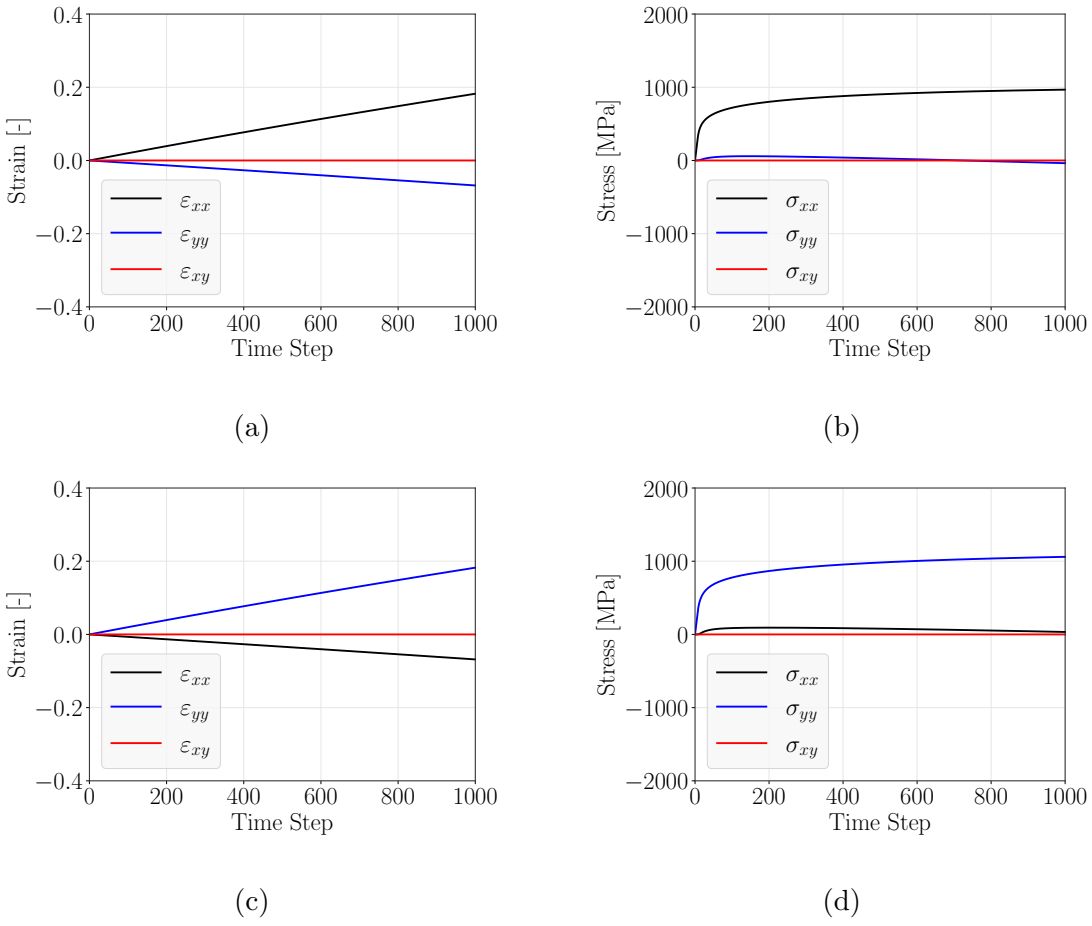


Figure D.1: Stress and strain evolution for uniaxial tension tests along the rolling (a–b) and transverse (c–d) directions; left: imposed strains ε_{xx}, ε_{yy}, ε_{xy}; right: resulting stresses σ_{xx}, σ_{yy}, σ_{xy}.

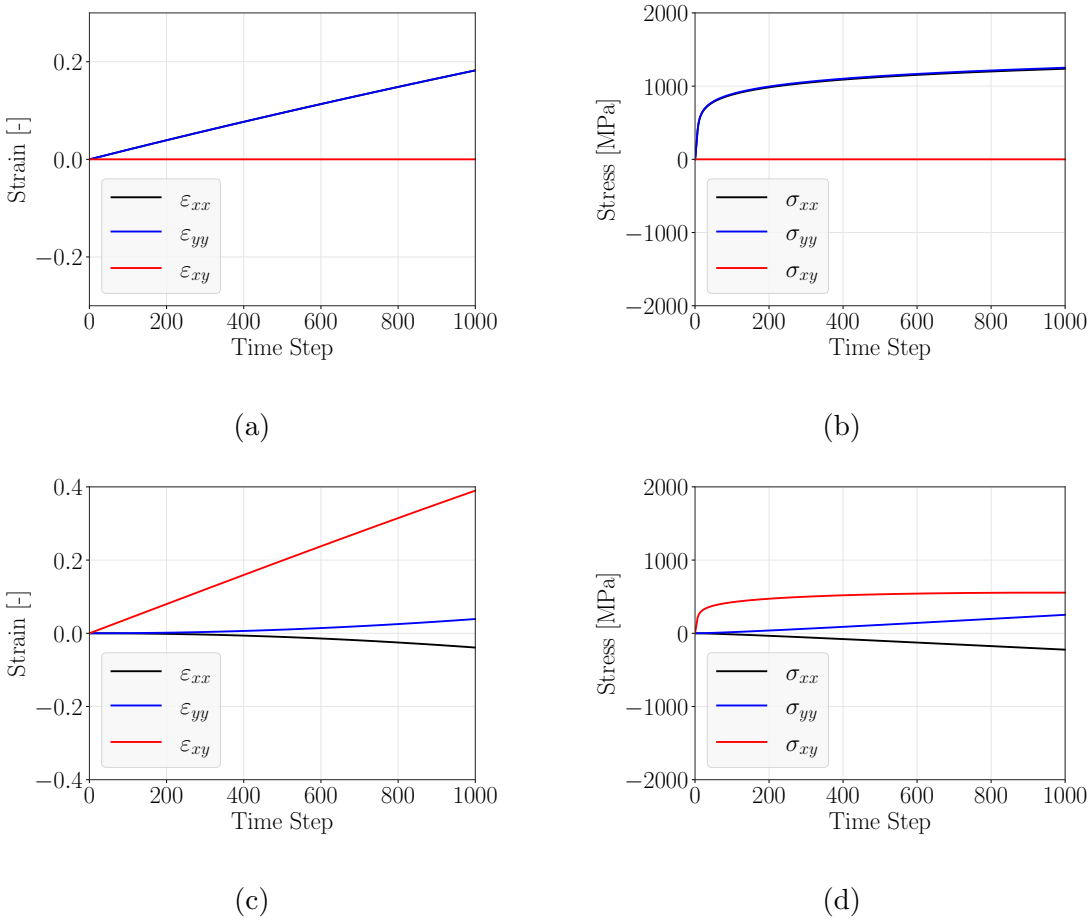


Figure D.2: Monotonic biaxial tension (a,b) and monotonic shear (c,d).

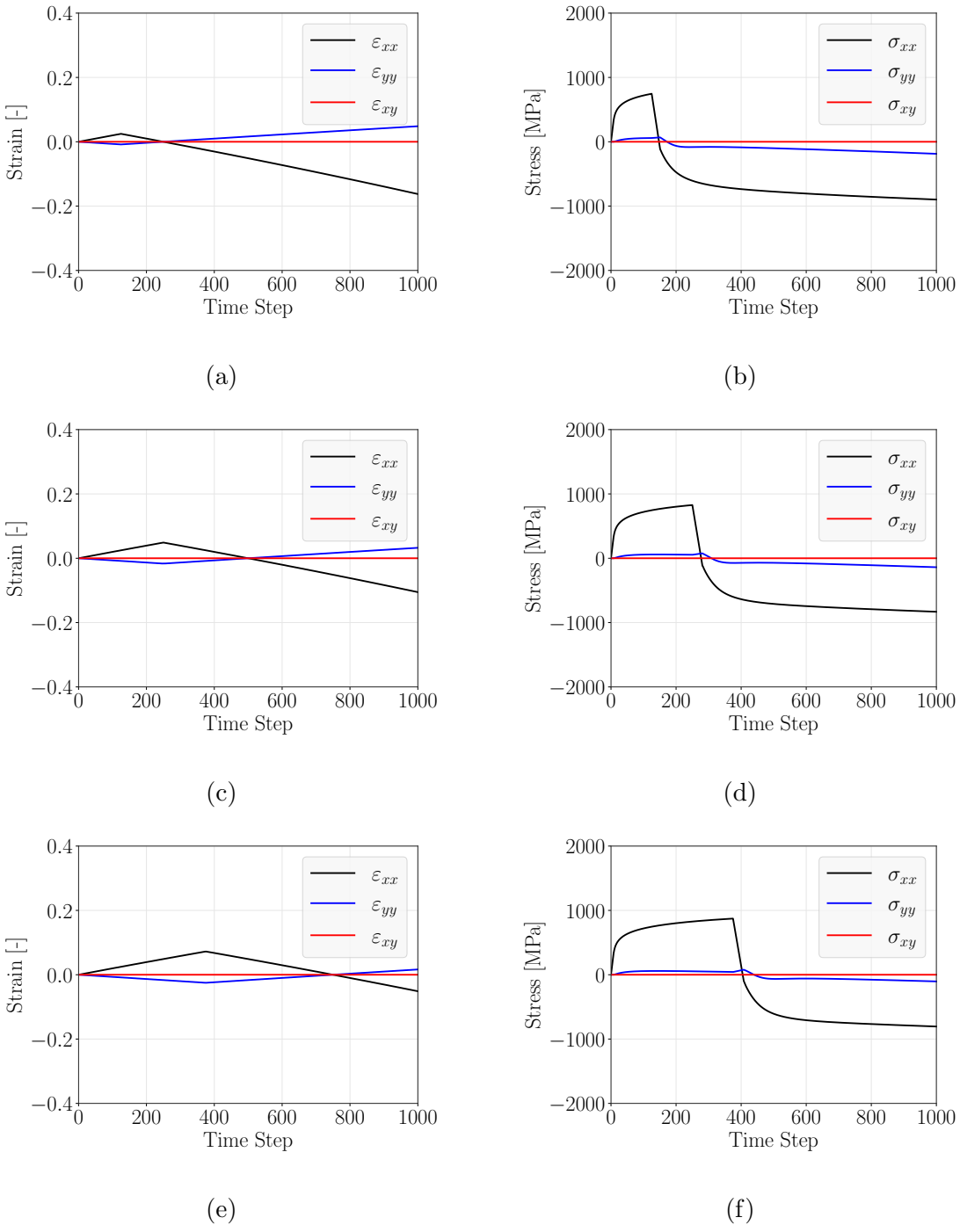


Figure D.3: Tension-compression paths showing reversal in loading direction (a–f).

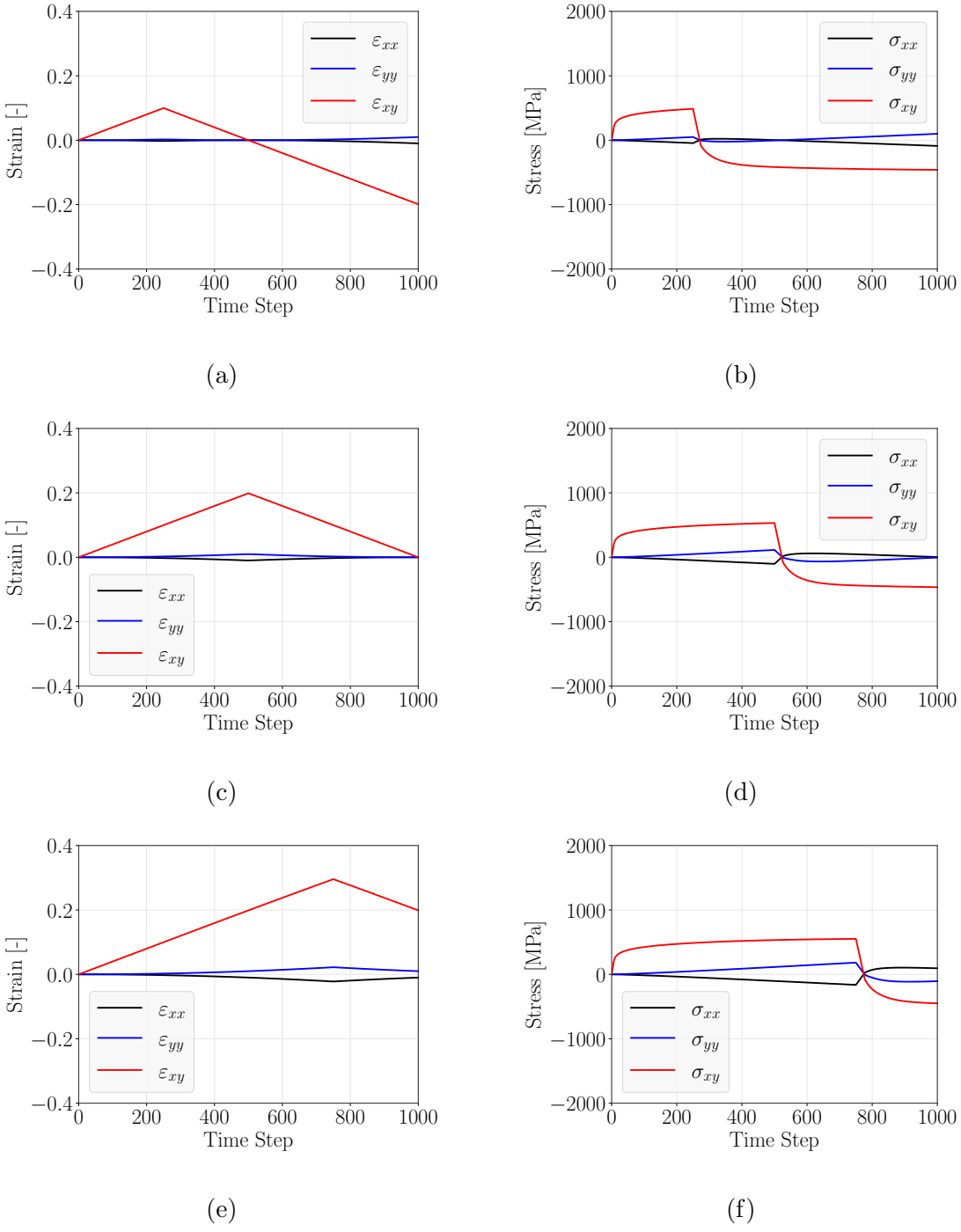
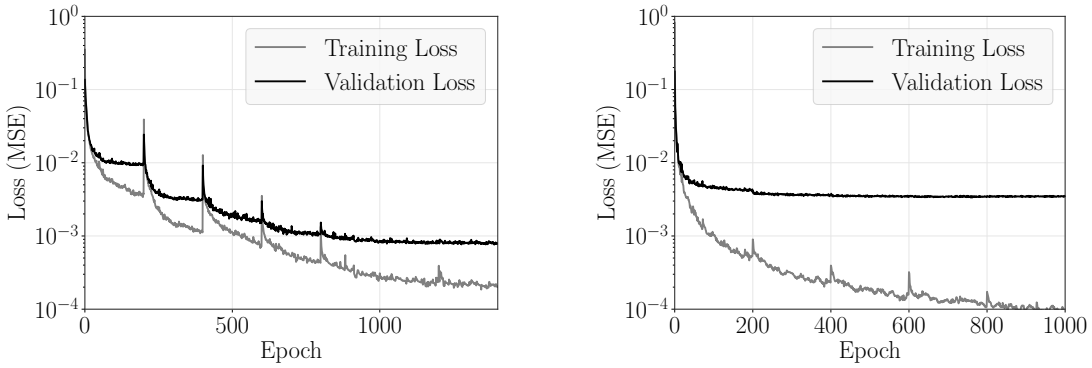


Figure D.4: Reverse shear tests with loading and unloading in ε_{xy}.

Appendix E

Training and Validation Loss Curves for Random-Walk and Smooth-Walk Models



(a) (b)

Figure E.1: MSE convergence during progressive training for the LMSC model ($n_s = 40$, $d = 4$, $w = 100$) trained exclusively on (a) random-walk (RW) data and (b) smooth-walk (SW) data.

Appendix F

Evaluation on FEA-Based Deformation Histories: Cylindrical Cup Forming

F.1 Results - Static/Implicit

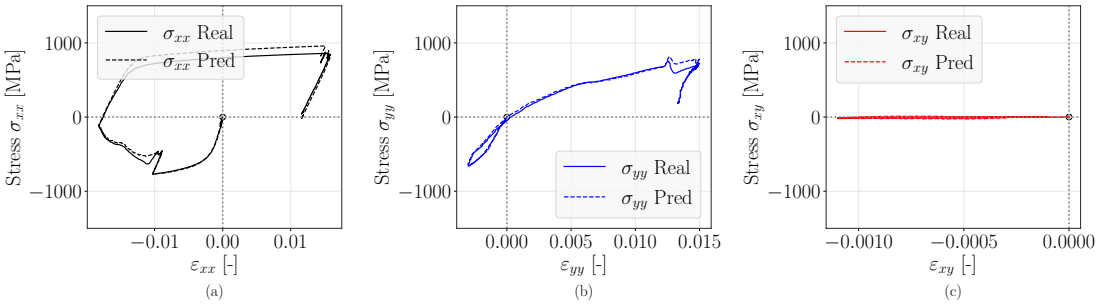


Figure F.1: Comparison of predicted and reference stress–strain evolution at IntPtA during cylindrical cup forming static/implicit simulation.

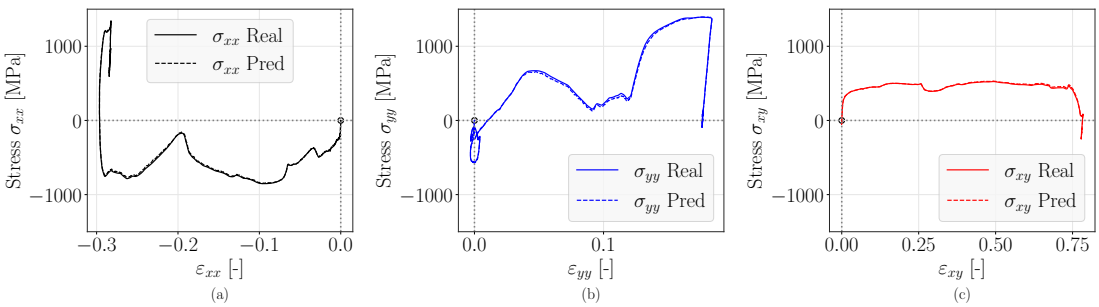


Figure F.2: Comparison of predicted and reference stress–strain evolution at IntPtC during cylindrical cup forming static/implicit simulation.

F.2 Strain Paths - Dynamic/Explicit

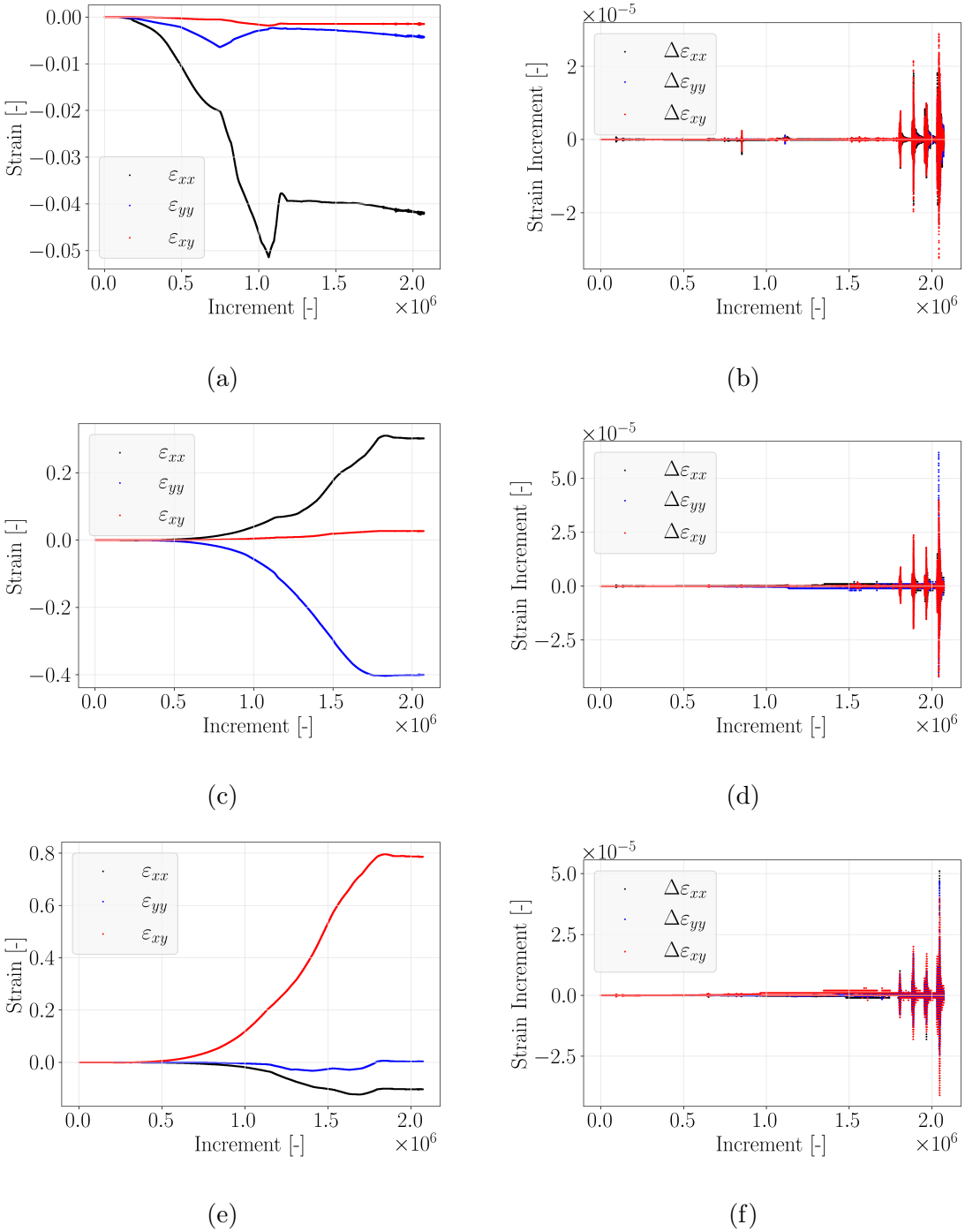


Figure F.3: Strain components (ε_{xx}, ε_{yy} and ε_{xy}) and corresponding strain increments ($\Delta\varepsilon$) for the selected integration points during the cup forming dynamic/explicit simulation: (a–b) IntPtA, (c–d) IntPtB and (e–f) IntPtC.

F.3 Results - Dynamic/Explicit

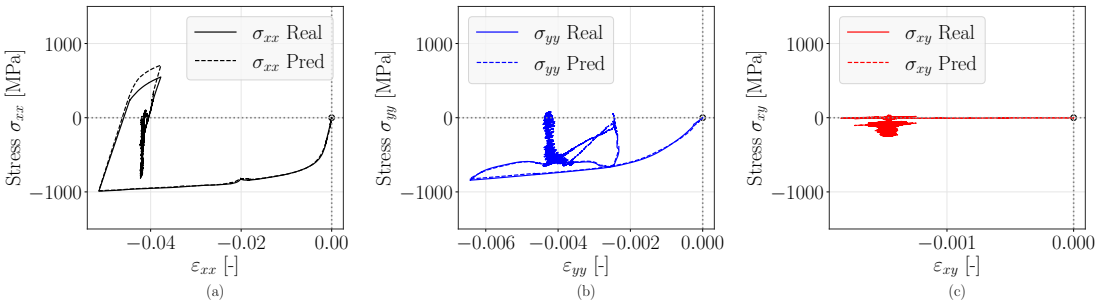


Figure F.4: Comparison of predicted and reference stress–strain evolution at IntPtA during cylindrical cup forming dynamic/explicit simulation.

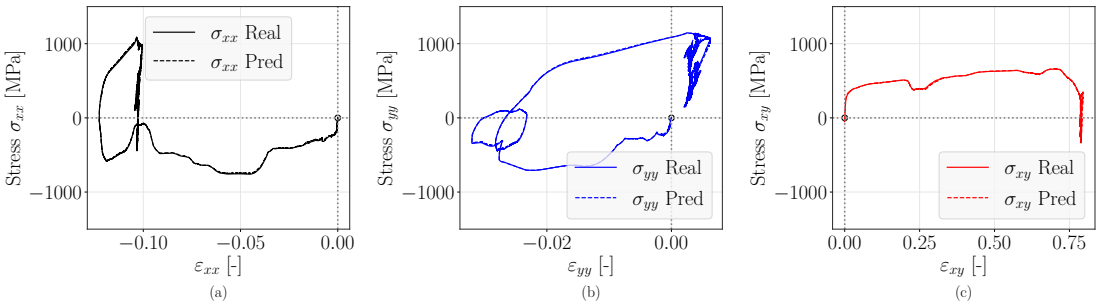


Figure F.5: Comparison of predicted and reference stress–strain evolution at IntPtC during cylindrical cup forming dynamic/explicit simulation.

Appendix G

Article: *"Application of Recurrent Neural Networks in Uncertainty Analysis of Sheet Metal Forming"*

Application of Recurrent Neural Networks in Uncertainty Analysis of Sheet Metal Forming

Daniel Cruz[1,2*], *Tomás* Parreira[3], *Armando* Marques[3], *Pedro* Prates[3,4], *Marta* Oliveira[3], *Diogo* Neto[3], *Abel* Santos[2], *Rui* Amaral[1], *Manuel* Barbosa[2], and *André* Pereira[3]

[1] Institute of Science and Innovation in Mechanical and Industrial Engineering (INEGI), Porto, Portugal
[2] Faculty of Engineering of University of Porto (FEUP), Porto, Portugal;
[3] Centre for Mechanical Engineering, Materials and Processes (CEMMPRE), Department of Mechanical Engineering, University of Coimbra, Portugal;
[4] Centre for Mechanical Technology and Automation (TEMA), Mechanical Engineering Department, University of Aveiro, Portugal.

Abstract. The quality of deep-drawn sheet metal components can be strongly influenced by different sources of uncertainty, such as variations in process conditions, deviations in tool geometry, and variations in material properties between coils. Identifying the underlying causes of forming defects remains a challenging and time-consuming task due to the complexity of the forming process. This study presents a machine learning (ML) framework for tracing sources of uncertainty in the forming of a cylindrical cup. By analysing key outputs from a standardized cylindrical cup test, including force-displacement sequences, earing evolution, and thickness distribution in different sections of the cup, the ML model aims to predict multiple sources of uncertainty. After identifying the principal sources of variation, numerical simulations using finite element analysis were performed to create a comprehensive dataset for the development and training of the ML model. The results from the simulated tests can be considered as sequential data, allowing their evaluation using recurrent neural networks (RNNs), which are particularly suited for modelling temporal or ordered datasets. The RNNs demonstrated strong performance in leveraging the temporal features of the forming data, achieving high accuracy in identifying the origins of uncertainty.

Keywords: Sheet metal forming; Uncertainty quantification; Machine Learning (ML); Recurrent Neural Networks (RNNs).

1 Introduction

Sheet metal forming is one of the most important and complex manufacturing processes in the production of metal components and is currently applied in a wide variety of industrial areas, such as the automotive, naval and aeronautical [1]. In these industries Finite Element Analysis (FEA) of sheet metal forming processes has become indispensable for predicting and optimizing the product's manufacturing process, allowing the prediction of deformation behavior and the identification of formability limits in components [2].

However, traditional FEA frequently relies on deterministic models that do not take into account the inherent uncertainties present in industrial environments [3]. These uncertainties, which can arise from variations in material properties, process conditions, tooling, lubrication, and other influencing factors [4,5], can have a critical impact on the quality of the final product [6,7]. As a result, they can lead to component rejection, unplanned production stops for troubleshooting and unexpected maintenance, thereby increasing manufacturing costs and causing production delays.

With the increasing availability of data and advances in computational power, there is a growing interest in applying stochastic modelling and uncertainty quantification to sheet metal forming processes. Several researchers have investigated the effects of different sources of uncertainty on final products using approaches such as Monte Carlo simulations [8-10], design of experiments [10,11] and meta-models [12]. However, these studies generally neglect the uncertainties associated with the forming tools (e.g. misalignment or geometric deviations). Hancock et al [7] and Majeske & Hammett [13] identified forming tools as a significant source of uncertainty associated with factors such as tool assembly, positioning errors and part bounce. This highlights the need for further research into the uncertainties associated with forming tools.

The uncertainties mentioned above can lead to significant deviations between the designed component and what is actually produced. Furthermore, it is often labour-intensive and time-consuming to find the source of the uncertainty responsible for the observed deviations. To address this challenge, this study introduces a machine learning (ML) approach to identify the sources of uncertainty that can affect the

* Corresponding author: dcruz@inegi.up.pt

final component in a forming process, using the cylindrical cup forming test [14], a widely recognized benchmark in sheet metal forming, to demonstrate the methodology [15-19]. FEA is used to create a virtual numerical database containing forming results under different uncertainty conditions. An ML framework is then developed as a metamodel that correlates these results with the uncertainty factors. This metamodel enables the identification of critical uncertainty factors influencing forming results and highlights the potential of artificial intelligence to improve troubleshooting processes in forming operations.

2 Methodology

2.1 Numerical model

The deep drawing process of a cylindrical cup, as presented in the ESAFORM 2021 benchmark [14], has been analysed. The numerical model of this forming process includes three main tools: the punch, the blank holder and the die, whose respective geometries and dimensions are shown in Fig. 1. The circular blank used has an average thickness of 0.82 mm and a diameter of 106 mm. The numerical simulation is performed in three distinct phases: (i) first, the blank holder moves downwards to press the blank against the die until a specified blank holder force (BHForce) is reached; (ii) next, the punch descends 54 mm, drawing the blank completely into the die while maintaining a constant BHForce; (iii) finally, the tools are removed, allowing the cup to springback. To prevent the formation of crushed cup ears during the second phase, a stopper of the same thickness as the blank is used.

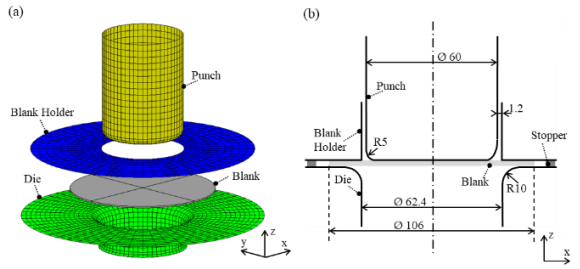


Fig. 1. Cylindrical cup forming process: (a) numerical model [20]; (b) dimensions of the tools and blank in mm (adapted from [14]).

In this study, a dual phase steel, DP600 with an initial thickness of 0.82 mm is considered. The mechanical behaviour of the material is assumed to be: isotropic elastic, described by the generalised Hooke's law, which has two parameters, the Young's modulus, E, and the Poisson's ratio, v; and orthotropic plastic, described by the Swift hardening law and the Hill'48 yield criterion. This yield criterion is defined by:

$$F(\sigma_{yy}-\sigma_{zz})^2 + G(\sigma_{zz}-\sigma_{xx})^2 + H(\sigma_{xx}-\sigma_{yy})^2 + 2L\tau_{yz}^2 + 2M\tau_{xz}^2 + 2N\tau_{xy}^2 = Y^2, \quad (1)$$

where σ_{xx}, σ_{yy}, σ_{zz}, τ_{xy}, τ_{yz} and τ_{xz} are the components of the Cauchy stress tensor; Y is the yield stress; F, G, H, L, M and N are the Hill'48 anisotropy parameters. These parameters follow the conditions $G + H = 1$ and $L = M = 1.5$ (von Mises). The Swift hardening law is defined by:

$$Y = C\,(\varepsilon_0 + \bar{\varepsilon}^p)^n, \quad (2)$$

where $\bar{\varepsilon}^p$ is the equivalent plastic strain and C, ε_0 and n are the hardening constants. The initial yield stress is given by $Y_0 = C\varepsilon_0^n$. The material parameters for the studied material are presented in Table 1 [20]

Table 1 – Constitutive Parameters of the Hill'48 Yield Criterion, the Swift Hardening Law, and the Generalized Hooke's Law for DP600 Steel [20]

F	***G***	***H***	***N***
0.506	0.590	0.410	1.572
n	***Y_0* [MPa]**	***C* [MPa]**	***E* [GPa]**
0.143	430.5	975.7	210

The frictional interaction between the tools and the blank is modelled using Coulomb's law, assuming a constant friction coefficient (μ). The blank is discretized with 23040 eight-node hexahedral solid elements, with two elements in thickness. The tools are modelled as rigid bodies and described by Bezier surfaces. Numerical simulations were performed using the DD3IMP (Deep Drawing 3D Implicit Code) software [21]. On average, each simulation required approximately 5 hours to complete on systems powered by an Intel® Core™ i7-13900K processor (5.8 GHz).

2.2 Uncertainty Model

Six sources of uncertainty related to friction, process conditions and misalignment are considered in this work. These uncertainties include the friction coefficient (μ); the blank holder force (BH_{Force}); the angular misalignment of the punch around the x-axis (α_x) and y-axis (α_y) and the linear misalignment of the blank along the x-axis (Δ_x) and y-axis (Δ_y). The angular and linear misalignments are shown schematically in Fig. 2. The ranges considered for each source of uncertainty are given in Table 2. Using these uncertainty values, the base numerical model (shown in Fig. 1(a)) is automatically adjusted to simulate the cylindrical cup forming process under uncertain conditions.

Table 2 – Minimum and maximum values for the six uncertainty sources.

	μ [-]	BH_{Force} [kN]	α_x [°]	α_y [°]	Δ_x [mm]	Δ_y [mm]
Max	0.05	40	-0.5	-0.5	-1.1	-1.1
Min	0.15	60	0.5	0.5	1.1	1.1

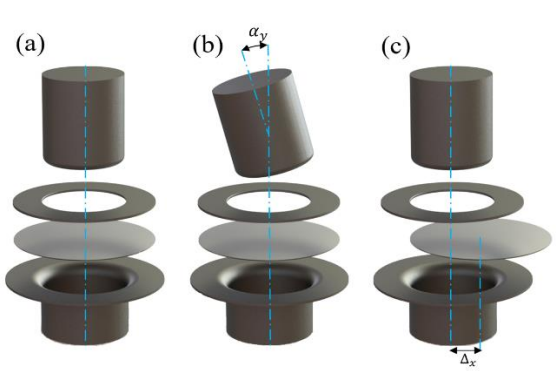


Fig. 2 – Illustrative representation of the uncertainty sources considered in the deep drawing of the cylindrical cup: (a) scenario without uncertainties; (b) punch with angular misalignment (α_y) and (c) blank with linear misalignment (Δ_x).

To develop the database required to train the metamodel, 2500 simulations of the cylindrical cup forming process were performed. Uncertainty values for these samples were generated using the Sobol sequence [22] to ensure uniform coverage of the uncertainty space, as shown in Fig. 3. This figure shows pairwise scatter plots of the six uncertainty variables, along with corresponding histograms, providing a comprehensive visualisation of the distribution of the input parameters across the dataset.

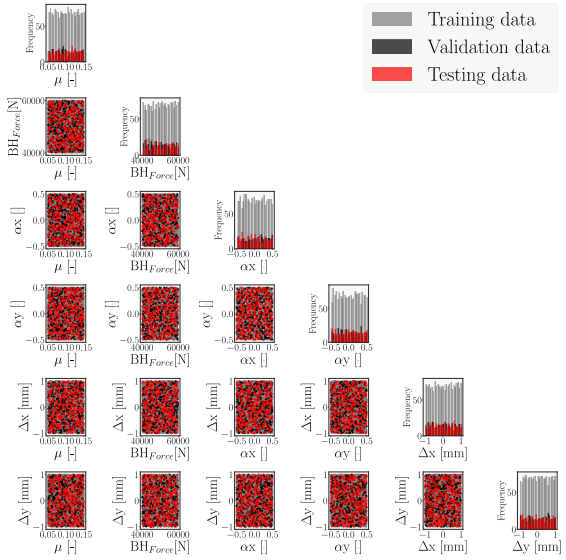


Fig. 3. Pairwise scatter plots and histograms illustrating the spatial distribution of the training (gray), validation (black), and testing (red) datasets, generated with the Sobol's sequence [22].

2.3 Machine Learning Modelling

In this study, a single metamodel was developed to predict all output variables simultaneously, based on a comprehensive database that integrates key results from the cylindrical cup forming process. As shown in Fig. 4, the inputs to the metamodel consist of three main types of data: (i) the punch force evolution, represented by 50 values uniformly distributed along the punch displacement; (ii) the cup height profile, evaluated at the top of the cup at different angles relative to the rolling direction (θ), as shown in Fig. 5, with 48 uniformly distributed values; and (iii) the cup thickness (t), measured around the cup for five specific cup heights (h = 10 mm, 15 mm, 20 mm, 25 mm and 30 mm), with 48 values for each height uniformly distributed along the circumference.

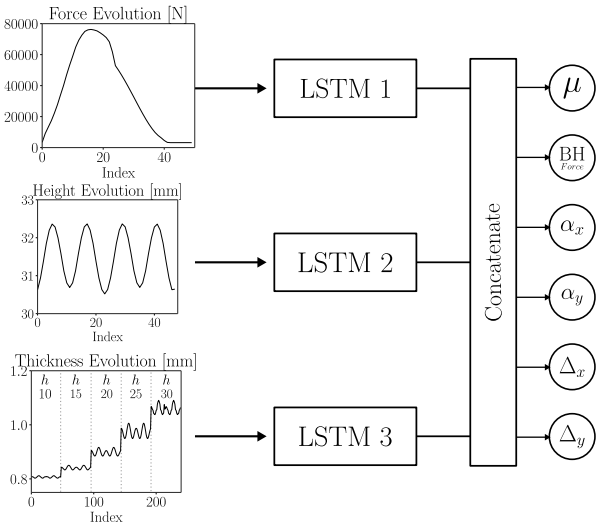


Fig. 4. Schematic representation of the input and output data used to train the metamodel.

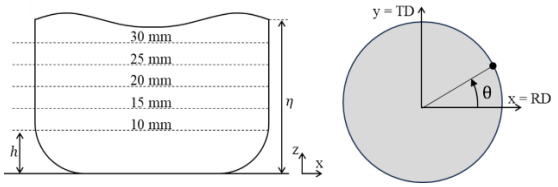


Fig. 5. Representation of the measurement locations for the height profile and thickness [3].

An architecture based on Long Short-Term Memory (LSTM) neural networks was used to model the relationships between the input data and the output variables. LSTMs are a type of recurrent neural network (RNN) specifically designed to handle sequential data, making them well suited to capturing temporal dependencies and long-range correlations within time series or spatially distributed data [23]. The input sequences were processed separately through dedicated LSTM layers, allowing the network to extract relevant features from each sequence. The outputs from these LSTM layers were then concatenated, allowing the model to integrate and capture the combined effects of different measurements involved in the cylindrical cup forming process.

For the training process of the LSTM metamodel, the dataset was divided into three subsets: training, validation and testing datasets. Specifically, 70% of the data was allocated to training, corresponding to 1750 cases, while the remaining 30% was divided equally between validation and testing, with 15% each, resulting in 375 cases for validation and 375 cases for testing. The training dataset is used to optimise the model parameters by minimising the Mean Square Error (MSE) of the

prediction. The validation dataset helps to fine-tune hyperparameters and prevent overfitting by assessing generalisation during training. The test dataset provides an unbiased evaluation of model performance after training. The uniform distribution of data across these datasets is visually confirmed in Fig. 3. These plots illustrate the consistency and diversity of the data in each subset, ensuring effective representation of the full range of input conditions and output responses. Throughout this article the datasets are colour coded as follows: grey for training data, black for validation data and red for test data. This colour scheme will be used consistently in all relevant figures and analyses.

A preliminary hyperparameter search was performed to identify the optimal configuration for training the LSTM metamodel. Several combinations of hyperparameters were evaluated to improve model performance, considering the number of units in each LSTM layer and the batch size as the main hyperparameters. For all trials, the Adam optimiser was used with a fixed learning rate of 0.001. In order to avoid overfitting and reduce unnecessary computational costs, early stopping was implemented with a *patience* of 10000 epochs, allowing the training process to stop if no significant improvement in validation performance was observed within this window. The best performance was achieved with 15 units I n each LSTM layer and a batch size of 128.

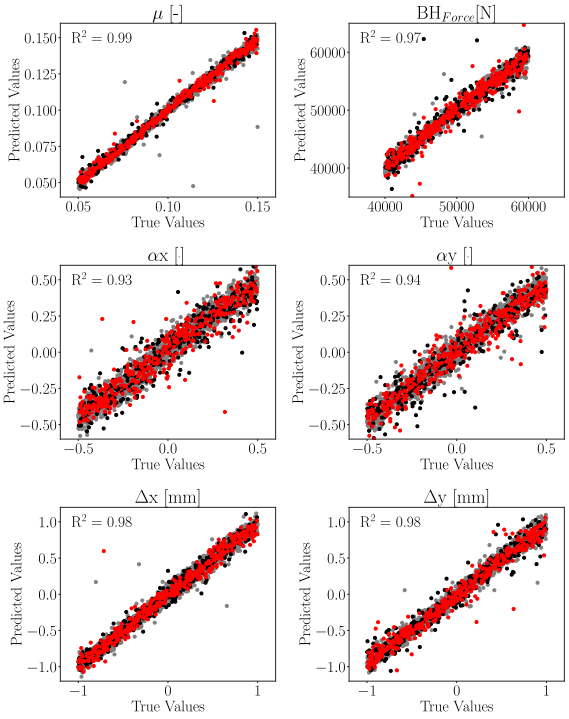


Fig. 6 – Predicted and true values of the uncertainty sources - μ, BH_{Force}, α_x, α_y, Δ_x, and Δ_y - across the training (grey), validation (black), and test (red) datasets.

3 Results and discussion

This section presents the results for the optimal meta-model. Fig. 6 shows the comparison between the predicted and expected values for the six output variables across the three datasets (training, validation and test). As can be seen, the coefficients of determination (R-squared values) for all variables are greater than 0.9, indicating strong model performance. In particular, the coefficient of friction (μ) is the best performing variable, followed by blank holder force (BH_{Force}) and blank misalignments (Δ_x and Δ_y).

In contrast, the angular misalignments (α_x and α_y) show a greater dispersion in the results and a higher presence of outliers, indicating a lower prediction accuracy for these variables. It is noteworthy that this behaviour is consistent across all three datasets, thus reinforcing the model's ability to generalise effectively.

Fig. 7 and 8 provide a comprehensive overview of the prediction performance of the model by illustrating the distribution of absolute and relative errors for the six sources of uncertainty.

Fig. 7 shows histograms of the absolute errors across the training, validation and test datasets. In general, the absolute errors for all variables follow a normal distribution with an average error close to zero, and extreme error values occur only in a small number of cases.

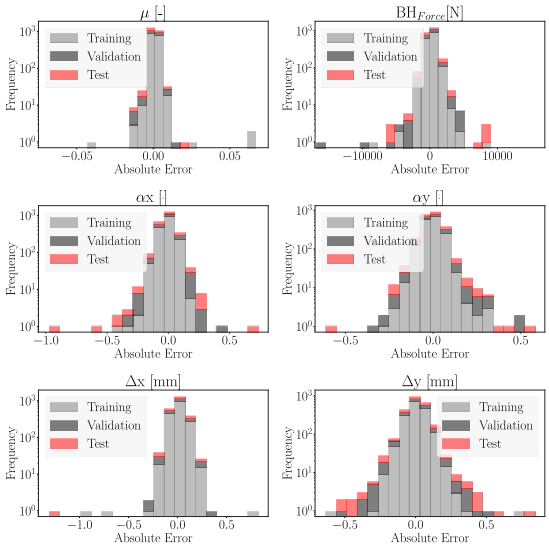


Fig. 7 – Histograms of the absolute error distributions for the six output variables - μ, BH_{Force}, α_x, α_y, Δ_x, and Δ_y - across the training (grey), validation (black), and test (red) datasets

Fig. 8 complements this analysis by showing the relative error distributions for the same variables through box plots. In this case, the relative error has been calculated by normalizing the error with respect to the range of each variable, allowing a consistent comparison across variables with different scales, as follows:

$$Relative\ Error\ (\%) = \frac{\hat{y} - y}{y_{max} - y_{min}}, \qquad (3)$$

where $\hat{y}$ is the predicted value and y represents the true value. The range is defined as the difference between the maximum and minimum values of the corresponding variable.

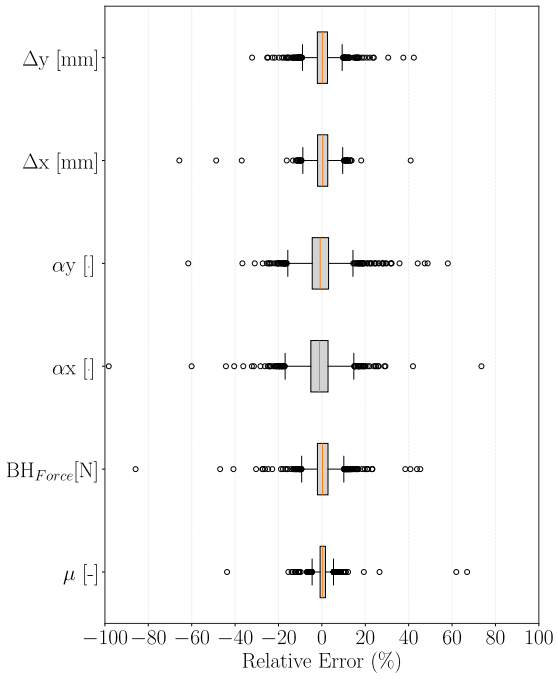


Fig. 8 – Boxplots of the relative error distributions (in %) - μ, BH_{Force}, α_x, α_y, Δ_x, and Δ_y for the test dataset.

As can be seen, the central tendency of the relative errors for μ, BH_{Force}, Δ_x, and Δ_y remain close to zero, with narrow interquartile ranges and a low number of outliers, reinforcing the high accuracy observed in Fig. 6. In particular, the interquartile range (IQR) for these variables is approximately 5%, indicating that 50% of the relative errors are within this narrow range around the median. Conversely, for the angular misalignments (α_x, α_y), the IQR is higher, around 10%, indicating a wider spread of errors and increased variability in the model predictions.

The minimum and maximum values are also higher for these two variables; however, they remain below 20%. Despite the lower prediction performance for the punch angular misalignment, it is still possible to reliably identify the sources of uncertainty that cause deviations in the forming results, even if the uncertainty values themselves cannot always be predicted with high accuracy.

All variables exhibit some outliers, in some cases with relatively high errors. Specifically, the variable μ has 106 outliers, BH_{Force}, has 115, α_x, α_y, have 72 and 78, respectively, while Δ_x, and Δ_y have 38 and 90 outliers, respectively. However, these outliers represent no more than 5% of the total cases for each variable, indicating that the vast majority of predictions remain within an acceptable error range.

4 Conclusions

This work proposes a methodology to identify the sources of uncertainty responsible for deviations in cylindrical cup forming results. The methodology uses machine learning to develop metamodels that establish a relationship between the cylindrical cup forming results (cup thickness, cup profile, and punch force evolution) and six uncertainty sources: the friction coefficient (μ); the blank holder force (BH_{Force},), the angular misalignment of the punch around the x-axis (α_x,) and y-axis (α_y) and the linear misalignment of the blank along the x-axis (Δx) and y-axis (Δy).

Due to the sequential nature of the cup forming results, recurrent neural networks (RNNs), specifically Long Short-Term Memory (LSTM) networks, were used to develop the metamodel. The LSTM-based metamodel was designed to predict all sources of uncertainty in a multi-output framework, using a database consisting of numerical results from cylindrical cup simulations along with the corresponding values of the six sources of uncertainty.

The results indicate that the trained metamodel accurately predicts the uncertainty source values for the coefficient of friction, blank holder force and blank misalignment. Although relatively higher relative errors were observed in the prediction of punch angular misalignment, approximately 95% of the cases have relative errors below 20%, demonstrating the overall reliability of the model in capturing the majority of uncertainty variations with reasonable accuracy.

Some outliers with excessively high relative errors were identified, highlighting areas where the performance of the model can be further improved. Addressing these outliers and improving the model's ability to generalise is likely to require the use of a larger and more diverse dataset, particularly for those cases that currently result in significant prediction errors.

In addition, experimental validation of the proposed methodology is planned to assess the performance on real experimental data from cylindrical cup forming. This validation will include controlled test conditions where uncertainties such as blank misalignment are deliberately introduced to assess the ability of the model to accurately identify and predict these deviations.

Acknowledgements

This work was sponsored by FEDER funds through the program COMPETE (Programa Operacional Factores de Competitividade), by national funds through FCT (Fundação para a Ciência e a Tecnologia) under the projects UIDB/00285/2020, UIDB/00481/2020, UIDP/00481/2020, CENTRO-01- 0145-FEDER-022083, LA/P/0104/2020 and LA/P/0112/2020. It was also supported by the projects RealForm (ref. 2022.02370.PTDC) and SmartBending (ref. 2023.14606.PEX), funded by Portuguese Foundation for Science and Technology. The authors Tomás Parreira, Daniel Cruz and Armando Marques were supported by doctoral grants from FCT (2024.00961.BD,2020.08449.BD and 2022.12657.BD). All the supports are gratefully acknowledged.

References

1. V. L. Hattalli, S. R. Srivatsa, *Materials Today: Proceedings* **5**, 2564-2574 (2018).

2. A. F. G. Pereira, P. A. Prates, M. C. Oliveira, J. V. Fernandes, *Int. J. Mech. Sci.* (2019), doi:10.1016/j.ijmecsci.2019.105169
3. A. F. G. Pereira, A. E. Marques, M. C. Oliveira, P. A. Prates, *Proceedings of the 2023 Esaform Conference*, doi:10.21741/9781644902479-129
4. A. Col, *Proceedings of the 6th International Conference on Material Forming* (2003)
5. T. de Souza, B. F. Rolfe, *Int. J. Mech. Sci.* (2010), doi:10.1016/j.ijmecsci.2010.09.009..
6. Y. Q. Li, *Proceedings of the AIP Conference Proceedings* (2005).
7. W. Hancock, M. Zayko, M. Autio, D. Ponagajba, *Qual. Eng.* (1997), doi:10.1080/08982119708919114.
8. M. Arnst, J.-P. Ponthot, R. Boman, *Comptes Rendus Mécanique* (2018), doi:10.1016/j.crme.2018.06.007.
9. V. J. Shahi, A. Masoumi, P. Franciosa, D. Ceglarek, *Procedia CIRP* (2018), doi:10.1016/j.procir.2018.02.022.
10. M. Dwivedy, V. Kalluri, *Procedia Manuf.* (2019), doi:10.1016/j.promfg.2019.02.116.
11. P. A. Prates, A. S. Adaixo, M. C. Oliveira, J. V. Fernandes, *Int. J. Adv. Manuf. Technol.* (2018), doi:10.1007/s00170-018-1604-y.
12. C. Huang, B. Radi, A. Hami, *Int. J. Adv. Manuf. Technol.* (2016), doi:10.1007/s00170-016-8436-4.
13. K. D. Majeske, P. C. Hammett, *Int. J. Flex. Manuf. Syst.* (2003), doi:10.1023/A:1023993806025.
14. A. M. Habraken, T. A. Aksen, J. L. Alves, et al., *Int. J. Mater. Form.* (2022), doi:10.1007/s12289-022-01672-w.
15. T. Hama, M. Takamura, A. Makinouchi, C. Teodosiu, H. Takuda, *Mater. Trans.* (2008), doi:10.2320/matertrans.PMRA2007885.
16. A. F. G. Pereira, M. F. Ruivo, M. C. Oliveira, J. V. Fernandes, P. A. Prates, *ESAFORM 2021* (2021), doi:10.25518/esaform21.2158.
17. Y. Q. Li, Z. S. Cui, X. Y. Ruan, D. J. Zhang, *Int. J. Adv. Manuf. Technol.* (2006), doi:10.1007/s00170-005-0121-y.
18. J. M. Gutiérrez Regueras, A. M. Camacho López, *Comput. Mater. Sci.* (2014), doi:10.1016/j.commatsci.2014.04.024.
19. E. Bayraktar, S. Altintaş, *Proceedings of NUMISHEET '93* (1993).
20. R. Amaral, *Development of Accurate Numerical Methodologies Applied to the Stamping of Advanced High Strength Steels and Experimental Validation*, PhD Thesis, Univ. of Porto (2020).
21. L. F. Menezes, C. Teodosiu, *J. Mater. Process. Technol.* (2000), doi:10.1016/S0924-0136(99)00345-3.
22. M. Sobol', *USSR Comput. Math. Math. Phys.* **7** (4), 86–112 (1967).
23. D. J. Cruz, M. R. Barbosa, A. D. Santos, R. L. Amaral, J. C. de Sá, J. V. Fernandes, *Metals* **14** (1), 84 (2024).